Optical Properties of Snow and Sea-Ice – A Field and Modelling Study

Holly J. Reay B.Sc. (hons)

A thesis submitted for the degree of Doctor of Philosophy at Royal Holloway, University of London.

Department of Earth Sciences
Royal Holloway College
University of London

February 2013

This thesis was funded by Royal Holloway, University of London

"*The best scientist is open to experience and begins with romance – the idea that anything is possible"* (Ray Bradbury)

I hereby declare that the work contained in this thesis and the work presented in it is my own, unless otherwise specified within the text

……..

Abstract:

The work contained within this thesis is a field and laboratory study of snowpack and sea-ice optical and physical properties, and a computation modelling study of photochemical reaction rates within snowpack. The contribution of snow photochemistry to snow and atmospheric oxidative capacity is controlled in part by snow albedo and *e*-folding depths in snow. Albedo and *e*-folding depths (and thus snow photochemistry) are a function of black carbon mass ratio in snow. The work contained within this thesis demonstrates the complicated response of albedo, *e*-folding depth (wavelengths 300–600 nm) and depth-integrated production rates of NO_2 and OH radicals to increasing black carbon mass ratio in well-characterised snowpacks of the Barrow OASIS campaign, Alaska. All snowpacks were reworked layered windpacks and were found to have similar responses to changes in black carbon mass ratio. The radiative-transfer calculations demonstrate two light absorption regimes: ice-dominated and black carbon dominated. The ice-dominated and black carbon dominated behaviour of albedo, *e*-folding depth and depth-integrated production rates with increasing black carbon mass ratios are presented. For black carbon mass ratios greater than 20 ng g^{-1} (wavelength range of 300–600 nm), *e*-folding depth and depth-integrated production rate have an inverse power law relationship with black carbon mass ratio. Doubling the black carbon mass ratio decreases the *e*-folding depth to ~70% of the initial value and for solar zenith angles greater than 60°, doubling the black carbon mass ratio decreases depth-integrated production rates of NO_2 and OH to ~70% and ~65% of their original values respectively. Black carbon mass ratios in snowpack were also calculated for glacial transects in Svalbard and Antarctic using a filtering technique developed by Clarke and

Noone (1985). The optical properties of Antarctic sea-ice were studied through bi-directional reflectance factor measurements using a Gonio Radiometric Spectrometer System (GRASS).

Table of Contents

List of Figures:

Chapter 1:

Chapter 2:

Chapter 2a:

Chapter 2b:

Chapter 2c:

Chapter 3:

Chapter 4:

Chapter 5:

Appendix 2:

Appendix 4:

List of Tables:

Acknowledgements

I would like to acknowledge my supervisor, Dr Martin King and Royal Holloway, University of London (Thomas Holloway Scholarship) for allowing me the opportunity to undertake this PhD. I am also thankful to other members of 'team snow' (Dr James France, Amelia Marks and Dr Claire Lucas) for all the help and advice they have given me over the years. I would like to acknowledge all the organisations that allowed me the opportunity to undertake fieldwork in extreme polar locations – For Barrow, NERC, NSF and Ocean-Atmosphere-Sea-Ice-Snowpack for funding and organisation of the campaign, NERC FSF for equipment hire; For Svalbard, BSES Expeditions and in particular Odobenus fire for all the hard work they put into the filter measurements; For Antarctica, Royal Holloway for funding, PNRA for organisation and NERC FSF for equipment hire. Finally, I would like to thank everybody else who supported me throughout my PhD, in particular all the other postgraduate students in the Earth Science department and my family who were always there when I needed a therapeutic cup of tea!

Chapter 1

Introduction

1.1 Outline

Through a combination of field, modelling and laboratory measurements, this study measures the optical properties of snow and sea-ice, the concentration of black carbon within snowpack and the effect of increasing black carbon and HULIS concentrations on albedo, *e*-folding depth and photochemical reactions within snowpack.

Background details of snow formation, snow optical properties, black carbon and the principles of photochemistryare covered in the introduction. Short literature reviews are given when needed and more comprehensive reviews for individual topics are found within the relevant chapters.

1.2 Aims

The thesis can be split broadly in 3 categories: fieldwork, modelling and laboratory studies. The main focus of the thesis is to improve the understanding of how black carbon affects albedo, *e*-folding depth and photochemical reactions within the snowpack.

The fieldwork aims were to:

- Measure the albedo, *e*-folding depths and snow stratigraphy for coastal and non-coastal snowpacks in Barrow, Alaska.
- Measure the concentration of black carbon for glaciers in Svalbard and Antarctica, using filtration methods developed by Clarke and Noone (1985).
- Test the ability of the Gonio RAdiometric Spectrometry System (GRASS) to undertake hemispherical-conical reflectance factor measurements in the polar environment of Antarctica.

The modelling aims were to:

- Calculate in-snow photochemical production rates for the photolysis of NO_3^-, NO_2^- and H_2O_2 for Barrow, Alaska using a snow-atmosphere coupled radiative transfer model (TUV-snow, Lee-Taylor and Madronich, 2002).
- Investigate the effect of impurities (black carbon and HULIS) on *e*-folding depth, albedo and snow photochemistry for four characteristic snowpacks measured during the Barrow 2009 campaign.
- Investigate the effect of black carbon on albedo and *e*-folding depth using data taken from previous studies at Greenland, Alert, Cairngorms and the South Pole (Fisher *et al.* (2005); Grenfell and Maykut (1977); Grenfell and Warren (1994); King and Simpson (2001) and Lee-Taylor and Madronich (2002)).

The laboratory aims were to:

- Determine the absorption due to black carbon and the concentration of black carbon for filter samples collected on glaciers in Oscar II Land, Svalbard and Victoria Land, Antarctica.

1.3 Formation of snow

Ice is a key component in the carbon cycle and therefore it is important to have an understanding of the different formations of ice crystals, from cirrus ice particles in the atmosphere to snow and sea-ice on the Earth's surface (McNeill, 2012). Snowflakes are single ice crystals that form and grow from water vapour. The morphology of snow has been studied for centuries (e.g. Frank, 1982; Kepler, 1966; Kobayashi and Kuroda, 1987; Mason, 1992; Nakaya, 1954; Wang, 2002); Around 1611, Kepler investigated the origins of snow crystal symmetry and Descartes described the forms of natural snow crystals in 1637. The work by Kepler and Descartes stemmed research into the variety of snow crystal morphologies found in natural snowfalls (e.g. Bentley and Humphrey, 1931; Chickering, 1864; Kobayashi and Kuroda, 1987; Libbrecht, 2005; Nakaya, 1954; Scoresby, 1820).

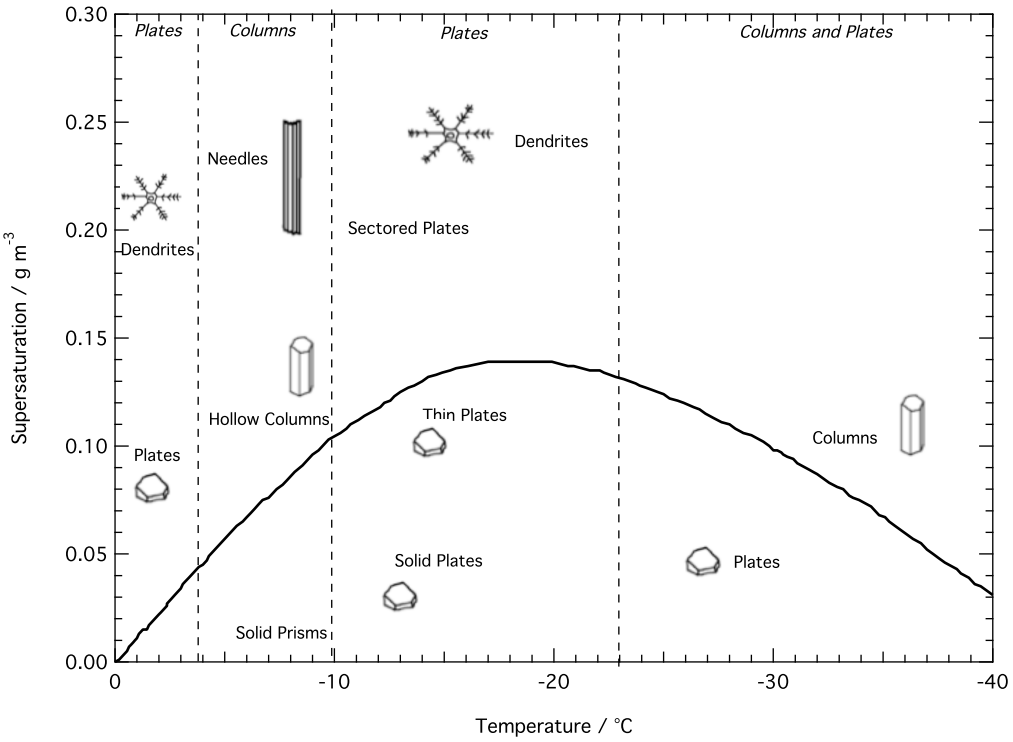

Figure 1.1. Diagram showing snow morphology with temperature and water saturation. Dotted black lines represent change in morpholoy, solid black line represents water saturation. (Adapted from Libbrecht (2005), Figure 2).

Figure 1.1 suggests a scheme for the morphological development of snowflakes indicating quantitatively the water saturation and temperature required to produce different morphological shapes. Crystal growth can be affected by air flow over the growing snowflake surface and laboratory studies undertaken in controlled conditions indicate that the morphology of individual snowflakes can vary greatly yet, for a representative sample of snowflakes, the snowflake morphology shown in Figure 1.1 holds true (Libbrecht, 2005).

Precipitation type is mainly determined by the vertical profile of the atmosphere. When temperaures at low levels of the atmosphere vertical profile are slightly above 0°C, snow is possible particularly if there is no freezing layer above the

lower level warmer layer (Bourgouin, 2000; Bluestine, 1993; Huffman and Norman, 1988). After snowfall, the snow on the ground is affected by solar radiation, windpumping and temperature variations that lead to water vapour and temperature fluxes within the snowpack causing a change to the size and shape of the snow crystals (Cabanes *et al.*, 2002; Domine and Shepson, 2002). Changes in the snow crystal size and shape are termed snow metamorphism and can affect the albedo, light penetration depth and response to impurities contained within snow for individual snowpacks.

Snow is comprised of a variety of phases e.g. air, ice and quasi-liquid water layers. McNeill *et al.* (2012) highlight that the state of the ice surface varies with temperature. A nanoscale region of surface on pure ice exists near the melting temperature, it is referred to as the quasi-liquid layer. The quasi-liquid layer is so thin that most molecules within the medium are affected by the nearest interface so the properties of the molecules in the quasi-liquid layer are different from the molecules in a liquid. Properties that could be affected are mobility, interactions with other molecules and reactivity. As temperature increases, the quasi-liquid layer increases in extent. In this thesis, snow is treated as a single phase of ice grains. It is unknown where the chemical reactions within snow occur; it could be within the air, or the ice, or the quasi-liquid layer. As there is no clear answer to where the chemical interactions within snow occur, the concept of multi-phase snow is too complicated for measurement processes used in this thesis and thus a single phase is used.

1.4 The response of snow to climate change

Over 30 % of the global land surface is covered in snow seasonally and sea-ice covers up to 7 % of the world's oceans (Dieckmann and Hellmer, 2005; Painter *et al.*, 1998; Robinson *et al.*, 1993). Understanding the controls on snow cover is important because climate sensitivity is often controlled by the cryospheric response to climate forcing (e.g. Flanner *et al.*, 2007; Jin and Simpson, 2001; Lemke *et al.*, 2007; Levis *et al.*, 2007; McNeill, 2012). Field and modelling studies have shown the influential role of snow on the global heat budget, particularly in areas with ephemeral snow cover (Barnett *et al.,* 1989; Berry, 1981; Gates *et al.*, 1992; Kukla *et al.*, 1986; Mitchell *et al.*, 1990; Robinson and Kukla, 1985; Walsh *et al.,* 1985).

1.4.1 Snow and sea-ice extent

Since the late 1960s, the extent of snow in the Northern Hemisphere has been monitored and the observations have indicated that the Arctic is the most sensitive area to climate change (Dewey and Heim, 1981; Iwasaki, 1991; Manabe *et al.,* 1992; Wang *et al.*, 2012). Recent observations have shown a decrease in the snow and sea-ice extent and thickness due to rapid warming, which can cause a variation of up to 50 % in the interannual planetary albedo (Browse *et al.,* 2012; Cavalieri *et al.,* 2003; Comiso, 2012; Curry *et al.,* 1996; Koch and Hansen, 2005; Kwok and Rothrock, 2009; Kwok and Untersteiner, 2011; Maslanik *et al.,* 2007; Parkison *et al.,* 1999; Qu and Hall, 2005; Rothrock *et al.,* 1999; Vinnikov *et al.,* 1999)

1.4.2 Albedo

The surface reflectance (surface albedo) of snow and sea-ice controls the proportion of solar radiation reflected or absorbed by the snow or sea-ice surface and thus is important for climate studies. Snow cover on sea-ice is a prominent feature, particularly in the Arctic Ocean (Jin and Simpson, 2001). Sea-ice can strongly influence local and global climate conditions by increasing surface albedo and insulating the relatively warm ocean from the atmosphere above thus modifying the air-sea energy exchange (Allison, 1982; Allison *et al.*, 1993; Curry, 1995; Ledley, 1991; Maykut, 1978; Walsh, 1993; Worby and Allison, 1991). Changes in snow and sea-ice cover control the variability of mid and high latitude albedo (e.g. Flanner *et al.*, 2007; Jin and Simpson, 2001; Lemke *et al.*, 2007; Levis *et al.*, 2007; McNeill, 2012; Qu and Hall, 2005). The albedo of snow and sea-ice is controlled by several factors including solar zenith angle, liquid water content, size of ice grains and impurities within the snowpack (e.g. Aoki and Tanaka, 2008; Aoki *et al.,* 1999; 2000; 2006; 2007; Flanner *et al.*, 2007; Grenfell and Warren, 1994; Motoyoshi *et al.*, 2005; Tanikawa *et al.*, 2006; 2009; Warren and Wiscombe, 1980; Wiscombe and Warren, 1980).

1.4.3. Light penetration depth

Light penetration depth (or *e*-folding depth) is the distance for the irradiance of diffuse light to decrease to $\frac{1}{e}$ (or ~37 %) of its initial value (King and Simpson, 2001). Only a handful of studies (e.g. Beine *et al*., 2006; Fisher *et al.*, 2005; France *et al.,* 2007; 2011a; 2011b; 2012; Gerland *et al.*, 1999; King and Simpson, 2001) have measured light penetration depth within snow, yet it is important for snow photochemistry, therefore the light penetration work undertaken in this

thesis will further the understanding of the behaviour of light in snowpack that contain impurities.

1.5 Photochemistry of snow

Photochemical dissociation is the breakdown of a molecule to its simpler components using the energy from photon excitation to break chemical bonds. There are two laws in photochemistry: (1) For a photochemical reaction to occur light must be absorbed by a reactant (the Grotthuss-Draper law), and (2) for each photon of light absorbed, only one molecule of reactant is given the activation energy needed for the reaction (the Stark-Einstein law) (Moser, n.d.).

The presence of chemicals within snow has been recognised for some time, however, recent evidence has shown that sunlit snowpack and ice play an important role in processing atmospheric species and the release of these photochemically generated species may significantly impact the chemistry of the overlying atmosphere (e.g. Beine *et al.,* 2002b; Fuhrer *et al.*, 1996; Grannas *et al.*, 2007; Honrath *et al.,* 1999; Jacobi *et al.*, 2004; Low *et al.*, 1990; Mulvaney *et al.*, 1998; Neftel *et al.*, 1985; Sumner and Shepson, 1999; Thomas *et al.*, 2012). The influence of snow photochemistry on the concentration of chemicals within the atmosphere has important implications for regional tropospheric chemistry and can lead to loss of snow and sea-ice through warming effects (Hansen *et al.,* 2005; Jones *et al.*, 2000). In snowpack, major elements and some compounds show little post-depositional change to the chemistry of the top 1 m of snow, however, post-depositional photochemistry can alter chemical concentrations, such as nitrate and hydroxyl radicals, within snowpack and therefore needs to be

considered when interpreting ice cores as a proxy for past atmospheric chemical concentrations (Blunier *et al.,* 2005; Domine and Shepson, 2002; Freyer *et al.,* 1996; Grannas *et al.*, 2004; Wolff, 1995; 1998).

For this thesis, the presence of nitrate (NO_3^-), nitrite (NO_2^-) and hydrogen peroxide (H_2O_2) within snowpacks is of interest as the species can react photochemically to produce product(s) that have been observed as fluxes above the snowpack surface (R1.1–1.3)(Beine *et al.*, 2001; 2002; 2003; 2008; Dibb *et al.*, 2004; Grannas *et al.*, 2007; Honrath *et al.*, 1999; 2000a; 2002; Jones *et al.*, 2000; 2001; Wang *et al.*, 2008).

$$\begin{aligned} NO_3^- + h\nu &\rightarrow NO_2 + O^- \\ O^- + H_2O &\rightarrow OH + OH^- \end{aligned} \qquad \text{(R1.1)}$$

$$H_2O_2 + h\nu \rightarrow 2OH \qquad \text{(R1.2)}$$

$$\begin{aligned} NO_2^- + h\nu &\rightarrow NO + O^- \\ O^- + H_2O &\rightarrow OH + OH^- \end{aligned} \qquad \text{(R1.3)}$$

Several field and laboratory studies have highlighted photochemical reactions involving nitrate within snowpack as a source of NO_x fluxes between the snowpack and the atmosphere, as shown in Figure 1.2 (Beine *et al.,* 2002a; 2002b; 2003; 2006; Boxe and Saiz-Lopez, 2008; Chu and Anastasio, 2003; 2005; 2007; Davis *et al.,* 2001; 2004; Dibb *et al.*, 2004; Dubowski *et al.*, 2002; 2001, Dubowski and Hoffmann, 2000; Fisher *et al.*, 2005; Grannas *et al.*, 2007; Honrath *et al.*, 1999; 2000a; 2000b; 2002; Jacobi and Hilker, 2007; Zhou *et al.*, 2001).

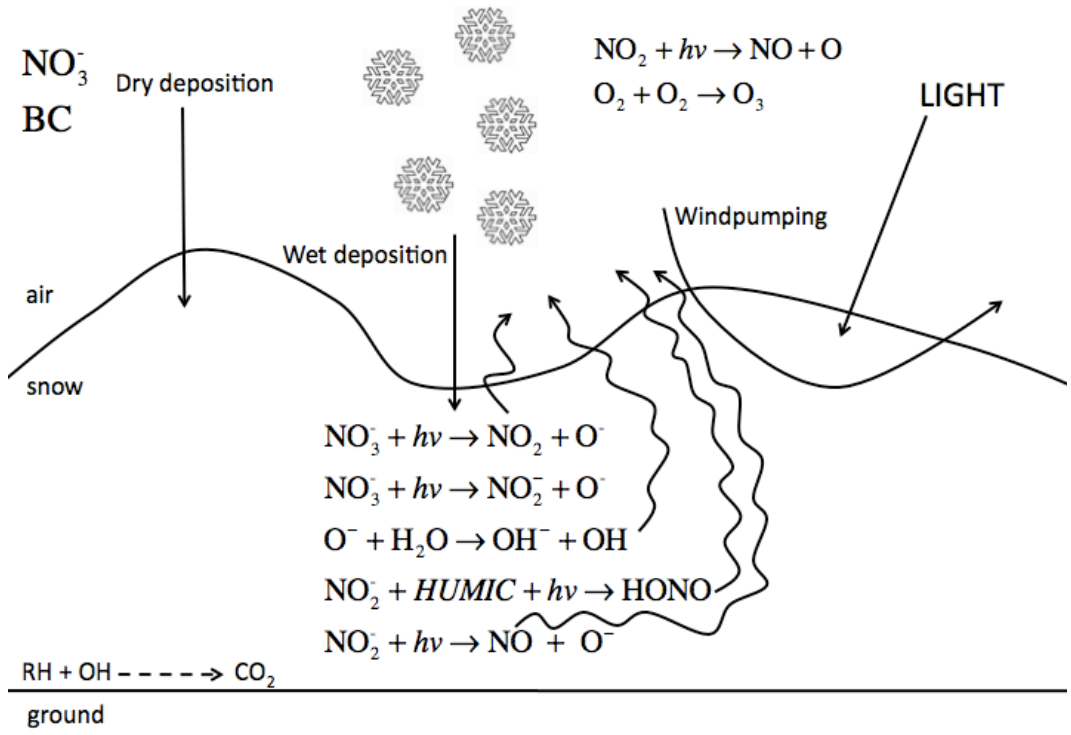

Figure 1.2. A schematic diagram showing the link between photochemical reactions within snowpack and chemical concentrations in the overlying atmosphere.

Measured concentrations of nitrate within polar snowpack range between 0.5–0.8 µmol dm^{-3} (Simpson *et al.*, 2002; Weller *et al.,* 2004). After deposition, the concentration of nitrate ions within snow can significantly change due to re-mobilisation of the ions to surface layers of snow crystals and the release of nitrate ions from top layers of snow (Beine *et al.,* 2002a; Rothlisberger *et al.*, 2002). As nitrate ions in ice-cores (used as a proxy for palaeoclimate conditions) are easy to measure, it is important to understand and quantify the post-deposition processes that affect the nitrate ions within the snowpack to calculate a meaningful record of palaeo-ozone levels (Grannas *et al.*, 2007; Hastings *et al.*, 2004; McCabe *et al.*, 2007). Sources of nitrate are from atmospheric deposition, generally in the form of fogs, precipitation and dry deposition (Bergin *et al.,* 1995). Ozone and particulate matter are formed using NO_x therefore the

atmospheric cycle of nitrogen, which influences the chemical composition of the lower atmosphere and the deposition pattern of nutrients at the Earth's surface, is important for regional air quality and radiative balance (Brown, 2006; Crutzen, 1970; Morin, 2008; Shindell, 2007).

Hydrogen peroxide concentrations in snow, measured in both the Arctic and the Antarctic, range between 1–18 μmol dm^{-3} (Hutterli *et al.,* 2001; Jacobi *et al.,* 2004; Kamiyana *et al.*, 1996; Puxbaum and Tscherwenka, 1998). The photochemical breakdown of hydrogen peroxide is likely to be the dominant source of OH radicals in snowpack as the small concentration of nitrite measured in snowpack, 0.01–0.02 μmol dm^{-3} (France *et al.*, 2007; King *et al.*, 2005), and a lack of nitrite measurements in comparison to hydrogen peroxide means that the role of nitrite ions in producing OH radicals is unclear (Chu and Anastasio, 2007). Hydrogen peroxide has previously been used as a palaeoclimate indicator and thus it is important to consider the role of photochemistry for ice cores as well as OH radical production (Jackson, 1999). It is imperative to understand the production process of OH radicals as the radicals have been implicated in the production of volatile compounds that, when emitted from snowpacks, can lead to changes in the chemistry of the overlying atmosphere boundary layer and destroy low level ozone (Dibb and Arsenault, 2002; Domine and Shepson, 2002; Grannas *et al.*, 2002; Houdier *et al.*, 2002; Impey *et al.*, 1999). Hydroxyl radicals can also oxidise organic carbon compounds and it has been suggested that trace organic compounds within ice cores may be used as palaeoclimate markers for palaeoatmospheric reconstruction (Grannas *et al.*, 2006).

1.6 The role of impurities within snowpack

A quarter of the global domestic product and a sixth of the world's population depend on snow melt for water resources (Barnett *et al.*, 2005). Light-absorbing impurities within snowpack may have a significant impact on polar climates by altering the seasonal cycle, temperature profile, cloud amount and temperature, contributing to the surface energy budget, influencing the polar radiative balance and dominating the absorption of solar radiation thus leading to accelerated snow and ice melt (Doherty *et al.*, 2010; Hegg *et al.*, 2009; Jacobson, 2001; Koch and Hansen, 2005). The work presented in this thesis investigates how impurities within snow can affect the behaviour of light (albedo and *e*-folding depth) and also the photochemical reactions within the snowpack.

1.6.1 Types of impurity

Many different impurities, i.e. dust, volcanic ash, HULIS (HUmic LIke Substances) and black carbon, can be found within snowpacks. Trace amounts of impurities within snowpack can affect the optical properties of the snow (Flanner *et al.*, 2007; France *et al.*, 2012; Reay *et al.*, 2012; Warren and Wiscombe, 1980). Black carbon, continental dust and volcanic ash are most likely to have widespread effects on snow albedo due long-range atmospheric transportation methods (Doherty *et al.*, 2010; Koch and Hansen, 2005; Stohl, 2006; Shindell *et al.*, 2008; Warren, 1984). However, black carbon is 50 times more efficient than dust and 200 times more efficient than volcanic ash at reducing albedo (Warren, 1984) thus, as it is the most efficient absorber per unit mass of carbon compared to other aerosol carbonaceous constituents (Hoffer *et al.*, 2006), this thesis concentrates on black carbon impurities within snow.

1.6.2 Black carbon

1.6.2.1 Sources of black carbon

Black carbon is produced from incomplete combustion of carbonaeous material by sources such as diesel engines, coal burning, residential wood burning, agricultural and forest fires (Bond and Bergstrom, 2006; Bond *et al.*, 2004; Hansen and Nazarenko, 2004; Menon *et al.*, 2009). Ice cores and glaciers contain a historical record of the atmospheric deposition of aerosols from natural and anthropogenic sources (McConnell *et al.*, 2007; Warren and Clarke, 1990; Warren and Wiscombe, 1980; Warren *et al.,* 2006). Black carbon concentrations have varied significantly in the past 215 years and observations indicate a seasonal cycle of Arctic pollution, with maximum long-range aerosol transport in winter/early spring and a maximum influence from regional sources in summer (Eleftheriadis *et al.*, 2009; Law and Stohl, 2007; McConnell *et al.*, 2007; Quinn *et al.*, 2007; Sharma *et al.*, 2006). McConnell *et al.* (2007) used ice cores from Greenland to study the black carbon variation in the Arctic over the last 215 years: Before industrilisation in the mid-1800s, the average annual concentration of black carbon was 1.7 ng g^{-1} with high seasonal variability. Annual black carbon concentrations rose after 1850, peaking at more than 20 ng g^{-1} in the early 1900s, then declined until the 1950s. From 1950 until the present day, the average annual black carbon concentration is characterised by high variability in summer and a gradual decline in winter black carbon concentrations, with a resulting average annual black carbon concentration of 2.3 ng g^{-1} (McConnell *et al.*, 2007). Present day Arctic black carbon concentration ranges from 0.2–60 ng g^{-1} with extreme values of 250 ng g^{-1} (Doherty *et al.*, 2010)

There have been several studies into the source regions and pathways for pollution in the Arctic (e.g. Browse *et al.* (2012); Polissar *et al.*, 1999, Sharma *et al.*, 2004; 2006; Xi *et al.*, 1999). A schematic diagram summarising the major transport pathways and removal processes that affect the seasonal cycle of Arctic aerosol concentrations can be seen in Figure 1.3.

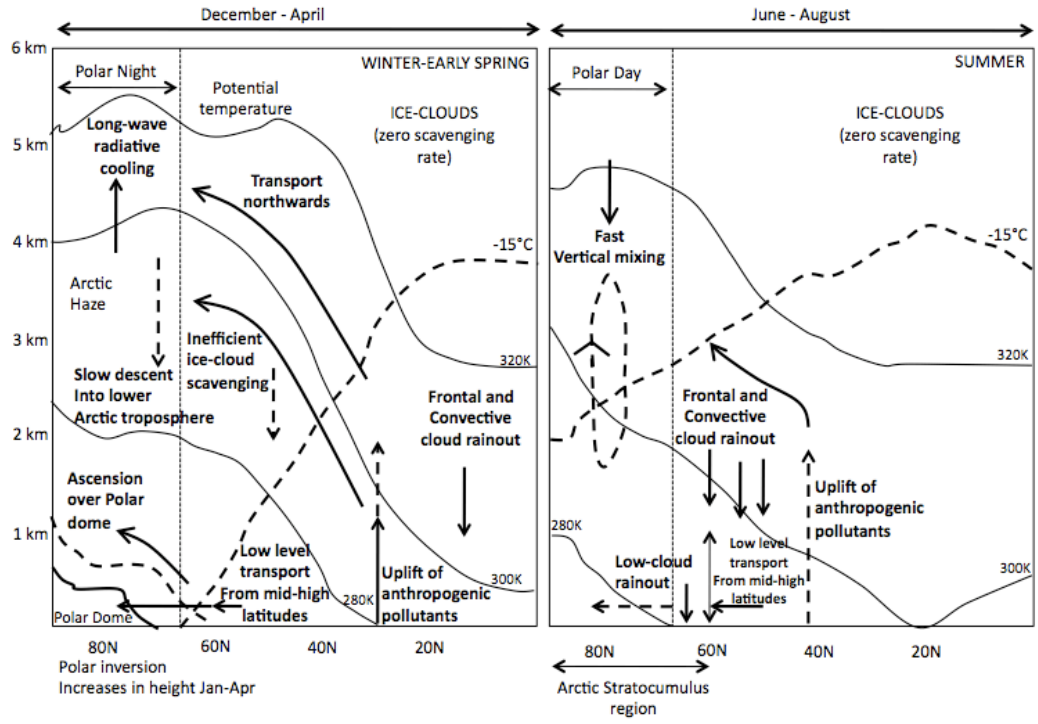

Figure 1.3. A schematic diagram showing the major transport pathways and removal processes that affect the seasonal cycle of Arctic aerosol concentrations in Winter-Early Spring (left) and Summer (right). (Adapted from Browse *et al.*, 2012, Figure 11).

The dominant source of black carbon in polar regions is anthropogenic, fossil fuels alone can produce over 8×10^9 kilograms of black carbon annually, but biomass burning is also an important aerosol source, contributing a maximum total of 6×10^9 kilograms of black carbon per year to the atmosphere (Cooke and Wilson, 1996; Gray, 1976; Hegg *et al.*, 2009; Koch and Hansen, 2005; Maenhaut

et al., 1989; Stohl *et al.*, 2006; Sturges and Barrie, 1989; Warren, 1984). As the source of black carbon is primarily anthropogenic combustion, including fossil fuel and biomass burning, human population restricts the geographical location of the sources (Highwood and Kinnersley, 2006). Figure 1.4 shows the distribution in global emissions of black carbon from fossil fuels and biomass burning. The proximity of pollution sources to the Arctic in comparison to the Antarctic makes the area more sensitive to changes in black carbon concentration.

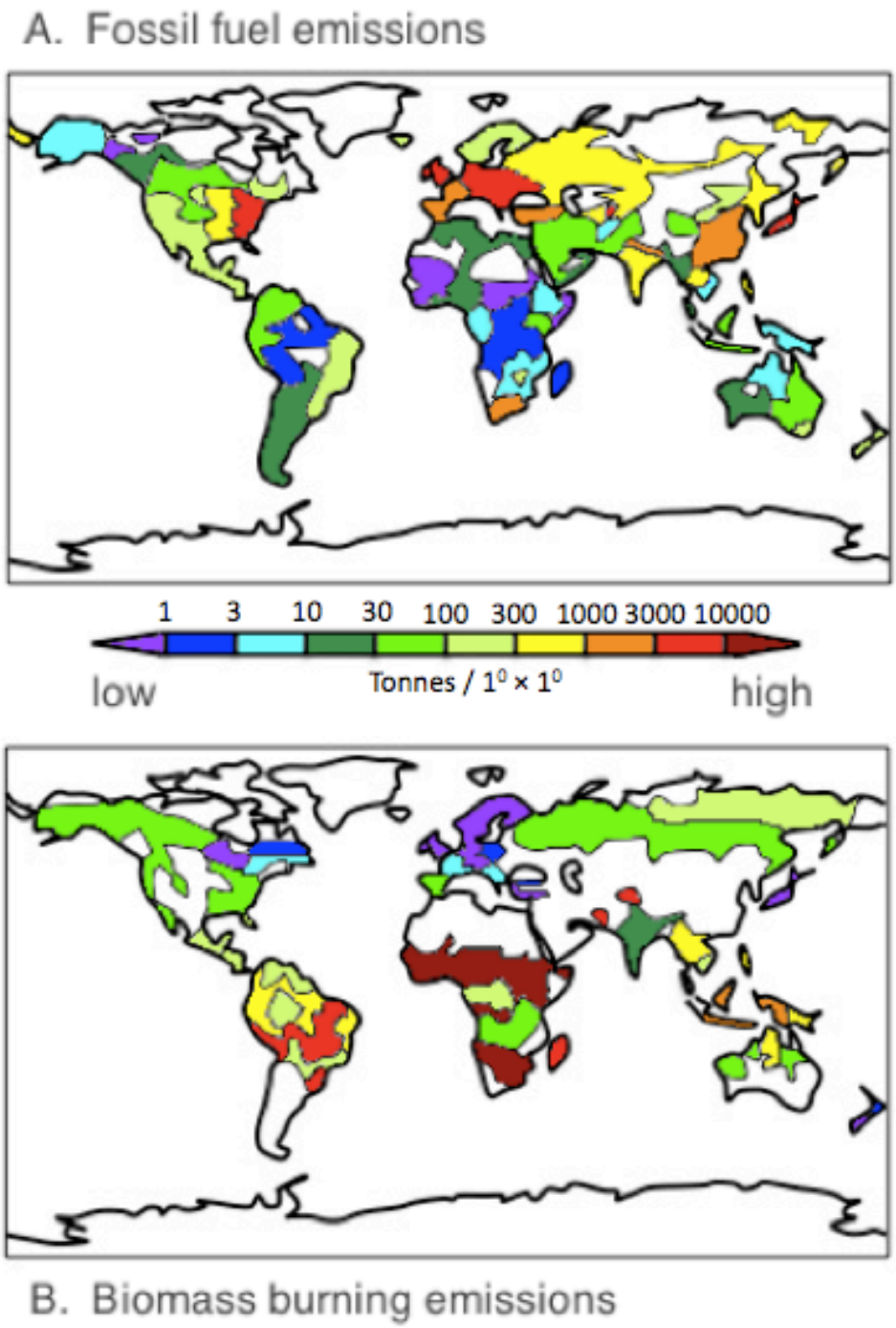

Figure 1.4. Global emissions of black carbon from a) fossil fuels and b) biomass burning. Data taken from the Global Emissions Inventory Activity (1985). (Adapted from Highwood and Kinnersley (2006), Figure 2).

1.6.2.2 Black carbon and climate change

It has been proposed that there are four ways in which black carbon affects climate: the direct effect, indirect effect, semi-direct effect and indirect surface albedo effect (Highwood and Kinnersley, 2006). When black carbon scatters or absorbs solar radiation it is termed the direct effect. An increase in atmospheric black carbon can decrease planetary albedo causing a 5% reduction in the amount of solar radiation that reaches the ground thus leading to changes in surface heat and moisture fluxes and the dynamics of the atmospheric boundary layer (Krishnan and Ramanathan, 2002; Liu *et al.*, 2002; Ramanathan *et al.*, 2001). Black carbon can be nucleated or scavenged within other aerosols thus altering the microphysics of clouds by causing changes in droplet size, the effect is termed the indirect effect (Baumgardener *et al.*, 2008; Conant *et al.,* 2002; Kireeva *et al.*, 2009; Nenes *et al.*, 2002). The semi-direct effect describes how atmospheric heating by black carbon can alter humidity profiles thus affecting how clouds form (Hansen *et al.*, 1997; Koch and Del Genio, 2010). Modelling and measurements undertaken over the Indian Ocean and South America suggest that the atmospheric heating rate can be increased by as much as 1–3 K per day when a layer of black carbon is introduced into the atmosphere (Ackerman *et al*, 2000; Johnson *et al.*, 2004; Koren *et al*., 2004). The final effect, the indirect surface albedo effect, occurs when black carbon is deposited onto snow and ice surfaces. The indirect surface albedo effect can cause changes to snow and ice melting patterns and induce planetary warming, it is the effect that is of interest to this thesis.

1.6.2.3 Black carbon in snow

The International Panel for Climate Change (IPCC) estimates that global climate forcing by black carbon aerosols is around 0.2 Wm^{-2} (Ramaswamy *et al.*, 2007). Hansen *et al.* (2005) calculated that black carbon in snow had 1.8 times the 'climatic warming effect' of anthropogenic CO_2 for a specified radiative forcing. However, Flanner *et al* (2007) considered several additions (described in detail in Chapter 4) and calculated that black carbon in snow may actually be 3.2 times more efficient at climatic warming than CO_2. It has been suggested that heating due to black carbon at the surface of the snowpack melts additional snow or sea-ice and the black carbon itself changes the reflectivity of the snow (Jacobson, 2004). Studies have shown that the albedo of snow can be reduced by ~1% with the addition of ~10 ng g^{-1} of black carbon in snow (Clarke and Noone, 1985; Flanner *et al.*, 2007; Grenfell *et al.*, 2002; Hansen and Nazarenko, 2004; Jaconson, 2004; Warren, 1982; Warren and Wiscombe, 1980; 1985). In West China, accelerated melting occurred due to a ~5% reduction in albedo caused in glaciers strongly contaminated by black carbon (Ming *et al.*, 2009).

Significant changes can be seen between the perceived concentration of black carbon in snowpack and the reduced reflectivity due to a number of factors, i.e. snow grain size, solar zenith angle, black carbon shape/size/morphology and whether black carbon is situated external or internal to the ice grain (Bohren, 1986). The absorbancy of black carbon is increased by 1.4 or more if the black carbon particles are intrinsic within the ice crystals rather than mixed externally because refraction focuses the light on the absorbers (Bohren, 1986; Chylek *et al.*, 1983; Dozier, 1989; Grenfell *et al.*, 1981). The shape of the black carbon particle

will also affects its absorptive power; randomly orientated discs or needles have an absorbance more than a factor of 2 greater than spherical shape particles (Bohren, 1986; Moosmüller *et al.*, 2009).

Laboratory studies undertaken by Hadley and Kirchstetter (2012) confirm that black carbon concentrations found in snow at natural settings (Aamaas *et al.*, 2011; Forsström *et al.*, 2012) noticeably reduced snow albedo. Increased snow grain size, seen naturally in the metamorphism of snow with age (Dirmhirn and Eaton, 1975) also decreased snow albedo and amplified the radiative effects of black carbon.

Several early studies have been conducted into the effect of black carbon in snow and the reduction of snow albedo (e.g. Aoki *et al.*, 2000; Chylek *et al.*, 1983; 1987; Clarke and Noone, 1985; Flanner *et al.*, 2007; Grenfell *et al.*, 2002; Hansen and Nazarenko, 2004; Jacobson, 2004; Warren and Wiscombe, 1980; 1985; Wiscombe and Warren, 1980) but there have been no previous studies into the effect of *e*-folding depth change with black carbon.

1.7 Thesis Overview

This thesis incorporates field, modelling and laboratory studies of snowpack photochemistry and the effect of black carbon concentrations within snow, along with the reflectance properties of sea-ice.

Chapter 2 focuses on a 2009 spring field campaign to Barrow, Alaska. Investigations of coastal and non-coastal snow albedo, light penetration and

stratigraphy are presented in Chapter 2a. The data from the study was modelled to derive optical co-efficients for each snowpack and produced depth-integrated photolytic production rates of NO_2 and OH radicals (Chapter 2b). Chapter 2c looks at the role of impurities (black carbon and HULIS) on snow albedo, light penetration depth and depth-integrated photochemical production rates. The consequences of black carbon in snow is further investigated in Chapter 3 by using the model to examine the effect of increasing black carbon concentration on the albedo and light penetration depth of four snowpacks; Greenland, Alert, Cairngorms and South Pole, previously studied by Fisher *et al.* (2005); Grenfell and Maykut (1977); Grenfell and Warren, (1994); King and Simpson (2001) and Lee-Taylor and Madronich (2002).

Chapter 4 moves away from the effect of black carbon on snow optical properties and photochemistry to consider the concentration of black carbon within snow. The field and laboratory study measured the concentration of black carbon in glacial snow at Svalbard and Antarctic using a filtration method developed by Clarke and Noone (1985).

Chapter 5 shows an assessment of a field study conducted at Tethys Bay, Antarctica that tested the ability of the Gonio Radiometric Spectrometer System to conduct reflectance measurements in polar environments. GRASS, originally built to measure reflectance in warm, desert environments, calculated the hemispherical-conical reflectance factor of the sea-ice at Tethys Bay, the results have been evaluated and improvements have been suggested to increase the quality of measurements for future polar field studies.

Chapter 2

Barrow, Alaska: OASIS Spring Campaign 2009

2.1 Overview

The town of Barrow, Alaska is situated on the Chukchi sea coast at 71°17'44"N, 156°45'59"W. Located 320 miles north of the Arctic Circle, Barrow experiences a cold, dry polar climate with seasonal snow settling from October to May each year. Owing to the topography surrounding the city, strong wind events are common and frequently cause blowing snow conditions which rework fallen snow into windpacks.

In Spring 2009, a large international campaign to Barrow was arranged by the organisation 'Ocean-Atmosphere-Sea-Ice-Snow' (OASIS) to instigate a collaborative project between scientists from atmospheric and snow research disciplines. The overall aim of the campaign was to investigate key science issues regarding air-surface chemical interactions and their evolution in future Arctic climates. Barrow was an ideal location for the collaborative project due to the proximity and accessibility of terrestrial and marine sampling sites plus the convenient transport links from Barrow to other parts of the United States of America. The campaign was based at the BARC (Barrow Arctic Research Centre) research facility and measurements were located within 0.3-15km of the site (Figure 2.1).

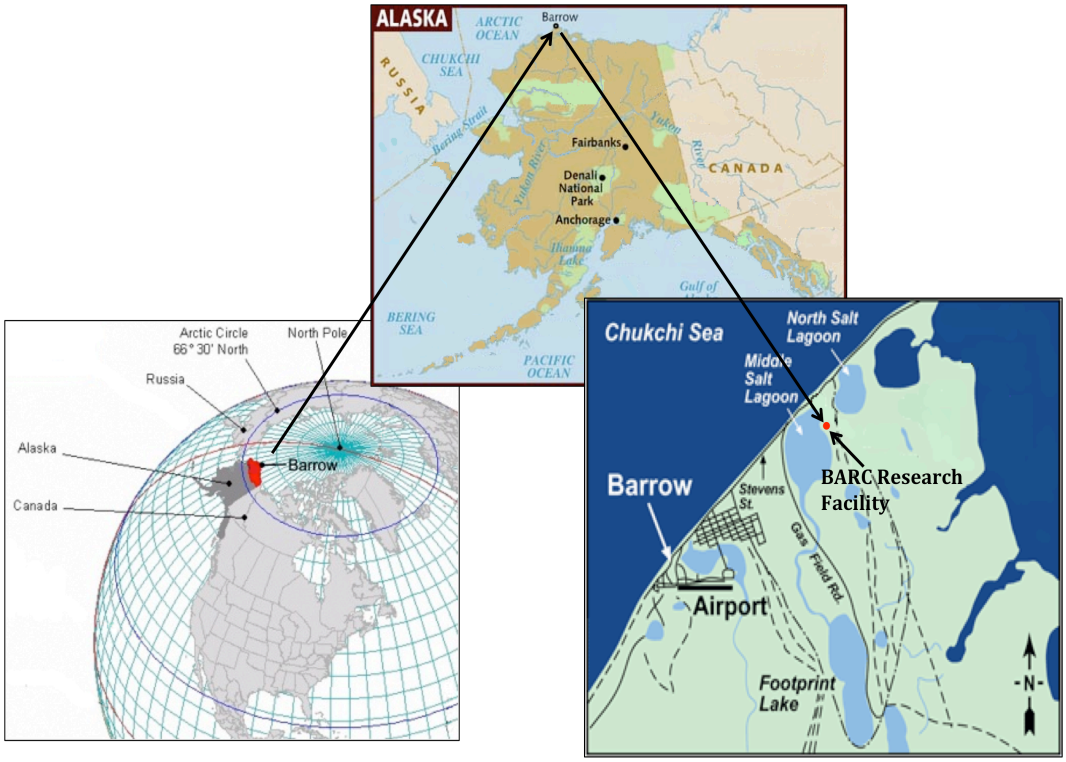

Figure 2.1. Relation of BARC research facility in terms of North America, Alaska and the city of Barrow. Adapted from www.lonelyplanet.com/maps/north-america/usa/alaska/ and www.eol.ucar.edu/projects/ceop/dm/insitu/sites/other/NSA/Barrow/

2.2 Experiments at Barrow

The following sections describe experiments undertaken by other research groups throughout the Barrow campaign:

2.2.1 Formaldehyde in the Alaskan Arctic snowpack: partitioning and physical processes involved in air-snow exchanges

The study investigated the physical processes involved in formaldehyde (HCHO) air-snow exchanges through atmospheric and snow measurements during the campaign. The project quantitatively explained HCHO concentration changes in a fresh diamond dust layer by the equilibration of a solid solution of HCHO in ice, through solid-state diffusion of HCHO within snow crystals. The investigation found that HCHO in snow equilibrates by solid state diffusion and photochemical production of HCHO takes place in the snowpack (Barret *et al.*, 2011).

2.2.2 Soluble chromophores in marine snow, seawater, sea-ice and frost flowers

The project measured light absorption in marine snow, sea-ice, seawater, brine and frost flower samples at multiple sites between land fast ice and open pack ice in coastal areas (~5 km west of Barrow). The investigation found that light absorption in frost flowers is 40 times larger than in terrestrial snow. Chromophoric dissolved organic matter was identified as a major source of OH in Barrow marine samples and H_2O_2, NO_3^- and NO_2^- contribruted <1% to light absorption in marine samples (Beine *et al.*, 2012).

2.2.3 Soluble, light-absorbing species in snow

Terrestrial melted snow samples were measured for light absorption, H_2O_2 and inorganic anion concentrations. The three key findings of this investigation were: snow choromophores are 50:50 HULIS and unknown with HOOH and NO_3^- making only minor contributions; there are four sources of chromophores in Barrow: vegetation, marine, diamond dust and atmospheric exchange; photo-bleaching of chromophores in snow is significant (Beine *et al.*, 2011).

2.2.4 Structure, specific surface area and thermal conductivity of the snowpack

Vertical profiles of density, specific surface area and thermal conductivity were measured on landfast ice, lakes and tundra to study the structure of the snowpack. The investigation found that snow properties are highly influenced by climate, particularly wind, and the properties of the snow at Barrow allow efficient storage of chemical species (Domine *et al.*, 2012).

2.2.5 The specific surface area and chemical composition of diamond dust

The specific surface area of diamond dust was measured along with the chemical composition including mineral and organic ions, dissolved organic carbon, aldehydes and hydrogen peroxide. The absorption spectra of water-soluble chromophores were also measured. The investigation found that ions, mercury, aldehydes, hydrogen peroxide and organic carbon and evidence of photochemistry were present in precipitated diamond dust (Domine *et al.*, 2011a).

2.2.6 Frost flowers growing in the Arctic: chemical composition and mercury exchange between the atmosphere, snow and frost flowers

The investigation had two aims: to determine the chemical composition of frost flowers and to measure the mercury exchange between the atmosphere, snow and frost flowers. The chemical composition was quantified by the major ion, stable oxygen and hydrogen isotope, alkalinity, light absorbance by soluble species, organochlorine and aldehyde composition of frost flowers, brine and sea-water. The investigation found that brine and frost flowers have interactions with the lower atmosphere, frost flowers have both a predictable and unpredictable chemical composition and changing sea-ice regimes is likely to mean more brine and frost flowers in the future (Douglas *et al.*, 2012). Stable isotopes of mercury were used to trace mercury cycling during atmospheric mercury depletion events (AMDEs). It was found that mercury re-emitted from snow during AMDEs was adsorbed by frost flowers and frost flowers helped to aid the local retention of mercury on sea-ice during AMDEs (Sherman *et al.*, 2012).

2.2.7 The vertical distribution of BrO and aerosol in the Arctic: Measurements by active and passive differential optical absorption spectroscopy

The study undertook simultaneous measurements of vertical profiles of aerosol extinction and BrO and found that BrO was released from aerosols and airborne ice particles as well as first-year sea-ice or frost flowers at low temperatures (Frieß *et al.*, 2011).

2.2.8 PTR-MS observations of photo-enhanced VOC release from Arctic and midlatitude snow

The study used proton transfer reaction-mass spectrometry (PTR-MS) was used to make real-time measurements of volatile organic species (VOC) from irradiated snow and found that similar VOCs were emitted from irradiated snow in vastly different locations (Barrow, Alaska; Alert, Nunavut; Egbert and Toronto, Ontario). The VOC emissions are potentially affected by snow composition (Gao, *et al.*, 2012).

2.2.9 Chemical composition of the snowpack during the OASIS spring campaign 2009 at Barrow, Alaska

The physical and chemical processes in the snow were investigated and used, along with the current chemical composition of Arctic snowpack, to determine the major processes influencing the chemistry of the snowpack. The snow samples collected were analysed for major sea salt components, bromide and nitrate (Jacobi *et al.*, 2012).

2.2.10 Observation of inorganic bromine (HOBr, BrO and Br_2) speciation

The investigation reported the first direct observations of hypobromous acid (HOBr) as well as measurements of bromine oxide (BrO) and molecular bromine (Br_2) by chemical ionization mass spectrometry. Direct evidence for the activation of bromine by high winds was found and it was proved that HOBr could be reproduced with a model including aerosol uptake (Liao *et al.*, 2012). A comparison was made between results of in situ BrO measured using a chemical ionisation mass spectrometer (CIMS) and the average concentration of BrO along light paths of either 7.2 or 2.1 km made using a long path-differential optical absorption spectrometer (LP-DOAS) (Liao *et al.*, 2011).

2.2.11 An isotopic view on the connection between photolytic emissions of NO_x from the Arctic snowpack and its oxidation by reactive halogens

The aim of the investigation was to provide a comprehensive (nitrogen and oxygen) isotopic composition of nitrate measured over one year at Barrow. The study found that NO_x emissions from the snowpack strongly interacted with reactive halogens and there was no significant correlation between the daily averaged ozone, BrO and $\Delta^{17}O$ (Morin *et al*., 2012).

2.2.12 Springtime boundary layer ozone depletion: Meteorological influence, year-to-year variation and long-term change.

A detailed picture was obtained from soundings for the vertical structure of the ozone depletion events observed in April 2009 and throughout the campaign (March-April 2009). The investigation found that changing sea-ice conditions were altering the ozone boundary layer chemistry and Spring boundary layer

ozone depletion events have increased in March in Barrow. Transport strongly influences the boundary layer ozone depletion at Barrow (Oltmans *et al.*, 2012).

2.2.13 The relative importance of chlorine and bromine radicals in the oxidation of atmospheric mercury

Previous to the Barrow campaign, the identities of halogen radicals that oxidize mercury in the Arctic were unknown. Through field measurements of GEM, RGM, ozone and a large suite of inorganic halogen and volatile organic compounds the investigation found that Br, BrO and Cl can be important and that measurements of temperature-dependent rate constants needed to be made, especially for Cl (Stephens *et al*., 2012).

2.2.14 Nitrous acid (HONO) during polar spring: a net source of OH radicals?

HONO was measured by a long path absorption photometer (LOPAP) for the duration of the campaign. Polar HONO concentrations measured at Barrow were much lower than values measured in other polar regions by previous studies using different methods. However, HONO is still a major source of OH radicals in the polar atmosphere. The photosensitized conversion of NO_2 from snow surfaces containing humic acid may be the more likely source of HONO in the polar atmosphere of Barrow than nitrate photolysis (Villena *et al.*, 2011).

2.2.15 Carbonaceous species and humic like substances (HULIS) in Arctic snowpack

Water insoluble organic carbon, dissolved organic carbon and elemental carbon were measured in various types of snow around the Barrow region. Snow type was used to determine the physical process that may influence the concentration of dissolved organic carbon measured. HULIS, short chain diacids and aldehydes were quantified and showed to represent <20 % of the total dissolved organic carbon concentration in snow. The optical properties of the HULIS were also measured (Voisin *et al.*, 2012).

2.3 Aim of Research

The overall aim of my research throughout the Barrow OASIS campaign was to calculate the in-snow production rates of NO, NO_2 and OH radicals and the absorption by impurities within the snowpack.

In-snow photochemistry has been implicated as a source of production for gaseous species such as NO_x and OH (hydroxyl) radicals in polar region (e.g. Beine *et al.*, 2001; 2002b; 2003; 2008; Dibb *et al*, 2004; Domine and Shepson, 2002; Grannas *et al.*, 2007; Honrath *et al.*, 1999; 2000a; 2002; Jones *et al.*, 2000; 2001; Wang *et al.*, 2008). The release of photochemical gases can impact the overlying atmospheric boundary layer chemistry (e.g. Dibb and Arsenault, 2002; Domine and Shepson, 2002; Grannas *et al.*, 2002; Houdier *et al.*, 2002; Impey *et al.*, 1999). The contribution of snow photochemistry to the atmosphere is controlled in part by the optical properties of the snowpack i.e. snow albedo and light penetration depths in snow. Photochemical reactions in snow can also reduce the amount of precursor material in the snow and ice thus causing false signal/proxies in ice cores leading to wrongly interpreted past environmental conditions. Reactions 2.1–2.3 show the mechanisms for the photolysis of nitrate, NO_3^-, in snowpack to produce a molecular flux of NO_2 from the snowpack to the atmosphere (Reaction 2.1) (Anastasio and Chu, 2009; Beine *et al*, 2006; Chu and Anastasio, 2007; Fisher *et al.*, 2005; France *et al.,* 2007; 2010; King and Simpson, 2001; Simpson *et al.*, 2002), and hydroxyl radical, OH, production through the photolysis of the nitrate anion (R2.1) (Anastasio *et al.,* 2007), hydrogen peroxide (Rb.2) and nitrite (Rb.3) (all naturally found in snowpacks).

$$\begin{aligned} NO_3^- + h\nu &\rightarrow NO_2 + O^- \\ O^- + H_2O &\rightarrow OH + OH^- \end{aligned} \qquad \text{(R2.1)}$$

$$H_2O_2 + h\nu \rightarrow 2OH \qquad \text{(R2.2)}$$

$$\begin{aligned} NO_2^- + h\nu &\rightarrow NO + O^- \\ O^- + H_2O &\rightarrow OH + OH^- \end{aligned} \qquad \text{(R2.3)}$$

To calculate the in-snow production rates and absorption by impurities for Barrow snowpack the spherical irradiance in snow is needed, a value that cannot be

measured and therefore needs to be modelled. To calculate the in-snow production rates and absorption by impurities using the TUV-snow radiative-transfer model (Lee-Taylor and Madronich, 2002) two optical measurements from Barrow were input into the model: albedo (snow reflectivity) and *e*-folding depth (light penetration depth). The methods for measuring albedo and *e*-folding depth, and calculating the in-snow production rates and absorption by impurities within snow are described in chapters 2a and 2b respectively.

Optical and physical properties measurements made in Barrow, Alaska were part of the larger OASIS international field campaign. The specific objectives of the work presented in chapter 2 were:

1. To determine the physical and visible optical properties of Barrow snowpack (350-700 nm) by measuring *e*-folding depth, surface nadir reflectance and snowpack stratigraphy.
2. Adapt a radiative-transfer model to include known photophysical data for natural organic matter and calculate wavelength dependent cross-sections from measurements of *e*-folding depth and snowpack surface reflectivity for scattering and light absorption due to impurities.
3. Calculate the in-snow production rates of NO, NO_2 and OH radicals for the duration of the OASIS campaign. The calculations can be used as an estimation of the potential flux of NO_2 or NO from the snowpack.
4. Determine the amount and type of light absorbing impurities in the Alaskan snowpack using the absorption cross-sections determined from field measurements of the snowpack.

Chapter 2a

Physical and Optical Properties of Snowpack in Barrow, Alaska: OASIS Spring Campaign 2009

Results from this chapter have been published in "Hydroxyl radical and NO_x production rates, black carbon concentrations and light-absorbing impurities from field measurements of light penetration and nadir reflectivity of on-shore and off-shore coastal Alaskan snow", J.L. France, H.J.Reay, M.D. King, D. Voisin, H.W. Jacobi, F. Domine, H. Beine, C. Anastasio, A. MacArthur and J. Lee-Taylor (2012), *Journal of Geophysical Research*, *117*(D00R12), doi:10.1029/2011JD016639 (see Appendix 1).

2a.1 Introduction

In polar regions, in-snow photochemistry has been implicated as a source of production for gaseous species such as NO_x gases and OH (hydroxyl) radicals (e.g. Beine *et al.*, 2001; 2002b; 2003; 2008; Dibb *et al*, 2004; Domine and Shepson, 2002; Grannas *et al.*, 2007; Honrath *et al.*, 1999; 2000a; 2002; Jones *et al.*, 2000; 2001; Wang *et al.*, 2008). The release of phototchemical gases can impact the overlying atmospheric boundary layer chemistry (e.g. Dibb and Arsenault, 2002; Domine and Shepson, 2002; Grannas *et al.*, 2002; Houdier *et al.*, 2002; Impey *et al.*, 1999). The main purpose of my work in Barrow was to predict the rate of hydroxyl production or NO_x formation in the surrounding

snowpack. The rate determining step in the production of photolytic chemicals is the photolysis (E2a.1),

$$x + h\nu \rightarrow y \qquad \text{(E2a.1)}$$

the rate of production can be determined using equation (2a.2):

$$\frac{d[y]}{dt} = J[x] \qquad \text{(E2a.2)}$$

where $J = \int \sigma\phi I \, d\lambda$. I is the spherical irradiance, σ is the absorption cross-section of the chromophore (NO_3^-, NO_2^- or H_2O_2), ϕ is the quantum yield for photolysis, d is depth and λ is the wavelength.

To calculate the flux of photochemicals from the snowpack (E2a.3), J needs to be known as a function of depth and solar zenith angle and I (irradiance) needs to be known as a function of solar zenith angle and depth also. Irradiance (I) cannot be measured directly and thus a radiative-transfer model coupling the atmosphere and snowpack must be used to find I.

$$F = [y] \int J \, dz \qquad \text{(E2a.3)}$$

The radiative-transfer model needs an input of a measure of the snowpack scattering coefficients and the snowpack absorption coefficient (more details in Chapter 2b). Lee-Taylor and Madronich (2002) have developed a radiative-transfer model where I is a function of solar zenith angle and depth can be calculated with two of three factors: *e*-folding depth, albedo or concentration of black carbon, thus a measure of *e*-folding depth and albedo is needed. Albedo (snow reflectivity) and *e*-folding depths are useful metrics and can also be used to describe snow climatically (see chapters 2c and 3).

The optical properties of the snowpack, i.e. snow reflectivity and *e*-folding depth, control in part the contribution of snow photochemistry to the atmosphere. Large *e*-folding depths (e.g. Fisher *et al*., 2005; France *et al.*, 2010) and less absorption by impurities within snowpack (i.e. less black carbon or other light absorbing snow impurities such as dust or HULIS) (e.g. Reay *et al.*, 2012) are consistent with solar irradiance penetrating deeper into snowpack, and therefore can potentially produce larger molecular fluxes of nitrogen dioxide from the snowpack or larger yields of hydroxyl radicals in the snowpack.

Measurements of the optical properties of snow (nadir reflectance and *e*-folding depth) along with snow type, density and temperature are used in a snow-atmosphere coupled radiative-transfer model to determine light absorption and scattering cross-sections. The absorption and scattering cross-sections are used to calculate spherical irradiance in the snowpack as a function of solar zenith angle and therefore allow the photolysis rate coefficients to be calculated, a full explanation of the calculations can be found in chapter 2c.

Chapter 2a reports field measurements of *e*-folding (light penetration) depth and nadir reflectivity (Duggin and Philipson, 1982) of Alaskan snowpacks on land and sea-ice.

2a.2 Aims

The physical (snow type and density) and optical (reflectivity and *e*-folding depth) properties measurements made in Barrow, Alaska were part of the larger OASIS international field campaign. The aims of the work presented in

this chapter were to determine the physical and optical properties of Barrow snowpack by measuring *e*-folding depth, surface nadir reflectance and snowpack type, density and temperature.

2a.3 Methods

Snowpacks located within 0.3-15 km of the Barrow Arctic Research Centre (BARC) (71.32063°N, 156.6748°W) were investigated as part of the OASIS (Ocean-Atmosphere-Sea-Ice-Snow) campaign during Spring 2009. The field season of 4th March 2009 to 1st April 2009 was designed to match the field seasons of our collaborators. The principal aim of the fieldwork was to measure the optical and physical properties of the snowpack at Barrow, Alaska.

Several snowpacks were optically studied in detail at locations around the OASIS field site and 4 snowpacks that represented different snowpack types were chosen for detailed analysis. The decision about where to conduct the field experiments was based on 3 main factors: how undisturbed the snow was, the depth of the snowpack and how close other collaborators on the campaign were. At each site, a snowpit (~1 m width by ~1 m length) was dug to the depth of the ground or the sea-ice surface. It was ensured that the snow was not contaminated by anthropogenic or animal influence. Measurements of light penetration depth, surface nadir reflectance and snowpack stratigraphy were undertaken at every site, the methods are described below:

2a.3.1 Light penetration depth

The *e*-folding depth (light penetration depth) is a useful metric in snow photochemistry and is the distance for solar irradiance to decrease to $\frac{1}{e}$ (or ~37%) of the initial value of incident light radiation within a snowpack. It is calculated for each wavelength resolved using the Beer-Lambert law (E2a.4). The light penetration depth for each snowpit was measured via a set of simultaneous irradiance measurements following the approach of King and Simpson (2001).

$$\frac{I_d}{I_{d'}} = e^{-\frac{d-d'}{\varepsilon}} \qquad \text{(E2a.4)}$$

where I_d is the irradiance in snow at a depth d relative to a reference irradiance $I_{d'}$ at depth d'. Depth, d, is deeper than d'. Note d' is a few cm below the surface of the snowpack where all irradiance is isotropic (e.g. King and Simpson, 2001).

To eliminate some effects caused by varying snow crystal morphology, the *e*-folding depth was scaled by the density of the snowpack.

Equipment used to measure the *e*-folding depth of the snow:

- Custom made spectrometer using 6 USB S2000 portable ocean optics spectroradiometers
- Custom made fibre optic cable with PTFE cosine corrector
- Panasonic toughbook portable laptop computer with appropriate cables
- Lead-acid batteries
- 50 cm lengths of ¼ inch diameter stainless steel tubing

To measure the *e*-folding depth of the snow, a pit was dug so as to expose a vertical surface into which 6 fibre optic probes were inserted horizontally with approximately 3-5 cm vertical separation and 5-20 cm horizontal separation between probes (Figure 2a.1). The probes were inserted into the wall that ensured no shadows would be cast over the measurement surface. On average, the pits were around 1 m by 2 m in size and the exposure to the sample area snow in the process of digging the pit was considered to clean the snow shovel to an extent where contamination would not be an issue. The fibre optic probes consisted of 50 cm long tubes of ¼ inch stainless steel with a fibre optic inside and a PTFE cosine diffuser was attached to the end of each fibre optic probe, thus the measuring end of the probe was situated 50 cm into the snowpack from the exposed vertical surface of the pit wall and any contamination could be considered reduced. In the ultra-violet and visible wavelengths of light, PTFE cosine diffusers are good diffusers but towards the infra-red end of the spectrum the quality is reduced. The fibre optic components were designed to operate in temperatures of −60 to +85 °C at a wavelength range of 280–750 nm and consisted of a 10 ± 3 μm fibre optic glass encased in 125 ± 2 μm Kevlar cladding and 245 ± 10 μm rubber tubing coating. There is a strain relief boot holding the stainless steel tubing and rubber inner tubing in place, this also acts to block out any light entering this end of the probe.

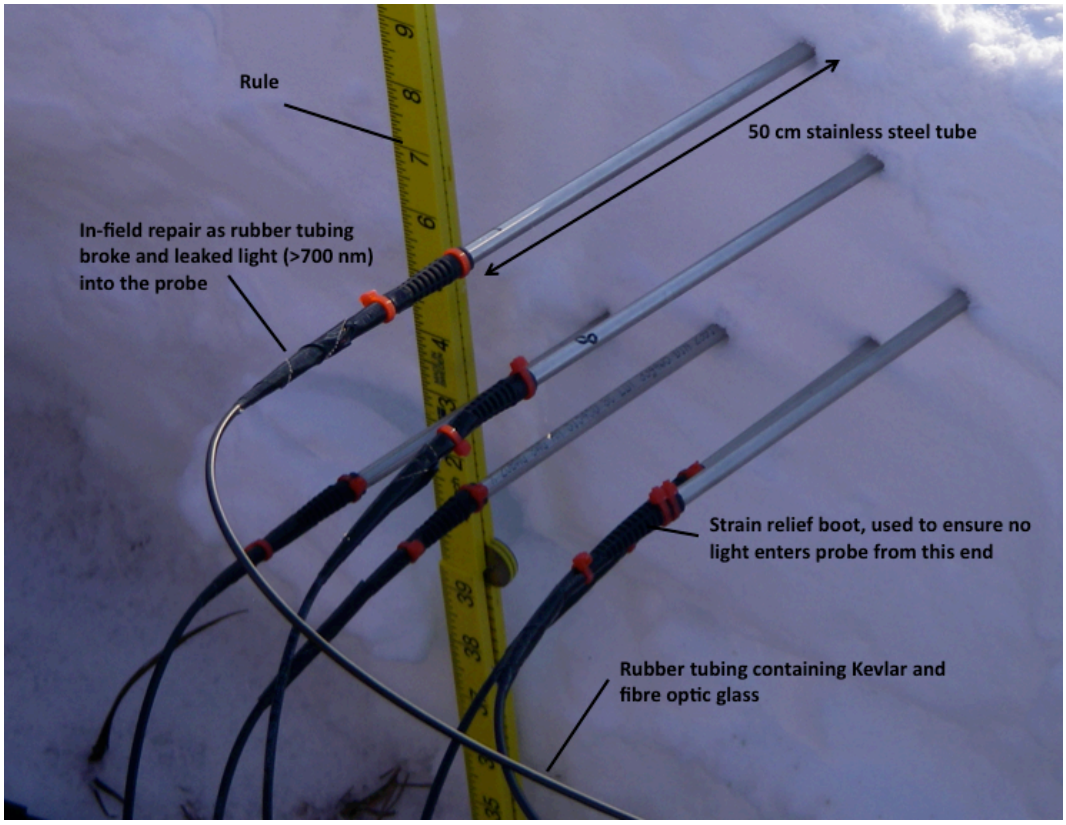

Figure 2a.1. An example of fibre optic probe arrangement.

The fibre optic probes were used to measure the intensity of light attenuated at different depths throughout the snowpack. Probes were placed into the fresh face of the snow pit facing away from the direction of sunlight so no shadows will be cast over the snow surface (Figure 2a.2).

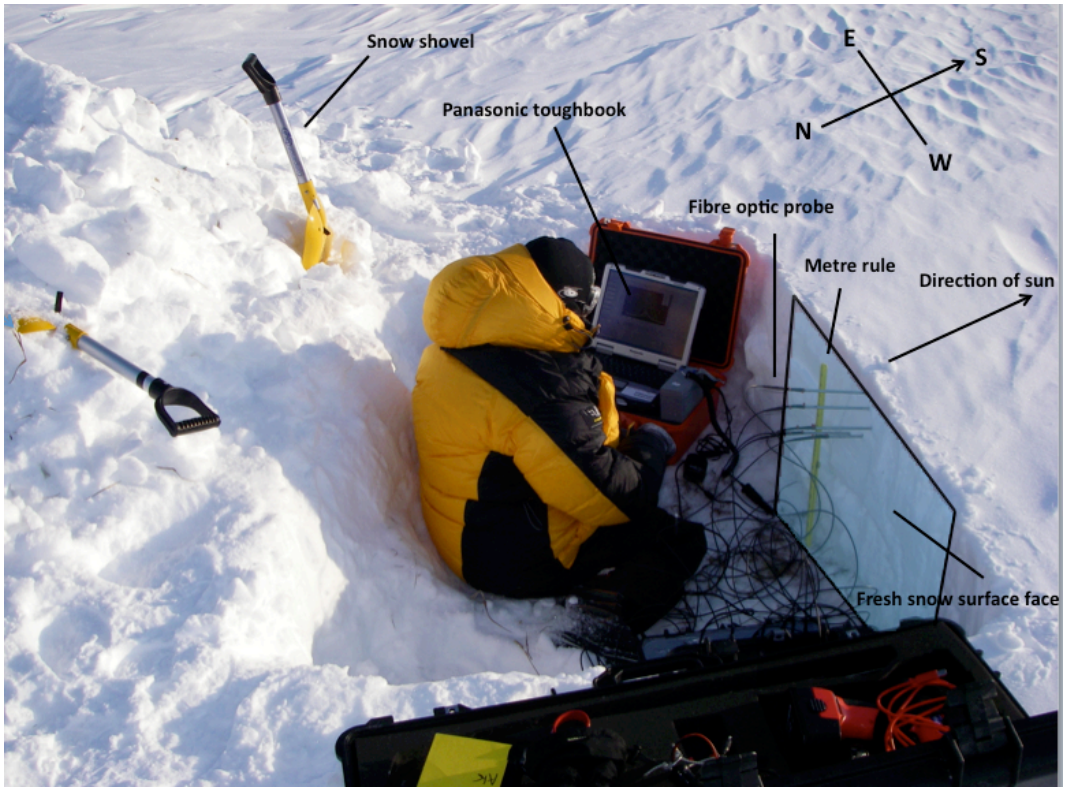

Figure 2a.2. An example of a snowpit set-up.

The probes were inserted horizontally into the snow at increasing depths using the arrangement shown in Figure 2a.1 to minimise light path disruption by probes higher in the snowpack. It was attempted to place the probes into the snow in the same order with the least sensitive probes near the surface as light intensity decreases with depth in the snowpack. Owing to the curvature of some of the metal encasing and the difficulty in keeping probes horizontal on insertion, the pit was excavated in the area where the tube tips had been and the depth of the cosine corrector was recorded after the measurements had been taken (Figure 2a.3). The probes were numbered and attached to a detector, a bespoke 6-channel spectrometer consisting of 6 independent spectrometers (Ocean Optics USB2000) assembled in a single portable housing and operated from batteries. The 6-channel spectrometer can simultaneously record spectral irradiance from 190–

1100 nm at a resolution of <1 nm, however the effective wavelength range of measurements within the snowpack was constrained to 350-700 nm due to the optical properties of the fibre optics, the cosine correctors and the ambient irradiance, i.e. the fibre absorbs light. The signal to noise ratio of the spectrometers is typically better than 300:1.

Using the method described in this chapter, the fibre optic probes were inserted into the snow only once per set of measurements, reducing the number of insertions reduced the variation in insertion angle and probe temperature fluctuations between probe measurements at varying depths.

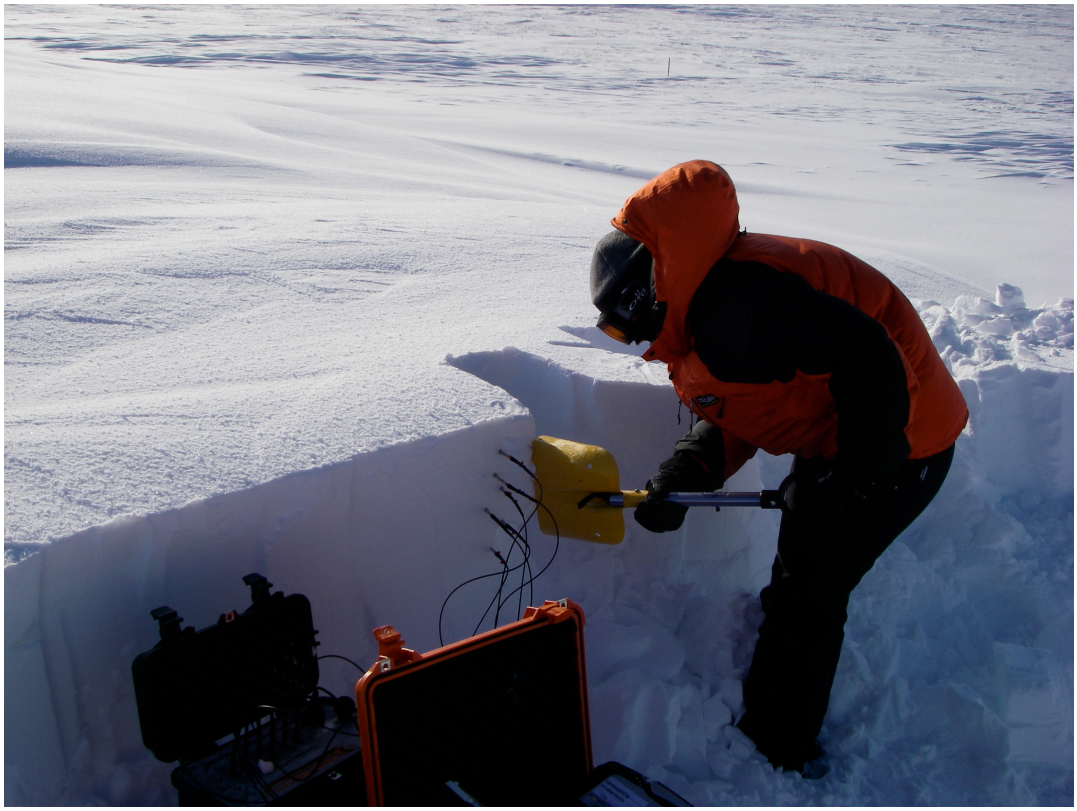

Figure 2a.3. An example of the probe recovery method.

Each fibre optic probe was connected to a separate spectrometer (channels) and the six individual spectrometers was controlled by a master unit, thus each "channel" has a different integration time. Measurement integration times were set once the probes had been inserted into the snow and the integration times varied with differing snowpits and snow types. After essential information such as the time and the file names of the measurements were recorded, the integration times were reset to the value at which the spectrometers were saturated in the wavelength region of 470–580 nm by sunlight and the essential information was recorded once more. The spectrometers were saturated to increase the signal to noise ratio in the wavelength regions of 300–400 nm and 650—700 nm. Typical saturated and unsaturated spectra can be seen in Figure 2a.4. Once all in-snow measurements were complete, the probes had to be dug up to record the depth of the cosine diffuser (Figure 2a.3).

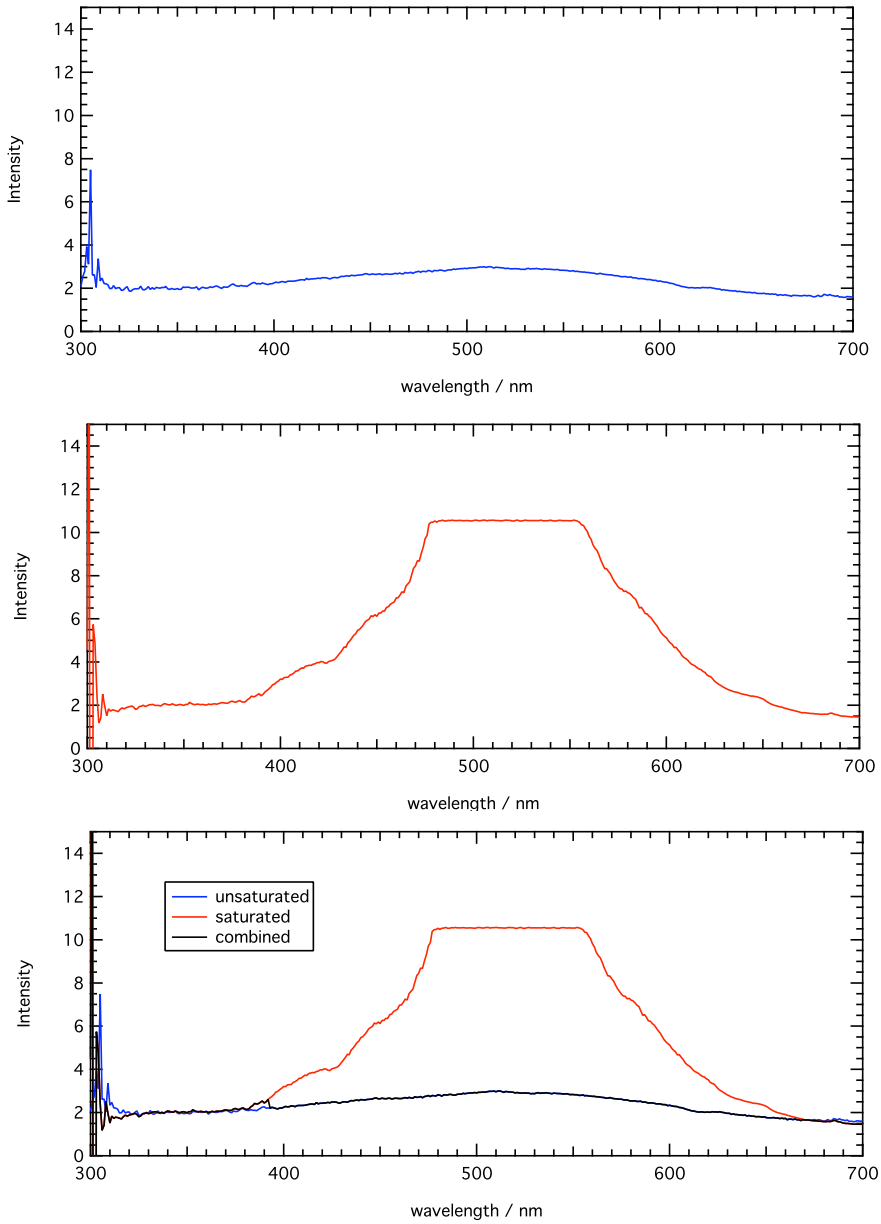

Figure 2a.4. Combining saturated and unsaturated intensity spectrum.

Dark spectra were also recorded in the field by capping the fibre optic probes thus allowing measurement of the electrical noise at ambient temperature. The sensitivity of each spectrometer and fibre were calibrated relative to each other by measuring the intensity of solar radiation above the snowpack simultaneously with all 6 fibre optic probes pointing at the same target. A wavelength calibration was performed for each spectrometer using a portable mercury-argon Pen-Ray

lamp in the field and an intensity calibration was performed for each channel using a NIST traceable halogen light source to monitor any decay in the fibre optical transmission.

To measure the *e*-folding depth of the sea-ice the method had to be adapted slightly (Figure 2a.5). The probes were inserted vertically into the sea-ice in an arc arrangement by drilling 6 holes, using a masonry drill bit and an electric drill, to different depths in the sea-ice. The method then follows that of snow *e*-folding depth measurements by measuring in-snow irradiance, saturation and dark spectra. Once all the measurements were complete, the probes were pulled out of the ice and the depth of the fibre optic end recorded using a measuring pole.

Figure 2a.5. An example of fibre optic probe arrangement in sea-ice.

Each measurement file taken was time stamped with GMT and informed about the spectrometer and solar zenith angle. To generate a useful data set for photochemical modelling from the in-field measurements, programs were run to combine the data and make corrections for wavelength, electrical noise and hot pixels. The files were corrected using labVIEW programs (Figure 2a.6) allowing for wavelength calibration using the daily Hg-Ar lamp reading and removal of the baseline using the dark spectra obtained for the same integration period.

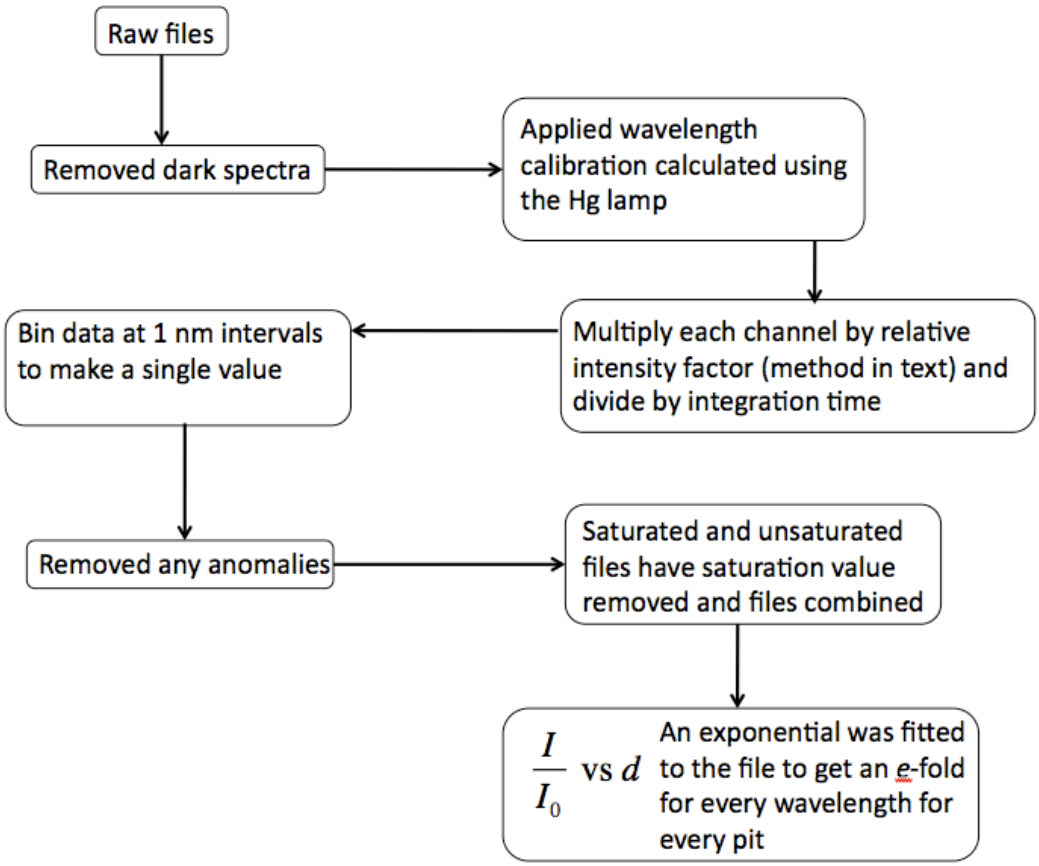

Figure 2a.6. Diagram showing the steps taken to analyse the data collected in the field.

The method used in this field experiment differs from that used by France (2011b) in previous studies. France (2011b) used a single fibre optic probe in conjunction with a spectroradiometer to measure the light attenuation every 3-5 cm in depth

with downwelling surface irradiance, i.e. the measurements were not concurrent and sky conditions could change. In contrast to previous studies (e.g. Beine *et al*, 2006; Fisher *et al*, 2005; France *et al*, 2011b) the method used here allows the light attenuation at varying depths to be measured simultaneously thus under the same sky conditions and therefore the need to calibrate each individual measurement of in-snow irradiance with a downwelling atmospheric irradiance measurement is removed. The new method removes the variation due to changing sky conditions between *e-folding depth* measurements at different depths within the snowpack.

2a.3.2 Albedo

The reflectance measurements were undertaken using the nadir reflectance method (Duggin and Philipson, 1982), a bi-conical method that compares the target radiance to that from a diffuse, lambertian reflective panel (E2a.5).

$$a_{\text{snow}} = \frac{R_{\text{snow}}}{R_{\text{panel}}} \qquad \text{(E2a.5)}$$

where a_{snow} is the albedo of the snow surface, R_{snow} is the relative reflectance of the snow surface and R_{panel} is the relative reflectance of the reflectance panel.

Two spectroradiometers (GER 1500s) were mounted on tripods, one to measure the radiance of a 10" square reference panel (Spectralon®) and the other to measure the radiance of the snow surface simultaneously. The reflectance of the panel is calibrated by NERC FSF. The GER 1500s can measure reflectance over the spectral range of 350-1050 nm, with a spectral resolution of 3.2 nm. The field of view used in the measurements at Barrow was 3°. The target and reference are

viewed under the same irradiation conditions and geometry therefore removing any influence of overhead sky conditions. Before and after the snow measurements, both spectrometers recorded the radiance of the same spectral panel and thus ensuring the spectrometers were calibrated to one another (Figure 2a.7).

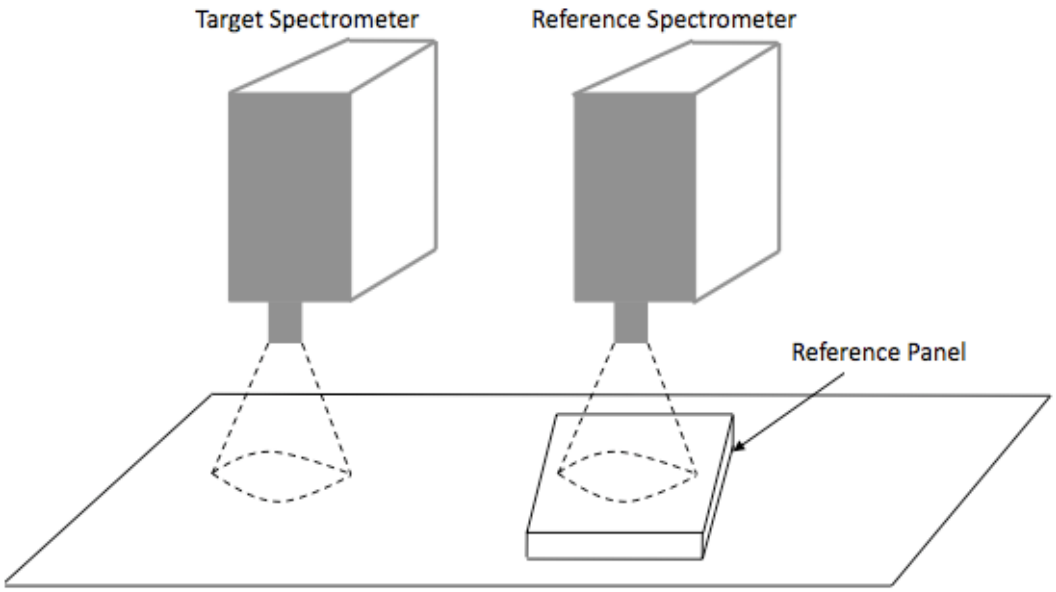

Figure 2a.7. Nadir surface reflectance equipment set-up. Field of view is 3°. Measurements taken over 350-1050 nm.

To measure the albedo, the following equipment was required:

- 2 x GER 1500 spectroradiometers
- 2 x tripod
- 1 x Panasonic Toughbook laptop
- 1 x Spectralon reference panel
- 3 x lead acid batteries

The technical specifications of the equipment used to measure reflectivity are show in Table 2a.1

Name	Part number	Specification
GER1500	2038 and 2039	Spectral Range 350-1050 nm 3º field of view
Spectralon Reference Panel	SRT 45230-1	Perfect white reflector

Table 2a.1. Specification of equipment used to measure snow surface albedo.

On average, up to 10 sites along ~1-10 m transect were measured for each snow surface with 5 measurements or more taken for each site and then the resultant albedo was averaged. When a transect was completed, both spectrometers were once again placed facing the reference panel for re-calibration to record any changes that may have occurred throughout the transect. All snowpack reflectance measurements were taken close to solar noon as the sun solar zenith angle is changing least at this time and during stable sky conditions. The reflectivity data was analysed using the NERC FSF (Field Spectroscopy Facility) template, it calculates a ratio between the spectrometer measuring the reference panel and the spectrometer measuring the snow surface. The method, recommended by MacLellan (2006), is the NERC (National Environmental Research Council) approved post-processing technique (and is part of their equipment hire process) for use with simultaneously collected files from two GER 1500 spectroradiometers in the dual field of view configuration and uses the following procedure:

1. The input parameters are set, e.g. the correct spectralon plate calibration factor is selected (all plates are pre-calibrated using lamps calibrated at the

NPL (National Physics Laboratory in Teddington) by NERC FSF prior to loan.

2. The average reflectance measurements from each GER 1500 are ratioed to produce a wavelength dependent inter-calibration factor (E2a.6).

$$\frac{I_{target}}{I_{panel}} \qquad \text{(E2a.6)}$$

where I_{target} is the downwelling irradiance measured on the snow surface and I_{panel} is the downwelling irradiance measured on the reflectance panel.

3. The data files of snow reflectance measurements for each site are interpolated to 1 nm intervals.
4. Ratioing the snow measurement to the reference measurement calculates the relative reflectance values for each measurement which can then be calibrated using the inter-calibration factor calculated in step 2 (E2a.7).

$$R_{target} = R_{panel} \times \frac{I_{target}}{I_{panel}} \qquad \text{(E2a.7)}$$

where R_{target} is the relative reflectance of the snow surface, R_{panel} is the relative reflectance of the reflectance panel, I_{target} is the downwelling irradiance measured on the snow surface and I_{panel} is the downwelling irradiance measured on the reflectance panel.

The GER 1500 measures over the spectral range of 350-1050 nm, sampling every 1.5 nm. For each measurement taken, the GER spectrometers were set to average over 16 wavelength scans, the recommended setting for balancing length of time to produce each measurement with signal:noise ratio (Fowgill, 2005). A representative snow surface reflectance measurement was chosen for the snowpit

and this process was repeated for each snowpit so several representative snow surface albedos were calculated.

2a.3.3 Snow Stratigraphy

The vertical profile of the snow texture and structure was recorded in each snow pit to understand the context of the optical measurements. Layers were found with brushing and each layer of the snow pit was recorded in a stratigraphic diagram showing the depth at which layers occurred, the type of snow within a layer and the hardness of the layer. The international classification for seasonal snow cover on the ground (Fierz *et al*, 2009) was used to establish the snowpack stratigraphy by identifying grain type/size and consistency. Snow was extracted from each layer, identified and the grain characteristics were examined under a hand lens. The hardness and snow morphology symbols used for the relevant classification of Barrow snowpacks are shown in Figures 2a.8 and 2a.9.

Term	Hand Test	Graphic Symbol
Very low	Fist	
Low	4 fingers	
Medium	1 finger	
High	Pencil	
Very high	Knife blade	
Ice		

Figure 2a.8. Snow hardness scale, penetration test. Adapted from Fierz et al (2009).

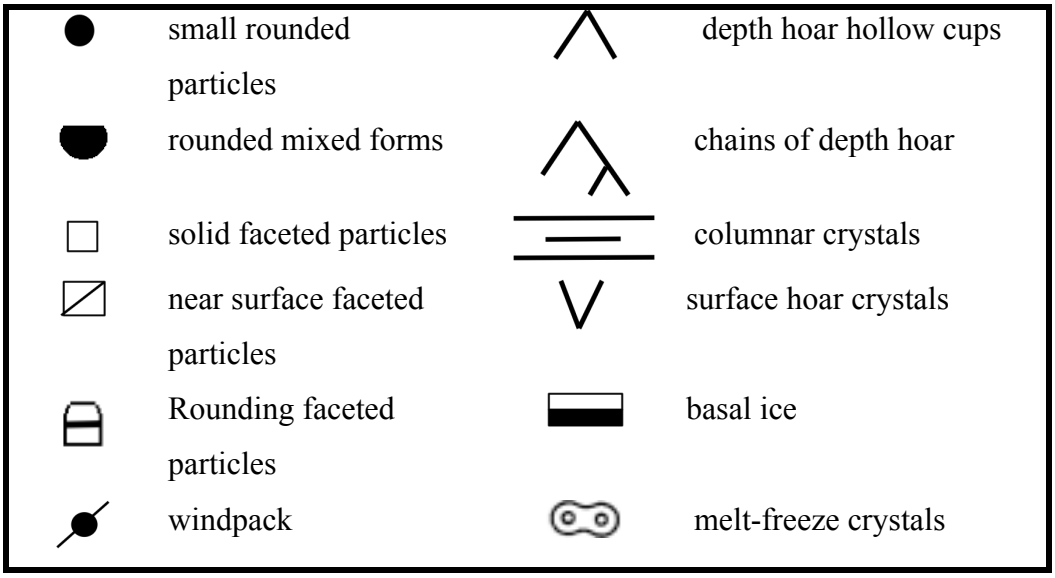

Figure 2a.9. Snow morphology symbols. Adapted from Fierz et al (2009).

The shape and size of a snow crystal are very important to scattering efficiency within the snowpack, this will be discussed further in chapter 2b. The density and temperature of the snowpack are parameters needed to model the snow photochemistry. Many photochemical reactions are temperature dependent (Chu and Anastasio, 2003; 2005; 2007) due to the energy required to break the bond between particles.

The density of the snowpack was measured using a bespoke 284 cm^3 snow block cutter (Fisher *et al*, 2005). Owing to the height of the snow block cutter (Figure 2a.10), the snow samples were taken every 5 cm through the vertical snow profile. A small quantity of snow could be encased in this box of known volume (284 cm^3) then transferred to a clean polythene sample bag for weight measurement. The snow + sample bag were weighed on a portable balance then the weight of the empty sample bag was deducted to produce a final snow weight. The two

known factors, mass and volume, were used to calculate the density of the snow samples.

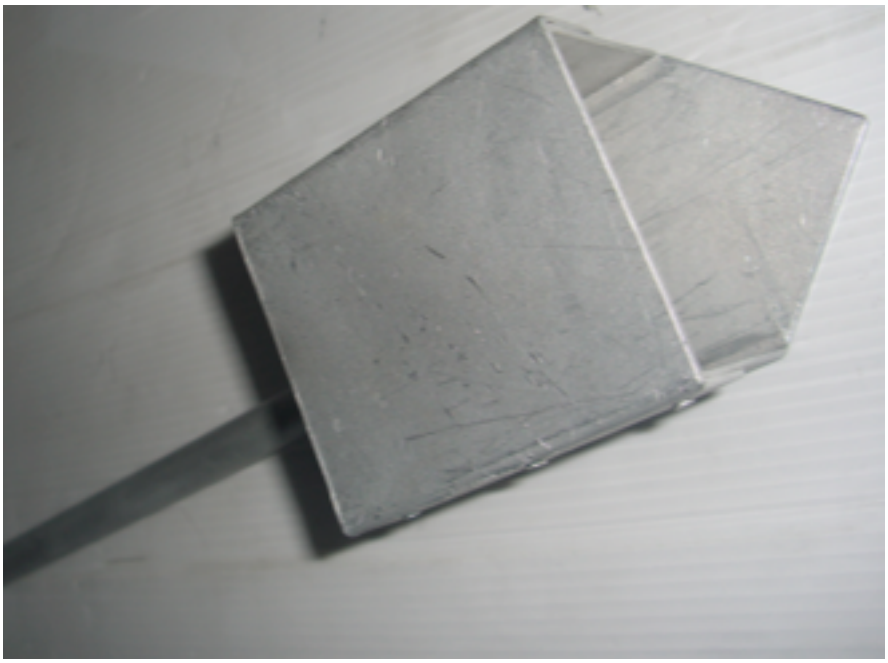

Figure 2a.10. The 284 cm^3 snow cutting tool was used to measure the density of the snow.

The temperature was taken every 5 cm down the vertical face of snowpack using a digital thermometer with a 20 cm stainless steel probe. The temperature was only recorded once the reading had stabilized as it has been noted that temperatures near the surface of snow can be unreliable due to the thermocouple becoming warmed by incoming solar radiation (Cathles and Albert, 2007). The error on the temperature probe is ± 0.5°C and thus is regarded as insignificant compared to other sampling errors.

2a.4 Processed field data: light penetration depth, albedo and physical snowpack properties

The following section aims to present the results of the processed field data in the following forms:

- Plots of *e*-folding depths versus wavelength
- Plots of reflectivity versus wavelength
- snowpack density and temperature profiles with depth
- snowpack stratigraphy

The snowpacks have been grouped depending on the locality of the snowpit. Each snowpack is named by the day of year on which the measurements were made with January 1st represented by day 0.

2a.4.1 BARC snowpits

Five snowpits were dug around the BARC science building, Barrow. The exact locations for each snowpit can be seen in Figure 2a.11. The snowpacks around the BARC building were measured to allow in-snow production rates of OH radicals and NO_2 to be derived and compared with collaborators' measured production rates around the BARC building area (chapter 2b).

Figure 2a.11. Locations of snowpits around the BARC building.

Day 68

The results of *e*-folding measurements, albedo and snowpit profiles for day 68 are presented. The weather conditions for this day were lightly blowing snow at the surface and continuous stratus clouds resulting in a diffuse light regime for the duration of the experiments. The air temperature was -16 to -28°C and there was a strong/moderate easterly wind. The surface snow morphology was soft windpacked snow with blowing snow precipitation. The site used for measurements on day 68 was an artificial snow drift built by a snow fence near an access route to the BARC building. Figure 2a.13 shows the *e*-folding depth and albedo, Figure 2a.14 shows the snowpack density and temperature profile and Figure 2a.15 shows the snowpack stratigraphy.

Figure 2a.12. Close-up of fibres inserted into the snowpack, day 68. The fibres are angled within the snowpack.

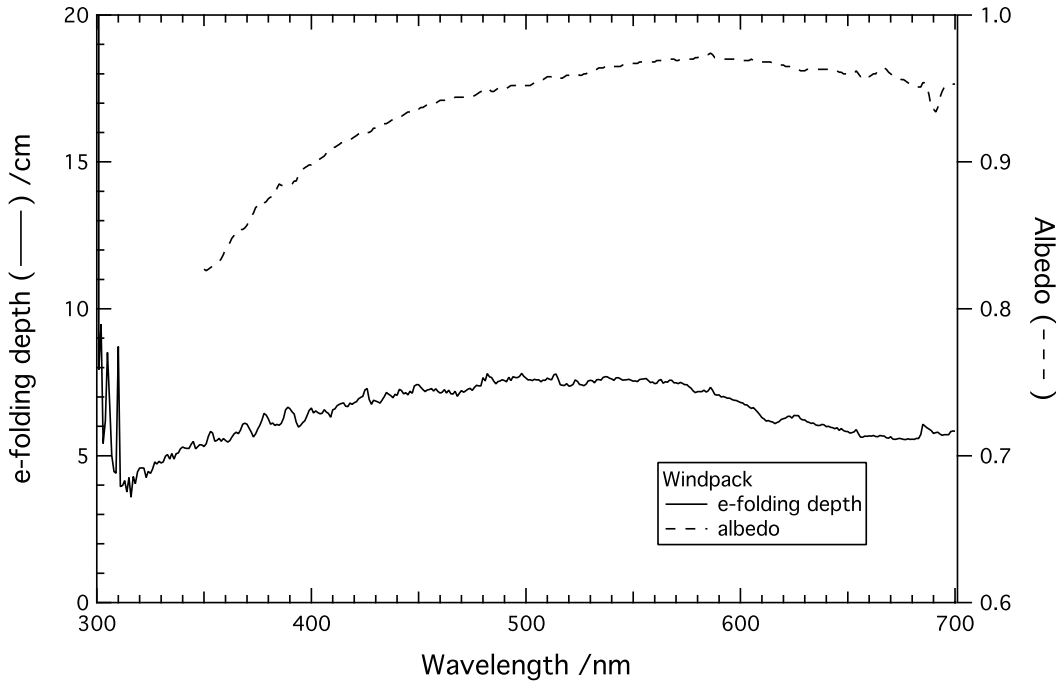

Figure 2a.13. *e*-folding depth and albedo vs wavelength for the snowpack measured on day 68, near to the BARC building.

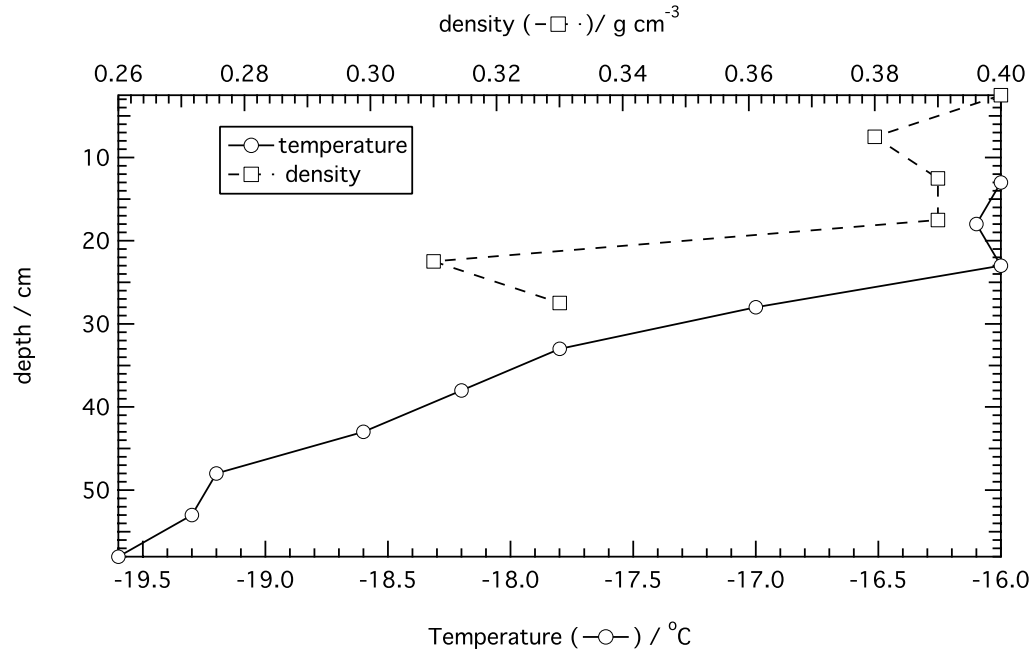

Figure 2a.14. Density and temperature changes with depth. Density inferred from a similar snowpack, day 70.

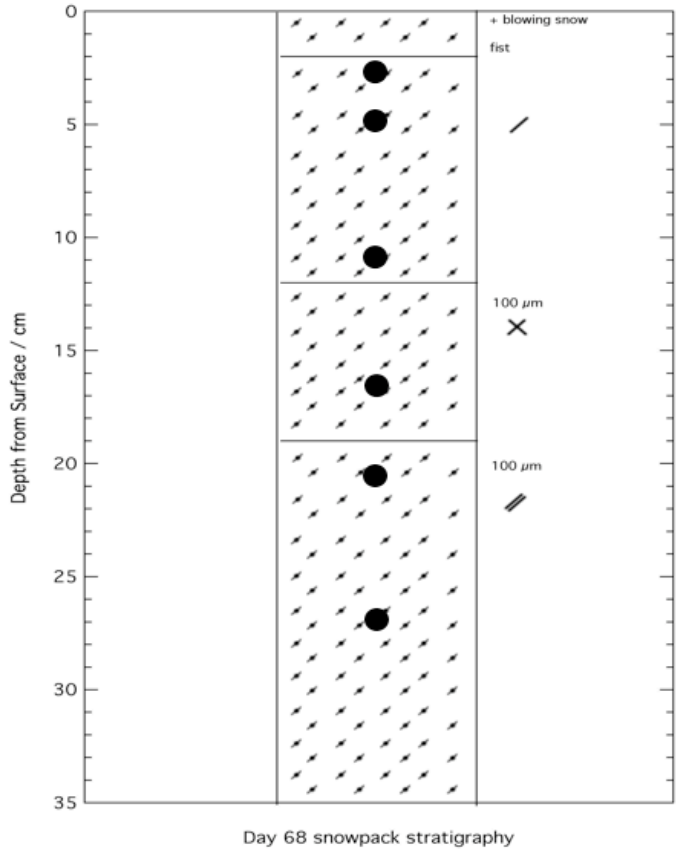

Figure 2a.15. Snowpack stratigraphy for day 68. The large black circles mark the depth of the fibre optic probes.

Day 69

The results of *e*-folding measurements, albedo and snowpit profiles for day 69 are presented. The weather conditions for this day were lightly blowing snow at the surface with low haze, however the Sun was clear resulting in a direct light regime for the duration of the experiments. The air temperature was -21°C and there was no notable wind. The surface snow morphology was hard eroding windpacked snow with blowing snow precipitation. Figure 2a.17 shows the *e*-folding depth and albedo, Figure 2a.18 shows the snowpack density and temperature profile and Figure 2a.19 shows the snowpack stratigraphy.

Figure 2a.16. Close-up of fibres inserted into the snowpack, day 69.

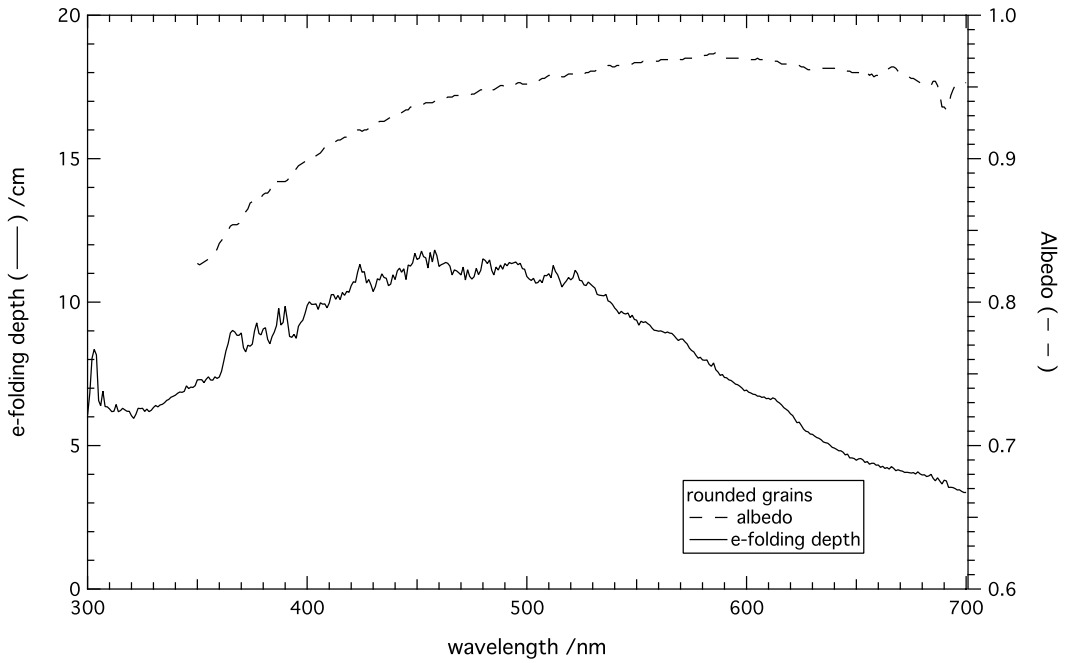

Figure 2a.17. *e*-folding depth and albedo for day 69.

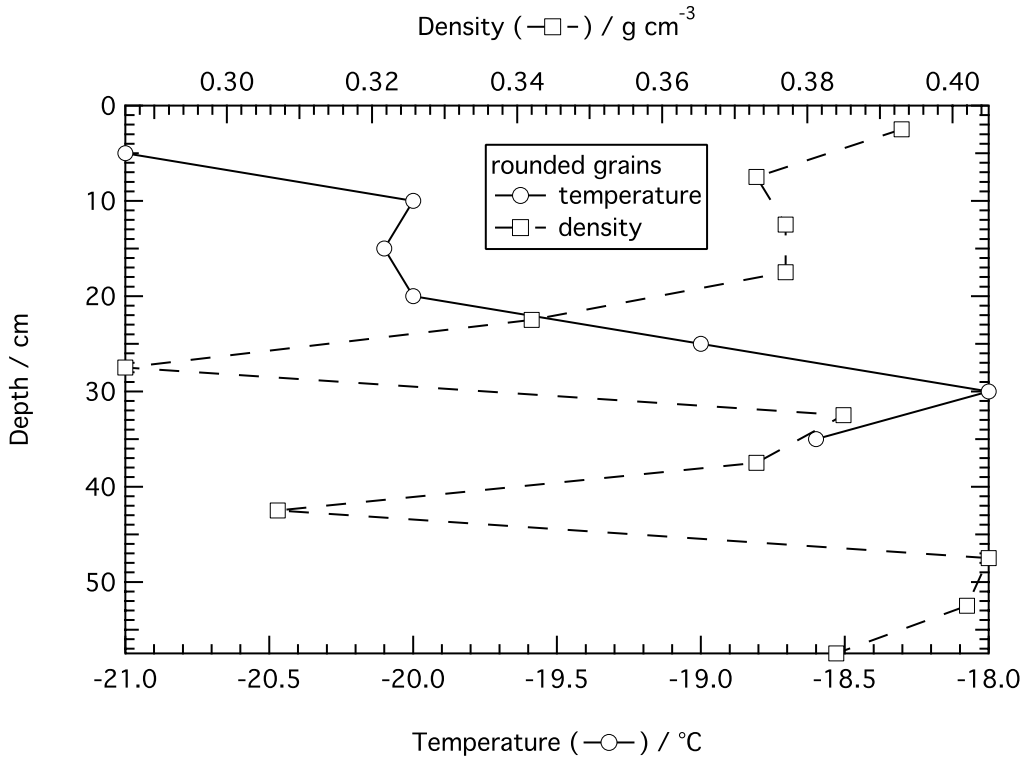

Figure 2a.18. Temperature and density with depth for day 69.

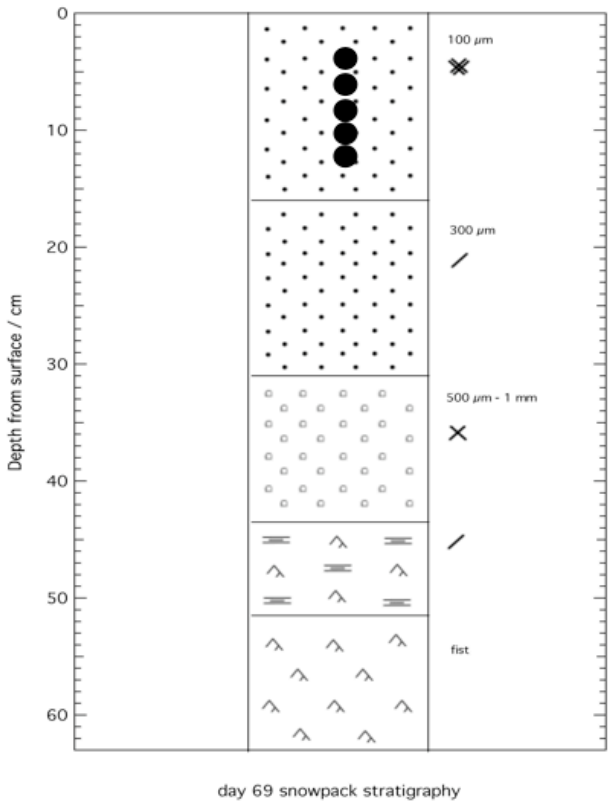

Figure 2a.19. Snowpit stratigraphy for day 69. The large black circles mark the position of the fibre optic probes.

Day 70

The results of *e*-folding measurements, albedo and snowpit profiles for day 70 are presented. The weather conditions for this day were light level blowing snow with a direct light regime for the duration of the experiments. The air temperature was -28°C and there was a strong/moderate easterly wind. The surface snow morphology was soft windpacked snow with blowing snow precipitation. Figure 2a.20 shows the *e*-folding depth and albedo, Figure 2a.21 shows the snowpack density and temperature profile and Figure 2a.22 shows the snowpack stratigraphy.

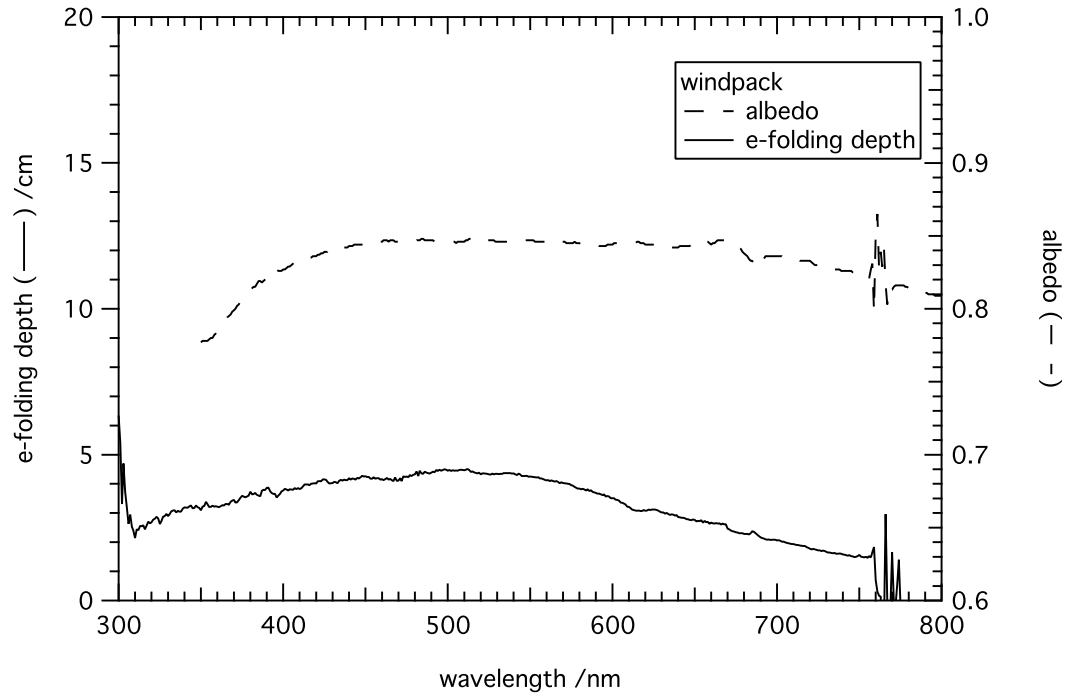

Figure 2a.20. *e*-folding depth and albedo of day 70.

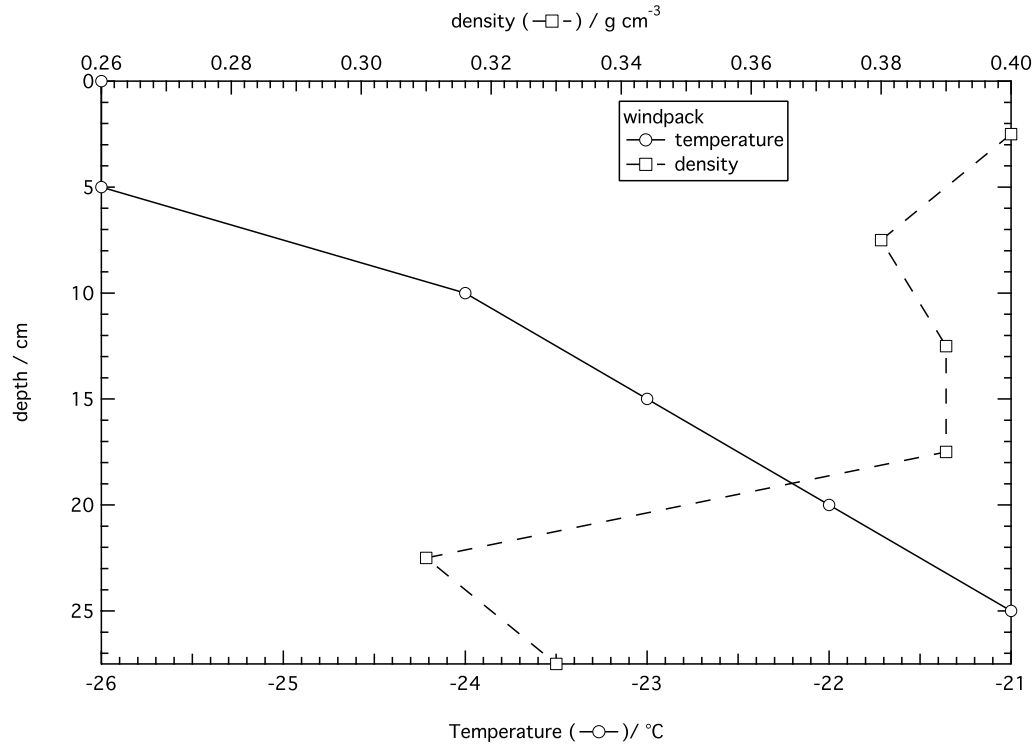

Figure 2a.21. Density and temperature profile of day 70 snowpit.

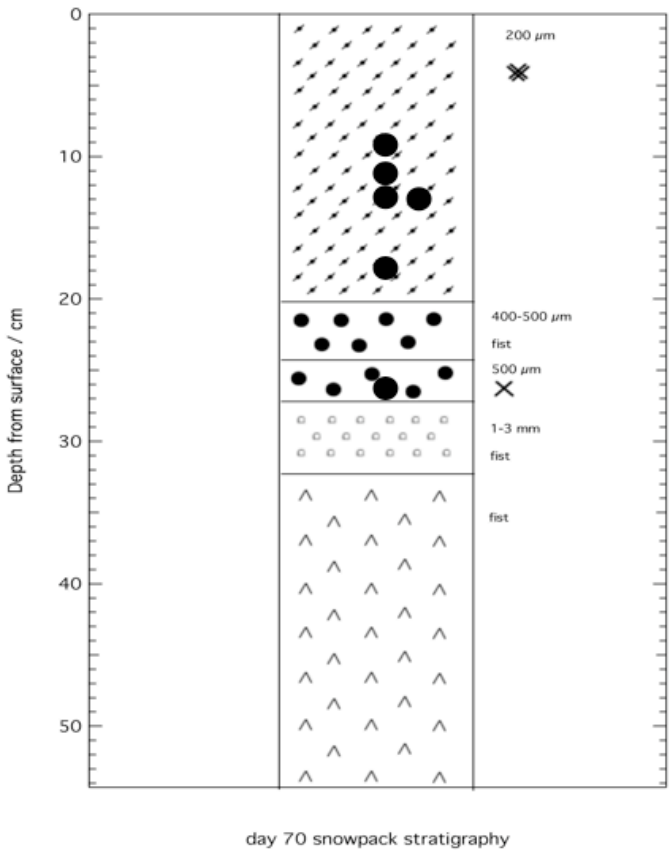

Figure 2a.22. Snow pack stratigraphy for day 70. The large black circles mark the position of the fibre optic probes.

Day 76

The results of *e*-folding measurements, albedo and snowpit profiles for day 76 are presented. The weather conditions for this day were very cloudy creating a diffuse light regime for the duration of the *e*-folding depth experiments but conditions changed and the albedo experiments were conducted under direct light conditions. The air temperature was -26°C and there was a light north-easterly wind. The surface snow morphology was small faceted particles. Figure 2a.24 shows the *e*-folding depth and albedo, Figure 2a.25 shows the snowpack density and temperature profile and Figure 2a.26 shows the snowpack stratigraphy.

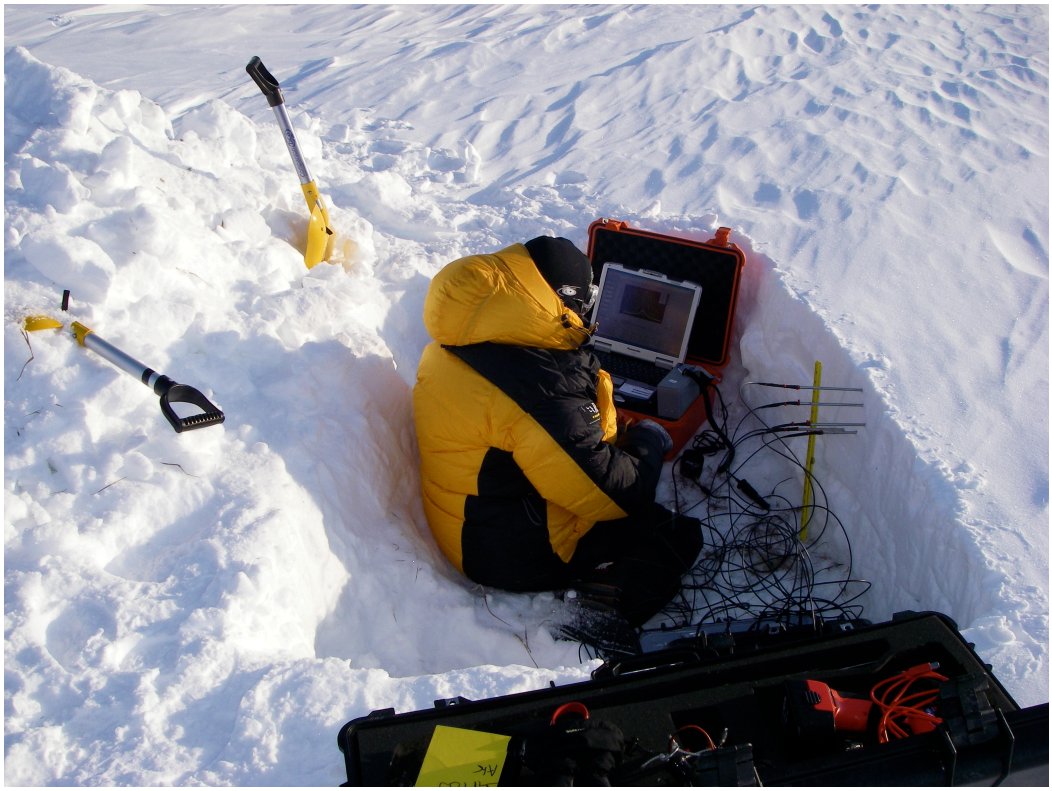

Figure 2a.23. Photograph of snowpit measured on day 76.

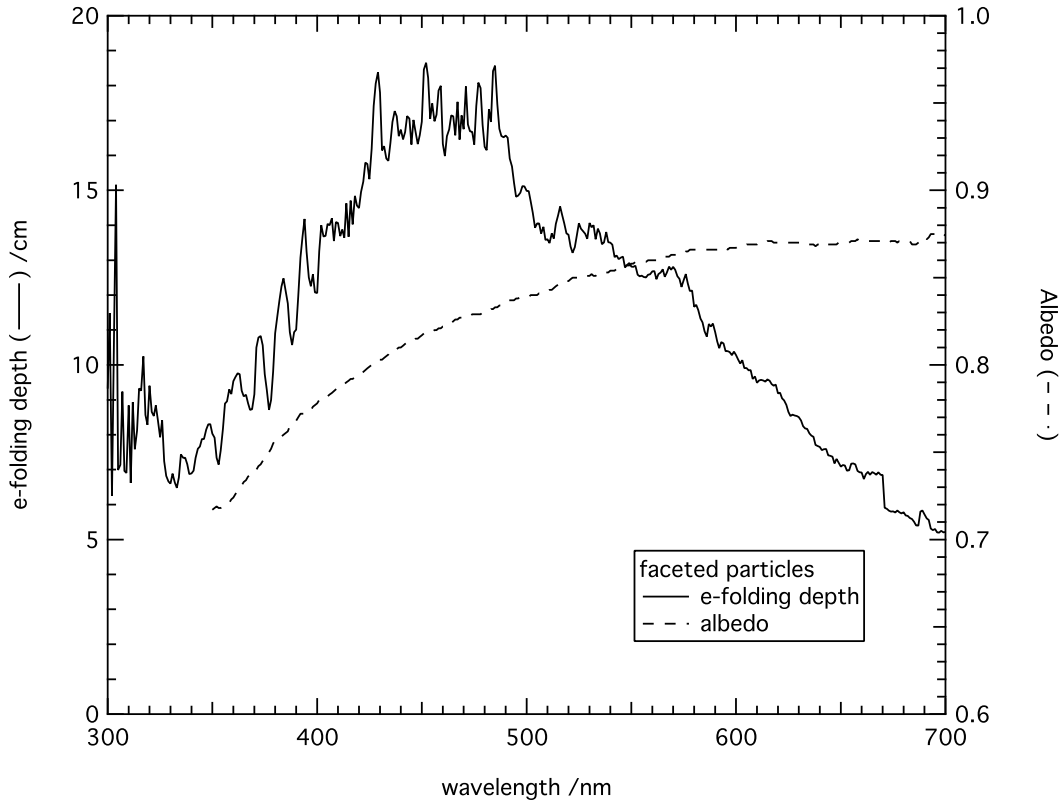

Figure 2a.24. *e*-folding depth and albedo for day 76.

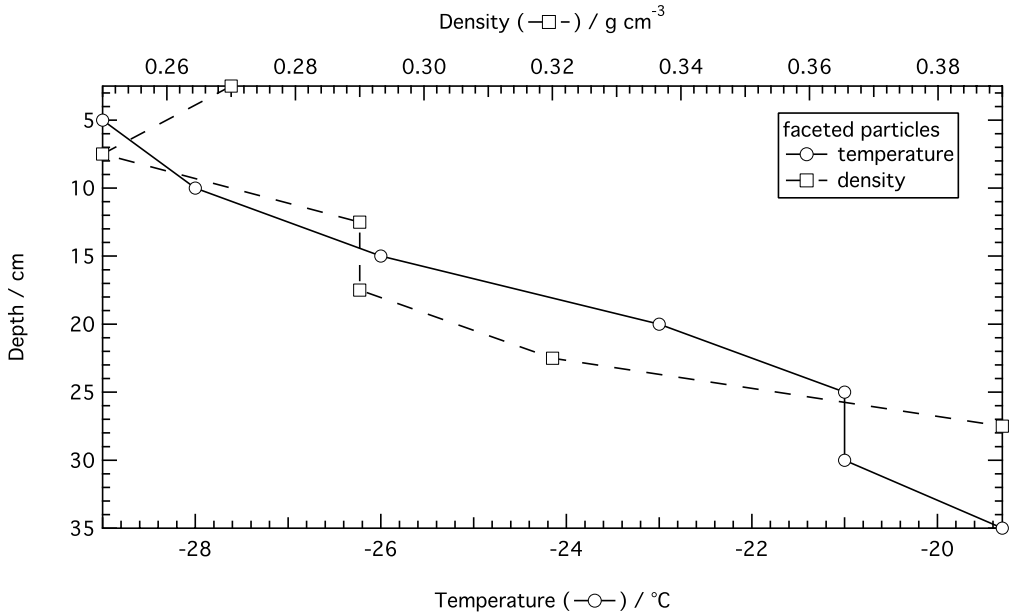

Figure 2a.25. Density and temperature profile with depth for the snowpit on day 76.

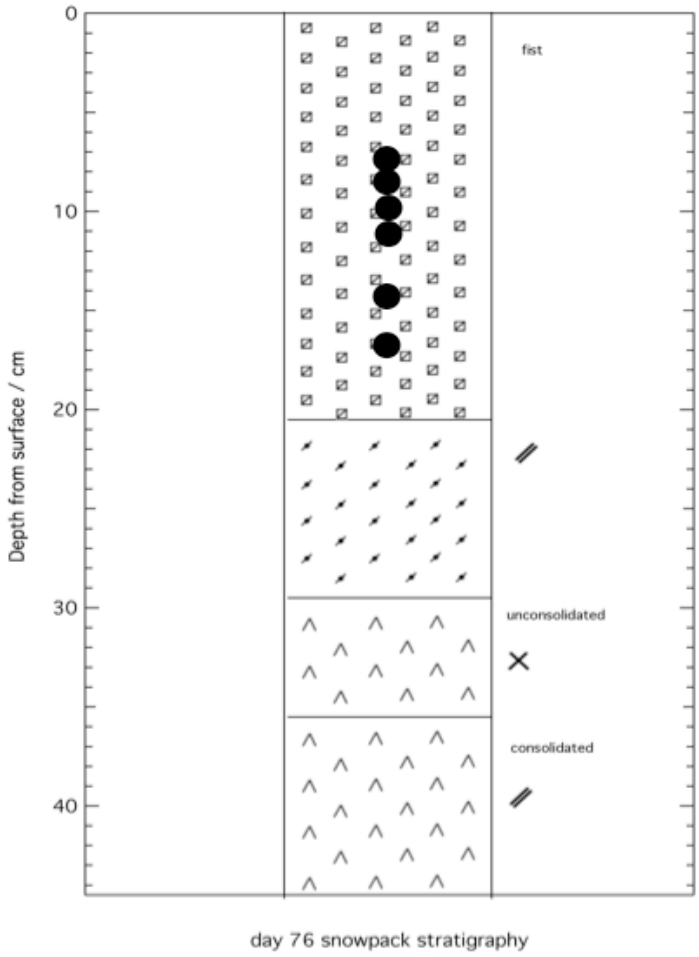

Figure 2a.26. Snowpack stratigraphy for day 76. The large black circles mark the position of the fibre optic probes.

Day 78

The snowpit on day 78 was dug to primarily test the consistency of optical measurements along a 4 m section of artificial snowdrift. Only *e*-folding depth measurements were undertaken and presented here. The weather conditions for this day were low haze covering sun therefore a diffuse light regime for the duration of the experiments. The air temperature was -28°C and there was light south-westerly winds. Figure 2a.28 shows the *e*-folding depth of all measurement snowpit sites on day 78. Figure 2a.29 shows the position of the probes within the snowdrift and solar conditions, sky conditions and time of measurement are shown in Table 2a.2.

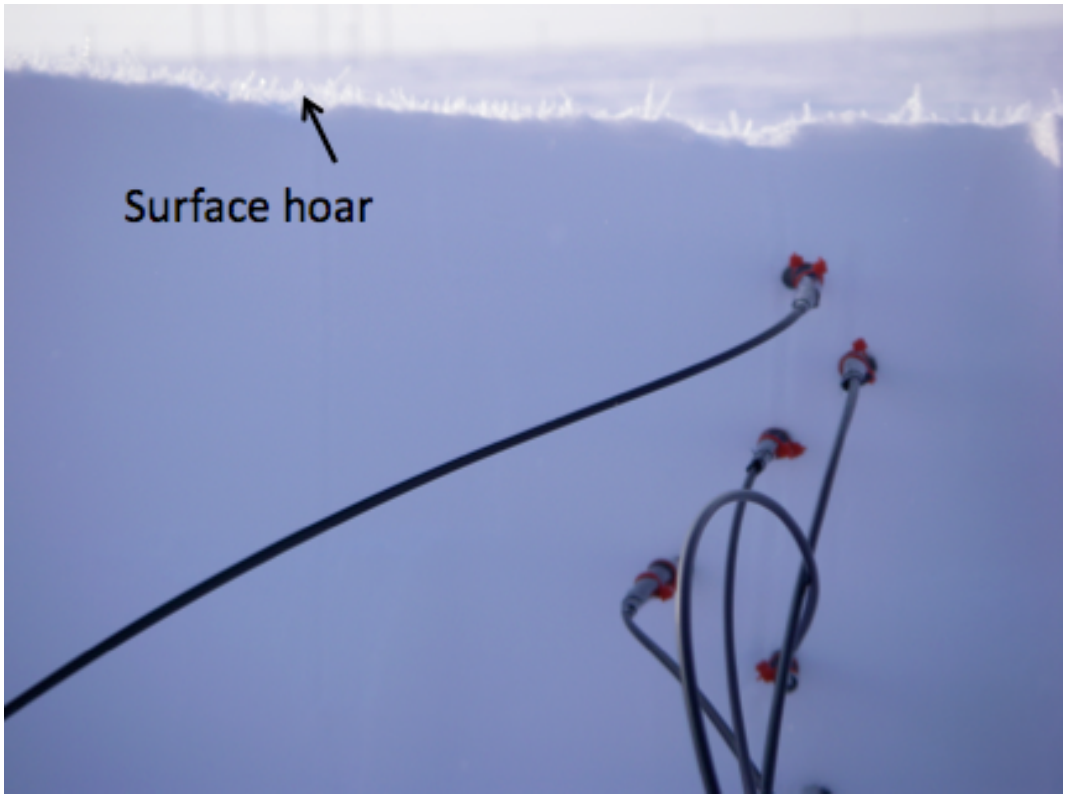

Figure 2a.27. Close-up of probes inserted into snowbank on day 78.

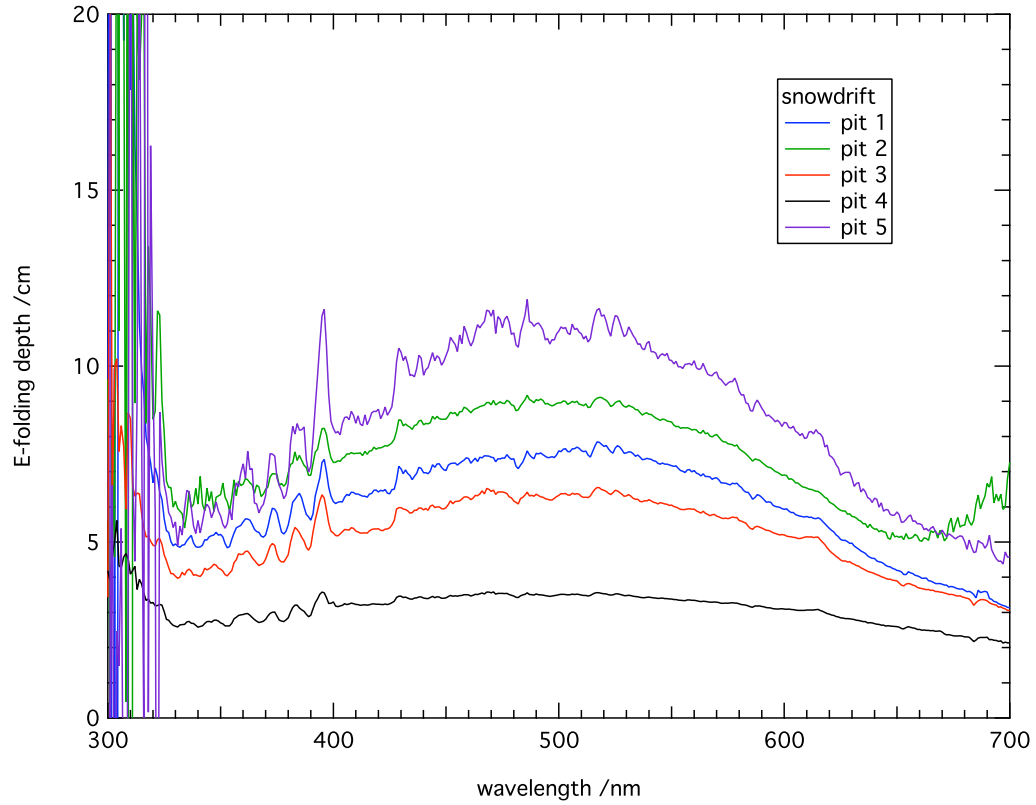

Figure 2a.28. *e*-folding depth of snowdrift, day 78.

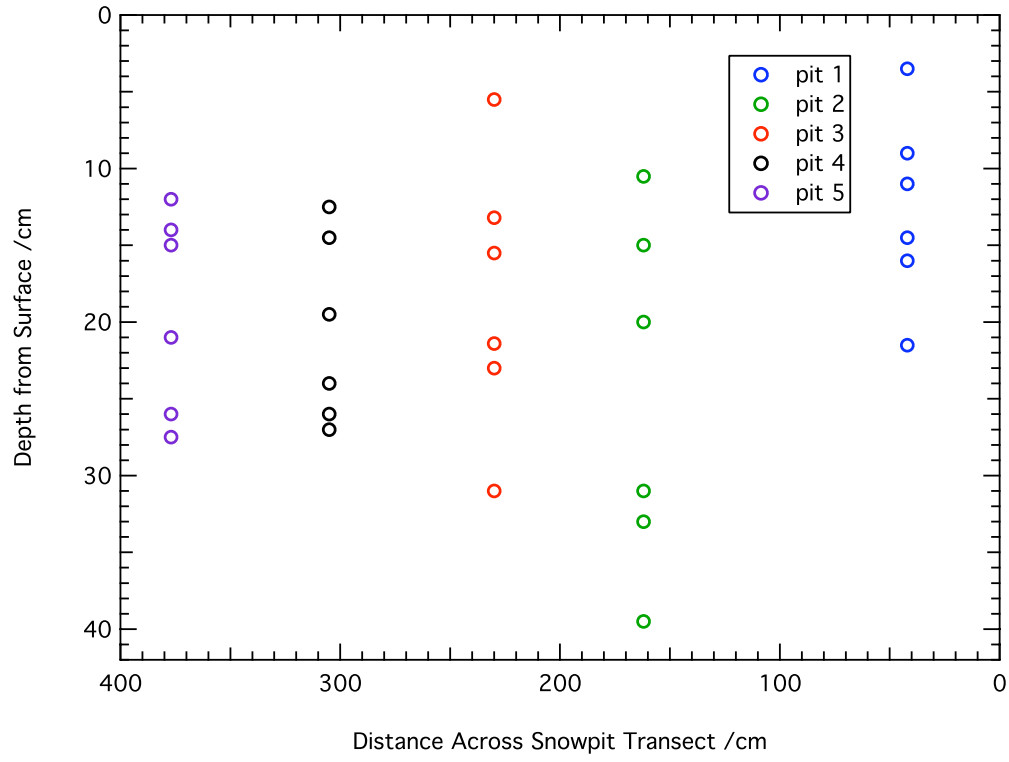

Figure 2a.29. Position of probes along the snowdrift transect.

Pit number	Time measurements were taken (GMT)	Sky Conditions	Zenith angles (°)
1	19:08:54	Overcast, low haze Light wind	78.85439
2	19:37:37	Overcast, low haze Light wind	77.11359
3	21:39:14	Few clouds Light wind	72.26473
4	22:16:10	Few clouds Light wind	71.76384
5	23:49:38	Clear skies Lighter wind than previous measurements	72.71393

Table 2a.2. Time measurements were taken, solar zenith angles and sky conditions along the transect.

Day 79

The results of *e*-folding measurements, albedo, and snowpit profiles for day 79 are presented. The snowpit was also sampled for specific surface area, black carbon and halogens by our collaborators on the campaign. The weather conditions for this day were clear skies and therefore a direct light regime for the duration of the experiments. The air temperature was -27°C and there was a light south-easterly wind. The surface snow morphology was hard windpacked snow.

The albedo for day 79 was measured along the crest of sastrugi. Figure 2a.31 shows the *e*-folding depth and albedo, Figure 2a.32 shows the snowpack density and temperature profile and Figure 2a.33 shows the snowpack stratigraphy.

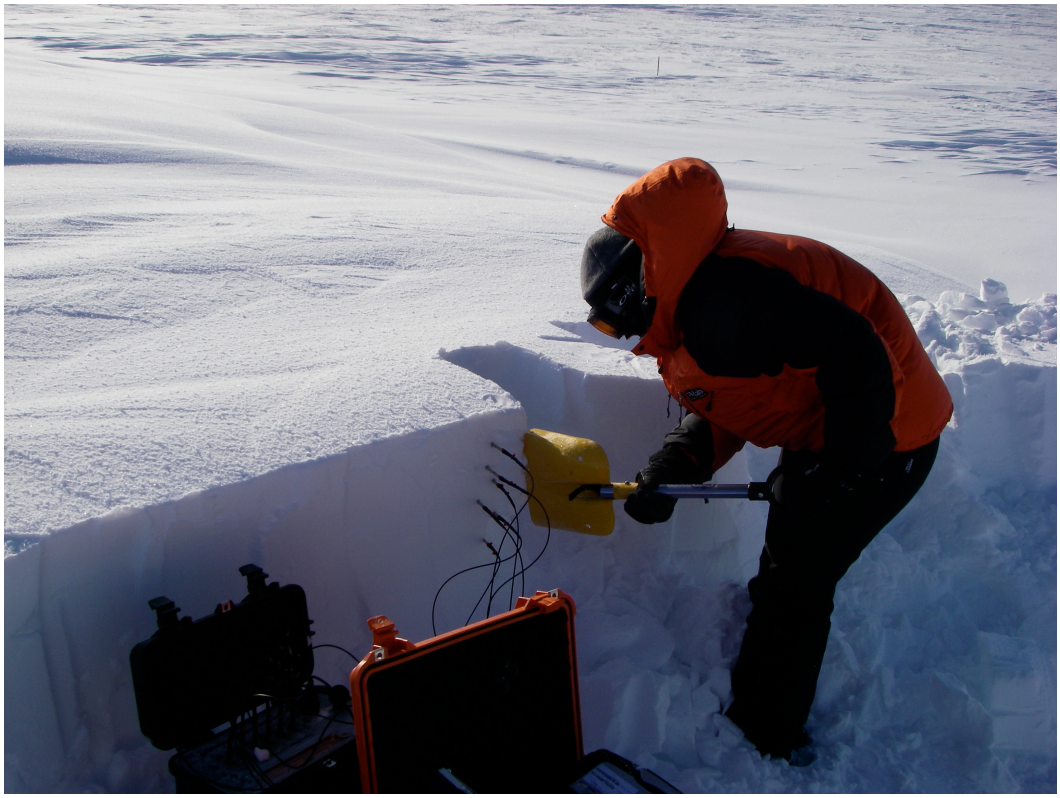

Figure 2a.30. Snowpit measured on day 79.

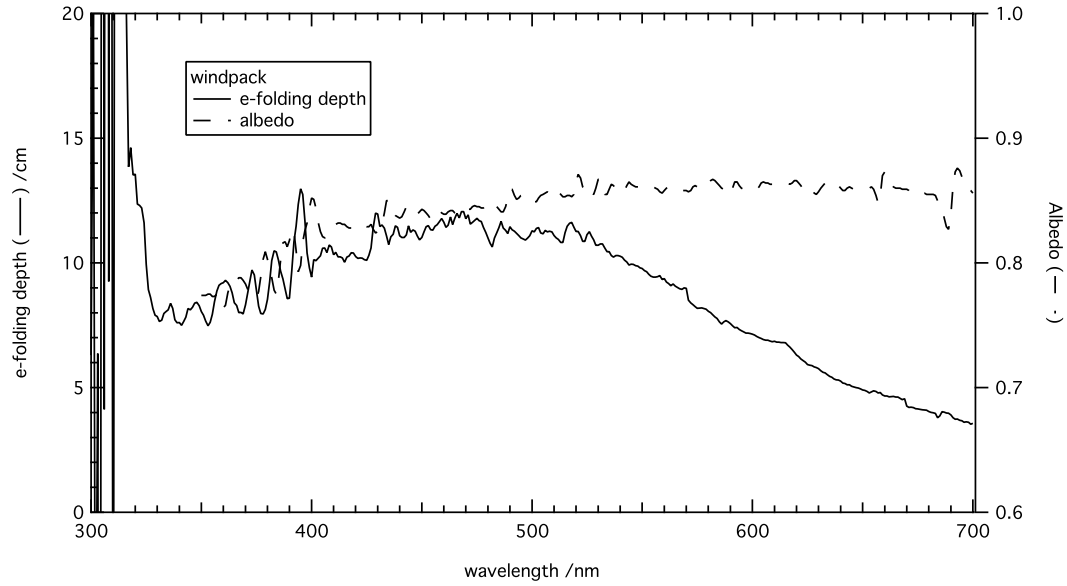

Figure 2a.31. *e*-folding depth and albedo for day 79.

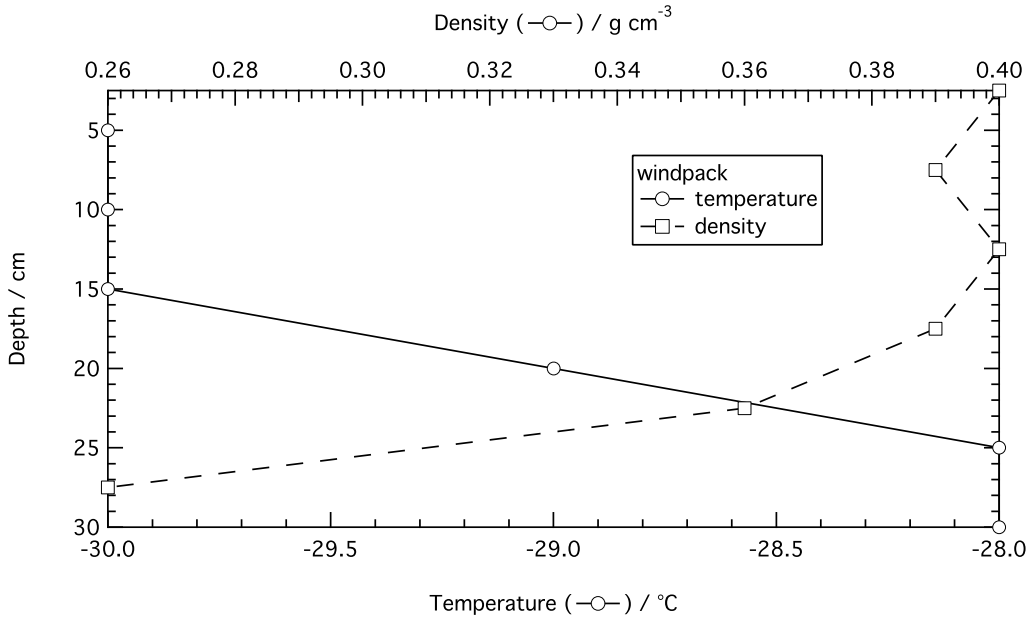

Figure 2a.32. Density and temperature profile with depth for the snowpit of day 79.

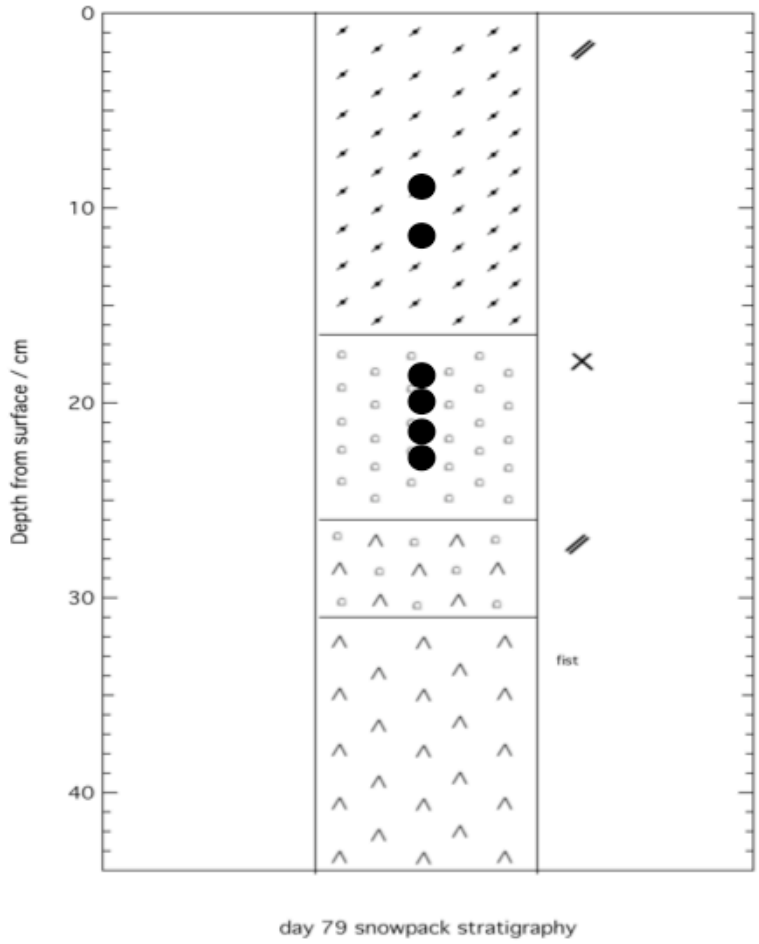

Figure 2a.33. Snowpit stratigraphy for day 79. The large black circles represent the fibre optic probes.

2a.4.2 Snowpits undertaken away from BARC

On days 72 and 85, optical measurements were undertaken at sites away from the BARC science base. Snow on sea-ice measurements were taken on day 72, just off point Barrow and measurements were taken 15 km inland on day 85. The locations of the sites in relation to the sites around the BARC building are shown in Figure 2a.34.

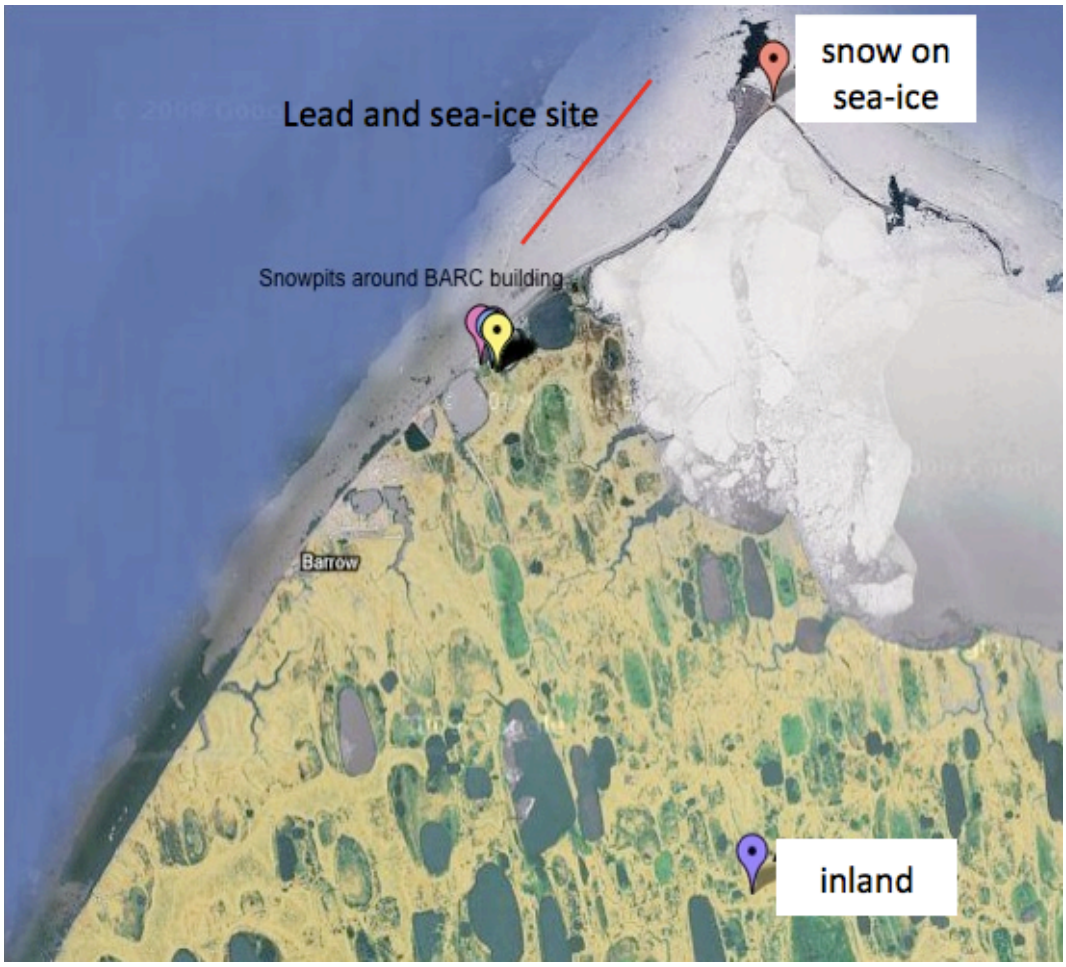

Figure 2a.34. Overview of snowpit measurement locations.

Day 72

The snowpit was dug with the purpose of measuring snow on sea-ice, just north of point Barrow (71.38469°N, 156.45239°W), to compare to terrestrial snow. The

weather conditions for this day were wispy clouds covering the sun therefore inducing a diffuse light regime for the duration of the experiments. The air temperature was -31°C and there was a light north-easterly wind. The surface snow morphology was hard windpacked snow. Figure 2a.35 shows the *e*-folding depth and albedo, Figure 2a.36 shows the snowpack density and temperature profile and Figure 2a.37 shows the snowpack stratigraphy.

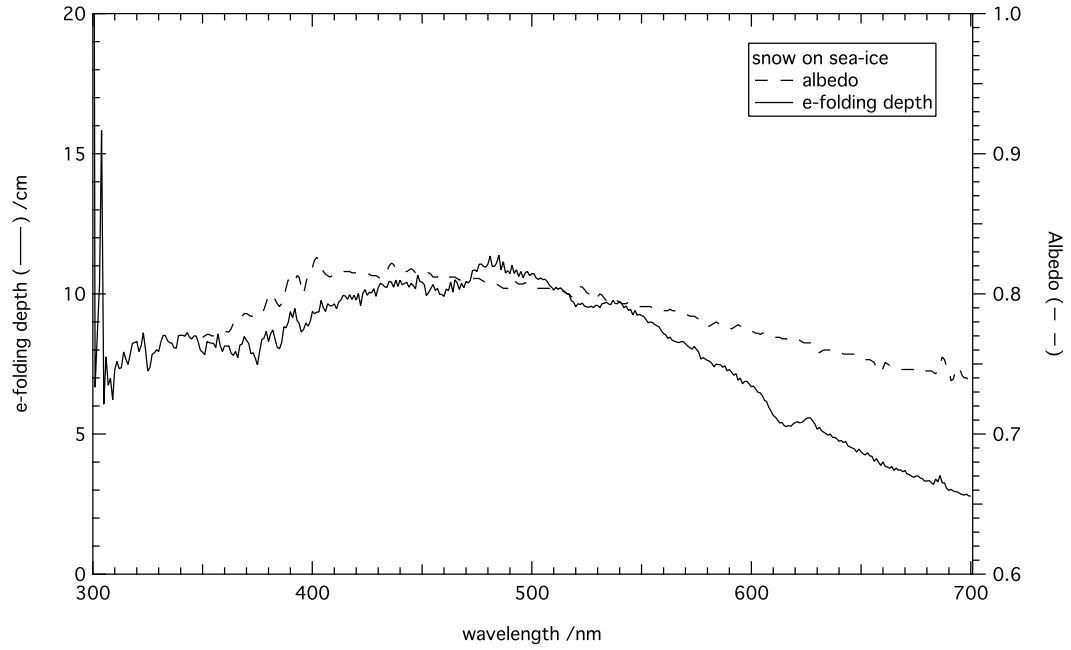

Figure 2a.35. *e*-folding depth and albedo for snowpack, day 72.

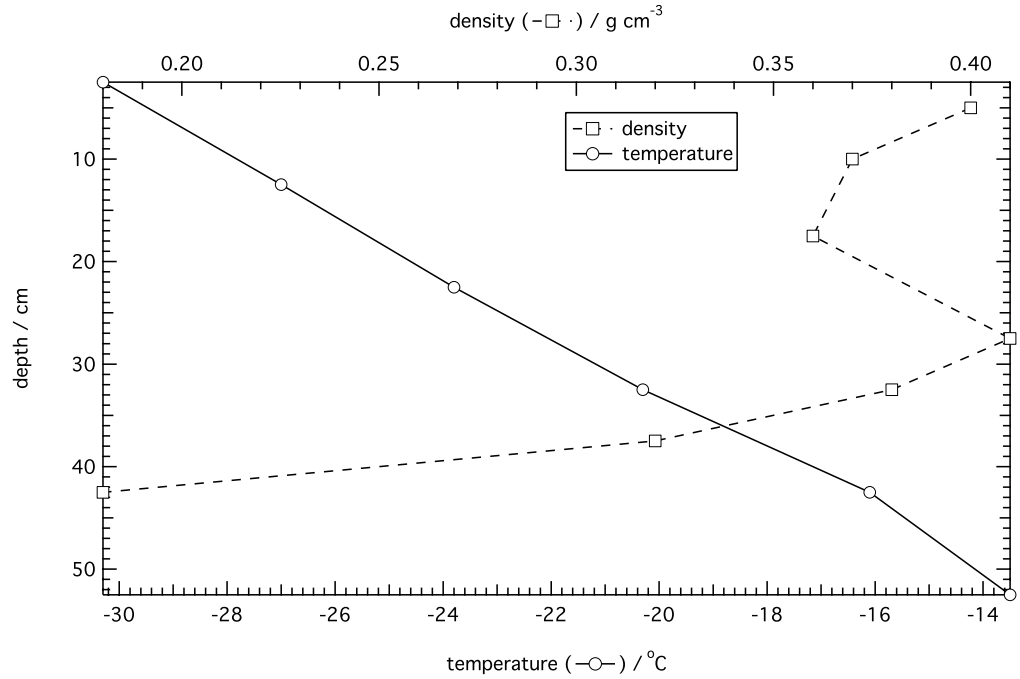

Figure 2a.36. Density and temperature profiles with depth for day 72.

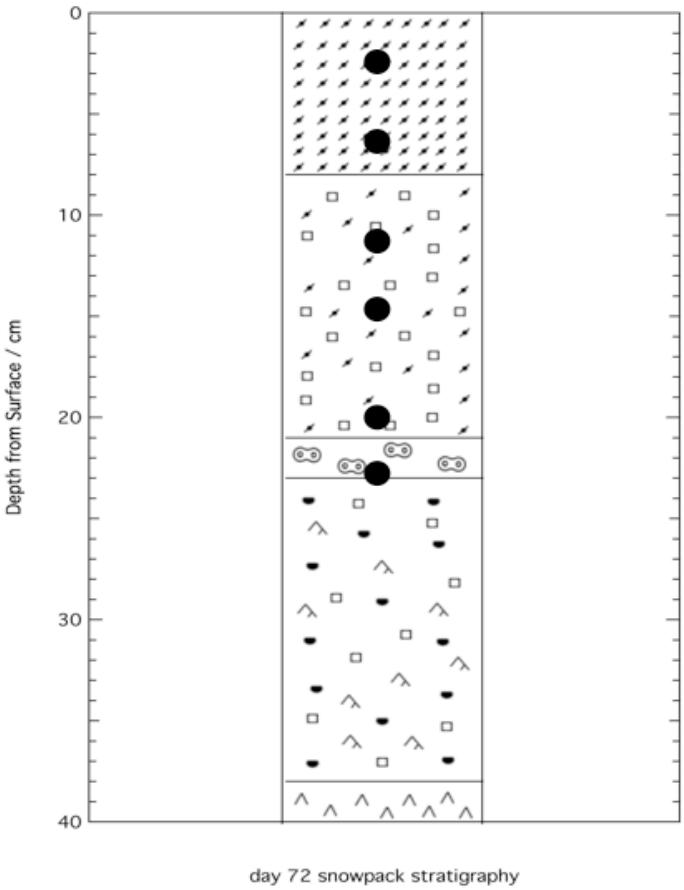

Figure 2a.37. Snowpack stratigraphy for day 72, measured by Florent Dominé. The large black circle represent the fibre optic probes.

Day 85

The snowpit was dug with the purpose of measuring snow 15 km inland from the science base (71.20259°N, 156.47471°W). The weather conditions for this day were clear skies inducing a direct light regime for the duration of the experiments. The air temperature was -27°C and there was a light north-easterly wind. The surface snow morphology was soft freshly blown snow with hard windpacked snow underneath. Figure 2a.38 shows the *e*-folding depth and albedo, Figure 2a.39 shows the snowpack density and temperature profile and Figure 2a.40 shows the snowpack stratigraphy.

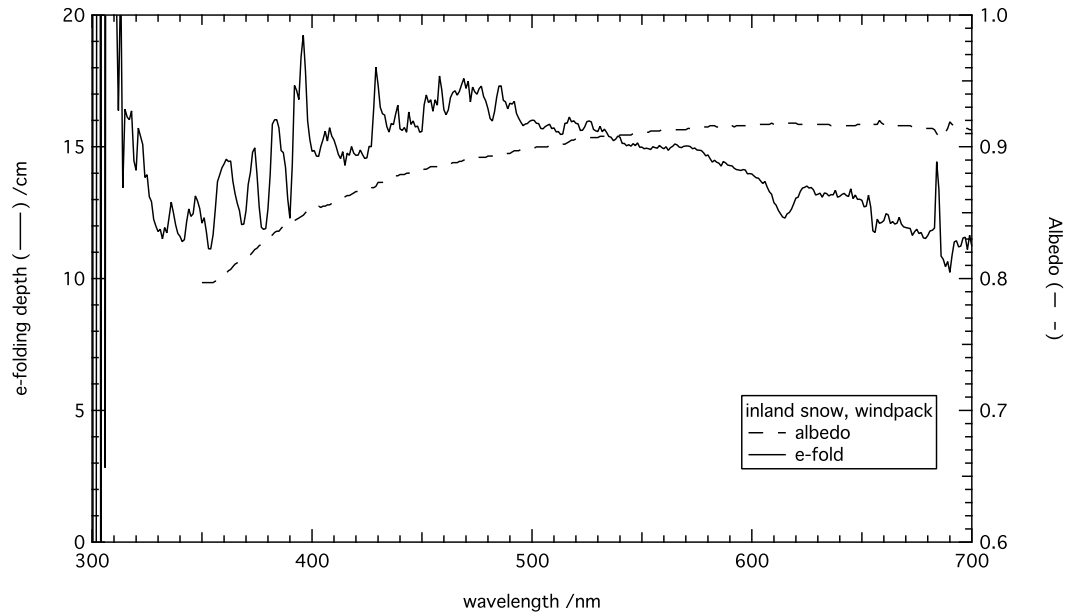

Figure 2a.38. *e*-folding depth and albedo for snowpack, day 85.

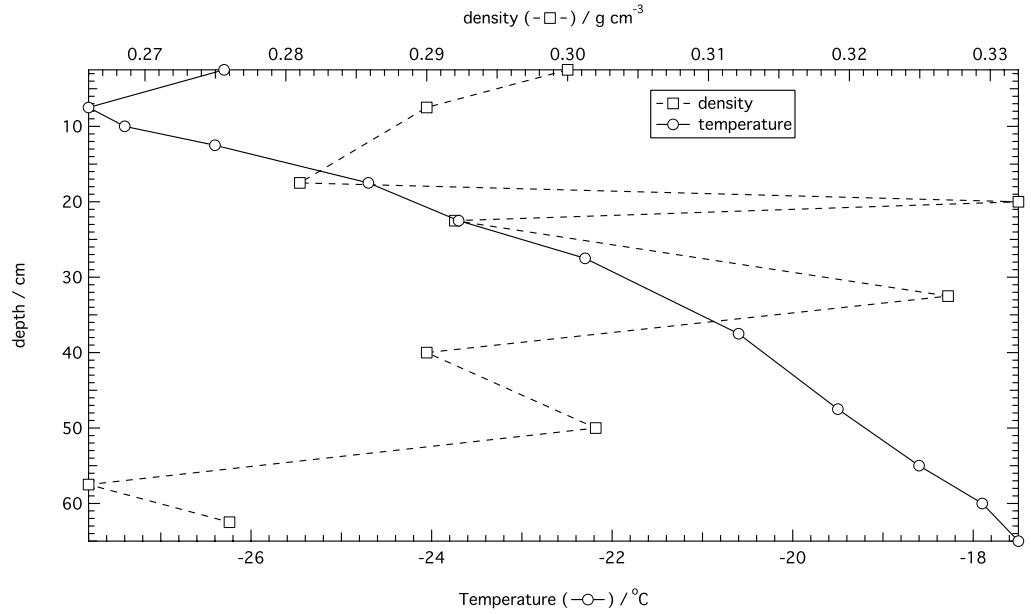

Figure 2a.39. Density and temperature profiles with depth the snowpack measured on day 85.

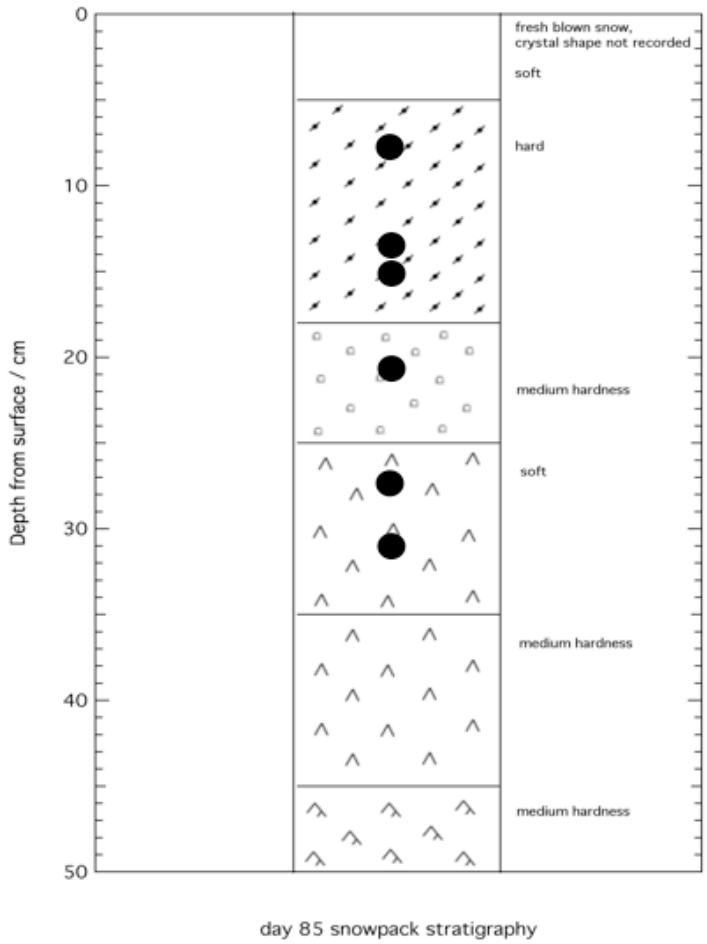

Figure 2a.40. Snowpack stratigraphy for day 85, measured by Jean-Charles Gallet. The large black circles represent the position of the fibre optic probes.

2a.4.3 Field Results

The snowpack stratigraphy shows the similarities between the snowpacks and also the differences. Generally, the stratigraphy consisted of a basal depth hoar with intermediate layers of faceted crystal and top layers of windpacks and/or recent wind-drift. The snowpacks were also often topped by a diamond dust layer of a millimetric scale (Domine *et al*, 2012). At several depths, a few thin melt-freeze crusts were sometimes observed. Depth hoar layers are typical of the snowpack of Alaska's Arctic Coastal Plain (Sturm and Liston, 2003) and are formed through

snowpack metamorphism due to the presence of a strong temperature gradient (Sturm and Listron, 2003).

The snow on sea-ice was similar to that on land but a greater variability of depth and stratigraphy could be seen with a greater frequency of occurrence of melt-freeze crusts. Supercooled droplets generated by nearby open leads may have frozen on the snow surface creating the frequent melt-freeze crusts.

The nadir reflectivity in the visible spectrum is similar for inland snow, snow on sea-ice and soft snowpack with a peak reflectance occurring at a wavelength of 600 nm. Clean snowpack measurements taken in central Antarctica by France *et al* (2011a) suggest a peak reflectance in the region of 470-520 nm, a shorter wavelength than that seen in Barrow. Warren *et al* (2006) has previously noted the shift in maximum albedo attributing it to the presence of dust or organic matter, therefore absorbing impurities within the snowpack cause the differences in reflectivity between Barrow snowpack and Antarctic snowpacks (France *et al*, 2011b).

The *e*-folding depths of the hard and soft snowpack measured around the BARC building and snow on sea-ice measured 1-2 km offshore away from the settlement are essentially the same. The inland snowpack shows the largest *e*-folding depth of ~15 cm at a wavelength of 400nm and soft snowpack shows the smallest *e*-folding depth of ~10 cm at 400 nm.

2a.5 Discussion

2a.5.1 Critique of technique

The main problem in the technique of measuring *e*-folding depth is placing the fibres horizontally into the snow due to the curvature of the metal section of the probe and minor variation in snow stratigraphy (Figure 2a.41). Fisher *et al.* (2005) calculated that imperfectly placing the probe by ±1 cm leads to an error of 9-14% in the calculated *e*-folding depth. However, as all probe measurements are taken simultaneously in the method used here, any error in probe placement was minimised by excavating the pit wall after measurements and recording the position of the cosine corrector.

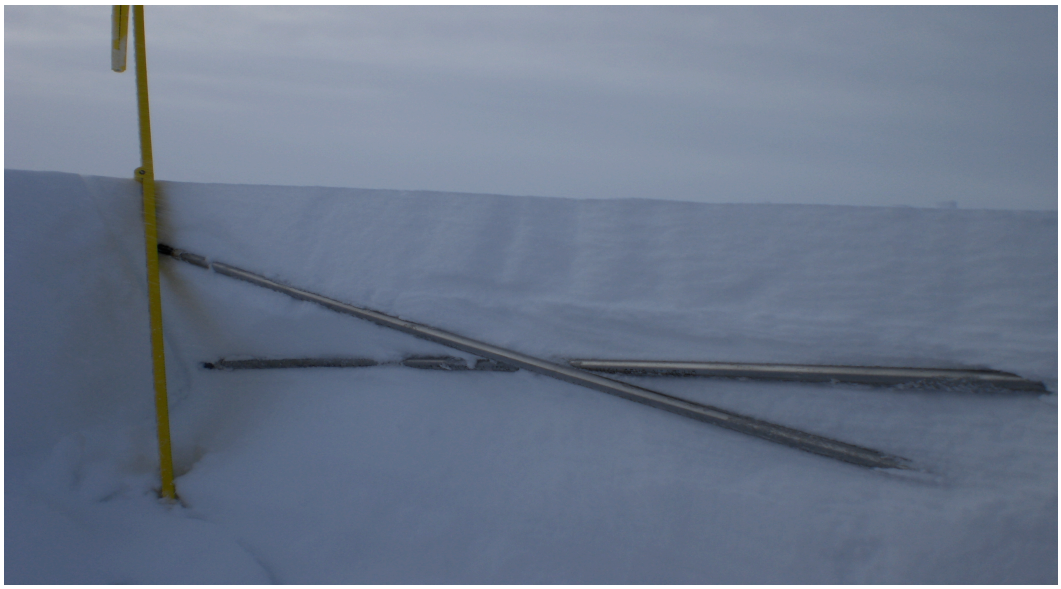

Figure 2a.41. Excavated pit showing placement of probes in snowpack. This is an extreme example.

The snow reflectivity measurements were averaged to remove any extreme values. The main problem with the bi-conical reflectance method is the small field of view produced using 3º lenses. The small field of view (3°) may cause

small surface features to be exaggerated or enhanced creating false reflectivity values (Grenfell *et al.*, 1994). To improve data the spectrometers should be elevated higher above the ground, this will enlarge the field of view and reduce the resolution. Changing weather and solar conditions may also influence reflectivity measurements; to reduce the impact, measurements were made under similar conditions as much as possible and bad data discarded when possible.

2a.5.2 Errors/uncertainties

The variability of reflectance and *e*-folding measurements are considered first. France *et al* (2011b) determined an uncertainty in *e*-folding depth for horizontally placed fibre optic probes. However, the study presented here uses fibre optics to record irradiance concurrently at 6 depths rather than at 4 depths consecutively (France *et al*, 2011b) therefore it is expected that the error of 1σ (~20%) can be considered a maximum. An example value for the maximum uncertainty in the *e*-folding depth measurements of day 69 at 400 nm was ±1.98 cm. The uncertainty of the fiber placement far exceeds the uncertainty in spectroradiometry and therefore dominates the uncertainty in the *e*-folding depth measurement technique. (France, 2011a). The angle of the fibre optic probe within the snowpack did not affect the *e*-folding depth measurement (France *et al.*, 2010).

Natural variation of the snowpack surface and measurement error in the set up of the equipment owing to topography are the most likely uncertainties in the reflectance data. To combat the likelihood of topographical error, the reflectance equipment should be elevated to extend the field of view per measurement and

reduce the effect of the natural variance of snow and sampling bias by small features. A 2° slope can give up to a 10% change in albedo, depending upon illumination angle (Grenfell *et al*, 1994). Repeat reflectance measurements have previously shown the variability to be ~10% using the single spectral radiometer method (Fisher *et al*, 2005) and a typical 2σ uncertainty using the dual beam system is ±5% of the mean average albedo (Anderson *et al*., 2006; Rollin *et al.*, 1998). An example for the uncertainty of the albedo value on day 69 at 400 nm is ±0.045. Different operating temperatures of the two spectrometers may cause the uncertainty. Matzl and Schneebeli (2006) used near infra-red photography to show, in terms of snow specific area, how laterally and vertically variable homogeneous snowpacks can be.

The methods for measuring snow stratgraphy, density and temperature have been used previously, e.g. Beine *et al* (2006), Fisher *et al* (2005) and no problems have been detected. Stratigraphic analysis can be subjective due to quantitative analysis. The detail of the stratigraphy provides sufficient information for snowpack analysis but could be improved with more advanced equipment.

The variation in the optical measurements can be rationalized due to locality with a large influence from marine sources shown in sites with close proximity to the coast.

To improve *e*-folding depth and reflectance measurements, a system should be constructed to allow measurements to be taken throughout the day therefore reducing solar condition influence. An attempt was made on day 78 to measure

successive sections of snowpack and determine the reproducibility of *e*-folding depth measurements. The measurements were undertaken along an artificial snowbank next to the access road from the base headquarters to the science building, a location where contamination of the snowpack may vary greatly within a short distance. The depth at which the fibre optic probes were placed in the snow ranged between 2–40 cm. The measurements were conducted over a 4 hour period, during which the sky conditions changed drastically from cloudy with low haze to clear skies. Considering all the aforementioned factors, the measurements taken on day 78 were not representative of the ability to reproduce *e*-folding results and thus have not been considered further.

2a.5.3 Comparison with previous work

For this work, the shortest wavelength that *e*-folding depths are reported at is 350 nm and the *e*-folding depths for the four representative Barrow snowpack types (hard snowpack, soft snowpack, inland snowpack and snow on sea-ice) range between 7-12 cm. Rowland and Grannas (2011) previously measured broadband *e*-folding depths in Barrow snowpack of 8 cm in spring and 26 cm in summer, using a solid-state chemical actinometry method. Only 3 depth measurements of in-snow actinometry were used to calculate the *e*-folding depths, the wavelength peak of the action spectrum was ~340 nm (Rowland and Grannas, 2011). The measurements of Rowland and Grannas (2011) are consist with the wavelength resolved measured *e*-folding depths presented in this study.

Previous work using fibre optic probes to measure *e*-folding depth by France *et al* (2011b) determined an uncertainty in *e*-folding depth of ± 20%. However, France *et al* (2011b) recorded irradiance at 4 depths consecutively so it is expected that the error can be considered a conservative maximum as the study presented here recorded irradiance at 6 depths concurrently. The three snowpacks within the vicinity of Barrow (snow on sea-ice, hard and soft) can be described as optically the same within uncertainty, but the inland snowpacks has a 50% longer *e*-folding depth at a wavelength of 400 nm.

To facilitate comparisons with previous work, the measured *e*-folding depths can be converted to liquid equivalent *e*-folding depths using E2a.5 (Lee-Taylor and Madronich, 2002; Warren, 1982).

$$\varepsilon_{liq} = \frac{\rho_{snow}}{\rho_{water}} \varepsilon \qquad \text{(E2a.5)}$$

where ρ is the density, ε is the measured *e*-folding depth and ε_{liq} is the equivalent *e*-folding depth.

Grenfell and Maykut (1977) reported liquid equivalent *e*-folding depths for Arctic snow on sea-ice of 2-3 cm and King and Simpson (2001) and Fisher *et al* (2005) reported liquid equivalent *e*-folding depths for Northern hemisphere snows of between ~1.5-~16 cm. For the snowpacks in Barrow, the liquid equivalent *e*-folding depths are in the range of 3.8-4.5 cm at a wavelength of 400 nm with the snowpacks studied on sea-ice and around the BARC building showing comparable values to springtime measurements made at Ny-Ålesund (France *et al*, 2011b; Gerland *et al*, 1999). It should be noted that *e*-folding depths will depend upon metamorphic history and season (France *et al*, 2010).

The nadir reflectivity was relatively consistent between snowpacks at Barrow, between 0.82 and 0.85 at 400 nm and between 0.84 and 0.91 at 500 nm. The reflectivity measurements typically have an uncertainty of two standard deviations and the variation at each site is likely to be caused by localized impurities or changes in surface topography. Previous work by Grenfell *et al* (1994) investigating albedo uncertainty suggests that a 2º slope, depending upon the illumination angle, can lead to a 10% change in albedo. Previous analysis of reflectance of dry snow at Barrow by Grenfell and Maykut (1977) recorded a value of 0.92 at a wavelength of 400 nm and France *et al* (2011b) recorded a reflectance value of 0.98 at a wavelength of 400 nm for clean Antarctic snow. It is thought that the low reflectivity of the Barrow snowpacks studied here is attributable to highly absorbing black carbon and humic material within and on

the snowpack and a detailed investigation of the effect of impurities on barrow snowpack can be found in chapter 2c.

2a.6 Conclusions

The use of optical properties and physical properties (snowpack stratigraphy) to classify snow have been shown to be valid methods. However, as seen by the four representative snowpacks of Barrow, even optically similar snowpacks can be stratigraphically different and therefore the physical and optical properties must be derived for each snowpack investigated rather than relying upon using 'typical' snowpacks from similar latitudes and localities.

The optical properties of the snowpack are important parameters needed to calculated in-snow photochemical production rates using a radiative-transfer model and a detailed description of their use can be found in chapter 2b.

Chapter 2b

Photolytic Production Rates of Snowpack in Barrow, Alaska: OASIS Spring Campaign 2009

Results from this chapter have been published in "Hydroxyl radical and NO_x production rates, black carbon concentrations and light-absorbing impurities from field measurements of light penetration and nadir reflectivity of on-shore and off-shore coastal Alaskan snow", J.L. France, H.J.Reay, M.D. King, D. Voisin, H.W. Jacobi, F. Domine, H. Beine, C. Anastasio, A. MacArthur and J. Lee-Taylor (2012), *Journal of Geophysical Research*, *117*(D00R12), doi:10.1029/2011JD016639 (see Appendix 1)

2b.1 Introduction

Recent evidence has shown that sunlit snowpack and ice play an important role in generating photochemical species and the subsequent release of these species may significantly impact the chemistry of the overlying atmosphere (e.g. Grannas *et al.,* 2007). Snowpack acts as an effective efficient medium for chemical photolysis of ice species that can be subsequently released into the atmosphere (Domine and Shepson, 2002; Grannas *et al.*, 2007). Several studies have observed the fluxes of gaseous NO, NO_2 and HONO from snow cover (Beine *et al.*, 2001; 2002; 2003; 2008; Dibb *et al*, 2004; Grannas *et al.*, 2007; Honrath *et al.*, 1999; 2000a; 2002; Jones *et al.*, 2000; 2001; Wang *et al.*, 2008). The contribution of snow photochemistry to the atmosphere is controlled in part by the

optical properties of the snowpack i.e. snow albedo and light penetration depths in snow. Laboratory studies have demonstrated that the source of gaseous NO_x (NO + NO_2) is from the photolysis of nitrate and nitrite within the snow/ice (Anastasio and Chu, 2009; Boxe and Saiz-Lopez, 2008; Chu and Anastasio, 2003; Cotter *et al.*, 2003; Couch *et al.*, 2000; Dubowski *et al.*, 2001; 2002; Honrath *et al.*, 2000b) and emissions can significantly impact the overlying boundary layer atmospheric chemistry (Dibb and Arsenault, 2002; Domine and Shepson, 2002; Grannas *et al.*, 2002; Houdier *et al.*, 2002; Impey *et al.*, 1999). Photochemical reactions can dilute the amount of precursor material in the snow and ice thus causing false signal/proxies in ice cores leading to wrongly interpreted past environmental conditions.

Photolysis of nitrate, NO_3^-, in the snowpack produces a molecular flux of NO_2 from the snowpack to the atmosphere (R2b.1) (Anastasio and Chu, 2009; Beine *et al*, 2006; Chu and Anastasio, 2007; Fisher *et al.*, 2005; France *et al.,* 2007; 2010; King and Simpson, 2001; Simpson *et al.*, 2002). Hydroxyl radicals, OH, are also produced in the snowpack by photolysis of the nitrate anion (R2b.1) (Anastasio *et al.,* 2007), hydrogen peroxide (R2b.2) and nitrite (R2b.3) (all naturally found in snowpacks).

$$\begin{aligned} NO_3^- + h\nu &\rightarrow NO_2 + O^- \\ O^- + H_2O &\rightarrow OH + OH^- \end{aligned} \qquad \text{(R2b.1)}$$

$$H_2O_2 + h\nu \rightarrow 2OH \qquad \text{(R2b.2)}$$

$$\begin{aligned} NO_2^- + h\nu &\rightarrow NO + O^- \\ O^- + H_2O &\rightarrow OH + OH^- \end{aligned} \qquad \text{(R2b.3)}$$

Hydroxyl radicals are extremely reactive and will react with snowpack chemical impurities releasing gaseous products from the snowpack into the interstitial air of the snow and to the atmosphere (Couch *et al.,* 2000; Dassau *et al.*, 2002, Grannas *et al.,* 2004; 2007; Hutterli *et al.,* 2003; 2004; Jacobi *et al.,* 2004b; Shepson *et al.*, 1996; Wang *et al.,* 2008). Production of hydroxyl radicals may be responsible for halogen activation and fluxes of organic chemicals from the snow (e.g. Abbatt *et al.,* 2010; Chu and Anastasio, 2005; Domine and Shepson, 2002; Oum *et al.,* 1998; Peterson and Honrath, 2001). It has been demonstrated through chemical modelling studies that 93-99% of hydroxyl radical production is due to hydrogen peroxide photolysis (Anastasio *et al.*, 2007; France *et al.,* 2007). Field measurements for photoformation rate of OH radicals in snow at Summit, Greenland agree with the modelling predictions (Bock and Jacobi, 2010; Thomas *et al.,* 2011). Larger *e*-folding depths (e.g. Fisher *et al*., 2005; France *et al.*, 2010) and less snowpack absorption (i.e. less black carbon or other light absorbing snow impurities such as dust or HULIS) (e.g. Reay *et al.*, 2012) are associated with larger molecular fluxes of nitrogen dioxide from the snowpack or larger yields of hydroxyl radicals in the snowpack. Chemical box modelling (Bock and Jacobi, 2010; Thomas *et al.,* 2011) has recently demonstrated that the concentration of OH radicals in the quasi-liquid layer surrounding snow grains may be a rate-controlling factor in the release of Br_2 into the interstitial air (Abbatt *et al*., 2010) thus OH radicals are important in snowpack chemistry. Similar reactions occur in sea-salt particles demonstrating that sea-ice is a source of gaseous bromine through the reaction of sea-ice with ozone (e.g. George and Anastasio, 2007, Oum *et al.* 1998) .

Photolytic production rates of OH radicals and NO_2 within snowpack have been previously calculated for several terrestrial snowpack environments including Arctic, Antarctica and mid-latitude snowpacks (e.g. Anastasio *et al.,* 2007; Beine *et al.,* 2006; Chu and Anastasio, 2007; Fisher *et al.,* 2005; France *et al.*, 2007; 2010; 2012; King and Simpson, 2001; Simpson *et al.,* 2002). The Alaskan site of Barrow allows the opportunity to measure the optical properties of coastal snow both on land and on sea-ice for snow that is much more characteristic of Arctic snow. Measurements of *e*-folding depth, nadir reflectance and snow stratigraphy taken at Barrow, Alaska are used to determine the light absorption and scattering cross-sections of the snowpack from snow-atmosphere coupled radiative-transfer calculations (Chapter 2a). The scattering and absorption cross-sections are used to calculate "actinic flux" (spherical or point irradiance) in the snowpack as a function of depth, solar zenith angle and atmospheric conditions, thus allowing the photolysis rate coefficients of reactions (2b.1-2b.3) to be calculated. The absorption cross-section of ice is well studied (Warren and Brandt, 2008) allowing the absorption spectrum of light-absorption impurities to be determined. In an attempt to identify and quantify the amount of absorbers within the snowpack, the variation of absorption cross-section due to impurities in the snowpacks with wavelength is compared to absorption cross-section of known absorbing species.

2b.2 Aims

The measurements of snowpack optical properties made at Barrow, Alaska were part of the larger OASIS international field campaign.

The aims of the work presented in this chapter are to:

1. Calculate wavelength-dependent cross-sections for light absorption due to impurities and for scattering for snowpack from measurements of *e*-folding depth and snowpack surface reflectivity (discussed in chapter 2a).
2. Calculate in-snow production rates of NO, NO_2 and OH radicals for the duration of the OASIS campaign as an estimation of the potential flux of NO_2 or NO from the snowpack.
3. Determine the identity and amount of light-absorbing impurities in the Alaskan snowpack from the absorption cross-sections determined from field measurements of the snowpack throughout the campaign.

2b.3 Methods

Snowpacks located within 1-15 km of the BARC (71.32063°N, 156.6748°W) were investigated as part of the OASIS campaign during Spring 2009. The field season of 4th March 2009 to 1st April 2009 was designed to match the field seasons of our collaborators. The principal aim of the fieldwork was to measure the optical and physical properties of the snowpack at Barrow, Alaska.

Several snowpacks were optically studied in detail at locations around the OASIS field site (data in appendix - Barrow) and 4 snowpacks that represented different snowpack types were chosen for detailed analysis. The decision about where to conduct the field experiments was based on 4 main factors: how undisturbed the snow was, how representative of general snow conditions the snowpacks were, the depth of the snowpack and the proximity to other collaborators. At each site, a snowpit (~1 m width by ~1 m length) was dug to the depth of the ground or the

sea-ice surface. The snow was not contaminated by anthropogenic or animal influence. Measurements of light penetration depth (*e*-folding depth), surface nadir reflectance and snowpack stratigraphy were undertaken at every site, the methods and results are described in chapter 2a.

In this chapter, four representative snowpacks from Barrow, Alaska are studied in greater detail – soft snowpack, hard snowpack, inland snowpack and snow on sea-ice, these four snowpacks represent the snows found around Barrow in Spring. Measurements of *e*-folding depth, nadir surface reflectance and snowpack stratigraphy from chapter 2a were used to calculate scattering and absorption cross-sections of the four snowpacks and photochemical production rates, the methods are described here:

2b.3.1 Determining Scattering and Absorption Coefficients

Using the method of Lee-Taylor and Madronich (2002), wavelength-dependent cross-sections of light scattering, $\sigma_{scatt}(\lambda)$, and absorption due to impurities, $\sigma^{+}_{abs}(\lambda)$, were determined for the four Barrow snowpacks from measurements of *e*-folding depth and surface reflectance.

The Tropospheric Ultraviolet Visible (TUV)-snow model (Lee-Taylor and Madronich, 2002) is a one-dimensional, 8-stream, discrete-ordinates (Stamnes *et al.,* 1988) radiative-transfer model that calculates the transfer of solar radiation through atmospheric and snow layers. The model couples atmosphere and snowpack. The snow layers are defined with similar optical properties to that of cloud, i.e. weakly or non-absorbing and highly scattering, and were added at the

base of the atmospheric model (Lee-Taylor and Madronich, 2002). Using the TUV-snow model, Lee-Taylor and Madronich (2002) demonstrate that knowledge of snow grain size or shape are not needed to derive the optical coefficients that characterize a snowpack, only knowledge of bulk optical properties (surface albedo, *e*-folding depth and snow density) are needed, making the process simpler. The optical coefficients are characterised in the radiative-transfer model by three quantities (Lee-Taylor and Madronich, 2002):

1. The scattering co-efficient, r_{scatt}, is estimated from the bulk optical properties and it is assumed to be independent of wavelength because the wavelengths of radiation are at least 2 orders of magnitude smaller than the irregularities in snow crystal structure (Domine *et al.,* 2001).
2. The absorption co-efficient, $\mu(\lambda)$, defined as the sum of the absorption by pure ice, μ_{ice}, and the absorption of impurities in the snowpack, μ^{+} (E2b.1).

$$\mu(\lambda) = \mu_{ice}(\lambda) + \mu^{+}(\lambda) \qquad \text{(E2b.1)}$$

   Values for pure ice absorption used in this work are from Warren and Brandt (2008). The value of $\mu(\lambda)$, $\mu_{ice}(\lambda)$ and $\mu^{+}(\lambda)$ are variable with wavelength.
3. The scattering phase function, *g*, is defined as the angular redistribution of radiation by each scattering event (Lee-Taylor and Madronich, 2002). A value of 0.89 for g is used in this based on a Mie calculation of 100 micron particles (Wiscombe and Warren, 1980). Grenfell and Warren (1999) state

that the value of *g* is reasonably insensitive to crystal size and structure at UV-visible wavelengths.

The radiative-transfer calculations of reflectance and *e*-folding depths were interpolated to find values of σ_{scatt} (E2b.2) and σ^{+}_{abs} (E2b.3) that satisfied the measured values of albedo and liquid equivalent *e*-folding depth for each wavelength.

$$\sigma_{scatt} = \frac{r_{scatt}}{\rho} \qquad \text{(E2b.2)}$$

$$\sigma^{+}_{abs} = \frac{\mu^{+}}{\rho} \qquad \text{(E2b.3)}$$

The dependencies of measured values of surface reflectance and liquid equivalent *e*-folding depth on σ_{scatt} and σ^{+}_{abs} were plotted an example of this is shown in Figure 2b.1. The intersection points of each wavelength curve represent the best σ_{scatt} and σ^{+}_{abs} for each snowpack.

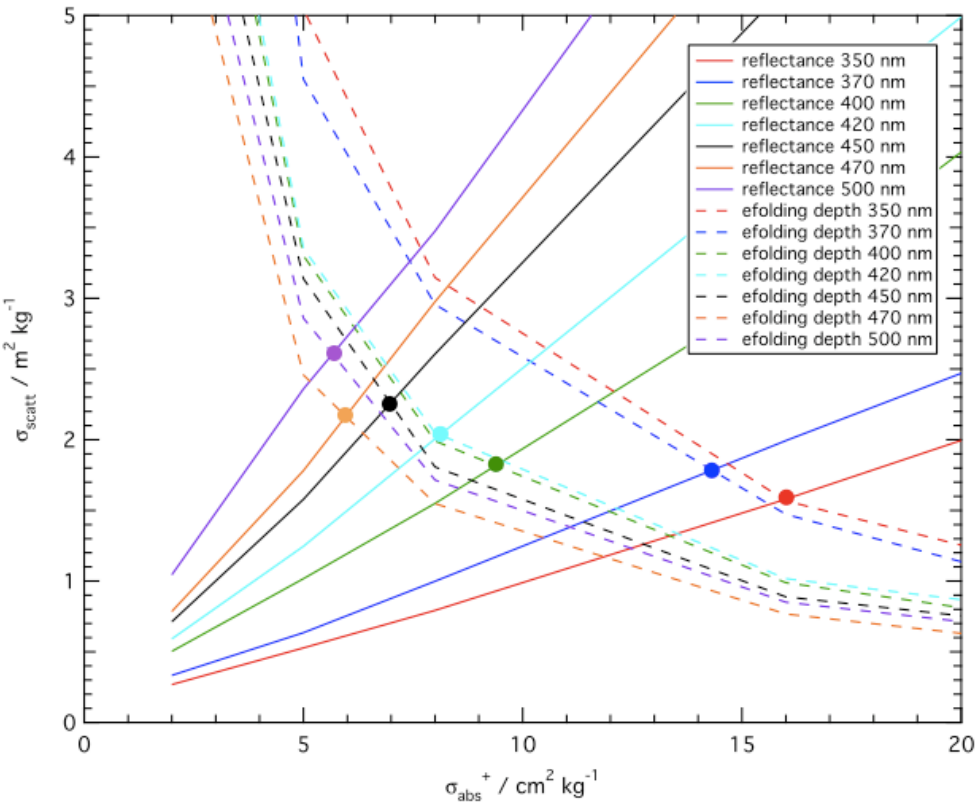

Figure 2b.1. σ_{scatt} and σ_{abs}^{+} derivation plot for inland snowpack (day 85). The point of intersection between lines of equal wavelength for albedo and *e*-folding depth (lines are the same colour) represents the values of absorption and scattering that best reproduce the measured field values of albedo and *e*-folding depth.

Figure 2b.1 gives a unique solution of σ_{scatt} and σ_{abs}^{+} for individual wavelengths, albedo and *e*-folding depth are required to derive σ_{scatt} and σ_{abs}^{+}. The lines represent values of σ_{scatt} and σ_{abs}^{+} that match albedo and *e*-folding depth therefore the intersection between the lines is the unique solution, and the reason why both albedo and *e*-folding depth have been measured.

For all the snowpits studied in Barrow, values of σ_{scatt} and σ_{abs}^{+} were derived using *e*-folding depths, surface reflectance, density and crossing-plots, as in

Figure 2b.1. The measured values used for the derivations of σ_{scatt} and σ^{+}_{abs} are shown in Table 2b.1.

Site / DOY	Snow Type	Location		Snow Density / g cm^{-3}	Column Ozone / Dobson Units	Representative snowpack
		Latitude	Longitude			
68	Soft	71.31987°N	156.67634°W	0.39	424	N
76	Soft	71.31903°N	156.67246°W	0.27	451	N
69	Hard	71.31896°N	156.67243°W	0.38	428	Y
70	Hard	71.31871°N	156.67175°W	0.39	444	N
79	Hard	71.31882°N	156.67113°W	0.39	450	Y
72	Snow on sea-ice	71.38469°N	156.45239°W	0.40	442	Y
85	Inland	71.20259°N	156.47471°W	0.29	459	Y

Table 2b.1. Locality, density and ozone conditions required for deriving absorption and scattering coefficients for each snowpit.

2b.3.2 Modelling Snowpack Absorption by Impurities

The absorption spectrum of the impurities in the snow is a summation of all the absorbers in the snowpack, it is derived by plotting the cross-section of absorption, $\sigma^{+}_{abs}(\lambda)$, owing to impurities in the snowpack versus wavelength for each snowpack. No previous study has calculated σ^{+}_{abs} in-situ snow before and most of the other studies found that an absorber was needed to make albedo values comparable to the measured snowpack. It is likely that absorbers at visible wavelengths are black carbon, brown carbon (including HULIS) and dust

(Anastasio and Robles, 2007; Doherty *et al.,* 2010; France *et al.,* 2011a; Grenfell *et al.,* 2011; Warren, 1984; Warren and Clarke, 1990; Warren *et al.,* 2006). Previous work by Lee-Taylor and Madronich (2002) assumed that all absorption by impurities was due to black carbon, a sensible assumption as black carbon is the strongest absorbing impurity. The range of wavelengths studied here (350-600 nm) allows the light-absorbing impurities to be identified by their different absorption spectra.

2b.3.3 Calculating Photolytic Rate Coefficients and Fluxes with Clear and Diffuse Skies

To calculate the photolytic rate coefficients for reactions 2b.1–3, the spherical or point irradiance ("actinic flux") in the snowpack is needed. The spherical irradiance is calculated using the TUV-snow model (Lee-Taylor and Madronich, 2002) at 1 nm intervals between 290-700 nm at 106 calculation depths in the 1 m model snowpack using the wavelength dependent snowpack optical properties, $\sigma_{scatt}(\lambda)$ and $\sigma^{+}_{abs}(\lambda)$, determined from field measurements (section 2b.10.1). Over 95% of sunlight is attenuated by 3 *e*-folding depths (France *et al.,* 2011b) thus any snowpacks thicker than 3-4 *e*-folding depths can be considered semi-infinite i.e. such a small amount of sunlight reaches past 3-4 *e*-folding depths that the reflectivity of the surface below the snow is irrelevant and the *e*-fold is asymptotic. All the snowpacks studied in Barrow, Alaska were optically semi-infinite therefore the actual recorded depth of the snowpack in the field can be considered without affecting the result when modelling photolysis rate constants and spherical irradiance in the snowpack. However, for comparison, all the snowpacks in this work are considered to be 1 m deep with conditions as shown in

Table 2b.1. Using a depth of 1 m is convenient for calculations and allows comparison between snowpacks but as long as the snowpack is semi-infinite the value of depth used is not important.

Photochemical rate coefficients, *J*, for the photolytic reactions 2b.1-3 were calculated using equation 2b.4 for solar zenith angles between 0 and 90° for both clear and diffuse sky conditions.

$$J(\theta,z) = \int_{\lambda_y}^{\lambda_x} \sigma(\lambda,T)\phi(\lambda,T)I(\lambda,\theta,z)d\lambda \qquad \text{(E2b.4)}$$

where σ is the absorption cross-section of the chromophore (NO_2^-, NO_3^- or H_2O_2), ϕ is the quantum yield for photolysis, *I* is the spherical irradiance, *T* is the snowpack temperature, λ is the wavelength, θ is the solar zenith angle, and *z* is depth in the snowpack.

The absorption cross-sections and temperature dependent quantum yields for the reactants in reactions 2b.1 and 2b.2 are from Chu and Anastasio (2003), Chu and Anastasio (2005) and Chu and Anastasio (2007). The choice of values will be jutified in the discussion section. For the calculation of photochemical rate coefficients, the average overhead column ozone, for the duration of the campaign, of 460 Dobson Units is used (McPeters *et al.,* 1998). Overhead ozone generates heat in the stratosphere by absorbing both solar radiation and upwelling radiation from the troposphere, thus increased ozone in the stratosphere results in higher temperatures (Allen, 2004). Photolysis rate coefficients were calculated for both diffuse sky (totally overcast) and clear sky (no cloud or aerosol) conditions. To obtain diffuse sky conditions, a layer of 100 m thick cumulous cloud with an optical depth of 16, an asymmetry factor of 0.85 and a single

scattering albedo of 0.9999 was placed 1 km above the ground in the model. Photolysis rate coefficients were calculated for both clear and diffuse sky conditions as the temporal and spatial variation in illumination intensity needed to be taken into account. A source of the variation is the discrimination between direct and diffuse sunlight (Spitters, 1986). For the purposes of the campaign, diffuse sky conditions were used for days when the sun was occluded. However, true diffuse sky conditions would be fog. Fog reflects less and absorbs more than cloud of the same density and thickness. To reflect 80 % of solar radiation a moderate cloud with a density of 1.0 gm m^{-3} would need a thickness of at least 150 m, whilst a dense cloud (fog) of 5 gm m^{-3} would need a thickness of at least ~50 m (Hewson, 1943).

Depth-integrated production rates, or maximum fluxes (assuming that all photoproduced NO_2 or NO is liberated from the snowpack), F, were calculated using equation 2b.5.

$$F = \int [x] J \, dz \qquad \text{(E2b.5)}$$

but if $[x]$ is independent of z then,

$$F = [x] \int_{z=0m}^{z=1m} J(z) \, dz$$

where z is the depth into the snowpack and $[x]$ is the concentration of the chromophore (H_2O_2, NO_3^- or NO_2^-). E2b.5 is independent of concentration but the equation could be written as $F \int_{z=0}^{z=1} J[x] \, dz$, if the depth profile was thought to be important.

The variation of chromophore, e.g. NO_3^-, NO_2^- or H_2O_2, concentration with depth has been shown by France *et al.* (2007) to be much less important relative to the depth-dependence of the spherical irradiance, as [*x*] varies by ~10 with depth but the spherical irradiance varies of many orders of magnitude, and therefore equation 2b.5 assumes a depth-independent concentration of chromophore. A constant nitrate concentration in the snowpack of 3.9 μmol $l_{(water)}^{-1}$ was used, this was an average concentration of more than 100 samples including all encountered snow types presented here (Jacobi *et al.,* 2012). Measurements of H_2O_2 concentration in snowpack were made at ~500 locations in the Barrow area during the campaign, concentrations were found to be fairly invariant with depth (Beine *et al.,* 2012). The calculated depth-integrated production rate of OH radicals used an average concentration of H_2O_2 measured in the top 10 cm of the snowpack, taken from Beine *et al.* (2012), of 0.4 μmol $l_{(water)}^{-1}$. Concentrations of NO_2^- were measured by Villena *et al.* (2012) at a single site near the BARC building (Figure 2b.11) over a period of 36h in surface snow and at a depth of 5 cm. The average measurement of NO_2^- in these samples was 0.02 μmol $l_{(water)}^{-1}$ and this single-site average nitrite concentration is used for all the snowpack calculations presented here.

2b.3.4 Calculating Photolytic Rate Coefficients and Fluxes From the Snowpack for Sky Conditions During the OASIS Campaign

To calculate the depth-integrated production rates (or fluxes) for the duration of the campaign an identification of sky conditions as "clear sky" or "diffuse" (i.e. thick cloud cover, an occluded solar beam) was required as the amount of cloud can affect the distribution and intensity of sunlight. The depth-integrated

production rates for UV downwelling irradiances were calculated as a function of solar zenith angle for clear sky and diffuse conditions then scaled by the measured downwelling UV atmospheric irradiance at the surface. The maximum in the action spectrums of NO_3^-, NO_2^- and H_2O_2 occur at 300 nm, 350 nm and 240 nm respectively thus UV irradiances were measured over the wavelengths of 295-385 nm as it is the wavelength region in which most photochemical reactions occur. It is assumed that $F(NO_2)$ can be scaled by the ratio of the calculated downwelling irradiance and measured downwelling irradiance. However, the relationships will be different for clear sky and diffuse sky conditions. Sky conditions throughout the campaign were monitored by two continuous measurements: broadband, downwelling irradiance for wavelengths of 295-385 nm using a TUVR (Tropospheric Ultraviolet and Visible Radiation) Eppley flat-plate radiometer sited 0.5 m above the snowpack approximately 800 m south of the BARC building, and hemispheric sky images (and retrievals of fractional sky cover for periods when the solar elevation was greater than 10 degrees) using a total sky imager (Yankee Environmental Systems). The total sky imager was based within a few kilometers of the measurement site and the Eppley TUVR at Atmospheric Radiation Measurement (ARM) site at the North Slope, Alaska (71° 19; 23.73" N, 156° 36' 56.70" W) (Long and DeLuisi, 1998; Long *et al.*, 2001). The ARM site is one of three premier solar irradiance sites and is known for high quality science, thus the data was used as supplied. Every minute of the measurement campaign, Julian Day 60-90, was assigned a sky condition (diffuse and direct) depending upon whether the sun's direct beam was occluded by cloud using the total sky imager (algorithm described in Long and DeLuisi, 1998; Long *et al.,* 2001). The radiative transfer calculations described in section 2b.10.3 were repeated to

calculate the 'flat-plate' broadband downwelling irradiance measured by the TUVR Eppley radiometer from 295 nm to 385 nm for the diffuse and clear sky conditions as a function of solar zenith angle under exactly the same conditions as the photolysis rate constants were calculated. The calculated photochemical fluxes of NO_2 and OH radicals were then used for equations 2b.6, 2b.7 or 2b.8 respectively to produce photochemical production rates of OH radicals, NO_2 and NO at a 1 min resolution for the whole period of the Barrow campaign.

$$\mathrm{F(OH)_{production}} = \frac{I_{\mathrm{TUVR\ measured}}}{I_{\mathrm{TUVR\ modelled}}} \mathrm{F(OH)_{modelled}} \qquad \text{(E2b.6)}$$

$$\mathrm{F(NO_2)_{production}} = \frac{I_{\mathrm{TUVR\ measured}}}{I_{\mathrm{TUVR\ modelled}}} \mathrm{F(NO_2)_{modelled}} \qquad \text{(E2b.7)}$$

$$\mathrm{F(NO)_{production}} = \frac{I_{\mathrm{TUVR\ measured}}}{I_{\mathrm{TUVR\ modelled}}} \mathrm{F(NO)_{modelled}} \qquad \text{(E2b.8)}$$

where $I_{TUVR\ measured}$ is the downwelling broadband irradiance for 295-285 nm measured by the Eppley TUVR and $I_{TUVR\ modelled}$ is the calculated downwelling broadband irradiance for 295-385 nm as a function of solar zenith angle and sky and snow conditions. The quantity F(OH) is the depth-integrated production rate of hydroxyl radicals and $F(OH)_{modelled}$ is the depth-integrated production rate of hydroxyl radicals calculated by the radiative-transfer modelling described in section 10.2.3. Note, the values of $F(OH)_{modelled}$ and $I_{TUVR\ modelled}$ correspond to the same solar zenith angle and sky conditions.

The relationships described in E2b.6-E2b.8 assume a linear dependence between F and *I*, and the theory will be tested later in the chapter.

2b.4 The Radiative-Transfer Model

TUV-snow (Tropospheric Ultraviolet and Visible-snow) model (Lee-Taylor and Madronich, 2002) was used to perform radiative-transfer calculations. TUV-snow is a discrete-ordinates (Stamnes *et al.,* 1988) coupled atmosphere-snow model running 8 streams with a pseudo-spherical correction. The model configuration for this study used 106 snowpack levels (with 1 mm spacing in the top 0.5 cm and 1 cm spacing for the rest of the 1 m snowpack) and 80 atmospheric levels spaced at 1 km intervals, clear skies, no atmospheric aerosol, and Earth-Sun distance based upon the day of measurements and an average overhead ozone column for the duration of the campaign (McPeters *et al.,* 1998). As stated in section 2b.3.1, the snow asymmetry factor, *g*, was set to 0.89 (Wiscombe and Warren, 1980). Tests were conducted to assess the impact of varying the asymmetry factor and are discussed later in the chapter. The recommended absorption cross-section for ice from Warren and Brandt (2008) was used and linearly interpolated from 200 nm to 400 nm where the complex index of refraction is too small to be reliably measured at present (Figure 2b.2).

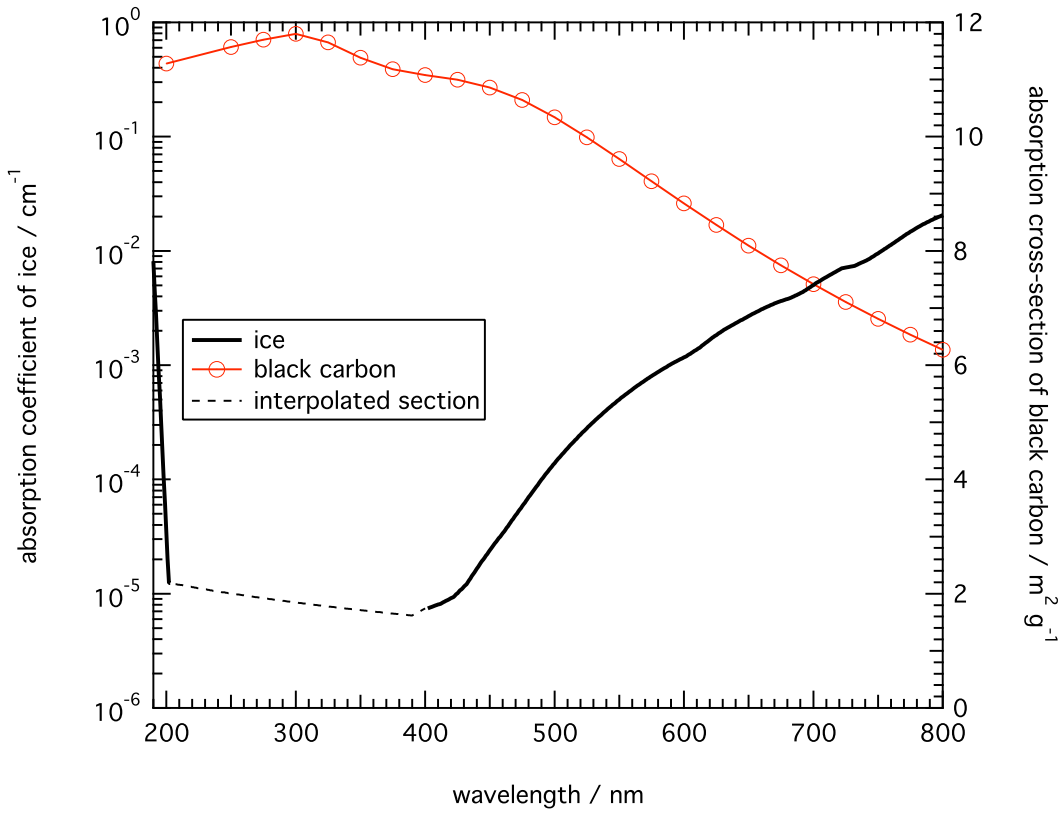

Figure 2b.2. Absorption coefficient of ice and the absorption cross-section of a spherical black carbon particle. The latter is calculated from Mie theory (density = 1 g cm^{-3}, complex index of refraction = 1.9-0.5i, media index of refraction = 1.0, particle size radius = 0.1 μm). See Warren and Brandt (2008, Figure 1), Warren and Wiscombe (1985, Figure 1) and Warren and Wiscomve (1980a; 1980b) for further details. Note, the absorption coefficient of ice is logged.

Table 2b.2 contains the data used as inputs for modelling the photolysis rate coefficients for the four representative Barrow snowpacks.

Snowpack	Snow Temperature / °C	Snow Density / g cm^{-3}	Location		Elevation / m	Average Column Ozone[a] /Dobson Units
			Latitude	Longitude		
Hard	-15	0.39	71.31896°N	156.67254°W	~5	460
Soft	-18	0.38	71.31987°N	156.67634°W	~5	460
Snow on sea-ice	-24	0.40	71.38469°N	156.45239°W	0	460
Inland	-28	0.30	71.20259°N	156.47471°W	~2	460

Table 2b.2. Data used as inputs for the modelling of photolysis rate coefficients using TUV-snow for the four representative Barrow snowpacks. [a] Ozone conditions determined from the NASA TOMS program as an average of the campaign duration to 2 significant figures (McPeters *et al.,* 1998).

2b.5 Results

The results focus on 4 key areas: snowpack optical coefficients determined from the field measurements, absorption by impurities, photolytic rate constants and the calculated depth-integrated production rates of NO_2, NO and OH radicals within the snowpack. Data from the four representative snowpacks are presented: hard and soft snows (prevalent around Barrow and the BARC building), snow on sea-ice and inland snow (~15 km inland from Barrow).

2b.5.1 Optical Coefficients of Barrow Snowpack

Figures 2b.3 and 2b.4 show the wavelength-dependent scattering, σ_{scatt}, and absorption, $\sigma^{+}_{abs}(\lambda)$ coefficients for the four representative Barrow snowpacks.

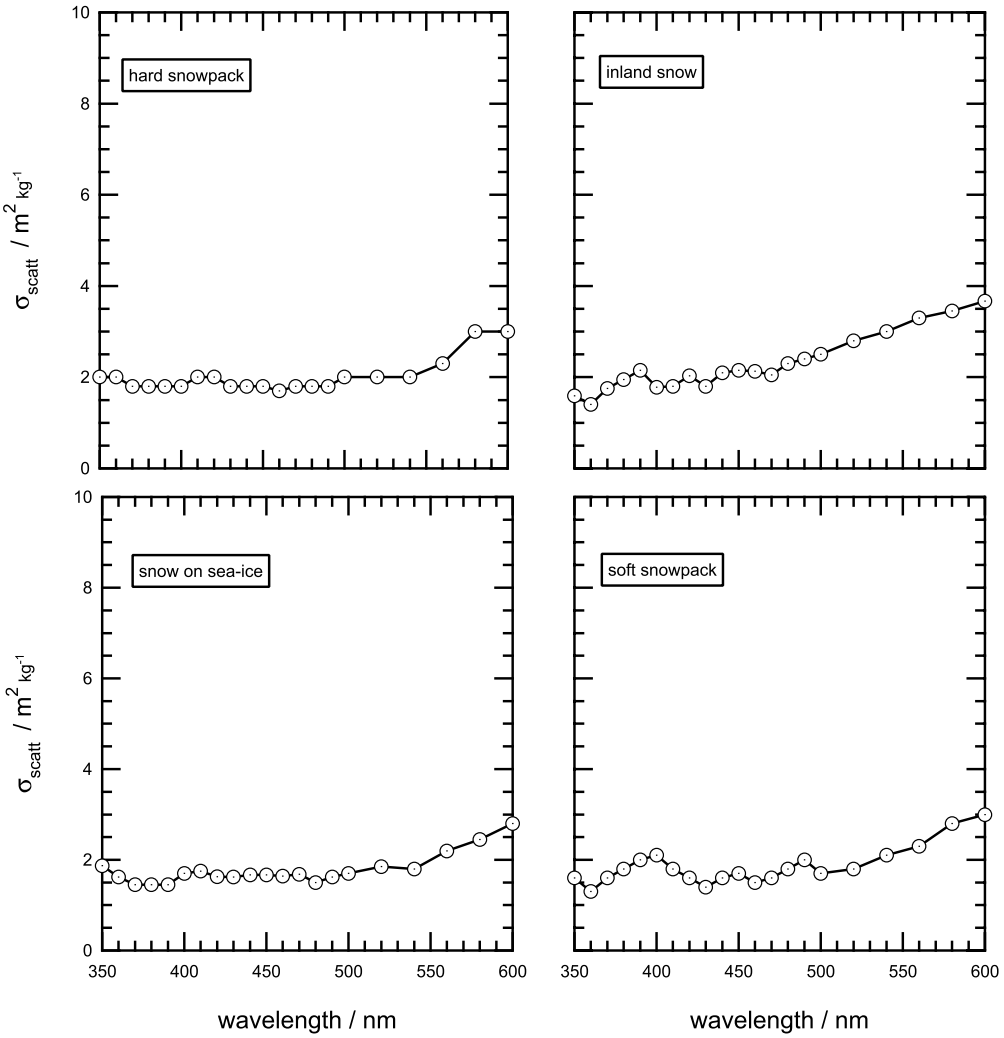

Figure 2b.3. Wavelength dependence of the scattering coefficient, σ_{scatt}, for the four snowpacks studied in Barrow, Alaska (France *et al.,* 2012). All the snowpacks demonstrate a broadly invariant relationship of scattering coefficient with wavelength. Conditions used to determine the values are described in Table 2b.2. The typical uncertainty in σ_{scatt} owing to a 5% change in snowpack density is $\pm^{7\%}_{5\%}$.

Several studies have previously determined snowpack optical extinction coefficients (Beine *et al.,* 2006; Fisher *et al.,* 2005; France *et al.,* 2010; Lee-Taylor and Madronich, 2002) at a wavelength of 400 nm in a variety of locations.

A comparison between the results from Barrow and previous studies can be found in Table 2b.3.

Study	Snow Description	σ_{scatt} / m^2 kg^{-1}	σ^{+}_{abs} / cm^2 kg^{-1}
Grenfell and Maykut (1977)	Arctic Summer dry[a]	6.4	7.3
	Arctic Summer melting[a]	1.1	7.8
Fisher *et al.* (2005)	Midlatitude windslab – melting	1	1
	Midlatitude windslab – dry	2-5	1-2
France *et al.* (2010)	Fresh Ny-Ålesund snowpack	16.7	2.7
	Melting Ny-Ålesund snowpack	0.8	19.8
France *et al* (2011b)	Ny-Ålesund – old windpack	9.5	1.4
	Ny-Ålesund – fresh windpack	7.7	5.4
	Ny-Ålesund – marine influenced	20	3.4
	Ny-Ålesund – glacial accumulation zone	25.5	0.5
King and Simpson (2001)	Arctic spring windblown[a]	6-30	4-25
This work	Barrow – hard snowpack	1.7	11
	Barrow – soft snowpack	2.0	11
	Barrow – snow of sea-ice	1.7	15
	Barrow – inland snowpack	1.8	9

Table 2b.3. A comparison of optical coefficients previously determined for Arctic and Northern Hemisphere snowpacks at a wavelength of 400 nm. Note that the values of σ^{+}_{abs} and σ_{scatt} for the four Barrow snowpacks are very similar. [a] Modelling optical coefficients conducted by Lee-Taylor and Madronich (2002), not in the original measurement study.

The typical error on the scattering coefficient has been calculated to be ~1 m^2 kg^{-1} (France *et al.,* 2012) and thus the scattering coefficient can be considered to be effectively constant (within uncertainty) across the wavelength range of 350-600 justifying the assumption by Lee-Taylor and Madronich (2002) that σ_{scatt} is wavelength-independent. The values of σ_{scatt} are ~2 m^2 kg^{-1} at 400 nm, similar to the midlatitude dry windslab studied by Fisher *et al.* (2005), and both the scattering and absorption coefficients are similar to snowpacks previously determined for summer Alaskan snow on sea-ice in Lee-Taylor and Madronich (2002) using data from Grenfell and Maykut (1977) as described in Table 2b.3.

The snowpack impurity absorption cross-sections were calculated over the wavelength range of 350-600 nm, this is work that has not been done before. The snowpack impurity absorption cross-sections (Figure 2b.4) all show a general trend of decreasing absorption with increasing wavelength from 350-550 nm and a smaller increase from 550-600 nm with the exception of inland snow. At longer wavelengths, the inland snowpack has a lower absorption cross-section that the other snowpacks. The comparison of Barrow snowpack absorption cross-sections in Table 2b.3 shows that the Barrow snowpacks are highly absorbing compared to other dry Arctic snowpacks. Lee-Taylor and Madronich (2002) assumed that both σ_{scatt} and σ^{+}_{abs} could be modelled as constant with wavelength, yet the value of σ^{+}_{abs} is clearly not constant with wavelength in the UV-visible wavelength region.

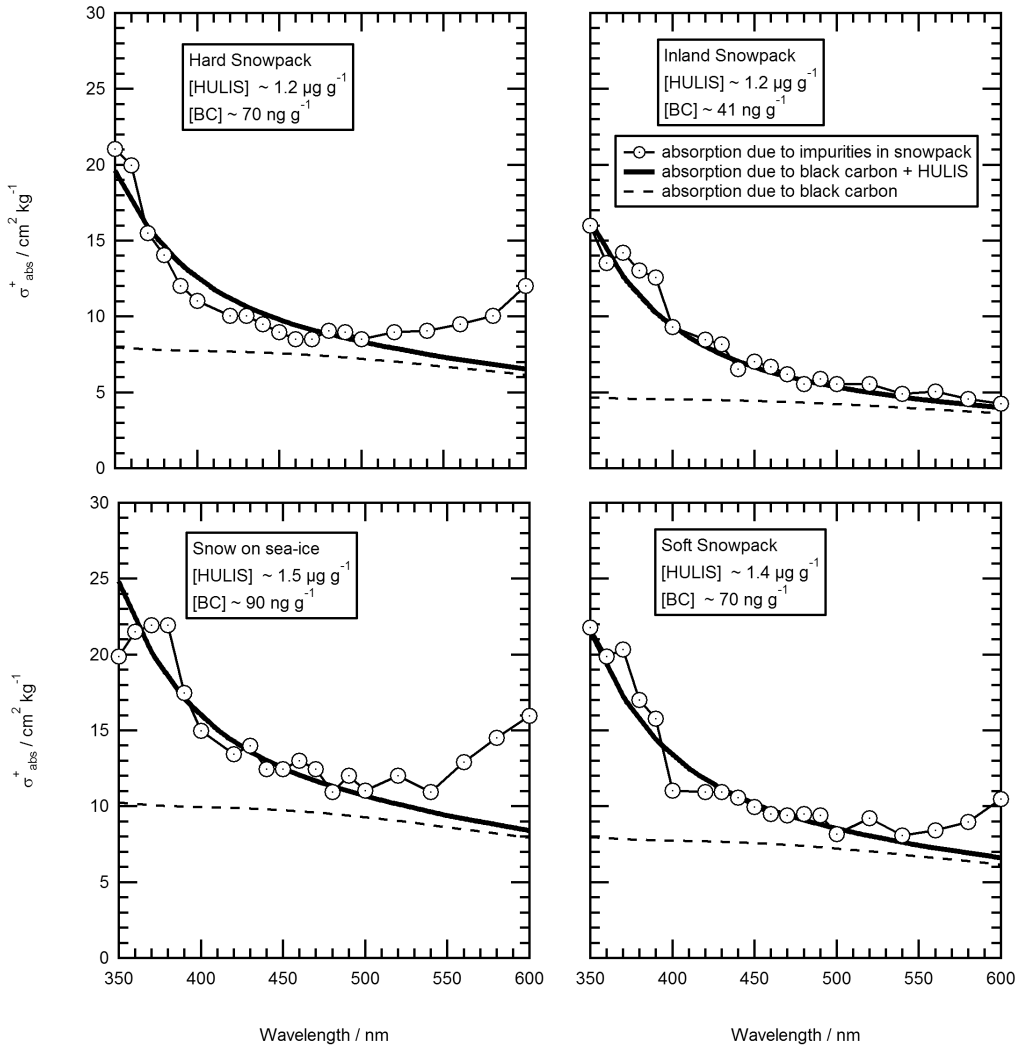

Figure 2b.4. Black carbon (BC) and HULIS (Humic Like Substances) absorption cross-sections fitted to total snowpack impurity absorbance for the four representative Barrow snowpacks. The lines with round markers are absorptions due to impurities within the snowpack derived from field measurements, the dashed line is black carbon absorption and the thick solid line is combined black carbon and HULIS absorption.

2b.5.2 Snowpack Absorption by Impurities

The majority of absorption by impurities can be fitted by combining absorption cross-sections of particulate black carbon and particulate HULIS (Figure 2b.4). Other impurities such as dust may also contribute to impurity absorption in

snowpacks, however, there was a lot of visual evidence of plant material and soil in the snow at Barrow.

The black carbon absorption spectrum was calculated from a Mie calculation that assumed spherical black carbon particles in the snow with a radius of 0.1 μm, density of 1 g cm^{-3} and a refractive index of 1.8-0.5i in concurrence with work by Warren and Wiscombe (1980; 1985). The black carbon absorption cross-section is presented in Figure 2b.5 along with black carbon absorption values reviewed by Bond and Bergstrom (2006).

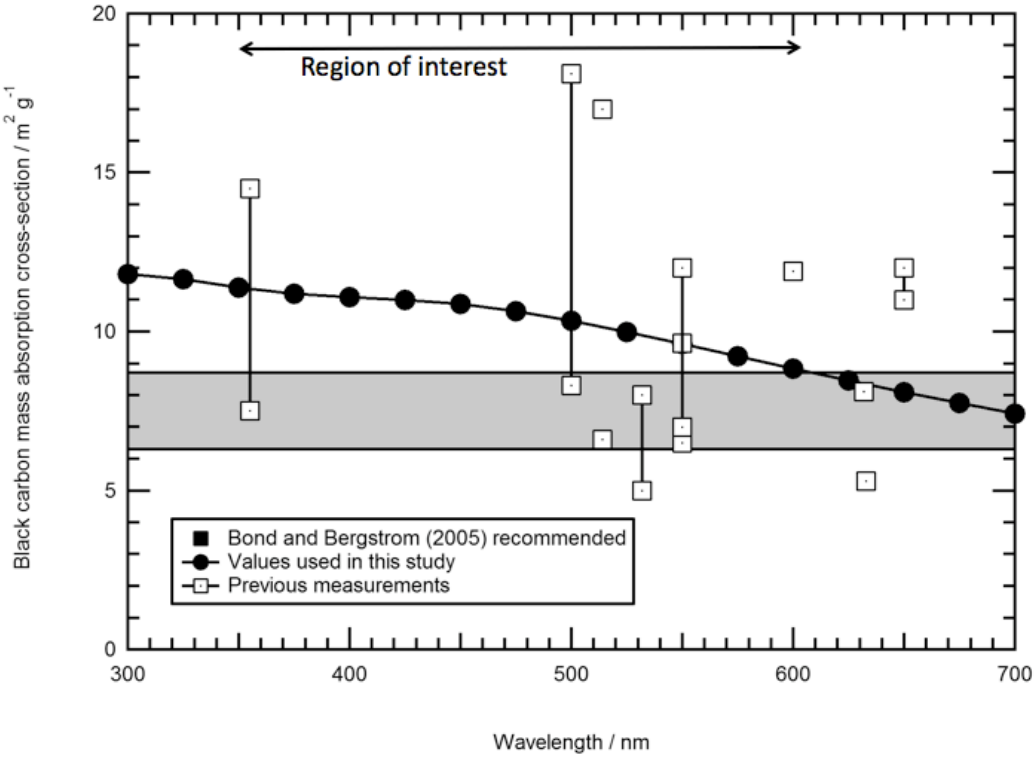

Figure 2b.5. Black carbon mass absorption cross-section. The filled circles are the absorption cross-section used in the work described here (based on the Mie calculation described in the text). Black carbon absorption cross-section values measured and reviewed by Bond and Bergstrom (2006) or measured by Adler *et al.* (2010) are represented by the unfilled squares. The value of 7.5 ± 1.2 m^2 g^{-1} recommended by Bond and Bergstrom (2006) for the black carbon mass absorption cross-section is represented by the shaded band. The values used in the work presented

here are in agreement with the values reviewed in the literature by Bond and Bergstrom (2006). The double-headed arrow represents the region of interest for the study presented here.

The absorption spectrum of HULIS used in this study was taken from Figure 4 of Hoffer *et al.* (2006) for biomass burning. Forest fires in Alaska and the soil beneath the snow in Barrow were probably the main sources of HULIS in Barrow snowpack (Clarke *et al.*, 2007; Stohl *et al.*, 2006; Voisin *et al.*, 2012). The linear combination of black carbon and HULIS absorption cross-sections was fitted to Figure 2b.4 by eye (France *et al.,* 2012). Both the HULIS absorption spectra (Hoffer *et al.,* 2006) and the black carbon absorption spectra (Warren and Wiscombe, 1980) are shown as per unit mass of carbon therefore it is possible to estimate crudely the amount of black carbon and HULIS found in the snowpack (Table 2b.4). The values for amount of black carbon and HULIS in the snowpack are considerably larger than the amount of impurities measured by chemical extraction in the windpack and windblown snowpacks at Barrow (Voisin *et al.*, 2012). The chemical extraction values ranged between 2-17 ng g^{-1} for black carbon, 30-200 ng g^{-1} for water insoluble organic carbon and 30-360 ng g^{-1} for dissolved organic carbon (Voisin *et al.*, 2012). The estimates shown in Table 2b.4 depend on many factors and are discussed later in this chapter.

Snowpack	*e*-folding depth		Black carbon	HULIS
	λ= 350 nm /cm	λ = 400 nm /cm	/ng-C g^{-1}	/μg-C g^{-1}
Hard	7	10	70	1.2
Soft	7.5	9	70	1.4
Snow on sea-ice	7.5	9	90	1.5
Inland	12	15	41	1.2

Table 2b.4. Estimated concentrations of black carbon and HULIS in the snowpacks around Barrow. Derived from fitting combinations of black carbon and HULIS absorption cross-sections to absorption cross-section of snowpack impurities in Figure 2b.4. Note that the concentration is per unit mass of carbon in HULIS or black carbon per gram of snow. The concentration of HULIS in the snowpack should be treated as an upper limit and representative of all light-absorption snowpack impurities. Values of *e*-folding depth are included for comparison.

2b.5.3 Photolytic Rate Coefficients and Fluxes as a Function of Solar Zenith Angle and Snowpack Depth

Photolysis rate coefficients, *J*, for the photolysis of hydrogen peroxide, nitrate and nitrite in the four representative snowpacks of Barrow were calculated for 106 depths in each snowpack at 30 separate solar zenith angles between 0 and 90° (equally spaced over cos θ). Contours of equal photolysis rate coefficients for reactions 2b.1 and 2b.2 are plotted versus depth and solar zenith angle in Figures 2b.5, 2b.6 and 2b.7 respectively. The photolysis rate coefficient for the production of OH radicals, NO_2 or NO in the snowpack can be interpolated from the plots for any solar zenith angle and for any depth in the semi-infinite snow, a nominal value of 1 m for this study.

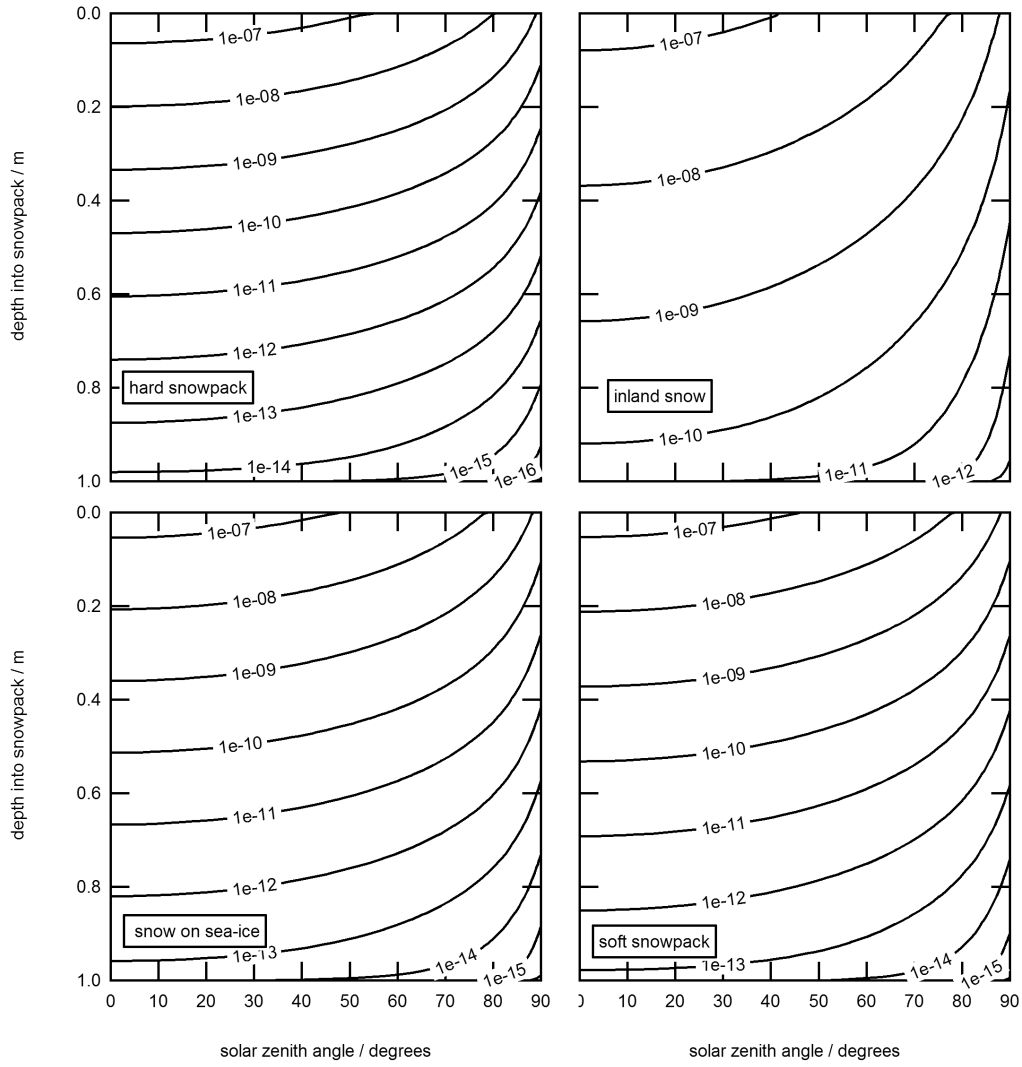

Figure 2b.6. Photolysis rate coefficients (s^{-1}) as a function of depth and solar zenith angle for the photolysis of NO_3^- to NO_2 (reaction 2b.1) for each of the four Barrow snowpacks. Values were determined using the conditions described in Table 2b.2 under clear sky conditions.

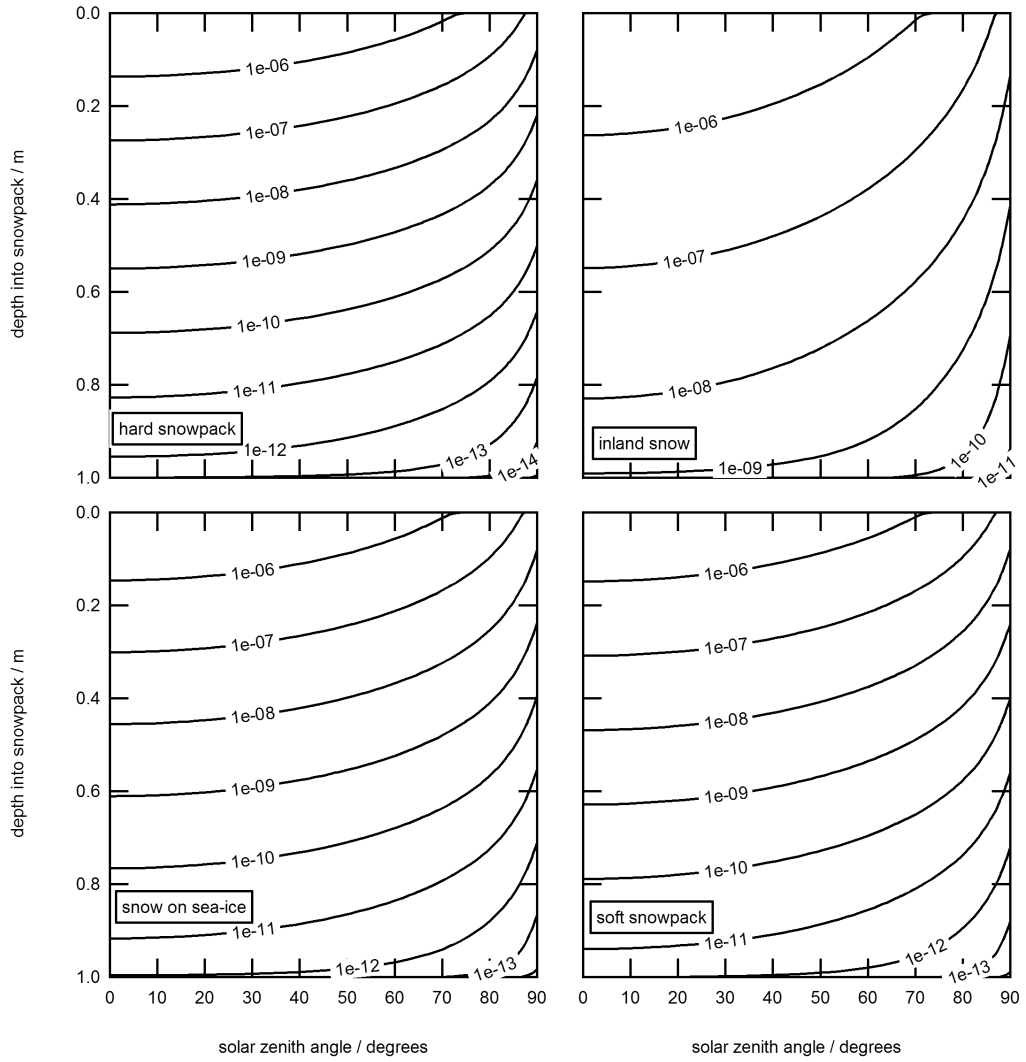

Figure 2b.7. Photolysis rate coefficients (s^{-1}) as a function of depth and solar zenith angle for the photolysis of H_2O_2 to produce to hydroxyl radicals (reaction 2b.2) for each of the four Barrow snowpacks. Values were determined using the conditions described in Table 2b.2 under clear sky conditions.

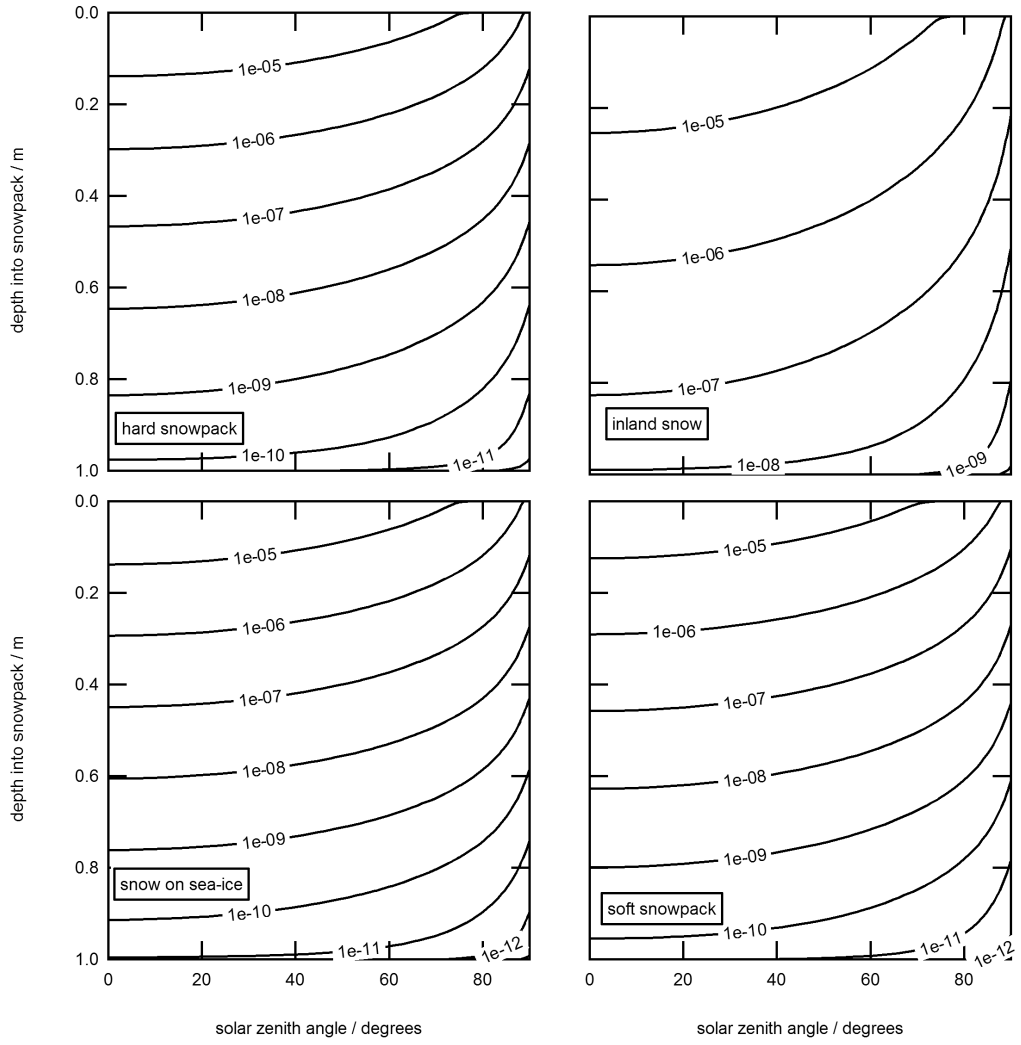

Figure 2b.8. Photolysis rate coefficients (s^{-1}) as a function of depth and solar zenith angle for the photolysis of NO_2^- to NO (reaction 2b.3) for each of the four Barrow snowpacks. Values were determined using the conditions described in Table 2b.2 under clear sky conditions.

2b.5.4 Depth-Integrated Production Rates (Fluxes) of NO, NO_2 and OH Radicals for the OASIS Field Campaign

Photochemical depth-integrated production rates (fluxes) of NO, NO_2 and OH radicals were calculated for the four snowpacks for every minute of the OASIS campaign (Figures 2b.9 and 2b.10).

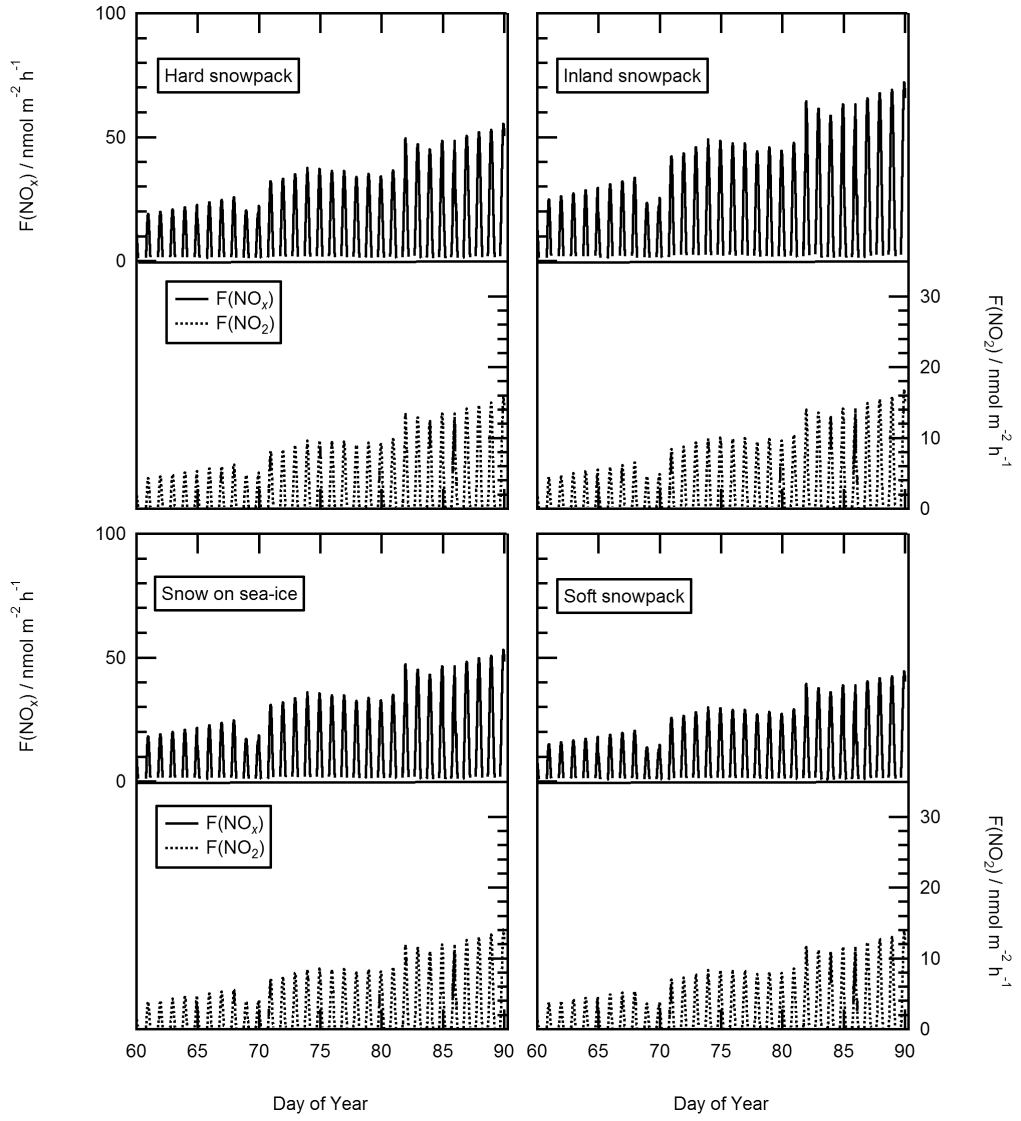

Figure 2b.9. Depth-integrated production (maximum fluxes) of NO_x and NO_2 in the snowpack for the duration of the Barrow OASIS campaign, assuming all in-snow photolytic production of NO_x from nitrate and nitrite is liberated from the snowpack. The top line in each graph is total NO_x photolytic production rates (NO + NO_2) and the lower line is NO_2 photolytic production rates for each snowpack. Note that the corresponding left and right hand side axes have different ranges. The depth-integrated production rates (maximum fluxes) are calculated with a concentration of 3.9 μmol l^{-1} of nitrate and 0.02 mol l^{-1}, an average of snow measurements during the OASIS campaign, with no depth dependence. Concentrations of chromophores are for melted snow.

Calculated photolytic production of NO_2 shows a variation between the Barrow snowpacks of less than a factor of 2. Julian Day 90 shows the maximum potential

fluxes of NO_2; 17 nmol m^{-2} h^{-1} for the inland snowpack, 15 nmol m^{-2} h^{-1} for the hard snowpack, 13 nmol m^{-2} h^{-1} for the soft snowpack and 14 nmol m^{-2} h^{-1} for the inland snowpack. The maximum photolytic production rate of NO from the photolysis of nitrite is 55 nmol m^{-2} h^{-1} for inland snowpack, 39 nmol m^{-2} h^{-1} for hard snowpack, 30 nmol m^{-2} h^{-1} for the soft snowpack and 36 nmol m^{-2} h^{-1} for snow on sea-ice. The maximum depth-integrated in-snow production rate of OH radicals also occurs on Day 90 with maximum potential fluxes of 160 nmol m^{-2} h^{-1} for inland snowpack, 110 nmol m^{-2} h^{-1} for the soft snowpack and 120 nmol m^{-2} h^{-1} for the snow on sea-ice and hard snowpack.

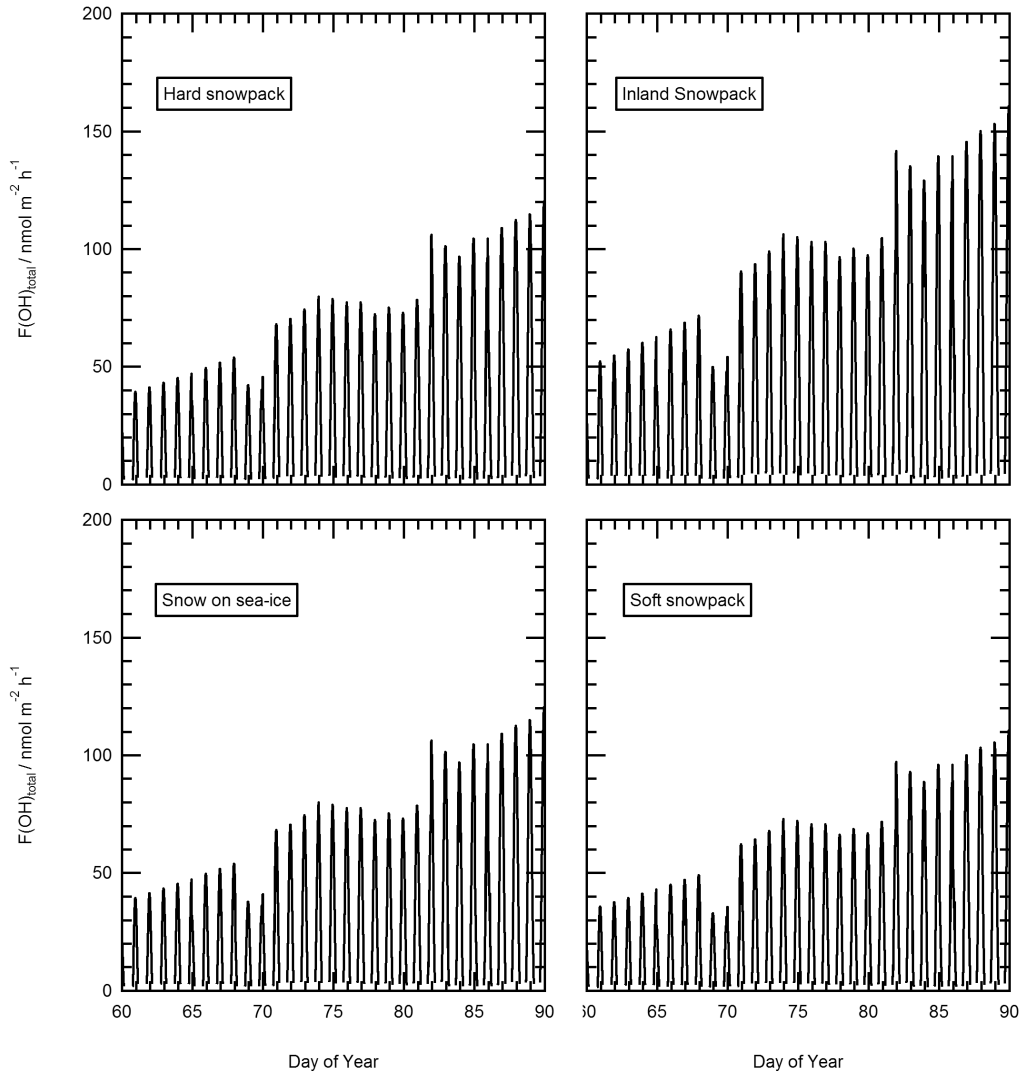

Figure 2b.10. Depth-integrated production rates (maximum fluxes) of OH radicals from the photolysis of hydrogen peroxide, nitrate and nitrite in the snowpack for the duration of the Barrow OASIS campaign. The depth-integrated production rates are calculated with a concentration of 0.4 μmol l^{-1} of hydrogen peroxide, 0.02 μmol l^{-1} of nitrite and 3.9 μmol l^{-1} of nitrate. Concentrations of chromophores are for melted snow.

The maximum in-snow production rate of NO_x is 72 nmol m^{-2} h^{-1} for inland snowpack and 44 nmol m^{-2} h^{-1} for soft snowpack. The production rate of OH radicals is a summation of OH radicals produced through nitrate, hydrogen peroxide and nitrite photolysis according to reactions 2b.1, 2b.2 and 2b.3 respectively.

While $F(NO_2)$, F(NO) and F(OH) are proportional to the downwelling broadband UV irradiance measured by the Eppley TUVR the depth-integrated production rate of NO_2, NO and OH radicals can be scaled by downwelling TUVR irradiance (295-385 nm broadband) measurement. There is an approximately linear relation between depth-integrated production rate of NO_2, NO or OH radicals and downwelling broadband UV irradiance, and Figure 2b.11 demonstrates that for diffuse and clear sky conditions between solar zenith angles of 51-90°.

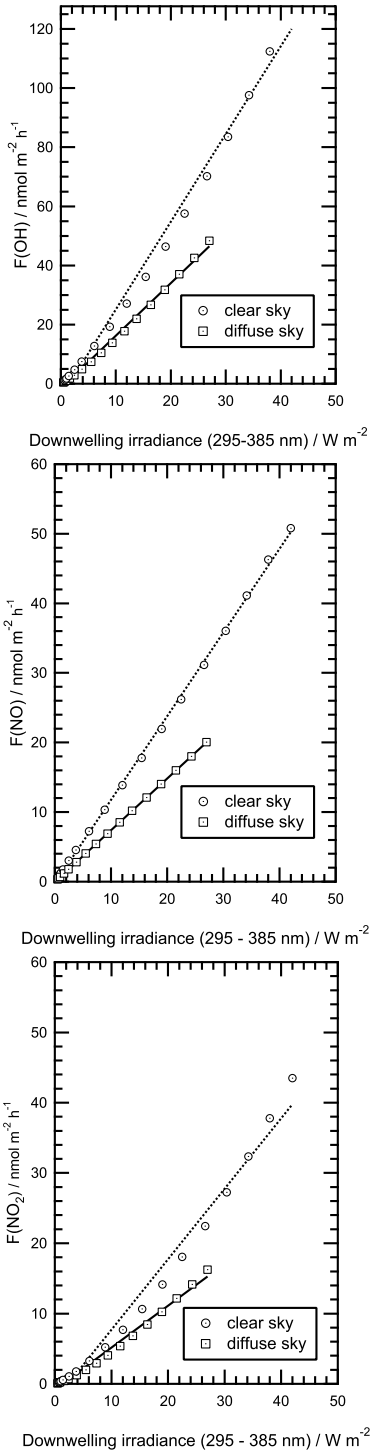

Figure 2b.11. Demonstrating the linear relationship and validity of scaling depth-integrated production rates of NO, NO_2 and OH radicals using broadband UV measurements (295-385 nm). Each point is a solar zenith angle between 51-90°. Minimum solar zenith angle was ~66° during the OASIS campaign. The snowpack presented here is the hard snowpack, modelled using the conditions in Table 2b.2.

TUVR downwelling irradiance measurements in Figure 2b.11 can be used to predict the depth-integrated production rates of NO_2, NO and OH radicals for the snowpacks and solar zenith angles studied here. The relationships shown here are only for these snowpack, however similar relationships should be possible for other snowpacks.

2b.6 Discussion

The discussion is broken into 4 sections: (a) the effect of grain size on the derivation of σ_{scatt} and σ^{+}_{abs}, (b) the scattering cross-sections of the Barrow snowpack, (c) the wavelength dependence of absorption in Barrow snowpack and (d) NO_x and OH radical in-snow production rates.

2b.6.1 The Effect of Grain Size on the Determination of σ_{scatt} or σ^{+}_{abs}

The effect of grain size on derived values of σ_{scatt} and σ^{+}_{abs} has not been considered in previous work using TUV-snow (France, King) because the values of σ_{scatt} and σ^{+}_{abs} along with the asymmetry parameter, *g*, were used to calculate irradiances and photolytic rate coefficients in the snow, i.e. it would not matter if σ_{scatt} and σ^{+}_{abs} were correlated as the resulting irradiance in the snowpack would be the same. However, the absorption cross-section of the impurities in the snowpack presented in this chapter were derived and it is useful to assess whether the grain size of the snow affects the value of the absorption cross-section derived for the impurities in the snowpack. As values of σ_{scatt} and σ^{+}_{abs} are empirically fitted to the measured albedo and *e*-folding depth, the only grain size dependent quantity used in the radiative-transfer calculation that is not empirically fitted is

the asymmetry parameter, *g* (Lee-Taylor and Madronich, 2002). Inspection of the Mie calculation for 100-2000 μm diameter ice spheres in Figure 4 of Wiscombe and Warren (1980) demonstrates that the value of the asymmetry parameter may be in the range of 0.885-0.895 for the wavelengths in the work considered here (Figure 2b.12).

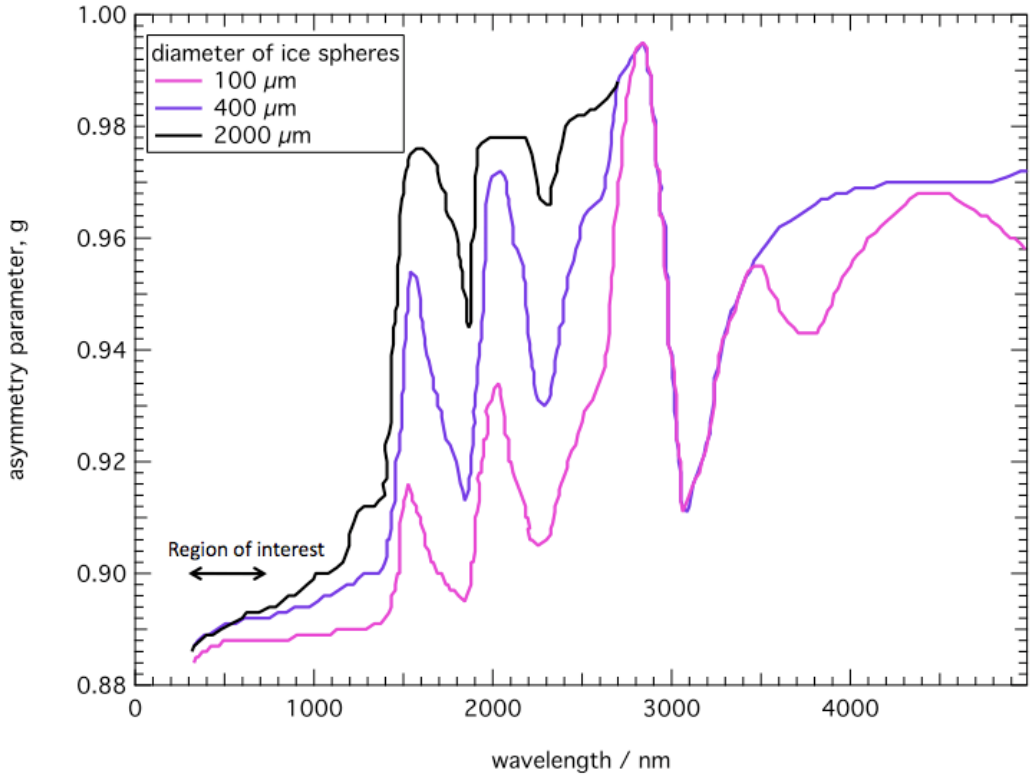

Figure 2b.12. Asymmetry parameter, *g*, for ice spheres of various diameter, as a function of wavelength. Adapted from Wiscombe and Warren (1980). The double-headed arrow represents the wavelength region of interest for work presented in this chapter.

To assess the effect of the value of the asymmetry parameter on the values of σ_{scatt} or σ^{+}_{abs}, the radiative-transfer calculations used to empirically fit σ_{scatt} and σ^{+}_{abs} for the hard snowpack were repeated with values of the asymmetry parameter, g = 0.880, 0.885, 0.890, 0.895 and 0.900. The results for wavelengths

of 400, 500 and 600 nm are displayed in Table 2b.5 and show that the values of σ_{scatt} and σ_{abs}^{+} derived are insensitive to the value of asymmetry parameter.

Asymmetry Parameter, g	λ = 400 nm		λ = 500 nm		λ = 600 nm	
	σ_{scatt} / m^2 kg^{-1}	σ_{abs}^{+} / cm^2 kg^{-1}	σ_{scatt} / m^2 kg^{-1}	σ_{abs}^{+} / cm^2 kg^{-1}	σ_{scatt} / m^2 kg^{-1}	σ_{abs}^{+} / cm^2 kg^{-1}
0.880	1.5	11.0	1.7	9.5	2.5	14.5
0.885	1.6	11.2	1.8	9.7	2.7	14.5
0.890	1.7	11.5	1.8	9.5	2.7	14.5
0.895	1.8	11.5	1.9	9.5	2.9	14.5
0.900	1.8	11.7	2.0	9.5	3.0	14.5

Table 2b.5. Values of σ_{scatt} and σ_{abs}^{+} calculated empirically by fitting the reflectance and *e*-folding depth for the hard snowpack using different values of the asymmetry factor, g. Note that the values of σ_{scatt} and σ_{abs}^{+} derived are insensitive to the value of g. Values are reported for the solar wavelengths of 400, 500 and 600 nm.

The effect of asymmetry parameter on the derived values of σ_{scatt} and σ_{abs}^{+} were also calculated for snowpacks in Dome C (France *et al.,* 2011) as a comparison for the Barrow hard snowpack, both results can be seen in Figure 2b.13. It can be seen from Figure 2b.13 that σ_{scatt} and σ_{abs}^{+} are relatively insensitive to values of *g*.

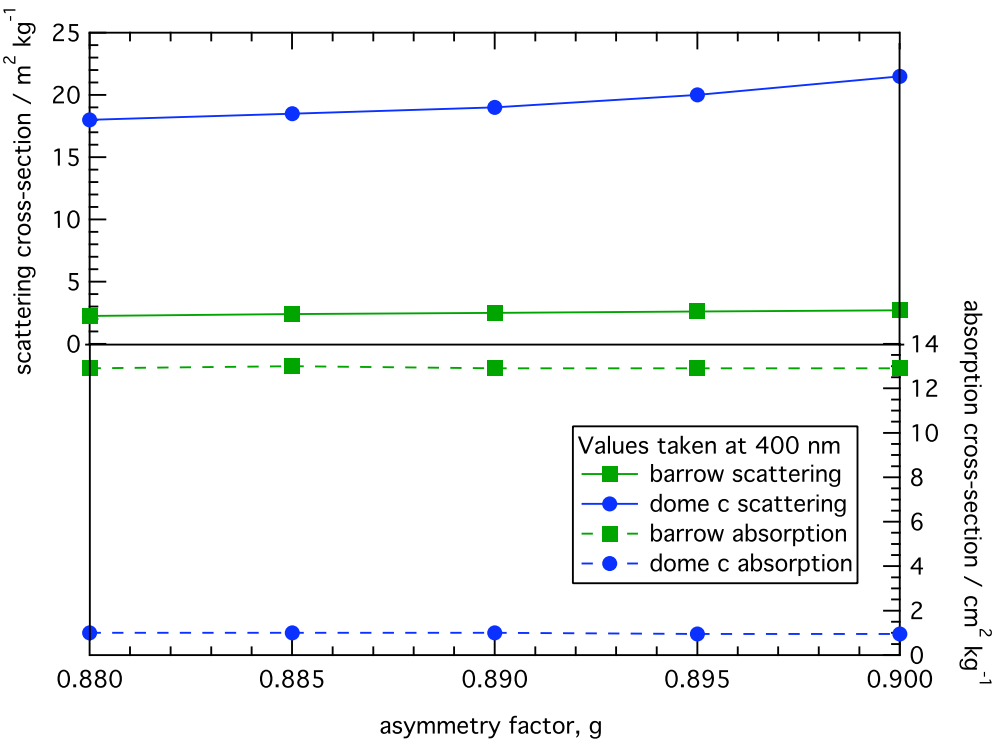

Figure 2b.13. The effect of varying asymmetry parameter, g, between values for typical ice grains (0.88-0.90) for Dome C (France *et al.*, 2011) and the Barrow hard snowpack. Note the values for the asymmetry parameter at 400 nm were taken from Wiscombe and Warren (1980, Figure 4).

To further test the procedure to determine values of σ_{scatt} and demonstrate that σ_{scatt} is sensitive to the grain size of the snowpack, the procedure outlined in section 2b.10.1 was used to fit the σ_{scatt} to the albedos and black carbon data (calculated by radiative-transfer) contained in Figure 8 of Warren and Wiscombe (1980). Figure 8 of Wiscombe and Warren (1980) shows semi-infinite direct beam albedo data as a function of wavelength, grain size (100 and 1000 μm) and black carbon content (50 and 500 ng g^{-1}). Values for σ_{scatt} were calculated for wavelengths of 300, 325, 350, 375, 400, 450 and 500 nm and were found to be 20 ± 3 m^2 kg^{-1} for the small grained snowpack (for all black carbon concentrations)

and 1.9 ± 0.1 m^2 kg^{-1} for the large grained snowpack (for all black carbon concentrations) over the wavelength range of 300-500 nm (Figure 2b.14). The above highlights that accurate values of σ_{scatt} can be determined irrespective of black carbon concentration. For the test presented in Figure 2b.14, black carbon concentration was constrained and therefore σ^{+}_{abs} was constrained also. The values for black carbon concentrations of 0 ng g^{-1} seen in Figure 2b.14 are representative of only σ_{scatt} as σ^{+}_{abs} was constrained so no absorption was modeled and thus the values are unrealistic for real snowpacks.

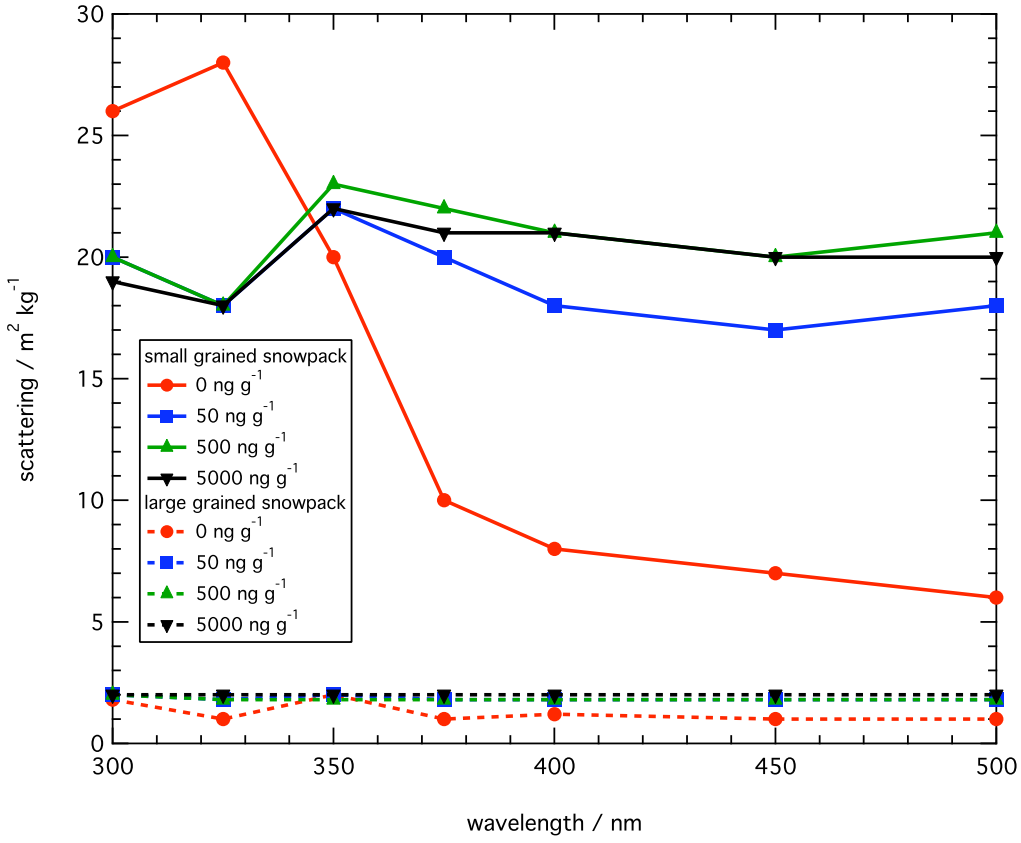

Figure 2b.14. Sensitivity of model to grain size and black carbon concentration.

Snowpacks are typically inhomogeneous layered structures yet in the work presented here the snowpacks are treated as one layer and the problems of treating the snowpack as one layer needs to be addressed. Previous work by France *et al.*

(2011a) used stratigraphic snowpack data to calculate the irradiance and photolytic rate coefficients in separate windpack layers in an Antarctic snowpack. The three layers considered were a surface soft windpack, a hard windpack and a hoar-like layer. The different layers of windpack had different properties, i.e. σ_{scatt} and σ^{+}_{abs}, in the radiative-transfer calculations due to different grain size and light-absorbing impurity content (Table 2b.6).

Snow description	σ_{scatt} /m^2 kg^{-1} (λ = 350 nm)	σ^{+}_{abs} /cm^2 kg^{-1} (λ = 350 nm)	Grain size / mm
Soft windpack	14-22 (20)	1.3-2.2 (1.7)	0.3-1
Hard windpack	17-24 (19)	1.3-1.8 (1.7)	0.3-2
Hoar-like layer	8-16 (10)	0.6-1.4 (1.2)	1-4

Table 2b.6. Snowpack properties for each snowpack layer at Dome C. Values in brackets are median value of the derived optical coefficients. Adapted from France *et al.* (2011a).

It can be seen from Table 2b.6 that France *et al.* (2011a) found that non-windpacked layers had very different optical properties to windpacked layers yet there was little or no change between the windpacked layers. As all the snowpacks measured in Barrow consisted solely of windpacked layers, radiative-transfer calculations for different layers were not undertaken due to the substantial increase in computational work needed to create layers within the snow similar to those described in chapter 2a ,with only a slight change to the irradiance-depth profiles. The typical uncertainty in σ_{scatt} owing to a 5% change in snowpack density is $\pm^{7\%}_{5\%}$ and the typical uncertainty in σ^{+}_{abs}, black carbon or HULIS owing to a 5% change in snowpack density is $\pm^{6\%}_{9\%}$.

2b.6.2 The Scattering Cross-Sections of Barrow Snowpack

Although the values of the scattering cross-section may be considered smaller than expected, a sensitivity analysis of the radiative-transfer modelling process to determine absorption and scattering cross-sections yielded no large changes in the values of σ_{scatt} or σ^{+}_{abs} for small changes in *e*-folding depth, albedo or the asymmetry parameter. A possible relationship between specific surface area of snow and scattering cross-section can lead to an expectation of greater values of $\sigma_{scatt}(\lambda)$ (Domine *et al.,* 2008). Domine *et al.* (2008) state that there is a mathematical relationship between scattering cross-section (σ_{scatt}) and the specific surface area (SSA) of snow, Kokhanovsky and Zege (2004, p. 1594, equation (22)) also describe this relationship. Scattering cross-sections recorded for coastal snowpacks in Antarctica (Beine *et al.,* 2006) show similar scattering cross-sections to Barrow. Values of snow specific surface area were derived from snow reflectivity in the near IR (Domine *et al.,* 2012) producing values of ~30-40 m^2 kg^{-1}, this suggests scattering cross-sections of 15-20 m^2 kg^{-1}. However, Figure 2b.3 and Table 2b.3 demonstrate typical σ_{scatt} values of ~2 m^2 kg^{-1}, these values were derived from *e*-folding depth and surface reflectance and a re-investigation of the modelling process used to calculate $\sigma_{scatt}(\lambda)$ revealed no errors or processes that could cause a large change in $\sigma_{scatt}(\lambda)$ for a small change in modelling parameters. Gallet *et al.* (2010) conducted a similar study at Dome C in Antarctica that found values of snow specific surface area of ~31 m^2 kg^{-1}, this would suggest σ_{scatt} values of ~25-16 m^2 kg^{-1}. For the same location, France *et al.* (2011a) determined σ_{scatt} values of 14-24 m^2 kg^{-1} using surface reflectance and *e*-folding depths for surface snows using the same technique described here. This

indicates that the relationship between snow specific surface area and σ_{scatt} appears to be valid for snow at Dome C but not valid at Barrow. An obvious difference between the study at Dome C and that at Barrow is the amount of light-absorbing impurities in the snowpack. The snowpacks studied at Barrow during the campaign were very dirty relative to the very clean snowpacks measured at Dome C. Scattering and absorption are independent quantities so the lowering of σ_{scatt} owing to increased absorption is unlikely.

It is not possible to drastically alter the value of σ_{scatt} and replicate the measured reflectivity and *e*-folding depth measurements by (1) varying the asymmetry parameter within the limits suggested by Wiscombe and Warren (1980), (2) varying nadir reflectivity or *e*-folding depth by amounts representing experimental error (i.e. measurement error), or (3) changing σ^{+}_{abs} by 20%. Occasionally proposed is the explanation that the measured reflectivity and measured *e*-folding depth are for different snow layers i.e. albedo for the surface layer and *e*-folding depth for another layer deeper in the snowpack with very different optical properties for different layers as the measurements of *e*-folding depth and nadir reflectance are taken in different parts of the snowpack, thus possibly having a thin (<1 cm) top layer of snowpack containing all the light absorbing impurities underlain by a clean snowpack. Exploratory calculations with TUV-snow and experience suggest that such conditions would be obvious to the naked eye as a dirty top layer would be a different colour to the rest of the snowpack. No such layer was observed at Barrow and all snowpits studied show similar values of σ_{scatt} (1.7-4 $m^2\ kg^{-1}$ (λ = 400 nm), see appendix - Barrow), thus to summarise there is no reason to suspect that the method of determining σ_{scatt} is not robust. At

present, there is no available explanation for the disagreement between snow specific surface area and σ_{scatt} for the snowpacks presented here.

2b.6.3 The Wavelength Dependence of Absorption in Barrow Snowpack

The absorption spectrum of light-absorbing impurities in the snowpack is plotted in Figure 2b.4. The absorption cross-section describes the total absorption of light-absorbing impurities whether they are internal or external to the snow grains. External light-absorbing impurities are particles such as soil or black carbon that were trapped or deposited since snowfall. Internal light-absorbing impurities have been incorporated into the snow grain as a deposited gas, during snow metamorphism or as part of the original snowfall. Figure 2b.5 compares the mass absorption cross-section used in previous work and the work presented here with measurements of the mass absorption coefficients found in Table 6 of the review by Bond and Bergstrom (2006) and in Adler *et al.* (2010). Figure 2b.5 demonstrates that values of the mass absorption cross-section from Bond and Bergstrom (2006) and Adler *et al.* (2010) are similar to the values used in this study. The interesting and important aspect of this work in this chapter is that both a HULIS and a black carbon absorber are required to explain the total absorption by impurities in the snowpack, not just black carbon. It may not be possible in the future to model UV-visible photolytic processes in the snowpack without considering both HULIS and black carbon absorptions.

Comparison of the absorption cross-sections of the four snowpacks in Figure 2b.4 demonstrate that the coastal snowpacks have an absorption in the wavelength region of 550-600 nm that is not present in the inland snowpack and not

accounted for by the HULIS or black carbon absorption spectrum used in this work (Hoffer *et al.*, 2006). For the three coastal snowpacks, a third light-absorbing impurity may be required. Marine microbiology could be responsible for this absorption and a similar feature has been noted in the extracted HULIS spectrum by Voisin *et al.* (2012). The noted feature is not visible in the inland snowpack absorption cross-section, only sites close to the open lead in Barrow have this feature. At present a realistic absorption spectra for marine microbiological detritus exists in Perovich *et al.* (1993, Figure 1) and this is a topic ripe for further fieldwork. The figure from Perovich *et al.* (1993) showing the absorption coefficients for bottom ice algae has been reproduced in Figure 2b.15.

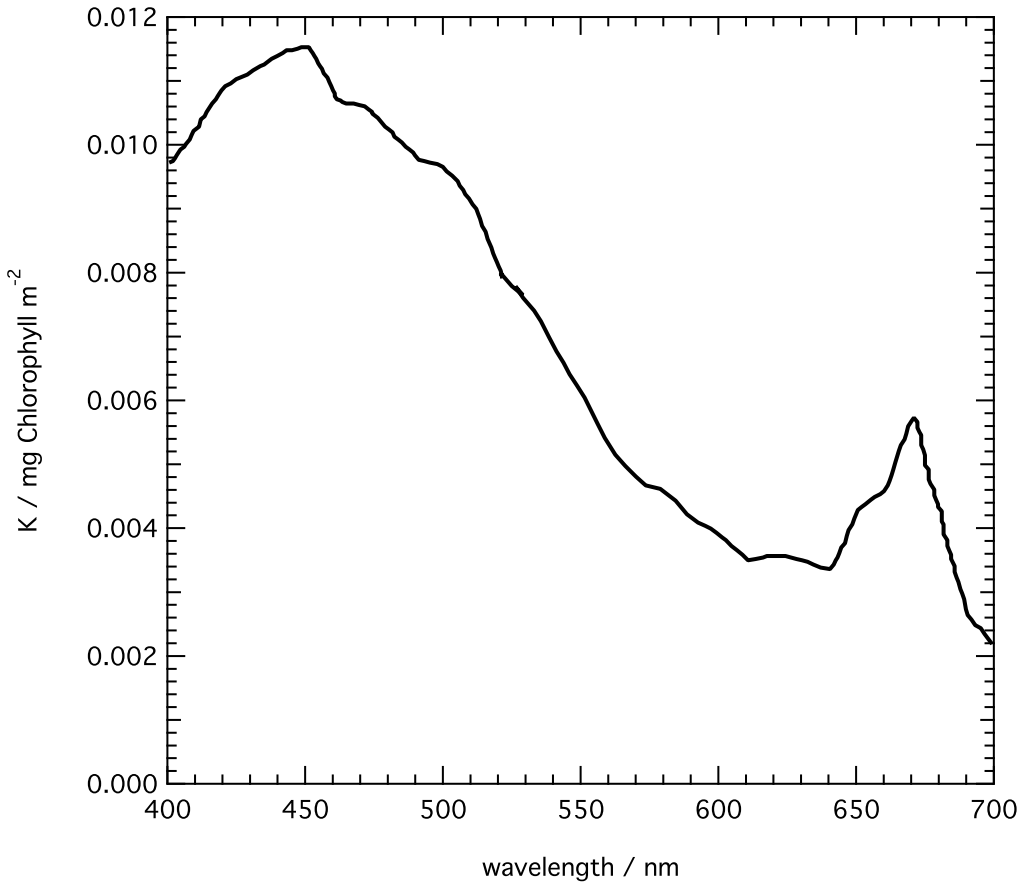

Figure 2b.15. Spectral absorption coefficients for bottom ice algae determine at a bare ice site, adapted from Perovich *et al.* (1993).

The amounts of black carbon predicted for Barrow snowpacks is much greater than in more remote regions of the Arctic, where the average black carbon concentrations range from 3 ng g^{-1} (Greenland) to 26 ng g^{-1} (West Russia) with an Alaskan snowpack average of 9 ng g^{-1} (Doherty *et al.,* 2010). The derived scattering and absorption coefficients from the work presented here are similar to previously determined values for Alaskan snow on sea-ice from Lee-Taylor and Madronich (2002) using data from Grenfell and Maykut (1977). In April 2007, Doherty *et al.* (2010) extracted and quantified black carbon in Barrow snow within 10 km of the snowpacks studied here. Lyapustin *et al.* (2010) show a photograph and reflectivity data for the snow sampled by Doherty *et al.* (2010) describing it as "fresh snow with minimal redistribution by the wind". The old windpacked snow described in this study is very different from the new unworked snow sampled by Doherty *et al.* (2010). The windpacked snows presented here were characteristic of the OASIS campaign and have clearly had the opportunity to accumulate more light-absorbing impurities through multiple wind events relative to the Doherty *et al.* (2010) sample. Doherty *et al.* (2010) highlight that they ignored samples from the lower 40% of some snowpacks to avoid bias in the samples due to windblown soil. Such sampling methods were not desired in the study presented here as the main aim of the work was to measure and model the optical properties of the Barrow snowpack during the OASIS campaign thus allowing photochemical production rates to be calculated. The original aim was not to measure black carbon concentration in the snowpack, thus a comparison between the snowpacks of Doherty *et al* (2010) and the work presented here is not sensible. The calculated amounts of black carbon in Barrow snow are comparable

to values measured in East Russian Arctic snow (~10-150 ng g^{-1}) where sampling was restricted to within 100 km of cities and local pollution sources could have become incorporated into the snowpack (Doherty *et al.,* 2010). Sources of black carbon in Barrow area could have been due to the frequent snow machine traffic and pollution from the local town.

Concentrations of various black and brown carbon species found in snow have been reported for some of the snowpacks studied in Barrow (Voisin *et al.*, 2012). Voisin *et al* (2012) determined the carbon concentrations in the snowpack by extracting carbon from the snowpack using various methods (e.g. SPE cartridge, filtering etc) and measuring the carbon content chemically, the method provided black carbon concentration values considerably higher than those measured in this study. The values stated here are reported optically after assumptions about the absorber identify have been made. The majority of the disagreement between Voisin *et al.* (2012) and the results shown in Table 2b.4 may be owing to the simple approximations for a HULIS and black carbon absorber in the snowpack made in this study. Bohren (1986) demonstrated that uncertainties in the shape, refractive index and internal/external position of the black carbon with respect to the snow grain could yield changes in the black carbon absorption cross-section by factors of 2.2, 5 and 1.4 respectively. Uncertainities in the HULIS absorption cross-section by factors of 1.8 and 1.3 for the shape and internal/external position of the HULIS particles were calculated using the refractive index of HULIS measured by Hoffer *et al.* (2006) and the mathematical approach of Bohren (1986)(E2b.9).

$$(C_{abs})_{sphere} = \frac{kv}{3}\left(\frac{27}{(\varepsilon'+2)^2+\varepsilon''^2}\right)\varepsilon''$$
$$(C_{abs})_{needle} = \frac{kv}{3}\left(\frac{8}{(\varepsilon'+1)^2+\varepsilon''^2}+1\right)\varepsilon'' \quad \text{(E2b.9)}$$
$$(C_{abs})_{disk} = \frac{kv}{3}\left(\frac{1}{(\varepsilon'^2+\varepsilon''^2}+2\right)\varepsilon''$$

where v is the volume of a particle, ε is its dielectric function relative to that of the surrounding medium (in air, ε=2.99+i1.8) and k is the wavenumber of the incident light. Taken from Bohren and Huffman (1983), p.350.

As there is more uncertainty in the identity of the UV absorber than the value of its refractive index, the uncertainty owing to the refractive index of HULIS was not considered. Any discrepancies between the measurements of Voisin *et al.* (2012) and the values presented in Table 2b.4 may be due to how black carbon and HULIS are measured and defined. Taking the previous statement into consideration it is important to understand what Figure 2b.4 demonstrates: (1) the total amount of light-absorbing impurity in the snowpack is not constant over 350-600 nm, (2) the light-absorbing impurities in the Barrow snowpack can be fitted to a combination of black carbon and HULIS absorbers but a third absorber based on marine microbiological detritus may also be required, and (3) estimated concentrations of black carbon and HULIS in snow can be calculated from optical measurements, however, these values depend on the location and the physical characteristics of the absorber. To clarify, it should be noted again that the absorption by snowpack impurities has been fitted to a linear combination of black carbon and HULIS absorption spectra to demonstrate that the total absorption is consistent with a mixture of light-absorbing impurities in the snowpack. It is possible to replace the material termed as HULIS with other light-

absorbing impurities such as brown carbon, dust or marine detritus. The concentration of HULIS in the snowpack should be treated as the upper limit and representative of all light-absorbing impurities. An advantage of the technique presented here is that the total absorption by light-absorbing impurities in the snowpack can be determined without melting or significantly altering the snowpack, in contrast to Voisin *et al.* (2012).

2b.6.4 NO_x and OH Radical In-Snow Production Rates (Fluxes)

It has been previously stated by King and Simpson (2001) that 85% of photochemistry occurs in the top 2 *e*-folding depths of the snowpack, therefore, using the *e*-folding depths measured at 350 nm, 85% of the photochemistry for the Barrow snowpack occurs in the top 14-24 cm of snow cover. The combined depth-integrated production rate of NO_2 and NO is the upper limit for the NO_x flux from the snowpack, it assumes that all photoproduced NO_x is able to escape from the snowpack. For a solar zenith angle of 66°, the maximum calculated noon-time NO_x flux from the inland snow at Barrow was 72 nmol m^{-2} h^{-1}, with 70% and 30% from photolysis of nitrite and nitrate respectively. The uncertainty of the depth-integrated production rates is approximately 20% (France *et al.,* 2010).

In the conditions at Barrow nitrite seems to dominate as a source of NO_x contributing approximately 3 times more NO_x than nitrate, however, the photolysis of NO_2^- to produce NO is not usually considered a significant source of NO_x. Previous analysis by Chu and Anastasio (2007) demonstrates that nitrate and nitrite photoproduction rates are comparable for OH production on ice grains

(therefore making the analysis applicable to NO_x in-snow production (reactions I, II and IV)) and a similar result was obtain by Jones *et al.* (2001) during the CHABLIS campaign. The conditions experienced at Barrow favour nitrite photolysis over nitrate photolysis due to: (1) the large value of $J_{NO_2^-}\left[NO_2^-\right]$ production relative to the value of $J_{NO_3^-}\left[NO_3^-\right]$, (2) the presence of a large ozone column attenuating the shorter UV wavelengths relative to longer UV wavelengths. The maximum of the action spectrum (the product of the absorption cross-section and the quantum yield) for nitrite photolysis is ~355 nm compared to the maximum of the action spectrum for nitrate photolysis of ~305 nm, and (3) the presence of a wavelength-dependent absorber in the snowpack that shows increasing absorption at shorter wavelengths. Thus, if the impact of nitrite photochemistry to form NO in the snowpack is also considered and added to the NO_2 production rate to give a total in-snow production rate of NO_x, the total in-snow production for the Barrow snowpacks of 33-72 nmol m^{-2} h^{-1} will become larger than 40 nmol m^{-2} h^{-1}, the maximum flux of NO_x measured at Alert Canada at a solar zenith angles of ~66° (Beine *et al.,* 2002). However, the depth-integrated production rate of NO is dependent upon the assumption that a single site measurements of nitrite concentration in the snowpack is valid across the whole Barrow region, i.e. the single measurement of $\left[NO_2^-\right]$ is a concern in this work.

It has previously been demonstrated that snowpack emissions of NO_x have an impact on the oxidative capacity of the lower troposphere (Bloss *et al.,* 2007; Morin *et al.,* 2008; Wang *et al.,* 2008; Yang *et al.,* 2002). It is likely that some of

the photoproduced NO_2 in the snowpack would be involved in some secondary chemistry within the snow matrix and therefore the depth-integrated production rates of NO_2 presented here can only be considered to be maximum fluxes. Anastasio and Chu (2003) previously suggested that 30% of the NO_2 is converted prior to release from the snowpack. Although the release of NO_2 from the snow cover to the atmosphere would be partly temperature controlled (Boxe *et al.,* 2006), it is unlikely that the photoproduced NO_x at Barrow will be trapped within the snow microstructure to a large degree as sunlight-dependent fluxes have already been observed over colder snowpacks in Alert (Beine *et al.,* 2002). The mechanism for movement of photoproduced NO_x from the snowpack to the atmosphere seems to be mostly influenced by windpumping at the surface of the snowpack and gas diffusion at greater depths within the snowpack (Thomas *et al.,* 2011). Bock and Jacobi (2010) discuss the complexity of the nitrate photochemical system in snow.

A reduction in predicted photolytic NO_x production is seen in the coastal snowpack by a factor of ~1.7 compared to the cleaner inland snowpack (Figure 2b.9) due to increased black carbon (and HULIS) absorption in the coastal snowpacks relative to the inland snow. The effect of increasing black carbon concentration and snowpack absorption upon the Alaskan snowpack is explored in chapter 2c (and Reay *et al.,* 2012).

The calculated depth-integrated production rates of total OH radical production from the photolysis of NO_3^-, H_2O_2 or NO_2^- in Barrow snowpacks are shown in Figure 2b.10, demonstrating that the variation in snowpack scattering and

absorption cross-sections between the four representative Barrow snowpacks only causes a small variation, a factor less than 2, in the in-snow photochemical production of OH radicals. The in-snow photochemical production of OH radicals may help in the formation and release from the snowpack of organic compounds that appear to have a photochemical source (Anastasio *et al.,* 2007; Hutterli *et al.,* 2004; Sumner *et al.,* 2002). The dynamically coupled atmospheric-snow modelling performed by Thomas *et al.* (2011) demonstrates the importance of OH radical production with respect to halogen release from the snowpack. The relative contributions to OH production by NO_3^-, H_2O_2 and NO_2^- are approximately 4%, 60% and 36% respectively. It was previously calculated by Chu and Anastasio (2007) that nitrite and nitrate photolysis contributed a similar amount of OH radicals to the snowpack but snowpack conditions in Barrow favour the production of OH radicals from nitrite (relative to nitrate) compared to previous calculations due to large nitrite concentrations and relatively low H_2O_2 concentrations, yet OH radical production from nitrite is still a factor of ~2 smaller than H_2O_2.

2b.7 Conclusions

The measurements of optical properties of snowpacks in Barrow and subsequent in-snow photochemical modelling have allowed a number of important conclusions to be drawn:

1. Non-black carbon impurities in the snowpack have a large absorption cross-section at the short solar wavelengths, responsible for photolytic reactions in the snowpack, therefore it is important to accurately account

for spectrally resolved absorption by both black carbon and non-black carbon impurities in the snowpack.

2. For individual snowpacks, estimates of depth-integrated production rates can be scaled and approximately correlated with downwelling UV irradiance.
3. The importance of NO fluxes from the snowpack owing to nitrite photolysis may have been significantly overlooked in previous campaigns. In this work, NO from nitrite photolysis has been calculated to be approximately three times larger than NO_2 from nitrate photolysis. In the snowpack the contribution of nitrite to OH radical production is approximately half that of hydrogen peroxide.

Chapter 2c

The effect of ng g^{-1} black carbon mass ratio on terrestrial and marine snowpacks at Barrow, Alaska: OASIS spring campaign 2009

Results from this chapter have been published in "Decreased albedo, light penetration depth and photolytic production of OH radicals and NO_2 in Barrow snowpack: A scenario of increasing black carbon in snow", H.J. Reay, J.L. France and M.D. King (2012), *Journal of Geophysical Research, 117*(D00R20), doi:10.1029/2011JD016630 (see Appendix 3)

2c.1 Introduction

Recent climatic changes in the Arctic i.e. thinning sea-ice, early springs and glacier retreat may be due to warming associated with increased black carbon content in Arctic snow (Hansen and Nazarenko, 2004**).** Trace amounts of dust, HULIS and black carbon deposited on or within a snowpack can reduce the albedo of that snowpack relative to pure snow (e.g. Clarke and Noone, 1985; France *et al.*, 2011b; Warren, 1982; Warren and Wiscombe, 1980; 1985). Changes in the extent of global snow and ice can account for up to fifty percent of interannual variability in planetary albedo (Qu and Hall, 2005). Studies have shown that the albedo of snow can be reduced by ~1% with the addition of ~10 ng g^{-1} of black carbon in snow (Clarke and Noone, 1985; Flanner *et al.*, 2007; Grenfell *et al.*, 2002; Hansen and Nazarenko, 2004; Jacobson, 2004). Hansen and Nazarenko (2004) suggest black carbon in snow is a factor of two more efficient than atmospheric carbon dioxide in altering global air temperatures and has a maximum global radiative forcing of +0.3 W m^{-2}. Typical

mass ratios of black carbon found in snow throughout the world (measured using filtration techniques, not optically) are 0.2–60 ng g^{-1} with extreme values greater than 250 ng g^{-1} (e.g. Clarke and Noone, 1985; Hansen and Nazarenko, 2004, Hegg *et al.*, 2010). Using the method developed by Clarke and Noone (1985), Doherty *et al.* (2010) reported equivalent black carbon, C_{equiv}^{BC}, (the mass of black carbon present in the snow to account for total light absorption in the snowpack) mass ratios in the Canadian and Alaskan Arctic as (14 ± 7) ng g^{-1}. Increasing mass ratios of black carbon in snow increases the amount of incident light absorbed by snow (Warren, 1984; Warren *et al.*, 2006) and decreases the light penetration depth (*e*-folding depth) of the snowpack. Light penetration depth (*e*-folding depth) is a useful metric in snow photochemistry and is the distance for irradiance to decrease to $\frac{1}{e}$ (or ~37%) of its initial value within a snowpack. The *e*-folding depth, ε, can be mathematically defined using Equation (2a.4), found in Chapter 2a.

Snowpack is an efficient medium for chemical photolysis (see reviews of Dominé and Shepson, 2002; Grannas *et al.*, 2007) and reduction of the *e*-folding depth by increasing black carbon mass ratio in the snow will reduce the rate of photolysis of impurities and pollutants in the snowpack such as nitrate (e.g. Fisher *et al.*, 2005; France *et al.*, 2010; King and Simpson, 2001). A decrease in the molecular flux of NO_2 (R2b.1, in Chapter 2b) is expected with increasing black carbon content.

The production of hydroxyl radicals (R2b.1, R2b.2 and R2b.3, found in Chapter 2b) may be responsible for fluxes of organic chemicals from the snow (e.g. Abbatt *et al.*, 2012; Chu and Anastasio, 2005; Dominé and Shepson, 2002; Peterson and Honrath,

2001). Larger molecular fluxes of NO_2 from the snowpack or larger yields of OH radicals in the snowpack are associated with a larger *e*-folding depth (e.g. Fisher *et al.*, 2005; France *et al.*, 2010) and less light absorption by snowpack or its impurities (i.e. less black carbon or other light-absorbing snow impurities such as dust or HULIS). Further work presented here focuses on the photolysis of nitrate (R2b.1) and hydrogen peroxide (R2b.3) as nitrite concentrations were not measured at Barrow for the OASIS 2009 campaign.

Previous radiative-transfer calculations of light propagation in snowpack undertaken by myself and my research group have always required the addition of black carbon to the snow to match the modelled snowpack reflectivity and *e*-folding depth with field measurements of *e*-folding depth and reflectivity of snowpacks (e.g. Beine *et al.*, 2006; Fisher *et al.*, 2005; France *et al.*, 2010; King *et al.*, 2005, Lee-Taylor and Madronich, 2002). Increases or decreases in the mass ratio of black carbon may respectively decrease or increase the albedo, *e*-folding depth and flux of chemicals from the snowpack respectively. Previous studies have considered the effect of black carbon on snowpack albedo (e.g. Aoki *et al.*, 2000; Chylek *et al.*, 1983; 1987; Flanner *et al.*, 2007; Warren and Wiscombe 1980; 1985) but to the author's knowledge the response of light penetration depth (*e*-folding depth) and depth-integrated production rate of chemicals from snowpack has not been quantified solely as a function of black carbon mass ratio in snowpack. The detailed field and modelling study of the Barrow snowpacks during the OASIS campaign (France *et al.*, 2012) provided enough good quality data to allow *e*-fold, albedo and depth-integrated production rates to be calculated as a function of black carbon.

Future deposition of black carbon from the atmosphere to the snowpack is expected to change (increase or decrease) and the resulting effect on albedo, *e*-folding depth and depth-integrated production rates is unknown. In this chapter, four snowpacks from Barrow, Alaska optically studied in chapters 2a and 2b are used to investigate the change in albedo, *e*-folding depth and depth-integrated production rate with increasing and decreasing amounts of black carbon using similar radiative-transfer calculations described by France *et al.* (2012). The calculations allow the variation of albedo and *e*-folding depth to black carbon mass ratios to be quantified in four snowpacks representative of the Barrow, Alaska region for the Barrow 2009 OASIS campaign. It is important to understand how black carbon mass ratio affects the albedo, *e*-folding depth and photochemical production rates within snowpack because variations in albedo and *e*-folding depth change the reflectivity and absorption properties of the snow thus contributing to the global heat budget. The release of chemicals through photochemical production rates in snow influences the overlying atmosphere, with important implications for the regional troposphere, ozone concentrations and the use of photochemical concentrations in ice cores as a proxy for past atmospheric photochemical concentrations (e.g. Beine *et al.,* 2002b; Blunier *et al.,* 2005; Domine and Shepson, 2002; Freyer *et al.,* 1996; Fuhrer *et al.*, 1996; Grannas *et al.*, 2004; 2007; Honrath *et al.,* 1999; Jacobi *et al.*, 2004a; Jones *et al.*, 2000; Low *et al.*, 1990; Mulvaney *et al.*, 1998; Neftel *et al.*, 1985; Sumner and Shepson, 1999; Thomas *et al.*, 2012; Wolff, 1995; 1998).

2c.2 Aims

The aims of the work presented in this chapter are to:

1. Calculate the effect of changing black carbon mass ratio on albedo, *e*-folding depth and depth-integrated production rates of OH and NO_2 radicals for four Barrow snowpacks.
2. Calculate the effect of changing HULIS mass ratio on albedo and *e*-folding depth.

2c.3 Methods

In this chapter, four representative snowpacks from Barrow, Alaska are studied in greater detail – soft snowpack, hard snowpack, inland snowpack and snow on sea-ice, these four snowpacks represent the snows around Barrow. Measurements of *e*–folding depth, nadir surface reflectance, snowpack stratigraphy and photochemical production rates from chapters 2a and 2b were used to calculate the effect of black carbon and HULIS on the four snowpacks. The methods are described here:

2c.3.1 Modelling Procedure

Albedo, *e*-folding depth and depth-integrated production rates of OH and NO_2 radicals for four Barrow snowpacks are calculated from irradiances within snowpack as a function of black carbon content, solar zenith angle and sky conditions (i.e. clear or completely cloudy skies). It is necessary to describe (a) the snowpacks selected for this study (b) the radiative-transfer calculations of irradiance in the snow and (c) the calculations of albedo, *e*-folding depth and depth-integrated production rates from irradiances in the snow.

2c.3.1.1 Snowpacks

Generally the snowpack stratigraphy constituted a basal depth hoar with intermediate layers of faceted crystals and windpacked top layers frequently coated with a thin layer of diamond dust (Dominé *et al.*, 2011a). The presence of a strong temperature gradient causes the depth hoar layers in all snowpacks to be formed through snowpack metamorphism, this is typical of Alaska's Arctic Coastal Plain (Sturm and Liston, 2003). The four snowpacks for the campaign were 'soft', 'hard', 'snow on sea-ice' and 'inland'. The depth and stratigraphy of the snow on sea-ice, although similar, contained greater variability than on land with occasional very thin (<1 mm) melt-freeze layers occurring more frequently in the snow on sea-ice. Supercooled droplets created by open leads and then frozen on the snow surface may have been the cause of the melt-freeze layers (France *et al*, 2012). Thin (< ~1 mm) melt-freeze layers do not measurably alter *e*-fold measurements (France *et al*, 2012). Details of the individual snowpack stratigraphy for the four snowpacks summarised in Table 2c.1 can be found in Figure 2c.1.

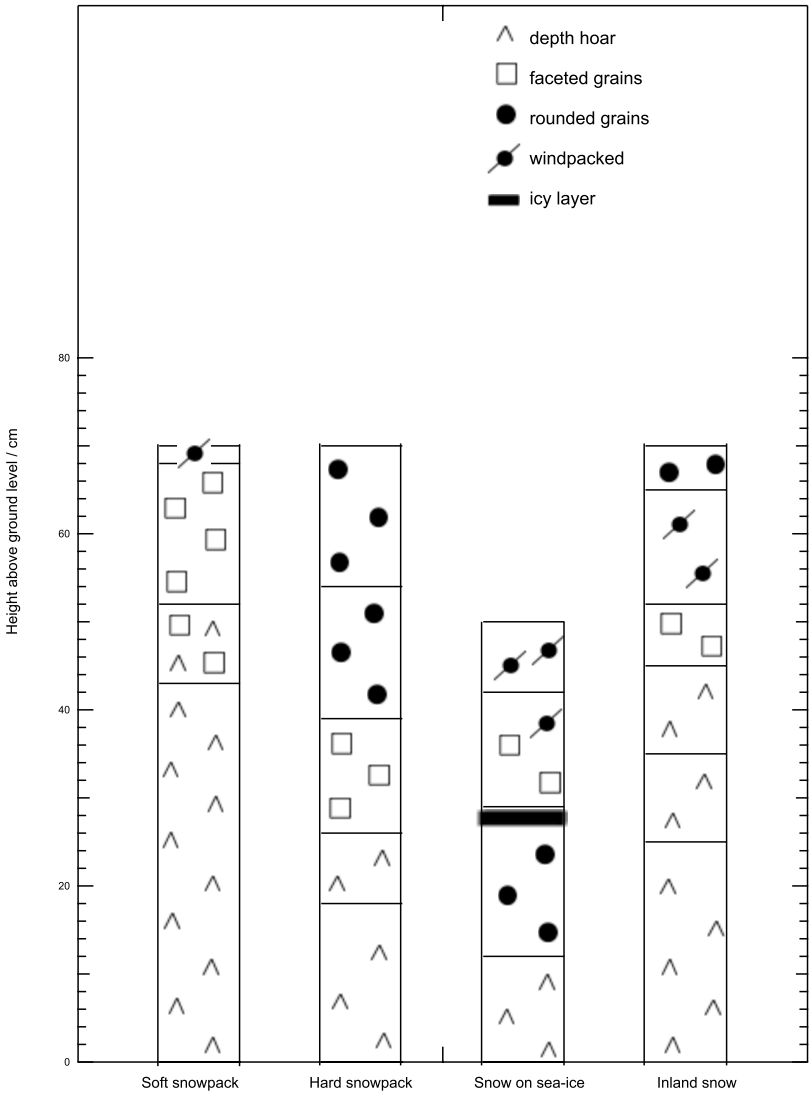

Figure 2c.1. Snowpack stratigraphy based on the notation of Fierz *et al.* (2009), adapted from France *et al.* (2012).

Snow Type	Date of measurement	Location		Column Ozone	Snow Density	Snow Temperature	Description of top snow layer	σ_{scatt} / m^2 kg^{-1} λ / nm						
		Longitude	Latitude	/Dobson Units	/g cm^{-3}	/°C		**300**	**350**	**400**	**450**	**500**	**550**	**600**
Hard snowpack	11th March 2009	71.31896°N	156.6723°W	428	0.38	-15	Windpack, rounded grains	2.0	2.0	1.8	1.8	2.0	2.2	3.0
Soft snowpack	21st March 2009	71.31987°N	156.67634°W	450	0.40	-18	Windpack, faceted grains	1.6	1.6	2.0	1.7	1.7	2.1	3.0
Inland snowpack	27th March 2009	71.20259°N	156.47471°W	459	0.29	-28	Windpack, faceted grains	1.6	1.6	1.7	2.2	2.5	2.9	3.7
Snow on sea-ice	14th March 2009	71.38469°N	156.45239°W	442	0.40	-24	Windpack, faceted grains	1.9	1.9	1.8	1.7	1.8	2.0	2.7

Table 2c.1. Physical properties of the four snowpacks studied and scattering cross-section, σ_{scatt}, for each snowpack. A more detailed description of the stratigraphy and physical properties of the four snowpacks can be found in Figure 2c.1 and Chapter 2a respectively.

The hard and soft snowpacks may be characteristic of the snowpacks around the atmospheric chemistry experiments near the BARC building. The inland snowpack is terrestrial and 15 km inland from the town of Barrow. The snow on sea-ice is located directly off Point Barrow (Figure 2c.2).

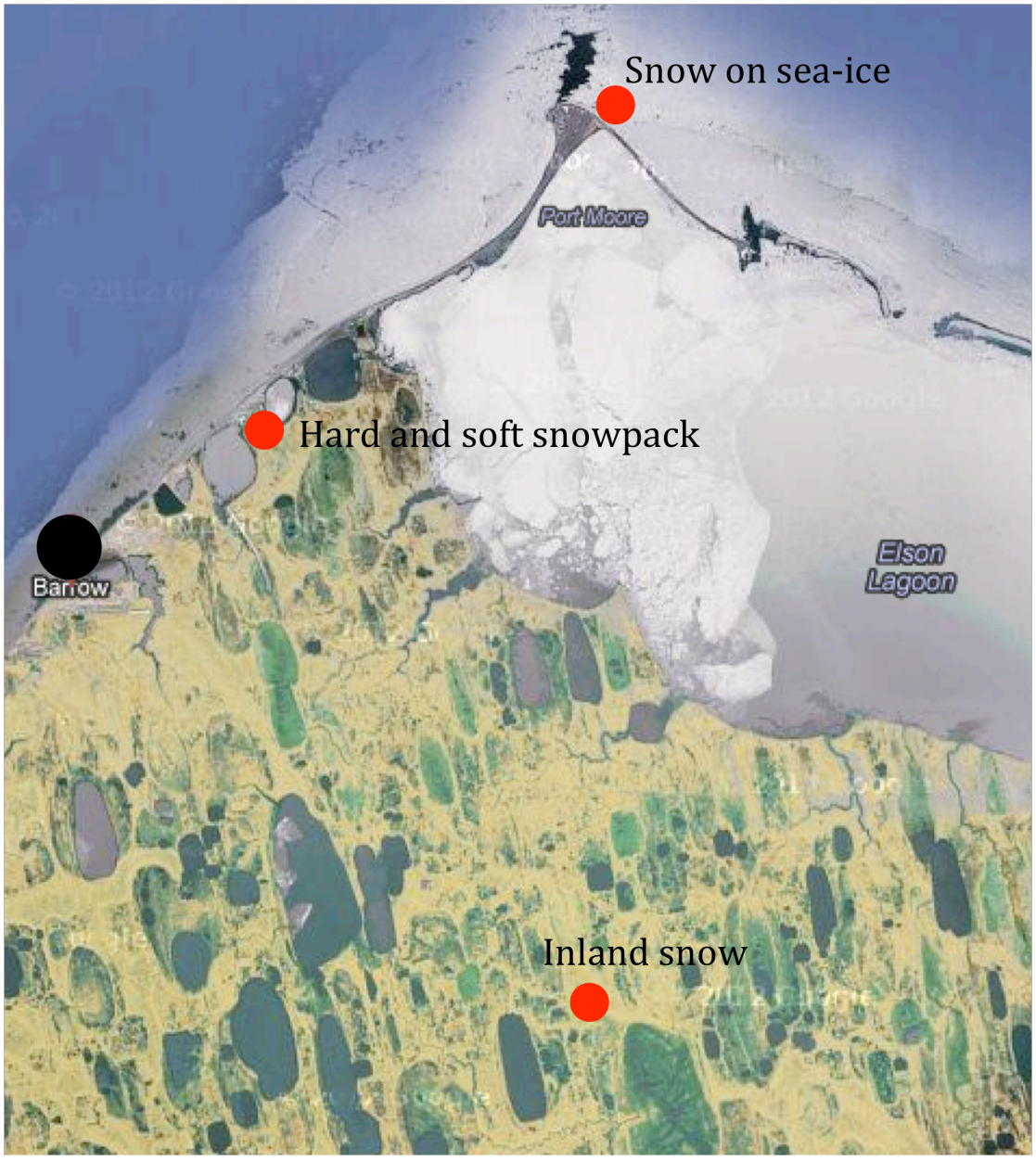

Figure 2c.2. Map showing location of four representative snowpacks in the region of Barrow, Alaska. Note, the leads shown on the map are indicative and do not represent conditions at time of measurement, i.e., the lead were not there on days when measurements were taken in March 2009.

2c.3.1.2 Radiative Transfer Calculations

Irradiances in the snowpack were calculated using the radiative-transfer code in the model TUV-snow (Lee-Taylor and Madronich, 2002). TUV-snow is a coupled atmosphere-snow radiative-transfer model with an eight-stream discrete-ordinates scheme (Stamnes *et al.*, 1988). Downwelling and spherical irradiances of short-wave radiation (λ=280–700 nm, $\Delta\lambda$=1 nm) were calculated from the top of the atmosphere through sixty-five unequal layers, varying from 0.001, 0.01, 1 or 2 km, to 30 unequal snow layers varying from either 0.1, 0.5, 1, 5 or 10 cm (5 thinner layers (1 mm) are at the snow surface) all within a 1 m snowpack. The atmosphere was modelled with and without clouds to calculate irradiances (and thus photolysis rate coefficients) for photochemical reactions in snow for clear sky conditions and to calculate albedo and *e*-folding depths for diffuse sky conditions respectively. To obtain diffuse sky conditions a 100 m thick cloud layer is placed 1 km above the ground with an optical depth of 16, an asymmetry factor of 0.86 and single scattering albedo of 0.9999. For the work presented here the albedo of the snowpack was calculated as a ratio of upwelling and downwelling irradiance at the snow surface. The *e*-folding depth, ε, was calculated by fitting Equation (E2a.4, found in Chapter 2a), to the downwelling irradiances, I_d, at depths, d, of 10, 20, 30 and 40 cm in the snowpack with a reference depth, d', of 10 cm. The depths of 10, 20, 30 and 40 cm are within the asymptotic zone (Simpson *et al.,* 2002; Warren, 1982) where any direct radiation entering the snowpack has been effectively diffused due to multiple scattering within the upper few cm of the snowpack.

The albedo of a snowpack is a function of solar zenith angle (Warren, 1984; 1986; Warren and Wiscombe, 1985), and the interaction of the direct component of solar

radiation with the snowpack is responsible for a solar zenith angle albedo dependency as detailed in Warren (1982). The albedo measured under diffuse-only solar illumination (i.e. no direct radiation or solely isotropic radiation) is not dependent on solar zenith angle. In the work presented here the albedos are reported for diffuse solar radiation to demonstrate the effect of increasing black carbon on snowpack albedo and not the effect of solar zenith angle on snowpack albedo. Diffuse-only sky conditions (i.e. no direct solar radiation) are achieved with thick cloud as described previously. The calculation of the *e*-folding depth is independent of the absolute values of irradiance incident to the snow surface and independent of the solar zenith angle of the solar irradiance, because the *e*-folding depth is the depth (normal to the surface) required to attenuate incident radiation to 37% (1/*e*) of the initial irradiance of a reference depth. The *e*-folding depth is only measured in the asymptotic zone of the snowpack (i.e. below the top few cm) where all solar direct radiation has been converted to diffuse radiation by multiple scattering in the top few cm of snow. The irradiances used in the calculation of the *e*-folding depth were recorded below the first 10 cm. Below a few cm, all radiation is isotropic (Lee-Taylor and Madronich, 2002) thus there can be no solar zenith angle dependence to *e*-folding depth (King and Simpson, 2001). The *e*-folding depth is independent of the absolute values of irradiance incident on the snow surface as the *e*-folding depth is the decay constant for an exponential decrease in relative irradiance. Depth-integrated production rates for the photolysis of H_2O_2 and NO_3^- (R2b.3 and R2b.1, found in Chapter 2b) were calculated for clear skies at four solar zenith angles: 60°, 69°, 75°, 86°. The Earth-Sun distance and ozone column were based on the date of field measurement for each snowpack (Table 1), and there was no atmospheric aerosol (the presence or absence of atmospheric aerosol will not effect the result of the calculation of *e*-folding depth or

diffuse albedo). The asymmetry factor, g, used for snow was 0.89 and an under-snow ground albedo of 0.1 was used (Lee-Taylor and Madronich, 2002). The value of under-snow albedo is not important in the work described here as the snowpack thickness is large enough (typical >3–5 *e*-folding depths) to ensure it is optically "semi-infinite" as demonstrated in France *et al*. (2010) and previously by Warren and Wiscombe (1980). Aoki *et al.* (2000) investigated the difference for single scattering parameters (g) for snow grains between Mie theory and Henyey-Greenstein theory and noted that for Bi-direction Reflectance Distribution Function (BRDF) calculations at greater than 1.4 μm there was a difference, but for albedo and at wavelengths less than 1.4 μm the Mie theory parameters gave the same results as the Henyey-Greenstein theory. As stated in the method section, the inclusion of atmospheric aerosol to the radiative-transfer calculations will not effect the calculation of asymptotic *e*-folding depth or diffuse albedo. However, exploratory calculations showed that the inclusion of an atmospheric aerosol profile described by Elterman (1968) reduces the photolysis coefficient for the photolysis of NO_2 by ~10% at 5 cm depth in the snowpack. Previous work by my research group (Fisher *et al.*, 2005; France *et al.,* 2007; 2010; 2011a; 2011b; King *et al.*, 2005) have neglected atmospheric aerosol column and the work presented here is consistent with that work.

The optical properties of the snowpack may be characterised by wavelength dependent scattering and absorption cross-sections (Lee-Taylor and Madronich, 2002). The absorption cross-section, σ_{abs}, is the sum of light absorption owing to water-ice, σ_{abs}^{ice}, and absorption owing to all light-absorbing species in the snowpack, σ_{abs}^{+}; for the study presented here, all absorption by light-absorbing species in the snowpack is due to black carbon. The absorption cross-section of ice used was taken

from Warren and Brandt (2008) and is plotted in Figure 2b.2 (found in Chapter 2b). The ice absorption cross-section is not well known in the wavelength region of 200–400 nm. Warren and Brandt (2008) noted the imaginary part of the refractive index of ice is effectively no different from zero (below 2×10^{-11}) in this wavelength region and therefore the value of the ice absorption cross-section used in this work is a linearly interpolated value between values for wavelengths of 200–400 nm.

The absorption cross-section used for the black carbon particle is reproduced in Figure 2b.2 (found in Chapter 2b). Details of the calculation can be found in Warren and Wiscombe (1980; 1985) but briefly the black carbon particles were assumed to be spheres of radius 0.1 μm, with a density of 1 g cm^{-3} and a complex refractive index of 1.8–0.5i. The uncertainty in these properties will be discussed later. The calculated absorption cross-section for black carbon agrees well with the measured black carbon absorption cross-section from Bond and Bergstrom (2006), as shown in Chapter 2b (Figure 2b.5). Albedo and *e*-folding depths were calculated at many wavelengths but reported at seven discrete wavelengths: 300, 350, 400, 450, 500, 550 and 600 nm whilst photolysis rate coefficients were calculated per 1 nm over 290–600 nm. The albedo, *e*-folding depth and photolysis rate coefficients for reactions 2b.1 and 2b.3 were calculated with mass ratios of black carbon in snow of 1, 2, 4, 8, 16, 32, 64, 128, 256, 512 and 1024 ng g^{-1}. The mass ratios of black carbon bracket the values found experimentally (Doherty *et al.*, 2010). Details of the individual Earth-Sun distances, ozone columns and values of scattering coefficient, σ_{scatt}, are presented in Table 2c.1. To demonstrate the accuracy of the radiative-transfer method described above, the albedo and *e*-folding depth were calculated for a Barrow snowpack described in France *et al.* (2012). Figure 2c.3 demonstrates a measured nadir reflectivity and *e*-

folding depth, and a sample model fit to the measurements using scattering cross-sections from Table 2c.1 and absorption cross-sections in France *et al.* (2012). Reproducing snow reflectivity and *e*-folding depth simultaneously is a rigorous test of the method as there are less parameters (more constrained) than fitting simply albedo (e.g. Jacobson, 2004).

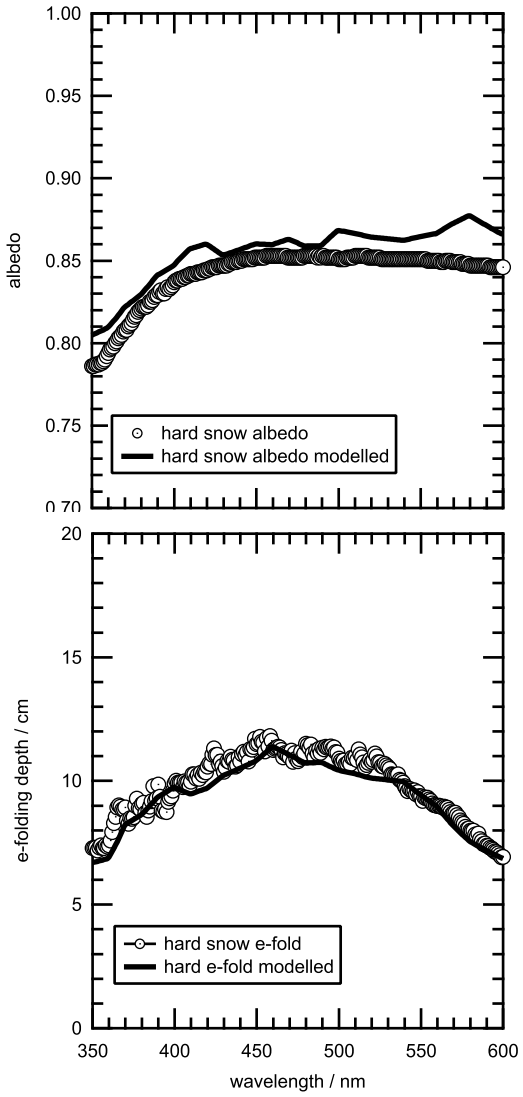

Figure 2c.3. Light penetration depth and reflectance measured for the hard snowpack during the Barrow OASIS campaign (France *et al.,* 2012) compared to modelled light penetration depth and

reflectance using TUV-snow (Lee-Taylor and Madronich, 2002), with wavelength variable snow optical properties (σ^{+}_{abs} and σ_{scatt}) and a snowpack density of 0.39 g cm^{-3}.

2c.3.1.3 Depth-Integrated Production Rate Calculations

Detailed descriptions for the calculation of photolysis rate coefficients, *J*, and depth-integrated production rates are found in chapter 2b. Briefly, photolysis rate coefficients, *J*, for reactions (R2b.1) and (R2b.3) were calculated using,

$$J = \int_{\lambda=290nm}^{\lambda=600nm} \sigma(\lambda,\mathrm{T})\Phi(\lambda,\mathrm{T})\mathrm{I}(\theta,\lambda)\mathrm{d}\lambda \qquad \text{(E2c.1)},$$

where σ is the absorption cross-section for NO_3^- or H_2O_2 taken from Chu and Anastasio (2003; 2005) respectively, Φ is quantum yield (0.71 for H_2O_2 and 0.34×10^{-3} for NO_3^-) with values adjusted for temperature (T = 263 K) taken from Chu and Anastasio (2003; 2005) respectively; I is the spherical irradiance, 'actinic flux', calculated using TUV-snow (Lee-Taylor and Madronich, 2002) within the snowpack, T is the snow temperature, λ is the wavelength and θ is the solar zenith angle.

Warren and Wiscombe (1980) note that the diffuse albedo for snowpacks is very similar to the direct albedo at a solar zenith angle of ~60˚. Thus, to a first approximation, the photolysis rate coefficient calculated at a solar zenith angle of 60˚ may be taken as representative of diffuse-only sky conditions (i.e. no direct solar beam). Depth-integrated production rates, F, of NO_2 and OH radicals were calculated using equation (E2c.2)

$$\mathrm{F} = [x] \int_{\mathrm{z}=0m}^{\mathrm{z}=1m} J\,\mathrm{dz} \qquad \text{(E2c.2)}$$

where z is the depth into the snowpack and $[x]$ is the concentration of NO_3^- or H_2O_2 : 3.9 μmol l^{-1} (Jacobi *et al.*, 2012) and 0.4 μmol l^{-1} (Beine *et al.*, 2011) respectively. A depth-integrated production rate of NO_2 may be considered equal to a potential molecular flux of photolytically produced NO_2 from the snowpack to the atmosphere in the absence of secondary reactions, photolysis or any impediment by the crystal matrix. Hydroxyl radicals are very reactive and have a very short lifetime thus they are not considered to advect from the snowpack.

Equation (2c.3) assumes a depth-independent concentration of hydrogen peroxide or nitrate. France *et al.* (2007) demonstrated depth independence of a chromophore to be a reasonable approximation for the type of work described here. The concentration-depth dependence of a chromophore tends to decrease over an order of magnitude with snow depth compared to light irradiance in the snowpack which will decrease over many orders of magnitude over the same snow depth. Thus concentration-depth dependence of a chromophore does not have a significant effect when determining depth-integrated production rates from snowpack. France *et al.* (2007) demonstrated the depth-integrated production rate of hydroxyl radical from the South Pole snowpit varied by 3–5% when considering depth-dependent chromophore concentrations or constant chromophore concentrations.

2c.4 Results

The effects (and parameterisation of the effects) of black carbon mass ratio in the snow on *e*-folding depth, albedo and depth-integrated production rates (summarized in Tables 2c.3, 2c.4 and 2c.6) will be considered individually:

2c.4.1 Effect of black carbon on light penetration depth (*e*-folding depth)

Light penetration depths (*e*-folding depths) versus black carbon mass ratio have been plotted for the four snowpacks in Figure 2c.4.

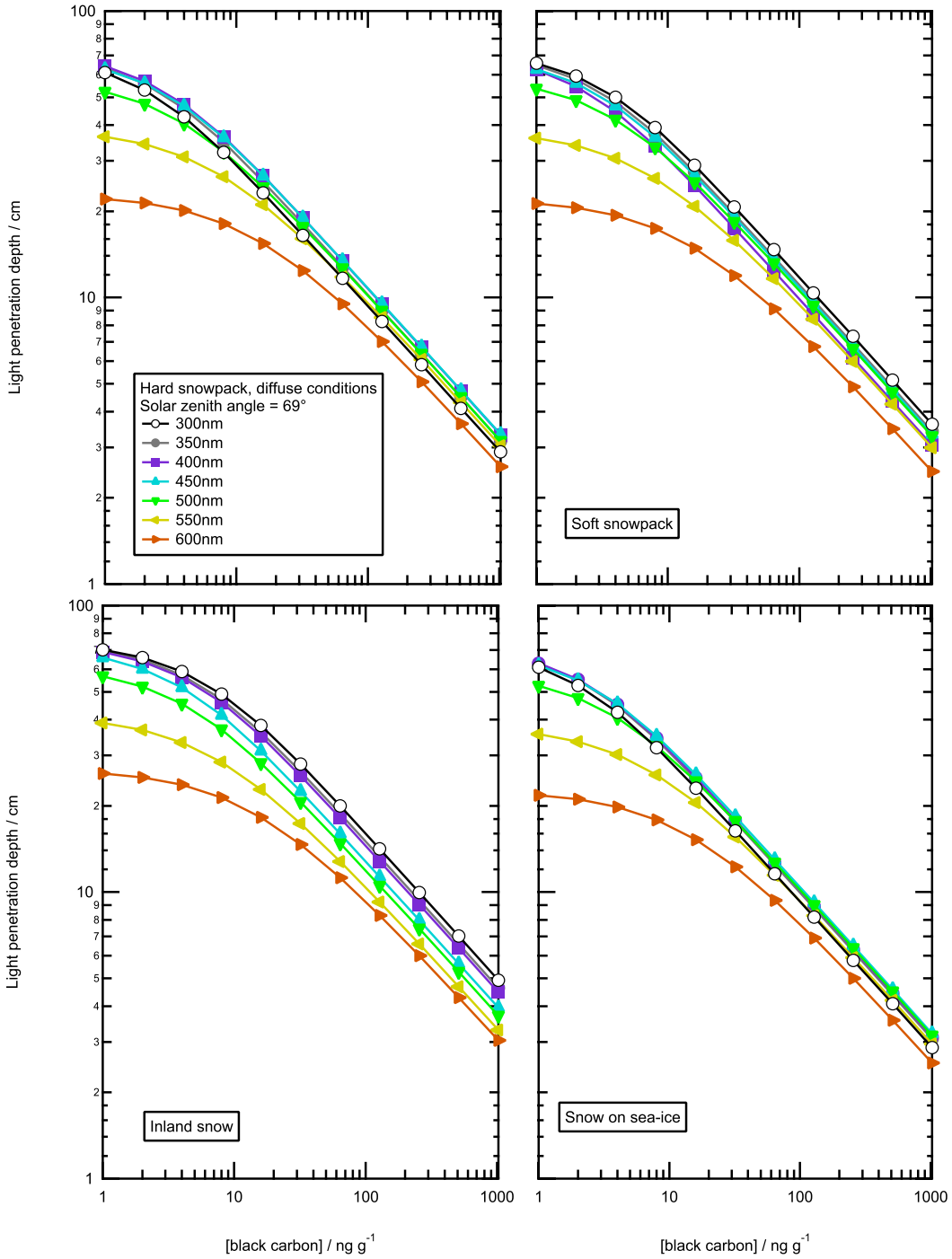

Figure 2c.4. Light penetration depths (*e*-folding depths) for four snowpacks plotted versus black carbon mass ratio for solar wavelengths of 300, 350, 400, 450, 500, 550 and 600 nm under diffuse sky conditions (nominal solar zenith angle of 69º).

The variation of *e*-folding depth with black carbon is not trivial and has two regimes dependent on black carbon mass ratio: If the mass ratio of black carbon is less than ~20 ng g^{-1} the absorption of solar radiation in the snowpack is dominated by ice and the *e*-folding depth develops a different wavelength dependence for each of the wavelengths of 450–600 nm relative to the *e*-folding depths at larger (>20 ng g^{-1}) black carbon mass ratios. The wavelength dependence of *e*-folding depths (for wavelengths 450–600 nm at black carbon mass ratios below 20 ng g^{-1}) is due to the absorption cross-section of ice, σ_{ice}, increasing quickly with wavelength over the range 450–600 nm, as shown in Figure 2b.2 (found in Chapter 2b). In the second regime, black carbon mass ratio is greater than ~20 ng g^{-1}, and the absorption of solar radiation in the snowpack is dominated by black carbon (Figure 2c.4 and 2c.5). The response of *e*-folding depth to increasing black carbon mass ratio becomes less wavelength dependent. The variation of the absorption cross-section of black carbon, σ^{+}_{abs}, with wavelength is small relative to ice and decreases from 300 nm to 1000 nm, i.e. opposite behaviour to the absorption cross-section of ice with wavelength (Figure 2b.2 (found in Chapter 2b)). It should be noted that for wavelengths less than 500 nm the transition between ice and black carbon dominated absorption is closer to 10 ng g^{-1}.

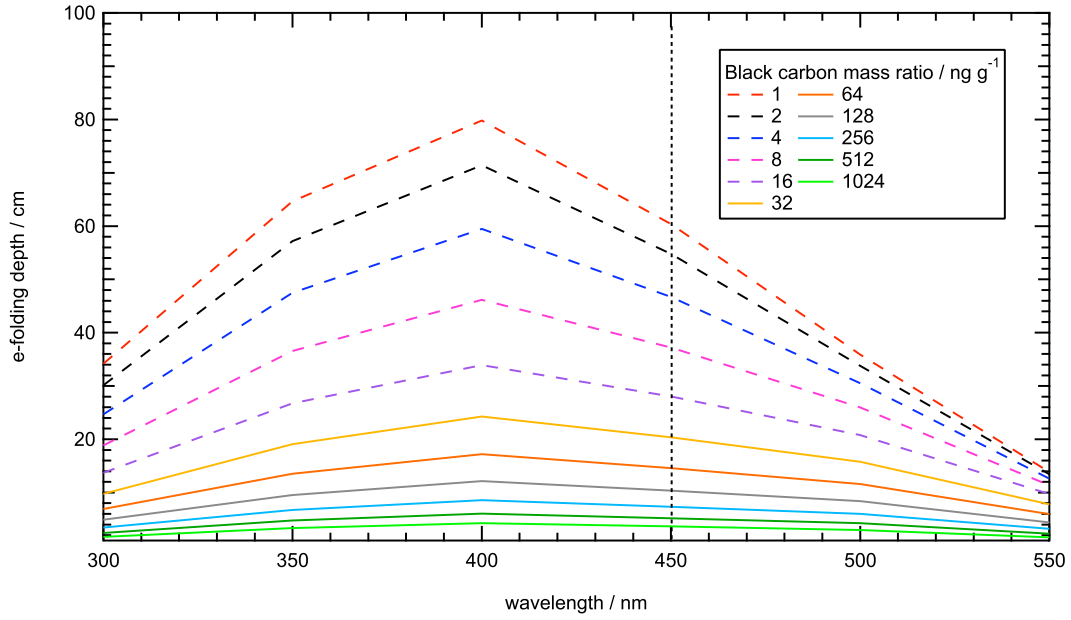

Figure 2c.5. *e*-folding depth vs wavelength for black carbon mass ratios of 1, 2, 4, 8, 16, 32, 64, 128, 256, 512, 1024 for the hard snowpack. The dashed lines represent black carbon mass ratios >20 ng g^{-1}, the solid lines represent black carbon mass ratios <20 ng g^{-1} and the dotted line represents a change in regime for wavelengths <450 nm.

For mass ratios of black carbon greater than 10-20 ng g^{-1} (depending on wavelength), the variation of *e*-folding depth with respect to black carbon obeys a simple power law, equation (2c.4) (as shown in Figure 2c.4). Equation 2c.4 is empirically derived.

$$e\text{-folding depth} = \alpha\left[\text{black carbon}\right]^{-\beta} \qquad \text{(E2c.3)}$$

The data in Figure 2c.4 are fitted to equation (E2c.3) for each wavelength. The values of α and β are displayed in Table 2c.2 along with the range of black carbon mass ratio over which the power law is valid. The power law is not valid over the whole range of black carbon considered. For all snowpacks the exponent, $-\beta$, in equation (E2c.3) is approximately -0.5 thus a doubling of the black carbon mass ratio (above 10-20 ng

g^{-1}) will reduce the light penetration depth to ~70% of its initial value. For the inland snow, a doubling of black carbon mass ratio will reduce light penetration depth to ~73%. All values have an error of 1 standard deviation from the fit of the power law.

Snow Type	Wavelength / nm	α / cm ng^{β} $g^{-\beta}$	$-\beta$	[Black Carbon] Range / ng g^{-1}
Hard	300	89.1 ± 0.911	0.489 ± 0.00353	8-512
	350	96.2 ± 1.36	0.485 ± 0.00487	8-512
	400	100 ± 1.63	0.482 ± 0.00562	8-512
	450	98.8 ± 1.79	0.479 ± 0.00624	8-512
	500	92.3 ± 1.5	0.480 ± 0.0046	16-512
	550	81.2 ± 2.28	0.467 ± 0.00675	32-512
	600	55.8 ± 2.94	0.406 ± 0.0125	32-512
Soft	300	106 ± 2.29	0.477 ± 0.00737	8-512
	350	102 ± 1.79	0.481 ± 0.00602	8-512
	400	86.0 ± 2.05	0.462 ± 0.0102	8-512
	450	99.1 ± 1.85	0.479 ± 0.00642	8-512
	500	95.9 ± 1.66	0.480 ± 0.0049	16-512
	550	80.1 ± 2.26	0.467 ± 0.00679	32-512
	600	53.7 ± 2.81	0.431 ± 0.0124	32-512
Snow on sea-ice	300	88.6 ± 0.911	0.489 ± 0.00356	8-512
	350	94.3 ± 1.19	0.487 ± 0.00435	8-512
	400	95.7 ± 1.25	0.487 ± 0.00449	8-512
	450	96.0 ± 1.59	0.481 ± 0.00569	8-512
	500	85.1 ± 2.27	0.459 ± 0.00904	8-512
	550	71.0 ± 2.75	0.443 ± 0.0108	16-512
	600	55.1 ± 2.87	0.431 ± 0.0124	32-512
Inland	300	126 ± 5.53	0.446 ± 0.0146	8-512
	350	123 ± 4.7	0.453 ± 0.0129	8-512
	400	135 ± 2.53	0.485 ± 0.00531	16-512
	450	121 ± 1.67	0.489 ± 0.00392	16-512
	500	106 ± 2.11	0.478 ± 0.0056	16-512
	550	87.8 ± 2.43	0.466 ± 0.00666	32-512
	600	65.9 ± 3.44	0.431 ± 0.0124	32-512

Table 2c.2. Power law coefficients for relating *e*-folding depth, ε, to black carbon mass ratio, i.e. $\varepsilon = \alpha[\text{black carbon}]^{-\beta}$, for black carbon mass ratios greater than 20 ng g^{-1}.

2c.4.2 Effect of black carbon mass ratio on albedo

Figure 2c.6 plots decreasing albedo with increasing black carbon mass ratio under diffuse sky conditions. Albedo can be defined as the ratio of upwelling irradiance to downwelling irradiance.

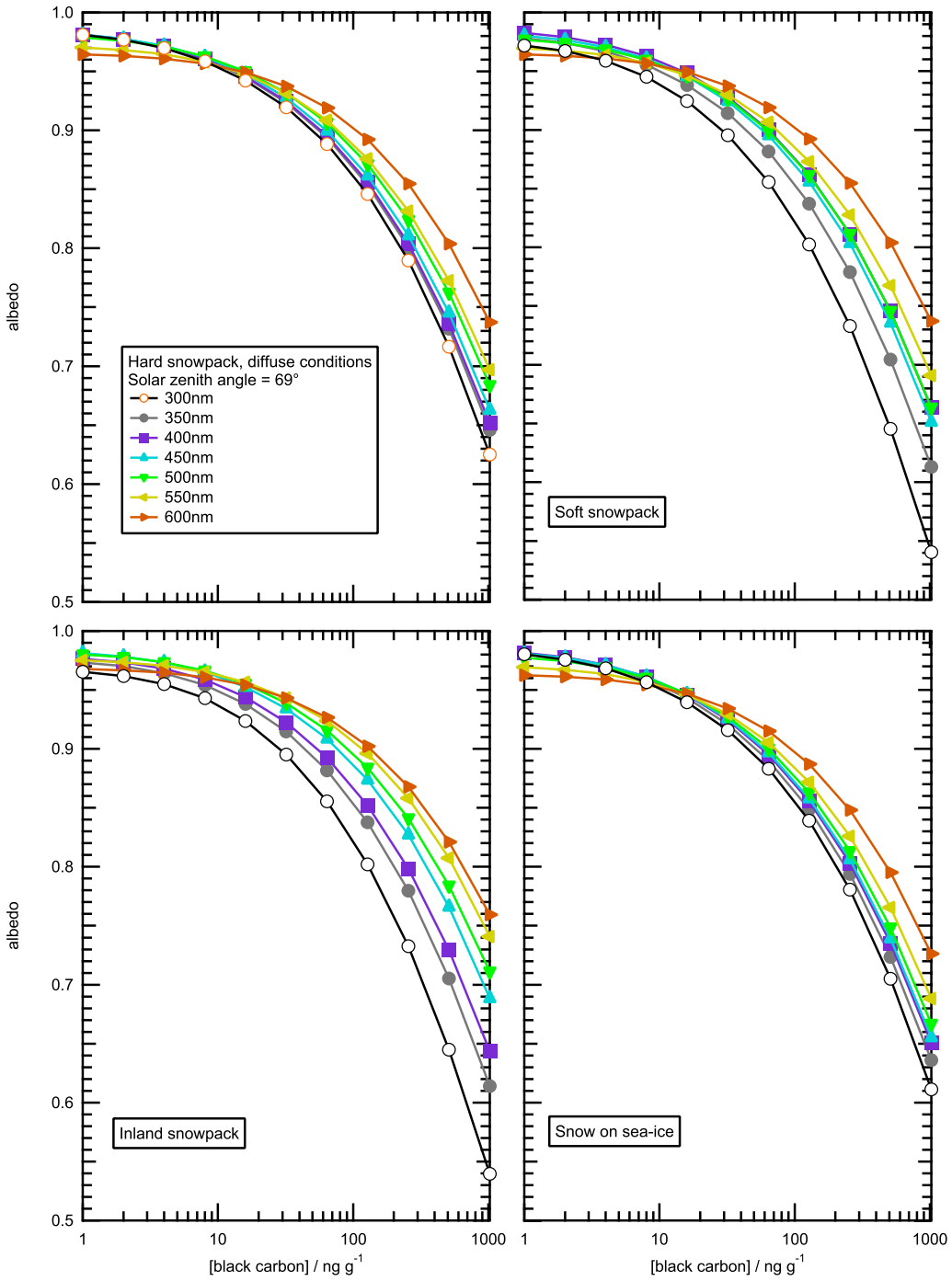

Figure 2c.6. Albedos i.e. ratio of upwelling and downwelling irradiance, for four snowpacks plotted versus black carbon mass ratio for light wavelengths of 300, 350, 400, 450, 500, 550 and 600 nm under diffuse sky conditions (nominal solar zenith angle of 69º).

Each snowpack albedo responds slightly differently to increased black carbon mass ratios. Large decreases of the albedo for increasing black carbon mass ratio are noted

for the inland snowpack and the soft snowpack but the albedo response for each wavelength is different, as demonstrated in Figure 2c.6. As the black carbon mass ratio increases the wavelength dependence of the albedo reverses as the absorption of light within the snowpack is influenced more by black carbon and less by water-ice. The relationship in equation (VII) is not valid for albedo. The decrease or increase in albedo for doubling or halving the mass ratio of black carbon around 32 ng g^{-1} is contained in Table 2c.3 and is approximately 2–3 %. The black carbon absorption spectrum used in this study (Figure 2b.2 (found in Chapter 2b)) decreases steadily from 350 nm to 600 nm, but with less and opposite gradient to the variation of water-ice with wavelength which generally increases from 400 nm to 600 nm.

Snow Type	$\frac{\text{Albedo([Black Carbon]=32 ng g}^{-1}\text{)}}{\text{Albedo([Black Carbon]=64 ng g}^{-1}\text{)}}$	$\frac{\text{Albedo([Black Carbon]=32 ng g}^{-1}\text{)}}{\text{Albedo([Black Carbon]=16 ng g}^{-1}\text{)}}$
Hard	1.033	0.978
Soft	1.033	0.978
Snow on sea-ice	1.031	0.979
Inland	1.033	0.978

Halving black carbon mass ratio from 64 to 32 ng g^{-1} increases albedo by 3%. Doubling black carbon mass ratio from 16 to 32 ng g^{-1} decreases albedo by 2%.

Table 2c.3. Relative changes in albedo with increasing and decreasing black carbon mass ratios, considering values typically found in Barrow snowpack (France *et al.*, 2012).

2c.4.3 The effect of black carbon mass ratio on snowpack photochemistry

Figures 2c.7 and 2c.8 plot the variation in depth-integrated production rates for NO_2, $F(NO_2)$, and OH radicals, F(OH), respectively, as a function of black carbon mass ratio. The dependence of $F(NO_2)$ and F(OH) on the mass ratio of black carbon matches the behaviour shown in Figure 2c.4 for the light penetration depths, with ice

dominated absorption below 20 ng g^{-1} and black carbon dominated absorption above 20 ng g^{-1}.

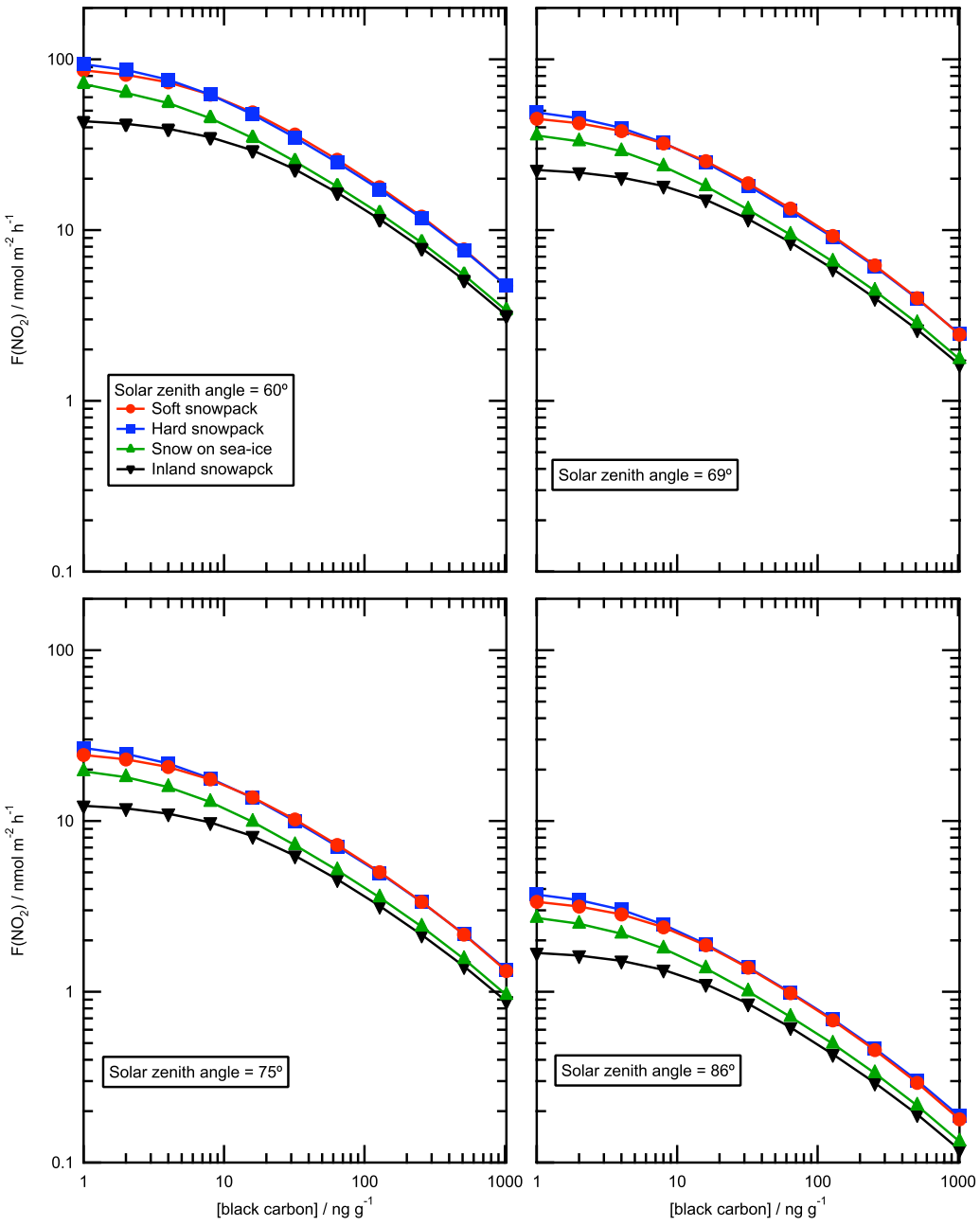

Figure 2c.7. Depth-integrated production rates of NO_2, $F(NO_2)$, versus black carbon mass ratio for the four snowpacks from the Barrow OASIS campaign. The depth-integrated production rates were calculated with a NO_3^- concentration of 3.9 µmol l^{-1} (Jacobi *et al.*, 2012) and at solar zenith angles of 60º, 69°, 75° and 86° under clear sky conditions. Note that all axes are plotted on a logarithmic scale.

The variation of $F(NO_2)$ and F(OH) with black carbon was fitted to the power law in equation (VII) and the values of α and β are in Table 2c.4. Note the value of $-\beta$ for all snowpack with black carbon mass ratios greater than 16 ng g^{-1} and a solar zenith angle of greater than 60° is ~–0.5 for $F(NO_2)$ and ~–0.6 for F(OH). Thus, a doubling of snowpack black carbon mass ratio will reduce $F(NO_2)$ and F(OH) to ~70% and ~65% of initial values respectively. It is worth noting that F(OH) decreases "quicker" than $F(NO_2)$ as $\phi\sigma F$ for F(OH) peaks at a shorter wavelength than $F(NO_2)$ and $\varepsilon_{\lambda=300nm} < \varepsilon_{\lambda=320nm}$.

Snow Type	Solar Zenith Angle / °	F(NO_2)			F(OH)		
		α / cm g ng $^{-1}$	-β	[Black Carbon] Range /ng g^{-1}	α /cm g ng^{-1}	-β	[Black Carbon] Range /ng g^{-1}
Hard	**60**	191 ± 9.39	0.497 ± 0.01	16-512	1650 ± 39.7	0.591 ± 0.01	16-512
	69	100 ± 4.93	0.497 ± 0.01	16-512	923 ± 22.6	0.591 ± 0.01	16-512
	75	54.8 ± 2.71	0.497 ± 0.01	16-512	541 ± 13.5	0.591 ± 0.01	16-512
	86	7.64 ± 0.38	0.495 ± 0.01	16-512	94.6 ± 2.4	0.591 ± 0.01	16-512
Soft	**60**	197 ± 12	0.496 ± 0.02	16-512	18900 ± 84.5	0.592 ± 0.01	16-512
	69	102 ± 6.2	0.497 ± 0.02	16-512	1030 ± 42.6	0.592 ± 0.01	16-512
	75	55.5 ± 3.35	0.497 ± 0.02	16-512	601. ± 26	0.592 ± 0.01	16-512
	86	7.54 ± 0.443	0.498 ± 0.02	16-512	89.2 ± 2.33	0.593 ± 0.01	16-512
Snow on sea-ice	**60**	140 ± 6.93	0.500 ± 0.01	16-512	1550 ± 38	0.593 ± 0.01	16-512
	69	73.0 ± 3.64	0.500 ± 0.01	16-512	868. ± 21.6	0.593 ± 0.01	16-512
	75	40.0 ± 2	0.500 ± 0.01	16-512	509. ± 12.9	0.593 ± 0.01	16-512
	86	5.56 ± 0.28	0.500 ± 0.01	16-512	103 ± 4.13	0.593 ± 0.01	16-512
Inland	**60**	135 ± 10.2	0.512 ± 0.02	32-512	1850 ± 118	0.612 ± 0.02	32-512
	69	69.5 ± 5.05	0.512 ± 0.02	32-512	1020 ± 60	0.613 ± 0.02	32-512
	75	37.6 ± 2.66	0.513 ± 0.02	32-512	589 ± 33.6	0.614 ± 0.01	32-512
	86	5.11 ± 0.351	0.514 ± 0.02	32-512	101. ± 5.45	0.614 ± 0.01	32-512

Table 2c.4. Power law coefficients for relating F(NO_2) and F(OH) to black carbon mass ratio, i.e. $\varepsilon = \alpha[\text{black carbon}]^{-\beta}$, for black carbon mass ratios greater than 20 ng g^{-1} and solar zenith angles greater than 60°.

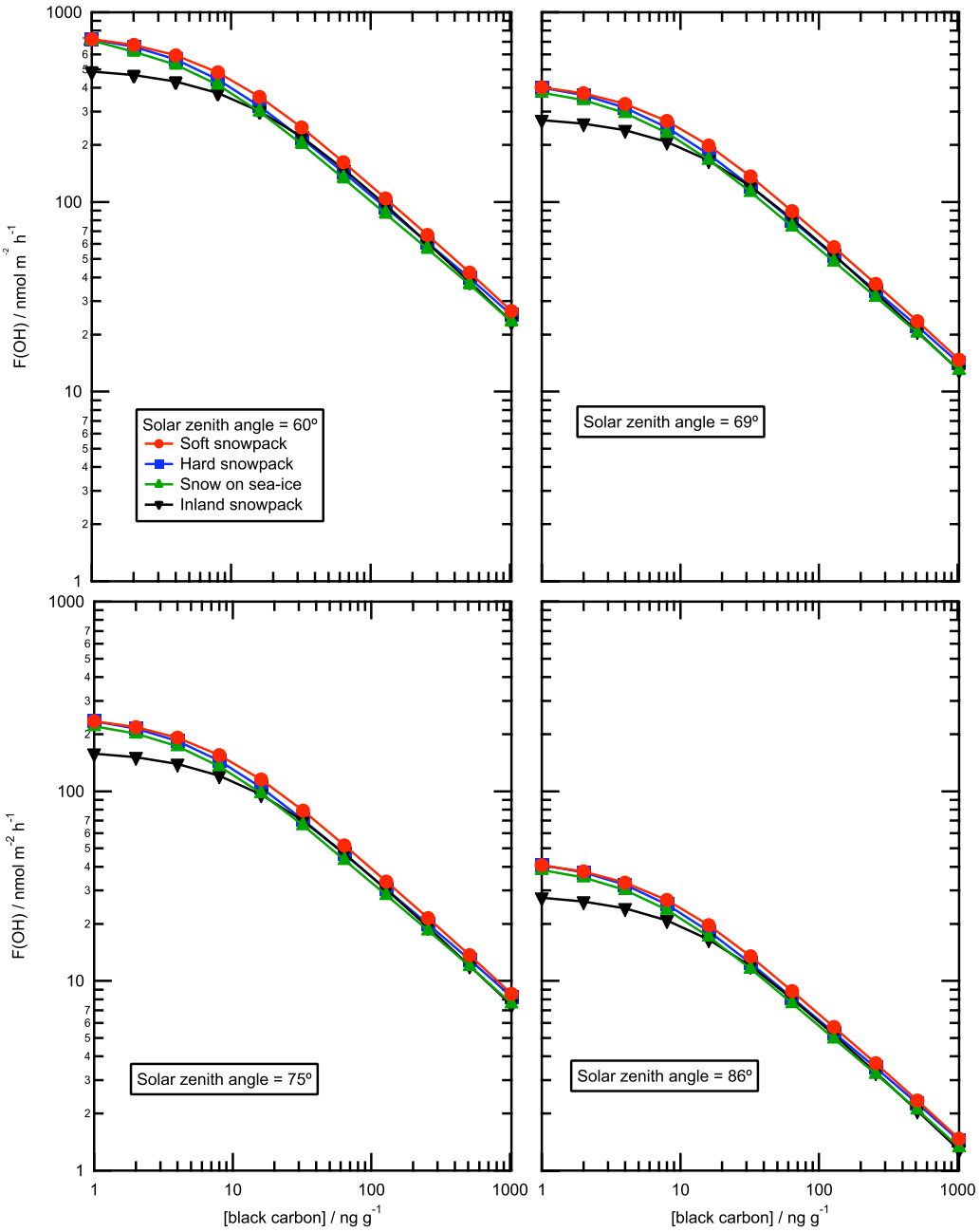

Figure 2c.8. Depth-integrated production rates of OH radicals, F(OH), from the photolysis of hydrogen peroxide in the snowpack for the four snowpacks from the Barrow OASIS campaign. The depth-integrated production rates are calculated with an H_2O_2 melted concentration of 0.4 µmol l^{-1} (Beine *et al.*, 2011) and at solar zenith angles of 60º, 69°, 75° and 86° under clear sky conditions. Note that all axes are plotted on a logarithmic scale.

The decrease in depth-integrated production rates of OH radicals, F(OH), and NO_2, $F(NO_2)$ with increasing black carbon mass ratios were calculated for the four snowpacks at four different solar zenith angles (Figures 2c.7 and 2c.8). The black carbon mass ratios used in the calculations were between 1–1024 ng g^{-1}, a range that encompasses the present-day black carbon mass ratios of the Barrow snowpack but also with higher and lower mass ratios to assess how increasing/decreasing black carbon mass ratio will affect snowpack photochemistry**.** Depth-integrated photolytic production rates reported in chapter 2b are the actual values calculated for the OASIS 2009 campaign as absorption by both HULIS and black carbon is considered. The study presented here considers only black carbon absorption (the strongest absorber among aerosol carbonaceous constituents (Hoffer *et al.*, 2006)) to assess how varying black carbon mass ratios will affect the photochemical production rates of snowpacks.

2c.5 Discussion

The discussion will focus on the following aspects of the work: the identity of the light-absorbing snowpack impurity, the absorption spectrum of black carbon and the effect of black carbon mass ratio on snowpack *e*-folding depth, albedo and snowpack photochemistry.

2c.5.1 Identity of the light-absorbing impurity

The main sources of organic carbon to the atmosphere and to snowpack are anthropogenic activities and biomass burning (e.g. Hegg *et al.*, 2009; Goldberg, 1985; McConnell *et al.*, 2007), the optical parameters of organic carbon from biomass burning aerosols have been reported by Kirchstetter *et al.* (2004). Brown carbon,

which includes HULIS (Humic Like Substances), is highly abundant yet a weaker absorber of visible light than black carbon which has the highest absorption cross-section among carbonaceous constituents of aerosols and therefore contributes significantly to atmospheric absorption by aerosols (e.g. Hoffer *et al.*, 2006). Chapter 2b demonstrated that black carbon alone could not account for all the absorption seen in the four Barrow snowpacks and an additional absorption by HULIS and other chromophores was necessary to explain variation of the cross-section of light-absorbing impurities in snowpack, σ^{+}_{abs}, with wavelength. It is important to note the effect of increased absorption due to impurities within the snowpack upon snowpack photochemistry, *e*-folding depth and albedo, especially black carbon as it is produced mainly by anthropogenic activity and therefore black carbon emissions are likely to be regulated or change in future. In the work presented here all absorption within the snowpack was attributed to black carbon for simplicity. However, the results of Figures 2c.7 and 2c.8 may be adjusted for another light-absorbing impurity (or a change in the properties of the black carbon particle) without repeating the radiative-transfer calculations, using E2c.4.

$$[\text{HULIS}] = [\text{BC}] \times \left(\frac{\text{wavelength dependent black carbon absorption}}{\text{wavelength dependent HULIS absorption}} \right) \qquad \text{(E2c.4)}$$

The mass ratio of black carbon may be converted to a specific absorption by snowpack light-absorbing impurities (i.e. σ^{+}_{abs}) by multiplying values on the ordinate of Figures 2c.7 and 2c.8 with the absorption cross-section of black carbon (at the correct wavelength) in Figure 2b.2 (found in Chapter 2b). Dividing the specific absorption (σ^{+}_{abs}) by the cross-section of the new absorber, such as HULIS (Figure

2c.9), at the correct wavelength will allow the albedo and *e*-folding depth to be reported as a function of mass ratios of the new absorber (Figures 2c.10 and 2c.11).

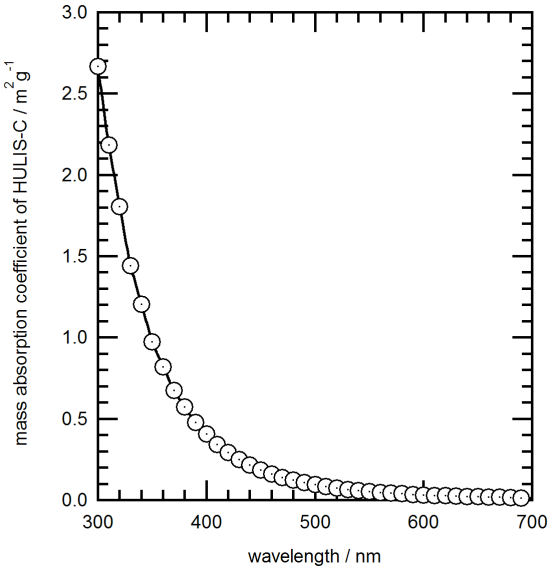

Figure 2c.9. HULIS absorption spectrum. The absorption cross-section is taken from the median value of the envelope given in Figure 5, Hoffer *et al.* (2006).

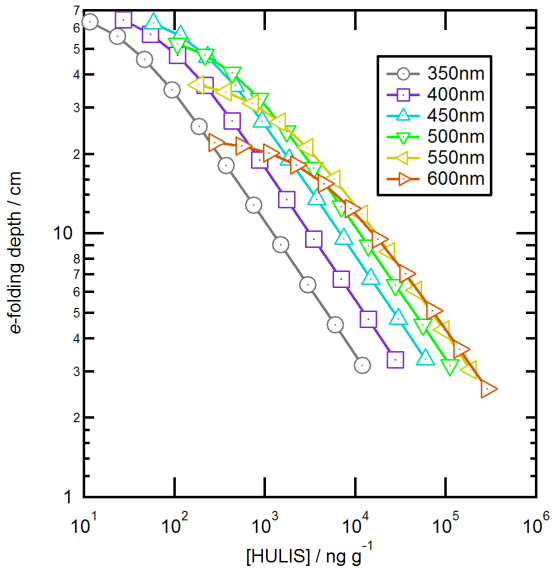

Figure 2c.10. *e*-folding depths for hard snowpack plotted versus HULIS concentrations for light wavelengths of 350, 400, 450, 500, 550 and 600 nm under diffuse sky conditions (nominal solar zenith angle of 69°).

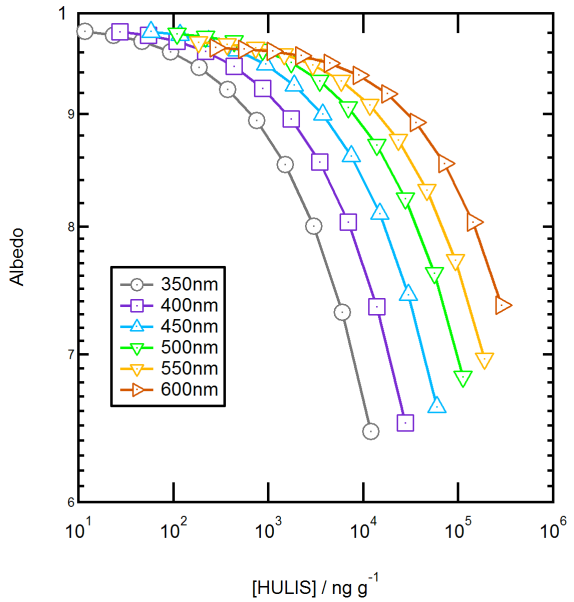

Figure 2c.11. Albedo for hard snowpack plotted versus HULIS concentrations for light wavelengths of 350, 400, 450, 500, 550 and 600 nm under diffuse sky conditions (nominal solar zenith angle of 69°).

2c.5.2 Black carbon absorption spectrum

For the work described here, a proxy for black carbon in snow was adopted from the literature (e.g. Bohren, 1986; Roessler and Faxvog, 1980; Warren and Wiscombe, 1980; 1985). It is useful to understand the sources of uncertainty that are introduced by adopting this proxy for black carbon in snow. The values of the index of refraction of the black carbon, size and location of the black carbon particle relative to the snow crystal/grain are the major sources of uncertainty on the calculation of the black carbon absorption cross-section. Bohren (1986) gives an excellent critique of the black carbon uncertainties of Warren and Wiscombe (1980) and Wiscombe and Warren (1980). A black carbon particle internal to the snow grain increases the absorption cross-section of the black carbon particle by a factor of 1.4 relative to the black carbon particle external to the snow grain (Bohren, 1986). In the work presented here, it was assumed that the black carbon has been deposited external to

the snowpack i.e. the black carbon was rimed onto the snow during snowfall or collected on the snowpack by atmospheric deposition or windpumping at a later date. Chylek *et al.* (1983) considered the effect on snow albedo of adding black carbon throughout the snow grain using a very similar radiative-transfer model to Warren and Wiscombe (1980) to calculate snow albedo. Chylek *et al.* (1983) found that values of black carbon deduced from their radiative-transfer model agreed well with measurements. It is not clear if black carbon should be modelled as internal or external to the snow grain and the study described here has taken the majority view i.e. external. A more detailed discussion can be found in Chylek *et al.* (1983). The imaginary index of refraction, and therefore the absorption spectrum, of different types of black carbon spans a factor of 5 (e.g. Roessler and Faxvog, 1980; Bohren, 1986) depending on the method of black carbon production. Chapter 2b (Figure 2b.5) demonstrated that the black carbon absorption spectra in Figure 2b.2 (found in Chapter 2b) is consistent with experimental measurements taken from the review of Bond and Bergstrom (2006). The third uncertainty is the shape of the black carbon particles and to remain consistent with previous works (e.g. France *et al*, 2011a; Warren and Wiscombe, 1980; 1985) a spherical black carbon particle was used. Bohren (1986) has shown that a needle or disk shape increases the absorption cross-section by a factor of 1.48 and 2.1 relative to the sphere using the equations shown in E2c.5. Comprehensive arguments by Bohren (1986) and Warren and Wiscombe (1980; 1985) justify the choice of black carbon properties used in this study.

$$(C_{abs})_{sphere} = \frac{kv}{3}\left(\frac{27}{(\varepsilon'+2)^2+\varepsilon''^2}\right)\varepsilon''$$
$$(C_{abs})_{needle} = \frac{kv}{3}\left(\frac{8}{(\varepsilon'+1)^2+\varepsilon''^2}+1\right)\varepsilon'' \quad \text{(E2c.5)}$$
$$(C_{abs})_{disk} = \frac{kv}{3}\left(\frac{1}{(\varepsilon'^2+\varepsilon''^2}+2\right)\varepsilon''$$

where v is the volume of a particle, ε is its dielectric function relative to that of the surrounding medium (in air, ε=2.99+i1.8) and k is the wavenumber of the incident light. Taken from Bohren and Huffman (1983), p.350.

Fieldwork investigating black carbon in snow (Table 2c.5) show that the mass ratio values of black carbon chosen in this work are reasonable.

Study	Black carbon mass ratio range /ng g^{-1}
Hegg *et al.* (2009)	0-40
Clarke and Noone (1985)	0.06-12.22
Doherty *et al.* (2010)	2-50
Ming *et al.* (2009)	5-981
Huang *et al.* (2011)	50-1000
Voisin *et al.* (2012)	2-17
France *et al.* (2012) and Chapter 2b	41-90

Table 2c.5. Range of black carbon mass ratios found through fieldwork by previous studies.

Jacobson (2004), Qian *et al.* (2009), Wang *et al.* (2011), Warren (1984; 1985) and Warren and Wiscombe (1980) have all investigated the effect of black carbon on albedo. The study presented here is different because it takes into account real snowpacks characterised both by light penetration depth and albedo, reports the effects of black carbon mass ratio on light penetration depth, albedo and

photochemical fluxes and the snow was not altered by measurement. Atmospheric deposition of black carbon to snowpack would (a) give a distribution of black carbon particle sizes from different sources and (b) give a distribution of different complex index of refractions from different sources. The work presented here has not considered such distributions and the reader could use the data plotted in Figures 3 and 4 to recalculate the effect on *e*-folding depth, albedo and depth-integrated production rates by different sized black carbon particles and a weighted sum of the distribution of absorption cross-sections corresponding to a distribution of particle size. The size distribution of black carbon particles in snow is not presently known.

2c.5.3 Effect of black carbon mass ratio on snowpack penetration depth

To the author's knowledge, there has been no systematic quantitative study on the effect of increasing black carbon mass ratios on *e*-folding depths in snowpacks. Table 2c.6 contains a survey of the previous light penetration depth measurements, their scattering and absorption cross-section as modelled by TUV-snow and the predicted *e*-folding depth using these cross-sections. Values of *e*-folding depth are reported for a wavelength of 400 nm.

Study	Snow Description	*e*-folding depth / cm (λ=400 nm)		σ_{scatt} / m^2 kg^{-1}	σ^{+}_{abs} / cm^2 kg^{-1}
		measured	predicted		
Grenfell and Maykut (1977)	Arctic summer, dry snow	2.4	2.3	6.4	7.3
	Arctic summer, melting snow	5.3	5.4	1.1	7.8
King and Simpson (2001)	Arctic Spring, windblown	1.3	1.3	25-30	4-5
Beaglehole *et al.* (1998)	Coastal Antarctic snowdrift, summer	6.6[a]	6.2	7	~0.4
Beine *et al.* (2006)	Antarctic coastal hard windpack	17[b]	17.3	1.3	4.3
	Antarctic coastal soft windpack	3.3	3.5	6.3	24
	Antarctic coastal recent windblown	4.5	4.3	3.7	37
	Antarctic coastal precipitation	15	14.8	4.3	17
Fisher *et al.* (2005)	Midlatitude maritime windslab, melting	13.9	-	1	1
	Midlatitude maritime windslab, dry	13.3	-	2–5	1–2
France *et al.* (2010)	Fresh Ny-Ålesund snowpack	6	5.7	16.7	2.7
	Melting Ny-Ålesund snowpack	9.9	9.7	0.8	19.8
This study	Hard snowpack	9.9	6.7	1.7	11
	Soft snowpack	9.4	7.7	2.0	11
	Inland snowpack	14.8	12.3	1.7	9
	Snow on sea-ice	9.4	7.5	1.8	15

[a] σ^{+}_{abs} and σ_{scatt} values suggest that Lee-Taylor and Madronich [2002] interpreted the data in Beaglehole et al. [1998] as liquid equivalent *e*-folding depth in contrast to King and Simpson [2001] who interpret the *e*-folding data in Beaglehole et al. [1998] as not corrected for density.

[b] in the original paper *e*-folding depth was incorrectly reported. Details of this snowpack can be found in France [2008].

Table 2c.6. Comparison of measured and predicted/modelled *e*-folding depths in snow and optical constants.

Figure 2c.3 shows the *e*-folding depth measured for the hard windpack in Barrow and the predicted *e*-folding depth using the model. The agreement between modelled and measured light penetration depths gives confidence to the method described in the work presented here. In the study presented here it was assumed the black carbon was uniformly mixed within the snowpack but the effect of layered snow containing different mass ratios of black carbon in different layers is possible. Preliminary field and modelling work on layered windpacks does not demonstrate any need to consider different black carbon mass ratios in different wind packed layers (France *et al.*, 2011a). Table 1 shows that all the snowpacks studied for work presented here have been re-worked by wind events and therefore the mass ratios of particles are assumed to be well-mixed in the top layers of the snowpack, thus, a constant black carbon mass ratio with depth is assumed. Owing to the close proximity of our study sites to human activity in Barrow, Alaska the regional black carbon concentrations given by Doherty *et al.* (2010) may not be representative of the black carbon mass ratio in snow found around Barrow; ~70 ng g^{-1} of black carbon was found in both the hard and the soft snowpacks, ~41 ng g^{-1} was found in the inland snowpack and ~90 ng g^{-1} was found in the snow on sea-ice (Chapter 2b; France *et al.*, 2012). The snow measured by Doherty *et al.* (2010) had recently fallen and therefore could be considered 'pristine' in comparison to the re-worked snow measurements (more typical snow surrounding Barrow) presented here, thus it may be better to consider the black carbon mass ratios in Barrow akin to that of Eastern Russia; mean C_{equiv}^{BC} values of (65 ± 44) ng g^{-1} (Doherty *et al.*, 2010).

2c.5.4 Effect of black carbon mass ratio on albedo

The amount of black carbon in snow controls the albedo and just a small fraction of black carbon, i.e. 5×10^{-8} ng g^{-1}, increases the imaginary part of the refractive index by more than a factor of 10 (Chylek *et al.*, 1983). There have been many modelling studies into the effect of black carbon mass ratio on albedo (e.g. Jacobson, 2004; Qian, 2009; Wang, 2011; Warren, 1984; 1985; Warren and Wiscombe, 1980) that have mainly dealt with hypothetical snowpacks and the study presented here, in contrast, uses measurements on real snowpack that were part of a wider field campaign and plots albedo versus black carbon mass ratio for a specific wavelength. Figure 2c.6 shows that even similar snowpacks will respond differently to black carbon mass ratio changes.

2c.5.5 The effect of black carbon mass ratio on snowpack photochemistry and future outlook

Lee-Taylor and Madronich (2002) produced a very useful plot to calculate $\int J(NO_3^-)dz / J(NO_2 \downarrow)$, i.e. the depth-integrated photolysis rate constant of nitrate photolysis relative to the surface photolysis coefficient for gaseous nitrogen dioxide, calculated for downwelling irradiance only, (which is frequently measured for field campaigns) as a function of snow albedo, *e*-folding depth or σ_{abs}^{+}. It is not possible to use Figure 5 in Lee-Taylor and Madronich (2002) to generate the figures (Figures 2c.5 and 2c.7) presented in this work as albedo and *e*-folding depth are also a function of black carbon. As shown in Figures 2c.5 and 2c.7, albedo and *e*-folding depth are sensitive functions of black carbon mass ratio and thus cannot be used to constrain a value of $\int J(NO_3^-)dz / J(NO_2 \downarrow)$ from Lee-Taylor and Madronich (2002). The work of

Figure 5 in Lee-Taylor and Madronich (2002) is an excellent resource for field workers who may have measurements of albedo, *e*-folding depth and $J(NO_2 \downarrow)$ and want to estimate $\int J(NO_3^-)dz$ whereas the work presented here demonstrates how the albedo, *e*-folding depth and depth-integration photolysis coefficients of reactions (2b.1) and (2b.3) respond to increasing or decreasing black carbon mass ratios for snowpacks characterised in Barrow, Alaska in Spring.

Inspection of Table 2c.4 demonstrates that for solar zenith angles greater than 60° and black carbon mass ratios greater than 20 ng g^{-1}, the depth-integrated production rate of NO_2 production from snow approximately follows the inverse square-root of the mass ratio of black carbon (i.e. $F(NO_2) \propto \frac{1}{\sqrt{[\text{black carbon}]}}$). The depth-integrated production rate of OH radicals is similar but the power is closer to 0.6 ($F(NO_2) \propto \frac{1}{[\text{black carbon}]^{0.6}}$). Such a simple approximate relationship can be used to estimate depth-integrated production rate response to increasing or decreasing black carbon scenarios for black carbon mass ratios greater than 20 ng g^{-1} i.e. doubling the black carbon in snow would reduce the depth-integrated production rates of NO_2 and OH radicals to ~70% and ~65% of their initial values.

As stated by Hansen *et al.* (2000), assessing climate forcing with consideration to changes in atmospheric aerosol (and thus its deposition) is a "wild card". Future trends of black carbon mass ratios within snow are difficult to predict as the main controls are anthropogenic processes that produce black carbon. Black carbon mass ratios in snow have varied significantly during the past 215 years, gradually rising

towards the mid 1800's until industrialisation caused a sharp increase in black carbon mass ratios (McConnell, 2007). For around 50 years, after 1900, the seasonal variability of black carbon mass ratios lessened as winter mass ratios matched the normally higher summer mass ratios but in the late 20th Century black carbon mass ratios once again became seasonal (McConnell, 2007). Ice cores from Greenland show that by 2000, black carbon mass ratios in snow/ice equalled the pre-industrial mass ratio of 1–2 ng g^{-1} in clean snowpack regions (Doherty *et al.*, 2010). Doherty *et al.* (2010) reported no increase in the black carbon mass ratios of Arctic snow since 1984 so it may be unlikely that black carbon in Arctic snow is causing the rapid decline of Arctic sea-ice as the snow is currently less polluted than in the 1980's. However, Flanner *et al.* (2009) does introduce the idea that black carbon in mid-latitude snow may be contributing indirectly to melt Arctic sea-ice by enhancing warm-air advection into the Arctic (Doherty *et al.*, 2010). Rosen *et al.* (1981) show that aerosol at Barrow, Alaska has a large increase in black carbon during winter to spring, the black carbon levels are almost as high as those found in urban areas. During February, the mass ratio of graphitic carbon is almost 40% of the carbonaceous mass (Rosen *et al.*, 1981). Sharma *et al.* (2006) and Garrett *et al.* (2011) highlight the seasonal variations of black carbon found in Barrow and indicate that the high black carbon mass ratios seen in winter and spring are due to long-range transport of pollutants. Black carbon removal is most efficient at warmer temperatures and higher humidities, thus a future warmer and wetter Arctic could be cleaner (Garrett *et al.*, 2011).

Hansen *et al.* (2000) suggest it should be easy to reduce black carbon emissions at fossil fuel power plants and Figures 2c.7 and 2c.8 show that a decrease in black

carbon will cause an increase in depth-integrated production rates of OH and NO_2 in snow at all studied solar zenith angles. Increased depth-integrated production rates of OH radicals and NO_2 molecules will increase the oxidative capacity of the snowpack and the atmospheric boundary layer above (e.g. Jones *et al.,* 2001). Bond and Sun (2005) take an opposing view to Hansen *et al.* (2000) stating that reducing black carbon cannot redress global warming because it has a different behaviour to greenhouse gases and thus may not diminish warming, it will be a costly process and the relevant emission sources are difficult to consign.

An increase in black carbon mass ratios in the snow will decrease depth-integrated production rates of OH and NO_2. "Warmer" snowpacks may produce larger depth-integrated production rates of OH radicals and NO_2 (Fisher *et al.*, 2005) and as black carbon in snow causes warmer snowpacks, a future warmer climate could have two effects on snow photochemistry: Firstly, snow photochemistry may become important (larger molecular fluxes from snowpack) in a warming world owing to more photochemistry occurring in the warm snowpack and secondly, a warming climate may cause a loss of snowpack thus snow photochemistry will become less important due to less snow cover. Thus a scenario may be envisaged where snow photochemistry may have a large effect on the oxidative potential of the overlying atmosphere but for a shorter duration.

2c.6 Conclusions

Increasing black carbon mass ratio in snow reduces albedo, *e*-folding depths and depth-integrated production rates of photochemically derived species in a complicated way. For black carbon mass ratios typically measured in the snow, *e*-folding depth, albedo and depth-integrated production rates of OH and NO_2 can switch from ice-

dominated absorption to black carbon dominated absorption. Light penetration depths and depth-integrated production rates (of NO_2 and OH radicals) follow a power law relationship for black carbon mass ratios greater than 10 ng g^{-1} and solar zenith angles greater than 60°.

The future is uncertain when considering the importance of photochemical production coefficients in snowpack owing to the dependence of black carbon production on human activity. Black carbon amounts in snow are very closely linked to human activity and therefore the reduction or increase of depth-integrated production rates of OH and NO_2 are linked to the increase or reduction of black carbon in the snow.

Chapter 3

Light Penetration Depths and Albedos in Arctic, Antarctic and Mid-Latitude Snowpacks Owing to Varying Black Carbon Mass Ratios

3.1 Introduction

Snow in the Arctic Ocean is presently suffering large-scale contamination by black carbon from anthropogenic sources (Bond and Bergstrom, 2006; Bond *et al*, 2004; Doherty *et al.*, 2010; Hansen and Nazarenko, 2004; Highwood and Kinnersley, 2006; Koch and Hansen, 2005; Stohl, 2006; Shindell *et al.*, 2008; Warren, 1984). Burning fossil fuels adds CO_2 to the atmosphere and also particulates, such as black carbon, which are the products of incomplete combustion (Browse *et al.*, 2012). The small black carbon particles are eventually scavenged from the atmosphere and incorporated into the Arctic snowpack (Baumgardner *et al.*, 2008; Browse *et al.*, 2012; Cooke and Wilson, 1996; Doherty *et al.*, 2010; Flanner *et al.*, 2007; Garrett *et al.*, 2011; Grenfell *et al.*, 2002; 2011; Noone and Clarke, 1998; Rahn and McCaffrey., 1979; Stohl *et al.*, 2006; Warren and Wiscombe, 1985). The major source of black carbon to the atmosphere at present is anthropogenic, burning of fossil fuels alone can produce over 8×10^9 kilograms of black carbon annually, but episodic biomass burning has been recognized as an important aerosol source that can also contribute a

maximum total of 6×10^9 kilograms of black carbon per year to the atmosphere (Cooke and Wilson, 1996; Gray, 1976; Harden *et al*., 2000; Hegg *et al.*, 2009; Holdsworth *et al.*, 1996; Koch and Hansen, 2005; Maenhaut *et al*., 1989; Saarikoski *et al.*, 2007; Stohl *et al.*, 2006; Sturges and Barrie, 1989; Warneke *et al.*, 2009; 2010; Warren, 1984). China and India are now the largest sources of black carbon emission (Jacobson, 2004) and although human population restricts the geographical location of the sources, long-range atmospheric transportation methods allow black carbon to have a globally widespread deposition extent (Doherty *et al.*, 2010; Highwood and Kinnersley, 2006; Koch and Hansen, 2005; Stohl, 2006; Shindell *et al.*, 2008; Warren, 1984). Local contamination from a permanent camp would have a greater influence on black carbon mass ratios within Antarctic snow in comparison to the Arctic as pollution sources are in closer proximity to the Arctic than the Antarctic thus black carbon in the Arctic may come from industrial sources in Europe (Hansen *et al.*, 2001; Warren, 1982).

Trace amounts of dust, HULIS, black carbon and other light-absorbing aerosols deposited within a snowpack can be measurably reduce the albedo of that snowpack relative to the albedo of pure snow (e.g. Clarke and Noone, 1985; Warren, 1982; Warren and Wiscombe, 1980; 1985; Wiscombe and Warren, 1980). Jacobson (2004) suggested that heating due to black carbon at the surface of the snowpack melts additional snow or sea-ice and the black carbon itself changes the reflectivity of the snow. Recent studies have shown that 10 ng g^{-1} of black carbon in snow reduces the albedo by 1% (Clarke and Noone, 1985; Flanner *et al.,* 2007; Grenfell *et al.,* 2002; Hansen and Nazarenko, 2004; Jacobson, 2004; Warren and Wiscombe, 1985). The reduction in visible surface albedo of snow

owing to absorption of solar radiation by black carbon in the snowpack may be responsible for a climatic warming and a reduction in snow and ice extent (Hansen and Nazarenko, 2004). Hansen and Nazarenko (2004) reported a radiative forcing of +0.3 W m^{-2} and suggested the black carbon in snow is a factor of two more efficient than atmospheric carbon dioxide in altering global air temperatures. Hansen and Nazarenko (2004) also suggested that recent climatic warmings seen in the Northern hemisphere Arctic i.e. early springs, thinning sea-ice and glacier retreat may be due to warming associated with black carbon in snow. Qu and Hall (2005) report that changes in the extent of global snow and ice can account for 50% of the observed changes in planetary albedo. Glaciers in West China that were strongly contaminated by black carbon at the surface experienced a ~5% reduction in albedo which caused accelerated melting (Ming *et al.,* 2009). Typical mass ratios of black carbon in snow have been reported in the range of 0.2-60 ng g^{-1} with extreme values of >250 ng g^{-1} (Clarke and Noone, 1985; Doherty *et al*, 2010; Hansen and Nazarenko, 2004; Hegg *et al.*, 2009; Huang *et al.*, 2011; Ming *et al.*, 2009; Voisin *et al.*, 2012). Black carbon, reported as an average mass ratio in the snow, could be concentrated at the surface where it would have more effect on albedo (Warren, 1982). Both absorption (by impurities) and scattering (influenced by grain size) control the albedo of snow. The shape and size of the snow crystals are changed by solar radiation, windpumping and temperature variations that lead to water vapour and temperature fluxes within snow on the ground (Cabanes *et al.*, 2002; Domine and Shepson, 2002). Albedo, light penetration depth and response to impurities contained within snow for individual snowpacks can be affected by snow metamorphism (changes in snow crystal shape and size). Snow grain size tends to

be larger in late winter/spring when there is enough sunlight to increase the importance of black carbon absorption (Hansen and Nazarenko, 2004). It is importance to bear in mind that the snow grain size, solar zenith angle, black carbon size/shape/morphology and whether the black carbon is situated external or internal to the ice grain can cause significant changes between the perceived mass ratio of black carbon in snowpack and the reduced reflectivity of the snowpack (Bohren, 1986). Figure 3.1 shows examples of different snow crystal morphology from snowpacks in Barrow, Alaska and Alert.

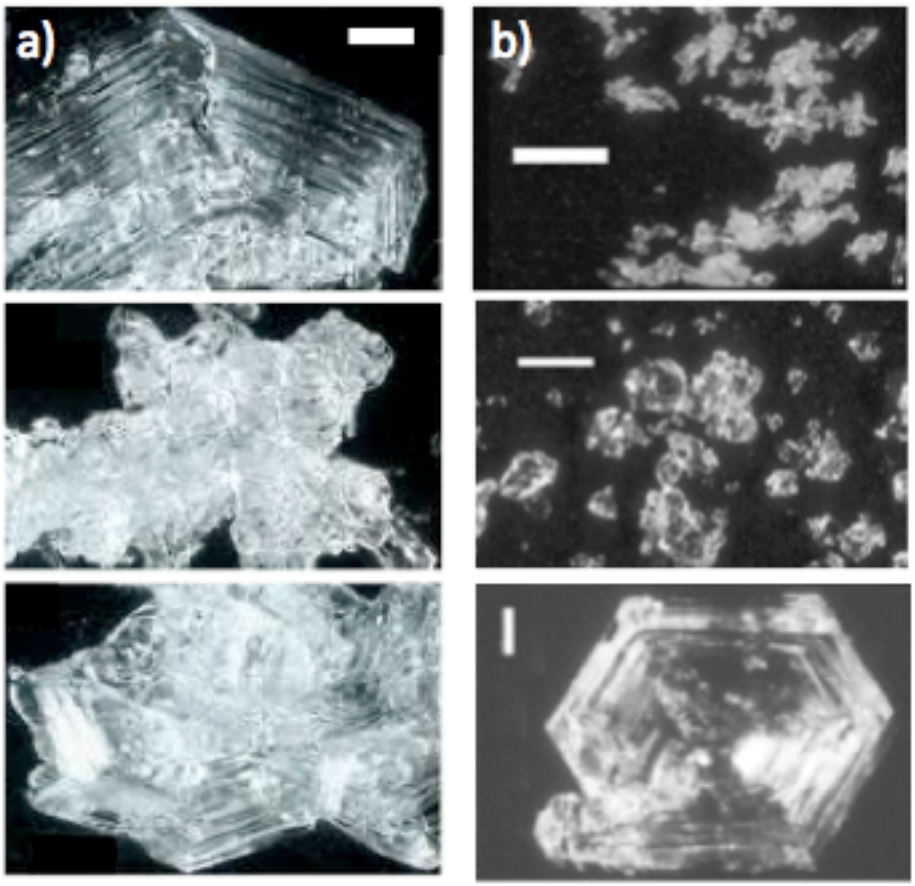

Figure 3.1. Examples of different snow crystal morphology from a) Barrow, Alaska and b) Alert. Scale bars = 1 mm. Adapted from Domine *et al.* (2002; 2012)

There have been several early studies on the effect of black carbon in snow and the reduction of snow albedo (e.g. Aoki *et al.*, 2000; Chylek *et al.*, 1983; 1987; Clarke and Noone, 1985; Flanner *et al.*, 2007; Warren and Wiscombe, 1980; 1985) but to the author's knowledge there have been no previous studies of the response of *e*-folding depth to increasing or decreasing black carbon mass ratio.

Light penetration depth (or *e*-folding depth) is the distance for the irradiance of diffuse light to decrease to $\frac{1}{e}$ (or ~37%) of its initial value (King and Simpson, 2001). The measure of light penetration is important in the field of snow photochemistry and snow optics. The photolysis of nitrate anion and hydrogen peroxide naturally found in snowpack produces fluxes of nitrogen dioxide from the snowpack and reactive hydroxyl radicals in the snowpack respectively. A large value for the *e*-folding depth is consistent with larger values of the solar irradiance penetrating deeper in the snowpack than snowpacks with smaller *e*-folding depth, potentially producing a larger flux of nitrogen dioxide from the snowpack or a larger yield of hydroxyl radicals in the snowpack. Absorption of solar radiation by black carbon in the snowpack will reduce the *e*-folding depth and any flux of photochemical materials from the snowpack.

Previous radiative-transfer modelling work of light propagation has always required the addition of black carbon absorber to the snowpack to match the modelled reflectivity and *e*-folding depth with field measurements of *e*-folding depth and reflectivity of snowpacks (e.g. Beine *et al.,* 2006; Fisher *et al.,* 2005; France *et al.,* 2007; France *et al.*, 2010; King *et al.,* 2005; Lee-Taylor and Madronich, 2002; Warren and Wiscombe, 1980). In the work presented in this chapter, a radiative-transfer model has been applied to four snowpacks previously

studied by fieldwork. The mass ratio of black carbon within the snowpack has been varied whilst all other snowpack properties have been kept constant, thus exploring the sensitivity of albedo, and for the first time, *e*-folding depth to black carbon mass ratio in four representative and field-studied snowpacks. Similar work was conducted in chapter 2c for the four representative Barrow snowpacks, however the Barrow snowpacks were very similar optically and in location, whereas the four snowpacks chosen for study in this chapter are located around the world and are optically different.

3.2 Aims

The aims of the work presented in this chapter are to:

1. Use published fieldwork albedo and *e*-folding depth values to calculate absorption and scattering parameters for four snowpacks.
2. Quantify the effect of black carbon on snowpack reflectivity.
3. Calculate the effect of black carbon on *e*-folding depth.

3.3 Modelling Procedure

Albedo and *e*-folding depth for four snowpacks located around the world were determined from calculations of irradiances within snowpack as a function of black carbon content, solar zenith angle and sky conditions. It is necessary to describe (a) the snowpits selected for this study, (b) the radiative-transfer calculations of irradiance in the snow and (c) the calculations of albedo and *e*-folding depth from irradiances in the snow.

3.3.1 Snowpacks

The four snowpacks chosen for this study (Table 3.1) are all from previous field studies and have previously determined values of scattering and impurity absorption cross-sections by the TUV-snow model (Lee-Taylor and Madronich, 2002). The four snowpacks chosen were: a cold Arctic snowpack, a cold Antarctic snowpack, a warm melting snowpack for contrast and a coastal windpack as most atmospheric chemistry experiments seem to occur at coastal snow sites. The four snowpacks represent different snow types and locations thus giving a greater understanding to the variation in snowpack behaviour (albedo and *e*-folding depth) with black carbon. The colder snowpacks are the South Pole and the Alert Arctic snowpack; a permanent snowpack located on the Antarctic plateau and a fine grained polar seasonal snowpack respectively. The two warmer snowpacks were located in coastal Greenland and the Cairngorm Mountains, UK. The Cairngorm snowpack was a mid-latitude, large grained, melting snowpack.

Location	σ_{scatt} / $m^2\ g^{-1}$	σ^{+}_{abs} / $cm^2\ g^{-1}$	Density /g cm^{-3}	Description
Alert [a]	27.5	4.5 [e]	0.24	Fine grained Arctic windpack
Cairngorm [b]	1.0	1.0 [b]	0.49	Coarse grained melting windslab
Coastal Greenland [c]	6.4	7.3 [e]	0.32	Dry, coastal snowpack
South Pole [d]	25	0 [e]	0.46	Dry, polar windpack

Table 3.1 Properties of the four snowpacks studied. Values of σ_{scatt} and σ^{+}_{abs} were derived from measurements of albedo and/or light penetration depths. [a] King and Simpson (2001), [b] Fisher *et al.* (2005), [c] Grenfell and Maykut (1977), [d] Grenfell *et al.* (1994), [e] Lee-Taylor and Madronich (2002).

3.3.2 Radiative Transfer Modelling

Upwelling and downwelling irradiances in the snowpack were calculated using TUV-Snow (Lee-Taylor and Madronich). TUV-Snow is an atmosphere-snowpack coupled radiative-transfer model based on the DISORT code (Stamnes *et al.,* 1988) that has been previously described by Lee-Taylor and Madronich (2002) and in earlier chapters. Downwelling and spherical irradiances of short-wave radiation (λ=280–700 nm, Δλ=1 nm) were calculated from the top of the atmosphere through sixty-five unequal layers, varying from 0.001, 0.01, 1 or 2 km, to 30 unequal snow layers varying from either 0.1, 0.5, 1, 5 or 10 cm (5 thinner layers (1 mm) are at the snow surface) all within a 1 m snowpack. The atmosphere was modelled free of cloud and aerosol with an ozone column of 300 Dobson units and an Earth-Sun distance based on the 4th October 2008, i.e. 1 AU. The snowpack is a multiple-scattering environment characterised by a wavelength independent scattering cross-section, σ_{scatt}, and wavelength dependent absorption cross-section, σ_{abs}, that is a sum of the absorption cross-section of water-ice, σ_{abs}^{ice} and a light-absorbing impurity, black carbon, σ_{abs}^{+}. For the work presented in this chapter, all absorption by light-absorbing species in the snowpack is attributed to black carbon because black carbon is the strongest absorber among aerosol carbonaceous constituents (Hoffer *et al.*, 2006). However, as described in chapters 2b and 2c, a variety of absorbers such as HULIS, dust and other chromophores may be present in the snowpack. Black carbon scattering properties were ignored. The asymmetry parameter, g, for the snowpack is 0.89 (Lee-Taylor and Madronich, 2002). Values of the ice absorption coefficient were taken from Warren and Brandt (2008) (Figure 2b.2, found in Chapter 2b).

The absorption cross-section of a black carbon particle was calculated using the Mie code of Bohren and Huffman (1983) and the work of Warren and Wiscombe (1985; 1980), i.e. the black carbon was represented by spheres of radius 0.1 μm externally mixed with the snow grains with a wavelength independent complex refractive index of 1.8-0.5i and a density of 1 g cm^{-3} (Figure 2b.2, found in Chapter 2b). Values of the absorption cross-section (taken from Figure 2b.2, found in Chapter 2b) were 11.4, 11.1, 10.9, 10.3, 9.6 and 8.8 m^2 g^{-1} for wavelengths of 350, 400, 450, 500, 550 and 600 nm respectively. Mass ratios of black carbon used in the model were 1, 2, 4, 8, 16, 32, 64, 128, 256, 512 and 1024 ng g^{-1}. The range of black carbon mass ratios encompasses the present-day mass ratio values of black carbon measured in snowpacks around the world (e.g. Clarke and Noone, 1985; Doherty *et al.*, 2010; France *et al.*, 2012; Hegg *et al.*, 2009; Huang *et al.*, 2011; Ming *et al.*, 2009; Voisin *et al.*, 2012). For each black carbon mass ratio, the solar zenith angles studied were 26°, 37°, 46°, 53°, 60°, 66°, 73°, 78°, 84° and 90° (linear in cos θ). Reflectivity and *e*-folding depths were calculated at six UV-Visible wavelengths of light: 350, 400, 450, 500, 550 and 600 nm (the wavelength region in which black carbon is most absorptive). The reflectivity of the snowpack was calculated as the ratio of upwelling to downwelling (flate plate) irradiance (calculated by the model) at the snow surface.

$$\text{reflectivity} = \frac{I_{upwelling}}{I_{downwelling}} \qquad \text{(E3.1)}$$

The *e*-folding depth, ε, was calculated by fitting equation (3.2) to the downwelling irradiances, I_d, at depths, d, of 10, 20, 30 and 40 cm in the snowpack.

$$\frac{I_d}{I_{d'}} = e^{\frac{d-d'}{\varepsilon}} \qquad \text{(E3.2)}$$

with a reference depth, d', of 10 cm. The solar radiation at depths of 10, 20, 30 and 40 cm is effectively diffuse owing to multiple scattering within the snowpack, sometimes described as the asymptotic zone (Simpson *et al.,* 2002; Warren, 1982).

3.4 Results

3.4.1 Effect of black carbon on *e*-folding depth

For mass ratios of black carbon greater than 20-30 ng g^{-1} (depending on wavelength), the variation of *e*-folding depth with respect to black carbon obeys a simple power law, equation (3.3) (as shown in Figure 3.2).

$$e\text{-folding depth} = \alpha\left[\text{black carbon}\right]^{-\beta} \qquad \text{(E3.3)}$$

The data in Figure 3.2 are fitted to equation (E3.3) for each wavelength. The values of α and β are displayed in Table 3.2 along with the range of black carbon mass ratio over which the power law is valid. The power law is not valid over the whole range of black carbon considered. For all snowpacks the exponent, $-\beta$, in equation (E3.3) is approximately -0.5 thus a doubling of the black carbon mass ratio (above 20-30 ng g^{-1}) will reduce the light penetration depth to ~70% of its initial value. All values have an error of 1 standard deviation from the fit of the power law.

Snow Type	Wavelength / nm	α / cm ng$^{\beta}$ g$^{-\beta}$	-β	[Black Carbon] Range / ng g^{-1}
South Pole	350	22.3 ± 0.107	0.499 ± 0.00123	32-512
	400	22.6 ± 0.109	0.499 ± 0.00123	32-512
	450	22.9 ± 0.0125	0.450 ± 0.000138	32-512
	500	22.4 ± 0.129	0.491 ± 0.00144	32-512
	550	19.7 ± 0.471	0.461 ± 0.00583	32-512
	600	16.4 ± 0.857	0.422 ± 0.0124	32-512
Greenland	350	63.9 ± 0.0703	0.501 ± 0.000276	32-512
	400	64.7 ± 0.0644	0.501 ± 0.000248	32-512
	450	64.6 ± 0.125	0.498 ± 0.000481	32-512
	500	63.1 ± 0.518	0.490 ± 0.002	32-512
	550	57.0 ± 1.56	0.466 ± 0.00652	32-512
	600	47.9 ± 2.53	0.430 ± 0.0122	32-512
Alert	350	40.999 ± 0.029	0.500 ± 0.000178	32-512
	400	41.6 ± 0.045	0.500 ± 0.00027	32-512
	450	41.4 ± 0.0808	0.4978 ± 0.000483	32-512
	500	41.0 ± 0.243	0.492 ± 0.00145	32-512
	550	36.7 ± 1.07	0.466 ± 0.00697	32-512
	600	30.9 ± 1.62	0.431 ± 0.0121	32-512
Cairngorms	350	47.0 ± 0.0467	0.500 ± 0.000249	32-512
	400	47.7 ± 0.0514	0.450 ± 0.000269	32-512
	450	47.7 ± 0.115	0.498 ± 0.000599	32-512
	500	46.6 ± 0.425	0.490 ± 0.00223	32-512
	550	42.2 ± 1.12	0.466 ± 0.00634	32-512
	600	35.4 ± 1.89	0.431 ± 0.0124	32-512

Table 3.2. Power law coefficients for relating *e*-folding depth, ε, to black carbon mass ratio, i.e. $\varepsilon = \alpha[\text{black carbon}]^{-\beta}$, for black carbon mass ratios greater than 20 ng g^{-1}.

For solar radiation wavelengths of 450-600 nm, the variation of light penetration depth with black carbon mass ratio has two regimes: When black carbon mass ratio is less than ~10 ng g^{-1}, the absorption of solar radiation in the snowpack is dominated by water-ice absorption and the response of *e*-folding depth to black carbon mass ratios is wavelength dependent. When black carbon mass ratio is greater than ~50 ng g^{-1}, the absorption of solar radiation in the snowpack is dominated by black carbon absorption. The absorption cross-section of black carbon is relatively invariant with wavelength (see Figure 2b.2, found in Chapter 2b) and thus the response of *e*-folding depth to black carbon mass ratio is effectively invariant with wavelength. The typical black carbon mass ratios for snowpacks and glaciers around the world ranges between 3-130 ng g^{-1} (Ming *et al.,* 2009), therefore the range modelled here considered the scenario of black

carbon mass ratios less and far greater than the typical amount. It can be seen from Figure 3.2 that typical black carbon mass ratios have a large effect on the *e*-folding depth within a snowpack. The *e*-folding depth is independent of solar zenith angle (King and Simpson, 2001). The lack of solar zenith angle dependence is expected because the metric of *e*-folding depth does not include the top few cm of the snowpack where direct and diffuse incoming radiation is converted to diffuse radiation by multiple scattering, i.e. although the absolute value of irradiance in snowpack is very sensitive to solar zenith angle, the attenuation (i.e. *e*-folding depth) depends only on the relative decrease in irradiance with depth.

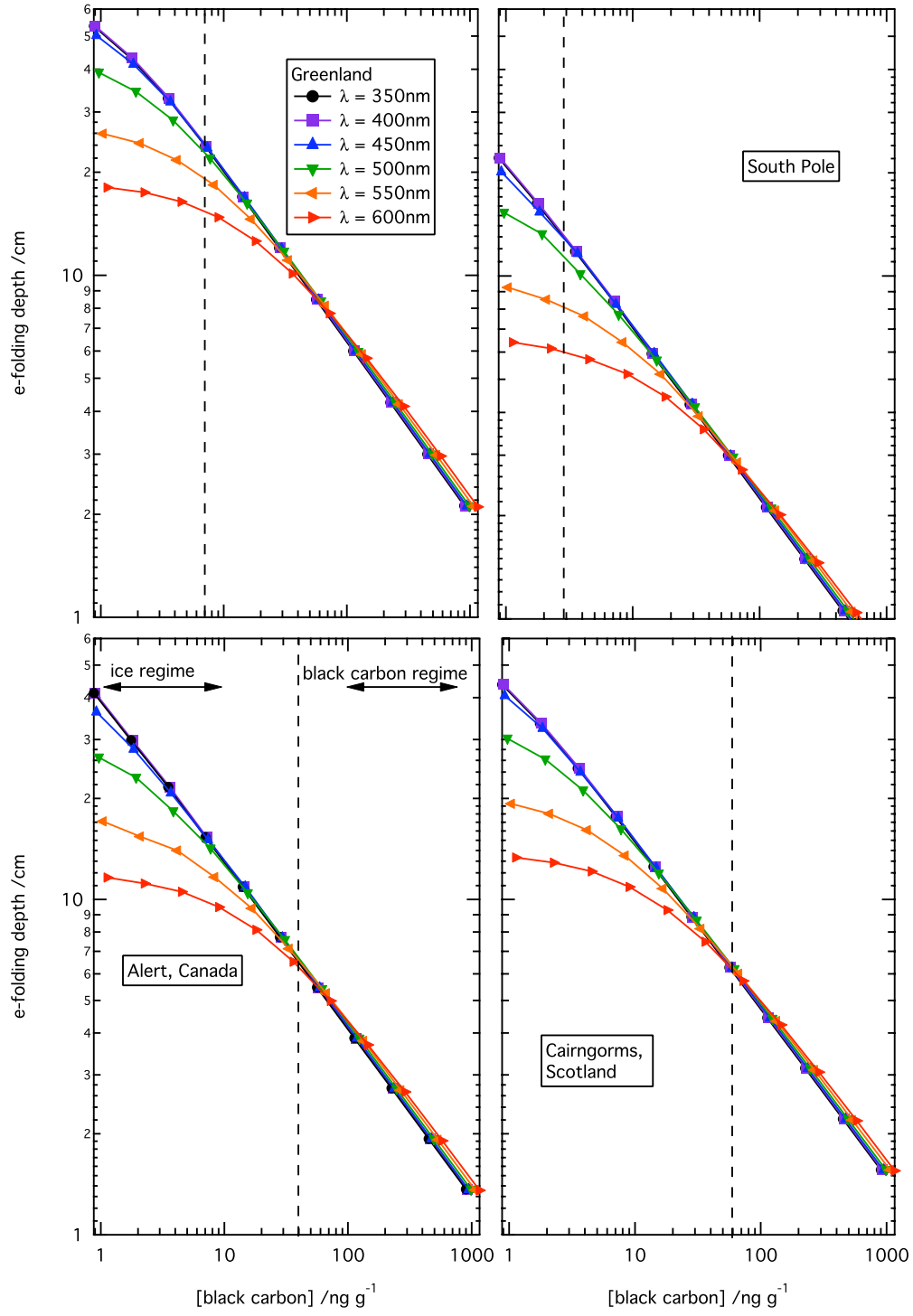

Figure 3.2. *e*-folding depths for four snowpacks plotted versus black carbon mass ratio for the wavelengths of 350, 400, 450, 500, 550 and 600 nm. Dotted lines represents mass ratio of black carbon presently found in snowpacks. Values of black carbon mass ratio in snow taken from Doherty *et al.* (2010) (Alert and Greenland), Warren and Clarke (1990) (South Pole) and Davies *et al.* (1992) (Cairngorms).

The response to increasing black carbon is not the same for each location or snow type (Figure 3.3). The *e*-folding depths of the warmer Cairngorm and coastal Greenland snowpacks undergo larger absolute decreases with increasing black carbon mass ratio than the colder South Pole and Alert snowpacks. The South Pole and Arctic (Alert) snowpacks have a small grain size relative to the Cairngorm and coastal Greenland snowpacks. A large grained snowpack tends to propagate light deeper into the snowpack thus the light experiences more potential interactions with black carbon particles in the snowpack (Warren, 1982; Fisher *et al.,* 2005). A photon experiences the same number of scattering events to get out of a coarse-grained snowpack as a fine-grained snowpacks, however, in each event the photon is more likely to be absorbed by a large grain than by a small grain and the scattering angle may be shallower for coarse grains therefore the light propagates deeper. A similar scenario can be seen for coarse and fine sand (Bohren, 1987)

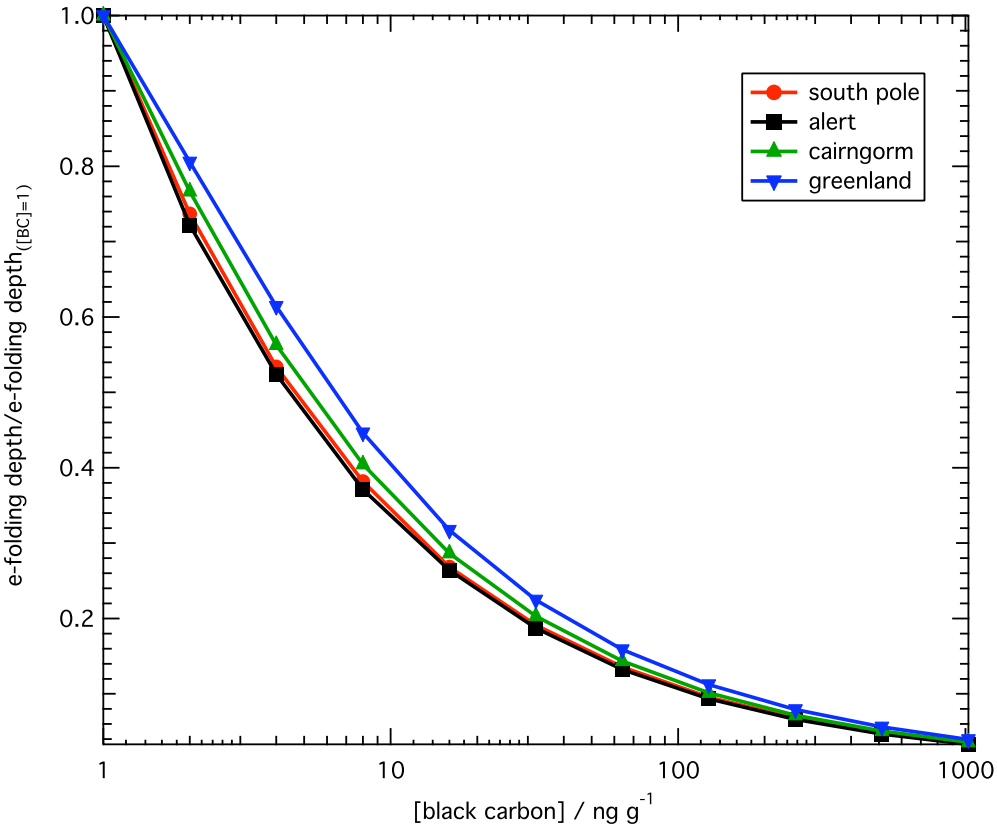

Figure 3.3. Response of snowpack *e*-folding depth to increasing black carbon mass ratios at 350 nm. Response is calculated as $\frac{e\text{-folding depth}}{e\text{-folding depth}_{[BC]=1}}$.

3.4.2 Effect of black carbon on albedo

Figure 3.4 and 3.5 plot the decreasing albedo with increasing black carbon mass ratio for solar zenith angles of 78° and 45° respectively. Large absolute decreases of albedo with increasing black carbon mass ratios are noted for the Cairngorm and coastal Greenland snowpacks, whereas the South Polar snowpack appears to be relatively insensitive. For smaller solar zenith angles, the albedo is lower at the same black carbon mass ratio thus a snowpack impacted by increased black carbon pollution would have a larger decrease in the albedo at small solar zenith angles.

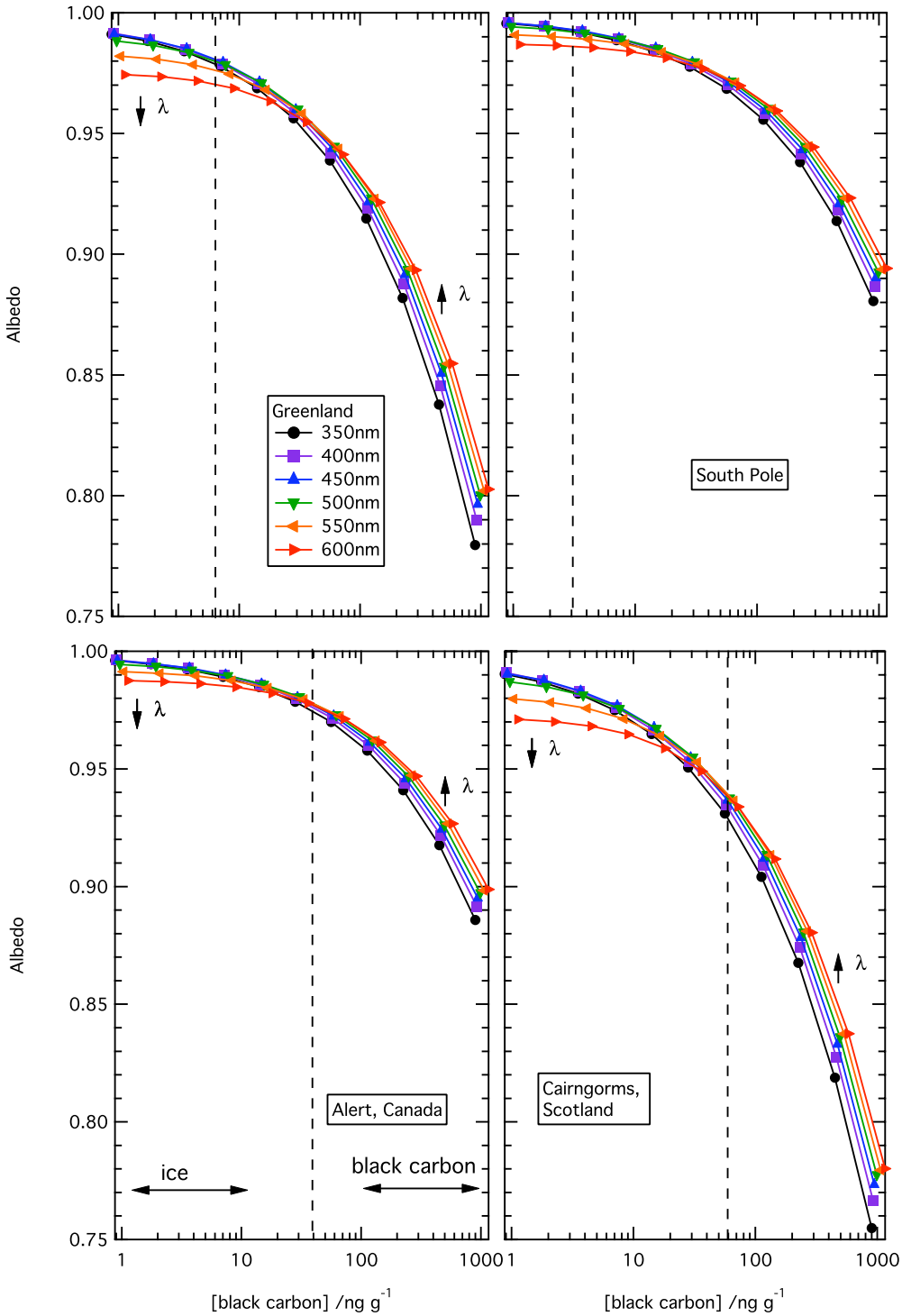

Figure 3.4. Albedos for four snowpacks plotted versus black carbon mass ratio for the wavelengths of 350, 400, 450, 550, 550 and 600 nm at a solar zenith angle of 45°. Dotted lines represents mass ratio of black carbon presently found in snowpacks. Values of black carbon mass ratio in snow taken from Doherty *et al.* (2010) (Alert and Greenland), Warren and Clarke (1990) (South Pole) and Davies *et al.* (1992) (Cairngorms).

Figure 3.4 demonstrates that the albedo response for each wavelength is different at small mass ratios of black carbon.

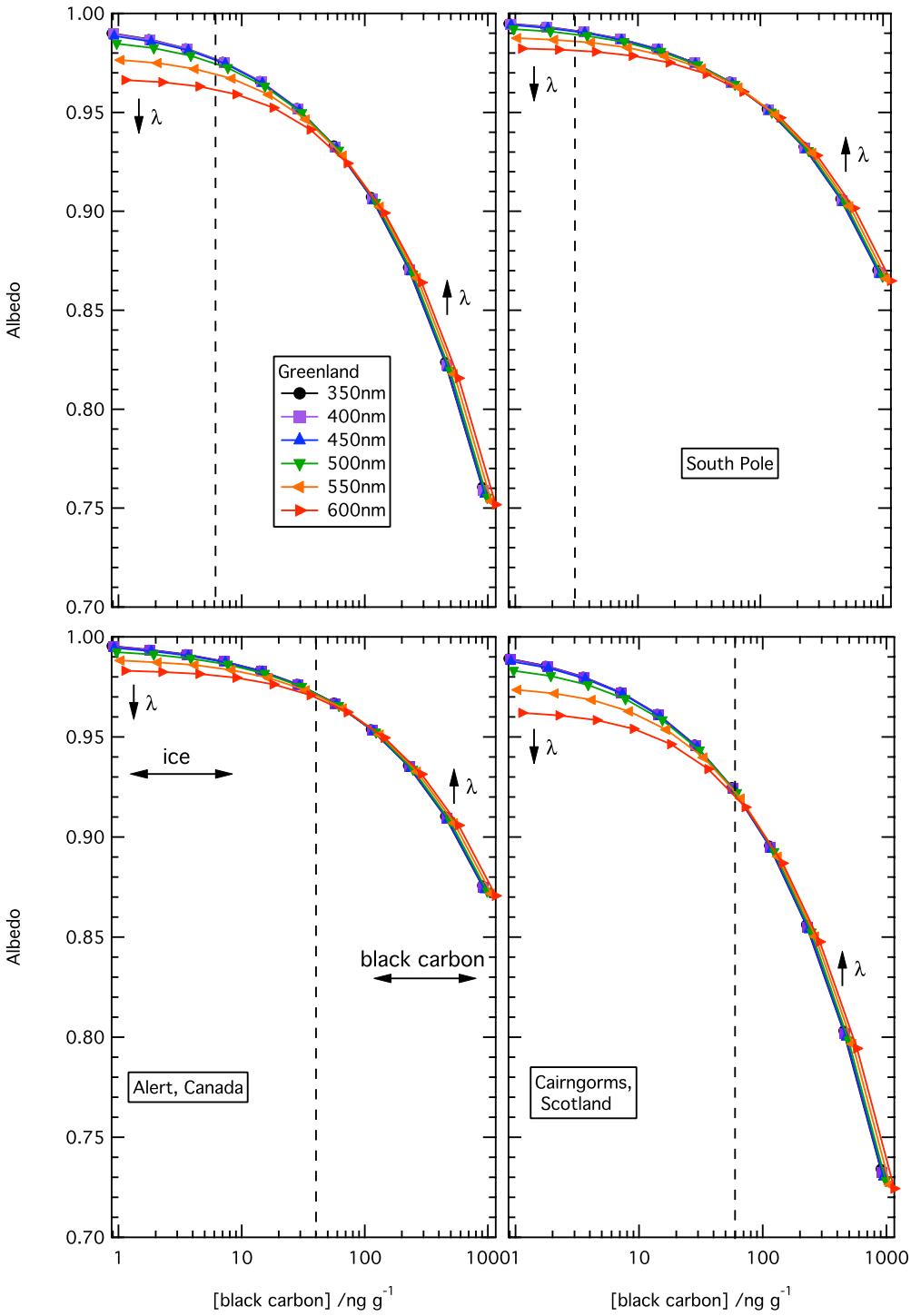

Figure 3.5 Albedos for four snowpacks plotted versus black carbon mass ratio for the wavelengths of 350, 400, 450, 500, 550 and 600 nm at a solar zenith angle of 78°.

It can be seen in Figure 3.5 that as black carbon mass ratios increase the wavelength dependence of the albedo reverses, this is due to the absorption of light becoming dominated by black carbon and not ice as the black carbon absorption spectrum used here (Figure 2b.2, found in Chapter 2b) decreases gently from 350 nm to 600 nm. For each solar zenith angle, albedo is equal for all wavelengths at a specific black carbon mass ratio e.g. ~100 ng g^{-1} in Figure 3.4 and ~15 ng g^{-1} in Figure 3.5, a decrease in specific black carbon mass ratio is seen with increasing solar zenith angle.

3.5 Discussion

The discussion will focus on: (a) a critique of the black carbon proxy, (b) the black carbon mass ratios presently found in the snowpack (c) the effect of black carbon on *e*-folding depth, (d) the effect of black carbon on snowpack albedo, (e) the effect of snow morphology on scattering and absorption values, (f) the effect of black carbon on snowpack photochemistry, (g) the uncertainties of the study presented here and (h) a comparison with previous work

3.5.1 Black carbon absorption spectrum

The major sources of uncertainty for the absorption of black carbon are the values of the index of refraction of the black carbon particle, size and position of the black carbon particle relative to the snow crystal/grain. Bohren (1986) demonstrates that black carbon internal to the snow grain increases the absorption spectrum by a factor of 1.4. The assumption in this work is that the black carbon has been deposited external to the snowpack by processes such as riming during snowfall or collection on the snowpack due to atmospheric deposition or

windpumping at a later date (Chylek *et al.* 1983). Roessler and Faxvog (1980) and Bohren (1986) highlight that the imaginary index of refraction, and thus the absorption spectrum, of different types of black carbon spans a factor of 5. Bond and Bergstrom (2006) reviewed the black carbon absorption values and the values for the black carbon absorption cross-section used in this work are in agreement (Figure 3.6). For consistency with previous workers, this study has chosen a spherical black carbon particle. Bohren (1986) has shown that a needle or disk shape increases the absorption cross-section by a factor of 1.48 and 2.1 respectively using equation 3.4.

$$
\begin{aligned}
(C_{abs})_{sphere} &= \frac{kv}{3}\left(\frac{27}{(\varepsilon'+2)^2+\varepsilon''^2}\right)\varepsilon'' \\
(C_{abs})_{needle} &= \frac{kv}{3}\left(\frac{8}{(\varepsilon'+1)^2+\varepsilon''^2}+1\right)\varepsilon'' \\
(C_{abs})_{disk} &= \frac{kv}{3}\left(\frac{1}{(\varepsilon'^2+\varepsilon''^2}+2\right)\varepsilon''
\end{aligned}
\qquad \text{(E3.4)}
$$

where v is the volume of a particle, ε is its dielectric function relative to that of the surrounding medium (in air, ε=2.99+i1.8) and k is the wavenumber of the incident light. Taken from Bohren and Huffman (1983), p.350.

The abscissa of Figures 3.2, 3.3 and 3.5 is therefore indicative of the amount of black carbon present and each snowpack will differ. The field measurements of black carbon in snow of Hegg *et al* (2009) and Clarke and Noone (1985) demonstrates that the values chosen in this and other work are sensible values.

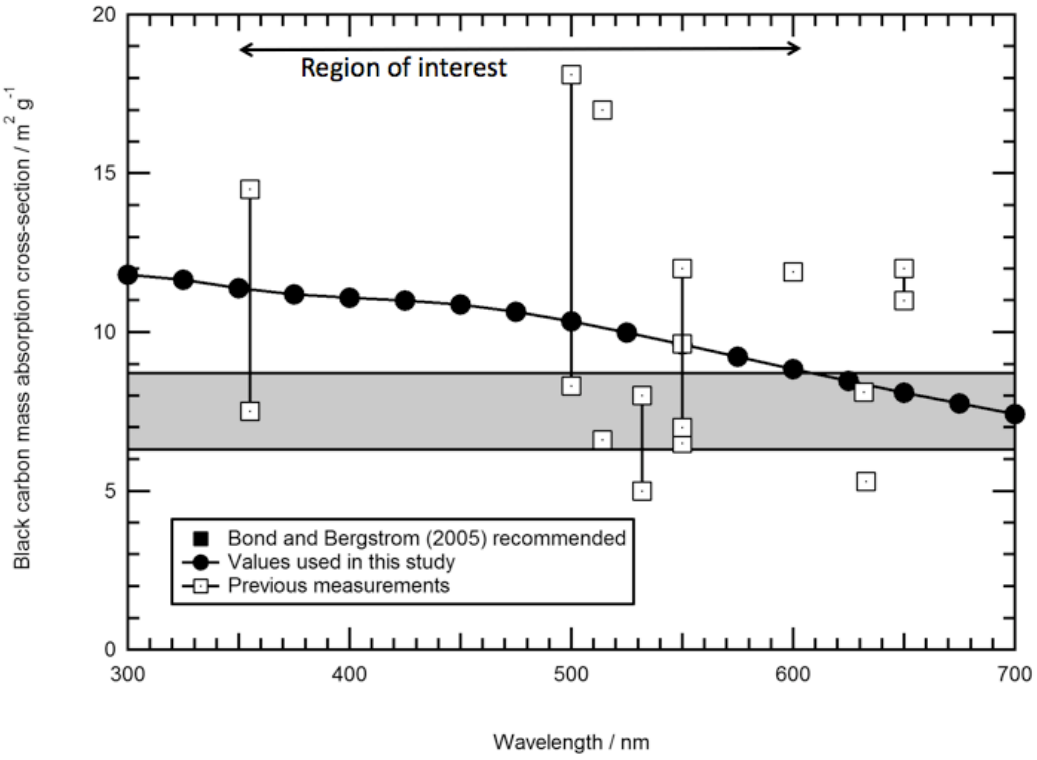

Figure 3.6. Black carbon mass absorption cross-section. The filled circles are the absorption cross-section used in the work described here (based on the Mie calculation described in the text). Black carbon absorption cross-section values measured and reviewed by Bond and Bergstrom (2006) or measured by Adler *et al.* (2010) are represented by the unfilled squares. The value of 7.5 ± 1.2 m^2 g^{-1} recommended by Bond and Bergstrom (2006) for the black carbon mass absorption cross-section is represented by the shaded band. The values used in the work presented here are in agreement with the values reviewed in the literature by Bond and Bergstrom (2006). The double-headed arrow represents the region of interest for the study presented here.

3.5.2 Black carbon mass ratios found within the snowpack

Typical black carbon mass ratios found in snowpack and glaciers around the world are 0.2-130 ng g^{-1} (Ming *et al*, 2009) and the four snowpacks studied here presently contain a variety of black carbon mass ratios within the typical range. The South Pole snowpack contains the lowest mass ratio of black carbon with a range of 0.25-3 ng g^{-1}, the highest black carbon mass ratio is marked on Figure

3.2 (Grenfell and Maykut, 1977; Grenfell *et al.*, 1994; Warren and Clarke, 1990). Black carbon mass ratios are also low in the coastal Greenland snowpack with a black carbon mass ratio range of 3.5-6 ng g^{-1}, the highest mass ratio of black carbon for Greenland is marked on Figure 3.2 (Clarke and Noone, 1985; Doherty *et al.*, 2010; Hansen and Nazarenko, 2004; Warren and Clarke, 1990). Larger black carbon mass ratios can be seen in both Alert and the Cairngorms snowpacks at present. Measurements of black carbon mass ratio at Alert found a large range of 14-45.5 ng g^{-1}, the highest value is marked on Figure 3.2 (Clarke and Noone, 1985). The Cairngorms contains the highest mass ratio of black carbon with a range of 40-60 ng g^{-1}, the highest value is marked on Figure 3.2 (Davies *et al.*, 1992; Hansen and Nazarenko, 2004). Other light-absorbing impurities i.e. HULIS and soil can also contribute to the absorption of snowpack and therefore the mass ratio values of black carbon are likely to be maximum mass ratios present in the individual snowpacks.

3.5.3 Effect of black carbon mass ratio on snowpack penetration depth

To my knowledge, there has been no systematic quantitative study on the effect of increasing black carbon mass ratios on *e*-folding depths in snowpack. The work presented here assumed the black carbon was uniformly mixed within the snowpack as it would have been difficult to obtain an *e*-folding depth from a study of varying layers. Table 3.1 shows that all the snowpacks studied here have been re-worked by wind events and therefore the mass ratio of particles are well-mixed in the top layers of the snowpack by their formation, thus for these snowpack layers with different black carbon mass ratios have not been considered.

3.5.4 Effect of black carbon mass ratio on albedo

It has been suggested that heating due to black carbon at the surface of the snowpack melts additional snow or sea-ice and the black carbon itself changes the reflectivity of the snow (Jacobson, 2004). In Western China, accelerated melting occurred due to a ~5% reduction in albedo caused in glaciers strongly contaminated by black carbon (Ming *et al.*, 2009). Laboratory studies undertaken by Hadley and Kirchstetter (2012) confirmed that black carbon mass ratios contaminating snow in natural settings (Aamaas *et al.*, 2011; Forsström *et al.*, 2012) reduced snow albedo. Increased snow grain size, seen naturally in the metamorphism of snow with age (Dirmhirn and Eaton, 1975), also decreased snow albedo and amplified the radiative effects of black carbon. For the given black carbon mass ratios in snow, a greater decrease in snow albedo can be seen for large grained snowpacks than small grained snowpack (Warren, 1982; 1984; Warren and Wiscombe, 1980). Comparing the Cairngorm and polar snowpacks shows how striking this effect is (Figures 3.5 and 3.5). Grenfell *et al.* (1994) demonstrated that increasing solar zenith angle caused an increase in albedo due to the photon undergoing its first scattering event closer to the surface when entering at closer to a grazing angle. The addition of black carbon to snow caused snow albedo to be changed at wavelengths where albedo was high, i.e. the visible. In spectral regions, increased absorption by ice allowed the black carbon to contribute less to the total absorption (Grenfell *et al.*, 1994). Comparison between Figure 3.4 (solar zenith angle of 45°) and Figure 3.5 (solar zenith angle of 78°) clearly demonstrates that increasing black carbon mass ratio exaggerates the effect. Previous studies on the effect of black carbon mass ratio on albedo have

dealt with hypothetical snowpacks whereas the snowpacks modelled here are based on measured optical properties of real snowpacks.

.

3.5.5 Snow morphology, scattering and absorption

The scattering in the snowpack is parameterised with a single wavelength independent variable, σ_{scatt}. The value of σ_{scatt} is fitted to experimentally studied snowpacks empirically. Grenfell *et al.* (1994) noted that (a) the absorption cross-section of a larger, nearly transparent particle is almost independent of its shape and proportional to its volume, and (b) the asymmetry parameter, g, of a large transparent particle is almost independent of its shape. Thus, by using empirically fitted values of σ_{scatt} the work described here has not had to assume any prior knowledge of the snow grain morphology.

The absorption cross-section of ice is not well known in the wavelength region of 200-400 nm, the imaginary part of the refractive index of ice is below 2×10^{-11} and, as noted by Warren and Brandt (2008), is effectively no different from zero. The extrapolation seen in Figure 3.3 is crude but it makes little or no difference as the ice absorption coefficient value is very small.

3.5.6 The effect of black carbon mass ratio on snowpack photochemistry

The top layers of solar illuminated snowpack are efficient media for the photolysis of chemicals within the snowpack to produce fluxes of chemicals from the snowpack involved in local atmospheric chemistry. Snowpack photochemistry may also modify deposited chemicals in the snowpack that are used in ice-cores to record previous climate. A well-used, approximate measure

of the amount of snow involved in snowpack photochemistry is two *e*-folding depths (King and Simpson, 2001), i.e. one can say 85% of the snowpack photochemistry occurring in the top x cm of snow, where x is equal to two *e*-folding depths. Figure 2b.2 (found in Chapter 2b) demonstrated that doubling the black carbon mass ratio decreases the amount of snowpack available for photochemistry by ~30 % and continued pollution of warmer snowpacks by black carbon would reduce the amount of photochemistry occurring in those snowpacks.

3.5.7 Uncertainties

To model the effect of black carbon mass ratios on snowpack, some approximations were made. The size, density and the external location of the black carbon particle relative to an ice grain were assumed. The model does not explicitly specify grain size, just a wavelength independent, σ_{scatt}, however the data was taken from four real snowpacks. The data taken from the real snowpacks mostly pertains to spring time so it is therefore a snapshot of the snowpack properties and may not necessarily be representative of all seasons or locations. The seasonality of the data may not affect the results of permanently snow-covered places such as the South Pole but will affect seasonally snow-covered places such as the Cairngorms and Greenland.

3.5.8 Previous studies

The effect of increasing black carbon mass ratio on albedo has been previously studied. Jacobson (2004) varied black carbon mass ratio between 0-500 ng g^{-1} at a solar zenith angle of 72°, producing albedos between 1-0.8. The solar zenith angle dependence of albedo makes it is difficult to compare this study with that of

Jacobson (2004). However, Figure 2 shows that at a solar zenith angle of 66° only the seasonal snowpacks, Greenland and Cairngorms, have albedos as low as 0.8 around 500 ng g^{-1}. Warren (1985) studied the effect of varying black carbon mass ratio between 1 ng g^{-1} to 1 μg g^{-1} at a solar zenith angle of 53°. The albedos produced ranged between 0.83-0.8. As with Jacobson (2004) it is difficult to compare this study exactly to Warren (1985) due to solar zenith angle dependence but both Figures 2 and 3 indicate that the only snowpacks reaching these albedo levels are the seasonal snowpacks, Greenland and the Cairngorms. In the boreal spring large portions of the Northern hemisphere are exposed to intense insolation whilst snow covered so snow-albedo feedback is at strongest (Hall and Qu, 2006; Flanner *et al*, 2009). Ming *et al* (2009) compared the percentage reduction in albedo with increasing mass ratios of black carbon showing that between 10 -100 ng g^{-1} albedo is reduced by less than 1%. Figures 2 and 3 from this study clearly show that albedo reduces by more than 1%. The difference in reduction of albedo between Ming *et al* (2009) and this study could be due to the different solar zenith angles, the black carbon mass ratio considered in this study is of a smaller range than that of Ming *et al* (2009) and therefore is a more concentrated study. Ming *et al* (2009) studied many measured and modelled snowpacks from worldwide locations whereas this study focuses on specific snowpacks.

Chapter 4

Investigating the variation of black carbon mass ratio across glaciers in Oscar II Land, Svalbard and Victoria Land, Antarctica

4.1 Introduction

Light-absorbing impurities in snow may have a significant impact on sensitive polar climates by altering the albedo and thus altering the temperature profile, cloud coverage, the seasonal cycle, contributing to the surface energy budget, influencing the polar radiative balance and dominating the absorption of solar radiation leading to accelerated snow and ice melt (Doherty *et al.,* 2010; Hegg *et al.*, 2009; Koch and Hansen, 2005). Burning of fossil fuels adds not only CO_2 to the atmosphere but also particulates produced by incomplete combustion, such as black carbon (Browse *et al.*, 2012). These particles may travel thousands of kilometres within the atmosphere before being removed by rain or snow precipitation (Doherty *et al,* 2010). Black carbon is produced from sources such as coal burning, diesel engines, residential wood burning, agricultural and forest fires (Bond and Bergstrom, 2006; Bond *et al*, 2004; Hansen and Nazarenko, 2004). The International Panel for Climate Change (IPCC) estimates that global climate forcing by black carbon in snow and ice is around 0.2 Wm^{-2}. Hansen *et al.* (2005) calculated that black carbon in snow had 1.8 times the 'climatic

warming effect' of anthropogenic CO_2 per Wm^{-2} for a specified radiative forcing. However, Flanner *et al* (2007) calculated that black carbon in snow may actually be 3.2 times more efficient at climatic warming than CO_2 because (1) the peak black carbon fallout coincides with the onset of snowmelt in Arctic springtime, (2) coarse-grained snow has a lower albedo than fine-grained snow, (3) dark underlying surfaces are exposed earlier by snowmelt, (4) rapid heat exchange is prevented by the stable atmospheric boundary layer over the snow thus warming is concentrated at the snow surface (Doherty *et al.*, 2010), (5) initial albedo reduction by black carbon can cause a temperature increase in snow thus initiating the growth of snow grain size before the onset of melting (LaChapelle, 1969; Flanner and Zender, 2006), (6) black carbon causes a greater reduction in the albedo of coarse-grained snow than fine-grained snow (Figure 7, Warren and Wiscombe, 1980), (7) melting may concentrate black carbon to the top surface of the snowpack where it is exposed to more sunlight (e.g. Flanner *et al.,* 2007).

Anthropogenic combustion, including fossil fuel (over 8×10^9 kilograms of black carbon to the atmosphere per year) and biomass burning (a maximum total of 6×10^9 kilograms of black carbon to the atmosphere per year), is the primary source of black carbon thus human population restricts the geographical location of the sources, but long-range atmospheric transportation methods allow black carbon to have a globally widespread deposition extent (Doherty *et al.*, 2010; Highwood and Kinnersley, 2006; Koch and Hansen, 2005; Stohl, 2006; Shindell *et al.*, 2008; Warren, 1984). The proximity of pollution sources to the Arctic in comparison to the Antarctic makes the area more sensitive to changes in black carbon concentration. Black carbon in the Arctic may come from industrial sources in

Europe, whereas local contamination from a permanent camp would have more influence on black carbon concentrations within Antarctic snow (Hansen *et al.*, 2001; Warren, 1982). Black carbon concentrations in snow are determined by the ambient concentrations in the air, wet and dry depositional processes, snowfall rate and in-snow processes, with aging, such as melting, sublimation and frost deposition (Browse *et al.*, 2012; Doherty *et al,* 2010).

Using modelling techniques, several studies have investigated the effect of black carbon in snow (e.g. Aoki *et al.*, 2000; Chylek *et al.*, 1983; 1987; Flanner *et al.*, 2007; France *et al*., 2012; Grenfell *et al.*, 2002; Hansen and Nazarenko, 2004; Jacobson, 2004; Reay *et al.*, 2012; Warren, 1980a; 1980b; 1985). The studies have shown that small (nanogram) quantities of black carbon in one gram of snow can significantly reduce albedo and light penetration depth (*e*-folding depth), i.e. 10 ng g^{-1} black carbon in snow can reduce the albedo by 1% (Clarke and Noone, 1985; Flanner *et al.,* 2007; Grenfell *et al.,* 2002; Hansen and Nazarenko, 2004; Jacobson, 2004) and doubling the black carbon concentration decreases the *e*-folding depth to ~70% of the initial value, for black carbon concentrations greater than 20 ng g^{-1} (France *et al.,* 2012; Reay *et al.*, 2012). Clarke and Noone (1985) pioneered the use of filtration techniques to measuring black carbon concentrations in the Arctic snow, and the work was continued by Doherty *et al*. (2010) and Hegg *et al.* (2009). Similar filtration techniques were used in the work presented here and the sample region has been extended to Antarctica, in addition to the Norwegian Arctic.

The work presented in this chapter is a combination of academic research and educational outreach. The field research undertaken in Svalbard was part of a British Schools Exploring Society (BSES) expedition to Oscar II Land.

The British Schools Exploring Society is one of the country's leading youth development charities undertaking scientific research expeditions. The expeditions combine a mixture of science and adventure using the underlying principal of 'adventure with purpose' to develop the next generation of leaders and scientists. BSES has been running extreme scientific research expeditions to remote wilderness areas around the world since 1932. The work undertaken on the Svalbard expedition presented here was a collaborative effort between 9 young explorers and 3 leaders. Due to the nature of the expedition, certain constraints were placed upon the science research: all scientific equipment had to be carried in a backpack along with day-to-day equipment therefore the weight, size and amount of equipment was limited; the entire expedition was spent living in tents in the remote wilderness of Oscar II Land with no external power sources and no inside laboratory facilities thus hand pumps were used and precautions had to be taken to keep the filtration method as clean as possible e.g. coveralls and Sigma-Aldrich glove bags; the ethos of BSES meant that the research needed to be undertaken by everyone, to inspire the next generation, therefore the filtration method was conducted by a variety of different people and the theory behind the research needed to be accessible to a variety of different scientific abilities.

The field research undertaken in Antarctica was part of a PNRA (Italian Antarctic Survey) campaign to Terra Nova Bay, Victoria Land. Bi-directional reflectance

distribution function measurements were undertaken on the same Antarctic campaign using a Gonio Radiometric Spectrometer System and the work is presented in chapter 5.

4.2 Study Area

4.2.1 Oscar II Land, Svalbard

The expedition area was based in Oscar II land, Svalbard. Svalbard is an archipelago situated between 74-81ºN and 10-35ºE. It was discovered in 1595 and is now home to around 2850 people. The main settlement on Svalbard, Longyearbyen, was situated on the opposite side of Isfjorden to Oscar II Land. The glaciers in Oscar II land were both surging and receding (Koryakin, 1986; Lankauf, 2002; Nuth *et al.*, 2007; 2010; Sobota, 2010; 2011; Wieslaw, 2005). Two smaller glaciers, Lappbreen and Lulefjellet, that fed into a larger glacier, Bardebreen, were focused on within the study area (Figures 4.1 and 4.2).

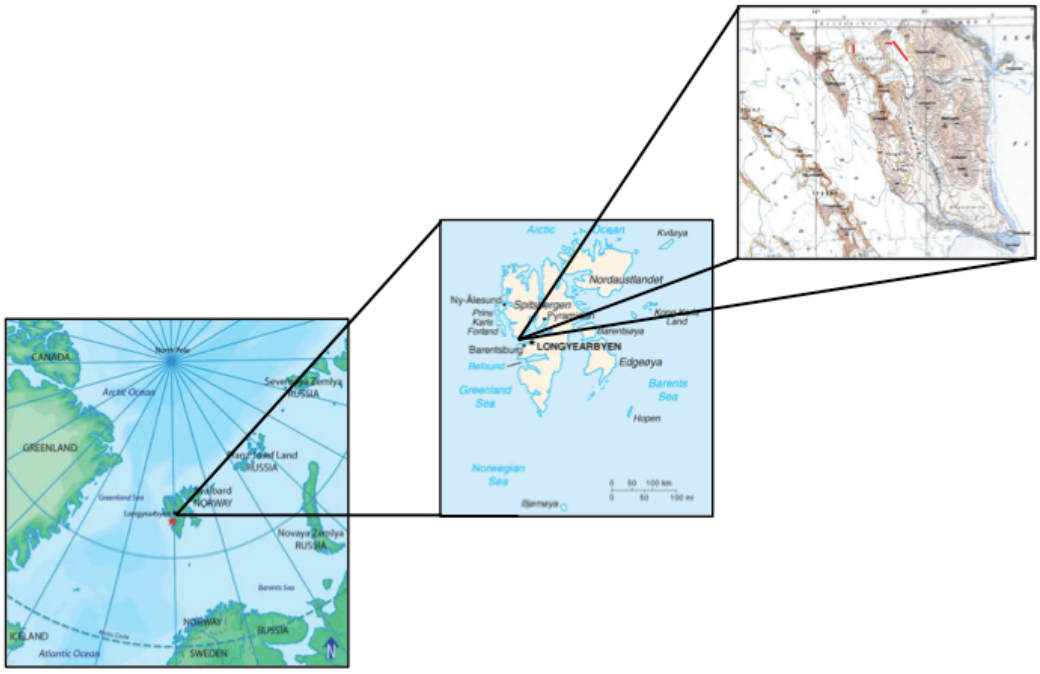

Figure 4.1. Maps of glacier transect locations in Oscar II Land, Svalbard.

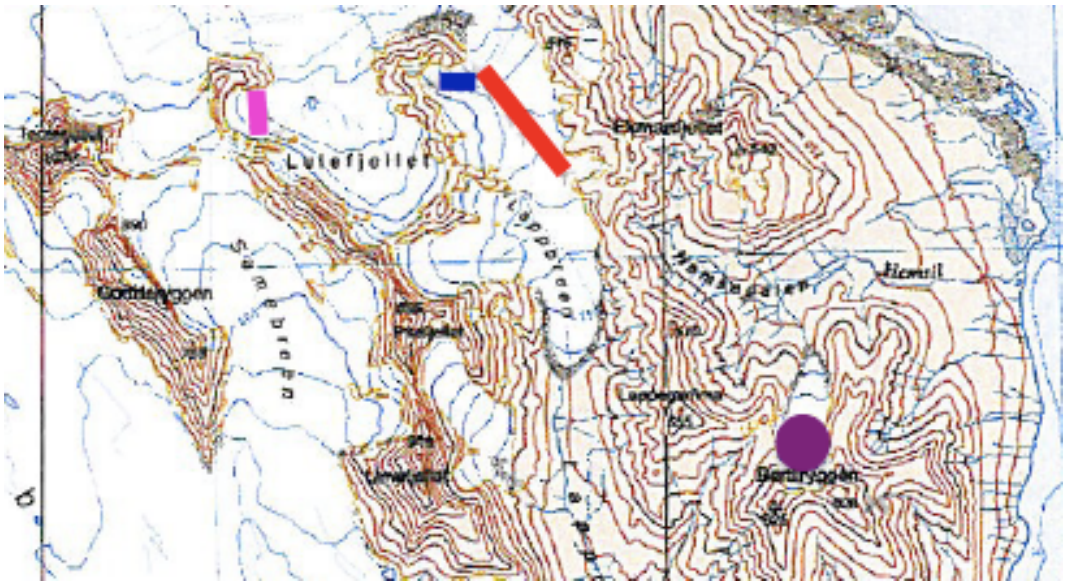

Figure 4.2. Close up map showing glacier transect locations.

Seasonally occupied huts can be found along the coast of Oscar II Land and it is often visited by small groups of kayaking tourists due to its accessibility from Longyearbyen.

4.2.2 Victoria Land, Antarctica

Victoria land is a region of Antarctica bound by the Ross Sea and Wilkes Land. It includes the Transantarctic mountains, the McMurdo dry valleys and a network of outlet glaciers that drain from the East Antarctic ice sheet (Figure 4.3). The campaign was based at the Mario Zucchelli station located in Terra Nova Bay.

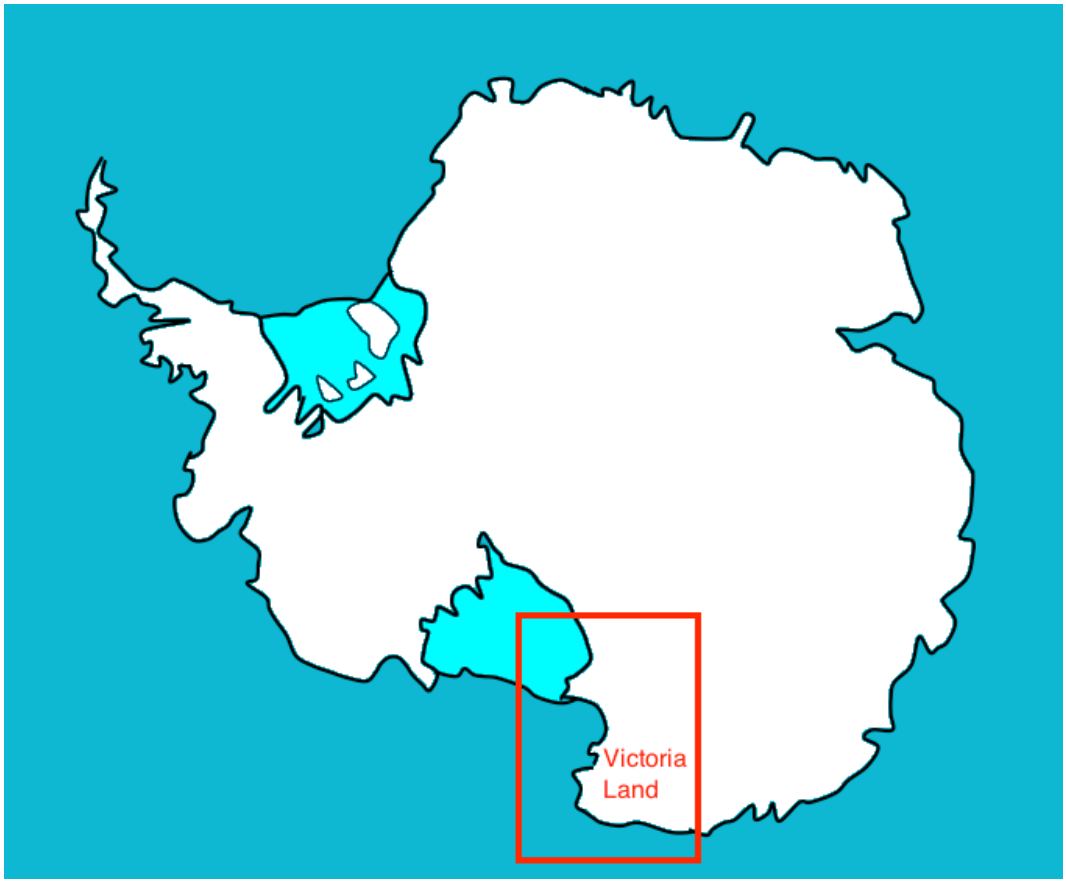

Figure 4.3. Location of Victoria Land within Antarctica.

The sample sites in Victoria Land (Figure 4.4) were visited by helicopter. Using helicopters to access areas of Antarctica meant that there were constraints on the size, weight and amount of sampling equipment transported. In contrast to the Svalbard expedition, filtering of the snow samples was done in a laboratory at the Mario Zucchelli station not in the field. However, filtering was still undertaken inside a Sigma-Aldrich glove bag to minimise contamination and the filtration technique remained consistent between the Antarctic and Svalbard filters.

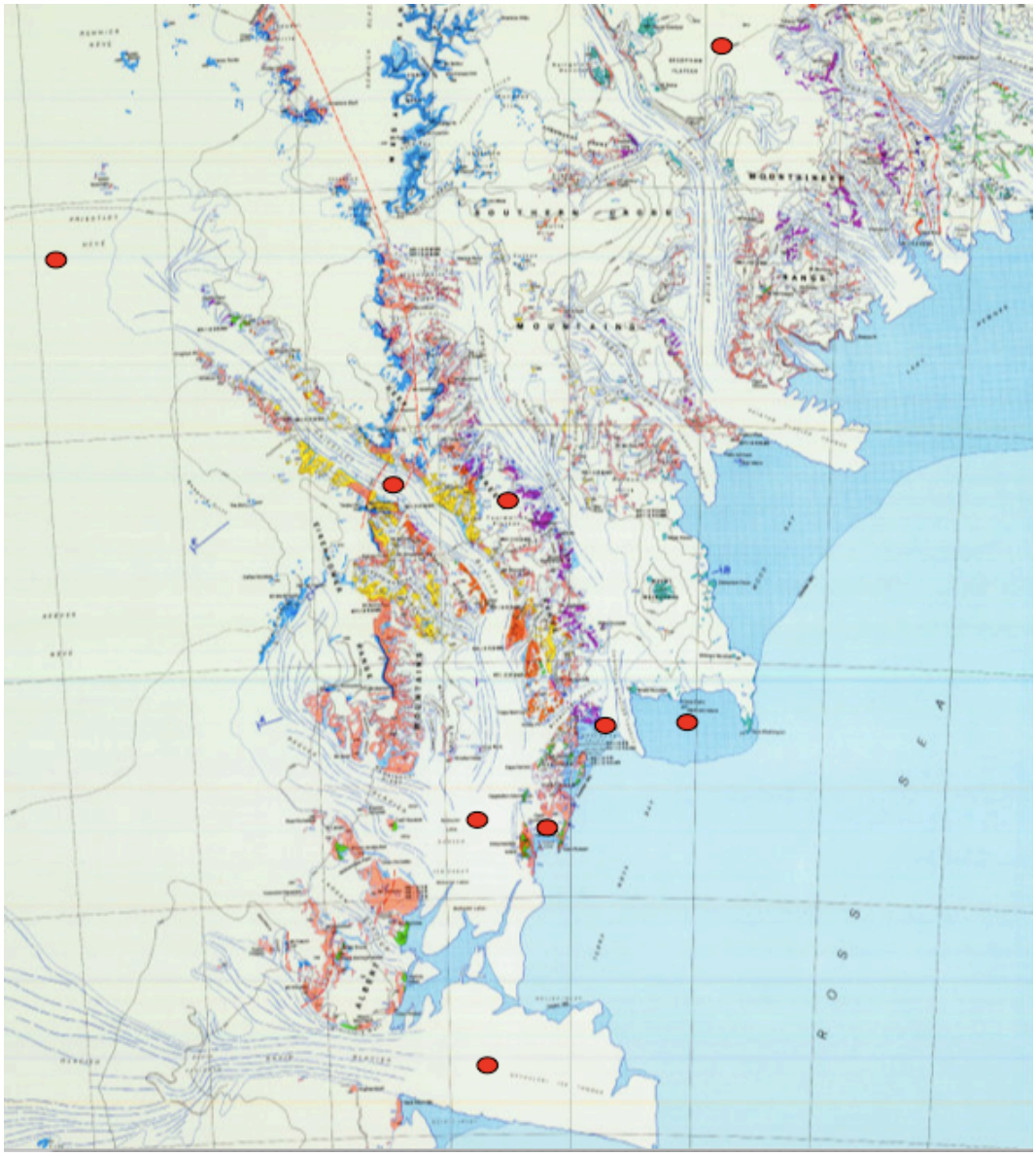

Figure 4.4. Location of sample sites in Victoria Land, Antarctica.

4.3 Aims

The aims of the work presented in this chapter are to:

1. Optically determine the amount of black carbon in snow and ice by taking filter samples from glaciers.
2. Investigate whether black carbon varies with depth.
3. Determine whether black carbon can be judged accurately from filters by eye.

4.4 Field Sampling Method

Two methods were used to analyse the amount of black carbon found in snow and ice on glaciers in Oscar II Land, Svalbard and Victoria Land, Antarctic. Firstly, a comparison was made between the sample filters from the field and pre-prepared comparison filters showing a variety of black carbon mass ratios. The method was used to produce 'instant' results in the field so the young explorers helping to conduct the research would have a greater understanding of the aim of the science work, and to test whether the amount of black carbon in snow can be judged by eye. The second method was a laboratory-based method that aimed to record the wavelength resolved spectrum of the filters to measure an accurate value for black carbon and identify other absorbers, if possible. It is beneficial to optically determine the mass ratio of black carbon because the chemical composition or origin of the black carbon are not necessary for analysis (Andreae and Glencser, 2006).

The work in Svalbard was undertaken as part of a BSES expedition and the Antarctica sampling was part of an Italian campaign. The extent of the field areas

and the nature of the campaigns meant that the scientific research needed to be suited to a variety of surface conditions, and the equipment needed to be small and portable.

4.4.1 Equipment

Below is a list of equipment needed to undertake the field experiments described in this chapter:

- 240 ml wide-mouth PTFE sample jars
- 0.4 μm Nuclepore membrane filters
- Vinyl gloves
- Clean lab coveralls
- Plastic vacuum filtration flasks (Erlenmeyer flasks)
- Tweezers
- Filter holders
- Glass vacuum filter holder
- Scientific tissues (Kim wipes)
- Sigma-Aldrich glove bag
- Permanent marker pens
- Sample bags
- Global Positioning System (GPS)

4.4.2 Oscar II Land, Svalbard

Measurements were taken in a variety of glacial locations between July-August 2010, as described below:

4.4.2.1 Transect

A GPS was used to determine the co-ordinates of the location. A bearing was used to conduct a transect across the glacier and samples were taken every 50 m along that bearing. As the sampling was undertaken during melt season, the location of the transect was determined by the accessibility of the glacier for safety reasons. To prevent contamination, overalls were worn when sampling.

Starting from the side of the glacier, three 240 ml PTFE pots were filled with snow at each sampling location to ensure that spatial variation was accounted for. No additional equipment was used to fill the pots; the pots were pushed horizontally into the snow surface, rotated and pulled out, thus ensuring that the snow was not artificially compacted into the pots or contaminated when filling. Each PTFE pot was cleaned 3 times, i.e. filled and emptied 3 times, using the same area of snow as sample to reduce contamination, and the fourth collection of the snow was kept. All samples were collected at the same depth. Areas containing red snow algae were avoided (as much as possible) when sampling as the red colour masks the black carbon colour results to the eye. The process was repeated at each sampling site location on the transect, using the GPS to determine distances of each sampling site and the bearing of the transect.

4.4.2.2 Snow Pit

A pit was dug in the snow, using ice axes and snow shovel, until the ice layer below the snow was reached. The snow pit was used to determine the variation of black carbon at different depths, thus samples were collected at different depths through a variety of snow layers. For each snow layer, three PTFE pots were used

to collect snow samples in the way as described for transect snow collection: each pot was cleaned out 3 times using the layer of snow to be sampled and the fourth collection was kept.

4.4.3 Victoria Land, Antarctica

Measurements were taken in a variety of locations around Victoria Land in December 2010.

Three PTFE sampling pots were filled at each glacial location. Before sampling, the PTFE pots were filled 3 times with snow from the sample site to ensure that the pot was clean. The fourth time the pot was filled, the snow was kept as the sample for the location.

4.4.4 Field Filtering Method

In Svalbard, once taken the samples were placed inside backpacks and the samples were left to melt naturally as the temperature was above 0 °C. In Antarctica, the samples were left to melt naturally inside the laboratory at the Mario Zucchelli station. Once the sample had melted, filtering could occur. The filtering was undertaken inside Sigma-Aldrich glove bag in order to prevent contamination (Figure 4.5).

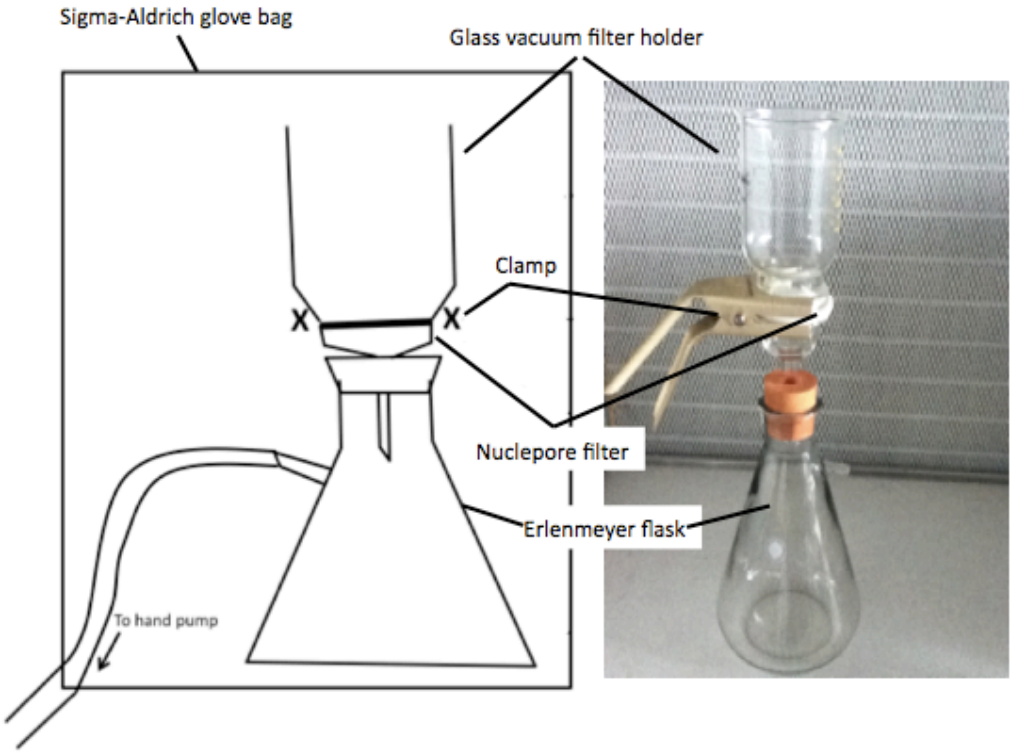

Figure 4.5. A diagram showing the field filtering equipment setup.

The filtering method was adapted from Clarke and Noone (1985). A 0.4 µm Nuclepore membrane filter was placed between the beaker and the conical flask using clean tweezers. A clamp was then attached to create a seal. The melted sample was poured into the top reciprocal and a vacuum hand pump was used to create a suction flow to 'pull' the water through the filter. Vacuum hand pumps were used as there was no electricity, electrical pumps required too much power for a solar panel and batteries were too heavy and not energy dense enough for the campaign. The sample drained into the conical flask through the 0.4 µm Nuclepore filter, leaving any black carbon residue on the membrane filter. The filter was removed and placed in a filter Petri slide to analyse against a pre-prepared filter colour chart (Figure 4.6; see section 4.5.1 for more detail). The filtering process was repeated for other sample and the beaker was cleaned using scientific tissues (Kim wipes) between the filtering of each sample.

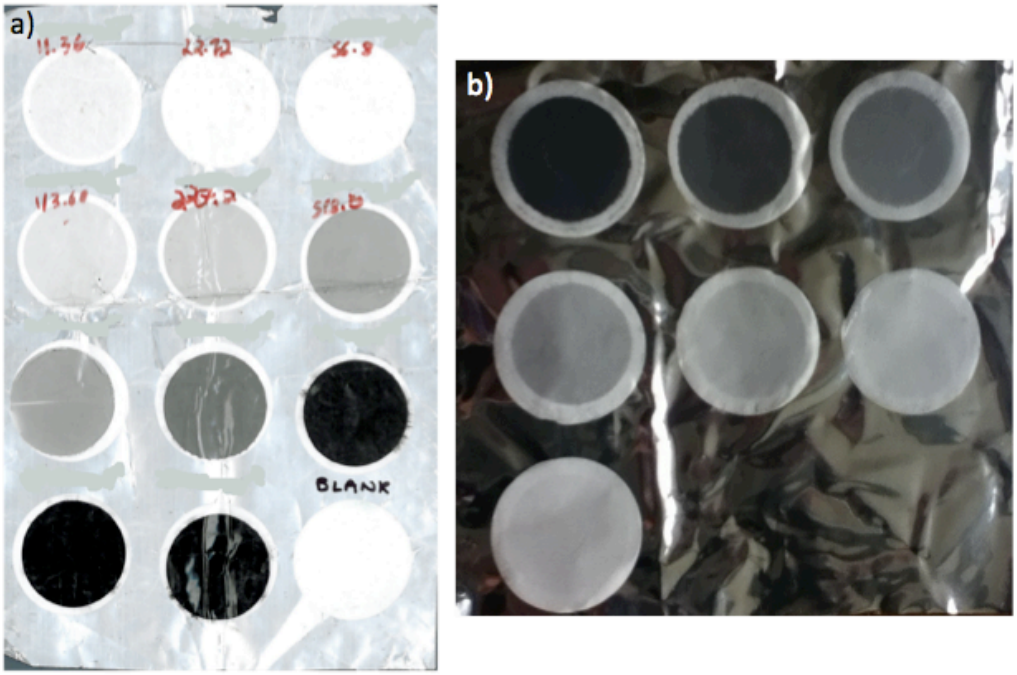

Figure 4.6. Filters created using varying mass ratios of black carbon, used as a comparison sheet for field sample filters to determine the mass ratio of black carbon by eye. Comparison sheet (a) was the sheet used in the field for both Svalbard and Antarctica. Comparison sheet (b) was a small range of filters for lower mass ratios of black carbon to be able to more accurately compare the field samples with the pre-made laboratory samples when using the integrating sandwich sphere.

4.5 Laboratory Method

The methods used to compile the comparison filters (e.g. Figure 4.6) and to measure the sample filters using an integrating sandwich sphere were adapted from the methods described in Clarke and Noone (1985).

4.5.1 Black carbon comparison filters

To make the comparison filters, solutions of known composition were made then filtered. The initial solution comprised of 1 g of black carbon (obtained from Cabot (M120) and was the closest available match to the black carbon used by Clarke and Noone (1985)), 800 ml of water and 200 ml of isopropanol were

mixed together. The stock solution was placed in an ultra-sonic bath for one hour to ensure the solution was fully saturated with black carbon particles, the solution was then filtered through 2 μm then 0.8 μm Nuclepore filters to remove the larger particles so the black carbon in the stock solution was roughly representative of atmospheric black carbon particles. The method described was a repeat of the method used by Clarke and Noone (1985).

To gain an accurate measurement of the black carbon concentration within the filtered stock solution 3 pre-weighed beakers were heated in an oven of 90 °C to remove any residual water from cleaning. The beakers were removed from the oven and aluminium foil was placed over the beakers to prevent any further contamination whilst the beaker was left to cool before weighing to obtain the mass of a dry beaker. Before being placed back in the oven, 525 ml of the filtered stock solution was accurately added to each beaker. Once all the solution has been evaporated, the beakers were removed from the oven and the tin foil was replaced whilst the beakers cooled before weighing. The final mass of the beaker minus the initial mass of the beaker, divided by the volume of stock solution added to the beaker gives the concentration of black carbon within the stock solution.

To make the comparison filters, pictured in Figure 4.6, 250 ml of the remaining stock solution was placed into a beaker marked ‘solution 1’, 125 ml of the solution was filter through 0.4 μm Nuclepore filter (this becomes a comparison filter) then the remaining 125 ml of stock was diluted with 125 ml of distilled water to make ‘solution 2’. The filtering and dilution process was repeated, i.e.

diluting by a factor of 2, until no visible black carbon was be collected on the 0.4 μm Nuclepore filter. Once the comparison filters were dry, the integrating sandwich sphere was used to measure the absorption due to black carbon on the filters. There was no evidence that black carbon was lost to the glass of the volumetric flask, isopropanol and the use of an ultra-sonic bath ensured that the black carbon in the solution settled but did not stick to the surface.

4.5.2 Integrating Sandwich Sphere Spectrometer

An integrating sandwich sphere spectrometer (ISSS) was used to measure the sample filters more accurately than by eye and a schematic diagram of the set-up of the ISSS can be seen in Figure 4.7. The principle of the ISSS is to create an isotropic environment by use of a highly scattering diffuser thus minimising any false measurement effects due to scattering. Any light scattered by particles on the sample filter is included in the multiple scattering radiation field caused by the diffuser surrounding the filter and thus very little light loss is experienced and the light passing through the sandwich to the detector is varied by only the absorption of the filter. The absorption of light by particles on the filter is amplified by the use of the ISSS as light passes multiple times through the filter. To produce the best results using the ISSS method, the measurements require either long integration times or a bright light source (Grenfell *et al.*, 2011).

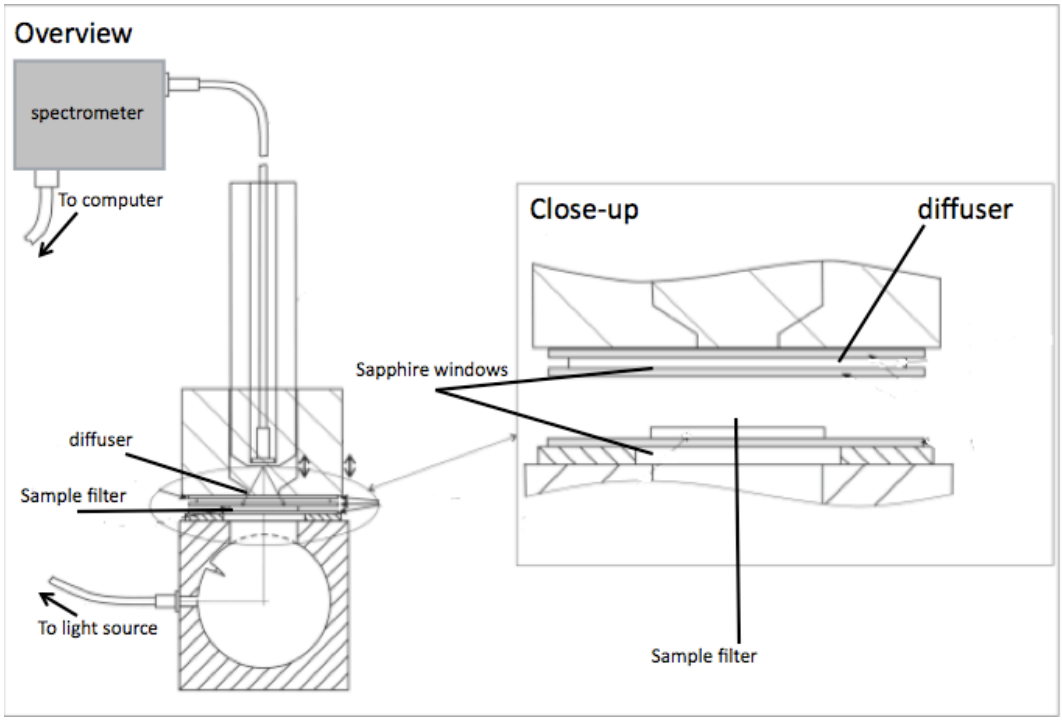

Figure 4.7. A schematic of the integrating sandwich sphere spectrometer. Adapted from Grenfell *et al.* (2011).

To make an absorption measurement using the ISSS, a blank filter was position using clean tweezers on the platform of the base to measure the background light received by the spectrometer (Figure 4.9).

Figure 4.8. Blank filter positioned on platform of base. Underneath the filter is a fixed position sapphire window.

The 'lid' of the ISSS was placed over the filter thus trapping the filter between two sapphire windows and ensuring no light other than the specific light source (a visible lamp) can be emitted through the filter (Figure 4.9 and 4.10).

Figure 4.9. Inside of 'lid' used to enclose the filter. The fixed position sapphire window can be seen and behind that is a small piece of quartz filter paper, used to diffuse light.

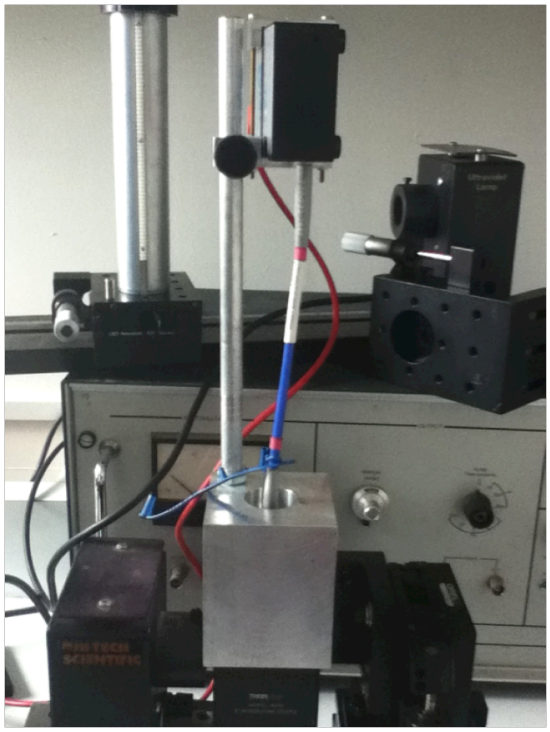

Figure 4.10. Set up of ISSS in laboratory.

The light passed from the visible lamp into a spectrolon integrating sphere to producing diffuse radiation. The diffuse light then passed through a 20 mm sapphire window before passing through the sample filter, another 20 mm sapphire window and the quartz fibre filter than acts as an upper diffuser. The radiation transmitted upwards through the quartz filter wass received by an Ocean Optics USB 2000+ spectrometer and the resulting spectrum was recorded, via a USB, on a Panasonic Toughbook laptop. After a spectrum of the background light was measured, a piece of aluminium foil was placed in between the visible lamp and the integrating sphere to block out any light so a dark spectrum could also be recorded. The integration time was adjusted to produce the best spectrum values, and the spectrometer undertook 10 measurements and averaged the results before printing the spectrum to screen. To minimise risk of moving the ISSS a UV lamp was not used, instead the visible lamp was saturated to produce a clearer absorption value between 300–400 nm. Once the background and dark spectra had been measured (both saturated and unsaturated), the blank filter was removed and a sample filter was position on the base. Ten separate spectra of the sample filters were taken the results were averaged to produce a better absorption value (in addition to the averaging undertaken by the spectrometer). The process was repeated for all sample and comparison filters. Examples of the intensity spectra detected for the comparison filters can be seen in Figure 4.11.

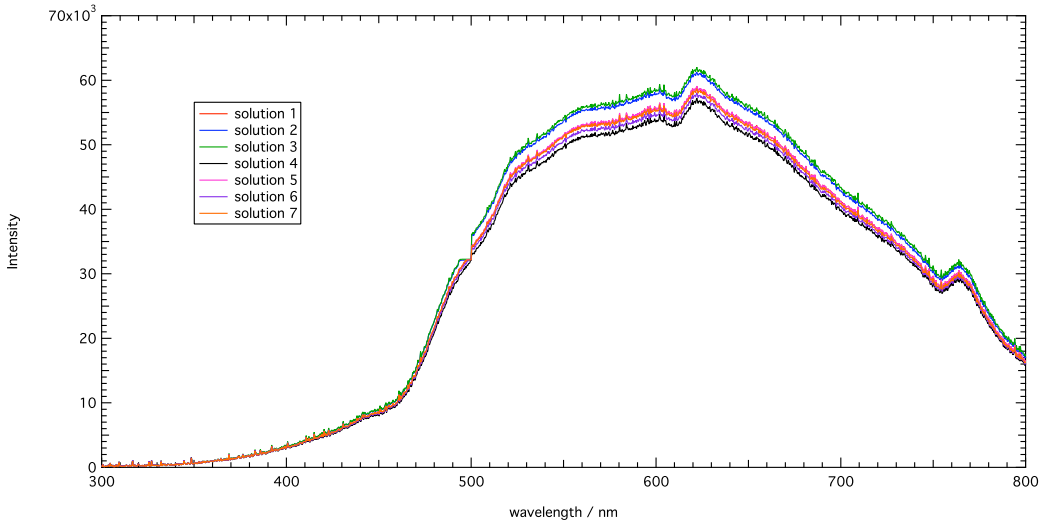

Figure 4.11. Background spectra of all 7 calibration solutions.

To determine the absorption by the sample filters, all spectra were divided by the integration time and then the dark spectra was removed from the correlating blank and sample filters. The absorption measured by the blank filter was removed from the sample filter absorption spectrum, thus all background noise experienced during measurements was removed. The absorption spectra for filters (Figure 4.12) was a combination of unsaturated and saturated absorption spectra and the 'bump' at 500 nm shows the join between the two spectra. The visible lamp was used for both the unsaturated and saturated absorption instead of using a UV lamp measure below 500 nm in wavelength to avoid changing lamps and therefore having calibration problems.

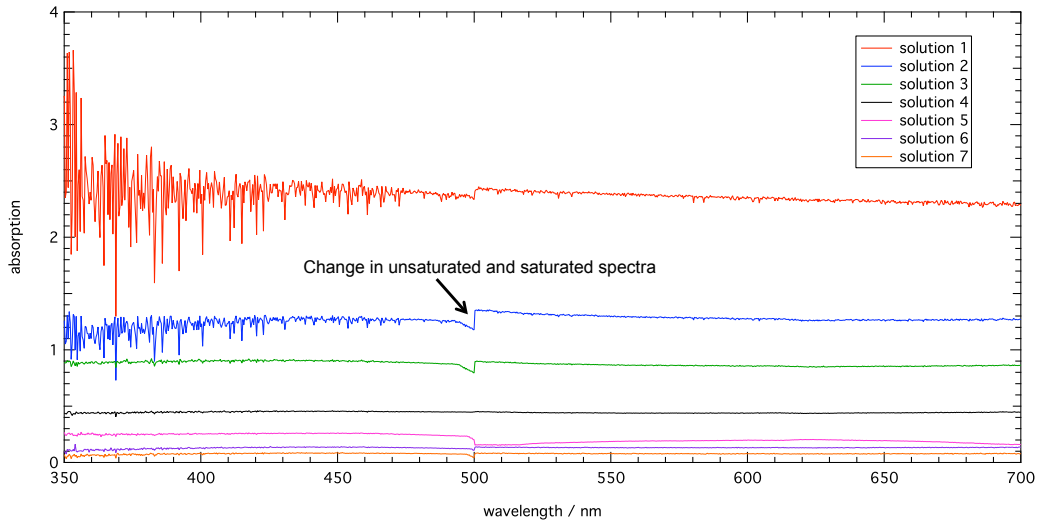

Figure 4.12. Absorption spectra of all 7 calibration solutions. The transition point between the two spectra occurs at 500 nm. There noise around 350 nm is due to lack of light from the lamp point. The black carbon standard used in further calibration measurements is solution 4 and the absorption spectum is perfectly flat.

4.6 Results

4.6.1 Comparison Filters

Calibrations of the ISSS system were based on a set of seven comparison filters with a series of loadings (g cm^{-3}) of commercially produced black carbon. The comparison filter loadings spanned a range sufficiently sized to produce sensitivity curves of the ISSS for the field filter samples. The average concentration of the stock solution was 2×10^{-3} g cm^{-3}. The black carbon concentrations of the individual comparison filters are shown in Table 4.1. The mass of the black carbon on the filter was calculated by multiplying the concentration of black carbon in solution by the volume of solution filtered.

Solution	Concentration of black carbon in solution /g cm^{-3}	Mass of black carbon on filter / g
1	2.29×10^{-3}	0.287
2	1.15×10^{-3}	0.143
3	5.73×10^{-4}	0.072
4	2.87×10^{-4}	0.036
5	1.43×10^{-4}	0.018
6	7.16×10^{-5}	0.009
7	3.58×10^{-5}	0.004

Table 4.1. Comparison filter black carbon concentrations.

The light transmitted through the comparison filter (F_C) was compared with the signal received for the blank filter (F_B) and the relative absorption is expressed as:

$$\text{absorption} = \ln(F_C(\lambda) / F_B(\lambda)) \qquad \text{(E 4.1)}$$

The calibration curves over wavelength for the comparison filters are shown in Figure 4.13 and the errors for the individual comparison filters can be seen in Table 4.2.

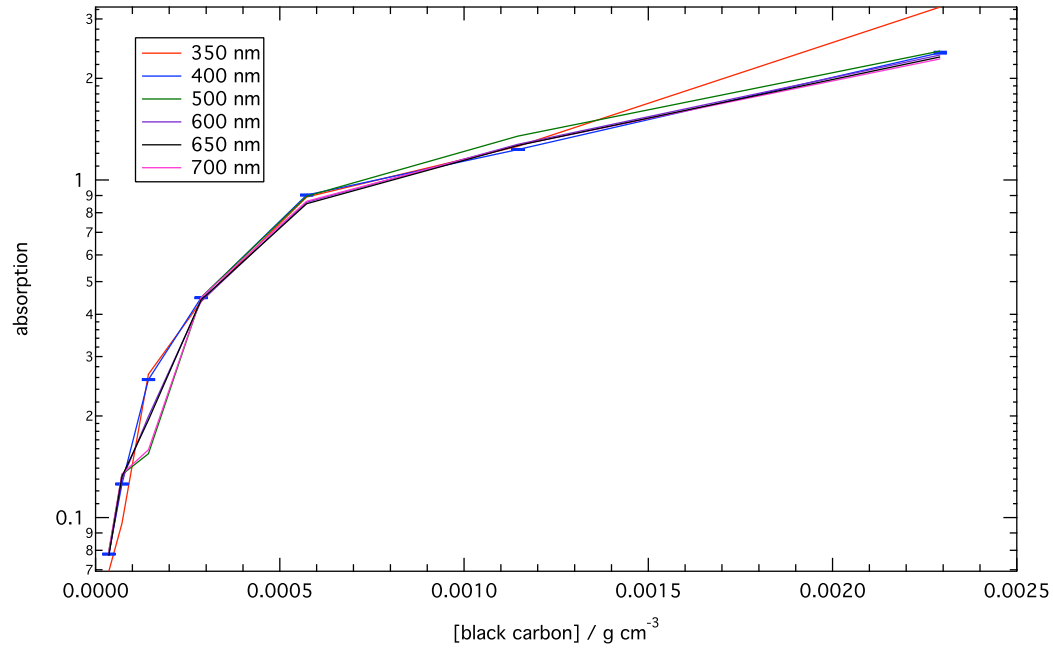

Figure 4.13. Calibration filters using solutions 1-7.

Concentration of black carbon / g cm^{-3}	**Absorption error**				
	λ = 350 nm	λ = 400 nm	λ = 500 nm	λ = 600 nm	λ = 700 nm
2.29×10^{-3}	3.72	0.0114	0.000102	4.76 e-05	4.76 e-05
1.15×10^{-3}	0.0169	0.000480	0.00168	0.000540	0.000434
5.73×10^{-4}	0.00785	0.000491	5.27 e-06	3.12 e-06	8.13 e-06
2.87×10^{-4}	0.00290	0.000165	4.42 e-06	2.14 e-06	2.15 e-06
1.43×10^{-4}	0.00184	0.000322	1.18 e-05	5.41 e-06	4.63 e-06
7.16×10^{-5}	0.00514	0.000219	1.04 e-06	4.02 e-06	2.17 e-06
3.58×10^{-5}	0.00329	7.17 e-05	1.27 e-05	8.08 e-06	4.56 e-06

Table 4.2. Absorption errors for calibration curves of comparison filters.

Multiple loadings of different concentrations were needed as the response of the system deviates from the Beer-Lambert law (Grenfell *et al.*, 2011). A power law (E4.2) was fitted to the comparison filters as it re-produces the calibration curve to within the accuracy of the measurement.

$$\text{Absorbance} = 0 + (6.3918 \pm 0.363)[\text{BC}]^{(0.80543 \pm 0.0337)} \qquad \text{(E4.2)}$$

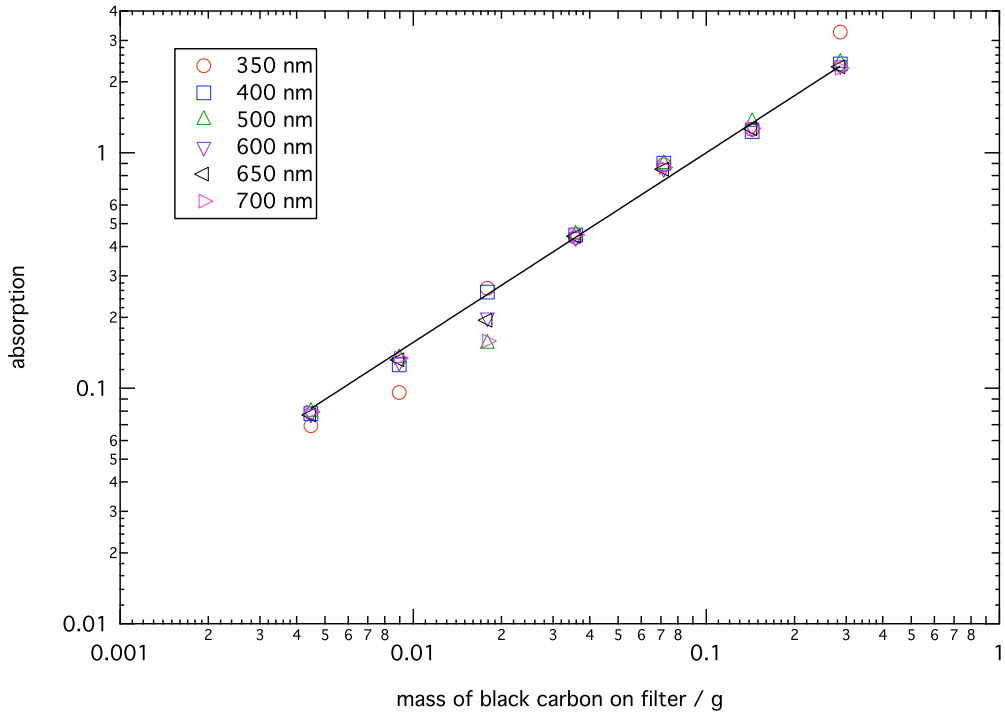

Figure 4.14. Calibration markers with a power fit using 600 nm. Absorbance = 0 + (6.3918 ± 0.363)[BC]$^{(0.80543 \pm 0.0337)}$. The absorption is on a ln scale. [BC]∝A^{x}.

Table 4.3 shows the results of comparing the sample filters with the comparison filter sheet in the field to judge the black carbon mass ratio by eye.

Location	Site number	Average black carbon mass ratio /ng g^{-1}
Hercules Neve		<11
Nansen Ice sheet		<11
Dryglowski Ice Tongue		~11
Hell's Gate		~11
Lappbreen	1	45
	2	11
	3	15
	4	15
	5	11
	6	15
Lappbreen slope	1	34
	2	76
	3	30
	4	94
	5	73
	6	19
Snow pit 1	Layer 1	23
	Layer 2	11
	Layer 3	30
Snow pit 2	Layer 1	34
	Layer 2	30
	Layer 3	45
Lulefjellet	1	45
	2	114
	3	76
	4	40
	5	46
	6	114

Table 4.3. Black carbon mass ratios for individual sites determined by comparing comparison sheet with sample filters and averaging the value for each site. The original field comparison sheet did not show black carbon mass ratio of <11 ng g^{-1} therefore this was the minimum value assigned.

4.6.2 Oscar II Land

All the data presented here are the worked up raw data. Stray light and electrical noise cause significantly less confidence in the data for wavelengths less than 350 nm and the data should not be used without extreme caution, however, snow photochemists have a strong interest in the wavelength region and so the raw data are presented. An example absorption spectrum for each sample region has been shown and the other absorption spectra can be found in Appendix 4.

4.6.2.1 Lappbreen Transect

The transect was across the Lappbreen glacier from one side to another on a specific bearing (Figure 4.15). The gradient of the glacier started off gently (~1 in 10) and became steeper through the transect (~2 in 10). Snow samples become icier throughout the transect. The transect used for sampling traversed from a high altitude on the glacier to a low altitude (i.e. across and down the glacier).

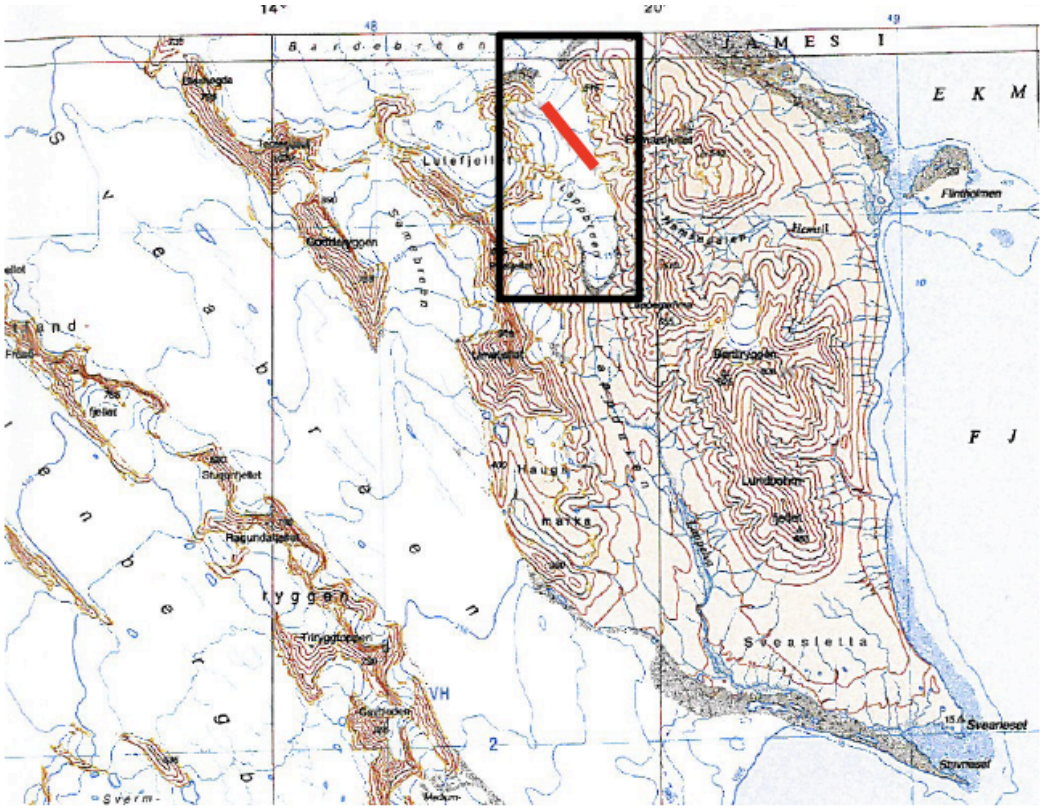

Figure 4.15. Map showing the location of the Lappbreen transect.

Figure 4.16 shows the absorption spectrum made from snow sampled along the transect. Each graph has been labelled with a subjective qualitative data quality score; A means the quality of data is good, B means the quality of data is subjective and C means the quality of data is poor. The filters were sampled by

'young explorers' on the expedition and the data quality is based on my confidence in the data taken by individuals.

Sampling site 1 of the Lappbreen transect (Figure 4.16) was situated beside a lake at 0 m along the transect.

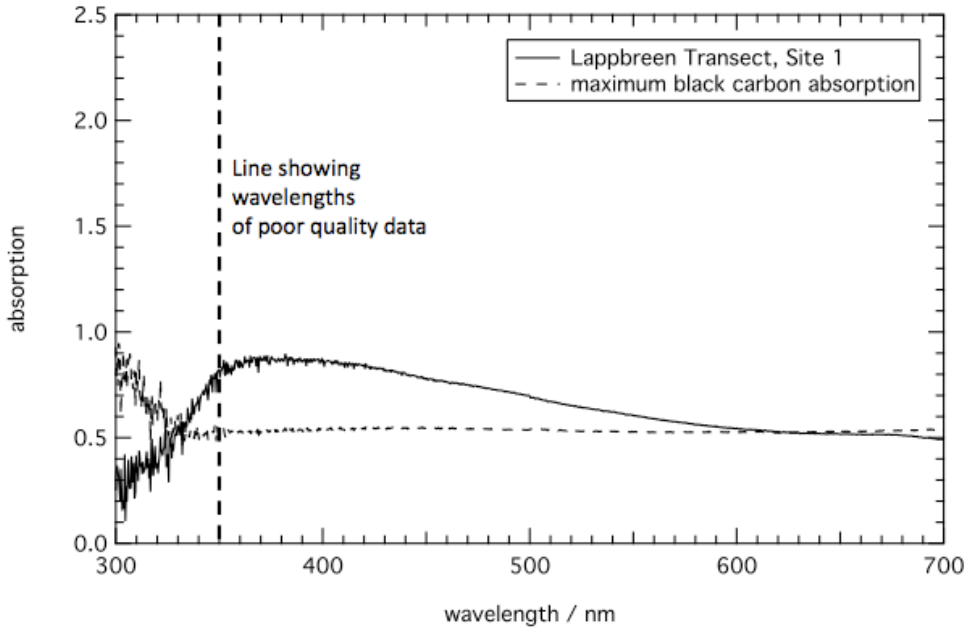

Figure 4.16. Absorption spectrum of site 1 of the Lappbreen transect. Data quality = A. Black carbon absorption factor = 1.2.

The maximum black carbon absorption was calculated by multiplying the comparison black carbon solution 4 by a factor until the maximum black carbon absorption aligns with the minimum filter absorption around 600 nm.

The absorption spectra for other sample sites along the Lappbreen transect can be found in Appendix 4, section A4.2.1.1.

4.6.2.2 Lulefjellet Transect

The transect was taken on a small sheltered glacier near the moraine between Lulefjellet and Samebreen (Figure 4.17). The centre of the glacier contained a high concentration of meltwater.

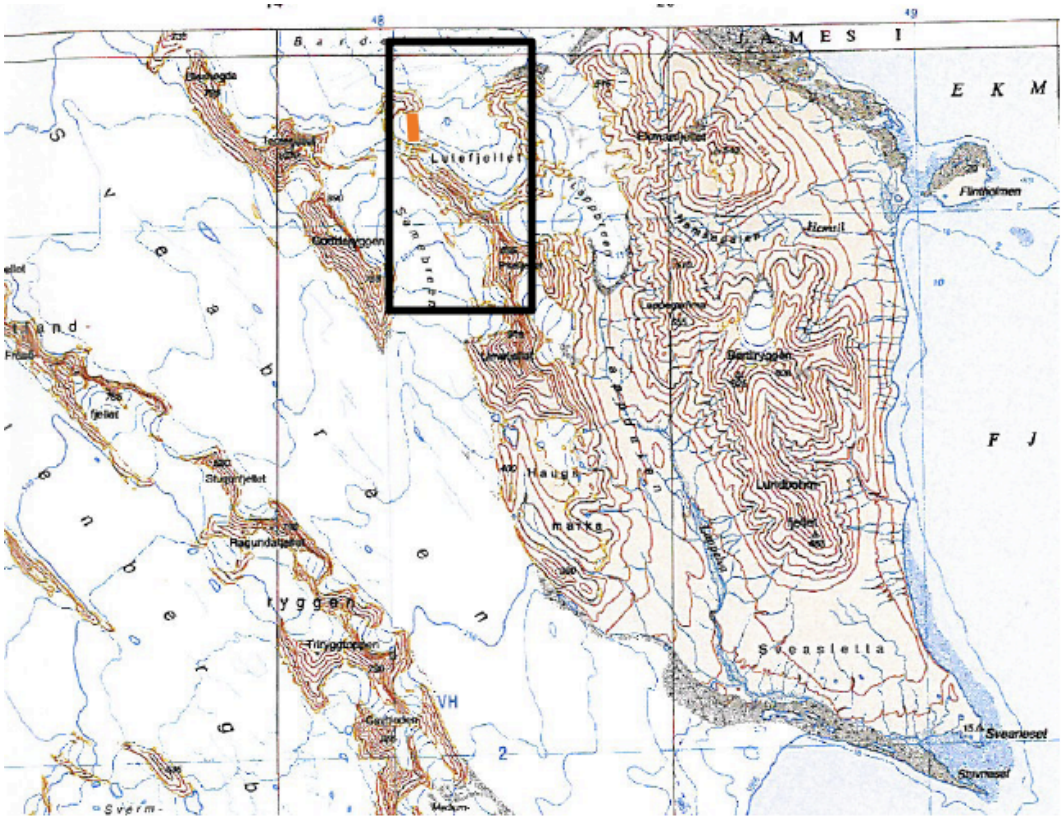

Figure 4.17. Map showing the location of the Lulefjellet transect.

Sampling site 1 (Figure 4.18) was located on a shaded icy slope at 0 m along the transect.

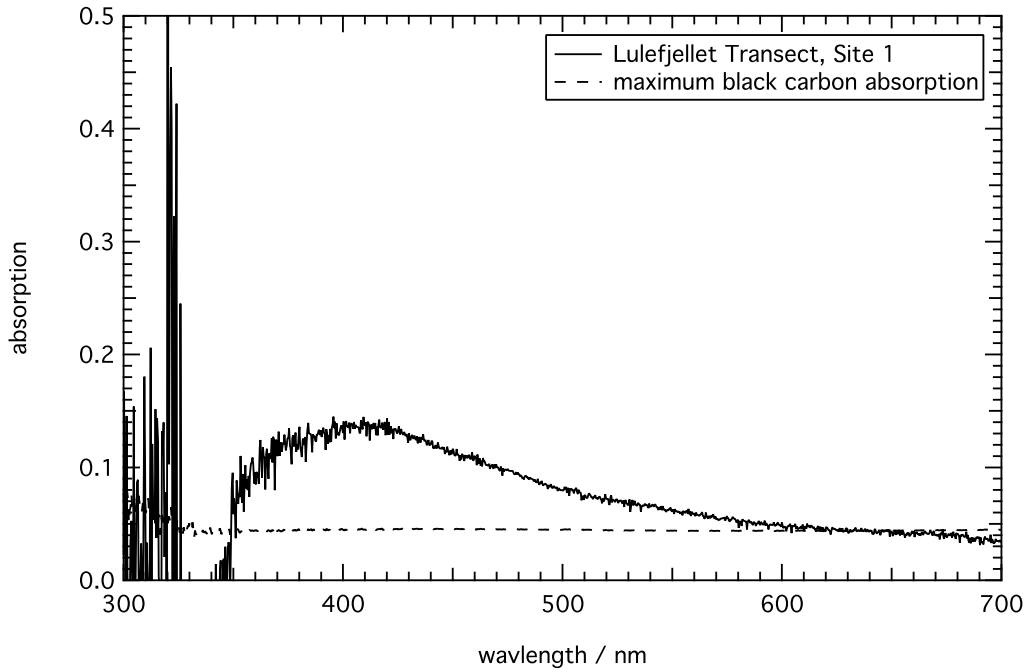

Figure 4.18. Absorption spectrum of site 1 of Lulefjellet transect. Data quality = A. Black carbon absorption factor = 0.1. Slightly influenced by stray light under 400 nm.

The absorption spectra for other sample sites along the Lulefjellet transect can be found in Appendix 4, section A4.2.1.2.

4.6.2.3 Lappbreen Slope Transect

The transect was taken of fine-grained snow on slope. The snow had a density of ~0.2 g cm^{-3}. The transect was taken up the snow slope at the side of Lappbreen towards the moraine peak between Lappbreen and Lulefjellet (Figure 4.19). It was noted that the top section of snow on the slope had melted significantly in comparison to the bottom section on days surrounding the measurement period, this is an indication of temporary snow cover and could be used to see if black carbon concentrates in illuminated snow.

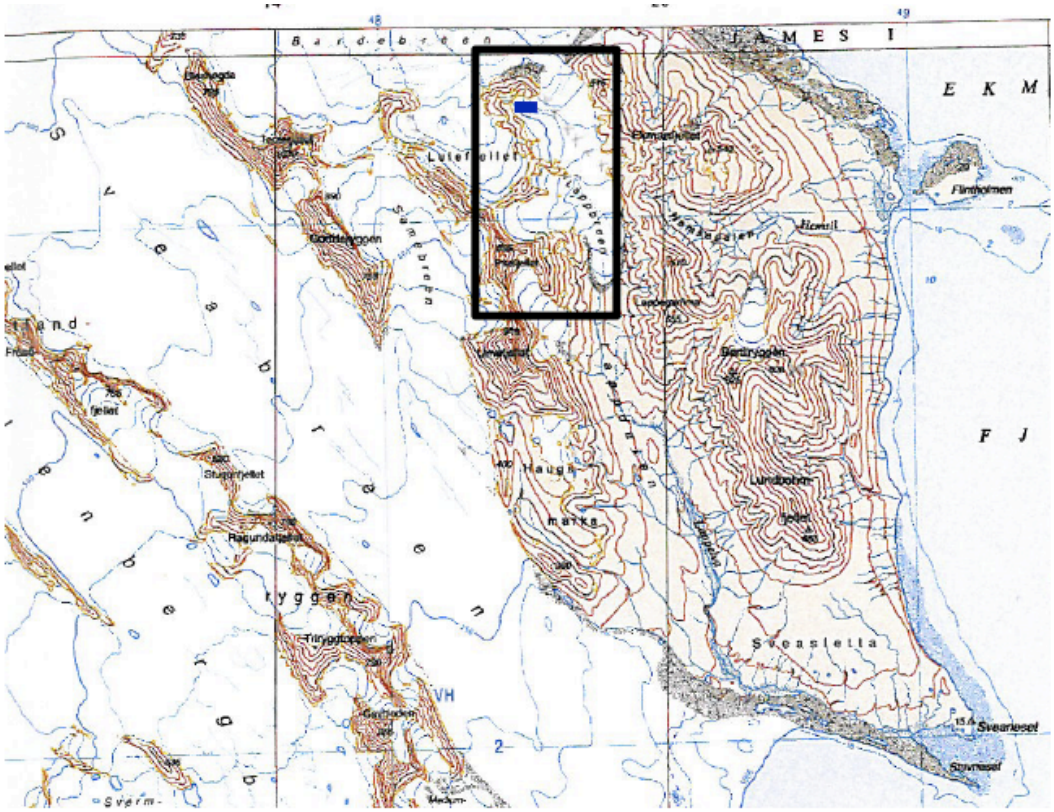

Figure 4.19. Map showing the location of the Lappbreen slope transect 2.

Sampling site 1 (Figure 4.20) was collected at the bottom of the slope.

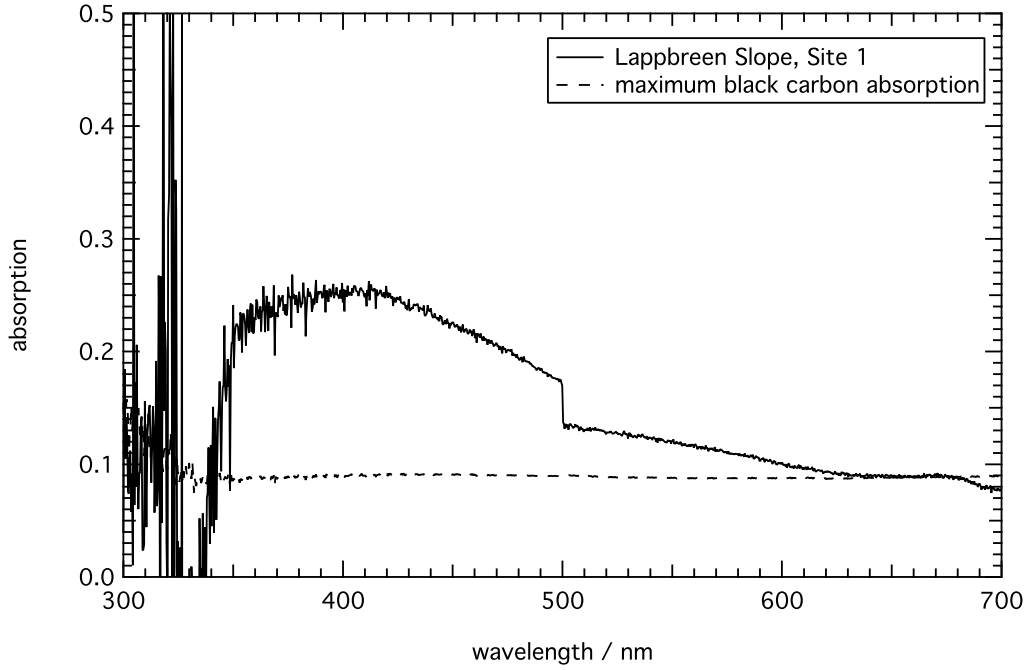

Figure 4.20. Absorption spectrum for site 1 of the Lappbreen slope transect. Data quality = B. Black carbon absorption factor = 0.2.

The absorption spectra for other sample sites along the Lappbreen slope transect can be found in Appendix 4, section A4.2.1.3.

4.6.2.4 Snowpits

The snowpits were located to the top of the Lappbreen slope near site 6 (Figure 4.19). The two snowpits were dug side-by-side. Layers 1 and 2 consisted of fine-grained snow with a density of ~0.2 g cm^{-3} and layer 3 was an icy layer with a density of ~0.5 g cm^{-3}.

Figures 4.21 – 4.23 show the individual snow layers for snowpit 1 and Figure 4.24 shows all 3 snow layers together. Similar graphs showing the absorption

spectrum of individual snow layers and all 3 snow layers together for snow pit 2 can be found in Appendix 4, section A4.2.1.4.

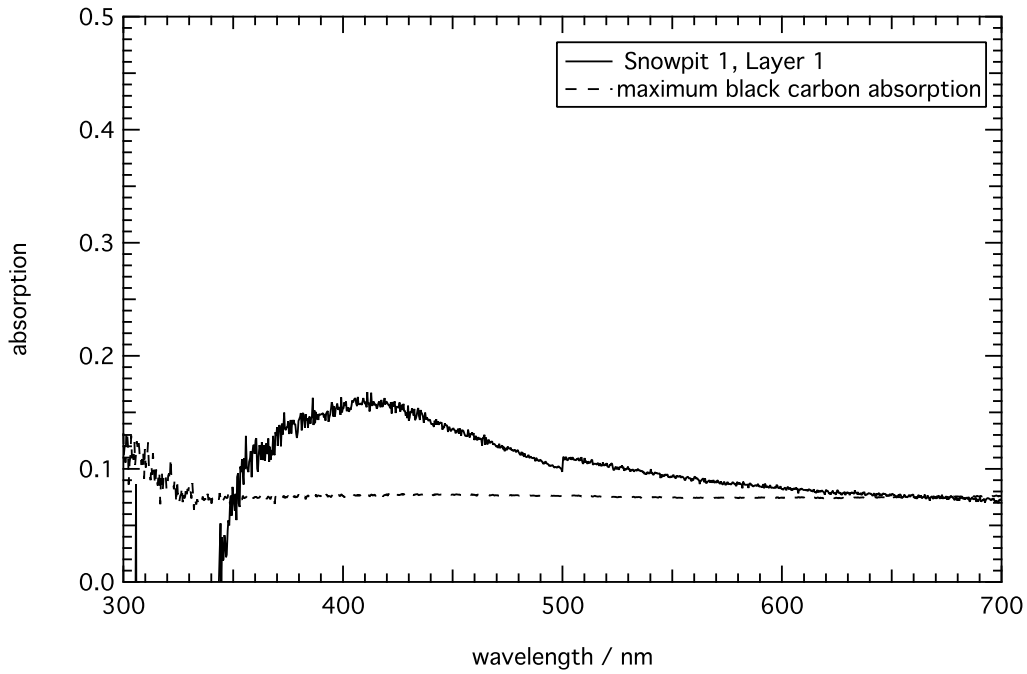

Figure 4.21. Absorption spectrum for layer 1 of snowpit 1 located on the slope of Lappbreen. Data quality = A. Black carbon absorption factor = 0.17.

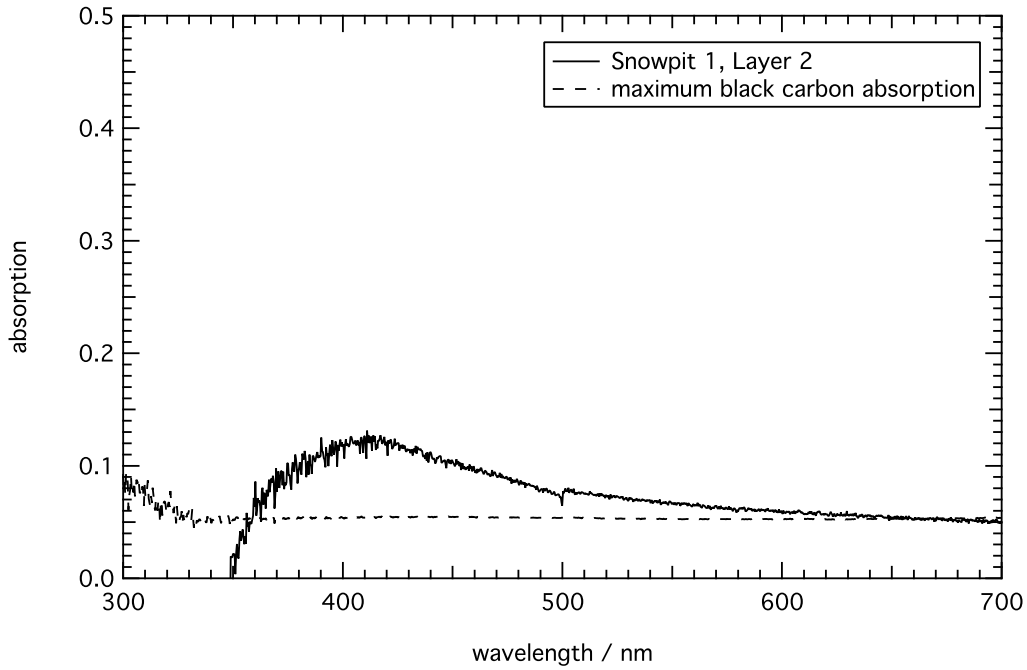

Figure 4.22. Absorption spectrum for layer 2 of snowpit 1 located on the slope of Lappbreen. Data quality = A. Black carbon absorption factor = 0.12.

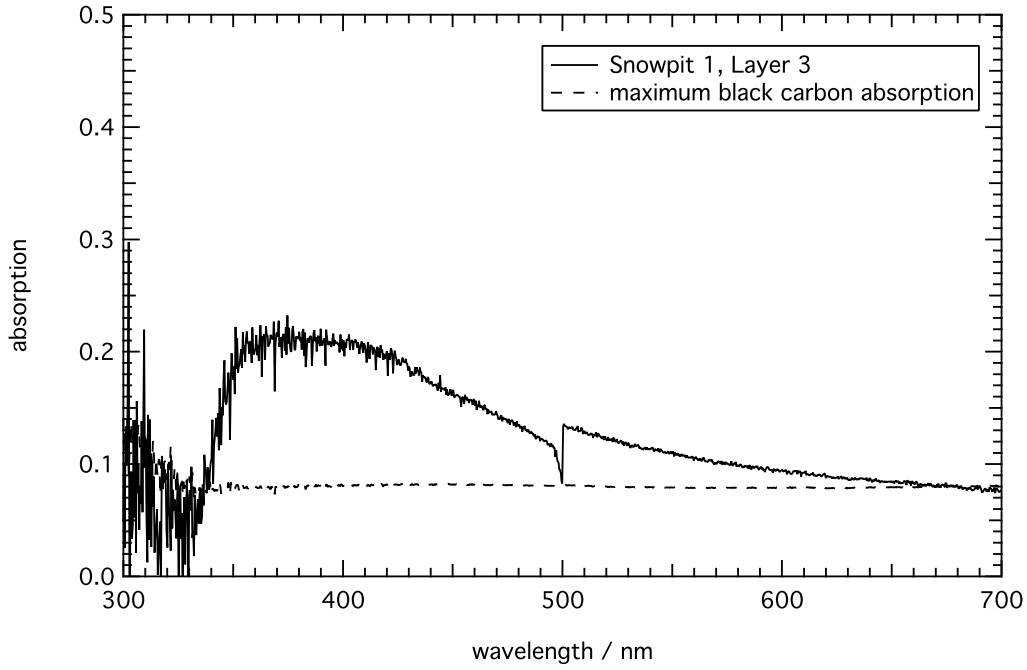

Figure 4.23. Absorption spectrum for layer 3 of snowpit 1 located on the slope of Lappbreen. Data quality = A. Black carbon absorption factor = 0.18.

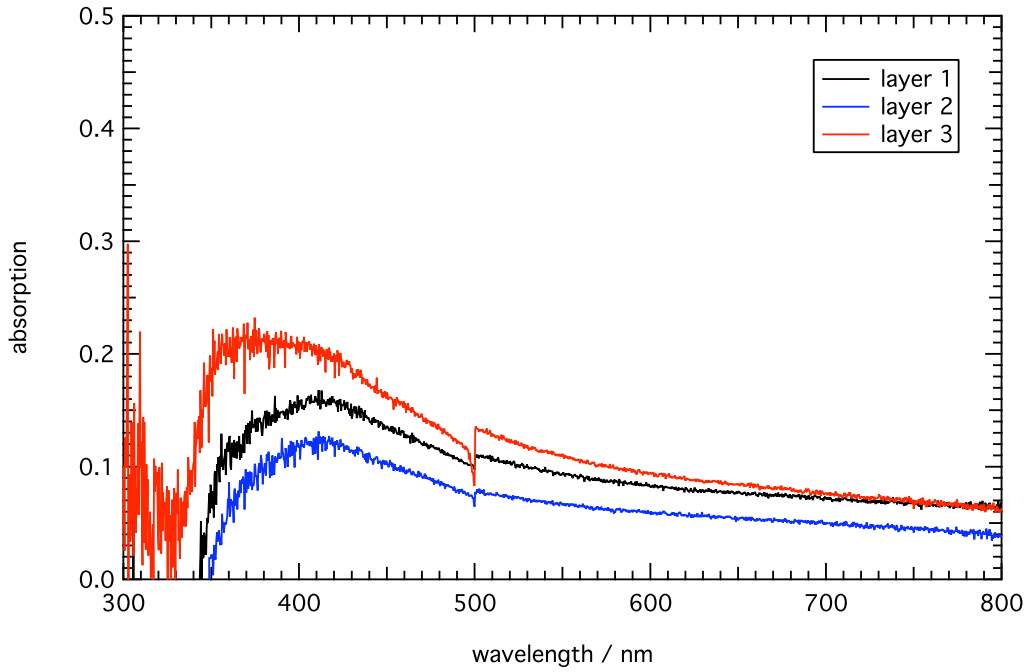

Figure 4.24. Absorption spectrum for layers 1, 2 and 3 of snowpit 1.

4.6.2.5 Bertilryggen

The snow sample was taken from a small snow patch just below the peak of Bertilryggen (Figures 4.25 and 4.26).

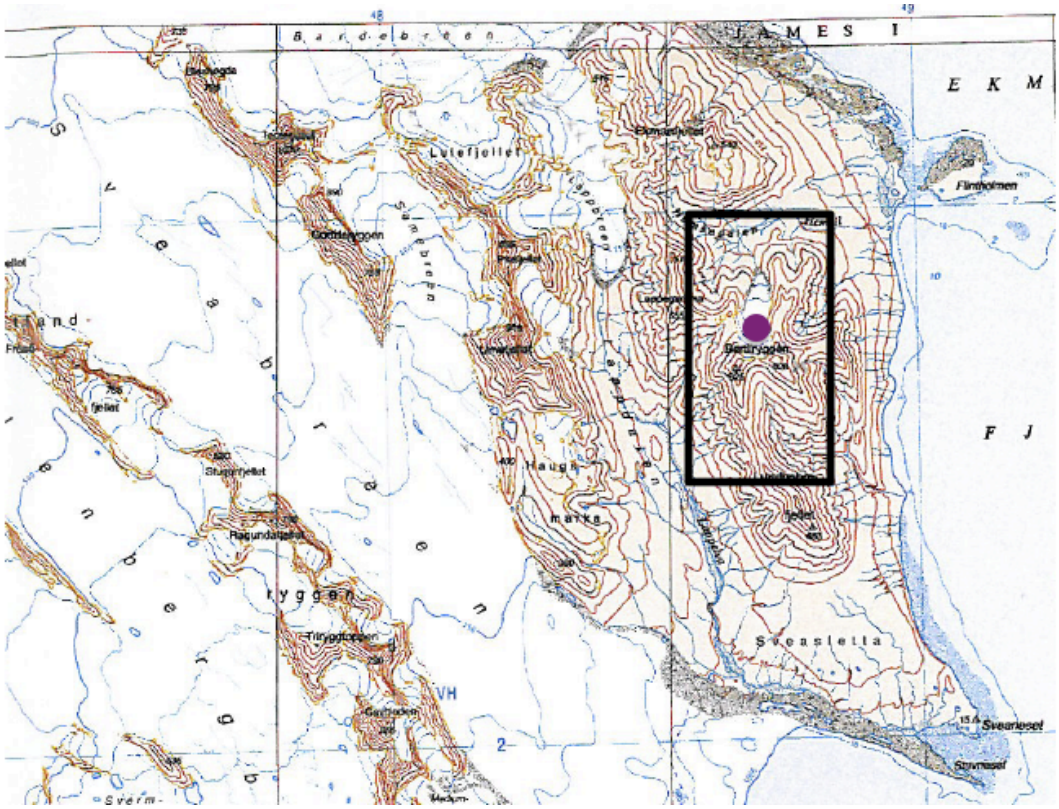

Figure 4.25. Map showing location of Bertilryggen snow sample.

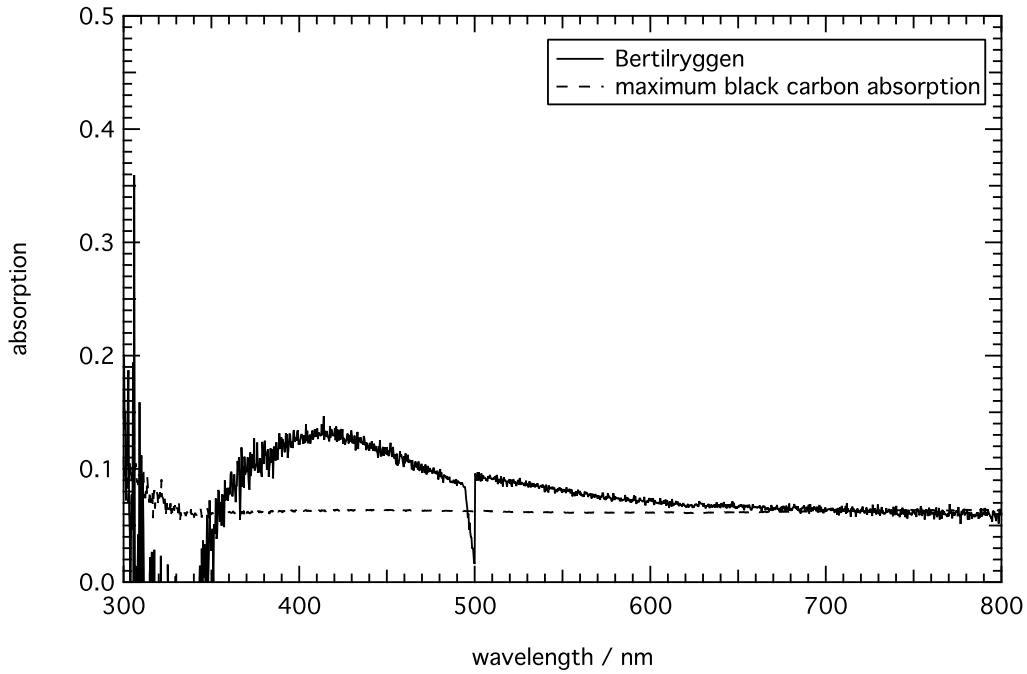

Figure 4.26. Absorption spectrum for snow sample taken from snow patch near the peak of Bertilryggen. Data quality = A. Black carbon absorption factor = 0.4.

4.6.3 Victoria Land, Antarctica

4.6.3.1 Dryglowski Ice Tongue

The Dryglowski Ice Tongue sampling site was located at 75°27.267 S, 164°29.321 E and an altitude of 30 m (Figure 4.27). The sampling surface consisted of mixed forms of faceted and rounded particles (Figure 4.28). The temperature taken between 0-5 cm depth in the snowpack ranged from -5.5 to -6.2 °C.

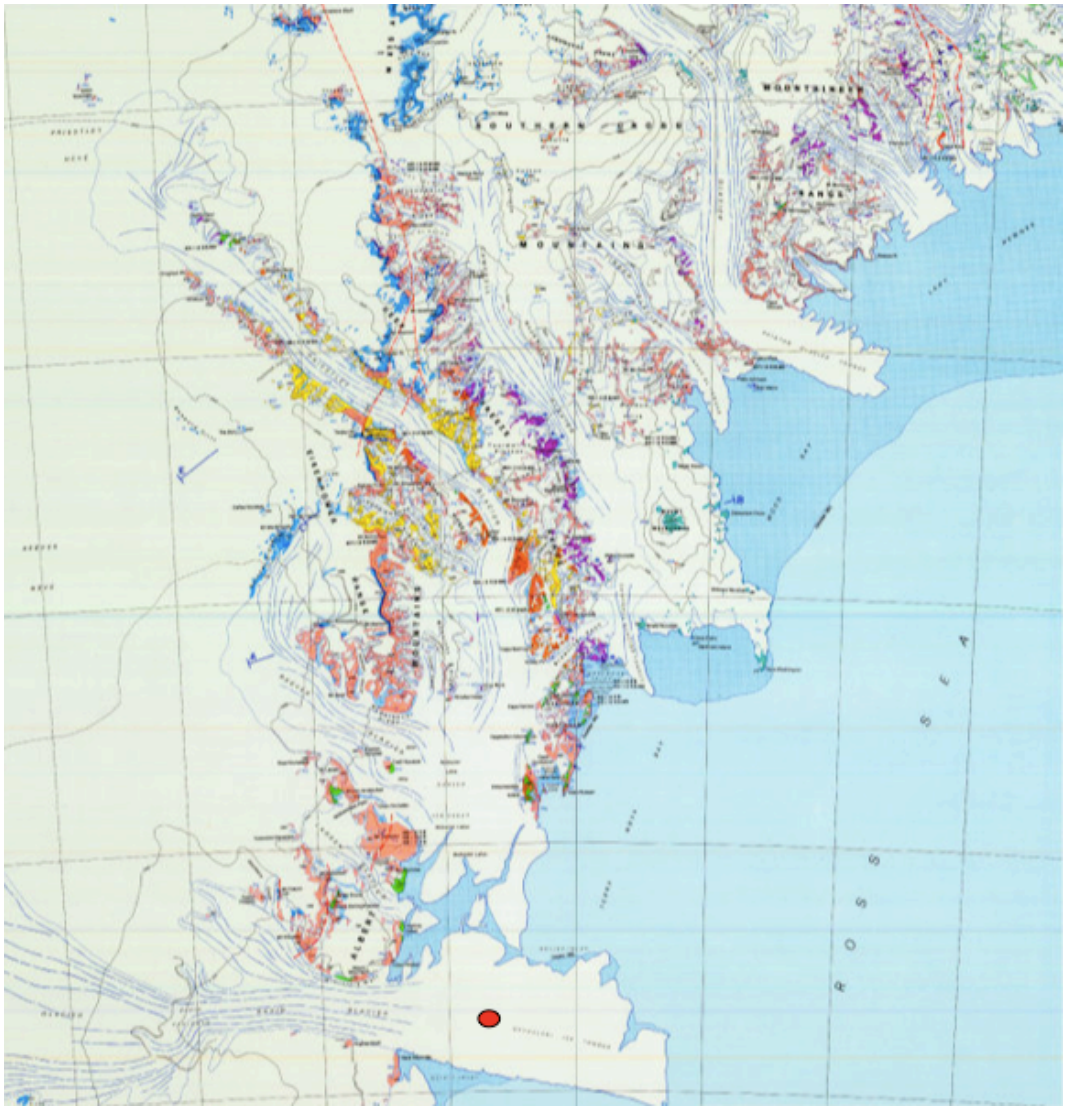

Figure 4.27. Map showing the location of the Dryglowski Ice Tongue.

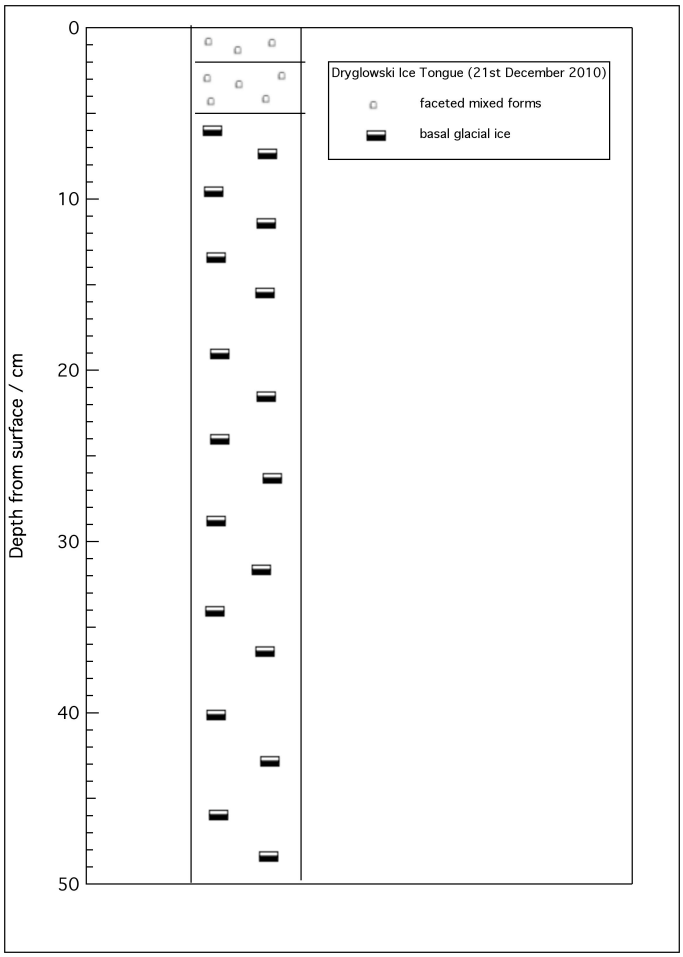

Figure 4.28. Stratigraphy of the sample site at the Dryglowski Ice Tongue.

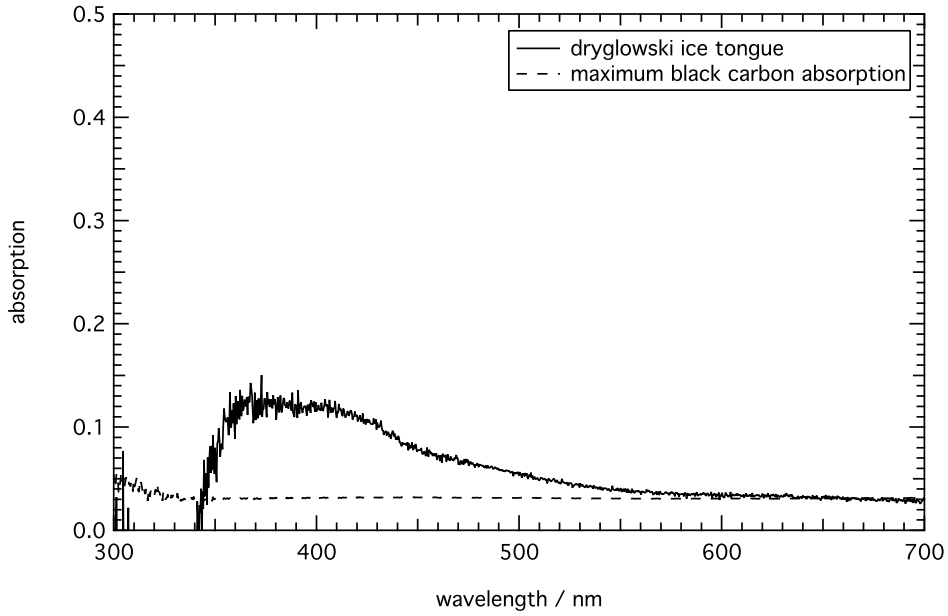

Figure 4.29. Absorption spectrum for Dryglowski ice tongue. Data quality = A. Black carbon absorption factor = 0.07.

4.6.3.2 Hell's gate

The Hell's gate sampling site was located at 74°51.299 S, 164°51.909 E and at an altitude of 30 m (Figure 4.30). The sampling surface was a heterogeneous melting surface (Figure 4.31). The temperature was 0.2 °C at a depth of 2 cm in the snowpack.

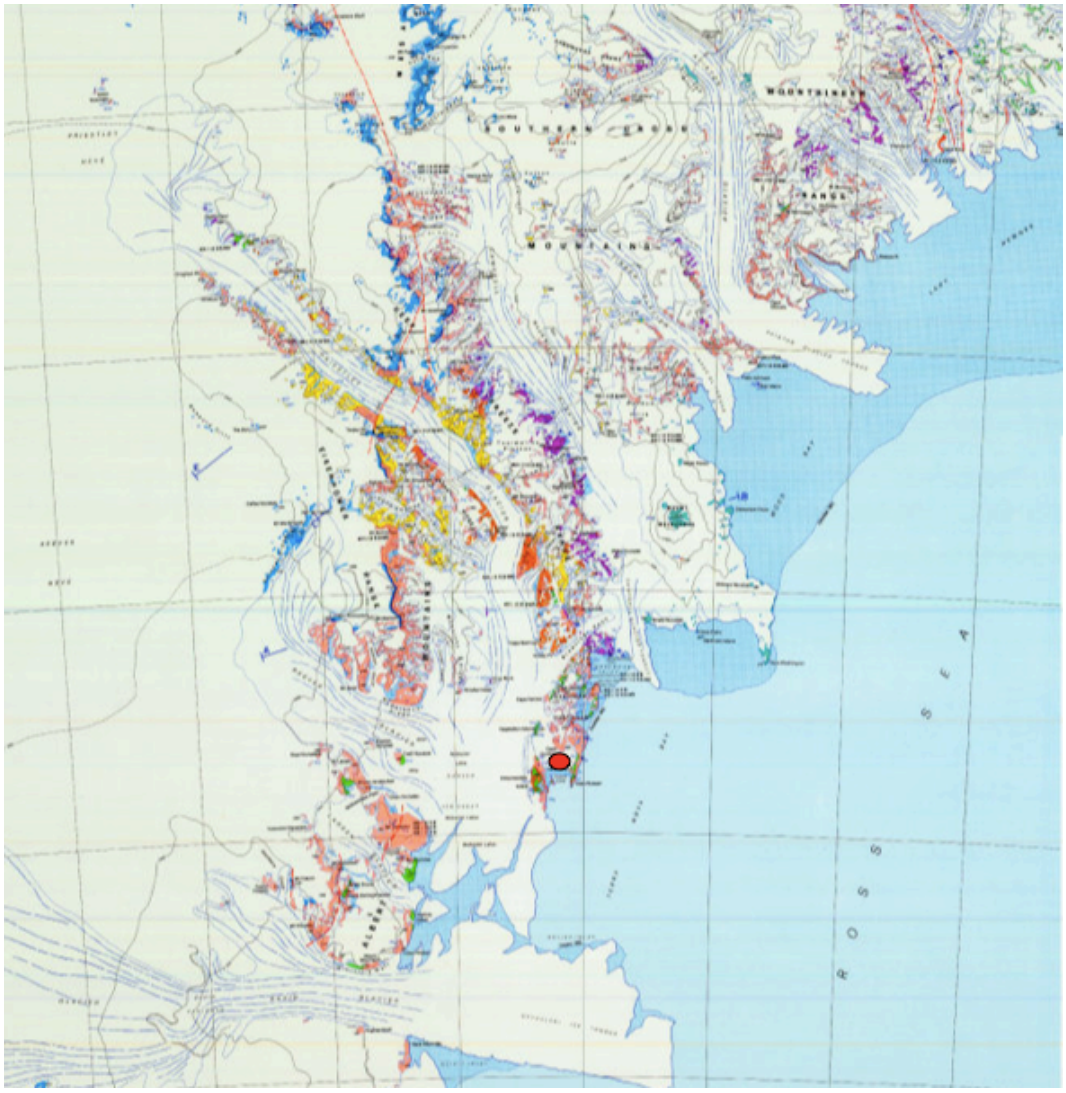

Figure 4.30. Map showing the location of Hell's gate.

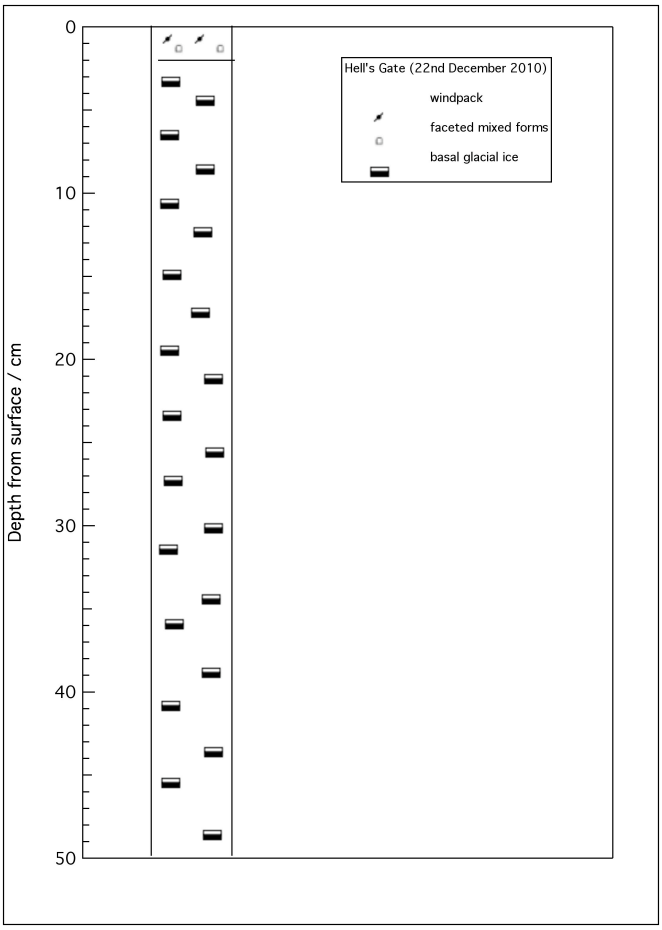

Figure 4.31. Stratigraphy of the sample site at Hell's gate.

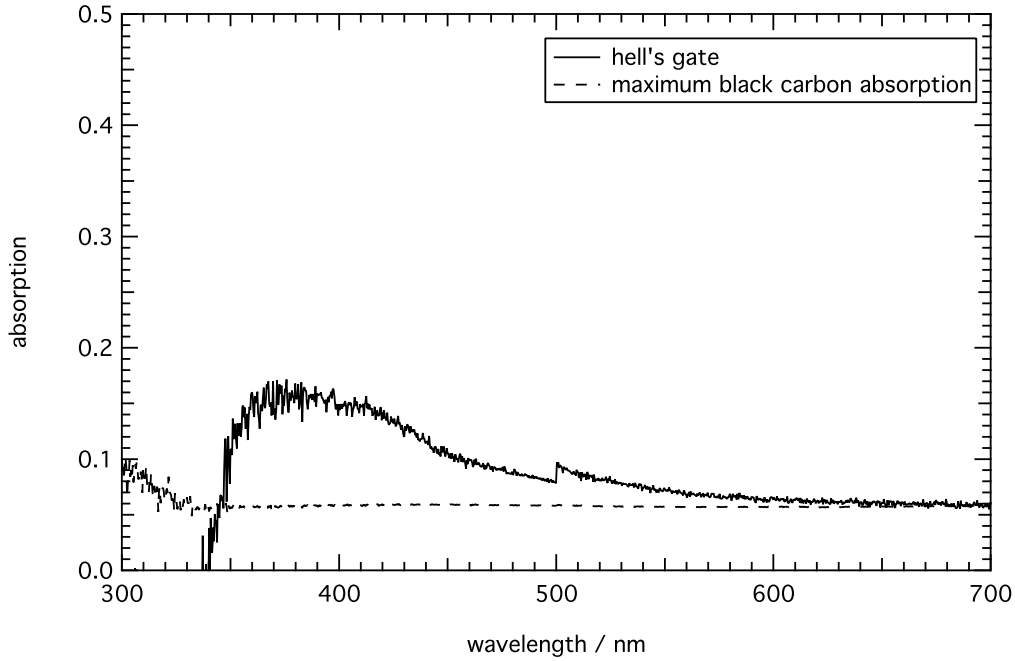

Figure 4.32. Absorption spectrum for Hell's gate. Data quality = A. Black carbon absorption factor = 0.13.

4.6.3.3 Nansen Ice Sheet

Two snow samples were taken on the Nansen ice sheet at a location of 74°45.143 S, 164°55.987 E and an altitude of 15 m (Figure 4.33). The snow surface was ice from melted snow on the ice shelf (Figure 4.34).

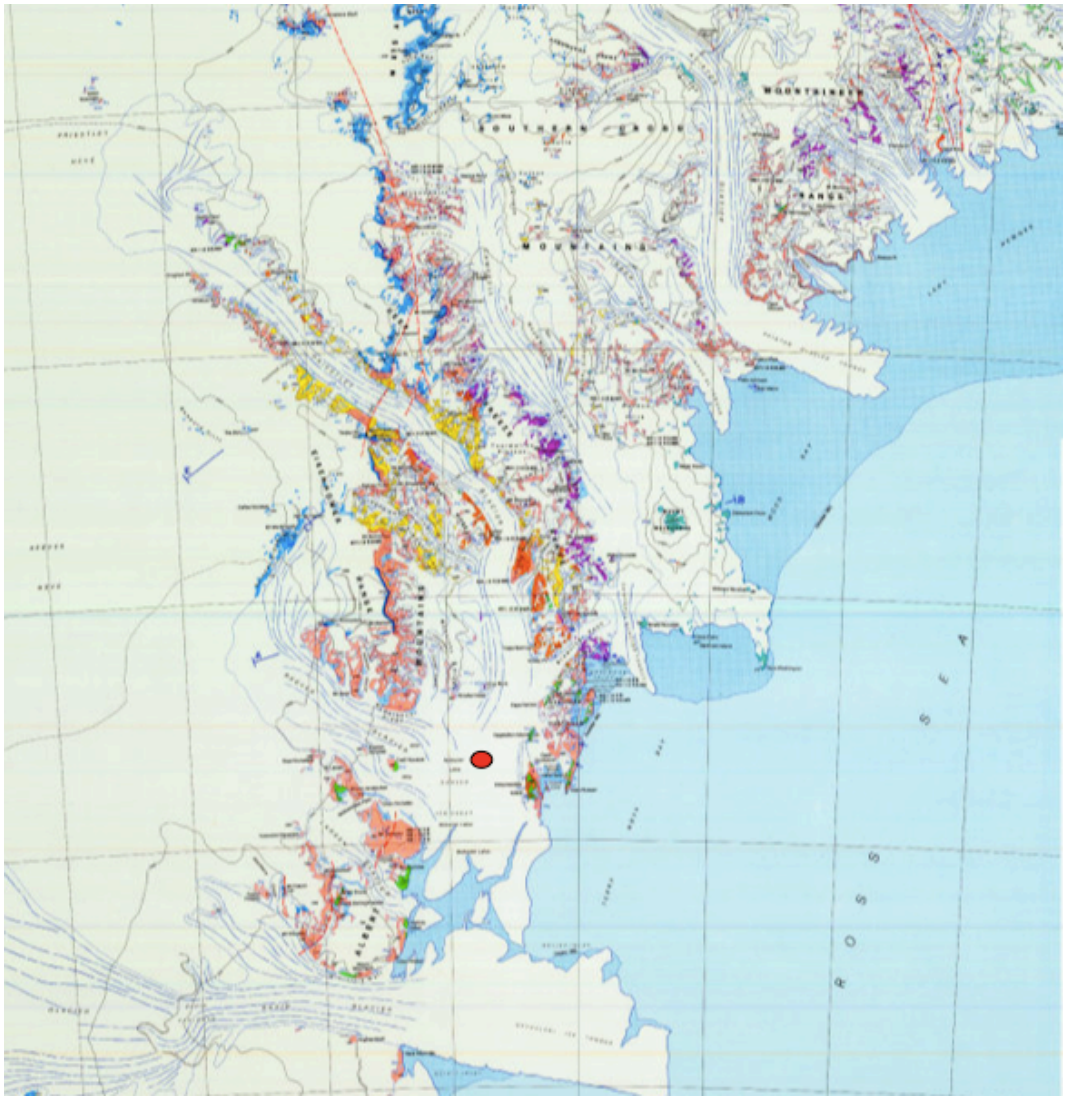

Figure 4.33. Map showing location of the Nansen Ice sheet.

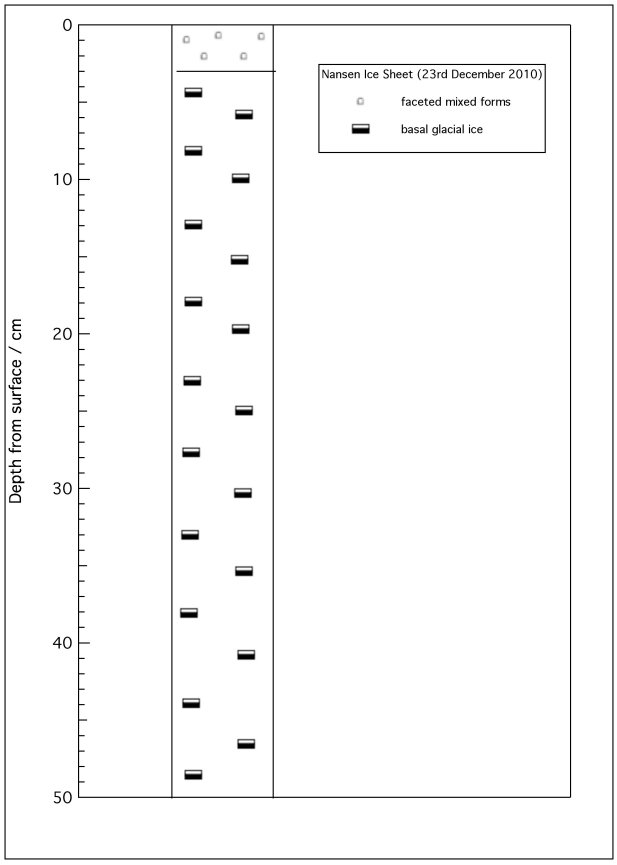

Figure 4.34. Snow stratigraphy of sampling site 2 on the Nansen ice sheet.

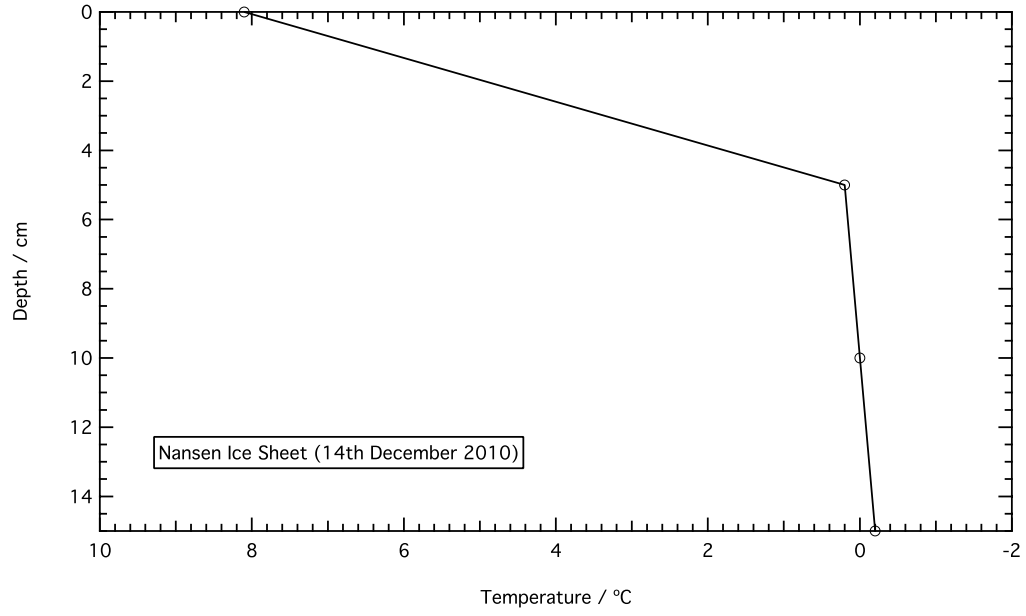

Figure 4.35. Temperature profile of sampling site on the Nansen ice sheet.

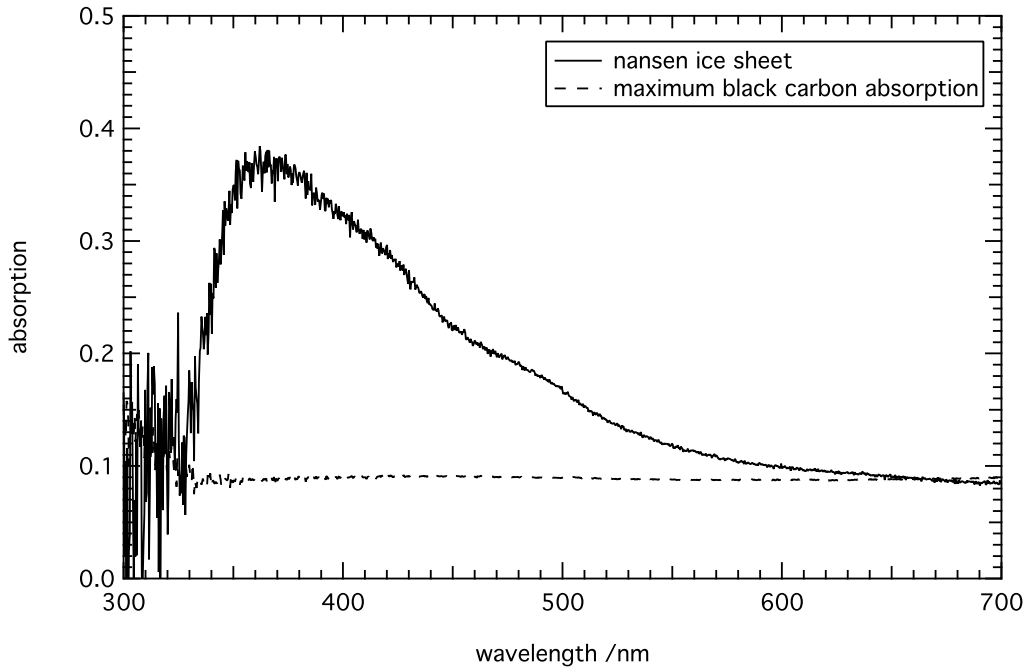

Figure 4.36. Absorption spectrum for snow sample 2 taken on the Nansen ice sheet. Data quality = A. Black carbon absorption factor = 0.2.

4.6.3.4 Hercules Neve

The Hercules Neve sampling site was located at 73°11.109 S, 164°45.730 E and an altitude of 2957 m (Figure 4.37). The surface snow was quite homogenous, aged snow consisting of small rounded grains (Figure 4.38).

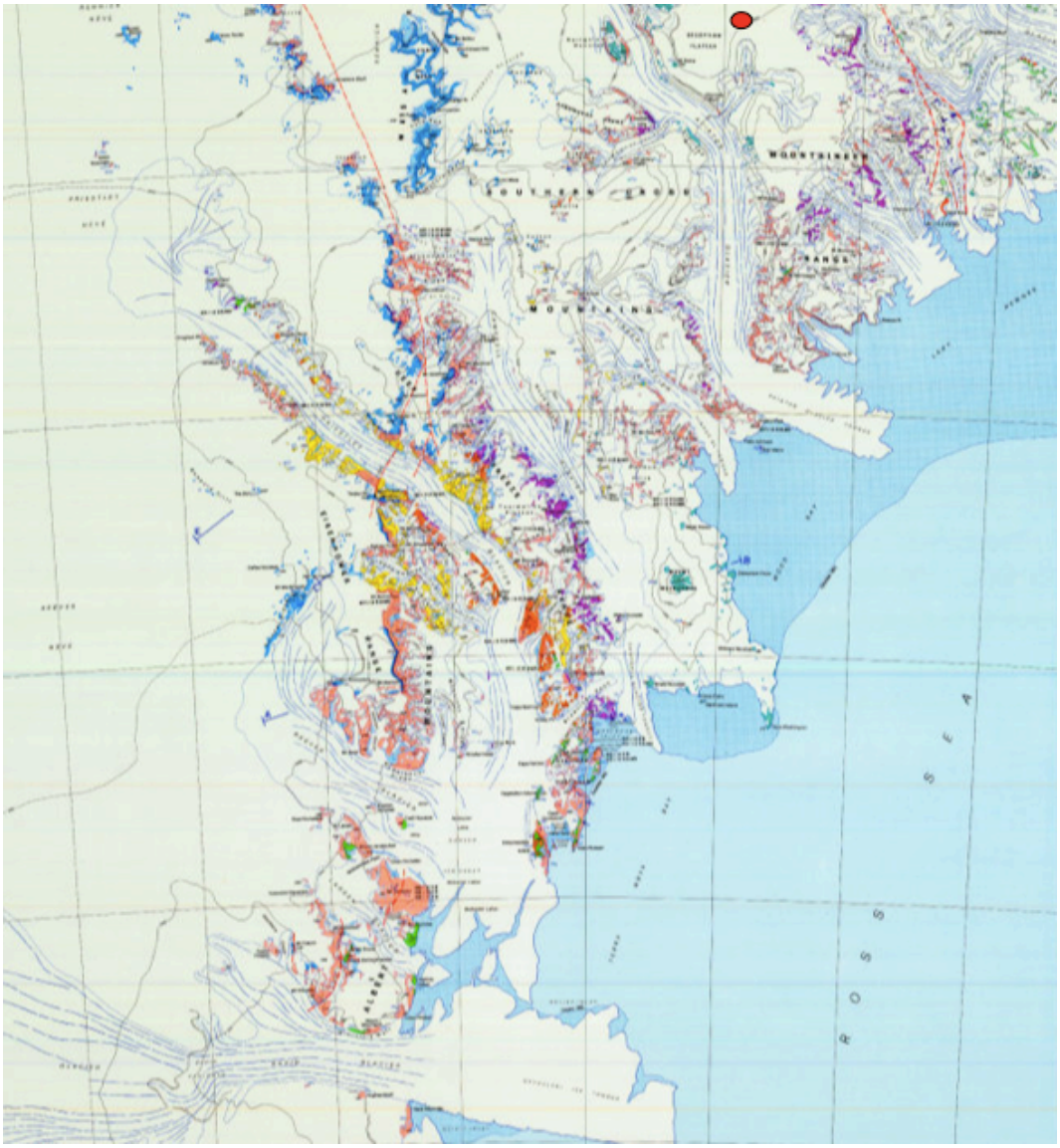

Figure 4.37. Map showing the location of Hercules Neve.

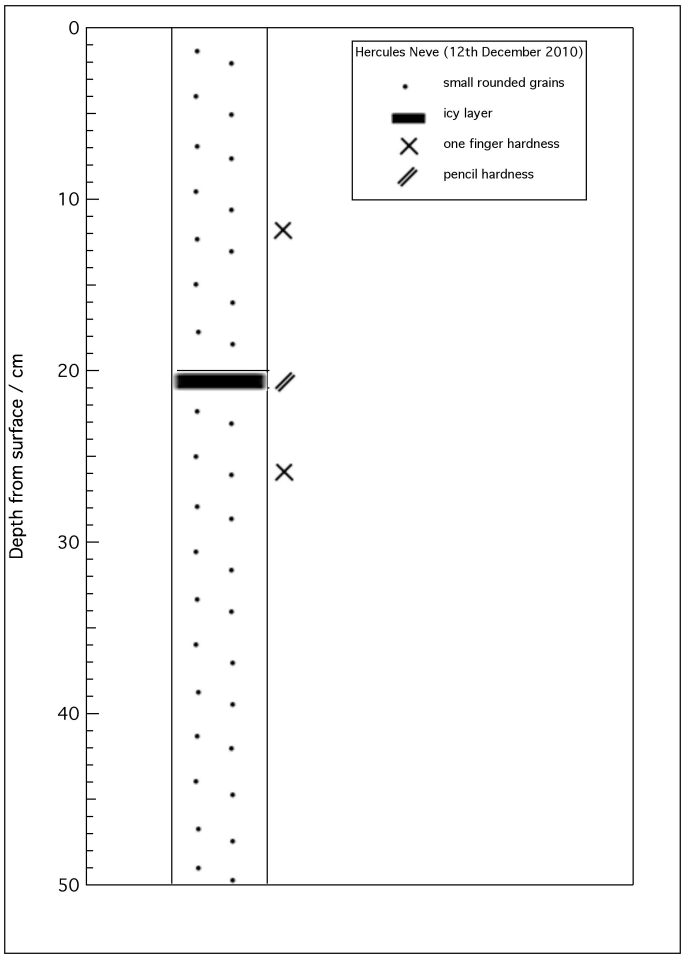

Figure 4.38. Snow stratigraphy at the sampling site on Hercules Neve.

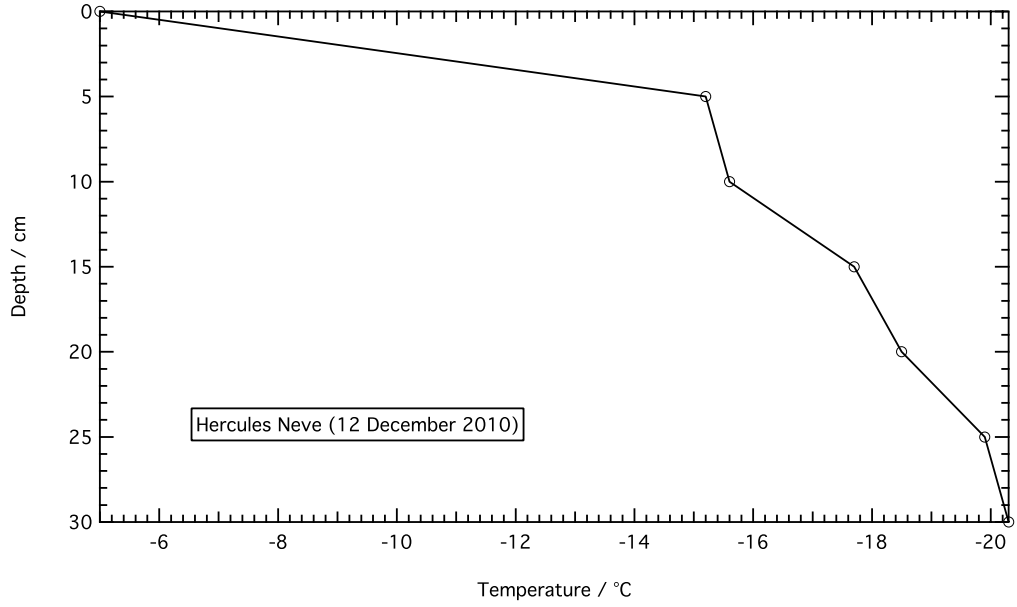

Figure 4.39. Temperature profile for the sampling site on Hercules Neve.

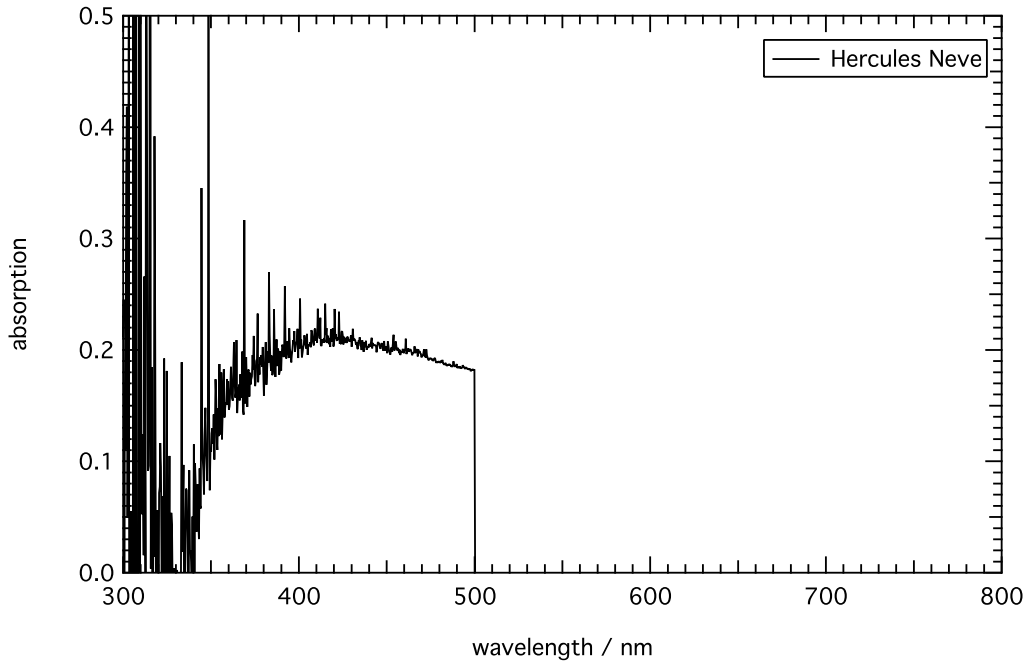

Figure 4.40. Absorption spectrum for Hercules Neve. Data quality = C. Black carbon absorption factor could not be fitted to the graph as the data quality was too poor.

4.7 Discussion

The discussion will focus on 3 main areas: (1) light-absorbing impurities seen within the snow, (2) factors influencing black carbon concentration within snow and the impacts, (3) comparison between judgement by eye and measurement using integrating sandwich sphere, (4) a comparison with previous studies and (5) the quality of the data gathered in the study presented here.

4.7.1 Light-absorbing impurities within snow

The main sources of organic carbon to the atmosphere and to snowpack are anthropogenic activities and biomass burning (e.g. Hegg *et al.*, 2009; Goldberg, 1985; McConnell *et al.*, 2007), the optical parameters of organic carbon from biomass burning aerosols have been reported by Kirchstetter *et al.* (2004). Brown carbon, which includes HULIS (Humic Like Substances), is highly abundant yet a

weaker absorber of visible light than black carbon which has the highest absorption cross-section among carbonaceous constituents of aerosols and therefore contributes significantly to atmospheric absorption by aerosols (e.g. Hoffer *et al.*, 2006). France *et al.* (2012) demonstrated that black carbon alone could not account for all the absorption seen in Barrow snowpacks and an additional absorption by HULIS and other chromophores was necessary to explain variation of the cross-section of light-absorbing impurities in snowpack, σ^{+}_{abs}, with wavelength. A similar situation can be seen in the work presented here, the light-absorbing impurities in the Svalbard and Antarctic snow can be fitted to black carbon but a combination with another absorber is required to explain all absorption i.e. soil, HULIS, mineral dust, red algae. Doherty *et al*. (2010) also calculate that ~20-50 % of the light-absorbing particles in the snowpack studied is by non-black carbon constituents. The total amount of light-absorbing impurity in the snow from Svalbard and Antarctica is not constant over 350-700 nm and therefore assumptions about the absorber identity have been made that the black carbon mass ratios presented here are a maximum and other light-absorbing impurities are needed to fully explain snowpack absorbtion. The work in this chapter shows that estimated concentrations of black carbon in snow can be calculated using the filtration method, however, the values depend on the location and physical characteristics of the absorber. Owing to the glacial location of the sampling sites it was hard to determine the other light-absorbing impurities within the filter samples, i.e. it could have been dust, HULIS, red algae; therefore only black carbon has been fitted to the graphs presented in section 4.6.

4.7.2 Factors influencing black carbon concentration and their impacts

4.7.2.1 Water

Svalbard shows a high temporal black carbon variability (Doherty *et al.,* 2010). The samples taken at 0 m on the Lappbreen transect (Figure 4.15) were situated near to a glacial lake, the samples taken at 0 m on the Lulefjellet transect were taken near a water accumulation area. Doherty *et al.* (2010) discovered that after the Svalbard melt season, black carbon concentrations in the surface snow increased from 18 ng g^{-1} to 56 ng g^{-1}, indicating that there was incomplete removal of the black carbon with melt water. For the work presented here, the areas near stagnant water represent snow after the seasonal melt. Meltwater channels could be found on the Lappbreen glacier in central areas indicating that part of the glacier was still undertaking seasonal melt.

The Arctic Climate Impact Assessment (2004) noted that seasonal weather patterns are changing with observed changes in timing, length and character of season including more rain in autumn and winter, and more extreme heat in the summer. If the trend continues, the melt season will increase in length causing an increased transportation of black carbon from the snow and thus lowering black carbon concentrations found within snowpacks during the melt season. After the melt season, any black carbon not removed will accumulate in the surface snow, lowering snow albedo and increasing snow melt.

4.7.2.2 Aspect

Wind movement will have a large effect on the concentration of black carbon found within snowpacks. A glacier with a strong prevailing wind will see greater

snow movement therefore allowing black carbon to be transported to other areas along the glacier. A glacier with little wind action will allow snow to accumulate thus little transport of black carbon to surrounding areas will occur. The terrain surrounding a glacier will determine the wind effect. A sheltered glacier such as Lulefjellet should show a higher black carbon concentration than an exposed glacier such as Lappbreen.

Slope gradient will have an affect on black carbon concentration. Snow on a steep slope is less stable than on a shallower slope, thus it is more vulnerable to melting and movement. Any black carbon within the snow will be transported until it settles at a more stable gradient. At shallower gradients, snow will accumulate causing an increase in black carbon concentrations.

4.7.2.3 Snow Type

Each snow layer signifies a different depositional event. The Arctic Climate Impact Assessment (2004) predicts there will be more freezing rain and an increasing frequency of freeze-thaw cycle causing hard-packed snow. Black carbon concentrations are higher in icy layers (Figure 4.23) due to reduced amounts of transportation. Taking the Arctic Climate Impact Assessment (2004) predictions of a regime change to hard-packed snow into account, and combining it with the investigative results shown in Figure 4.23, it seems likely that there will be an increase in black carbon concentrations in Svalbard snow in the future.

4.7.2.4 Variability of measurements and proximity to sources

Black carbon concentrations are more variable in the Eastern Arctic than for the Alaskan/Arctic ocean thus reflectivity a close proximity to sources (Doherty *et al.*, 2010). Previous literature implies there are no previous black carbon measurements in Oscar II Land, Svalbard. Clarke and Noone (1985) and Doherty *et al.* (2010) conducted prior measurements in Svalbard using the technique described in this chapter at Ny-Alesund, a research station (78° 55' 60 N, 11° 56' 60 E). The black carbon concentration medians measured were 22 ng g^{-1} (Clarke and Noone, 1985) and 14 ng g^{-1} (Doherty *et al.,* 2010). The black carbon concentration medians recorded by Clarke and Noone (1985) and Doherty *et al.* (2010) are taken from many sites over Svalbard, whilst the investigation presented in this chapter focuses on a small region of Oscar II Land. The different in study area is dictated by transport, budget and style of expedition. However, given the spatial diversity of Svalbard, it seems erroneous to generalize the black carbon measurements.

The Arctic Climate Impact Assessment (2004) predicts that summer temperatures may jump from 9.8-15.3 °C in the Arctic, increasing forest fires by as much as 80 % over the next 100 years. A rise in the number of forest fires will release more black carbon into the atmosphere therefore increasing the change of black carbon being deposited within Svalbard snowpacks and glaciers. Black carbon emissions from China and India alone account for 25-35 % of global emissions (Ramanathan and Carmichael, 2008). With increasing industrialisation, the proximity of black carbon sources will become close to Svalbard and the local black carbon concentration will increase. Increasing the black carbon will lower

the snow albedo (Warren and Wiscombe, 1985), decrease *e*-folding depth and reduce depth-integrated production rates within snowpacks (France *et al.,* 2012; Reay *et al.,* 2012).

4.7.3 Judgements by eye and integrating sandwich sphere

The mass of black carbon on the comparison filter can be used to calculate the mass ratio of black carbon on the sample filter, using the absorption measured by the ISSS (E4.33).

$$m_n^{BC} = m_o^{BC} \left(\frac{A_n}{A_o} \right)^{1/\alpha} \quad \text{(E4.3)}$$

where m_n^{BC} is the mass of black carbon on the sample filter, m_o^{BC} is the mass of black carbon on the comparison filter, A_n is the absorption due to black carbon on the sample filter, A_o is absorption measured using the comparison filters (6.3918) and α is the power stated in Equation 4.2 (0.80543).

Calculations made using E4.3 are not comparable to the black carbon mass ratios judged by eye using the comparison sheet. The values are also not comparable to measurements by previous studies using the same technique. An extreme example of the discrepancy: The black carbon mass ratio judged by eye at Lappbreen, site 1 is 45 ng g^{-1}, the value of black carbon mass ratio calculated from the absorption spectrum of the filter is 11845 ng g^{-1}. There are three possible reasons for this discrepancy: human error, the diffusing environment inside the ISSS is not diffuse enough, and the black carbon was more absorptive than expected. As the comparison sheet values correlate with values measured by previous studies it seems unlikely that the black carbon is absorbing light in an

unaccounted manner, i.e. light is being absorbed as expected. As the sample filters have now degraded too much to repeat the measurements, future investigations need to conduct a series of measurements using the ISSS to establish the problem.

4.7.4 Previous Studies

Doherty *et al.* (2010) conducted a similar study to the work presented here across larger regions of the Arctic. In March-April 2007 and April 2009 Doherty *et al* (2010) sampled snow around Ny-Alesund, Svalbard (78.9° N, 11.9° E), a region further north than Oscar II land. The samples were taken on tundra and glaciers and an equivalent black carbon value was calculated as 18 ± 12 ng g^{-1} with a 15 % variability on black carbon values measured for Svalbard calculated (Doherty *et al.,* 2010). The range of values, in this chapter, determined using the comparison sheet for Svalbard is 11–114 ng g^{-1} with a mean value of 45 ng g^{-1}. The average value of black carbon mass ratio measured here is larger than the values measured by Doherty *et al.* (2010) but many black carbon mass ratio fall within error of the Doherty *et al*. (2010) equivalent black carbon value. None of the snow sampled by Doherty *et al.* (2010) had experienced melt as the sampling was undertaken in spring time and snow from Svalbard indicated a larger role of fossil-fuel aerosol than other sites measured in the study. Flanner *et al.* (2007) and Hansen *et al*. (2005) hypothesize that melting concentrates black carbon at the snow surface thus the value measured in Svalbard for this chapter would be expected to be larger than those measured by Doherty *et al*. (2010).

4.7.5 Data Quality

The work presented in this chapter was outreach and also research.

4.7.5.1 Field Data Quality

Several influences on the quality of the data taken in the field are listed below:

1. Owing to the outreach element of the work, the samples were not always taken or filtered by the same person and therefore with varying skill and ability, variations in method procedure were introduced.
2. The sampling was undertaking within a challenging expedition environment with limited weight restrictions on equipment as it all had to be carried in backpacks along with personal kit, plus with no transportation only sites that were accessible by foot could be sampled. No electrical sources or batteries were accessible.
3. In the cold Arctic climate the snow took a while to melt thus, in conjunction with the weight restrictions, only one transect could be undertaken per day. To increase the number of transects per day and introduce a non-carbon production melting method, a larger amount of sample pots would have been needed therefore adding to the overall equipment weight.
4. Red algae is abundant throughout glacial snow in the summer. The sampling process was biased by making efforts to gather snow samples away from icy areas, areas containing red algae and only including absorbing filters.

4.7.5.2 Laboratory Data Quality

Several factors influencing laboratory data quality are listed below:

1. The sample is unevenly distributed on the Nuclepore filter so to minimise the bias when measuring the absorption using the integrating sandwich sphere, each sample filter was measured 10 times then a mean absorption was calculated.
2. When using the integrating sandwich sphere, instrumental noise and instability, i.e. the temperature, conditions and time of measurement, can affect the absorption value as demonstrated in Figure 4.20.
3. Figures 4.13 and 4.14 show the absorption spectra of the calibration filters. It can be seen that solution 1 gives a large absorption i.e. the absorption is greater than 1, therefore this filter should be used with caution as Beer-Lambert may not be reliable (Grenfell *et al.*, 2011)

4.8 Conclusions

- Non-black carbon impurities in the snowpack have a large absorption cross-section at the short solar wavelength, responsible for photolytic reactions in the snowpack, therefore it is important to accurately account for the spectrally resolved absorption by both black carbon and non-black carbon impurities in the snowpack.
- Spatial features create a large variation in black carbon concentrations and therefore only local black carbon concentrations can be determined using this technique.
- Black carbon concentrations are affected by slope angle, aspects of the sampling locations, presence of melt water and snow type.

- The proximity of black carbon sources are likely to increase in the future thus giving rise to the increasing concentration of black carbon in snow.

Chapter 5

Assessment of Bi-Directional Reflectivity Distribution Function Measurements in Cold Climates

5.1 Introduction

Snow has the highest albedo of any naturally occurring and spatially extensive surface on Earth therefore more solar radiation is reflected from snow-covered areas than any other surface (Dumont *et al.*, 2010; Painter *et al.,* 1998). The albedo of snow has a significant influence on the radiation budget of the Earth and the areal extent of snow cover may be an indicator of climate change. Thus, measurements of the surface reflectivity are needed to accurately calculate the radiation budget of areas covered in permanent or seasonal snow (Budyko, 1969; Cubasch and Cess, 1990; Gleick, 1987, Jin *et al.,* 2008). For climate modelling, an accurate assessment of reflected solar radiation over snow and ice covered ocean is needed as the solar energy partitioning between the atmosphere and the ocean is critical (Curry, 1995; Ledley, 1991; Walsh, 1993). Albedo of snow is governed by several factors such as solar zenith angle, size of the snow grains, liquid water content and impurities within the snowpack (e.g. Aoki and Tanaka, 2008; Aoki *et al.,* 1999; 2000; 2006; 2007; Flanner *et al.,* 2007; Grenfell *et al.,* 1994; Motoyoshi *et al.*, 2005; Tanikawa *et al.*, 2006; 2009; Warren and Wiscombe, 1980; Wiscombe and Warren, 1980). The spectral signature of the reflectance of clean snow is characterised by moderate reflectance in the near-

infrared and almost 100% reflectance at visible wavelengths whereas ice is moderately absorptive in the near-infrared and highly transparent in the visible wavelengths (Painter *et al.,* 2004). The IPCC report (2007) highlighted surface albedo as a radiative forcing term affected by land use and black carbon in snow. Hansen and Nazarenko (2004) suggest that radiative forcing could be as high as +0.3 W m^{-2} for the Arctic. With climatic change, the albedo of the polar oceans (both Arctic and Antarctic) may change due to a change in the position of the ice margin, the ice concentration within the pack, the mixture of ice types or a change in snow cover, depth and wetness (Brandt *et al.*, 2005).

Recent evidence has shown that snowpack is highly photochemically active as reactive trace gases from photolysed snowpack impurities are released into the boundary layer of the overlying atmosphere (Fuhrer *et al.,* 1996; Grannas *et al.,* 2007; Honrath *et al.,* 1999; Sumner and Shepson, 1999). Emissions from snow influence the concentration of chemicals within the atmosphere and have been shown to be fundamental in driving local and regional boundary layer chemistry (e.g. Beine *et al.,* 2002b; Fuhrer *et al.*, 1996; Grannas *et al.*, 2007; Honrath *et al.,* 1999; Jacobi *et al.*, 2004a; Low *et al.*, 1990; Mulvaney *et al.*, 1998; Neftel *et al.*, 1985; Sumner and Shepson, 1999; Thomas, 2012). Post-depositional photochemical processes need to be considered in the interpretation of ice cores as a proxy for past atmospheric chemical concentrations (Grannas *et al.,* 2004; Wolff, 1995). Any process that influence the concentration of active chemicals in the atmosphere have important implications for regional tropospheric chemistry and can lead to sea-ice loss through warming effects (Hansen *et al.,* 2005; Jones *et al.,* 2000). Antarctica is remote from major pollution sources in comparison to

the Arctic and therefore photochemical emissions from snow may be more influential (Jones *et al.,* 2000).

To study the influence of snow cover changes on climate, a better understanding of albedo and its behaviour with solar zenith angle, wavelength and snow physical properties is needed (Xie *et al.,* 2006). Taking into account the high spatial and temporal variability of albedo, remote sensing is used to measure the reflectivity of the snow surface yet remote sensing sensors measure the bi-conical reflectance not albedo (Dumont *et al.,* 2010). To calculate the spectral albedo from bi-conical reflectance, the angular distribution of the reflected radiation on snow must be known (Dumont *et al.,* 2010; Li *et al.,* 2007; Warren *et al.,* 1998). If both the solid angles of light and view are infinitesimal, the bi-conical reflectance is called the bidirectional reflectance and the angular distribution over the upper hemisphere is known as the bi-directional reflectivity distribution function (BRDF) (Nicodemus *et al.,* 1977). Nicodemus (1965) first used the term BRDF to describe the intrinsic reflectance properties of a surface, properties that cannot be measured directly, it is a theoretical concept that describes directional reflectance by relating the contribution of the incident irradiance from a given direction to the reflected radiance in another specific direction (Nicodemus *et al.,* 1977; Schaepman-Strub *et al.,* 2006).

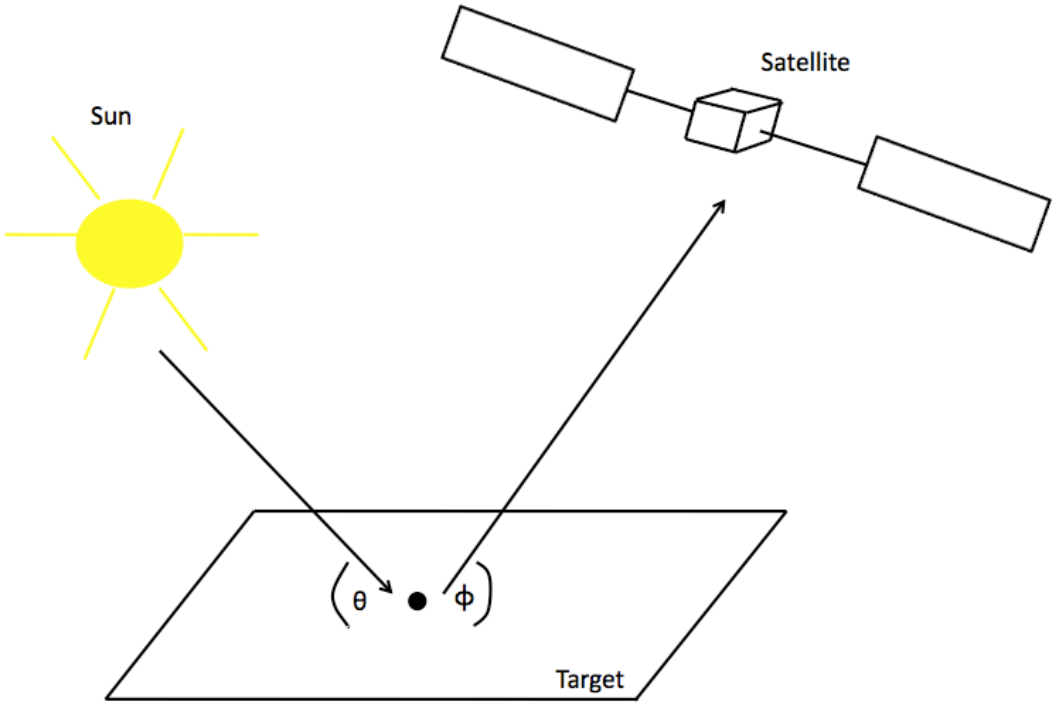

Figure 5.1. Using satellites to detect the reflectivity of snow.

A diagrammatic representation of the relationship between the angle of incidence and the angle of reflectance is shown in Figure 5.1. Reflectivity is dependent on wavelength (λ), the intensity of reflected radiation is a function of both the incident direction (θ_i, ϕ_i) and the reflected direction (θ_r, ϕ_r). There are two types of reflection (Figure 5.2), (1) specular reflection, where the direction of the reflected radiation is determined uniquely by the incident angle, and (2) Lambertian reflection, where the direction of reflected radiation is uniform and therefore completely independent of the incident direction (Petty, 2006). Specular reflection (Figure 5.1) is measured by satellites and can be used to calculate BRDF.

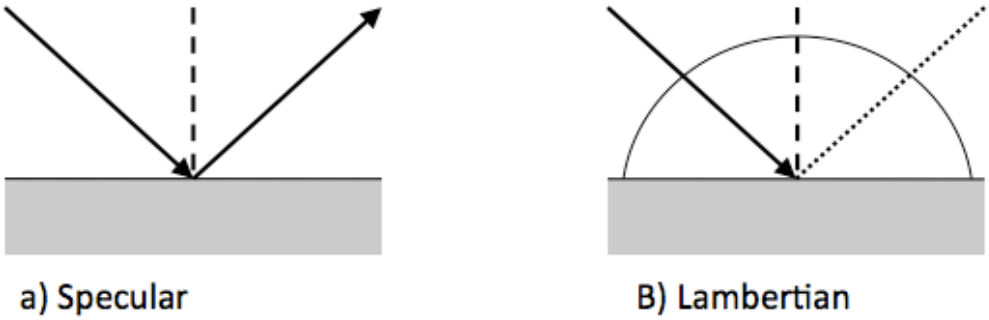

Figure 5.2. Reflectance of light with a) specular reflection and b) Lambertian reflection.

Natural surface targets are usually illuminated by the whole hemisphere of the sky so receive scattered light from the sky in addition to a direct solar flux therefore the measurements presented in this chapter represent hemispherical-conical reflectance function (HCRF) not bi-directional reflectivity distribution function (BRDF) (Figure 5.1).

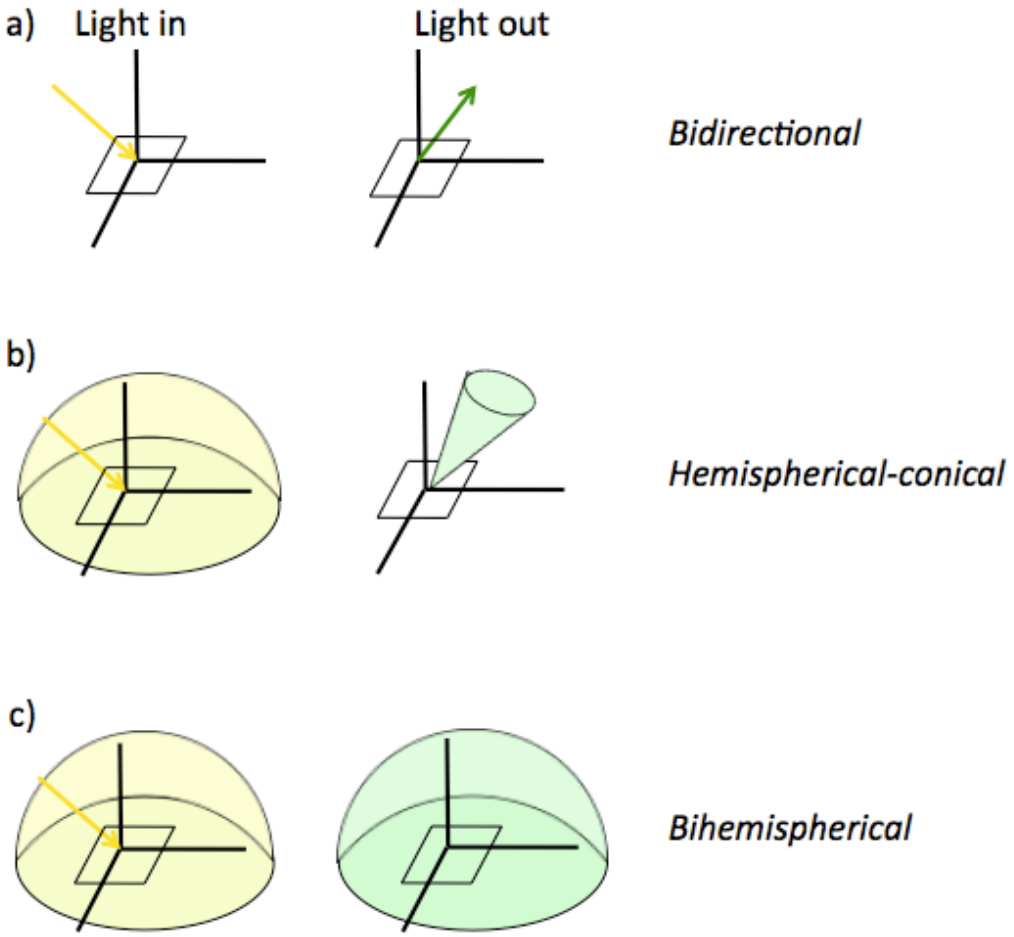

Figure 5.3. Terminology used to described reflectance quantities (adapted from Shaepman-Strub *et al.* (2006), Table 2).

Figure 5.3 shows diagrammatic representations for three reflectance terminologies associated with the measurements described in this chapter. To briefly explain Figure 5.3: Figure 5.3a is a visual representation of the bi-directional reflectivity distribution function (BRDF). A single incident flux enters the measurement area and is reflected as a single reflected flux. Figure 5.3b is a visual representation of the hemispherical-conical reflectance factor. The incident flux is a combination of the whole hemisphere, i.e. light from the sun and sky light, and the reflected flux is measured using a sensor with a specific field of view. The measurements

presented in this chapter were taken using one single fibre optic sensor at a time and therefore the data is representative of HCRF. In remote sensing, HCRF is the most common field spectral measurement, however it is often encompassed under the term BRDF. Figure 5.3c is a visual representation of the bi-hemispherical reflectance factor. The incidence flux is a combination of whole hemisphere (sun and sky) and the reflected flux is also a total hemisphere. The reflected flux is expressed as a proportion of the incident flux on the measurement surface from the whole hemisphere.

Reflectance measurements taken under hemispherical conditions, i.e. all outdoor measurements, depend on several factors including the scattering properties of the observed surface, the surroundings and the topography in expression with different wavelengths (Schaepman-Strub *et al.*, 2006). Several investigations have studied hemispherical-directional reflectance of smooth snow on a macro-scale using the understanding of snow structure and dependencies (Aoki *et al.,* 2000; Dozier *et al.,* 1988; Kuhn, 1985; Leroux *et al.,* 1998; O'Brien and Munis, 1975; Steffen, 1987), the effect of macro-scale roughness on the directional reflectance of snow using modelling and field measurements (Leroux and Fily, 1998; Warren *et al.,* 1998) and the effect of morphology on the single-scattering phase function and multiple scattering measurement values (Leroux *et al.,* 1998; Liou, 1980; Mischenko *et al.,* 1999). Schaepman-Strub *et al.* (2006) highlight that natural incidence is composed of 3 components: non-scattering radiation (a direct component), a diffuse component scattered by the atmosphere e.g. clouds and aerosols, and the surroundings of the observed surface, with atmospheric conditions, topography and the reflectance properties of the topography

influencing the magnitude and spectral distribution of the diffuse irradiance. Reflectance factors can be greater than the value of 1, particularly for strong forward reflecting surfaces such as snow (Painter and Dozier, 2004). The reflectance factor is the ratio of the radiant flux reflected by a surface to the radiant flux reflected by an ideal and diffuse (Lambertian) standard surface, e.g. a spectralon panel, into the same reflected-beam geometry and wavelength range under the same conditions (Schaepman-Strub *et al.,* 2006). All ground surfaces have different properties, i.e. surface type, grain size, surface features, which control the amount of light reflected (or absorbed) at different wavelengths. Satellites are used to measure the reflectance of various surfaces and provide an understanding of the reflectivity properties, however the satellite sensor data needs to be validated. Field goniometers such as GRASS allow ground BRDF data to be acquired under natural illumination conditions that can be used as a ground reference for remote sensing applications and BRDF models (Sandmeier, 2000).

Using satellites to produce multiangular remote sensing data means that it is increasingly important to use ground bidirectional reflectance data as a tool to (1) calibrate satellite measurements with ground measurements, (2) validate current and develop new, more accurate BRDF models, (3) investigate the physical mechanisms of BRDF effects, (4) study the relationship between BRDF effects and biogeophysical parameters, (5) compare with BRDF measurements made using satellites (Sandmeier, 2000), and (6) developed spectral libraries (Clarke *et al.*, 2002)

5.2 Aims

- Record the BRDF of sea-ice and surface snow in and around Tethys Bay, Antarctica.
- Prove that the GRASS system is capable of undertaking measurements in polar environments.
- Assess GRASS as a cold polar field instrument.

5.3 Study Area

The Italian research base, Mario Zucchelli station (also known as Terra Nova Bay), is located at 74° 41' 42'' S, 164° 7' 23'' E on the western side of the Ross Sea (Figure 5.4). Tethys Bay is a small cove located close to the Mario Zucchelli station (Figure 5.5).

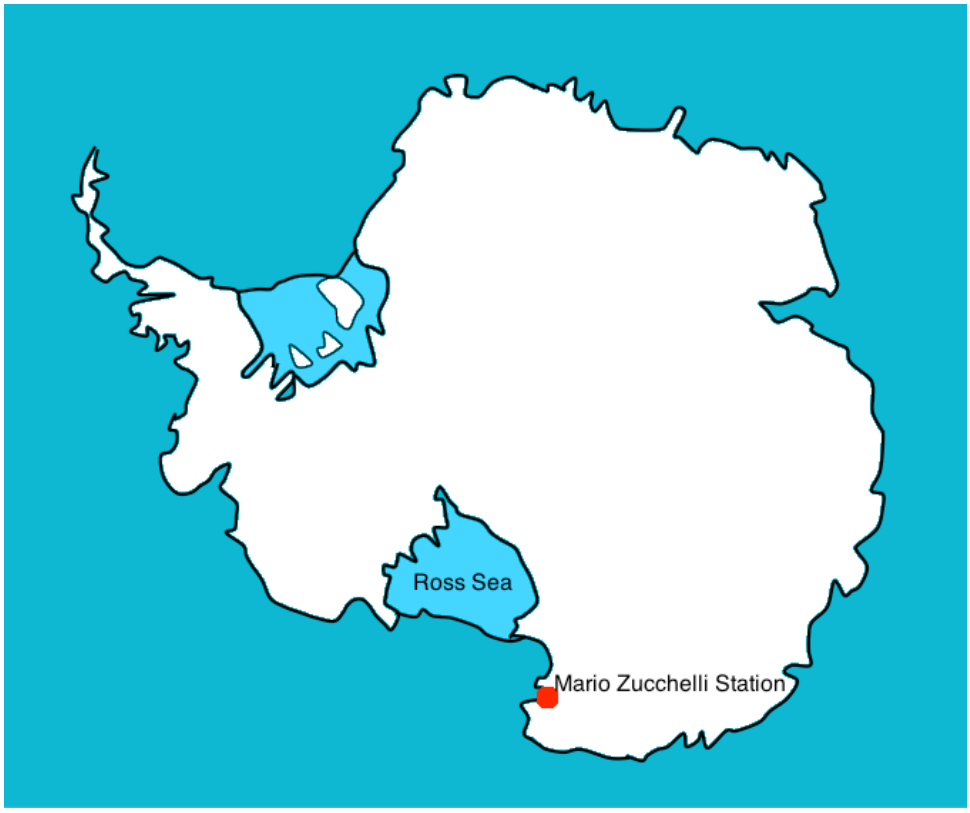

Figure 5.4. Map showing location of Mario Zucchelli Station in Antarctica.

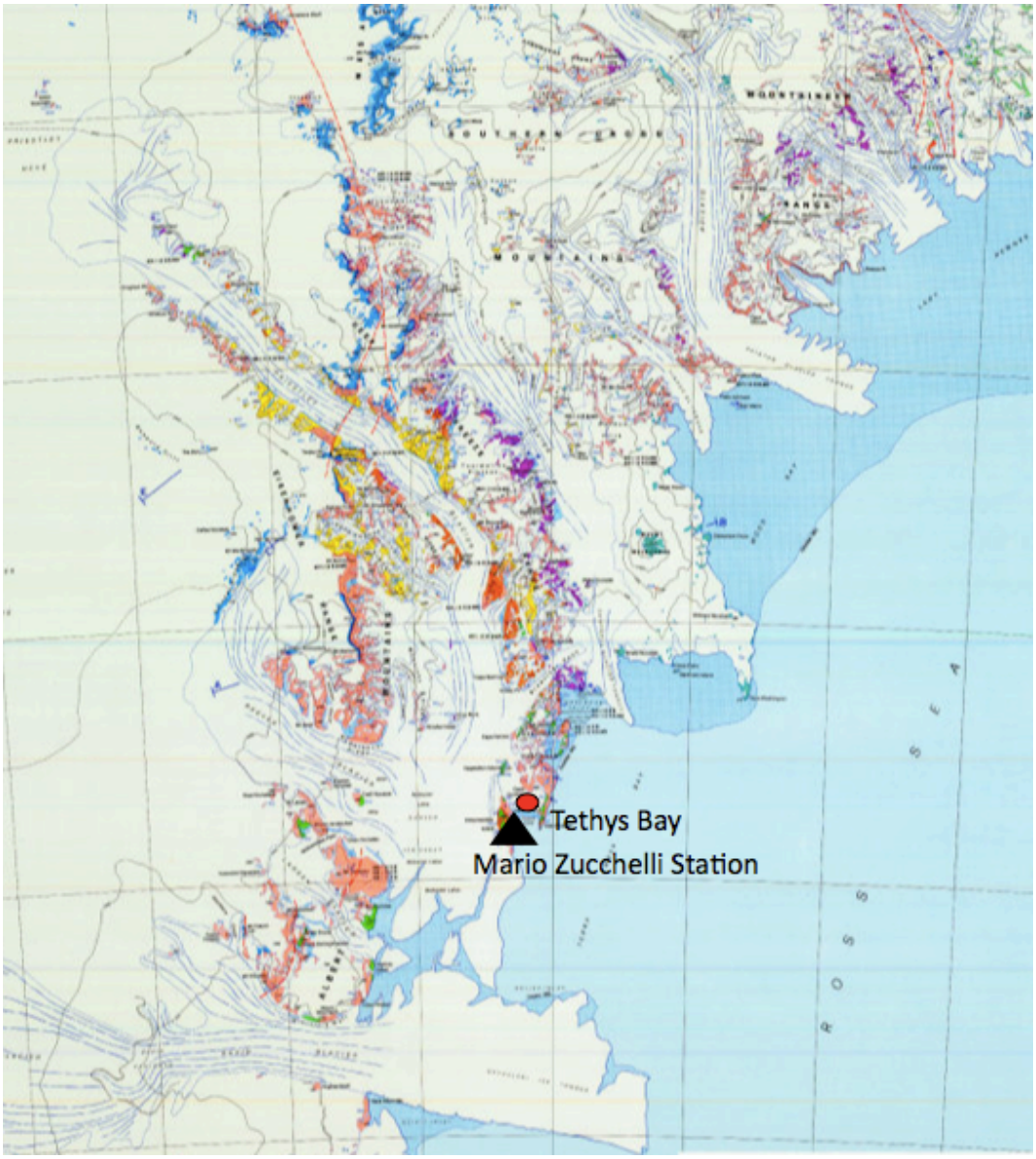

Figure 5.5. Map showing location of Tethys Bay and the Mario Zucchelli Station in Victoria Land, Antarctica.

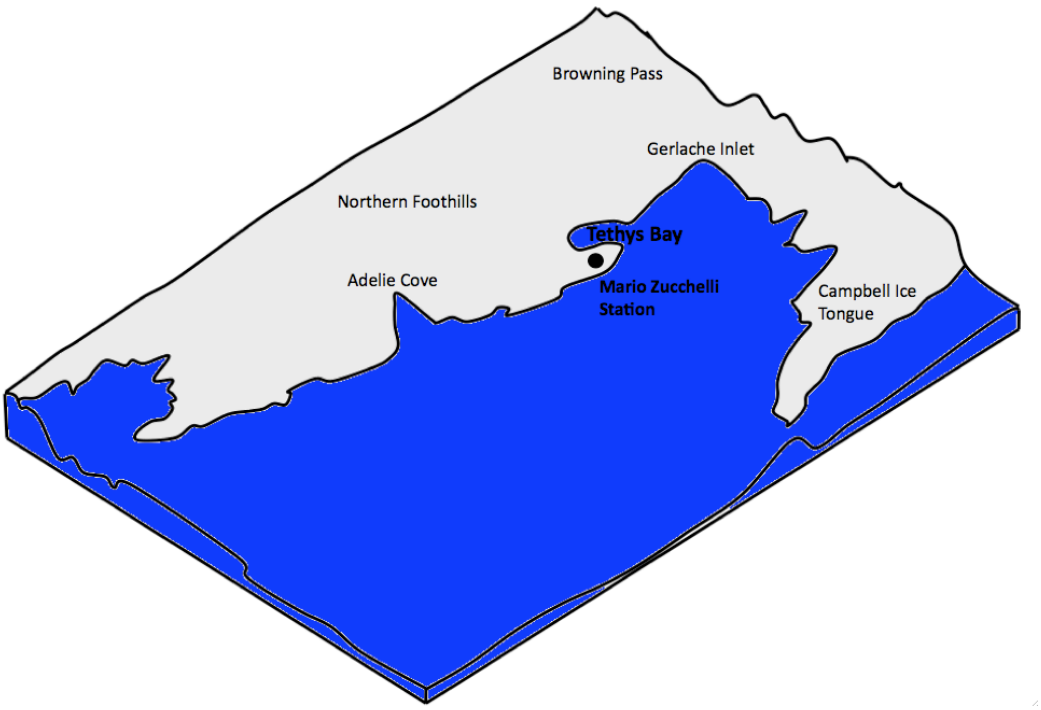

Figure 5.6. A diagram showing the location of Tethys Bay in relation to the Mario Zucchelli Station (adapted from Turner and Pendlebury (2004), Figure 7.12.2.1.1). Note, sea-ice normally covers Tethys Bay, yet the sea-ice is free of snow cover.

Two ice tongues (Campbell and Dryglowski) protect Tethys Bay from sea swell and the Northern Foothills located to the west shield the bay against katabatic winds (Figure 5.6).

5.4 Gonio Radiometric Spectrometer System (GRASS)

A Gonio Radiometric Spectrometer System (GRASS) was used to measure the hemispherical-conical reflectance factor (HCRF) of Tethys Bay sea-ice (Figure 5.7). GRASS was a new instrument that needed to be tested before being taken on a measurement campaign to Dome C, Antarctica, as it had only been used once previously in a Turkish salt flat (i.e. hot and dry environment).

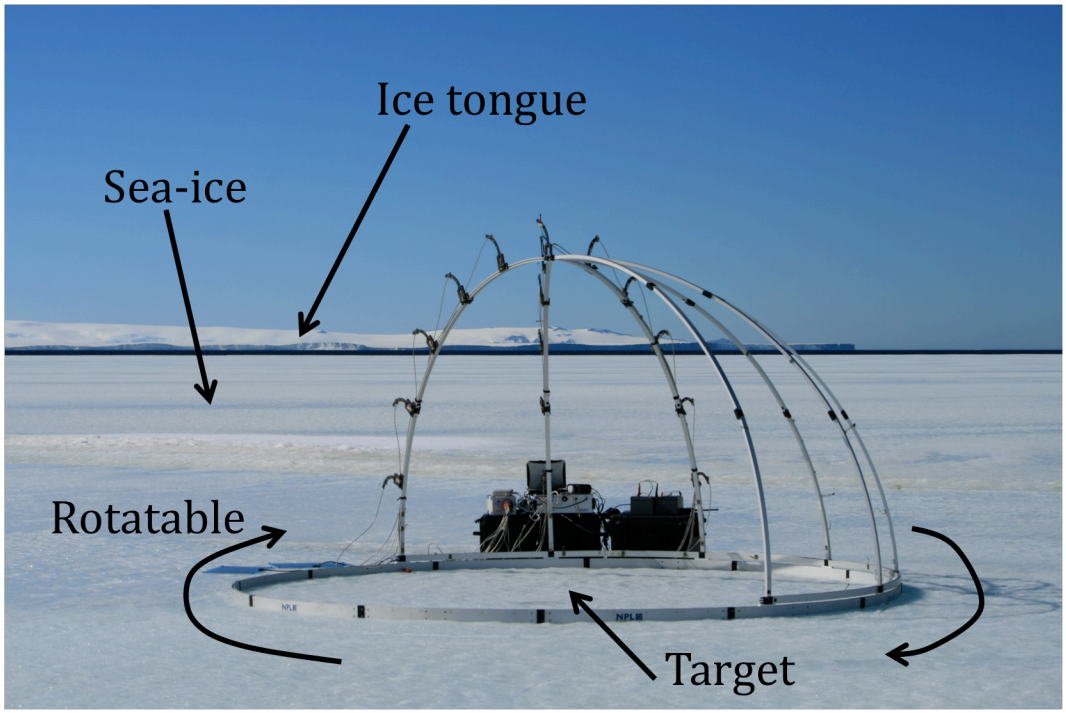

Figure 5.7. The Gonio Radiometric Spectrometer System (GRASS) at Tethys Bay.

The GRASS system is a hemisphere comprised of 7 arms. On a quarter of the hemisphere (arms 1 – 3), 5 fibre optics with 4° field of view lenses were placed on each arm at zenith angles of 15°, 30°, 45°, 60° and 75°. Two fibre optics were placed at the nadir, one with a 4° field of view lens to measure upwelling radiance and the other with a cosine diffuser to measure downwelling irradiance. The optical fibres are Vis-NIR low OH content with a fibre diameter of 400 μm and work most efficiently in the wavelengths of 400-2100 nm. All fibre optics were connected through a multiplexer and a VSWIR to a Panasonic toughbook. The VSWIR system is a dual field of view portable spectroradiometer covering the spectral range of 400-1700 nm. The two spectrometers inside the VSWIR, visible and short-wave infra-red, joined at ~900 nm. The fibre optic sensors on arms 1-3 and the upwelling radiance fibre optic sensor at nadir were attached to the multiplexer via 16 individual fibre ports (Figure 5.8). A fibre optic inside the

multiplexer rotated to align with each individual fibre port thus allowing measurement to be taken in turn for each fibre optic sensor. The upwelling radiance (via the multiplexer) and the downwelling radiance (the fibre optic sensor placed at nadir) were connected to fibre inputs on the VSWIR and a pair of spectra for an individual fibre optic sensor could be acquired within 30 seconds.

Figure 5.8. Close up of fibre optics attached to multiplexer.

5.5 Field Measurement Method

5.5.1 Setting up GRASS

Figure 5.9 describes the individual component of the Gonio Radiometric Spectrometer System (GRASS) in the final assemblage position.

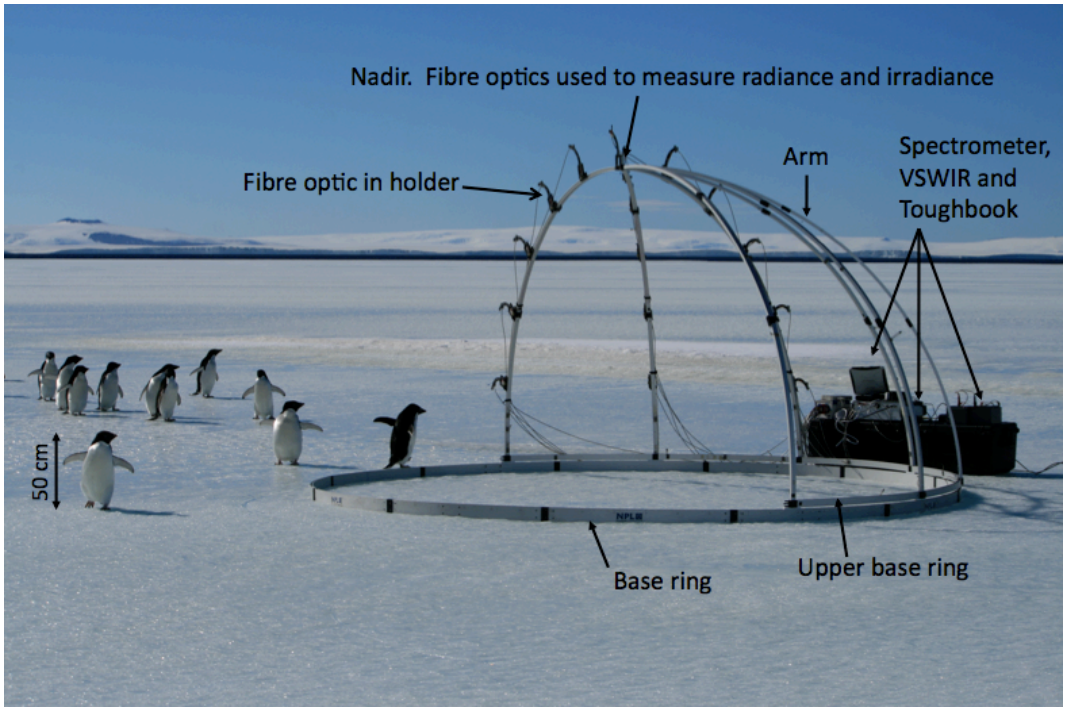

Figure 5.9. Individual components of GRASS.

GRASS is modular for transportation and has a mass of ~40 kg. GRASS was set up by firstly connecting the base ring together (Figure 5.10) and the 7 arms were inserted into the upper base ring at fixed positions, 22.5° apart at the base. Attached to arms 1-3 were 5 fibre optics arranged at zenith angle positions of 15°, 30°, 45°, 60° and 75° and two fibre optics were also attached at the nadir to measure radiance and irradiance (Figures 5.10 and 5.11).

Figure 5.10. Setting up the base ring of GRASS. The structure of GRASS was assembled then moved to a fresh snow surface before measurements were taken.

Figure 5.11. Setting up the fibre optics on the arms of GRASS.

Figure 5.12. Close up of fibre optic arrangement along arms of GRASS.

All fibre optics were connected through a multiplexer and a VSWIR to a Panasonic toughbook computer thus allowing measurements for the hemisphere of GRASS (Figure 5.12).

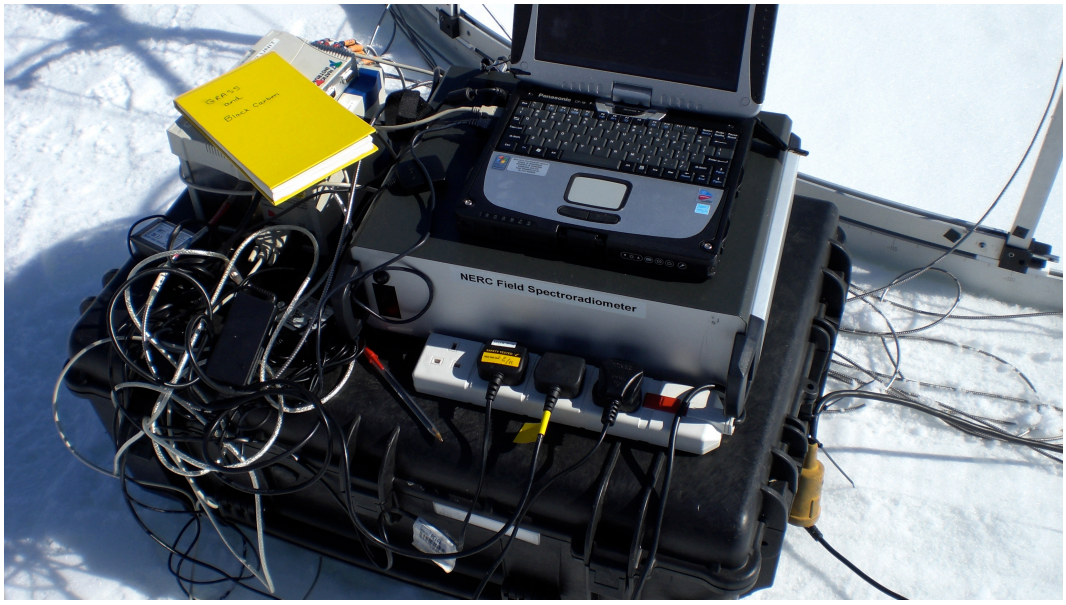

Figure 5.13. Computer equipment needed to measure reflectivity using GRASS. The Panasonic Toughbook is sitting on top of the VSWIR. Powered by a portable generator, not seen in photograph.

5.5.2 Using GRASS to measure reflectivity

Measurements were taken in a fixed pattern: Firstly a measurement at nadir was taken followed by the fibre at 15° on arm 1, the fibre at 30° on arm 1, the fibre at 45° on arm 1, the fibre at 60° on arm 1 and the fibre at 75° on arm 1. Another measurement at nadir was taken and the pattern was repeated for both arms 2 and 3.

Once a measurement of the quarter of a hemisphere had been taken, the arms were rotated 90° and the process was repeated until the whole sphere had been measured. Spectral measurements over a range of wavelengths were acquired as digital numbers using GRASS then used to calculate the HCRF of a target. The measurement points lie on the surface of a hemisphere i.e. each measurement point is defined by a zenith angle between 0° and 90° and an azimuth angle

between 0° and 360°. Each separate file measured using GRASS contained the spectral measurements for a single point. Reflectance calculations required two sets of measurements: one set using the target and one set using a calibrated reference panel. A spectralon reference panel was placed in the centre of GRASS beneath the nadir and the measurement sequence was repeated at the same angles previously used for the target measurements (Figure 5.14).

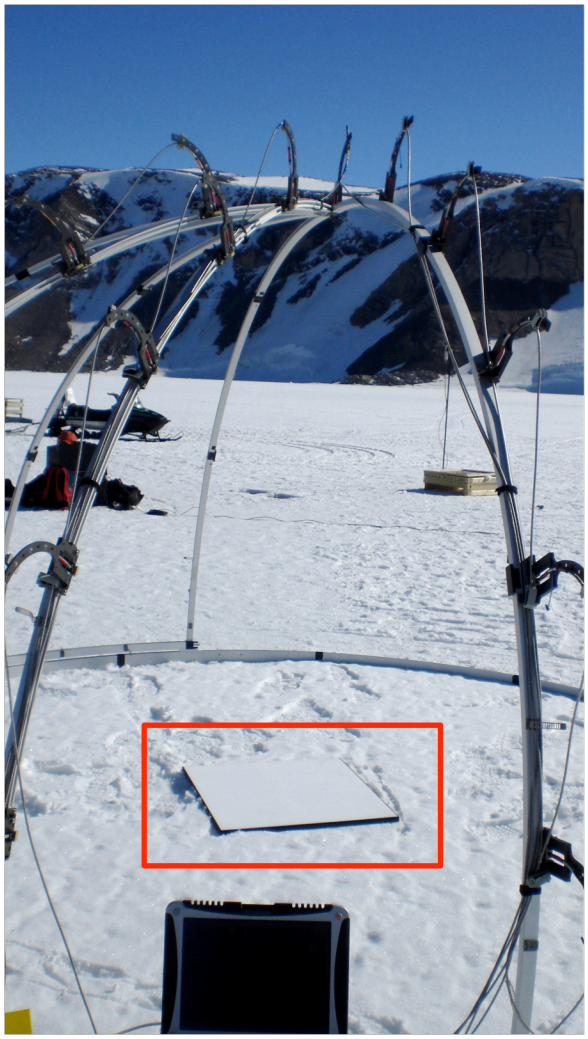

Figure 5.14. An example of the spectralon reference panel position used with GRASS. Red highlights position of reference panel on snow.

The 'MADAT' software processed the multi-angular measurement data acquired by GRASS and allowed it to be presented in a visual manner. The reflectance at

each wavelength was calculated from the measurement data and the locations at which the data was gathered for both the target and the reference panel, using equation (5.1).

$$R_t(\theta_i,\varphi_i;\theta_r,\varphi_r) = \frac{f_t(\theta_i,\varphi_i;\theta_r,\varphi_r)}{f_p(\theta_i,\varphi_i;\theta_r,\varphi_r)} R_p(\theta_i,\varphi_i;\theta_r,\varphi_r) \qquad \text{(E5.1)}$$

where $f_t(\theta_i,\varphi_i;\theta_r,\varphi_r)$ is the measured digital number of the target surface at the point (θ_r,φ_r), $f_p(\theta_i,\varphi_i;\theta_r,\varphi_r)$ is the measured digital number of the reference panel at the point (θ_r,φ_r), and $R_p(\theta_i,\varphi_i;\theta_r,\varphi_r)$ is the calibrated reflectance of the reference panel (calibrated previous to campaign by NPL).

Linear interpolation techniques generated approximate reflectance values at 1° intervals in the azimuth and zenith directions. The resulting surface was then 'visualised' using 2- or 3-dimensions, measured values could be reflected to form a symmetric 2d plot.

Figure 5.15 is an example of four quarter measurements taken for each sector of a site.

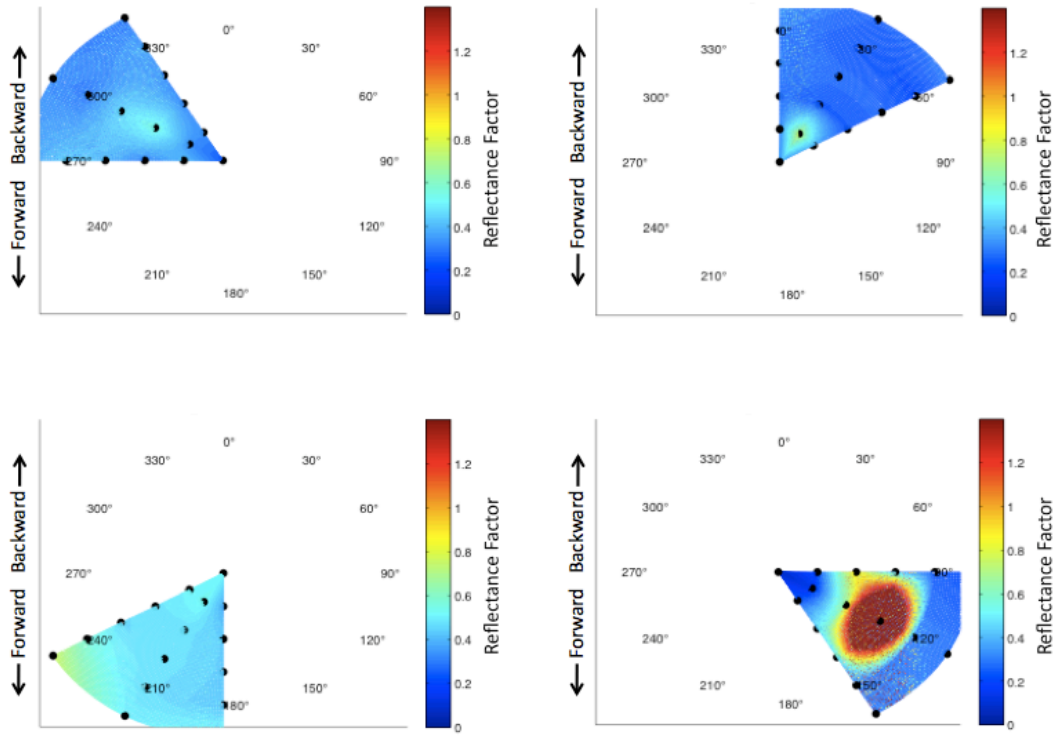

Figure 5.15. Four quarter HCRF measurements made at Tethys Bay at a wavelength of 400 nm. The radial distance represents the field of view zenith angle, the rotation about the centres is the field of view azimuth angle and the HCRF value is shown by the intensity (indicated on the colour scale). Any forward scattering of light is shown in a downward direction and any back scattering of light is shown in an upwards direction.

5.6 Field Measurements in Tethys Bay

5.6.1 Day 1

The first day of measurements taken at Tethys Bay using GRASS occurred on the 11th December 2010. The location for the measurements was 74° 41.3306 S, 164° 03.1543 E, the temperatures was -2.4 °C and sky conditions consisted of no cloud but high wind. The sea-ice was > 1 m thick and the measurements surface was bare sea-ice with a melting surface (Figure 5.16).

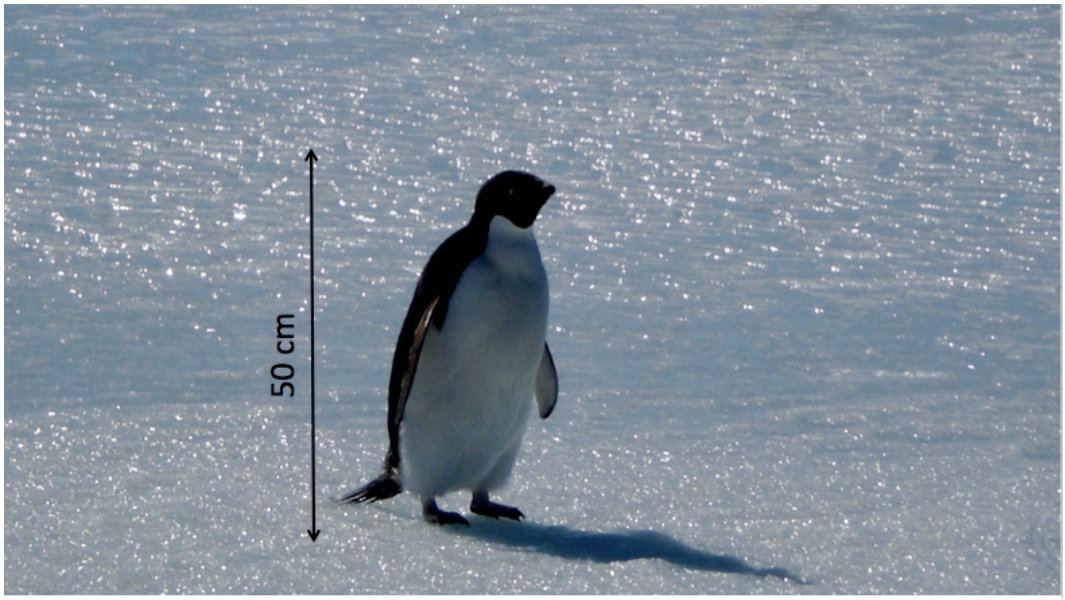

Figure 5.16. Close up of bare sea-ice surface measured using GRASS. Penguin is useful to approximate scale of surface features.

Figure 5.17 and 5.18 show reflected contour plots for site 1 of day 1 at two representative wavelengths, 500 nm and 1100 nm respectively. The radial distance of Figures 5.17 and 5.18 represents the field of view zenith angle, the rotation about the centres is the field of view azimuth angle and the HCRF value is shown by the intensity (indicated on the colour scale). Any forward scattering of light is shown in a downward direction, on Figures 5.17 and 5.18, and any back scattering of light is shown in an upwards direction.

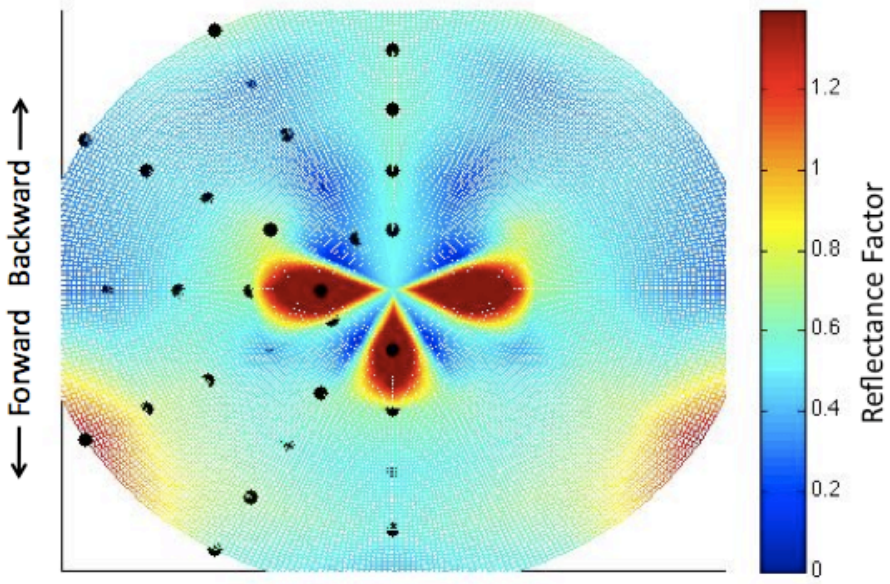

Figure 5.17. Reflected contour plots presenting the intensity of reflectivity at 500 nm. Reflectivity measurements taken on 11th December 2010 at Tethys Bay. The HCRF value is the intensity (indicated by the colour scale). The solar zenith angle at which the measurements were taken was 52°. Data is averaged to produce symmetrical plot.

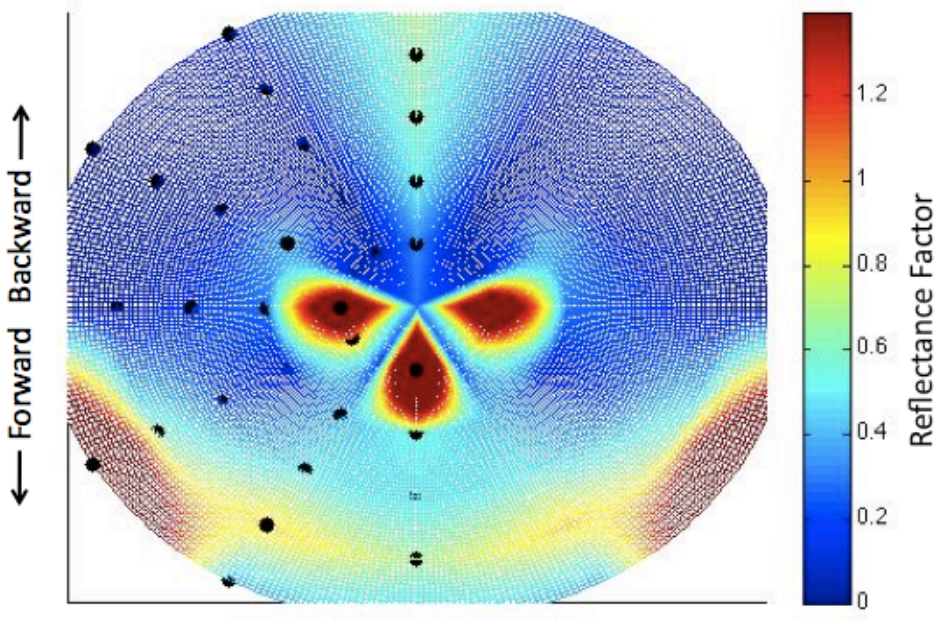

Figure 5.18. Reflected contour plots presenting the intensity of reflectivity at 1100 nm. Reflectivity measurements taken on 11th December 2010 at Tethys Bay. The HCRF value is the intensity (indicated by the colour scale). The solar zenith angle at which the measurements were taken was 52°. Data is averaged to produce symmetrical plot.

A complete set of contour plots for the wavelength range of 400–1500 nm for day 1 can be found in Appendix 5, section A5.2.2.

5.6.2 Day 2

The second day of measurements taken at Tethys Bay using GRASS occurred on the 20th December 2010. The location for the measurements was 74° 41.3306 S, 164° 03.1543 E, the temperatures was -2.46 °C and sky conditions consisted of no cloud and no wind. The sea-ice was > 1 m think and the measurement surface was sea-ice covered in a faceted snow crystal layer 1-2 cm thick (Figure 5.19).

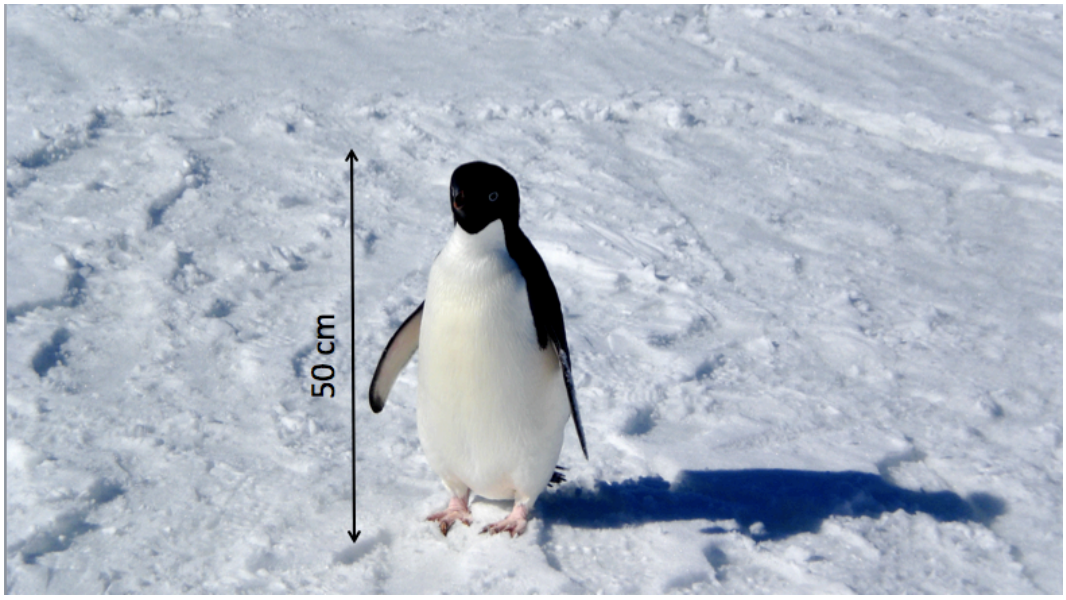

Figure 5.19. Close up of the sea-ice surface covered in a 1-2 cm layer of faceted snow crystals measured using GRASS. Penguin is useful to approximate scale of surface features.

Figure 5.20 and 5.21 show contour plots comprised of the 4 GRASS rotations for site 1 of day 2 at two representative wavelengths, 500 nm and 1100 nm respectively. The radial distance of Figures 5.20 and 5.21 represents the field of view zenith angle, the rotation about the centres is the field of view azimuth angle

and the HCRF value is shown by the intensity (indicated on the colour scale). Any forward scattering of light is shown in a downward direction, on Figures 5.20 and 5.21, and any back scattering of light is shown in an upwards direction.

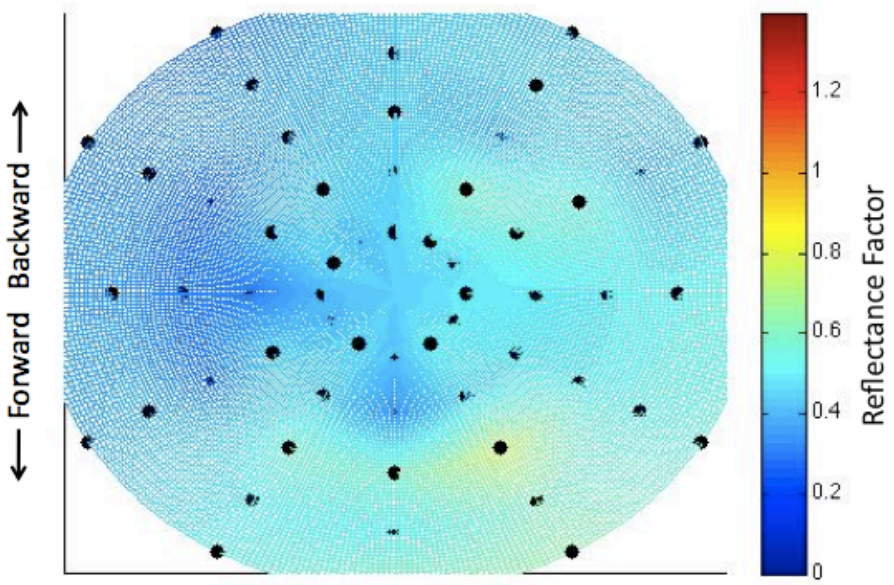

Figure 5.20. Rotated contour plots presenting the intensity of reflectivity at 500 nm. Reflectivity measurements taken on 20th December 2010 at Tethys Bay. The HCRF value is the intensity (indicated by the colour scale). The solar zenith angle at which the measurements were taken was ~53°.

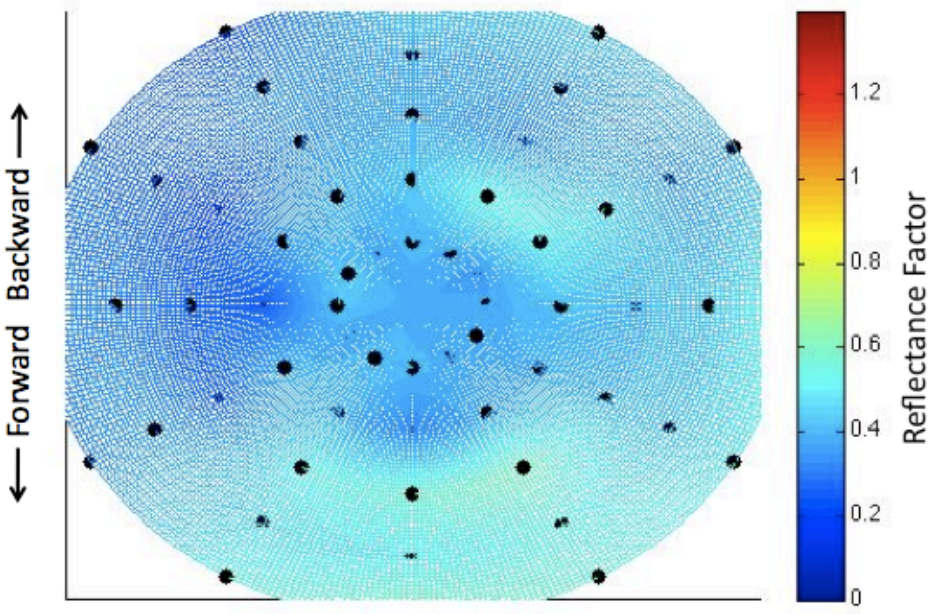

Figure 5.21. Rotated contour plots presenting the intensity of reflectivity at 1100 nm. Reflectivity measurements taken on 20th December 2010 at Tethys Bay. The HCRF value is the intensity (indicated by the colour scale). The solar zenith angle at which the measurements were taken was ~53°.

Figure 5.22 and 5.23 show reflected contour plots for site 2 of day 2 at two representative wavelengths, 500 nm and 1100 nm respectively. The radial distance of Figures 5.22 and 5.23 represents the field of view zenith angle, the rotation about the centres is the field of view azimuth angle and the HCRF value is shown by the intensity (indicated on the colour scale). Any forward scattering of light is shown in a downward direction, on Figures 5.22 and 5.23, and any back scattering of light is shown in an upwards direction.

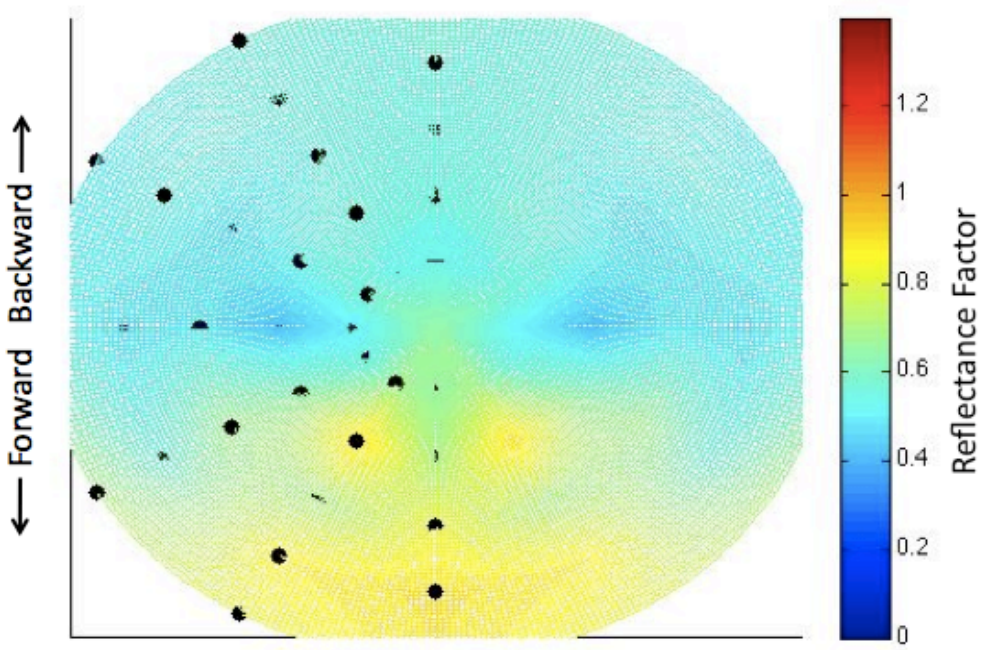

Figure 5.22. Reflected contour plots presenting the intensity of reflectivity at 500 nm. Reflectivity measurements taken on 20th December 2010 at Tethys Bay. The HCRF value is the intensity (indicated by the colour scale). The solar zenith angle at which the measurements were taken was 57°. Data is averaged to produce symmetrical plot.

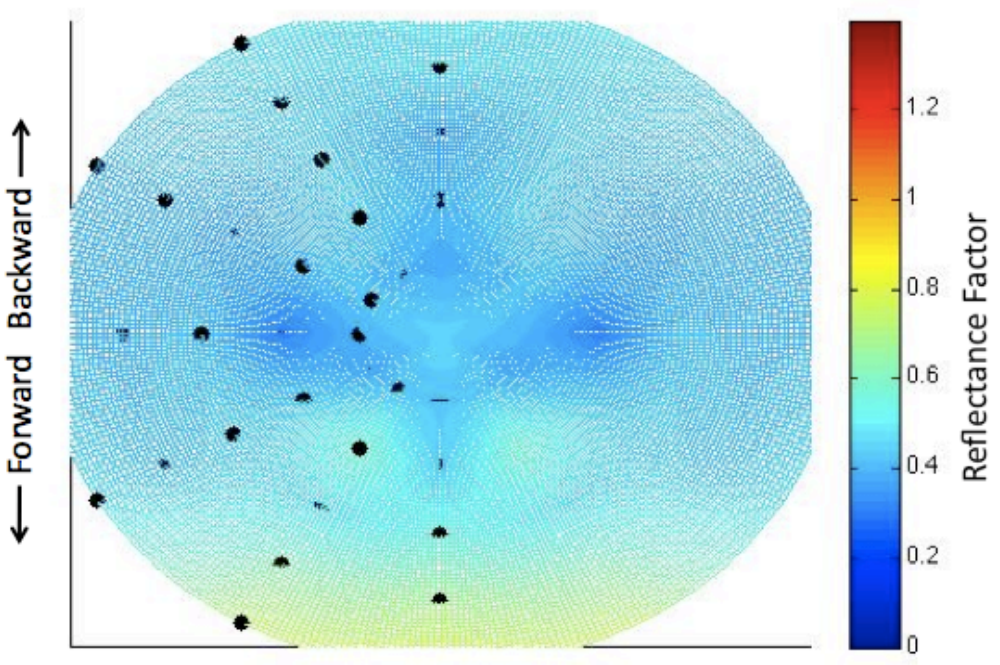

Figure 5.23. Reflected contour plots presenting the intensity of reflectivity at 1100 nm. Reflectivity measurements taken on 20th December 2010 at Tethys Bay. The HCRF value is the intensity (indicated by the colour scale). The solar zenith angle at which the measurements were taken was 57°. Data is averaged to produce symmetrical plot.

Figure 5.24 and 5.25 show contour plots comprised from the 4 GRASS rotations for site 2 of day 2 at two representative wavelengths, 500 nm and 1100 nm respectively. Figure 5.22 and 5.23 show the same data presented by a reflected contour plot. The radial distance of Figures 5.24 and 5.25 represents the field of view zenith angle, the rotation about the centres is the field of view azimuth angle and the HCRF value is shown by the intensity (indicated on the colour scale). Any forward scattering of light is shown in a downward direction, on Figures 5.24 and 5.25, and any back scattering of light is shown in an upwards direction.

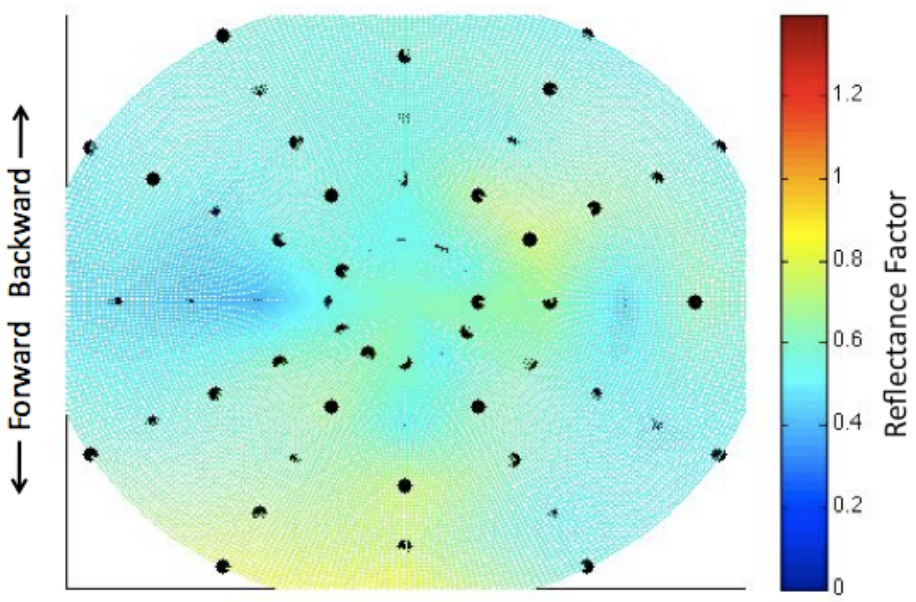

Figure 5.24. Rotated contour plots presenting the intensity of reflectivity at 500 nm. Reflectivity measurements taken on 20th December 2010 at Tethys Bay. The HCRF value is the intensity (indicated by the colour scale). The solar zenith angle at which the measurements were taken was 57°.

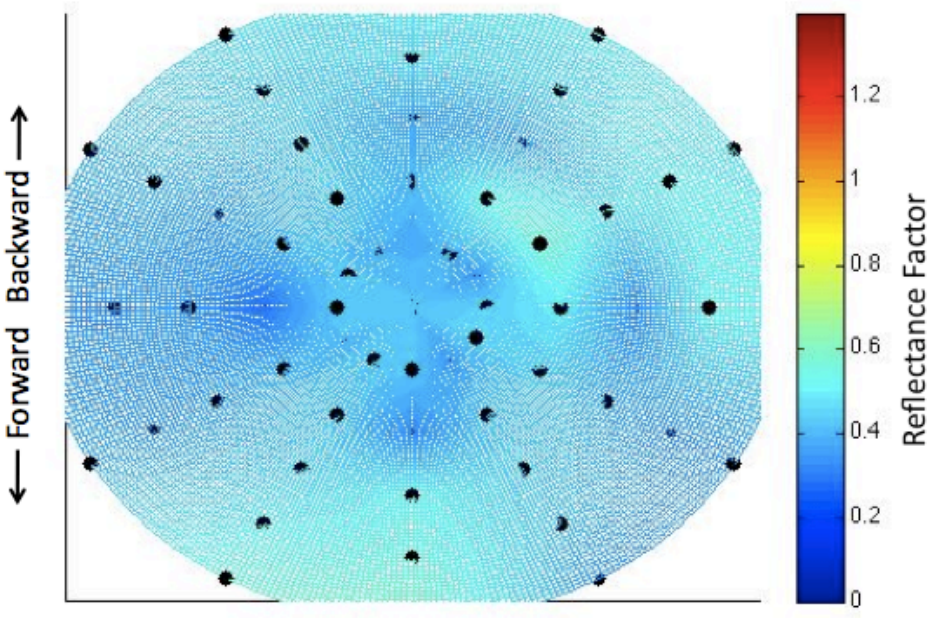

Figure 5.25. Rotated contour plots presenting the intensity of reflectivity at 1100 nm. Reflectivity measurements taken on 20th December 2010 at Tethys Bay. The HCRF value is the intensity (indicated by the colour scale). The solar zenith angle at which the measurements were taken was 57°.

A complete set of contour plots for the wavelength range of 400–1500 nm for day 1 can be found in Appendix 5, section A5.2.3.

5.7 Discussion

The discussion will be divided into 3 sections: (1) an evaluation of the advantages and disadvantages when using field measurement and satellite data retrieval techniques, (2) a comparison between the reflectance data measured using GRASS and previous studies calculating reflectance using field measurements and satellite data and (3) a detailed examination of the GRASS system to assess the ability to capture reflectance data in a polar environment, including suggested improvements to the system for future polar work.

5.7.1 Advantages and disadvantages of field and satellite measurements

Field measurements of HCRF (ground data measurements taken under natural illumination conditions) are used to calibrate and validate remote sensing instruments and climate models (Sandmeier, 2000; Schaepman-Strub *et al.*, 2006) thus reducing uncertainties, however, it is worth considering the advantages and disadvantages of both satellite and field measurement techniques.

Optical remote sensing equipment attached to satellites or aircraft typically has a narrow field of view and reflected radiance is measured rather than irradiance. To convert the reflected radiance observations to an estimate of irradiance, measurements of BRDF are needed (Perovich, 1996). Each pixel in a satellite

observation is limited to a certain angular direction therefore, due to the inherent anisotropy of snow reflectance, if the angular dependence of snow reflectance is ignored the albedo derived from the remote sensing data may have a large error (Jin and Simpson, 2000). Polar regions usually exhibit a large variety of ice types with varying thickness and snow cover resulting in a corresponding large variety in values of measured albedo (Brandt *et al.,* 2005). Satellite observations indicate large-scale, high spatial and temporal coverage of albedo that in-situ measurements cannot capture (Jin and Simpson, 2000).

There are many advantages and disadvantages of undertaking goniometer field experiments, as reviewed by Sandmeier (2000): Measurements can be taken in the natural environment of the target, under natural illumination conditions and can be replicated for parts of the target surface but may be affected by environmental factors, e.g. wind and varying atmospheric conditions. An identical illumination source, i.e. the sun, for both ground and remote sensing measurements increases the comparability of data, however, the illumination conditions constantly change with the movement of the sun causing the data collection period to be kept as short as possible which may compromise the angular sampling resolution.

Stroeve *et al.* (2001) compared ground-based albedo measurements taken in Greenland with remote sensing albedo data from the same area, a better agreement between the two sets of measurements was seen at sites where seasonal changes in surface conditions occurred producing a large range in albedo, compared to sites with constant surface albedo because the measurement

uncertainty at the sites exceeded the natural variability. To improve the consistency of albedo measurements, Stroeve *et al.* (2001) suggested that an improved angular model was used to convert the directional reflectance measurement to hemispherical albedo.

5.7.2 Comparison with previous studies

Antarctic sea-ice plays an important part in climate change (e.g. Holland and Bitz, 2003; Holland *et al.,* 2001; Rind *et al.,* 1995) and therefore knowledge of the albedo of Antarctic sea-ice is needed to create accurate climate simulations (Meehl and Washington, 1990; Rind *et al.,* 1997). Sea-ice has an intricate structure consisting of an ice matrix with inclusion of brine, air and salts (Perovich, 1996). The inclusions cause sea-ice to be a highly scattering medium as the differences between the index of refraction for the inclusions and for the surrounding ice creates strong scattering, however, at visible wavelengths, and when temperature increases, the scattering inclusion can be larger than the light wavelength thus allowing spectral variation to be determined by the absorption spectrum of the ice (Barber and Ngheim, 1999; Grenfell, 1983; Perovich, 1996). For the measurements taken on day 1 using GRASS, bare sea-ice was measured and the contour plots (Figure 5.17 and 5.18) show high values of HCRF indicating a large amount of scattering. For the measurements taken on day 2 using GRASS, the target surface was sea-ice covered in 1-2 cm of snow type material and the contours plots (Figures 5.20-5.25) show low values of HCRF indicating less scattering, however, snow is more scattering than ice (Kong, 1989). The contribution of scattering from snow covering a sea-ice surface depends on the roughness, water and brine volumes, dielectric contrast between the ice and its

interfaces (air-snow, air-ice, snow-ice) and inhomogeneities within the snow (Barber and LeDrew, 1994; Winebrenner *et al.*, 1989). Snow particle morphology can lead to an underestimation of the snow hemispherical-directional reflectance factor (HDRF) when using stereological analysis as a larger absorbing volume for snow particles is calculated by assuming a spherical shape regardless of the true particle shape (Painter and Dozier, 2004). Stamnes *et al.* (2011) modelled the effect that varying snow layer thickness had on sea-ice reflectance and discovered that when the snow layer is thin, the specular reflection is important but as the snow layer thickness increases, the direct light component becomes weaker. Only the surface layer affects the anisotropy of the hemispherical-directional reflectance factor, larger grain sizes and lower density allow fewer scattering events to occur within the surface layer and therefore there is a higher probability of photons reaching the absorbing substrate (Nolin *et al.*, 1990; Painter and Dozier, 2004). The *e*-folding depth (depth at which light decays to ~37% of its initial value) of the sea-ice measured in Tethys Bay was ~10 cm, thus to see any contributing effect of snow cover on reflectivity the surface snow layer would need to be thicker (at least one *e*-fold). Snow cover on sea-ice is a major characteristic of polar oceans; it is highly reflective of solar radiation and also interrupts the energy exchange between the atmosphere and the ocean (Jin and Simpson, 2000). Optically-thin snow can present a problem for remote sensing, reflectance differences can be as great as 60% depending on viewing geometry and the substrate (i.e. sea-ice) reflectance can significantly influence the snow reflectance, particularly at Nadir viewing angles (Nolin *et al.*, 1990). Dozier *et al.* (1988) used a model to calculate the BRDF of semi-infinite snow, when compared to field measurements of BRDF for similar snow a good agreement was seen

between the modelled and measured values. Nolin *et al.* (1990) used the same model to calculate BRDF of finite depth snow and, when compared to field measurements of BRDF, the model was unable to successfully estimate the reflected intensity. Snow particle morphology can lead to an underestimation of the snow HDRF when using stereological analysis as a larger absorbing volume for snow particles is calculated by assuming a spherical shape regardless of the true particle shape (Painter and Dozier, 2004).

De Abreu *et al.* (1994) calculated a satellite derived surface albedo of snow-covered sea-ice as 0.68-0.82, yet Jin and Simpson (2000) speculate that studies that retrieved snow and sea-ice albedo from AVHRR satellite albedo data (e.g. De Abreu *et al.*, 1994; Haefliger *et al.,* 1993; Lindsay and Rothrock, 1997; Nolin and Stroeve, 1997; Schweiger *et al.*, 1993; Stroeve *et al.*, 1997) had not generally considered and corrected the effect of BRDF on the satellite measurement data. In an alternative technique, Brandt *et al.* (2005) and Briegleb and Light (2007) undertook field experiments to measure the albedo of first year sea ice with and without snow, bare ice and ponded ice. Brandt *et al.* (2005) measured an albedo for first year Antarctic sea-ice with a thickness of >70 cm topped with a thin layer (<3 cm) of snow of 0.75 (within the range calculated from satellite data by De Abreu *et al.* (1994)) and an albedo for bare first year Antarctic sea-ice with a thickness of >70 cm of 0.49. Briegleb and Light (2007) measured an albedo for bare Arctic sea-ice with a thickness of 2 m of 0.8 and 0.4 at wavelengths of 500 nm and 1100 nm respectively. Ponded ice with a thickness of 1.5 m and a pond layer of 0.35 m had an albedo of 0.3 at 500 nm (Briegleb and Light, 2007). Melt

ponds on sea-ice occur commonly in the Arctic Ocean but are almost non-existent in Antarctica (Andreas and Ackley, 1982).

Painter and Dozier (2004) measured the hemispherical-directional reflectance facor (HDRF) of snow in California and at a wavelength of 550 nm, the HRDF ranged between 0.8-1.0 for a solar zenith angle of ~50° whilst at a wavelength of 1030 nm the HDRF ranged between 0.6-0.8 at a solar zenith angle of 50°. The average HCRF measured using GRASS for snow on sea-ice, day 2, at a wavelength of 500 nm (Figures 5.20, 5.22 and 5.24) ranges between 0-0.8 and at a wavelength of 1100 nm (Figures 5.21, 5.23 and 5.25) ranges between 0-0.6. The range of HCRF values measured using GRASS are more extensive and lower at both 500 nm and 1100 nm in comparison to the HDRF value observed by Painter and Dozier (2004). The Californian snow measured by Painter and Dozier (2004) was thick in comparison to the snow measured in Antarctic therefore the sea-ice under the snow measured using GRASS may have influenced the Antarctic HCRF values.

The Antarctic measurements taken on day 1 for bare sea-ice (Figures 5.17 and 5.18) show an average HCRF range of 0-1.2 at both 500 nm and 1100 nm. The greater range in HCRF values taken on day 1 in comparison to day 2 measurements are indicative of the increased scattering caused by inclusions in sea-ice. However, as the scatterers can be larger than the light wavelength, the absorption spectrum of ice should determine the spectral variation (Grenfell, 1983). The absorption spectrum of ice shows a minimum absorption (and therefore a maximum scattering) at 470 nm and a maximum absorption (therefore

a minimum scattering) at 1030 nm (Grenfell and Perovich, 1984; Grenfell *et al.,* 1994), two features that are not represented in the HCRF values for day 1.

5.7.3 Developments for GRASS to improve polar field measurements

In the section presented here, developments for GRASS will be discussed with a view to improving the quality of measurements in future polar field campaigns. The focus of the discussion will be on the ability of using GRASS to undertake quality polar HCRF measurements and measurement a variety of target surface locations. Most of the suggestions made here had been implemented before GRASS was used on another polar campaign at Dome C, Antarctic.

5.7.3.1 Access to field study areas

Owing to the coastal location of the Mario Zucchelli station, most fieldwork was conducted by using a helicopter to fly to surrounding locations. The GRASS measurements were restricted to Tethys Bay as it could be accessed by motor vehicles because GRASS was unable to be flown by helicopter. The weight of GRASS was not over the helicopter limit but it needed to be slung below the helicopter and due to a recent accident at a nearby base, stricter helicopter operational procedures were enforced including a reduced weight limit and the rule that equipment could not be hung below the helicopter whilst passengers were aboard. The stricter operational procedures meant that two helicopters would have been needed to transport GRASS and that was not possible.

The power requirement of the multiplexers was larger in the cold weather. GRASS was unable to be powered by batteries as the multiplexers used in the

system were power hungry and the batteries could not provide enough power, a generator was used to run the system instead. The use of a generator compounded the decision to limit GRASS measurements to Tethys Bay as generators cannot be carried inside a helicopter for safety reasons so two helicopters would be needed and as previously mentioned two helicopters were not available.

Using Tethys Bay as the measurement site solved transportation issues because the bay was accessible by car but as the sea-ice was in a melting phase it was not possible to leave GRASS in situ between measurements therefore GRASS had to be constructed and de-constructed between days of measurements. The system was not designed for multiple constructions as it was a lengthy process (over 1 hr) to assemble the system and it took around 45 mins to disassemble when the measurements have been concluded. In cold conditions, simple tasks, such as slotting the metal pieces of GRASS together, took longer because the material itself was very cold, gloves had to be worn to protect hands from frostbite and fingers lost dexterity. To combat the assemblage problems, GRASS should be used in an area where it can remain permanently erected for the measurement campaign. Dome C was an ideal location for measurements as GRASS could be left as a whole for the campaign plus there were a variety of measurement areas surrounding Dome C accessible by foot or snow mobile.

5.7.3.2 Cold Weather

GRASS was designed for use in warm, desert conditions and the aim of the fieldwork in Antarctica was to prove that GRASS was capable of taking measurements in polar conditions. As GRASS had not been originally designed

for polar fieldwork, elements of the system struggled with the low temperatures. The multiplexer did not cope well with the sub zero temperatures, the fibre optic inside the multiplexer that rotated to align with the individual fibre optics attached the outside of the multiplexer was unable to rotate in the cold conditions and the multiplexer would 'cut out'. In future measurements, steps should be made keep the multiplexer as warm as possible. The multiplexer should be kept in a box to protect the machine from outside elements, the box may contain bubble wrap and foam for insulation plus hot packs can be used to raise the temperature inside the box further if needed. Taking precautions to keep the multiplexer warm will increase the ability of the multiplexer to last through the measurement sequence.

At cold temperatures, the cladding around the fibre optics froze causing the fibres to become rigid and therefore the chance of a fibre breaking was increased, especially as the fibres frequently became tangled during the rotations of GRASS (Figure 5.26) and needed to be removed from the fibre optic housing plus detached from the multiplexer when disassembling the system.

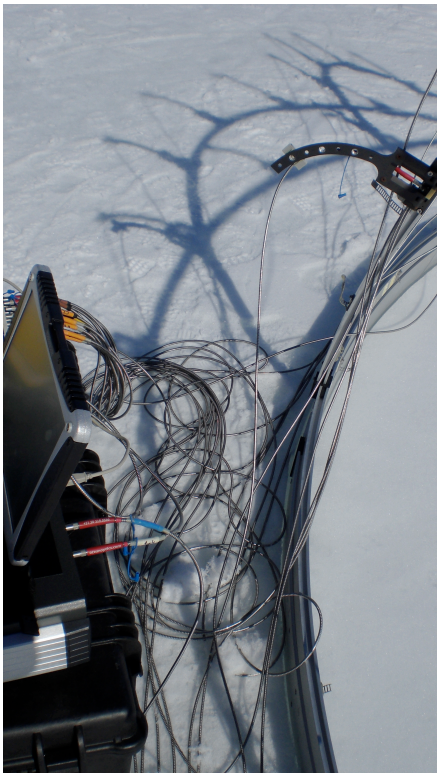

Figure 5.26. Tangled frozen fibre optics after a rotation of GRASS.

To combat the issues of working with GRASS at cold temperatures, the system should be assembled inside a warm hanger before being transported to the measurement site. Assembling GRASS at warmer temperatures will alleviate the problem of the fibre cladding freezing and also make it easier to assemble GRASS as gloves may not necessarily need to be worn.

5.7.3.3 Stability of system

The frame of GRASS consists of a full circle base ring and attached the base ring are 7 arms in a vertical position converging in the centre to form half a hemisphere. Due to only being half a hemisphere, the system was not stable and was affected by conditions such as wind. Although the system was too heavy to blow over in windy conditions the 7 arms swayed thus affecting any measurements taken. When the fibre optics in the holders were added to arms 1-3

the weight of the fibre holders caused the frame of GRASS to sag and the structure was no longer the shape of a perfect half-hemisphere. A change in shape meant the fibres may not have all been pointing at the same target area thus reducing the quality of the data collected. A pole reaching from the nadir point to the upper base ring of GRASS on the opposite side to the half hemisphere (Figure 5.27) would increase the stability and rigidity of the structure yet still allow rotation. The stability of downwelling measurements will increase with the stability of the structure.

Figure 5.27. Photo taken of GRASS with line showing the position of the bar recommended for increased structural stability.

5.7.3.4 Confidence in GRASS measurements

Confidence in the reflectance data produced by GRASS was not high due to the following reasons:

The hot spots seen on the reflected contour plots, e.g. Figure 5.17, indicate that individual fibre optic sensors were receiving either too little or too much light. To

ensure the amount of light received by each sensor is equal, each fibre optic sensor could be calibrated using an integrating sphere illumination source. Glinting from the base ring may have also affected the reflectance measurement data, at high solar zenith angles the fibre optics were calculating speculative data from the base ring caused by an increased reflected flux. A distinctive increase in reflectivity around the edge of the reflected contour plots is indicate of glint from the base ring, e.g. Figure 5.18. To check that the fibres are all measuring the same portion of snow surface, a laser can be fired back through the fibre optic sensors. Once the frame has been stabilised a large indoor uniform test surface (both uniformly flat and uniformly illuminated) of around 5 m × 5 m should be used to test the measurement area of the fibre optic sensors in a controlled environment so that further adjustments can be made if necessary. Linoleum is ideally suited as a measurement surface.

The heterogeneity of the target surface can affect measurement data. To reduce the affect of heterogeneity, the footprint of the measurement surface should be increased. Although the measurement will be less representative of BRDF, the overall data will be more useful. The footprint of the measurement surface can be expanded by increasing the acceptance cone of the fibre optic sensor.

The VSWIR spectrometer captures light from both the target and the sky simultaneously and channels the light into visible/near-IR wavelengths and short wave IR wavelengths to produce measurement spectrum. The individual spectrum, UV and IR, produced by the VSWIR did not overlap as the

spectrometer was not stable over time. The spectrometer has been sent back to the manufacture to be repaired and re-calibrated.

Field goniometry was an advantageous technique to use to measure surface reflectance as the target could be left in its natural environment and be illuminated naturally by the sun whilst measurements were conducted. However, the atmospheric effects and variations in illumination over time were a disadvantage and needed to be considered. To measure a full rotation using GRASS took around 1.5 hours, over the time sky conditions were changing thus affecting measurements. To assess the reproducibility of measurements, the variability of the Nadir reflectance was assessed during a full HCRF measurement (one full rotation) (Figure 5.28).

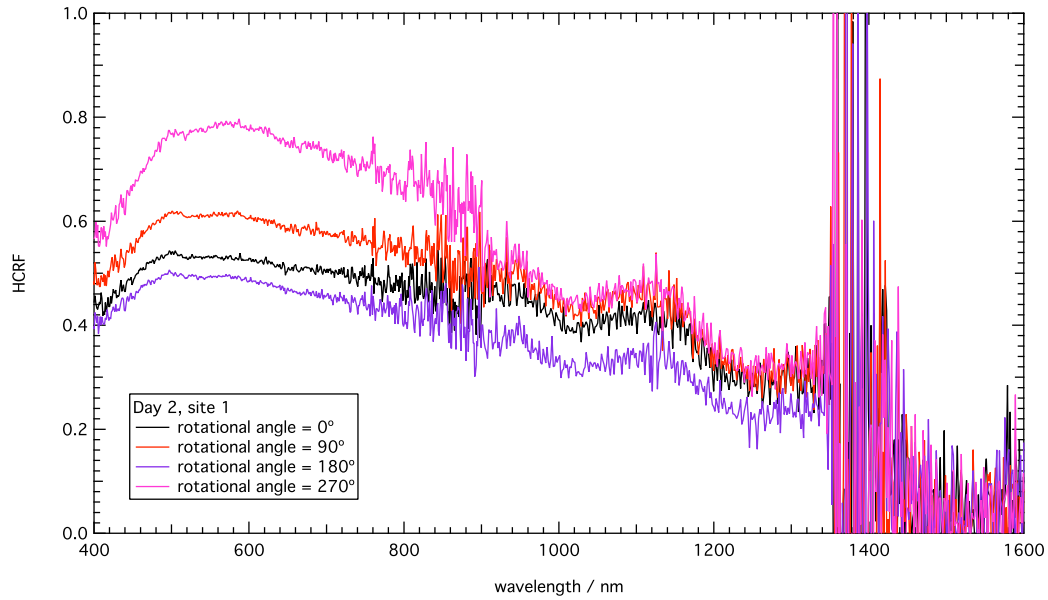

Figure 5.28. Reproducibility of measurements over 400-1500 nm for day 2, site 1. HCRF values shown represent downwelling irradiance.

Figure 5.28 shows that there was a larger variation in downwelling irradiance between each rotational angle of measurements taken using GRASS. Only one

downwelling irradiance measurement is taken per arm of measurement on GRASS and, as the length of time taken for measurements cannot be reduced, more downwelling irradiance should be conducted, i.e. one per fibre optic sensor measurement, to increase the reliability of the reflectance data.

5.8 Conclusions

The field work presented in this chapter proved that GRASS has the ability to undertake HCRF measurements in polar conditions, however, improvements need to be made to ensure the quality of the measurements taken. The main categories for the development of GRASS are the structural stability, the adaptation of computational machines to cope in cold temperatures and the variation of sites that can be accessed.

Chapter 6

Conclusion of Thesis

6.1 Introduction

The overall aim of this thesis was to conduct a field and laboratory study of snowpack and sea-ice optical and physical properties. In chapter 6, the conclusion of each individual study will be presented and the overall conclusion of the thesis will be discussed.

6.2 Individual Studies

6.2.1 Barrow OASIS 2009 campaign

Chapter 2a-c included research undertaken as part of the Barrow OASIS 2009 Spring campaign. The overall conclusions for the campaign were:

- Using optical properties and physical properties (snowpack stratigraphy) to classify snow have been shown to be valid methods.
- Optically similar snowpacks can be stratigraphically different and therefore the physical and optical properties must be derived for each snowpack investigated rather than relying upon using 'typical' snowpacks from similar latitudes and localities.
- The optical properties of the snowpack are important parameters needed to calculated in-snow photochemical production rates using a radiative-transfer model.

- Non-black carbon impurities in the snowpack have a large absorption cross-section at the short solar wavelengths, responsible for photolytic reactions in the snowpack, therefore it is important to accurately account for spectrally resolved absorption by both black carbon and non-black carbon impurities in the snowpack.
- Estimates of depth-integrated production rates, for individual snowpacks, can be scaled and approximately correlated with downwelling UV irradiance.
- The importance of NO fluxes from the snowpack owing to nitrite photolysis may have been significantly overlooked in previous campaigns. The work conducted at Barrow has calculated that NO from nitrite photolysis was approximately three times larger than NO_2 from nitrate photolysis.
- Increasing black carbon mass ratio in snow reduces albedo, *e*-folding depths and depth-integrated production rates of photochemically derived species in a complicated way.
- For black carbon mass ratios typically measured in snow, *e*-folding depth, albedo and depth-integrated production rates of OH and NO_2 can switch from ice-dominated absorption to black carbon dominated absorption.
- Light penetration depths and depth-integrated production rates (of NO_2 and OH radicals) follow a power law relationship for black carbon mass ratios greater than 10 ng g^{-1} and solar zenith angles greater than 60°.
- The future is uncertain when considering the importance of photochemical production coefficients in snowpack due to the dependence of black carbon production on human activity.

6.2.2 Black carbon in Arctic, Mid-Latitude and Antarctic Snowpacks

Chapter 3 presented a modeling study investigating the effect of black carbon in Arctic, Mid-Latitude and Antarctic snowpacks. The overall conclusions were:

- For mass ratios of black carbon greater than 20-30 ng g^{-1} (depending on wavelength), the variation of *e*-folding depth with respect to black carbon obeys a simple power law.
- Doubling the black carbon mass ratio (above 20-30 ng g^{-1}) will reduce the light penetration depth to ~70% of its initial value.
- When black carbon mass ratio is less than ~10 ng g^{-1}, the absorption of solar radiation in the snowpack is dominated by water-ice absorption and the response of *e*-folding depth to black carbon mass ratios is wavelength dependent.
- When black carbon mass ratio is greater than ~50 ng g^{-1}, the absorption of solar radiation in the snowpack is dominated by black carbon absorption and the response of *e*-folding depth to black carbon mass ratios is effectively invariant with wavelength.
- The response to increasing black carbon is not the same for each location or snow type.
- A snowpack impacted by increased black carbon pollution would have a larger decrease in the albedo at small solar zenith angles.

6.2.3 Black carbon mass ratios in Svalbard and Antarctic snowpack

Chapter 5 investigated the black carbon mass ratios found in Svalbard and Antarctic snowpack. The overall conclusions of the study were:

- Non-black carbon impurities in the snowpack have a large absorption cross-section at the short solar wavelength, responsible for photolytic reactions in the snowpack, therefore it is important to accurately account for the spectrally resolved absorption by both black carbon and non-black carbon impurities in the snowpack.
- Spatial features create a large variation in black carbon concentrations and therefore only local black carbon concentrations can be determined using this technique.
- Black carbon concentrations are affected by slope angle, aspects of the sampling locations, presence of melt water and snow type.
- The proximity of black carbon sources are likely to increase in the future thus giving rise to the increasing concentration of black carbon in snow.

6.2.4 The Bi-Directional Reflectance Distribution Function of Antarctic Snow

Chapter 5 presented research undertaken using GRASS in a polar environment. The overall conclusions were:

- GRASS has the ability to undertake HCRF measurements in polar conditions.
- Improvements to GRASS need to be made to ensure the quality of the measurements taken.
- The main categories for the development of GRASS are the structural stability, the adaptation of computational machines to cope in cold temperatures and the variation of sites that can be accessed

6.3 Conclusions of the thesis

The work presented in this thesis involved a variety of techniques to investigate the optical and physical properties of snowpack around the world. The key theme for the thesis was absorbers in snow. Each individual research study undertaken had an underlying theme of investigating the impact of absorbers in snowpack. The main absorber investigated was black carbon as this is the most efficient carbonaceous absorber; other absorbers were also considered including HULIS. The individual chapter conclusions have shown that absorbers in snow have an impact on the behaviour of light within snowpack. The work in chapters 2a-c and 3 concluded that a small amount of black carbon had a significant effect on the behaviour of light with regards to *e*-folding depth and albedo of the snowpack. The conclusion came from investigating the optical properties from a variety of snow types and locations throughout the world. An alternative method was used to research the impact of black carbon mass ratio on snow in chapter 4: a filtration technique. The filtration technique allowed the mass ratio of black carbon within snowpack to be measured at individual sampling sites without considering the optical properties of the snow. The technique allowed a general idea of snowpack black carbon mass ratio to be gain in the field through comparison with pre-prepared filters of varying black carbon mass ratios. Only location black carbon mass ratios could be determined by the filtration technique as spatial features created a large variation in black carbon mass ratio. It was concluded that black carbon concentrations are affected by slope angle, aspects of the sampling locations, presence of melt water and snow type.

The main aim of the Barrow campaign was to provide photochemical production rates of NO_2 and OH radicals within snowpack. Chapter 2c considered the effect of black carbon on the depth-integrated photochemical production rates of NO_2 and OH within snow. It was concluded that depth-integrated production rates follow a power law relationship for black carbon mass ratios greater than 10 ng g^{-1} and solar zenith angles greater than 60°; doubling the black carbon mass ratio within the snowpack will reduce $F(NO_2)$ and F(OH) to ~70% and ~65% of initial values respectively. Photochemical reactions within snowpack are important processes and, as black carbon is mainly controlled by human activity, the future of snow photochemistry remains uncertain. The proximity of black carbon sources to snow regions are likely to increase in the future therefore the concentration of black carbon in snow may increase and impact upon *e*-folding depth, albedo and snow photochemistry.

The work undertaken to investigate the ability of GRASS to measurement HCRF in a polar environment does not fit into the overall thesis theme of absorbers in snow. The aim of the reflectivity measurements made in Antarctic using GRASS was to test whether the machine had the ability to work in extreme polar conditions. It was concluded that GRASS could undertake measurements in a cold environment but improvements and adaptations were suggested to improve the accuracy of the measurements and thus allow the reflectivity to be linked to absorbers in snow, such as the reflectivity of Barrow snowpack has been linked to absorbers found within snowpack in this thesis.

6.4 Further Recommendations

To improve future research based on the work presented in this thesis a number of factors need to be considered:

- The seasonality of measurements needs to be taken into account and thus optical measurements of *e*-folding depth and albedo should be undertaken in one location for a variety of seasons to gather an accurate assessment of light behaviour within the snowpack.
- Time should be considered with regards to the BRDF measurements. The current measurements were a 'snap shot' of the surface reflectivity and to gain more accurate and informative values, measurements should be taken over a longer time period.
- An easier way to measure *e*-folding depths should be developed. Although the work presented in this thesis improved the technique in comparison to previous methods used to measure *e*-folding depth, there were still problems (such as the non-horizontal insertion of fibres) that may have affected the accuracy of the measurements. To improve fibre insertion, the fibre optics could be attached to a large pole that is subsequently inserted into the snowpack horizontally.

Definitions

AMDEs	Atmospheric Mercury Depletion Events - The cycling of mercury during depletion events in the Arctic Spring time.
BARC	Barrow Arctic Research Centre – The base for the 2009 OASIS campaign.
BRDF	Bi-directional reflectance distribution function – A function that defines how light is reflected on an opaque surface.
Brown carbon	A type of absorbing carbon that is not black.
CIMS	Chemical Ionisation Mass Spectrometer – Used to measure chemical composition of atmosphere.
***e*-folding depth**	The distance for solar irradiance to decrease to $\frac{1}{e}$ (or ~37%) of the initial value of incident light radiation within a snowpack. Can also be termed light penetration depth.
g	The asymmetry factor for a single ice grain. It is the mean cosine of the scattering angle. Can be plotted as a function of wavelength.
GEM	Gaseous Elemental Mercury - GEM counts for up to 98% of airborne mercury.

GER 1500s	A light-weight, high performance single-beam field spectroradiometer made by the Geophysical and Environmental Research Corporation (GER) used to measure over the visible to near infrared wavelength range.
GRASS	Gonio Radiometric Spectrometer System - Used to measure the HCRF of surfaces.
HCRF	Hemispherical Conical Reflectance Factor – A function that defines how light is reflected on an opaque surface.
HONO	Nitrous acid.
HULIS	Humic Like Substances
LabVIEW	A system design software that uses a visual programming language.
LOPAP	Long Path Absorption Photometer – Used to measure concentrations of HONO during the Barrow 2009 campaign.
LP-DOAS	Long Path-Differential Optical Absorption Spectrometer – Used to measure the average concentration of Br) during the Barrow 2009 campaign.
MADAT	Computational software that uses MATLAB programming software as a base, developed by the National Physics Laboratory (NPL) for use with GRASS.
NERC FSF	Natural Environmental Research Council Field Spectroscopy Facility. An organisation that promotes the use of field instruments in research science through

	training, equipment hire and calibration. Based in Edinburgh.
NIST	National Institute of Standards and Technology – Produced the traceable halogen light source used to monitor any decay in the fibre optical transmission during the Barrow 2009 campaign.
NO_x	A generic term for the nitrogen oxides produced during combustion. It includes NO (nitric oxide) and NO_2 (nitrogen dioxide).
OASIS	Ocean-Atmosphere-Sea-Ice-Snow – The organisation that ran the 2009 Barrow campaign.
PTFE	Polytetrafluoroethylene – Material from which the robust pots used to collect snow samples on the Svalbard 2010 expedition were made.
PTR-MS	Proton Transfer Reaction Mass Spectrometry – A technique used to monitor VOCs in ambient air.
RGM	Reactive Gaseous inorganic Mercury. GEM is oxidised to RGM species that are deposited to the snow surface during AMDEs.
Short chain diacids	Short chain dicarboxylic acids – Organic compounds that contain two carboxylic acid functional groups.
TUVR	Total Ultraviolet Radiometer – A detector for measuring solar UV radiation.
TUV-snow	Total Ultraviolet-Snow – Model used to calculate absorption and scattering in snowpack.

VOCs	Volatile Organic Compounds – Organic chemicals that have a high vapour pressure at ordinary, room-temperature conditions.

References

Aamaas, B., C. Boggild, F. Stordal, T. Berntsen, K. Holmen and J. Ström (2011), Elemental carbon deposition to Svalbard snow from Norwegian settlements and long-range transport, *Tellus, 63B,* 340-351

Abbatt, J., N. Oldridge, A. Symington, V. Chukalovskiy, R.D. McWhinney, S. Sjostedt and R.A. Cox (2010), Release of gas-phase halogens by photolytic generation of OH in frozen halide-nitrate solutions: An active halogen formation mechanism?, *Journal of Physical Chemistry A, 114*(23), 6526-6533, doi:10.1021/jp102072t

Abbatt, J.P.D., J.I. Thomas, K. Abrahamsson *et al.* (2012), Halogen activation via interactions with environmental ice and snow in the polar lower troposphere and other regions, *Atmospheric Chemistry and Physics, 12*, 6237-6271, doi: 10.5194/acp-12-6237-2012

Ackerman, A.S., O.B. Toon, D.E. Stevens, A.J. Heymsfield, V. Ramanathan and E.J. Welton (2000), Reduction of tropical cloudiness by soot, *Science, 288*, 1042-1047

Adler, G., A.A. Riziq, C. Erlick and Y. Rudich (2010), Effect of intrinsic organic carbon on the optical properties of fresh diesel soot, *Proceedings of the National Academy of Sciences U.S.A., 107*(15), 6699-6704

Allen, J. (2004), Tango in the Atmosphere: Ozone and Climate Change, *NASA Earth Observatory, Goddard Institute for Space Studies,* accessed 1st September 2012, www.giss.nasa.gov/research/features/200402_tango

Allison, I. (1982), The role of sea ice in climate variations, in: *Report of the WMO/CAS-JSC-CCCO Meeting of Experts on the Role of Sea Ice in Climate Variations, WCP-26,* World Meteorological Organisation, Geneva, 27-50

Allison, I., R.E. Brandt and S.G. Warren (1993), East Antarctic sea ice: albedo thickness distribution and snow cover, *Journal of Geophysical Research, 98*(C7), 12417-12429

Anastasio, C. and L. Chu (2009), Photochemistry of Nitrous Acid (HONO) and Nitrous Acidium Ion (H_2ONO^+) in aqueous solution and ice, *Environmental Science and Technology, 43*(4), 1108-1114, doi: 10.1021/es802579a

Anastasio, C., E.S. Glabavy, M.A. Hutterli, J.F. Burkhart and D.K. Friel (2007), Photoformation of hydroxyl radical on snow grains at Summit, Greenland, *Atmospheric Environment, 41*(24), 5110-5121, doi: 10.1016/j.atmosenv.2006.12.011

Anastasio, C. and L. Chu (2009), Photochemistry of Nitrous Acid (HONO) and Nitrous Acidium Ion (H_2ONO^+) in aqueous solution and ice, *Environmental Science and Technology, 43*(4), 1108-1114, doi: 10.1021/es802579a

Anderson, K., E.J. Milton and E.M. Rollin (2006), Calibration of dual-beam spectroradiometric data, *International Journal of Remote Sensing, 27*(5), 975-986

Andreae, M.O. and A. Glencser (2006), Black carbon or brown carbon? The nature of light-absorbing carbonaceous aerosols, *Atmospheric Chemistry and Physics Discussion, 6*. 3419-3463

Andreas, E.L. and S.F. Ackley (1982), On the differences in ablation seasons of Arctic and Antarctic sea ice, *Journal of Atmospheric Science, 39*, 440-447

Aoki, Te. And T. Tanaka (2008), Atmospheric aerosol deposition impact on snow albedo, *Tenki, 55*(7), 538-546

Aoki, Te., T. Aoki, M. Fukabori and A. Uchiyama (1999), Numerical simulation of the atmospheric effects on snow albedo with a multiple scattering radiative transfer model for the atmosphere-snow system, *Journal of Meteorological Society Japan, 77*(2), 595-614

Aoki, T., T. Aoki, M. Fukabori, A. Hachikubo, Y. Tachibana and F. Nishio (2000) Effects of snow physical parameters on spectral albedo and bidirectional reflectance of snow surface, *Journal of Geophysical Research, 105*(D8), 10219-10236, doi: 10.1029/1999JD901122

Aoki, Te., H. Motoyoshi, Y. Kodama, T.J. Yasunari, K. Sugiura and H. Jobayashi (2006), Atmospheric aerosol deposition on snow surfaces and its effect on albedo, *SOLA, 2,* 13-16, doi: 10.2151/sola.2006-003

Aoki, Te., H. Motoyoshi, Y. Kodama, T.J. Yasunari and K. Sugiura (2007), Variations of the snow physical parameters and their effects on albedo in Sapporo, Japan, *Annals of Glaciology, 46,* 375-381

Aubin, D.G. and J.P.D. Abbatt (2007), Interaction of NO_2 with hydrocarbon soot: focus on HONO yield, surface modification and mechanism, *Journal Of Physical Chemistry A, 111,* 6263-6273, doi: 10.1021/jp068884h

Barber, D.G. and E.F. LeDrew (1994), Modeling synthetic aperture radar (SAR) scattering from a seasonally varying snow-covered sea ice volume at 5.3 and 9.25 GHz, *Polar Research, 13,* 35-54

Barber, D.G. and S.V. Ngheim (1999), The role of snow on the thermal dependence of microwave backscatter over sea ice, *Journal of Geophysical Research (Oceans), 104*(C11), 25789-25803, doi: 10.1029/1999JC900181

Barnett, T.P., L. Dumenil, U. Schlese, E. Roeckner and M. Latif (1989), The effect of Eurasian snow cover on regional and global climate variations, *Journal of Atmospheric Science, 46,* 661-685

Barret, M., F. Domine, S. Houdier, J.-C. Gallet, P. Weibring, J. Walega, A. Fried and D. Richter (2012), Formaldehyde in the Alaskan Arctic snowpack: partitioning and physical processes involved in air-snow exchanges, *Journal of Geophysical Research, 116*(D00R03), doi:10.1029/2011JD016038

Baumgardner, D., R. Subramanian, C. Twohy, J. Stith and G. Kok (2008), Scavenging of black carbon by ice crystals over the northern Pacific, *Geophysical Research Letters, 35*(L22815), doi: 10.1029/2008GL035764

Beaglehole, D., B. Ramanathan and J. Rumberg (1998), The UV to IR transmittance of Antarctic snow, *Journal of Geophysical Research, 103*(D3), 8849-8857, doi: 10.1029/97JD03604

Beine, H. J., I. Allegrini, R. Sparapani, A. Ianniello, and F. Valentini (2001), Three years of springtime trace gas and particle measurements at Ny-Alesund, Svalbard, *Atmospheric Environment*, *35*(21), 3645-3658.

Beine, H.J., F. Dominé, W.R. Simpson, R.E. Honrath, R. Sparapani, X.L. Zhou, and M.D. King (2002a), Snow-pile and chamber experiments during the Polar Sunrise Experiment 'Alert 2000': exploration of nitrogen chemistry, *Atmospheric Environment*, *36*(15-16), 2707-2719

Beine, H.J., R.E. Honrath, F. Domine, W.R. Simpson and J.D. Fuentes (2002b), NOx during background and ozone depletion periods at Alert: Fluxes above the snow surface, *Journal of Geophysical Research (Atmosphere), 107*(D21), art. no. -4584, doi: 10 10.29/2002JD002082

Beine, H.J., F. Domine, A. Ianniello, M. Nardino, I. Allegrini, K. Teinila and R. Hillamo (2003), Fluxes of nitrates between snow surfaces and the atmosphere in the European high Arctic, *Atmospheric Chemistry and Physics, 3,* 335-346, doi: 10.1594/acpd-3-75-2003

Beine, H., A. Amoroso, F. Domine, M. King, M. Nardino, A. Ianniello and J. France (2006), Surprisingly small HONO emissions from snow surfaces at browning pass, Antarctic, *Atmospheric Chemistry and Physics*, *6*, 2569-2580, doi: 10/5194/acpd-6-615-2006

Beine, H, A.J. Colussi, A. Amoroso, G. Esposito, M. Montagnoli and M.R. Hoffman (2008), HONO emissions from snow surfaces, *Environmental Research Letters, 3*, 045005, doi:10.1088/1748-9326/3/4/045005

Beine, H., C. Anastasio, G. Esposito, K. Patten, E. Wilkening, F. Domine, D. Voisin, M. Barret, S. Houdier and S. Hall (2011), Soluble, light-absorbing species in snow at Barrow, Alaska, *Journal of Geophysical Research, 116*(D00R05), doi:10.1029/2011JD16181

Beine, H., C. Anastasio, F. Domine, T. Douglas, M. Barret, J. France, M. King, S. Hall and K. Ullmann (2012), Soluble chromophores in marine snow, seawater, sea ice and frost flowers near Barrow, Alaska, *Journal of Geophysical Research, 117*(D00R15), doi:10.1029/2011JD016650

Bentley, W. and W.J. Humphreys (1931), *Snow Crystals*, McGraw-Hill, New York

Bergin, M.H., J.L. Jaffrezo, C.I. Davidson, J.E. Dibb, S.N. Pandis, R. Hillamo, W. Maenhaut, H.D. Kuhns, and T. Makela (1995), The Contributions of Snow, Fog, and Dry Deposition to the Summer Flux of Anions and Cations at

Summit, Greenland, *Journal of Geophysical Research (Atmospheres)*, *100*(D8), 16275-16288

Berry, M.O. (1981), Snow and climate, *Handbook of snow,* Pergamon Press, 32-59

Bloss, W.J., J.D. Lee, D.E. Heard, R.A. Salmon, S.J.B. Bauguitte, H.K. Roscoe and A.E. Jones (2007), Observations of OH and HO_2 radicals in coastal Antarctica, *Atmospheric Chemistry and Physics, 7*(16), 4171-4185, doi:10.5194/acp-7-4171-2007

Bluestein, H.B. (1993), *Synoptic-Dynamic Meteorology in Midlatitudes. Vol II,* Oxford University Press, 594

Blunier, T., G.L. Floch, H.W. Jacobi, and E. Quansah (2005), Isotopic view on nitrate loss in Antarctic surface snow, *Geophysical Research Letters*, *32*(13)

Bock, J. and H.W. Jacobi (2010), Development of a mechanism for nitrate photochemistry in snow, *Journal of Physical Chemistry A, 114*(4), 1790-1796, doi: 10.1021/jp909205e

Bohren, C. (1986), Applicability of effective-medium theories to problems of scattering and absorption by nonhomogeneous atmospheric particles, *Journal of Atmospheric Science, 43*(5), 468-475

Bohren, C. (1987), *Clouds in a glass of beer: simple experiments in atmospheric physics,* Dover Publications Inc, New York, 114

Bohren, C. and D. Huffman (1983), *Absorption and scattering of light by small particles,* New York, Wiley-Interscience, 1983

Bond, T.C. and H. Sun (2005), Can reducing black carbon emissions counteract global warming?, *Environmental Science and Technology*, *39,* 5921-5926, doi: 10.1021/es0480421

Bond, T.C. and R.W. Bergstrom (2006), Light absorption by carbonaceous particles: an investigative review, *Aerosol Science and Technology, 40*, 27-67, doi: 10.1080/02786820500421521

Bond, T.C., D.G. Streets, K.F. Yarber, S.M. Nelson, J.-H. Woo and A. Kilmont (2004), A technology-based global inventory of black and organic carbon emissions from combustion, *Journal of Geophysical Research, 109*(D14203), doi: 10.1029/2003JD003697

Bourgouin P. (2000), A method to determine precipitation types, *Weather and Forecasting*, *15*(5), 583-592

Boxe, C.S. and A. Saiz-Lopez (2008), Multiphase modeling of nitrate photochemistry in the quasi-liquid layer (QLL): implications for NOx release from the Arctic and coastal Antarctic snowpack, *Atmospheric Chemistry and Physics, 8*(2), 6009-6034, doi: 10.5194/acp-8-4855-2008

Boxe, C.S., A.J. Colussi, M.R. Hoffmann, I.M. Perez, J.G. Murphy and R.C. Chohen (2006), Kinetics of NO and NO_2 evolution from illuminated frozen nitrate solutions, *Journal of Physical Chemistry A., 110*(10), 3578-3583, doi:10.1021/jp055037q

Brandt, R.E., S.G. Warren, A.P. Worby, T.C. Grenfell (2005), Surface albedo of the Antarctic sea ice zone, *Journal of Climate, 18*, 3606-3622

Briegleb, B.P. and B. Light (2007), A Delta-Eddington multiple scattering parameterization of solar radiation in the sea ice component of the community climate system model, NCAR Technical Note NCAR/TN-472+STR

Brown, S.S., T.B. Ryerson, A.G. Wollny, *et al.* (2006), Variability in noctural nitrogen oxide processing and its role in regional air quality, *Science, 311*, 67-70, doi: 10.1126/science.1120120

Browse, J., K.S. Carslaw, S.R. Arnold, K. Pringle and O. Boucher (2012), The scavenging processes controlling the seasonal cycle in Arctic sulphate and black carbon aerosol, *Atmospheric Chemistry and Physics, 12*, 6775-6798, doi: 10.5194/acp-12-6775-2012

Budyko, M.I. (1969), The effect of solar radiation variations on the climate of the Earth, *Tellus, 21*, 611-619

Cabanes, A., L. Legagneux, and F. Dominé (2002), Evolution of the specific surface area and of crystal morphology of Arctic fresh snow during the ALERT 2000 campaign, *Atmospheric Environment*, *36*(15-16), 2767-2777

Cathles, L.M., and M.R. Albert (2007), Instruments and methods - A physically based method for correcting temperature profile measurements made using thermocouples, *Journal of Glaciology*, *53* (181), 298-304

Cavalieri, D.J., C.L. Parkinson and K.Y. Vinnikov (2003), 30-year satellite record reveals contrasting Arctic and Antarctic decadal sea ice variability, *Geophysical Research Letters, 30*(18), 4

Chickering, F. (1864), *Cloud crystals: A snow flake album*, Appleton Company, New York

Chu, L. and C. Anastasio (2003), Quantum yield of hydroxyl radical and nitrogen dioxide from the photolysis of nitrate on ice, *Journal of Physical Chemistry A, 107*(45), 9594-9602, doi: 10.1021/jp0349132

Chu, L. and C. Anastasio (2005), Formation of hydroxyl radical from the photolysis of frozen hydrogen peroxide, *Journal of Physical Chemistry A, 109*(28), 6264-6271, doi:10.1021/jp051415f

Chu L. and C. Anastasio (2007), Temperature and wavelength dependence of nitrite photolysis in frozen and aqueous solutions, *Environmental Science and Technology, 41*(10), 3626-3632, doi: 10.1021/es062731q

Chylek, P., V. Ramaswamy and V. Srivastava (1983), Albedo of soot-contaminated snow, *Journal of Geophysical Research, 88*(C15), 10837-10843, doi: 10.1029/JC088iC15p10837

Chylek, P., V. Srivastava, L. Cahenzli, R.G. Pinnick, R.L. Dod, T. Novakov, T.L. Cook and B.D. Hinds (1987), Aerosol and graphitic carbon content of snow, *Journal of Geophysical Research, 92*(D8), 9801-9809, doi: 10.1029/JD092iD08p09801

Clarke A.D. and K. Noone (1985), Soot in the arctic snowpack: a cause for perturbations in radiative transfer, *Atmospheric Environment*, *19*(12), 2045-2053

Clark, R.N., G.A. Swayze, K.E. Livo *et al.* (2002), Surface reflectance calibration of terrestrial imaging spectroscopy data: a tutorial using AVIRIS, *Proceedings of the 10th Airborne Earth Science Workshop,* p.21

Clarke, A., C. NcNaughton, V. Kapustin, Y. Shinozuka, S. Howell, J. Dibb, J. Zhou, B. Anderson, V. Brekhovskikh, H. Turner and M. Pinkerton (2007), Biomass burning and pollution aerosol over North America: Organic components and their influence on spectral optical properties and humidification response, *Journal of Geophysical Research, 112*(D12S18), doi:10.1029/2006JD007777

Comiso, J.C. (2012), Large decadal decline of the Arctic multiyear ice cover, *Journal of Climate, 25*(4), 1176-1193

Conant, W.C., A. Nenes and J.H. Seinfeld (2002), Black carbon radiative heating effect on cloud microphysics and implications for the aerosol indirect effect: 1. Extended theory, *Journal of Geophysical Research (Atmospheres), 107*(4604), 9, doi: 10.1029/2002JD002094

Cooke W.F. and Wilson J.N (1996), A global black carbon aerosol model, *Journal of Geophysical Research, 101*(D14), 19395-19409

Cotter, E.S.N., A.E. Jones, E.W. Wolff and S.J.B. Bauguitte (2003), What controls photochemical NO and NO_2 production from Antarctic snow? Laboratory investigation assessing the wavelength and temperature dependence, *Journal of Geophysical Research (Atmosphere), 108*(D4), art. no. -4147, doi: 10.1029/2002JD002602

Couch, T.L., A.L. Sumner, T.M. Dassau, P.B. Shepson and R.E. Honrath (2000), An investigation of the interaction of carbonyl compounds with the snowpack, *Geophysical Research Letters, 27*(15), 2241-2244, doi: 10.1029/1999GL011288

Crutzen, P.J. (1970), The influence of nitrogen oxides on the atmospheric ozone content, *Quarterly Journal of the Royal Meteorological Society, 96*, 320-325

Cubasch, V and R.D. Cess (1990), Processes and modeling, In: Houghton, J.T., G.J. Jenkins, J.J. Ephraumus, efs. Climate change, the IPCC scientific assessment, Cambridge: Cambridge University Press, p. 364

Curry, J.A., J.L. Schramm and E.E. Ebert (1995), On the ice albedo climate feedback over the Arctic ocean, *Journal of Climate, 8*, 240-247

Curry, J.A., W.B. Rossow, D. Randall and J.L. Schramm (1996), Overview of Arctic cloud and radiation characteristics, *Journal of Climate, 9*(8), 1731-1764

Dassau, T.M. *et al.* (2002), Investigation of the role of the snowpack on atmospheric formaldehyde chemistry at Summite, Greenland, *Journal of Geophysical Research, 107*(D19). 4394, doi:10.1029/2002JD002182

Davies, T.D., M. Tranter, T.D. Jickells, P.W. Abrahams, S. Landsberger, K. Jarvis and C.E. Pierce (1992), Heavily-contaminated snowfalls in the remote Scottish highlands: a consequence of regional-scale mixing and transport, *Atmospheric Environment, 26A*(1), 95-112

Davis, D., J.B. Nowak, G. Chen, M. Buhr, R. Arimoto, A. Hogan, F. Eisele, L. Mauldin, D. Tanner, R. Shetter, B. Lefer, and P. McMurry (2001), Unexpected high levels of NO observed at South Pole, *Geophysical Research Letters*, *28*(19), 3625-3628

Davis, D., G. Chen, M. Buhr, J. Crawford, D. Lenschow, B. Lefer, R. Shetter, F. Eisele, L. Mauldin, and A. Hogan (2004), South Pole NOx Chemistry: an assessment of factors controlling variability and absolute levels., *Atmospheric Environment*, *38*, 5375-5388

De Abreu, R.A., J. Key, J.A. Maslanik, M.C. Serreze and E.F. LeDrew (1994), Comparison of in situ and AVHRR-derived broadband albedo over Arctic sea-ice, *Arctic, 47*(3), 288-297

Dewey, K.F. and R. Heim Jr. (1981), Satellite observations of variations in Northern Hemisphere seasonal snow covered, *NOAA Technical Report, NESS 87,* Washington D.C., 83

Dibb, J.E., and M. Arsenault (2002), Shouldn't snowpacks be sources of monocarboxylic acids?, *Atmospheric Environment*, *36*(15-16), 2513-2522

Dibb, J.E., L.G. Huey, D.L. Slusher and D.J. Tanner (2004), Soluble reactive nitrogen oxides at South Pole during ISCAT 2000, *Atmospheric Environment, 38*(32), 5399-5409, doi: 10.1016/j.atmosenv.2003.01.001

Dieckmann, G.S. and H.H. Hellmer (2005), The importance of sea ice: an overview in: D.N. Thomas, G.S. Dieckmann (eds), *sea ice: an introduction to its physics, chemistry, biology and geology*, Blackwell publishing, oxford, 1-21

Dirmhirn, I. and F.D. Eaton (1975), Some characteristics of the albedo of snow, *Journal of Applied Meteorology, 14*, 375-379

Doherty, S.J., S.G. Warren, T.C. Grenfell, A.D. Clarke and R.E. Brandt (2010), Light-absorbing impurities in Arctic snow, *Atmospheric Chemistry and Physics Discussion, 10*, 18807-18878, doi: 10.5194/acp-10-11647-2010

Dominé, F. and P.B. Shepson (2002), Air-snow interactions and atmospheric chemistry, *Science, 297*(5586), 1506-1510, doi: 10.1126/science.1074610

Domine, F., A. Cabanes, A.S. Taillandier, and L. Legagneux (2001), Specific surface area of snow samples determined by CH4 adsorption at 77 K and estimated by optical, microscopy and scanning electron microscopy, *Environmental Science & Technology*, *35* (4), 771-780

Domine, F., A. Cabanes and L. Legagneux (2002), Structure, microphysics and surface area of the Arctic snowpack near Alert during the ALERT 2000 campaign, *Atmospheric Environment, 36*(15-16), 2753-2765

Domine, F., M. Albert, T. Huthwelker, H.W. Jacobi, A.A. Kokhanovsky, M. Lehning, G. Picard and W.R. Simpson (2008), Snow physics as relevant to

snow photochemistry, *Atmospheric Chemistry and Physics, 8*(2), 171-208, doi:10.5194/acp-8-171-2008

Domine, F., J.-C. Gallet, M. Barret, S. Houdier, D. Voisin, T.A. Douglas, J.D. Blum, H.J. Beine, C. Anastasio and F.-M. Bréon (2011a), The specific surface area and chemical composition of diamond dust near Barrow, Alaska, *Journal of Geophysical Research, 116*(D00R06), doi:10.1029/2011JD016162

Domine, F., J.-C. Gallet, J. Bock and S. Morin (2012), Structure, specific surface area and thermal conductivity of the snowpack around Barrow, Alaska, *Journal of Geophysical Research, 117*(D00R013), doi:10.1029/2011JD016647

Douglas, T.A., F. Domine, M. Barret, C. Anastasio, H.J. Beine, J. Bottenheim, A. Grannas, S. Houdier, S. Netcheva, G. Rowland, R. Staebler and A. Steffer (2012), Frost flowers growing in the Arctic ocean-atmosphere-sea ice-snow interface: 1. Chemical composition, *Journal of Geophysical Research, 117*(D00R09), doi:10.1029/2011JD016460

Dozier, J. (1989), Spectral signature of alpine snow cover from the Landsast Thematic mapper, *Remote Sensing Environments, 28,* 9-22

Dozier, J., R.E. Davis, A.T.C. Chang and K. Brown (1988), The spectral bidirectional reflectance of snow, paper presented at 4th international colloquium of Spectral Signatures of Objects in Remote Sensing, Aussois, France, 87

Dubowski, Y., and M.R. Hoffmann (2000), Photochemical transformations in ice: Implications for the fate of chemical species, *Geophysical Research Letters*, *27*(20), 3321-3324

Dubowski, Y., A.J. Colussi and M.R. Hoffman (2001), Nitrogen dioxide release in the 302 nm band photolysis of spray-frozen aqueous nitrate solutions. Atmospheric implications, *Journal of Physical Chemistry A, 105*(20), 4928-2932, doi: 10.1021/jp0042009

Dubowski, Y., A.J. Colussi, C. Boxe and M.R. Hoffman (2002), Monotonic increase of nitrite yields in the photolysis of nitrate in ice and water between 238 and 294 K, *Journal of Physical Chemistry A, 106*(30), 6967-6971, doi: 10.1021/jp0142942

Duggin, M.J. and W.R. Philipson (1982), Field measurement of reflectance: some major considerations, *Applied Optics, 21*(15), 2833-2840, doi: 10.1364/AO.21.002833

Dumont, M., O. Brissaud, G. Picard, B. Schmitt, J.-C. Gallet and Y. Arnaud (2010), High-accuracy measurements of snow Bidirectional Reflectance Distribution Function and visible and NIR wavelengths – comparison with modelling results, *Atmospheric Chemistry and Physics, 10,* 2507-2520

Eleftheriadis, K., S. Vratolis and S. Nyeki (2009), Aerosol black carbon in the European Arctic: Measurements at Zepplin station, Ny-Alesund, Svalbard from 1998-2007; *Geophysical Research Letters, 36*(L02809), doi: 10.1029/2008GL035741

Elterman, L. (1968), UV, visible and IR attenuation for altitudes up to 50 km, *Environmental Research,* No. 285, AFCRL-680153

Fierz, C., R.L. Armstrong, Y. Durand, P. Etchevers, E. Greene, D.M. McClung, K. Nishimura, P.K. Satawali and S.A. Sokratov (2009), The International Classification for Seasonal Snow on the Ground, *IHP-VII Technical Documents in Hydrology N°83, IACS Constribution N°1,* United Nations

Educational Scientific and Cultural Organiszation International Hydrological Progressions, Paris

Fisher F.N., King M.D. and J. Lee-Taylor (2005), Extinction of UV-visible radiation in wet midlatitude (maritime) snow: Implications for increased NO_x emission, *Journal of Geophysical Research, 110*(D21301), doi: 10.1029/2005JD005963

Flanner M.G. and C.S. Zender (2006), Linking snowpack microphysics and albedo evolution, *Journal of Geophysical Research, 111*(D12), doi: 10.1029/2005JD006834

Flanner, M.G., C.S. Zender, J.T. Randerson and P.J. Rasch (2007), Present-day climate forcing and response from black carbon in snow, *Journal of Geophysical Research (Atmospheres), 112*(D11), D11202, doi:10.1029/2006JD008003

Flanner, M.G., Zender C.S., Hess P.G., Mahowald N.M., Painter T.H., Ramanathan V. and P.J. Rasch (2009), Springtime warming and reduced snow cover from carbonaceous particles, *Atmospheric Chemistry and Physics, 9*, 2481-2497

Forsström, S., J. Ström, C. Pedersen, E. Isaksson and S. Gerland (2009), Elemental carbon distribution in Svalbard snow, *Journal of Geophysics Research, 114*(D19112), 8, doi: 10.1029/2008JD011480

Fowgill, F. (2005), Field Guide for the GER1500 - Dual Beam Mode, *FSF Technical Report*

France, J.L. (2008), Chemical oxidation in snowpack, PhD thesis, Dep. Of Earth Science, Royal Holloway, University of London, Egham, Surrey, UK

France, J.L. and M.D. King (2012), The effect of measurement geometry on recording solar radiation attenuation in snowpack (*e*-folding depth) using fibre-optic probes, *Journal of Glaciology, 58*(208), doi: 10.3189/2012JoG11J227

France, J.L, M.D. King and J. Lee-Taylor (2007), Hydroxyl (OH) radical production rates in snowpack from photolysis of hydrogen peroxide (H_2O_2) and nitrate (NO_3^-), *Atmospheric Environment, 41*(26), 5502-5509, doi: 10.1016/j.atmosenv.2007.03.056

France, J.L, M.D. King and J. Lee-Taylor (2010), The importance of considering depth-resolved photochemistry in snow: a radiative-transfer study of NO_2 and OH production in Ny-Alesund snowpacks, *Journal of Glaciology, 56*(198), 655-663, doi: 10.3189/002214310793146250

France, J.L., M.D. King, M.M. Frey, J. Erbland, G. Picard, S. Preunkert, A. MacArthur and J. Savarino (2011a), Snow optical properties at Dome C (Concordia), Antarctica; implications for snow emissions and snow chemistry of reactive nitrogen, *Atmospheric Chemistry and Physics, 11*(18), 9787-9801, doi: 10.5194/acp-11-9787-2011

France, J.L., M.D. King, J. Lee-Taylor, B.H.J., A. Ianniello, A. Macarthur and F. Domine (2011b), A field and radiative-transfer study of the optical properties of Svalbard (Ny-Ålesund) snowpacks: Predications of in-snow NO_2 and OH photochemical production rates, *Journal of Geophysical Research (Surface)*

France, J.L., H.J. Reay, M.D. King, D. Voisin, H.W. Jacobi, F. Domine, H. Beine, C. Anastasio, A. MacArthur and J. Lee-Taylor (2012), Hydroxyl radical and nitrogen dioxide production rates, black carbon concentrations and light-

absorbing impurities from field measurements of light penetration and nadir reflectivity of on-shore and off-shore coastal Alaskan snow, *Journal of Geophysical Research*, doi: 10.1029/2011JD016639

Frank, F.C. (1982), Snow crystals, *Contemp. Phys., 23*, 3-22

Freyer, H.D., K. Kobel, R.J. Delmas, D. Kley, and M.R. Legrand (1996), First results of N-15/N-14 ratios in nitrate from alpine and polar ice cores, *Tellus Series B-Chemical and Physical Meteorology*, *48*(1), 93-105

Frieß, U., H. Sihler, R. Sander, D. Pöhler, S. Yilmaz and U. Platt (2011), The vertical distribution of BrO and aerosols in the Arctic: Measurements by active and passive differential optical absorption spectroscopy, *Journal of Geophysical Research, 116*(D00R04), doi:10.1029/2011JD015938

Fuhrer, K., M. Hutterli and J.R. McConnell (1996), Overview of recent field experiments for the study of the air-snow transfer of H_2O_2 and HCHO, NATA ASI Ser., vol. 1, 43, *Chemical exchange between the atmosphere and polar snow*, Wolff, E.W. and R.C. Bale (eds), Springer-Verlag, Berlin Heidelberg

Gallet, J.C., F. Domine, L. Arnaud, G. Picard and J. Savarino (2010), Vertical profiles of the specific surface area of the snow at Dome C, Antarctica, *Cryosphere Discussion, 4*(3), 1647-1708, doi:10.5194/tcd-4-1647-2010

Gao, S.S., S.J. Sjostedt, S. Sharma, S.R. Hall, K. Ullmann and J.P.D. Abbatt (2012), PTR-MS observations of photo-enhanced VOC release from Arctic and midlatitude snow, *Journal of Geophysical Research, 117*(D00R017), doi:10.1029/2011JD017152

Garrett, T.J., S. Brattström, S. Sharma, D.E.J. Worthy and P. Novelli (2011), The role of scavenging in the seasonal transport of black carbon and sulfate to

the Arctic, *Geophysical Research Letters, 38*(L16805), doi: 10.1029/2011GL048221

George, I.J. and C. Anastasio (2007), Release of gaseous bromine from the photolysis of nitrate and hydrogen peroxide in simulated sea-salt solutions, *Atmospheric Environment, 4*(3), 543-553, doi: 10.1016/j.atmosenv.2006.08.022

Gerland, S., J.G. Winther, J.B. Orbaek, G.E. Liston, N.A. Oritsland, A. Blanco and B. Ivanov (1999), Physical and optical properties of snow covering Arctic tundra on Svalbard, *Hydrological Processes, 13*(14-15), 2331-2343

Gleick, P.H. (1987), Regional hydrologic consequences of increases in atmospheric CO_2 and other trace gases, *Climate Change, 10,* 137-161

Goldberg, E.D. (1985), *Black carbon in the environment: properties and distribution,* New York, John Wiley and Sons, 1985

Grannas, A.M., P.B. Shepson, C. Guimbaud, A.L. Sumner, M. Albert, W. Simpson, F. Dominé, H. Boudries, J. Bottenheim, H.J. Beine, R. Honrath, and X.L. Zhou (2002), A study of photochemical and physical processes affecting carbonyl compounds in the Arctic atmospheric boundary layer, *Atmospheric Environment*, *36*(15-16), 2733-2742

Grannas, A.M., P.B. Shepson and T.R. Filley (2004), Photochemistry and nature of organic matter in Arctic and Antarctic snow, *Global Biogeochemical Cycles, 18*(10), GB1006, doi: 10.1029/2003GB002133

Grannas, A.M., W.C. Hockaday, P.G. Hatcher, L.G. Thompson, and E. Mosley-Thompson (2006), New revelations on the nature of organic matter in ice cores, *Journal of Geophysical Research (Atmospheres)*, *111*(D4)

Grannas, A.M., A.E. Jones, J. Dibb, M. Ammann, C Anastasio, H.J. Beine, M. Bergin, K. Bottenheim, C.S. Boxe, G. Carver, G. Chen, J.H. Crawford, F. Domine, M.M Frey, M.I. Guzman, D.E. Heard, D. Helmig, M.R. Hoffman, R.E. Honrath, L.G. Huey, M. Hutterli, H.W. Jacobi, P. Klan, B. Lefer, J. McConnel, J. Plane, R. Sander, J. Savarino, P.B. Shepson, W.R. Simpson, J.R. Sodeau, R. von Glaow, R. Weller, E.W. Wolff and T. Zhu (2007), An overview of snow photochemistry: evidence, mechanisms and impacts, *Atmospheric Chemistry and Physics, 7*(16), 4329-4373, doi: 10.5194/acp-7-4329-2007

Gray W.M., Frank W.M., Corrin M.L. and C.A. Stokes (1976), Weather Modification by Carbon Dust Absorption of Solar Energy, *Journal of Applied Meteorology, 15,* 355-386

Grenfell, T.C. (1983), A theoretical model of the optical properties of sea ice in the visible and near infrared, *Journal of Geophysical Research, 88,* 9723-9735

Grenfell, T.C. and D.K. Perovich (1984), Spectral albedos of sea ice and incident solar irradiance in the Souther Beaufort Sea, *Journal of Geophysical Research, 89,* 3573-3580

Grenfell T.C. and G.A. Maykut (1977), The optical properties of ice and snow in the Arctic basin, *Journal of Glaciology, 10*, 445-463

Grenfell, T.C. and S.G. Warren (1994), Reflection of solar radiation by the Antarctic snow surface at ultraviolet, visible, and near-infrared wavelengths, *Journal of Geophysical Research*, *99*(D9), 18669-18684

Grenfell, T.C., and S.G. Warren (1999), Representation of a nonspherical ice particle by a collection of independent spheres for scattering and absorption

of radiation, *Journal of Geophysical Research (Atmospheres)*, *104* (D24), 31697-31709

Grenfell, T.C., S..G. Warren and P.C. Mullen (1994), Reflection of solar radiation by the Antarctic snow surface at ultraviolet, visible and near-infrared wavelengths, *Journal of Geophysical Research, 99*(18), 669-618, doi: 10.1029/94JD01484

Grenfell, T., B. Light and M. Sturm (2002), Spatial distribution and radiative effects of soot in the snow and sea-ice during the SHEBA experiment, *Journal of Geophysical Research (Oceans), 107*(C10), 8032, doi:10.1029/2000JC000414

Grenfell, T.C., S.J. Doherty, A.D. Clarke and S.G. Warren (2011), Light absorption from particulate impurities in snow and ice determined by spectrophotometric analysis of filters, *Applied Optics, 50,* 2037-2048, doi:10.1364/AO.50.002037

Hadley, O. and T. Kirchstetter (2012), Black-carbon reduction of snow albedo, *Nature Climate Change, 2*, 437-330, doi: 10.1038/nclimate1433

Haefliger, M., K. Steffen and C. Fowler (1993), AVHRR surface temperature and narrow-band albedo comparison with ground measurements for the Greenland ice sheet, *Annals of Glaciology, 17*(1), 49-54

Hall, A. and X. Qu (2006), Using the current seasonal cycle to constrain snow albedo feedback in future climate change, *Geophysical Research Letters*, *33*(L03502)

Hansen, J. and L. Nazarenko (2004), Soot climate forcing via snow and ice albedos, *Proceedings of the National Academy of Sciences USA, 101*(2), 423-428, doi: 10.1073/pnas.2237157100

Hansen, J., M. Sato and R. Ruedy (1997), Radiative forcing and climate response, *Journal of Geophysical Research, 107*, 6831-6863

Hansen, J., M. Sato, R. Ruedy, A. Lacis and V. Oinas (2000), Global warming in the twenty-first century: an alternative scenario, *PNAS, 97*(18), 9875-9880, doi: 10.1073/pnas/170278997

Hansen, A.D.A., R.H. Lowenthal, J.C. Chow and J.G. Watson (2001), Black carbon aerosol at McMurdo Station, Antarctica, *Journal of the Air and Waste Management Association, 51*(4), 593-600

Hansen, J., M. Sato, R. Ruedy *et al.* (2005), Efficacy of climate forcings, *Journal of Geophysical Research, 110*(D18104), doi: 10.1029/2005JD005776

Harden, J.W., S.E. Trumbore, B.J. Stocks, A. Hirsch, S.T. Gower, K.P. O'Neill and E.S. Kasischke (2000), The role of fire in the boreal carbon budget, *Global Change Biology, 6*(Suppl 1), 174-184

Hastings, M.G., E.J. Steig, and D.M. Sigman (2004), Seasonal variations in N and O isotopes of nitrate in snow at Summit, Greenland: Implications for the study of nitrate in snow and ice cores, *Journal of Geophysical Research (Atmospheres)*, *109*(D20)

Hegg, D.A., S.G. Warren, T.C. Grenfell, S.J. Doherty, T.V. Larson and A.D. Clarke (2009), Source attribution of black carbon in arctic snow, *Environmental Science and Technology, 43*(11), 4016-4021, doi: 10.1021/es803623f

Hegg, D.A., S.G. Warren, T.C. Grenfell, S.J, Doherty and A.D. Clarke (2010), Sources of light-absorbing aerosol in arctic snow and their seasonal variation, *Atmospheric Chemistry and Physics, 10*, 10923-10938, doi: 10.5194/acp-10-10923-2010

Hewson, E.W. (1943), The reflection, absorption and transmission of solar radiation by fog and cloud, *Quarterly Journal of the Royal Meteorology Society, 69,* 47-62, doi:10.1002/qj.49706929808

Highwood, E.J. and R.P. Kinnersley (2006), When smoke gets in our eyes: The multiple impacts of atmospheric black carbon on climate, air quality and health, *Environment International, 32*, 560-566

Hoffer, A., A. Gelencsér, P. Guyon, G. Kiss, G.P. Frank, P. Artaxo and M.O. Andreae (2006), Optical properties of humic-like substances (HULIS) in biomass-burning aerosols, *Atmospheric Chemistry and Physics, 6*(11), 3563-3570

Holdsworth, G., K. Higuchi, G.A. Zielinski, P.A. Mayewski, M. Wahlen, B. Deck, P. Chylek, B. Johnson and P. Damiano (1996), Historical biomass burning: Late 19th century pioneer agriculture revolution in northern hemisphere ice core data and its atmospheric interpretation, *Journal of Geophysical Research, 101*(D18), 23317-23334 doi: 10.1029/96JD01158

Holland, M.M. and C.M. Bitz (2003), Polar amplification of climate change in coupled models, *Climate Dynamics, 21*, 221-232

Holland, M.M., C.M. Bitz and A.J. Weaver (2001), The influence of sea ice physics on simulations of climate change, *Journal of Geophysical Research, 106,* 19639-19655

Honrath, R.E., M.C. Peterson, S. Guo, J.E. Dibb, P.B. Shepson, and B. Campbell (1999), Evidence of NOx production within or upon ice particles in the Greenland snowpack, *Geophysical Research Letters*, *26*(6), 695-698, doi: 10.1029/1999GL9000779

Honrath, R.E., M.C. Peterson, M.P. Dziobak, J.E. Dibb and M.A. Arsenault and S.A. Green (2000a), Release of NOx from sunlight-irradiated midlatitude snow, *Geophysical Research Letters, 27*(15). 2237-2240, doi: 10.1029/1999GL011286

Honrath, R.E., S. Guo, M.C. Peterson, M.P. Dziobak, J.E. Dibb and M.A. Arsenault (2000b), Photochemical production of gas phase NOx from ice crystal NO_3^-, *Journal of Geophysical Research (Atmosphere), 105*(D19), 24183-24190, doi: 10.1029/2000JD900361

Honrath, R.E., Y. Lu, M.C. Peterson, J.E. Dibb, M.A. Arsenault, N.J. Cullen, and K. Steffen (2002), Vertical fluxes of NOx, HONO, and HNO_3 above the snowpack at Summit, Greenland, *Atmospheric Environment*, *36*(15-16), 2629-2640, doi: 10.1016/S1352-2310(02)00132-2

Houdier, S., S. Perrier, F. Dominé, A. Cabanes, L. Legagneux, A.M. Grannas, C. Guimbaud, P.B. Shepson, H. Boudries, and J.W. Bottenheim (2002), Acetaldehyde and acetone in the Arctic snowpack during the ALERT2000 campaign. Snowpack composition, incorporation processes and atmospheric impact, *Atmospheric Environment*, *36*(15-16), 2609-2618

Huang, J., Q. Fu, W. Zhang, X. Wang, R. Zhang, H. Ye and S.G. Warren (2011), Dust and black carbon in seasonal snow across northern china, *Bulletin of the American Meteorological Society, 92*(2), 175-181, doi:10.1175/2010BAMS3064.1

Huffman, G.J. and G.A. Norman (1988), The supercooled warm rain process and the specification of freezing precipitation, *Monthly Weather Review, 116*, 2172-2182

Hutterli, M.A., J.R. McConnell, R.W. Stewart, H.W. Jacobi, and R.C. Bales (2001), Impact of temperature-driven cycling of hydrogen peroxide (H_2O_2) between air and snow on the planetary boundary layer, *Journal of Geophysical Research (Atmospheres)*, *106*(D14), 15395-15404

Hutterli, M.A., J.R. McConnell, R.C. Bales and R.W. Stewart (2003), Sensitivity of hydrogen peroxide (H_2O_2) and formaldehyde (HCHO) preservation in snow to changing environmental conditions: Implications for ice core records, *Journal of Geophysical Research (Atmosphere), 108*(D1), art. no.-4023, doi: 10.1029/2002JD002528

Hutterli, M.A., J.R. McConnell, G. Chen, R.C. Bales, D.D. Davis and D.H. Lenschow (2004), Formaldehyde and hydrogen peroxide in air, snow and interstitial air at South Pole, *Atmospheric Environment, 38*(32), 5439-5450, doi: 10.1016/j.atmosenv.2004.06.003

Impey, G.A., C.M. Mihele, K.G. Anlauf, L.A. Barrie, D.R. Hastie, and P.B. Shepson (1999), Measurements of photolyzable halogen compounds and bromine radicals during the Polar Sunrise Experiment 1997, *Journal of Atmospheric Chemistry*, *34*(1), 21-37

Iwasaki, T. (1991), Year-to-year variation of snow cover area in the Northern Hemisphere, *Journal of the Meteorological Society Japan, 69,* 209-217

Jackson, A.V. (1999), Atmosphere hydrogen peroxide and organic hydroperoxides: A review, *Critical Reviews in Environmental Science and Technology*, *29*(2), 175-228

Jacobi, H.W., and B. Hilker (2007), A mechanism for the photochemical transformation of nitrate in snow, *Journal of Photochemistry and Photobiology A (Chemistry)*, *185*(2-3), 371-382

Jacobi, H.W., R.C. Bales, R.E. Honrath, M.C. Peterson, J.E. Dibb, A.L. Swanson, and M.R. Albert (2004a), Reactive trace gases measured in the interstitial air of surface snow at Summit, Greenland, *Atmospheric Environment*, *38*(12), 1687-1697

Jacobi, H.W., B. Kwakye-Awuah and O. Schrems (2004b), Photochemical decomposition of hydrogen peroxide (H_2O_2) and formaldehyde (HCHO)in artificial snow, *Annals of Glaciology., 39,* 29-33

Jacobi H.-W., D. Voisin, J.-L. Jaffrezo, J. Cozic and T. Douglas (2012), Chemical composition of the snowpack during the OASIS spring campaign 2009 at Barrow, Alaska, *Journal of Geophysical Research*, 117(D00R13), doi: 10.1029/2011JD016654

Jacobson, M.Z. (2001), Strong radiative heating due to the mixing state of black carbon in atmospheric aerosols, *Nature, 409,* 695-697

Jacobson, M.Z. (2004), Climate response of fossil fuel and biofuel soot, accounting for soot's feedback to snow and sea ice albedo and emissivity, *Journal of Geophysical Research, 109*(D21201), doi: 10.1029/2004JD004945

Jin, Z. and J.J. Simpson (2000), Bidirectional anisotropic reflectance of snow and sea ice in AVHRR channel 1 and channel 2 spectral regions – part II: correction applied to imagery of snow on sea-ice, *IEEE Transactions on Geoscience and Remote Sensing, 38*(2), 999-1015

Jin, Z. and J.J. Simpson (2001), Anisotropic reflectance of snow observed from space over the Arctic and its effect on solar energy balance, *Remote Sensing Environment,, 75*, 63-75

Jin, Z., T.P. Charlock, P. Yang, Y. Xie and W. Miller (2008), Snow optical properties for different particle shapes with application to snow grain size retrieval and MODIS/CERES radiance comparison over Antarctica, *Remote Sensing Environment, 112*, 3563-3581, doi: 10.1016/j.rse.2008.04.011

Johnson, B., K. Shine and P. Forster (2004), The semi-direct aerosol effect: impact of absorbing aerosol on marine stratocumulus, *Quarterly Journal of the Royal Meteorological Society, 130*, 1407

Jones, A.E., R. Weller, E.W. Wolff and H.W. Jacobi (2000), Speciation and rate of photochemical NO and NO_2 production in Antarctic snow, *Geophysical Research Letters, 27*(3), 345-348, doi: 10.1029/1999GL010885

Jones, A.E., R. Weller, P.S. Anderson, H.W. Jacobi, E.W. Wolff, O. Schrems and H. Miller (2001), Measurements of NOx emissions from the Antarctic snowpack, *Geophysical Research Letters, 28*(8), 1499-1502, doi: 10.1029/2000GL011956

Kepler, J. (1966), *On the Six-Cornered Snowflake* (english translation), Clarendon, Oxford

King M.D. and W.R. Simpson (2001), Extinction of UV radiation in Arctic snow at Alert, Canada (82ºN), *Journal of Geophysical Research, 106*(D12), 12499-12507, doi: 10.1029/2011JD900006

King, M., J. France, F. Fisher and H. Beine (2005), Measurement and modelling of UV radiation penetration and photolysis rates of nitrate and hydrogen peroxide in Antarctic sea-ice: an estimate of the production rate of hydroxyl radicals in first year sea-ice, *Journal of Photochemistry and Photobiology A: Chemistry, 176*, 39-49, doi: 10.1016/j.jphotochem.2005.08.032

Kirchstetter, T.W., T. Novakov and P.V. Hobbs (2004), Evidence that the spectral dependence of light absorption by aerosols is affected by organic carbon, *Journal of Geophysical Research (Atmospheres), 109*(D21208), doi: 10.1029/2004JD004999

Kireeva, E.F., O.B. Popovicheva, N.M. Persiantseva, T.D. Kokhlova and N.K. Shonija (2009), Effect of black carbon on the efficiency of water droplet freezing, *Colloid Journal, 70*(3), 353-359, doi: 10.1134/51061933X09030090

Kobayashi, T. and T. Kuroda (1987), snow crystals in: *Morphology of crystals – Part B*, I. Sunagawa (ed), Terra Scientific, Tokya, 645-743

Koch, D. and A.D. Del Genio (2010), Black carbon semi-direct effects on cloud cover: review and synthesis, *Atmospheric Chemistry and Physics, 10*, 7685-7696

Koch D. and J. Hansen (2005), Distant origins of Arctic black carbon: a Goddard Institute for space studies modelE experiment, *Journal of Geophysical Research, 110*(D04204), doi: 10.1029/2004JD005296

Kong, J.A. (1989), Active and passive remote sensing of ice, *Office of Naval Research, Massachusetts Institute of Technology, Report no. AD-A214 863*

Koren, I., J. Kaufman, L. Remer and J. Martins (2004), Measurement of the effect of Amazon smoke on inhibition of cloud formations, *Science, 303,* 1342-1345

Koryakin, V.S. (1986), Decrease in glacier cover on the islands of the Eurasian Arctic during the 20th Century, *Polar Geography and Geology, 10*(2), 157-165, doi: 10.1080/10889378609377283

Krishnan, R. and V. Ramanathan (2002), Evidence of surface cooling from absorbing aerosols, *Journal of Geophysical Research, 29*(1340)

Kuhn, M. (1985), Bidirectional reflectance of polar and alpine snow surfaces, *Annals of Glaciology, 6,* 164-167

Kukla, G., R.G. Barry, A. Hecht and D. Wiesnet (eds) (1986), *Snow Watch '85, Glaciological data,* Report GD-18, 276

Kwok, R. and D.A. Rothrock (2009), Decline in Arctic sea ice thickness from submarine and ICESat records: 1958-2008, *Geophysical Research Letters, 36*(L15501), 36-41

Kwok, R. and N. Untersteiner (2011), The thinning of Arctic sea ice, *Physics Today, 64*(4), 36-41

Law, K.S. and A. Stohl (2007), Arctic air pollution: Origins and impacts, *Science, 315*(5818), 1537-1540, doi: 10.1126/science.1137695

LaChapelle, E.R. (1969), Field guide to snow crystals, University of Washington Press, Seattle.

Lankauf, K.R. (2002), The retreat of glaciers in the Kaffiøyra region (Oscar II Land – Spitsbergen) in the 20th Century, *Geographical Studies, 183,* 221 (in Polish with English summary)

Ledley, T.S. (1991), Snow on sea ice: competing effects in shaping climate, *Journal of Geophysical Research, 96*(D9), 17195-17208

Lee-Taylor, J. and S. Madronich (2002), Calculation of actinic fluxes with a coupled atmosphere-snow radiative-transfer model, *Journal of Geophysical Research (Atmospheres), 107*(D24), 4796, doi: 10.1029/2002JD002084

Lemke, P., P.J. Ren, R.B. Alley, I. Allison, J. Carrasco, G. Flato, Y. Fujii, G. Kaser, P. Mote, R.H. Thomas and T. Zhang (2007), Observations: changes

in snow, ice and frozen ground in: *Climate change 2007: the physical science basis*, Cambridge University Press, UK

Leroux C. and M. FIly (1998), Modeling the effect of sastrugi on snow reflectance, *Journal of Geophysical Research, 103*(E11), 25779=25788

Leroux, C., J.L. Deuze, P. Goloub, C. Sergent and M. Fily (1998), Ground measurements of the polarized bidirectional reflectance of snow in the near-infrared spectral domain: comparisons with model results, *Journal of Geophysical Research, 103*(D16), 19721-19731

Levis, S., G.B. Bonan and P.J. Lawrence (2007), Present-day spring-time high-latitude surface albedo as a predictor of simulated climate sensitivity, *Geophysical Research Letters, 34*(L17703), doi: 10.1029/2007GL030775

Li, W., K. Stamnes, H. Eide and R. Spurr (2007), Bidirectional reflectance distribution function of snow: correction for the Lambertian assumption in remote sensing applications, *Optical Engineering, 46*(6), 066201, doi: 10117/1.2746334

Liao, J., H. Sihler, L.G. Huey *et al.* (2011), A comparison of Arctic BrO measurements by chemical ionization mass spectrometry and long path-differential optical absorption spectroscopy, *Journal of Geophysical Research, 116*(D00R02), doi:10.1029/2010JD014788

Liao, J., L.G. Huey, D.J. Tanner *et al.* (2012), Observation of inorganic bromine (HOBr, BrO and Br_2) speciation at Barrow, Alaska in spring 2009, *Journal of Geophysical Research, 117*(D00R16), doiL10.1029/2011JD016641

Libbrecht, K.G. (2005), The physics of snow crystals, *Reports on Progress in Physics, 68,* 855-895

Lindsay, R.W and D.A. Rothrock (1994), Arctic sea ice albedo from AVHRR, *J. Climate, 7*(11), 1737-1749

Liou, K.N. (1980), *An Introduction to Atmospheric Radiation,* pp. 392, Academic. San Diego, California

Liu, L., M.I. Mischenko, S. Menon, A. Macke and A.A. Lacis (2002), The effect of black carbon on scattering and absorption of solar radiation by cloud droplets*, Radiative Transfer, 74*, 195-204

Long, C.N. and J.J. DeLuisi (1998), Development of an automated hemispheric sky imager for cloud fraction retrievals, paper presented at 10th Symposium on Meteorological Observations and Instrumentation, Am. Meteorological Society, Phoenix, Ariz.

Long, C.N., D.W. Slater and T. Tooman (2001), Total Sky Imager model 880 status and testing results, *ARM TR-006,* 30 pp., U.S. Dep. of Energy, Washington, D.C.

Low, G.K.C., S.R. McEvoy, R.W. Matthews, and J.A. Warburton (1990), Content of chloride, nitrate, and sulphate in snow samples collected from the Snowy Mountain region of Australia., *The Science of the Total Environment.*, *94*, 221-234

MacLellan, C. (2006), Guidelines for Post Processing GER 1500 Dual Field of View Data Files using a FSF Excel Templates, *FSF Technical Report*

Maenhaut, W., P. Cormille, J.M. Pacyna and V. Vitols (1989), Trace element composition and origin of the aerosol in the Norwegian Arctic, *Atmospheric Environment, 19*, 2011-2024

Manabe, S., M.M. Spelman and R.J. Stouffer (1992), Transient responses of a couples ocean-atmosphere model to gradual changes in atmospheric CO_2, *Journal of Climate, 5,* 105-126

Maslanik, J.A., C. Fowler, J. Stroeve *et al.* (2007), A younger, thinner Arctic ice cover: increased potential for rapid, extensive sea-ice loss, *Geophysical Research Letters, 34*(24), Art. No. L24501

Mason, B.J. (1992), Snow crystals, natural and man made, *Contemporary Physics, 33,* 227-243

Matzl, M. and Schneebeli, M. (2006), Measure specific surface area of snow by near-infrared photography, *Journal of Glaciology, 52*(179), 558-564, doi:10.3189/172756506781828412

Maykut, G.A. (1978), Energy exchange over young sea ice in the central Arctic, *Journal of Geophysical Research, 83,* 3646-3658

McCabe, J.R., M.H. Thiemens, and J. Savarino (2007), A record of ozone variability in South Pole Antarctic snow: Role of nitrate oxygen isotopes, *Journal of Geophysical Research (Atmospheres)*, *112*(D12)

McConnell, J.R., R. Edwards, G.L. Kok, M.G. Flanner, C.S. Zender, E.S. Saltzman, J.R. Banta, D.R. Pasteris, M.M. Carter, J.D.W. Kahl (2007), 20^{th}-century industrial black carbon emissions altered Arctic climate forcing, *Science, 317*(5743), 1381-1384, doi: 10.1126/science.1144856

McNeill, V.F., A.M. Grannas, J.P.D. Abbatt, M.Ammann, P.Ariya, T.Bartels-Rausch, F. Domine, D.J. Donaldson, M.I. Guzman, D. Heger, T.F. Kahan, P. Klan, S. Masclin, C. Toubin and D. Voisin (2012), Organic in environmental ices: sources, chemistry and impacts, *Atmospheric Chemistry and Physics Discussion, 12,* 8857-8920, doi: 10.5194/acpd-12-8857-2012

McPeters, R.D., A.J. Krueger, P.K. Chartia and J.R. Herman (1998), Earth Probe Total Ozone Mapping Spectrometer (TOMS) data products user's guide, *NASA Technical Publicaton, 18870296895*, 70 pp.

Meehl, G.A. and W.M. Washington (1990), CO_2 climate sensitivity and snow-sea-ice albedo parameterization in an atmospheric GCM coupled to a mixed-layer ocean model, *Climate Change, 16,* 283-306

Menon, S., D. Koch, G. Beig, S. Sahu, J. Fasullo and D. Orlikowski (2009), Black carbon aerosol and the third polar ice cap, *Atmospheric Chemistry and Physics Discussion, 9*, 26593-26625, doi: 10.5194/acpd-9-26503-2009

Ming, J.*, C.* Xiao, H. Cachier, D. Qin, X. Qin, Z. Li, J. Pu (2009), Black carbon (BC) in the snow of glaciers in west China and its potential effects on albedo, *Atmospheric Research, 92*(1)*,* 114-123, doi: 10.1016/j.atmosres.2008.09.007

Mischenko, M., J.M. Blugach, E.G. Yanovitskij and N.T. Zakharova (1999), Bidirectional reflectance of flat, optically thick particulate layers: An efficient radiative transfer solution and applications to snow and soil surfaces, *Journal of Quantitative Spectroscopy and Radiative Transfer, 63*, 409-432

Morin, S., J. Savarino, M.M. Frey, N. Yan, S. Bekki, J.W. Bottenheim and J.M.F. Martins (2008), Tracing the origin and fate of NO_x in the Arctic atmosphere using stable isotopes in nitrate, *Science, 322*(5902), 730-732, doi:10.1126/science.1161910

Morin, S., J. Erbland, J. Svarino, F. Domine, J. Bock, U. Friess, H.-W. Jacobi, H. Sihler and J.M.F. Martins (2012), An isotopic view on the connection between photolytic emissions of NO_x from the Arctic snowpack and its

oxidation by reactive halogens, *Journal of Geophysical Research, 117*(D00R08), doi:10.1029/2011JD016618

Moser, J.-E. (n.d.), Photochemistry I, lesson 1, *Ecole Polytechnique federale de Lausanne,* accessed 21st August 2012, http://photochemistry.epfl.ch/PC.html

Mossmüller, H., R.K. Chakrabarty and W.P. Arnott (2009), Aerosol light absorption and its measurement: A review, *Journal of Quantitative Spectroscopy and Radiative Transfer, 110*(11), 844-878

Motoyoshi, J., Te. Aoki, M. Hori, O. Abe and S. Mochizuki (2005), Possible effect of anthropogenic aerosol deposition on snow albedo reduction at Shinjo, Japan, *Journal of Meteorological Society Japan, 83A,* 137-148

Mulvaney, R., D. Wagenbach, and E.W. Wolff (1998), Postdepositional change in snowpack nitrate from observation of year-round near-surface snow in coastal Antarctica, *Journal of Geophysical Research (Atmospheres)*, *103*(D9), 11021-11031

Nakaya, U. (1954), *Snow crystals: Natural and Artificial*, Harvard University Press, Cambridge

Neftel, A., J. Beer, H. Oeschger, F. Zurcher, and R.C. Finkel (1985), Sulphate and nitrate concentrations in snow from south Greenland 1895-1978, *Nature*, *314*, 611-613

Nenes, A., W.C. Conant and J.H. Seinfeld (2002), Black carbon radiative heating effects on cloud microphysics and implications for the aerosol indirect effect: 2. Cloud microphysics, *Journal of Geophysical Research (Atmospheres), 107*(4605), 11, doi: 10.1029/2002JD002101

Nicodemus, F.E. (1965), Directional reflectance and emissivity of an opaque surface, *Applied Optics, 4,* 767-773

Nicodemus, F.E., J.C. Richmond, J.J. Hsia, I.W. Ginsberg and T. Limperis (1977), *Geometrical considerations and nomenclature for reflectance*, Washington DC: National Bureau of Standards, US Department of Commerce

Nolin, A.W. and J.C. Stroeve (1997), The changing albedo of the Greenland ice sheet: implications for climate modeling, *Annals of Glaciology, 25*, 51-57

Nolin, A.W., J. Dozier and R.E. Davis (1990), Bidirectional reflectance of optically-thin snow, *Proceedings IGARSS '90,* 1159

Noone, K.J. and A.D. Clarke (1998), Soot scavenging measurements in Arctic snowfall, *Atmospheric Environment, 22*, 2773-2778

Nuth, C., J. Kohler, H.F. Aas, O. Brandt and J.O. Hagen (2007), Glacier geometry and elevation changes on svalbard (1936-90): a baseline dataset, *Annals of Glaciology, 46*(1), 106-116

Nuth, C., G. Moholdt, J. Kohler, J.O. Hagen and A. Kääb (2010), Svalbard glacier elevation changes and contribution to sea level rise, *Journal of Geophysical Research, 15*(F01008), doi: 10.1029/2008JF001223

O'Brien, H. and R.H. Munis (1975), Red and near-infrared spectral reflectance of snow, *Cold Region Research And Engineering Laboratory,* Hanover, N.H.

Oltmans, S.J., B.J. Johnson and J.M. Harris (2012), Springtime boundary layer ozone depletion at Barrow, Alaska: Meteorological influence, year-to-year variation and long-term change, *Journal of Geophysical Research, 117*(D00R18), doi:10.1029/2011JD016889

Oum, K.W., M.J. Lakin and B.J. Finlayson-Pitts (1998), Bromine activation in the troposphere by the dark reaction of O_3 with seawater ice, *Geophysical Research Letters, 25*(21), 3923-3926, doi:10.1029/1998GL900078

Painter, T.H. and J. Dozier (2004), Measurements of the hemispherical-directional reflectance of snow at fine spectral and angular resolution, *Journal of Geophysical Research, 109*(D18115), doi: 10.1029/2003JD004458

Painter, T.H., D.A. Roberts, R.O. Green and J. Dozier (1998), The effect of grain size on spectral mixture analysis of snow-covered area from AVIRIS data, *Remote Sensing of Environment, 65*(3)*,* 320-332

Perovich, D.K. (1996), The optical properties of sea ice, *U.S. Cold Region Research and Engineering Laboratory Monographs, 99,* 3351-3359

Perovich, D.K., G.F. Cota, G.A. Maykut and T.C. Grenfell (1993), Bio-optical observations of first-year arctic sea ice, *Geophysical Research Letters, 20*(11) 1059-1062

Peterson M.C. and R.E. Honrath (2001), Observations of rapid photochemical destruction of ozone in snowpack interstitial air, *Geophysical Research Letters, 28*(3), 511-514, doi:10.1029/2000GL012129

Petty, G.W. (2006), *A First Course in Atmospheric Radiation* (2nd edition)*,* Sundog Publishing, Wisconsin, USA, p. 105

Puxbaum, H., and W. Tscherwenka (1998), Relationships of major ions in snow fall and rime at sonnblick observatory (SBO, 3106 m) and implications for scavenging processes in mixed clouds, *Atmospheric Environment*, *32*(23), 4011-4020

Qian Y., W.I. Gustafson Jr, L.R. Leung and S.J. Ghan (2009), Effects of soot-induced snow albedo change on snowpack and hydrological cycle in western United States based on weather research and forecasting chemistry and regional climate simulations, *Journal of Geophysical Research, 114*(D03108), doi: 10-1029/2008JD011039

Qu, X. and A. Hall (2005), Surface contribution to planetary albedo variability in cryosphere regions, *Journal of Climate, 18*(24), 5239-5252, doi: 10.1175/JCLI3555.1

Quinn, P.K., G. Shaw, E. Angrews, E.G. Dutton, T. Ruoho-Airola and S.L. Gong (2007), Arctic haze: current trends and knowledge gaps, *Tellus B, 59*(1), 99-113, doi: 10.1111/j.1600-0889.2006.00238.x

Rahn, K.A. and R.J. McCaffrey (1979), Long-range transport of pollution aerosol to the Arctic: A problem without borders, *Corrosion Science,* 25-35

Ramanathan, V., P.J. Crutzen, J.T. Kiehl and D. Rosenfield (2001), Atmosphere-Aerosols, climate and the hydrological cycle, *Science*, *294*, 2119-2124

Ramanathan V., Crutzen P., Lelieveld J. *et al* (2008), Global and regional climate changes due to black carbon, *Nature Geoscience*, 1, 221-227

Ramaswamy, V., O. Boucher, J. Haigh *et al.* (2007), Radiative forcing of climate change, in: *IPCC Fourth Assessment Report: Climate Change 2007 (AR4)*, Cambridge University Press, UK

Reay, H.J., J.L France and M.D. King (2012), Decreased albedo, *e*-folding depth and photolytic OH radical and NO_2 production with increasing black carbon content in Arctic snow, *Journal of Geophysical Research, 117*(D00R20), doi: 10.1029/2011JD016630

Rind, D., R. Healy, C. Parkinson and D. Martinson (1995), The role of sea ice in 2 × CO_2 climate model sensitivity. Part I: The total influence of sea ice thickness and extent, *Journal of Climate, 8,* 449-463

Rind, D., R. Healy, C. Parkinson and D. Martinson (1997), The role of sea ice in 2 × CO_2 climate model sensitivity. Part II: Hemispheric dependencies, *Geophysical Research Letters, 24,* 1491-1494

Robinson, D.A. and G. Kukla (1985), Maximum surface albedo of seasonally snow covered lands in the Northern Hemisphere, *Journal of Climate Applied Meteorology, 24.,* 402-411

Robinson, D.A., K.F. Dewey, and R.R. Heim (1993), Global Snow Cover Monitoring - an Update, *Bulletin of the American Meteorological Society*, *74* (9), 1689-1696

Roessler, D. and F. Faxvog (1980), Optical properties of agglomerated acetylene smoke particles at 0.5145-mu m and 10.6-mu m wavelengths, *Journal of the Optical Society of America, 70*(2), 230-235, doi: 10.1364/JOSA.70.000230

Rollin, E.M., D.R. Emery, C.H. Kerr and E.J. Milton (1998), Dual beam reflectance measurements and the need for a field intercalibration procedure, *Developing International Connections, Proceedings of the 24th Annual Conference of the Remote Sensing Society,* Remote Sensing Society, Nottingham, UK, 552-558

Rosen, H., T. Novakov and B.A. Bodhaine (1981), Soot in the arctic, *Atmospheric Environment, 15*(8). 1371-1374

Rothlisberger, R., M.A. Hutterli, E.W. Wolff, R. Mulvaney, H. Fischer, M. Bigler, K. Goto-Azuma, M.E. Hansson, U. Ruth, M.L. Siggaard-Andersen, and J.P. Steffensen (2002), Nitrate in Greenland and Antarctic ice cores: a detailed description of post-depositional processes, *Annals of Glaciology, 35*, 209-216

Rothrock, D.A., Y. Yu and G.A. Maykut (1999), Thinning of the Arctic sea-ice cover, *Geophysical Research Letters, 26*(23), 3469-3472

Saarikoski, S., M. Sillanpää, M. Sofiev, H. Timonen, K. Saarnio, K. Teinilä, A. Karppinen, J. Kukkonen and R. Hillamo (2007), Chemical composition of

aerosols during a major biomass burning episode over northern Europe in spring 2006: Experimental and modeling assessments, *Atmospheric Environment, 41*, 3577-3589

Sandmeier, S.R. (2000), Acquisition of bidirectional reflectance factor data with field goniometers, *Remote Sensing of Environment, 73,* 257-269

Schaepman-Strub, G. M.E. Schaepman, T.H. Painter, S. Dangel and J.V. Martonchik (2006), Reflectance quantities in optical remote sensing – definitions and case studies, *Remotes sensing of environment, 103,* 27-42

Schweiger, A.J., M.C. Serreze and J.R. Key (1993), Arctic sea ice albedo: A comparison of two satellite-derived data sets, *Journal of Geophysical Letters, 20*(1), 41-44

Scoresby, W. (1820), *An account of the Arctic regions with a history and description of the Northern Whale-Fishery (Archibald Constable)*

Sharma, S., D. Lavoue, H. Cachier, L.A. Barrie and S.L. Gong (2004), Long-term trends of the black carbon concentrations in the Canadian Arcitc, *Journal of Geophysical Research, 109*(D15203), doi: 1029/2003JD004331

Sharma, S., E. Andrews, L.A. Barrie, J.A. Ogren and D. Lavoue (2006), Variations and sources of the equivalent black carbon in the high Arctic revealed by long-term observations at Alert and Barrow: 1989-2003, *Journal of Geophysical Research, 111*(D14207), doi: 10.1029/2005JD006581

Shepson, P.B., A.P. Sirju, J.F. Hopper, L.A. Barrie, R.E. Honrath and X.L. Zhou (2002), Radition-transfer modelling of snow-pack photochemical processes during ALERT 2000, *Atmospheric Environment, 26*(15-16), 2663-2670, doi:10.1016/S1352-2310(02)00124-3

Sherman, L.S., J.D. Blum, T.A. Douglas and A. Steffen (2012), Frost flowers growing in the Arctic ocean-atmosphere-sea ice-snow interface: 2. Mercury exchange between the atmosphere, snow and frost flowers, *Journal of Geophysical Research, 117*(D00R10), doi:10.1029/2011JD016186

Shindell, D. (2007), Local and remote contributions to Arctic warming, *Geophysical Research Letters, 34*(L14704), 5, doi: 1029/2007GL030221

Shindell, D.T., M. Chin, R. Dentener *et al.* (2008), A multi-model assessment of pollution transport to the Arctic, *Atmospheric Chemistry and Physics, 8,* 5353-5372

Simpson, W.R., M.D. King, H.J. Beine, R.E. Honrath, and X.L. Zhou (2002), Radiation-transfer modeling of snow-pack photochemical processes during ALERT 2000, *Atmospheric Environment*, *36*(15-16), 2663-2670, doi: 10.1016/S1352-2310(02)00124-3

Sobota, I. (2011), Snow accumulation, melt, mass loss, and the near-surface ice temperature structure of Irenebreen, Svalbard, *Polar Science, 5,* 327-336

Sobota, I. and K.R. Lankauf (2010), Recession of Kaffiøyra region glaciers, Oscar II land, Svalbard, *Bulletin of Geography, 3,* 27-45

Stamnes, K., S.-C. Tsay, W. Wiscombe and K. Jayaweera (1988), Numerically stable algorithm for discrete-ordinate-method radiative-transfer in multiple scattering and emitting layered media, *Applied Optics, 27*(12), 2502-2509, doi: 10.1364/AO.27.002502

Stamnes, K., B. Hamre, J.J. Stamnes, G. Ryzhikov, M. Biryulina, R. Mahoney, B. Hauss and A. Sei (2011), Modeling of radiation transport in coupled atmosphere-snow-ice-ocean systems, *Journal of Quanitative Spectroscopy and Radiative Transfer, 112,* 714-726

Steffen, K. (1987), Bidirectional reflectance of snow at 500-600 nm, in *Large-Scale Effects of Seasonal Snow Cover,* edited by B. Goodison, R.G. Barry and J. Dozier, *IAHS Publ., 166*, pp. 415-425, International Association of Hydrological Science, Wallingford, UK

Stephens, C.R., P.B. Shepson, A. Steffen *et al.* (2012), The relative importance of chlorine and bromine radicals in the oxidation of atmospheric mercury at Barrow, Alaska, *Journal of Geophysical Research, 117*(D00R11), doi: 10.1029/2011JD016649

Stohl A., E. Burkhart, J.F. Forster *et al.* (2006), Pan-Arctic enhancements of light absorbing aerosol concentrations due to North American boreal forest fires during summer 2004. *Journal of Geophysical Research, 111*(D22214), doi: 10.1029/2006JD007216

Stroeve, J.C., A.W. Nolin and K. Steffen (1997), Comparison of AVHRR-derived and in situ surface albedo over the Greenland ice sheet, *Remote Sensing Environment, 62,* 262-276

Sturges, W.T. and L.A. Barriw (1989), Stable lead isotope ratios in arctic aerosols: evidence for the origin of Arctic air pollution, *Atmospheric Environment, 23*(11), 2514-2519

Sturm, M., and G. E. Liston (2003), The Snow Cover on Lakes of the Arctic Coastal Plain of Alaska, *Journal of Glaciology*, *49*(166), 370-380

Sumner, A.L. and P.B. Shepson (1999), Snowpack production of formaldehyde and its effect on the Arctic troposphere, *Nature, 398*, 230-233

Sumner, A.L. *et al.* (2002), Atmospheric chemistry of formaldehyde in the Arctic troposphere at polar sunrise, and the influence of the snowpack,

Atmospheric Environment, 36(15-16), 2553-2562, doi:10.1016/S1352-2310(02)00105-X

Tanikawa, T., T. Aoki, M. Hori, A. Hachikubo, O. Abe and M. Aniya (2006), Monte Carlo simulations of spectral albedo for artificial snowpacks composed of spherical and nonspherical particles, *Applied Optics, 45,* 5310-5319

Tanikawa, T., K. Stamnes, T. Aoki, K. Kuchiki, A. Hachikubo and K. Sugiura (2009), Effect of snow impurities and vertical profile on snow albedo and reflectance, *Eos. Transactions AGU, 90*(52), Fall Meet. Suppl. Abstract C33C-0519

Thomas, J.L., J. Stutz, B. Lefer, L.G. Huey, K. Toyota, J.E. Dibb and R. von Glasow (2011), Modeling chemistry in and above snow at Summit, Greenland – Part 1: Model description and results, *Atmospheric Chemistry and Physics, 11*(10), 4899-4914, doi: 10.5194/acp-11-4899-2011

Thomas, J.L., J.E. Dibb, L.G. Huey, J. Liao, D. Tanner, B. Lefer, R. von Glasow and J. Stutz (2012), Modeling chemistry in and above snow at Summit, Greenland – Part 2: Impact of snowpack chemistry on the oxidation capacity of the boundary layer, *Atmospheric Chemistry and Physics Discussion, 12*, 555105699, doi: 10.5184/acpd-12-5551-2012

Turner, J. and S. Pendlebury (eds.) (2004), The international Antarctic weather forecasting handbook, *British Antarctic Survey* NERC, Cambridge, UK, p. 440

Villena, G. *et al.* (2011), Nitrous acid (HONO) during polar spring in Barrow, Alaska: A net source of OH radicals?, *Journal of Geophysical Research, 116,* D00R07, doi:10.1029/2011JD016643

Villena, G., P. Wiesen, C.A. Cantrell *et al.*, (2012), Nitrous acid (HONO) during polar spring in Barrow, Alaska: A net source of OH radicals?, *Journal of Geophysical Research, 116*(D00R07), doi:10.1029/2011JD016643

Vinnikov, K.Y., A. Robock, R.J. Stouffer *et al.* (1999), Global warming and Northern Hemisphere sea ice extent, *Science,* 286(5546), §934-1937

Voisin, D., J.-L. Jaffrezo, S. Houdier, M. Barret, J. Cozic, M.D. King, J.L. France, H.J. Reay, A. Grannas, G. Kos, P.A. Ariya, H.J. Beine and F. Domine (2012), Carbonaceous species and HUmic LIke Substances (HULIS) in Arctic snowpack during OASIS field campaign in Barrow, *Journal of Geophysical Research, 117*(D00R19), doi: 10.1029/2011JD016612

Walsh, J.E., W.H. Jasperson and B. Ross (1985), Influences of snow cover and soil moisture on monthly air temperature, *Monthly Weather Review, 113,* 756-768

Walsh, J.E., A. Lynch and W. Chapman (1993), A regional model for studies of atmosphere-ice-ocean interaction in the Western Arctic, *Meteorology and Atmospheric Physics, 51*(3-4), 179-194

Wang, P.K. (2002), Shape and microdynamics of ice particles and their effects in cirrus clouds, *Advanced Geophysics, 45,* 1-258

Wang, Y.H., Y. Choi, T. Zheng, D. Davis, M. Buhr, L.G. Huey and W. Neff (2008), Assessing the photochemical impact of snow NOx emissions over Antarctica during ANTCI 2003 (reprinted from Atmospheric Environment, volume 41, p. 3944-3958, 2007), *Atmospheric Environment, 42*(12), 2849-2863, doi: 10.1016/j.atmoserv.2007.07062

Wang, Q, D.J. Jacob, J.A. Fisher, J. Mao, E.M. Leibensperger, C.C. Carouge, P. Le Sager, Y. Kondo, J.L. Jimenez, M.J. Cubison and S.J. Doherty (2011),

Sources of carbonaceous aerosols and deposited black carbon in the Arctic in winter-spring: implications for radiative forcing, *Atmospheric Chemistry and Physics Discussion, 11*, 19395-19442, doi: 10.5194/acpd-11-19395-2011

Wang, X., J. Key, Y. Liu, C. Fowler, J. Maslanik and M. Tschudi (2012), Arctic climate variability and trends from satellite observations, *Advances in Meteorology,* Art. no. 505613

Warneke, C., R. Bahreini, J. Brioude *et al.* (2009), Biomass burning in Siberia and Kazakhstan as an importance source for haze over the Alaskan Arctic in April 2008, *Geophysical Research Letters, 36*(L02813), 6, doi: 10.1029/2008GL036194

Warneke, C., K.D. Froyd, K. Brioude *et al.* (2010), An important contribution to springtime Arctic aerosol from biomass burning in Russia, *Geophysical Research Letters, 37*(L01801), doi; 10.1029/2009GL041816

Warren, S. (1982), Optical properties of snow, *Reviews of Geophysics, 20*(1), 67-89, doi: 10.1029/RG020i001p00067

Warren S.G. (1984), Impurities in snow: effects on albedo and snowmelt, *Annals of Glaciology, 5*, 177-179

Warren, S. (1986), Soot from arctic haze: radiative effect on the arctic snowpack, *Glaciological Data Report GD-18,* p.p.73-77, World Data Center A for Glaciology (snow and ice), Boulder, Colorado

Warren, S.G. and W.J. Wiscombe (1980), A model for the spectral albedo of snow I. Pure snow, *Journal of Atmospheric Science, 37*, 2712-2733

Warren, S. and W. Wiscombe (1980), A model for the spectral albedo of snow II. snow containing atmospheric aerosols, *Journal of Atmospheric Science, 37*(12), 2734-2745

Warren S.G. and Wiscombe W.J. (1985), Dirty snow after nuclear war, *Nature, 313*(6002), 467-470

Warren, S.G. and A.D. Clarke (1990), Soot in the atmosphere and snow surface of Antarctica, *Journal of Geophysical Research, 113,* D14220, doi:10.1029/2007JD009744

Warren, S.G. and R.E. Brandt (2008), Optical constants of ice from the ultraviolet to the microwave: A revised compilation, *Journal of Geophysical Research (Atmospheres), 113*(D14220, doi: 10.1029/2007JD009744

Warren, S.G., R.E. Brandt and P.O. Hinton (1998), Effect of surface roughness on bidirectional reflectance of Antarctic snow, *Journal of Geophysical Research, 103*(E11), 25789-25807

Warren, S.G., R.E. Brandt and T.C. Grenfell (2006), Visible and near-ultraviolet absorption spectrum of ice from the transmission of solar radiation into snow, *Applied Optics, 45*(21), 5320-5334, doi: 10.1354/AO.45.005320

Weller, R., F. Traufetter, H. Fischer, H. Oerter, C. Piel, and H. Miller (2004), Postdepositional losses of methane sulfonate, nitrate, and chloride at the European Project for Ice Coring in Antarctica deep-drilling site in Dronning Maud Land, Antarctica, *Journal of Geophysical Research-Atmospheres*, *109*(D7), art. no.-D07301

Wieslaw, Z. (2005), Response of the Nordenskiöld Land (Spitsbergen) glaciers Grumantbreen, Håbergbreen and Dryadbreen to the climate warming after the Little Ice Age, *Annals of Glaciology, 42*(1), 189-194(6)

Winebrenner, D.P., L. Tsang, B. Wen and R. West (1989), Sea ice characterization measurements needed for testing of microwave remote sensing models, *IEEE Journal of Oceanic Engineering, 14*(2), 149-158

Wiscombe, W.J. and S. Warren (1980), A model for the spectral albedo of snow. I: Pure snow, *Journal of Atmospheric Science, 37*(12), 2712-2733

Wolff, E. (1995), Nitrate in polar ice, in: *Ice core studies of global biochemical cycles,* NATO ASI Series I, vol. 30, R.J. Delmas (ed), Springer-Verlag, New York, N.Y., 195-224

Wolff, E.W., J.S. Hall, R. Mulvaney, E.C. Pasteur, D. Wagenbach, and M. Legrand (1998), Relationship between chemistry of air, fresh snow and firn cores for aerosol species in coastal Antarctica, *Journal of Geophysical Research-Atmospheres*, *103*(D9), 11057-11070

Worby, A.P. and I. Allison (1991), Ocean-atmosphere energy exchange over thin, variable concentration Antarctic pack ice, *Annuals of Glaciology, 15*, 184-190

Xie, Y., P. Yang, B.-C. Gao, G.W. Kattawar and M.I Mischchenko (2006), Effect of ice crystal shape and effective size on snow bidirectional reflectance, *Journal of Quantitative Spectroscopy and Radiative Transfer, 100,* 457-469, doi: 10.1016/j.jqsrt.2005.11.056

Yang, J., R.E. Honrath and T.C. Grenfell (2006), Visible and near-ultraviolet absorption spectrum of ice from transmission of solar radiation into snow, *Applied Optics, 45*(21), 5320-5334, doi:10.1364/AO.45.005320

Zhou, X.L., H.J. Beine, R.E. Honrath, J.D. Fuentes, W. Simpson, P.B. Shepson, and J.W. Bottenheim (2001), Snowpack photochemical production of

HONO: a major source of OH in the Arctic boundary layer in springtime, *Geophysical Research Letters*, *28*(21), 4087-4090

Impacts of a Warming Arctic: Arctic Climate Impact Assessment (2004), ACIA Overview report, Cambridge University Press

Appendix 1

Hydroxyl radical and NO_x production rates, black carbon concentrations and light-absorbing impurities from field measurements of light penetration and nadir reflectivity of on-shore and off-shore coastal Alaskan snow

Hydroxyl radical and NO_x production rates, black carbon concentrations and light-absorbing impurities in snow from field measurements of light penetration and nadir reflectivity of onshore and offshore coastal Alaskan snow

J. L. France,[1] H. J. Reay,[1] M. D. King,[1] D. Voisin,[2] H. W. Jacobi,[2] F. Domine,[2] H. Beine,[3] C. Anastasio,[3] A. MacArthur,[4] and J. Lee-Taylor[5]

Received 28 July 2011; revised 6 January 2012; accepted 6 January 2012; published 9 March 2012.

[1] Photolytic production rates of NO, NO_2 and OH radicals in snow and the total absorption spectrum due to impurities in snowpack have been calculated for the Ocean-Atmosphere-Sea-Ice-Snowpack (OASIS) campaign during Spring 2009 at Barrow, Alaska. The photolytic production rate and snowpack absorption cross-sections were calculated from measurements of snowpack stratigraphy, light penetration depths (*e*-folding depths), nadir reflectivity (350–700 nm) and UV broadband atmospheric radiation. Maximum NO_x fluxes calculated during the campaign owing to combined nitrate and nitrite photolysis were calculated as 72 nmol m^{-2} h^{-1} for the inland snowpack and 44 nmol m^{-2} h^{-1} for the snow on sea-ice and snowpack around the Barrow Arctic Research Center (BARC). Depth-integrated photochemical production rates of OH radicals were calculated giving maximum OH depth-integrated production rates of ~160 nmol m^{-2} h^{-1} for the inland snowpack and ~110–120 nmol m^{-2} h^{-1} for the snow around BARC and snow on sea-ice. Light penetration (*e*-folding) depths at a wavelength of 400 nm measured for snowpack in the vicinity of Barrow and snow on sea-ice are ~9 cm and 14 cm for snow 15 km inland. Fitting scaled HULIS (HUmic-LIke Substances) and black carbon absorption cross-sections to the determined snow impurity absorption cross-sections show a "humic-like" component to snowpack absorption, with typical concentrations of 1.2–1.5 μgC g^{-1}. Estimates of black carbon concentrations for the four snowpacks are ~40 to 70 ng g^{-1} for the terrestrial Arctic snowpacks and ~90 ng g^{-1} for snow on sea-ice.

Citation: France, J. L., H. J. Reay, M. D. King, D. Voisin, H. W. Jacobi, F. Domine, H. Beine, C. Anastasio, A. MacArthur, and J. Lee-Taylor (2012), Hydroxyl radical and NO_x production rates, black carbon concentrations and light-absorbing impurities in snow from field measurements of light penetration and nadir reflectivity of onshore and offshore coastal Alaskan snow, *J. Geophys. Res.*, *117*, D00R12, doi:10.1029/2011JD016639.

1. Introduction

[2] It has been widely demonstrated that snowpack acts as a photolytic source of gaseous species that can be subsequently released to the atmosphere. Fluxes of NO, NO_2 and HONO have been observed from snow cover [*Beine et al.*, 2001, 2002, 2003, 2008; *Dibb et al.*, 2004; *Grannas et al.*, 2007; *Honrath et al.*, 1999, 2000a, 2002; *Jones et al.*, 2000, 2001; *Wang et al.*, 2008], with laboratory studies demonstrating that the source of NO_x ($NO + NO_2$) is through the photolysis of nitrate and nitrite [*Anastasio and Chu*, 2009; *Boxe and Saiz-Lopez*, 2008; *Chu and Anastasio*, 2003; *Cotter et al.*, 2003; *Couch et al.*, 2000; *Dubowski et al.*, 2001, 2002; *Honrath et al.*, 2000b]:

$$NO_3^- + h\nu \xrightarrow{J_{NO_3^-}} NO_2 + O^- \quad (1a)$$

$$O^- + H_2O \rightarrow OH + OH^- \quad (1b)$$

Snowpack may be a highly-oxidizing medium through the photoproduction of hydroxyl radicals from the photolysis

[1]Department of Earth Sciences, Royal Holloway, University of London, Egham, UK.
[2]Laboratoire de Glaciologie et Géophysique de l'Environnement, CNRS/Université Joseph Fourier – Grenoble 1, St Martin d'Hères, France.
[3]Department of Land, Air, and Water Resources, University of California, Davis, California, USA.
[4]NERC Field Spectroscopy Facility, Grant Institute, School of GeoSciences, University of Edinburgh, Edinburgh, UK.
[5]Atmospheric Chemistry Division, National Center for Atmospheric Research, Boulder, Colorado, USA.

0148-0227/12/2011JD016639

of hydrogen peroxide (2), of nitrite (3) and nitrate anions (1).

$$H_2O_2 + h\nu \xrightarrow{J_{H_2O_2}} 2OH \quad (2)$$

$$NO_2^- + h\nu \xrightarrow{J_{NO_2^-}} NO + O^- \quad (3)$$

[3] Hydroxyl radicals, OH, are very reactive and will react with snowpack chemical impurities, and may release gaseous products from the snowpack. Hydroxyl radicals are implicated in the production of acetaldehyde, formaldehyde and oxygenated organic compounds in the snow, [*Anastasio et al.*, 2007; *Couch et al.*, 2000; *Dassau et al.*, 2002; *Grannas et al.*, 2004, 2007; *Shepson et al.*, 1996; *Wang et al.*, 2008]. Some of these species are subsequently released to the interstitial air of the snow and to the atmosphere. [*Couch et al.*, 2000; *Grannas et al.*, 2007; *Hutterli et al.*, 2003, 2004; *Jacobi et al.*, 2004; *Shepson et al.*, 1996].

[4] Field measurements of photoformation rates of OH radicals in snow at Summit, Greenland show that photolysis of hydrogen peroxide is the main source, with a small contribution from photolysis of nitrate (reaction (1)) [*Anastasio et al.*, 2007] and nitrite (reaction (3)) [*Bock and Jacobi*, 2010; *Thomas et al.*, 2011]. Modeling studies have demonstrated that 93–99% of OH radical production in snowpack is likely to be due to hydrogen peroxide photolysis [*Anastasio et al.*, 2007; *France et al.*, 2007]. The importance of OH radicals in snowpack chemistry has been recently demonstrated through chemical box modeling [*Bock and Jacobi*, 2010; *Thomas et al.*, 2011], showing that the concentration of OH radicals in the quasi-liquid layer surrounding snow grains is a rate controlling factor in the release of Br_2 into the interstitial air [*Abbatt et al.*, 2010]; similar reactions also occur in sea-salt particles [e.g., *George and Anastasio*, 2007]. Sea-ice has also been demonstrated to be a source of gaseous bromine through the reaction of sea-ice with ozone [*Oum et al.*, 1998]. Mixing ratios and measurements of reactive gas-phase halogens have been compared to modeled values with good agreement, giving evidence that emissions from snow covered surfaces may be responsible for gas-phase halogens in the boundary layer [*Domine and Shepson*, 2002; *Thomas et al.*, 2011].

[5] Photolytic production rates of NO_2 and OH radicals within snowpack have been calculated previously for several terrestrial snowpack environments by some of the authors of this work, including Arctic, midlatitude and Antarctic snowpacks [*Anastasio et al.*, 2007; *Beine et al.*, 2006; *Chu and Anastasio*, 2007; *Fisher et al.*, 2005; *France et al.*, 2007, 2010; *King and Simpson*, 2001; *Simpson et al.*, 2002], but the Alaskan site of Barrow provides an opportunity to measure optical properties of coastal snow both on land and on sea-ice.

[6] The work described in this paper reports field measurements of *e*-folding (light penetration) depths and nadir reflectivity [*Duggin and Philipson*, 1982] of Alaskan snowpacks on land and on sea-ice. Light penetration (*e*-folding depths) are defined as in (4) below.

$$I_d = I_{d'} e^{\frac{d'-d}{\varepsilon(\lambda)}} \quad (4)$$

where I_d is the irradiance at a depth d within the snowpack, d' is the initial depth into the snowpack (d is a deeper depth than d'), $\varepsilon(\lambda)$ is the asymptotic *e*-folding depth (the depth at which irradiance becomes $1/e$ ($\sim$37%) of its initial value) for a specific wavelength. Note, both d and d' are usually greater than a few cm into the snow to ensure the measured irradiance is diffuse only.

[7] Measurements of nadir reflectance, *e*-folding depth and snow stratigraphy (including snow density) are used to determine light absorption and scattering cross-sections from snow-atmosphere coupled radiative-transfer calculations. The scattering and absorption cross-sections are used to calculate spherical irradiance ("actinic flux") in the snowpack as a function of solar zenith angle and depth to allow photolysis rate coefficients of reactions (1) and (2) to be calculated. The variation of the absorption cross-section with wavelength is due to changes in the absorption cross-section of ice and the absorption due to impurities within the snow. The absorption cross-section of ice is well studied [*Warren and Brandt*, 2008], so the absorption spectrum of light-absorbing impurities can be determined. The variation of absorption cross-section due to impurities of the snowpacks with wavelength is compared to absorption cross-sections of known absorbing species in the snowpack in an attempt to identify and quantify the amount of absorbers.

[8] The measurements of snowpack optical and physical properties made at Barrow, Alaska were part of the larger OASIS (Ocean-Atmosphere-Sea Ice-Snowpack) international field campaign.

[9] The aims of the work presented here were as follows:

[10] 1. Measure the optical properties of Barrow snowpacks by measuring light penetration depth, surface nadir reflectance and the snowpack stratigraphy.

[11] 2. Calculate wavelength-dependent cross-sections for light absorption due to impurities and for scattering from measurements of *e*-folding depth and snowpack surface reflectivity.

[12] 3. Calculate in-snow production rates of NO, NO_2 and OH radicals for the duration of the campaign as an estimation of the potential flux of NO_2 or NO from the snowpack.

[13] 4. Determine the identity and amount of light-absorbing impurities in the Alaskan snowpack from the absorption cross-section determined from field measurements of the snowpack.

2. Methods

[14] The majority of the basic fieldwork and modeling methodologies used here have been described in detail previously [e.g., *Beine et al.*, 2006; *Fisher et al.*, 2005; *France et al.*, 2007, 2010, 2011a]. Only a brief description will be given here, with emphasis given to the new and improved sections of the methodology.

2.1. Field Methods

[15] Snowpacks within 1–15 km of the coastal Barrow Arctic Research Centre (BARC) (71.32063°N, 156.6748°W) were investigated during the spring of 2009 as part of the Barrow OASIS (Ocean-Atmosphere-Sea Ice-Snowpack) campaign. Approximately 50 test snowpits were dug, with 15 snowpacks studied optically at locations around the OASIS field site and 4 snowpacks of the 15 (with stratigraphic sequences representative of the different snowpack

types) chosen for detailed analysis: (1) a soft snowpack close to the BARC, (2) a hard snowpack close to the BARC, (3) a snowpack 15 km inland, and (4) a snowpack on sea-ice near Point Barrow. Snowpits at these four locations were deeper than average [see *Domine et al.*, 2012] to facilitate optical measurements. Furthermore, as also detailed by *Domine et al.* [2012], the snowpack stratigraphy was variable at the 1 m horizontal scale.

[16] At each of the 15 sites, a snowpit was dug ~1 m wide by ~1 m length, down to the ground or to the sea-ice, ensuring the snow was not contaminated by human or animal influence. At each site, measurements of light penetration depth, surface reflectance and stratigraphy were undertaken as described below.

2.1.1. Light Penetration (*e*-Folding) Depth

[17] Light-penetration depth was measured via a set of simultaneous irradiance measurements, after the approach of *King and Simpson* [2001]. Probes consisted of bundles of six fiber optics encased separately in 1/4 inch diameter stainless-steel tubing and with a cosine diffuser on the end of each fiber. The probes were 50 cm long and 49 cm was inserted into the snowpack. Probes were placed horizontally into the snowpack with 5–20 cm horizontal separation between the fibers, and with approximately 3–5 cm vertical separation between different probes, i.e., six irradiance measurements were taken concurrently at different depths in the same snowpack. The detector comprised 6 independent spectrometers (Ocean Optics USB2000) assembled in a single field-portable housing and operated from batteries. The snow pits were not back-filled with excavated material during irradiance measurements for calculation of *e*-folding depth because this would not reproduce the irradiance field within the snowpit owing to the mechanical properties of the snow. Previously, *France et al.* [2011a] have crudely argued that only 1% of the diffuse light measured by the deepest fiber optic probes has originated from the snowpit wall with the rest originating from the snow surface. For the shallowest probes the diffuse light measured by the probes from the snowpit wall is significantly less [*France et al.*, 2011a].

[18] The 6-spectrometer instrument is capable of recording spectral irradiance from 190 nm to 1100 nm at a resolution of < 1 nm simultaneously. The optical properties of the fiber optics constrained the effective wavelength range of measurements within snowpack from 350 nm to 700 nm. The 6-spectrometer instrument removes the need to calibrate each individual measurement of in-snow irradiance with a downwelling atmospheric irradiance measurement as the measurements at all depths are effectively simultaneous, in contrast to previous studies [e.g., *Beine et al.*, 2006; *Fisher et al.*, 2005; *France et al.*, 2011b]. Dark spectra were recorded in the field by capping the fiber optic probes to allow measurement (and the removal) of electrical noise. The spectrometers were used at ambient temperature, which significantly reduces the electrical noise. The sensitivity of each fiber and spectrometer were calibrated relative to each other by simultaneously measuring the intensity of the solar radiation above the snowpack with all 6 fiber optic probes pointing at the same target. The determination of an *e*-folding depth does not require an absolute calibration of the fiber optic probes or spectrometer efficiency, just the relative calibration between fibers and spectrometers. A wavelength calibration for each spectrometer was performed using a mercury-argon lamp in the field and an intensity calibration for each fiber was performed using a NIST traceable halogen light source to monitor fiber optical transmission for any decay. The signal-to-noise ratio of the spectrometers is typically better than 300:1.

2.1.2. Nadir Reflectivity

[19] The reflectance measurements were carried out using a portable nadir reflectance method [*Duggin and Philipson*, 1982], previously employed in midlatitude and polar environments to measure the reflectivity of the snowpack surface [*Beine et al.*, 2006; *Fisher et al.*, 2005]. The method uses two spectroradiometers (GER 1500 s) mounted upon tripods, one to measure radiance of a reference panel and one to measure the radiance of the snow surface simultaneously. Simultaneous measurement removes any influence of changing overhead sky conditions. The spectroradiometers were calibrated in the field by simultaneous measurement of the reflectance of the standard reference panel with both spectroradiometers before and after measurements of the snowpack. All measurements of snowpack reflectance were taken close to solar noon and during stable sky conditions. At each site, a transect of 10–15 reflectance measurements (within ~1–10 m) was averaged.

[20] The snowpack stratigraphy was measured using the guidelines from the international classification of seasonal snow [*Fierz et al.*, 2009], with measurements of snow density made every 5 cm using a snow cutter (volume = 284 cm^3) and temperature-depth profiles of the snowpack recorded using a NIST traceable temperature probe.

2.2. Radiative-Transfer Modeling and Photolysis Calculations

2.2.1. Determining Absorption and Scattering Coefficients

[21] Wavelength-dependent cross-sections of light scattering, $\sigma_{scatt}(\lambda)$, and absorption due to impurities, $\sigma^{+}_{abs}(\lambda)$, were determined for the four Barrow snowpacks from measurements of light penetration (*e*-folding depth) and surface reflectance by the method of *Lee-Taylor and Madronich* [2002]. Briefly, this involves performing radiative-transfer calculations of reflectance and *e*-folding depths for a range of combinations of σ_{scatt} and σ^{+}_{abs}, and interpolating to find unique solutions for $\sigma_{scatt}(\lambda)$ and $\sigma^{+}_{abs}(\lambda)$ that satisfy the field measurements of both reflectivity and *e*-folding depth at each wavelength. Radiative-transfer calculations were performed using the TUV-snow (Tropospheric Ultraviolet and Visible-snow) model [*Lee-Taylor and Madronich*, 2002], a discrete-ordinates [*Stamnes et al.*, 1988] coupled atmosphere-snow model running 8 streams with a pseudo-spherical correction. The model configuration in the current study used 106 snowpack levels (with 1 mm spacing in the top 0.5 cm and 1 cm spacing for the rest of the 1 m snowpack) and 80 atmospheric levels spaced at 1 km intervals, clear skies, no atmospheric aerosol, an Earth-Sun distance (based upon the day of measurement), and overhead ozone column (from the day of measurement [*McPeters et al.*, 1998]). The snow asymmetry factor, g, was set to 0.89 based on a Mie calculation of a 100 micron particles [*Wiscombe and Warren*, 1980]. As in previous work we have not adjusted the size of the snow grain. An under-snow albedo of 0.1 was specified. The recommended absorption cross-section for ice from Warren and Brandt [*Warren and*

Table 1. Data Used As Inputs for the Modeling of Photolysis Rate Coefficients Using TUV-Snow for Each of the Barrow Snowpacks

Snowpack	Snow Temperature (°C)	Snow Density (g cm^{-3})	Location		Elevation (m)	Average Column Ozone[a] (Dobson Units)
			Longitude	Latitude		
Hard	−15	0.39	156.67243°W	71.31896°N	∼5	460
Soft	−18	0.38	156.67634°W	71.31987°N	∼5	460
Snow on sea-ice	−24	0.40	156.45239°W	71.38469°N	0	460
Inland	−28	0.30	156.47471°W	71.20259°N	∼2	460

[a]Ozone conditions determined from the NASA TOMS program as an average of the campaign duration to 2 significant figures [*McPeters et al.*, 1998].

Brandt, 2008] was used, and linearly interpolated from 200 nm to 400 nm where the absorption is too small to be reliably measured at present.

2.2.2. Modeling Snowpack Absorption By Impurities

[22] Plotting the cross-section owing to absorption by impurities versus wavelength for each snowpack results in the absorption spectrum of all the light-absorbing impurities in the snowpack. The absorption spectrum is a summation of all of the absorbers in the snowpack. The absorbers in the visible wavelengths are probably black carbon, brown carbon (including HULIS) and dust [*Anastasio and Robles*, 2007; *Doherty et al.*, 2010; *France et al.*, 2011b; *Grenfell et al.*, 2011; *Warren*, 1984; *Warren and Clarke*, 1990; *Warren et al.*, 2006]. Previous work assumed that absorption due to impurities was due to black carbon [*Lee-Taylor and Madronich*, 2002]. However, in the work presented here the range of wavelengths (350–600 nm) studied allows identification of the light-absorbing impurities by their different absorption spectra.

2.2.3. Calculating Photolytic Rate Constants and Fluxes With Clear and Diffuse Skies

[23] The spherical irradiance ("actinic flux") in the snowpack is needed to calculate the photolytic rate constants for reactions (1)–(3). Spherical irradiance was calculated using the TUV-snow model [*Lee-Taylor and Madronich*, 2002] at 1 nm intervals from 290 to 700 nm and at 106 calculation depths in the 1 m model snowpack, using the wavelength dependent snowpack optical properties $\sigma^{+}_{abs}(\lambda)$ and $\sigma_{\mathrm{scatt}}(\lambda)$, determined from field data in section 2.2.2. Snowpacks thicker than 3–4 *e*-folding depths can be considered optically semi-infinite as over 95% of sunlight is attenuated by 3 *e*-folding depths [*France et al.*, 2011a]. All the snowpacks studied in the field work were optically semi-infinite. Thus, for modeling photolysis rate constants and spherical irradiance in the snowpack, the actual recorded depth of the snowpack in the field or a larger depth can be considered without affecting the result. In this work all snowpacks are considered to be 1 m deep for comparison. All other conditions are as stated in section 2.2.1.

[24] Photochemical rate coefficients, *J*, for the photolytic reactions (1)–(3) were calculated according to equation (5) for solar zenith angles between 0 and 90° for clear sky and diffuse sky conditions.

$$J(\theta,z)=\int_{\lambda_y}^{\lambda_x}\sigma(\lambda,T)\Phi(\lambda,T)I(\lambda,\theta,z)d\lambda \tag{5}$$

where σ is the absorption cross-section of the chromophore (NO_2^-, NO_3^- or H_2O_2), Φ is the quantum yield for photolysis, I is the spherical irradiance, T is the snowpack temperature, λ is the wavelength and θ is the solar zenith angle.

[25] The absorption cross-sections and temperature dependent quantum yields for reactions (1), (2) and (3) are from *Chu and Anastasio* [2003]; *Chu and Anastasio* [2005] and *Chu and Anastasio* [2007], respectively. For the calculation of photochemical rate constants, the average campaign overhead column ozone is used [*McPeters et al.*, 1998]; the snowpack location, temperatures and densities are also shown in Table 1.

[26] Photolysis rate coefficients were calculated for clear skies (no cloud or aerosol) and diffuse sky conditions. To obtain diffuse sky conditions a cloud layer 1 km above the ground, 100 m thick, with an optical depth of 16, an asymmetry factor of 0.85 and a single scattering albedo of 0.9999 was included. Depth-integrated production rates, or maximum fluxes (assuming that all the photoproduced NO_2 or NO is liberated from the snowpack), *F*, are calculated using (6).

$$F=[x]\int_{z=0}^{z=1}J\,dz \tag{6}$$

where z is the depth into the snowpack, and [*x*] is the concentration of the chromophore, H_2O_2, NO_2^- or NO_3^-.

[27] Equation (6) assumes a depth-independent concentration of chromophore. *France et al.* [2007] showed depth variation of chromophore concentration to be much less important relative to the depth-dependence of the spherical irradiance. A constant nitrate concentration in the snowpack of 3.9 μmol l^{-1} was used (an average concentration of more than 100 samples including all encountered snow types as shown in Figure 1a [*Jacobi et al.*, 2012]). Measurements of [H_2O_2] in snowpack during the Barrow campaign were

Figure 1. (a) snowpack stratigraphy based on the notation of *Fierz et al.* [2009], (b) wavelength dependent snowpack nadir reflectance (markers every 10 data points for clarity), (c) wavelength dependent *e*-folding depths (markers every 10 data points for clarity), (d) snowpack density profiles and (e) snowpack temperature profiles for each characteristic snowpack. For the *e*-folding depths plotted in Figure 1c, the fiber optic probes were placed between the following depths: hard snow 6 cm to 19 cm, snow on sea-ice 4 cm to 20 cm, soft snow 3 cm to 28 cm and for the inland snowpack the probes were placed at depths between 7 cm and 31 cm.

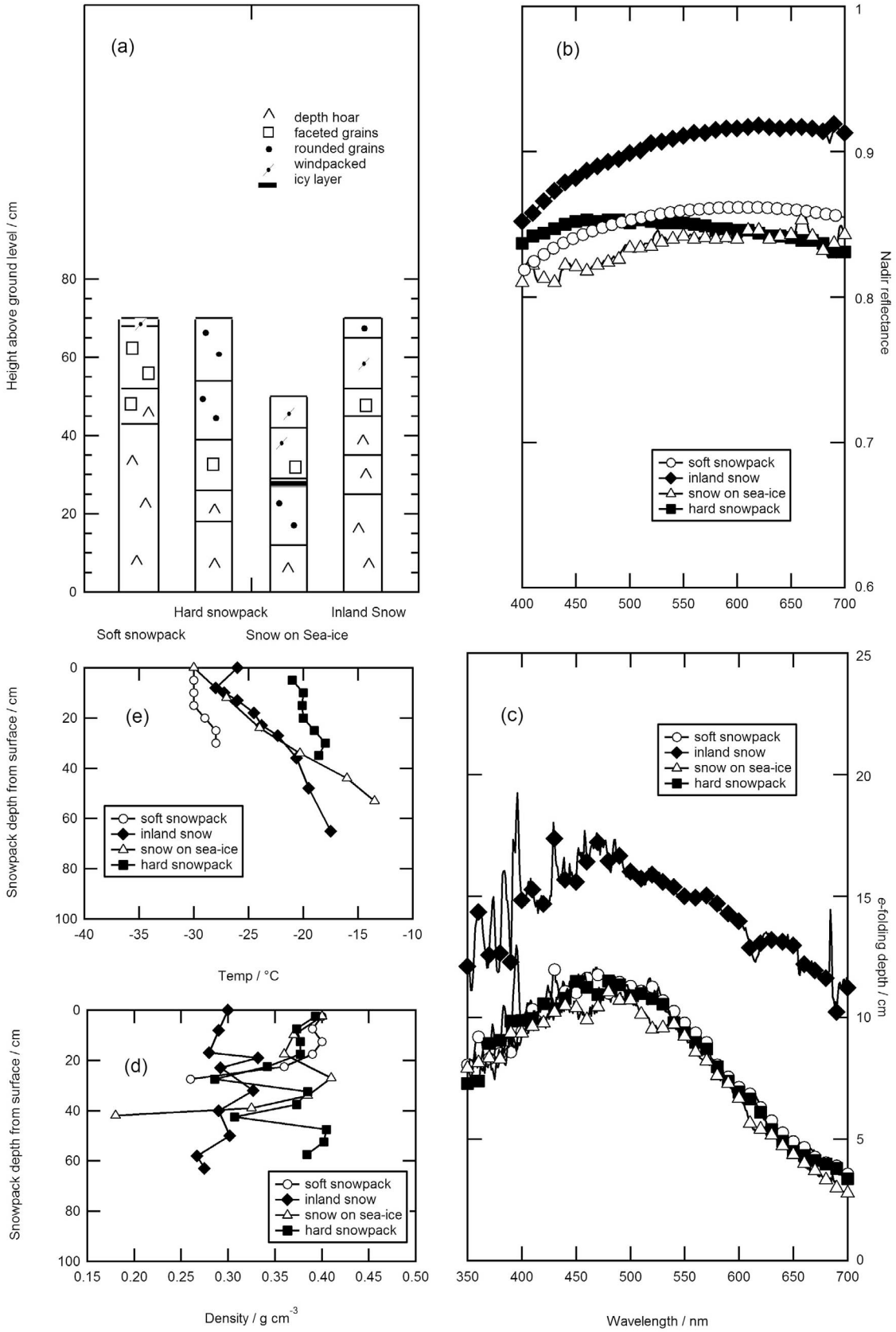
(a)
depth hoar
faceted grains
rounded grains
windpacked
icy layer
Height above ground level / cm
Soft snowpack
Hard snowpack
Snow on Sea-ice
Inland Snow
(b)
soft snowpack
inland snow
snow on sea-ice
hard snowpack
Nadir reflectance
(e)
Snowpack depth from surface / cm
Temp / °C
(d)
Density / g cm-3
(c)
e-folding depth / cm
Wavelength / nm

Figure 1

made at ~500 locations in the Barrow area, with concentrations found to be fairly invariant with depth [*Beine et al.*, 2012]. The calculated depth-integrated production rates of OH radicals used a concentration of H_2O_2 of 0.4 μmol l^{-1}, the average concentration measured in the top 10 cm of snowpack [*Beine et al.*, 2012]. Concentrations of NO_2^- were measured at a single site near the BARC over a period of 36 h in surface snow and at depth of 5 cm [*Villena et al.*, 2012]. The average NO_2^- measured in these samples was 0.02 μmol l^{-1}. The single-site average nitrite concentration is used for all of our snowpack calculations.

2.2.4. Calculating Photolytic Rate Constants and Fluxes From the Snowpack for Sky Conditions During the OASIS Campaign

[28] Depth-integrated production rates or fluxes were calculated as a function of solar zenith angle for clear sky or thick cloud cover (i.e., completely diffuse). To calculate the depth-integrated production rates (fluxes) for the duration of the campaign required an identification of sky conditions as "clear sky" or "diffuse" and then a scaling of depth-integrated production rates (calculated from a solar zenith angle dependence) by actual downwelling UV atmospheric irradiance at the surface. The sky conditions were monitored using two continuous measurements: broadband, downwelling irradiance (wavelength 295 nm to 385 nm) using a TUVR (Tropospheric Ultraviolet and Visible Radiation) Eppley flat-plate radiometer sited 0.5 m above the snowpack approximately 800 m South of the BARC, and hemispheric sky images (and retrievals of fractional sky cover for periods when the solar elevation was greater than 10 degrees) using a total sky imager (Yankee Environmental Systems). The total sky imager was based at Atmospheric Radiation Measurement site at the North Slope, Alaska (71° 19′ 23.73" N, 156° 36′ 56.70" W) [*Long and DeLuisi*, 1998; *Long et al.*, 2001], within a few kilometers of the measurement site and the Eppley TUVR. Every minute of the measurement campaign from Julian Day 60 to Day 90 was assigned as diffuse sky conditions or clear (diffuse and direct), depending on whether the sun's direct beam was occluded by cloud using the total sky imager [*Long and DeLuisi*, 1998; *Long et al.*, 2001]. The radiative-transfer calculations of section 2.2.3 were repeated to calculate the 'flat-plate' broadband downwelling irradiance from 295 nm to 385 nm as measured by a surface TUVR Eppley radiometer for the diffuse and clear sky conditions described in section 2.2.3 as a function of solar zenith angle under exactly the same conditions as the photolysis rate constants were calculated. The calculated photochemical fluxes of NO_2 and OH radicals were then scaled using,

$$F(\mathrm{OH}) = \frac{I_{\mathrm{TUVR\ measured}}}{I_{\mathrm{TUVR\ modeled}}} \times F(\mathrm{OH})_{\mathrm{modeled}}, \quad (7)$$

$$F(\mathrm{NO_2}) = \frac{I_{\mathrm{TUVR\ measured}}}{I_{\mathrm{TUVR\ modeled}}} \times F(\mathrm{NO_2})_{\mathrm{modeled}}, \quad (8)$$

$$F(NO) = \frac{I_{\mathrm{TUVR\ measured}}}{I_{\mathrm{TUVR\ modeled}}} \times F(\mathrm{NO})_{\mathrm{modeled}}, \quad (9)$$

to produce photochemical production rates of OH radicals, NO_2 and NO at a 1 min resolution for the whole of the Barrow campaign period. In equations (7), (8) and (9), $I_{\mathrm{TUVR\ measured}}$ is the downwelling broadband irradiance for 295–385 nm measured by the Eppley TUVR and $I_{\mathrm{TUVR\ modeled}}$ is the calculated downwelling broadband irradiance for 295–385 nm as a function of solar zenith angle and sky conditions. The quantity F(OH) is the depth-integrated production rate of hydroxyl radicals and $F(\mathrm{OH})_{\mathrm{modeled}}$ is the depth-integrated production rate of hydroxyl radicals calculated by the radiative-transfer modeling of section 2.2.3. Note that the values of $F(\mathrm{OH})_{\mathrm{modeled}}$ and $I_{\mathrm{TUVR\ modeled}}$ correspond to the same solar zenith angle and sky conditions (i.e., clear or diffuse sky). The linear relationship of $F(\mathrm{OH})_{\mathrm{modeled}}$ and $I_{\mathrm{TUVR\ modeled}}$ for diffuse and clear sky conditions is demonstrated in section 3.

3. Results

[29] The results are presented in three sections: field measurements, snowpack optical coefficients determined from the field measurements, and the calculated production rates of NO_2, NO and OH radical within the snowpack. Data from the four snowpacks are presented: Soft and hard snows (prevalent around Barrow and BARC), snow on sea-ice, and inland snow (~ 15 km inland from Barrow).

3.1. Field Results

[30] Measurements of snowpack stratigraphy, snowpack depth, *e*-folding depth, surface reflectance, snowpack density and temperature are shown in Figure 1 for each of the four individual, representative snowpacks. The snowpack stratigraphy in Figure 1 illustrates the variability between snowpacks, as well as the similarities: in general the stratigraphy featured basal depth hoar, intermediate layers of faceted crystals, and top layers comprised of windpacks and/or recent unsintered wind-drift, often topped by a millimetric diamond dust layer [*Domine et al.*, 2012]. A few very thin melt-freeze crusts were also sometimes observed at several depths. The snow on sea-ice was essentially similar to that on land, but the depth and stratigraphy were much more variable. Melt-freeze layers were also more frequent (this may have been caused by supercooled droplets generated by nearby open leads, which froze on the snow surface). Depth hoar layers in all the snowpacks are formed through snowpack metamorphism due to the presence of a strong temperature gradient and are typical of the snowpack of Alaska's Arctic Coastal Plain [*Sturm and Liston*, 2003].

[31] The nadir reflectivity of the snowpack across the visible spectrum is similar for three of the snowpacks: the inland snowpack, soft snowpack and the snow on sea-ice. The peak reflectance occurs at a wavelength of 600 nm, a longer wavelength than that of clean snow, as reflectance measurements in central Antarctica suggest peak reflectance in the region of 470–520 nm [*France et al.*, 2011b]. Peak reflectance at 470 nm is seen only in the hard snowpack at Barrow. A shift in maximum albedo has been previously noted by *Warren et al.* [2006] and mostly attributed to the presence of dust or organic matter. The differences in reflectivity between Barrow snow and the cleaner Antarctic snow [*France et al.*, 2011b] are due to absorbing impurities within the snowpack. The impurities absorb light over the visible and near UV wavelength range. The *e*-folding depths, reported in Figure 1c, are largest for the inland snowpack,

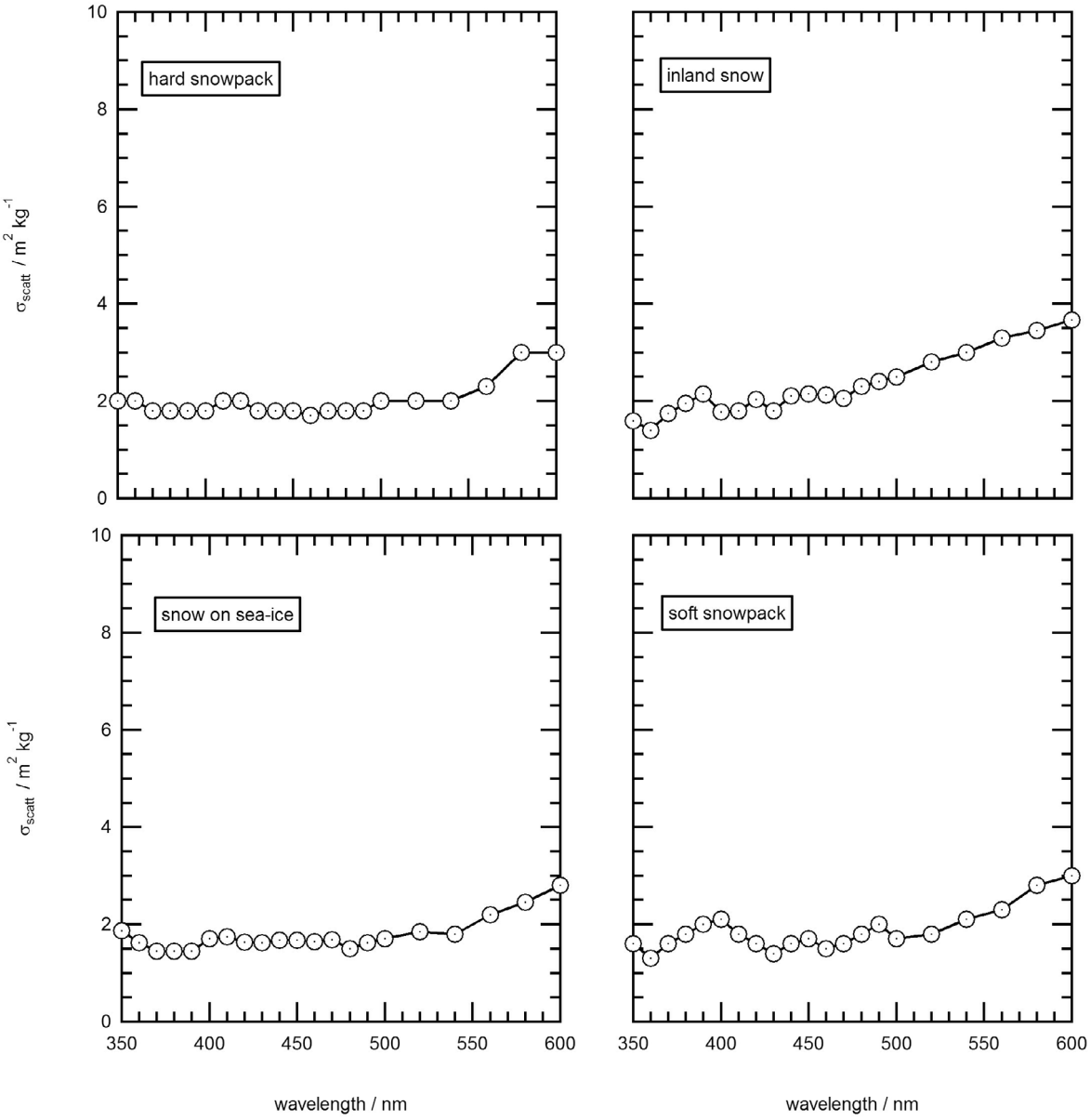

Figure 2. Wavelength dependence of the scattering coefficient, σ_{scatt}, for each of the four snowpacks investigated at Barrow. All snowpacks demonstrate a broadly invariant relationship of scattering coefficient with wavelength. Determined using the conditions described in Table 1.

with an *e*-folding depth of ~15 cm at a wavelength of 400 nm, and smallest in the soft snowpack, ~10 cm at 400 nm. The *e*-folding depths of the snowpacks at the BARC (hard and soft snowpack) and on the sea-ice (only 1–2 km offshore away from the settlement) are essentially the same.

3.2. Optical Coefficients of Barrow Snowpack

[32] The wavelength-dependent absorption and scattering coefficients $\sigma_{scatt}(\lambda)$ and $\sigma^{+}_{abs}(\lambda)$ determined for the Barrow snowpacks are shown in Figures 2 and 3, respectively. Table 2 reports these values relative to previously determined snowpack coefficients [*Beine et al.*, 2006; *Fisher et al.*, 2005; *France et al.*, 2010; *Lee-Taylor and Madronich*, 2002] at a wavelength of 400 nm.

[33] The typical error on the scattering coefficient has been calculated to be ~1 m^2 kg^{-1}, and therefore the scattering coefficient can be considered effectively constant across the wavelength range 350 to 600 nm, justifying the assumption of wavelength-independent σ_{scatt} in the original work by *Lee-Taylor and Madronich* [2002]. The values of σ_{scatt} at 400 nm are ~2 m^2 kg^{-1}, and are similar to those for midlatitude dry windslab [*Fisher et al.*, 2005] and both the absorption and scattering coefficients are similar to snowpacks previously determined for summer Alaskan snow on sea-ice in *Lee-Taylor and Madronich* [2002] using data from *Grenfell and Maykut* [1977] as shown in Table 2.

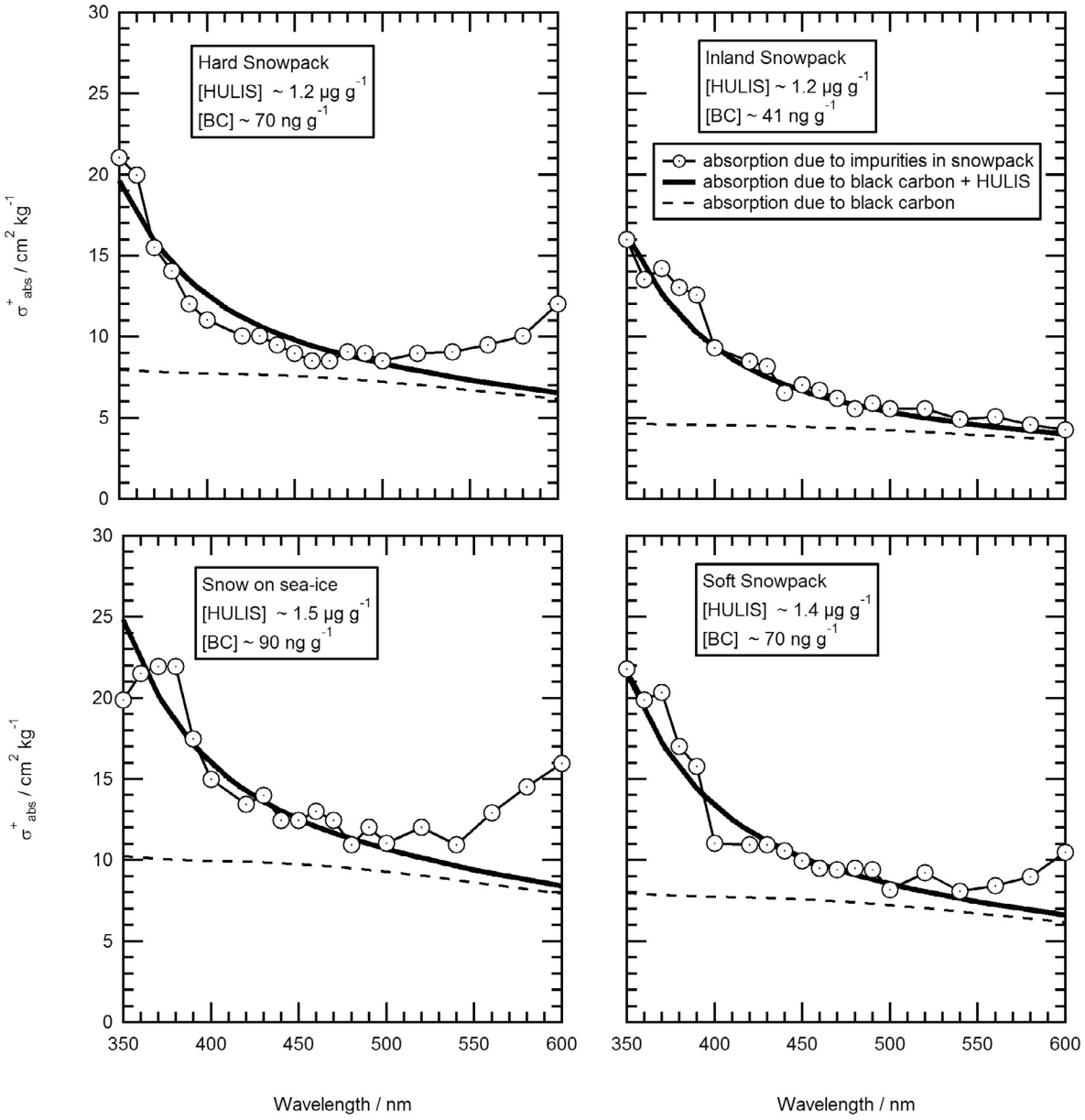

Figure 3. Black Carbon (BC) and HULIS (Humic Like Substances) absorption cross-sections fitted to total snowpack absorbance due to impurities for each of the four Barrow snowpacks. The lines with round markers are absorptions due to impurities in the snowpack derived from field measurements, the dashed line is black carbon absorption and the thick solid line is combined black carbon and HULIS absorption.

[34] The absorption cross-sections of snowpack impurities shown in Figure 3 all demonstrate a general trend of decreasing absorption with increasing wavelength from 350 nm to 550 nm and a smaller increase from 550 nm to 600 nm with the exception of inland snow. The inland snow has a lower absorption cross-section at longer wavelengths than the other snowpacks. Comparison of absorption cross-sections at a wavelength of 400 nm (Table 2) shows that the Barrow snowpacks are highly absorbing when compared to other dry Arctic snowpacks. *Lee-Taylor and Madronich* [2002] assumed that both σ^{+}_{abs} and σ_{scatt} could be modeled as constant with wavelength, however the value of σ^{+}_{abs} is highly variable with wavelength in the UV-visible wavelength range.

3.3. Snowpack Absorption By Impurities

[35] Figure 3 demonstrates that the majority of absorption can be fitted by a linear combination of absorption cross-sections of particulate black carbon and particulate HULIS. The black carbon absorption spectrum was calculated from a Mie calculation assuming spherical black carbon particles in the snow of 0.1 μm radius, 1 g cm^{-3} density and a refractive index of 1.8–0.5i, as in work by *Warren and Wiscombe* [1980, 1985]. The black carbon cross-section is shown in

Table 2. A Comparison of Optical Coefficients Previously Determined for Arctic and Northern Hemisphere Snowpacks at a Wavelength of 400 nm[a]

Study	Snow Description	σ_{scatt} (m^2 kg^{-1})	σ^+_{abs} (cm^2 kg^{-1})
Grenfell and Maykut [1977]	Arctic Summer dry[b]	6.4	7.3
	Arctic Summer melting[b]	1.1	7.8
King and Simpson [2001]	Arctic spring windblown[b]	6–30	4–25
Fisher et al. [2005]	Midlatitude windslab - melting	1	1
	Midlatitude windslab - dry	2–5	1–2
France et al. [2010]	Fresh Ny-Ålesund snowpack	16.7	2.7
	Melting Ny-Ålesund snowpack	0.8	19.8
France et al. [2011a]	Ny-Ålesund – old windpack	9.5	1.4
	Ny-Ålesund – fresh windpack	7.7	5.3
	Ny-Ålesund – marine influenced	20	3.4
	Ny-Ålesund – glacial accumulation zone	25.5	0.5
This work	Barrow – soft snowpack	2.0	11
	Barrow – hard snowpack	1.7	11
	Barrow – inland snowpack	1.8	9
	Barrow – snow on sea-ice	1.7	15

[a]Note the values of σ^+_{abs} and σ_{scatt} for the four Barrow snowpacks studied are very similar.
[b]Modeling of optical coefficients conducted by *Lee-Taylor and Madronich* [2002], not in the original measurement study.

Figure 4. The absorption spectrum for the HULIS absorber was taken from Figure 4 of *Hoffer et al.* [2006]. The linear combination of absorption cross-sections was fitted to the experimental data in Figure 3 by eye. The HULIS and the black carbon absorption spectra from *Hoffer et al.* [2006] and *Warren and Wiscombe* [1980] are presented as per unit mass of carbon, thus it is possible to crudely estimate the amount of black carbon and HULIS in the snowpack. The amounts of HULIS and black carbon in the snowpack determined in this work are presented in Table 3. These values are considerably larger than the amounts of impurities measured by chemical extraction in the windpack and windblown snowpacks at Barrow, which were in the range of 2–17 ng g^{-1} for black carbon, water insoluble organic carbon of 30–200 ng g^{-1} and 30–360 ng g^{-1} of dissolved organic carbon (D. Voisin et al., Carbonaceous species and

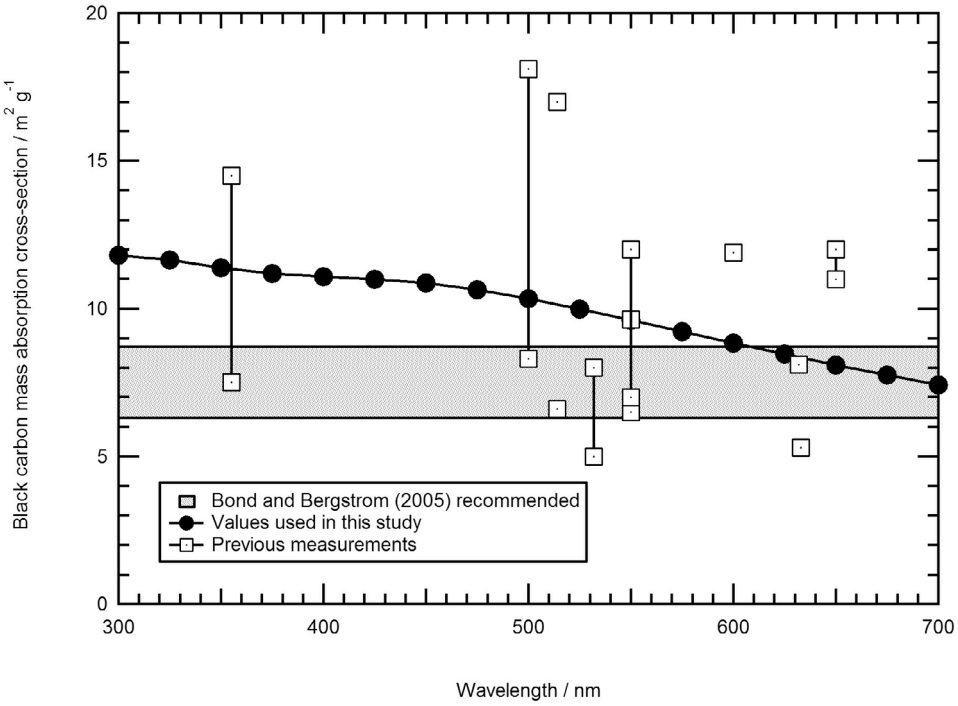

Figure 4. Mass absorption cross-section for black carbon. Filled circles are the absorption cross-section used in the work described here based on a Mie calculation described in the text. The unfilled squares represent values of the black carbon absorption cross-section measured and reviewed by *Bond and Bergstrom* [2006] or measured by *Adler et al.* [2010]. The shaded band represents the value recommended by *Bond and Bergstrom* [2006] for the black carbon mass absorption cross-section. The values used in this work are in agreement with the values reviewed in the literature by *Bond and Bergstrom* [2006].

Table 3. Estimated Concentrations of Black Carbon and HULIS in the Snowpacks Around Barrow, Derived From Fitting Linear Combinations of Black Carbon and HULIS Absorption Cross-Sections to Absorption Cross-Section of Snowpack Impurities in Figure 3[a]

	e-Fold			
Snowpack	λ = 350 nm (cm)	λ = 400 nm (cm)	Black Carbon (ng-C g^{-1})	HULIS (μg-C g^{-1})
Hard	7	10	70	1.2
Soft	7.5	9	70	1.4
Snow on sea-ice	7.5	9	90	1.5
Inland	12	15	41	1.2

[a]Note that the concentration is per unit mass of carbon in HULIS or black carbon per gram of snow. The concentration of HULIS in the snowpack should be treated as an upper limit and to represent all light-absorbing snowpack impurities. Values of *e*-folding depth are included for comparison.

humic-like substances (HULIS) in Arctic snowpack during OASIS field campaign in Barrow, submitted to *Journal of Geophysical Research*, 2012). These estimates depend upon many factors and are discussed in section 4.4.

3.4. Photolytic Rate Constants and Fluxes As a Function of Solar Zenith Angle and Snowpack Depth

[36] Photolysis rate coefficients, *J*, for the photolysis of hydrogen peroxide, nitrate and nitrite within the four Barrow characteristic snowpacks were calculated for 106 depths within each snowpack for 30 separate solar zenith angles between 0 and 90° (equally spaced over Cos θ). Figures 5, 6 and 7 plot contours of equal photolysis rate coefficients for reactions (1), (2) and (3) respectively versus depth and solar zenith angle. The photolysis rate coefficient for the production of OH radicals, NO_2 or NO in the snowpack may be

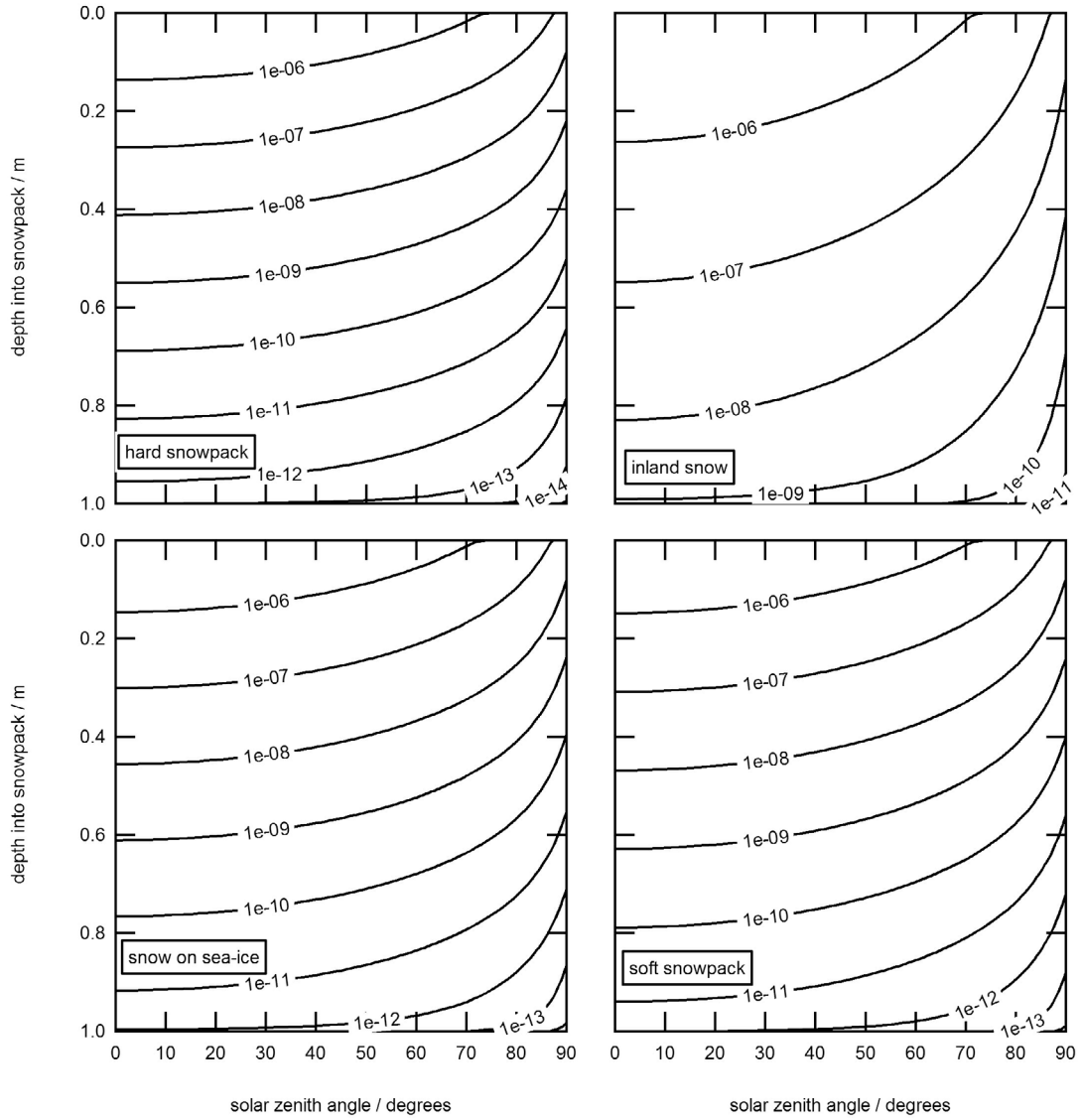

Figure 5. Photolysis rate coefficients (s^{-1}) as a function of depth and solar zenith angle for the photolysis of H_2O_2 to produce two hydroxyl radicals (reaction (2)) for each of the four Barrow snowpacks, determined using the conditions described in Table 1 under clear skies.

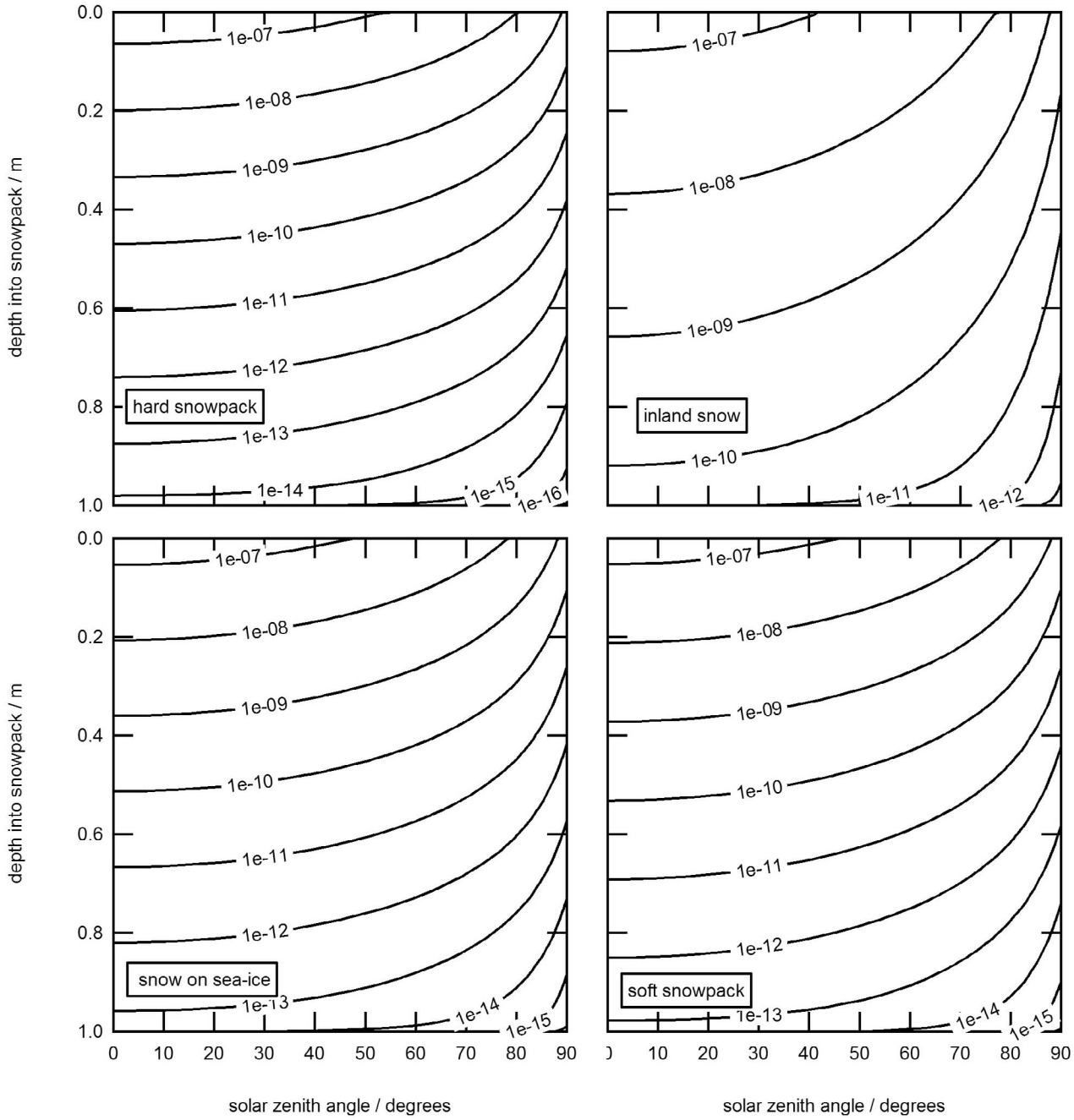

Figure 6. Photolysis rate coefficients (s^{-1}) as a function of depth and solar zenith angle for the photolysis of NO_3^- to NO_2 and OH (reaction (1)) for each of the four Barrow snowpacks. Values were determined using the conditions described in Table 1 under clear skies.

interpolated from the plot for any depth in the top 1 m of snow and for any solar zenith angle.

3.5. Depth-Integrated Production Rates (Fluxes) of NO, NO_2 and OH Radicals for the OASIS Field Campaign

[37] Photochemical depth-integrated production rates (fluxes) of OH radicals, NO_2 and NO were calculated for each of the four snowpacks for every minute of the OASIS campaign and are presented in Figures 8 and 9. The variation in calculated photolytic production of NO_2 between the Barrow snowpacks is less than a factor of 2, with maximum potential fluxes of NO_2 on Julian Day 90 of 17 nmol m^{-2} h^{-1} for the inland snowpack, 15 nmol m^{-2} h^{-1} for the hard snowpack and 13 nmol m^{-2} h^{-1} for the soft snow and 14 nmol m^{-2} h^{-} for the snow on sea-ice. The maximum depth-integrated in-snow production rate of OH radicals for Day 90 is 160 nmol m^{-2} h^{-1} for the inland snowpack, 110 nmol m^{-2} h^{-1} for the soft snowpack and 120 nmol m^{-2} h^{-1} for the snow on sea-ice and hard snowpack. The maximum photolytic production rate of NO from the photolysis of nitrite is 30 nmol m^{-2} h^{-1} for the soft snowpack and 55 nmol m^{-2} h^{-1} for the inland snowpack and 36 nmol m^{-2} h^{-1} snow

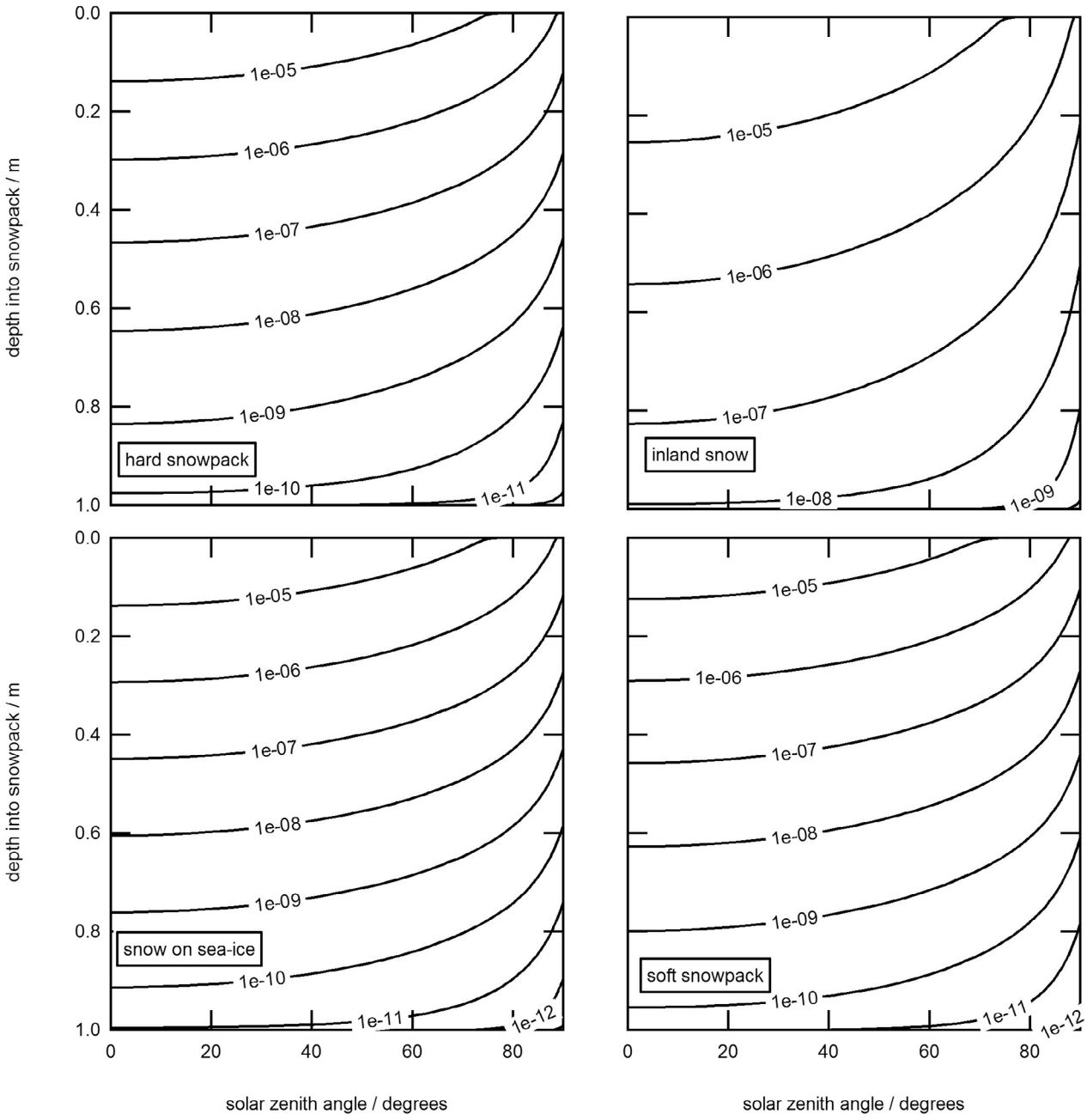

Figure 7. Photolysis rate coefficients (s^{-1}) as a function of depth and solar zenith angle for the photolysis of NO_2^- to NO and OH (reaction (3)) for each of the four Barrow snowpacks. Values were determined using the conditions described in Table 1 under clear skies.

on sea-ice and 39 nmol m^{-2} h^{-1} for the hard snowpack. The maximum in-snow NO_x production rate is therefore 72 nmol m^{-2} h^{-1} for the inland snowpack and 44 nmol m^{-2} h^{-1} for the soft snowpack. The total OH radical production rate is a summation of OH radicals produced through nitrate, hydrogen peroxide and nitrite photolysis according to reactions (1), (2) and (3) respectively.

[38] Scaling the depth-integrated production rate (or flux) of NO_2, NO and OH radicals by downwelling TUVR downwelling irradiance (295–385 nm broadband) measurement is only valid while F(NO), F(NO_2) or F(OH) is proportional to the downwelling broadband UV irradiance measured by the Eppley TUVR. Figure 10 demonstrates that for diffuse conditions and clear sky conditions between solar angles of 51–90°, there is an approximately linear relationship between depth-integrated production rate of OH radicals, NO_2 or NO and downwelling broadband UV irradiance. As a wider point, depth-integrated production rates (fluxes) of NO_2, NO and OH radicals can be predicted from the TUVR downwelling irradiance measurements using Figure 10 for the snowpacks and solar zenith angles studied here. Similar relationships may be possible for other

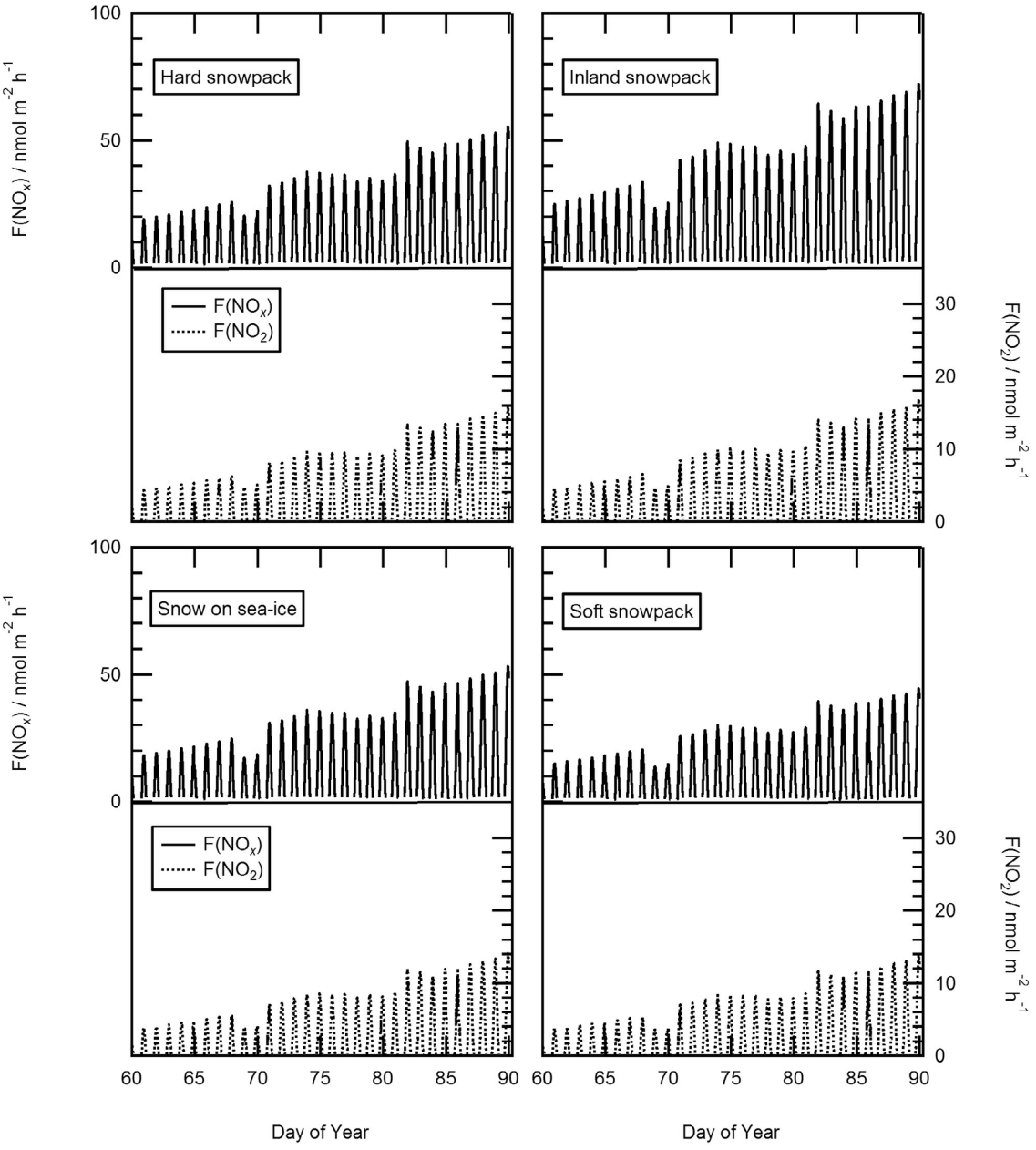

Figure 8. Depth-integrated production (maximum fluxes) of NO_x and NO_2 in the snowpack for the duration of the Barrow OASIS campaign, assuming all in-snow photolytic production of NO_x from nitrate and nitrite is liberated from the snowpack. The top line in each graph is total NO_x photolytic production rates ($NO + NO_2$) and the lower line is NO_2 photolytic production rates for each snowpack; note that the corresponding left and right hand side axes have different ranges. The depth-integrated production rates (maximum fluxes) are calculated with a concentration of 3.9 μmol l^{-1} of nitrate and 0.02 μmol l^{-1}, an average of snow measurements during the OASIS campaign, with no depth dependence. Concentrations of chromophores are for melted snow.

snowpacks and the relationships shown here are only for these snowpacks.

4. Discussion

4.1. Comparison With Previous Work

[39] Previous measurements of *e*-folding depths in snowpack at Barrow gave values of 8 cm and 26 cm for spring and summer respectively [*Rowland and Grannas*, 2011]. Those results were obtained using a solid-state chemical actinometry method and *e*-folding depths calculated using only 3 depth measurements of in-snow actinometry with the wavelength peak of the action spectrum at ~340 nm [*Rowland and Grannas*, 2011]. The shortest wavelength at which *e*-folding depths are reported in this work is at 350 nm, with *e*-folding depths for four Barrow snowpacks

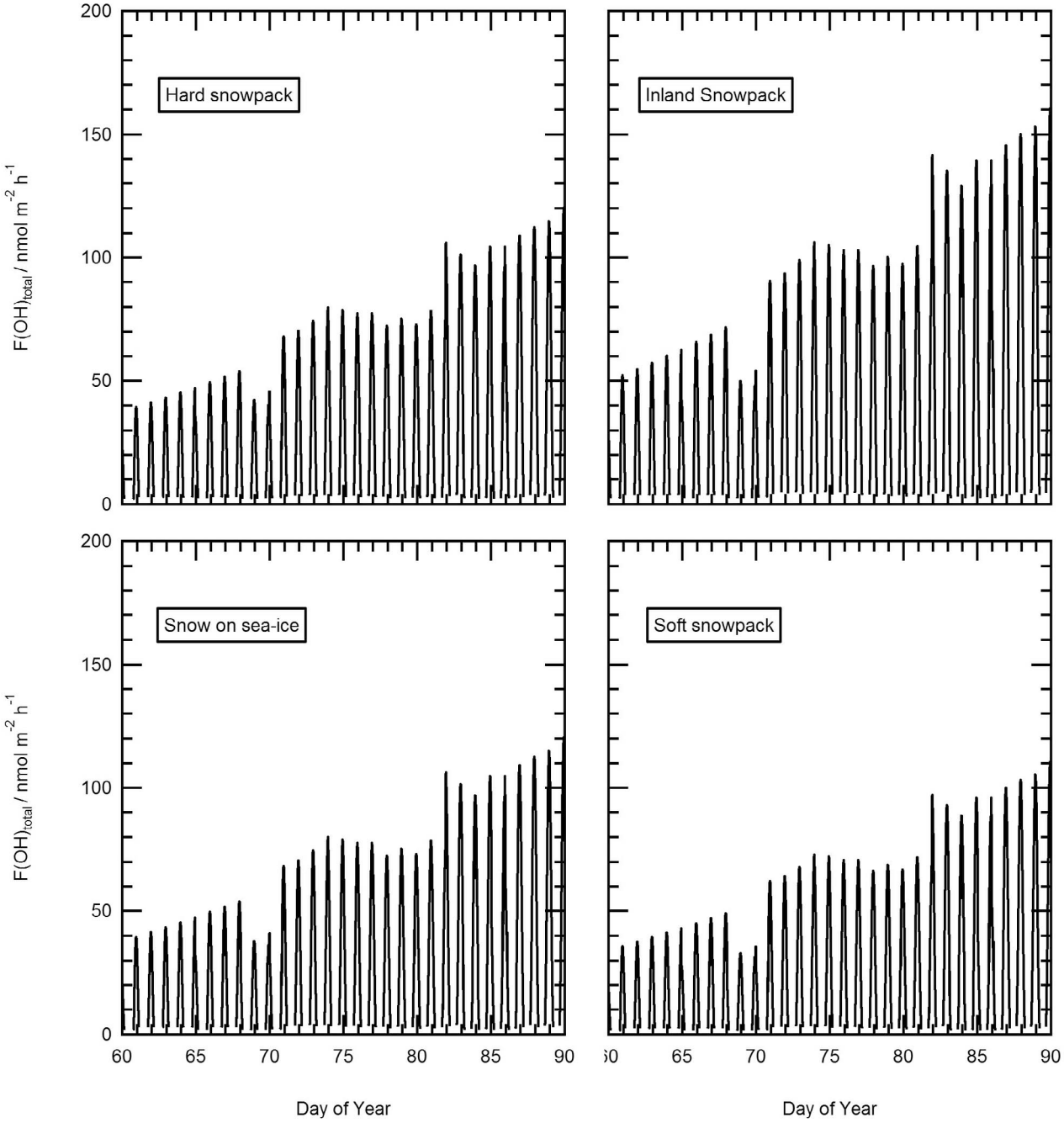

Figure 9. Total depth-integrated production rates of OH radicals from the photolysis of hydrogen peroxide, nitrite and nitrate in the snowpack for the duration of the Barrow OASIS campaign. The depth-integrated production rates are calculated with a concentration of 0.4 μmol l^{-1} of hydrogen peroxide, 0.02 μmol l^{-1} of nitrite and 3.9 μmol l^{-1} of nitrate. Concentrations of chromophores are for melted snow.

of 7–12 cm. Thus the values of measured *e*-folding depths presented here are consistent with those of *Rowland and Grannas* [2011] for Spring snowpacks. Previous analysis of the error in determining *e*-folding depths using a fiber optic probe placed horizontally into a snowpack determined an uncertainty in *e*-folding depth of ± 20% [*France et al.*, 2011a]. As this study recorded irradiance at 6 depths concurrently rather than at the 4 depths consecutively used in the uncertainty analysis, it is expected that the error of 20% can be considered a very conservative maximum. The three snowpacks within the vicinity of Barrow (hard, soft and snow on sea-ice) can all be effectively described as the same (optically) within uncertainty, whereas the inland snowpack has a 50% longer *e*-folding depth at a wavelength of 400 nm.

[40] The measured *e*-folding depths can be converted to liquid equivalent *e*-folding depths in order to facilitate

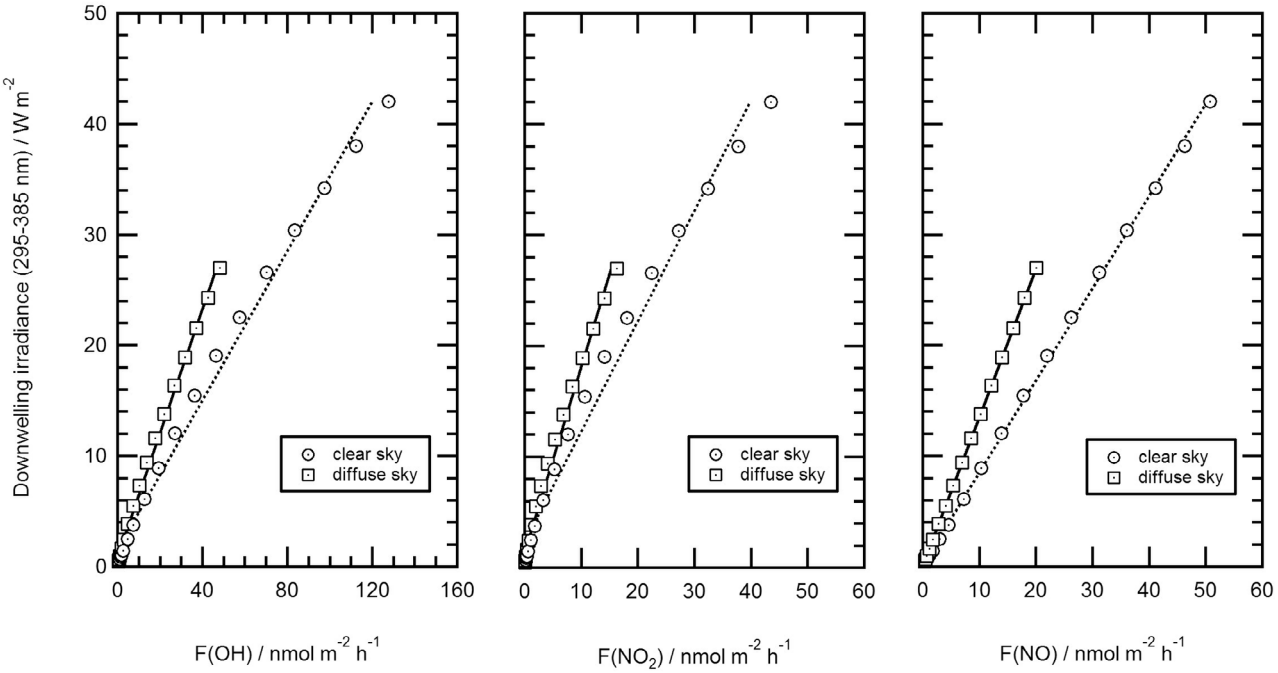

Figure 10. Demonstrating the linear relationship and validity of scaling NO, NO_2 and OH depth-integrated production rates of NO, NO_2 and OH radicals using broadband UV measurements (295–385 nm). Each point is a solar zenith angle between 90° and 51°, Minimum solar zenith angle was ~66° during the OASIS campaign. The snowpack was the hard snow using conditions as described in Table 1. Similar relations exist for the other three snowpacks.

comparison between different snowpacks [*Lee-Taylor and Madronich*, 2002; *Warren*, 1982], using equation (12).

$$\varepsilon_{liq} = \frac{\rho_{snow}}{\rho_{water}}\varepsilon, \tag{10}$$

where ρ is the density, ε is the measured e-folding depth and ε_{liq} is the liquid equivalent *e*-folding depth.

[41] The liquid equivalent *e*-folding depths for the snowpacks in Barrow are in the range 3.8–4.5 cm (for a wavelength of 400 nm) which are a little larger than liquid equivalent *e*-folding depths previously reported for Arctic snow on sea-ice of 2–3 cm [*Grenfell and Maykut*, 1977], but are within the large range of liquid equivalent *e*-folding depths for Northern hemisphere snows (~1.5 cm [*King and Simpson*, 2001] to ~16 cm [*Fisher et al.*, 2005]). The snowpacks near to the Barrow Science Centre and the snowpack on sea-ice have a liquid equivalent *e*-folding depth of ~4 cm at a wavelength of 400 nm, which is comparable to springtime measurements made at Ny-Ålesund [*France et al.*, 2011a; *Gerland et al.*, 1999]. Previously it has been stated that 85% of photochemistry occurs in the top 2 *e*-folding depths of snowpack [*King and Simpson*, 2001], therefore for the Barrow snowpacks 85% of the photochemistry occurs within the top 14–24 cm of snow cover using *e*-folding depths measured at 350 nm. It should be noted that the *e*-folding depths will depend upon the season [*France et al.*, 2010] and the metamorphic history of the snowpack, and that the above comparison does not take this into account.

[42] The nadir reflectivity of the snowpacks at Barrow was relatively consistent between snowpacks, between 0.82 and 0.85 at 400 nm, and between 0.84 and 0.91 at 500 nm. The reflectivity measurements typically have an uncertainty of 0.04 (two standard deviations), with the variation at each site likely due to changes in surface topography and localized impurities. Previous work investigating albedo uncertainty suggests that a 2° slope can lead to a 10% change in albedo depending upon illumination angle [*Grenfell et al.*, 1994]. Previous analysis of reflectance of dry snow at Barrow recorded a value of 0.92 at a wavelength of 400 nm [*Grenfell and Maykut*, 1977] and clean Antarctic snow a value of 0.98 at a wavelength of 400 nm [*France et al.*, 2011b]. As discussed in the next section, the low reflectivity of the Barrow snowpacks is attributable to highly absorbing black carbon and humic material within and on the snowpack.

4.2. The Effect of Grain Size on the Determination of σ_{scatt} or σ^{+}_{abs}

[43] In previous publications by the main (U.K) authors of this work the effect of snow grain size on derived values of σ_{scatt} or σ^{+}_{abs} has not been considered in a systematic manner because the values of σ_{scatt} and σ^{+}_{abs}, along with the asymmetry parameter, g, were used to calculate irradiances and photolytic rate constants in the snow. In the work described here the absorption cross-section of the impurities in the snowpack are derived and it is prudent to assess whether the grain size of the snow affects the value of the absorption cross-section derived for the impurities in the snowpack. As described by *Lee-Taylor and Madronich* [2002], the only

grain-size-dependent quantity used in the radiative-transfer calculation that is not empirically fitted to the measured albedo and *e*-folding depth (values of σ_{scatt} and σ^{+}_{abs} are empirically fitted) is the asymmetry parameter, g. Inspection of the Mie calculation for 100–2000 μm diameter ice spheres by *Wiscombe and Warren* [1980, Figure 4] demonstrates that the value of the asymmetry parameter may be bracketed by values between 0.885 and 0.895 for the wavelengths considered in the work presented here. As a sensitivity study of the effect of the asymmetry parameter on the values of σ_{scatt} or σ^{+}_{abs} the radiative-transfer calculations to empirically fit σ_{scatt} and σ^{+}_{abs} for the hard snowpack described in Figure 1 were repeated with values of the asymmetry parameter, g = 0.880, 0.885, 0.890, 0.895 and 0.900. The results are displayed in Table 4 for solar wavelengths of 400, 500 and 600 nm. Table 4 demonstrates the values of σ_{scatt} and σ^{+}_{abs} derived are insensitive to the value of asymmetry parameter.

[44] As a further test of the procedure to determine values of σ_{scatt} and demonstrate that σ_{scatt} is sensitive to the grain size of the snowpack the authors used the procedure outlined in section 2.2.1 to fit σ_{scatt} to the albedos (calculated by radiative-transfer) contained in Figure 7 of *Wiscombe and Warren* [1980]. Figure 7 of *Wiscombe and Warren* [1980] contains semi-infinite direct beam albedo data as a function of wavelength, grain size (100 and 1000 μm) and black carbon content (50, 500 and 500 ng g^{-1}). Values of σ_{scatt} were determined for solar wavelengths of 300, 325, 350, 375, 400, 450 and 500 nm. Values of σ_{scatt} were found to be 20 ± 3 m^2 kg^{-1} for the small grained snowpack (for all black carbon concentrations) and 1.9 ± 0.1 m^2 kg^{-1} for the large grained snowpack (for all black carbon concentrations) over the wavelengths 300–500 nm.

[45] In previous work by *France et al.* [2010], stratigraphic snowpack data was used to calculate the irradiance and photolytic rate coefficients in separate windpack layers in an Antarctic snowpack. The different windpack layers had slightly different optical properties in the radiative-transfer calculations owing to slightly different grain size and light-absorbing impurity content. For windpack layers similar to those in Figure 1 the very slight change to irradiance-depth profiles calculated from the radiative-transfer calculations was not worth the increase in substantial computational effort. The typical uncertainty in σ_{scatt} owing to a 5% change in snowpack density is $\pm^{7\%}_{5\%}$ and the typical uncertainty in σ^{+}_{abs}, black carbon or HULIS owing to a 5% change in snowpack density is $\pm^{6\%}_{9\%}$.

4.3. The Scattering Cross-Sections of Barrow Snowpack

[46] The values of the scattering cross-section may be considered to be smaller than expected, but a sensitivity analysis of the radiative-transfer modeling process to determine absorption and scattering cross-sections yielded no large changes in the values of σ_{scatt} or σ^{+}_{abs} for small changes in albedo, *e*-folding depth or the asymmetry parameter, g. An expectation of greater values of $\sigma_{scatt}(\lambda)$ is due to a possible relationship between specific surface area of snow and scattering cross-sections [*Domine et al.*, 2008]. *Domine et al.* [2008] state there is a mathematical relationship between snow specific surface area (SSA) and the scattering cross-section, (σ_{scatt}) and *Kokhanovsky and Zege* [2004, p. 1594, equation (22)] describe this relationship. Similar values of scattering cross-sections were recorded for coastal snowpacks similar to Barrow in Antarctica [*Beine et al.*, 2006]. *Domine et al.* [2012] have derived values of SSA from snowpack reflectivity in the near IR of ~30–40 m^2 kg^{-1} for surface snow, which would suggest scattering cross-sections of 15–20 m^2 kg^{-1}. However, the results in Figure 2 and Table 2 demonstrate typical values of $\sigma_{scatt} \sim 2$ m^2 kg^{-1} were derived from the measurements of *e*-folding depth and surface reflectance, and a re-investigation of the modeling process to calculate $\sigma_{scatt}(\lambda)$ revealed no errors or processes that could cause a large change in $\sigma_{scatt}(\lambda)$ for a small change in the modeling parameters. An almost identical study using identical techniques by the same authors at DOME C in Antarctica found values of SSA of ~31 m^2 kg^{-1} [*Gallet et al.*, 2010], which would suggest σ_{scatt} values of ~15–16 m^2 kg^{-1}, and values of σ_{scatt} of 14–24 m^2 kg^{-1} were determined for surface snows [*France et al.*, 2011b]. Thus the relationship between SSA and σ_{scatt} appears to be valid for snow at Dome C, but not valid for Barrow. One obvious difference between these two studies is the amount of light-absorbing impurities in the snowpack as the snowpacks studied at Barrow during this campaign are very dirty relative to the very clean snowpacks measured at DOME C. Scattering and absorption are independent quantities.

[47] It is not possible to drastically alter the value of σ_{scatt} and replicate the measured *e*-folding depth and reflectivity measurements by (1) changing σ^{+}_{abs} by 20%, (2) varying the asymmetry parameter, g, within the limits suggested by *Wiscombe and Warren* [1980] or (3) varying nadir reflectivity or *e*-folding depth (i.e., measurement error) by amounts representing experimental error. An explanation that is occasionally proposed is the measured reflectivity and measured *e*-folding depth are for different snow layers with very different optical properties, as the measurements of *e*-folding depth and nadir reflectance are in different parts of the snowpack. Thus, it may be possible to have a thin (<1 cm) top layer of snowpack containing all the light-absorbing impurities, underlain by a clean snowpack. Experience and exploratory calculations with TUV-snow suggest such a condition would be obvious to the naked eye as a dirty top layer of a different color to the rest of the snowpack. No such layer was observed at Barrow and all 15 snowpits studied had similar values of σ_{scatt} (1.7–4 m^2 kg^{-1} (λ = 400 nm)). To surmise, there is no reason to suspect that the method of determining σ_{scatt} is not robust. At the present time an explanation for the disagreement between SSA and σ_{scatt} for the snowpacks presented here is not available.

4.4. The Wavelength Dependence of Absorption in Barrow Snowpack

[48] The absorption spectrum of light-absorbing impurities in the snowpack is plotted in Figure 3. The absorption cross-section represents the total absorption of light-absorbing impurities whether they are internal or external to the snow grains. External light-absorbing impurities include particles such as soil or black carbon that were trapped or deposited since snow fall. An internal light-absorbing impurity is likely to have been part of the original snow fall or has been incorporated into the snow grain as a deposited gas or during snow metamorphism. Figure 4 also compares

Table 4. Values of σ_{scatt} and σ^{+}_{abs}, Calculated Empirically By Fitting the Reflectance, and *e*-Folding Depth for the Hard Snowpack Using Different Values of the Asymmetry Factor g[a]

	λ = 400 nm		λ = 500 nm		λ = 600 nm	
Asymmetry Parameter, g	σ_{scatt} (m^2 kg^{-1})	σ^{+}_{abs} (cm^2 kg^{-1})	σ_{scatt} (m^2 kg^{-1})	σ^{+}_{abs} (cm^2 kg^{-1})	σ_{scatt} (m^2 kg^{-1})	σ^{+}_{abs} (cm^2 kg^{-1})
0.880	1.5	11.0	1.7	9.5	2.5	14.5
0.885	1.6	11.2	1.8	9.7	2.7	14.5
0.890	1.7	11.5	1.8	9.5	2.7	14.5
0.895	1.8	11.5	1.9	9.5	2.9	14.5
0.900	1.8	11.7	2.0	9.5	3.0	14.5

[a]Note that the values of σ_{scatt} and σ^{+}_{abs}, derived are insensitive to the value of g. Values are reported for the solar wavelengths of 400, 500 and 600 nm.

the mass absorption cross-section used in this and previous work with measurements of the mass absorption coefficients found in Table 6 of the review by *Bond and Bergstrom* [2006], and in work by *Adler et al.* [2010]. Figure 4 demonstrates the values of the mass absorption cross-section from *Bond and Bergstrom* [2006], and *Adler et al.* [2010] are similar with values used in this study. The very interesting result of this work is that a HULIS absorber and a black carbon absorber are required to explain the total snowpack impurity absorption, not just black carbon. In future it may not be possible to model UV-visible photolytic processes in the snowpack without considering HULIS and black carbon absorptions.

[49] Comparison of the four snowpacks in Figure 3 demonstrates that the coastal snowpacks have an absorption in the wavelength region 550–600 nm that is not present at the inland site and not accounted for by the HULIS or black carbon absorption spectrum used in this work [*Hoffer et al.*, 2006]. Thus, for the three coastal snowpacks a third light-absorbing impurity may be required. Marine microbiology may be responsible for this absorption and a similar feature has been noted in the extracted HULIS spectrum by Voisin et al. (submitted manuscript, 2012) and melted snow samples by *Beine et al.* [2012]. The feature is not present in the inland snowpack and only sites close to the open lead at Barrow have this absorption feature. Continued investigation is underway, but at present a realistic absorption spectra for marine microbiological detritus in snowpack does not exist to the authors' knowledge. The amounts of black carbon predicted for Barrow snowpacks are much greater than in more remote regions of the Arctic, where average black carbon concentrations range from 3 ng g^{-1} (Greenland) to 26 ng g^{-1} (West Russia), with an Alaskan snowpack average of 9 ng g^{-1} [*Doherty et al.*, 2010]. However, the derived absorption and scattering coefficients from the work presented here are similar to previously determined values for Alaskan snow on sea-ice from *Lee-Taylor and Madronich* [2002] using data from *Grenfell and Maykut* [1977]. *Doherty et al.* [2010] extracted and quantified black carbon in Barrow snow in April 2007 within 10 km of the snowpacks studied and shown in Figure 1. *Lyapustin et al.* [2010] have a photograph and reflectivity data of the snow sampled by *Doherty et al.* [2010] and describe it as "fresh snow with minimal redistribution by the wind." The new unworked snow sampled by *Doherty et al.* [2010] is very different to the old windpacked snow described in this work in Figure 1. The windpacked snows in Figure 1 were characteristic of the OASIS campaign and have clearly had the opportunity to accrue more light-absorbing impurities through multiple wind events relative to the *Doherty et al.* [2010] sample. *Doherty et al.* [2010] highlight that they ignored samples from the lower 40% of some snowpacks to avoid biasing their samples with windblown soil. Such sampling measures were not possible or desired in the study presented here as the main aim of this work was to measure and model the optical properties of the Barrow snowpack during the OASIS campaign to allow photochemical production rates to be calculated. The initial aim was not to measure black carbon concentrations in the snowpack. Thus a comparison of the black carbon concentrations between snowpacks of *Doherty et al.* [2010] and those in Figure 1 is not sensible. The calculated amounts of black carbon in Barrow snow are comparable to values measured in East Arctic Russian snow ($\sim$10 to 150 ng g^{-1}), where sampling was restricted to within 100 km of cities and local sources of pollution could have become incorporated into the snowpack [*Doherty et al.*, 2010]. Snow machine traffic and the local town pollution could be the sources of the high amount of black carbon in the Barrow area.

[50] Voisin et al. (submitted manuscript, 2012) reported concentrations of various brown and black carbon species in snow for some of the snowpacks studied in this work. The values reported here are considerably higher than those of Voisin et al. (submitted manuscript, 2012) where the carbon concentrations in the snowpack were determined by extracting carbon from the snowpack using various methods (e.g., SPE cartridge, filtering etc.) and measuring carbon content chemically. However, the values reported here are reported optically after making assumptions about the absorber identity. The majority of the disagreement between Voisin et al. (submitted manuscript, 2012) and the results shown in Table 3 may be owing to our simple approximations for a HULIS absorber and black carbon absorber in the snowpack. *Bohren* [1986] demonstrated that reasonable uncertainties in the shape, refractive index, and internal / external nature of black carbon with respect to the snow grain could yield changes in the black carbon absorption cross-section of factors of 2.2, 5 and 1.4 respectively, Using the refractive index of HULIS measured by *Hoffer et al.* [2006] and the mathematical approach of *Bohren* [1986] results in uncertainties in the HULIS absorption cross-section of factors of 1.8 and 1.3 for the shape and internal / external nature of the HULIS particles respectively. The uncertainty owing to refractive index of HULIS was not considered, as there is more uncertainty in the identity of the UV absorber than the value of its refractive index. There may be a small measure of disagreement between Voisin et al. (submitted manuscript, 2012) and

values presented in Table 3 owing to how HULIS and BC are measured and defined. It is therefore important to understand what Figure 3 demonstrates: (1) that the total snowpack light-absorbing impurity is not constant over 350–600 nm, (2) that the light-absorbing impurities in snowpack can be fitted to a combination of HULIS and black carbon absorber and a third absorber based on marine microbiological detritus may be required, and (3) estimates of concentration of black carbon and HULIS in snow can be calculated from optical measurements, but these values depend upon the physical characteristics and location of the absorber. It should again be noted that the absorption by snowpack impurities has been fitted to a linear combination of black carbon and HULIS absorption spectra to demonstrate that the absorption is consistent with a mixture of light-absorbing snowpack impurities. It is quite possible that the material termed HULIS could be replaced by other forms of brown carbon, dust or other light-absorbing impurities. The concentration of HULIS in the snowpack should be treated as an upper limit and to represent all light-absorbing snowpack impurities. One advantage of the technique presented here is that the total absorption of light-absorbing impurities in the snowpack is determined without melting or significantly perturbing the snowpack.

4.5. NO_x and OH Radical in-Snow Production Rates (Fluxes)

[51] The combined depth-integrated production rate of NO_2 and NO is the upper-bound for the NO_x flux from the snowpack, assuming all photoproduced NO_x is able to escape from the snowpack. The maximum calculated noontime NO_x flux from the inland snow at Barrow for a solar zenith angle of 66° is 72 nmol m^{-2} h^{-1}, with 30% and 70% from photolysis of nitrate and nitrite, respectively. The uncertainty in the depth-integrated production rates is approximately 20% [*France et al.*, 2010].

[52] The photolysis of NO_2^- to produce NO is not usually considered as a significant source of NO_x, but in the conditions at Barrow nitrite appears to dominate, contributing approximately 3 times more NO_x than nitrate. Previously, analysis by *Chu and Anastasio* [2007] demonstrate that for OH production on ice grains (and therefore applicable to NO_x in-snow production (reactions (1) and (3)), nitrate and nitrite photoproduction rates are comparable. A similar result was obtained for Antarctic snow during the CHABLIS campaign [*Jones et al.*, 2001]. However, under the conditions in Barrow nitrite photolysis is favored relative to nitrate due to: (1) the large value of the product $J_{NO_2^-}[NO_2^-]$ relative to the value of $J_{NO_3^-}[NO_3^-]$, (2) the presence of large ozone column, which attenuates the shorter UV wavelengths relative to longer UV wavelengths. The maximum of the action spectrum (product of absorption cross-section and quantum yield) for nitrate photolysis is ~302 nm, whereas the maximum of the action spectrum of nitrite photolysis is ~355 nm. (3) the presence of a wavelength-dependent absorber in the snowpack, with increasing absorption at shorter wavelengths. Therefore, if the impact of nitrite photochemistry to form NO in the snowpack is also considered and added to the NO_2 production rate to give a total NO_x in-snow production rate, then the total in-snow production for the Barrow snowpacks of 44–72 nmol m^{-2} h^{-1} is larger than the maximum flux of 40 nmol m^{-2} h^{-1} NO_x measured at Alert, Canada for a solar zenith angle of ~66° [*Beine et al.*, 2002]. The depth-integrated production rate of NO is dependent upon the assumption that the single site measurement of nitrite concentration in the snowpack is valid across the Barrow area.

[53] Snowpack emissions of NO_x have previously been demonstrated to have an impact on the oxidative capacity of the lower troposphere [*Bloss et al.*, 2007; *Morin et al.*, 2008; *Wang et al.*, 2008; *Yang et al.*, 2002]. The depth-integrated production rates of NO_2 presented here can only be considered to be maximum fluxes because some of the photoproduced NO_2 in the snowpack is likely to be involved in some secondary chemistry within the snow matrix. It has previously been suggested that 30% of the NO_2 is converted prior to release from the snowpack [*Anastasio and Chu*, 2009]. The release of NO_2 from the snow cover to the atmosphere is likely to be at least partly temperature controlled [*Boxe et al.*, 2006], but as sunlight-dependent fluxes of NO_x have been already observed over colder snowpacks in Alert [*Beine et al.*, 2002], it is unlikely that the NO_x photoproduced at Barrow in the warmer snowpacks will be trapped within the snow microstructure to a large degree. The mechanism for movement of photoproduced NO_x from snowpack to the atmosphere appears to be mostly influenced by windpumping at the surface of the snowpack and gas diffusion deeper into the snowpack [*Thomas et al.*, 2011]. The complexity of the nitrate photochemical system in snow is discussed by *Bock and Jacobi* [2010].

[54] The increased black carbon (and HULIS) absorption in the coastal snowpacks relative to inland snow reduces the predicted amount of photolytic NO_x production in the coastal snowpack by a factor of ~1.7 relative to the cleaner inland snowpack (Figure 8). The effect of increasing black carbon concentration upon the Alaskan snowpack photochemistry is explored in detail by H. J. Reay at al. (Decreased albedo, light penetration depth and photolytical production of OH radicals and NO_2 in Barrow snowpack: A scenario of increasing black carbon, submitted to *Journal of Geophysical Research*, 2012).

[55] The calculated depth-integrated production rates of total OH radical production from the photolysis of H_2O_2, NO_3^- or NO_2^-IO in Barrow snowpacks are shown in Figure 9, demonstrating that the variation in snowpack absorption and scattering cross-sections between the Barrow snowpacks only causes a small variation of the in-snow photochemical production of OH by a factor of less than 2. The in-snow photochemical production of OH radicals may well be a driving factor in the formation and release from the snowpack of organic compounds that appear to have a photochemical source [*Anastasio et al.*, 2007; *Hutterli et al.*, 2004; *Sumner et al.*, 2002]. The importance of OH radical production with respect to halogen release from snowpack is demonstrated through the dynamically coupled atmospheric-snow modeling performed by *Thomas et al.* [2011]. The relative contributions of OH production by H_2O_2, NO_3^- or NO_2^- are approximately 60%, 4% and 36%, respectively. It was previously calculated that nitrite and nitrate photolysis contributed a similar amount of OH radicals to the snowpack inventory [*Chu and Anastasio*, 2007], but the snowpack conditions in Barrow with large nitrite concentrations and

relatively low H_2O_2 concentrations favor the production of OH radicals from nitrite (relative to nitrate) compared to previous calculations, but still a factor of ~2 smaller than H_2O_2.

5. Conclusions

[56] The investigations into the optical properties of the snowpacks at Barrow and subsequent in-snow photochemical modeling have allowed a number of important conclusions to be drawn from the work:

[57] 1. It is important to accurately account for spectrally resolved absorption by both black carbon and non-black carbon impurities in the snowpack because non-black carbon impurities have a large absorption cross-section at the short solar wavelengths, responsible for photolytic reactions in the snowpack. The relative importance of the photolysis of nitrite (versus nitrate) as a source of NO_x from the snowpack is increased when absorption of short wavelength solar radiation by non-black carbon impurities is considered.

[58] 2. Estimates of depth-integrated production rates can be scaled and approximately correlated with downwelling UV irradiance for individual snowpacks.

[59] 3. The importance of NO fluxes from the snowpack owing to nitrite photolysis may have been significantly overlooked during previous campaigns. From the calculations in this work, NO from nitrite photolysis is approximately three times larger than NO_2 from nitrate photolysis. The contribution of nitrite to OH radical production in the snowpack is approximately half that of hydrogen peroxide.

[60] **Acknowledgments.** This work is part of the international multidisciplinary OASIS (Ocean-Atmosphere-Sea Ice-Snowpack) program. J.L.F. and M.D.K. thank NERC for support through grants NE/F010788/1 and NE/F004796/1, NERC FSF for support through grant 555.0608 and the RHUL research strategy fund. Funding for this work was also gratefully received from NSF grant ATM-0807702. H.J.R. thanks RHUL for support through the Thomas Holloway Scholarship scheme. D.V., H.W.J. and F.D. acknowledge financial support by the LEFE-CHAT program of CNRS-INSU. The participation of LGGE was funded by the French Polar Institute (IPEV) grant 1017 to F.D. The National Center for Atmospheric Research is sponsored by the National Science Foundation. All sky camera data were obtained from the Atmospheric Radiation Measurement (ARM) Program sponsored by the U.S. Department of Energy, Office of Science, Office of Biological and Environmental Research, Climate and Environmental Sciences Division.

References

Abbatt, J., N. Oldridge, A. Symington, V. Chukalovskiy, R. D. McWhinney, S. Sjostedt, and R. A. Cox (2010), Release of gas-phase halogens by photolytic generation of OH in frozen halide-nitrate solutions: An active halogen formation mechanism?, *J. Phys. Chem. A*, *114*(23), 6527–6533, doi:10.1021/jp102072t.

Adler, G., A. A. Riziq, C. Erlick, and Y. Rudich (2010), Effect of intrinsic organic carbon on the optical properties of fresh diesel soot, *Proc. Natl. Acad. Sci. U. S. A.*, *107*(15), 6699–6704.

Anastasio, C., and L. Chu (2009), Photochemistry of nitrous acid (HONO) and nitrous acidium ion (H_2ONO^+) in aqueous solution and ice, *Environ. Sci. Technol.*, *43*(4), 1108–1114, doi:10.1021/es802579a.

Anastasio, C., and T. Robles (2007), Light absorption by soluble chemical species in Arctic and Antarctic snow, *J. Geophys. Res.*, *112*, D24304, doi:10.1029/2007JD008695.

Anastasio, C., E. S. Galbavy, M. A. Hutterli, J. F. Burkhart, and D. K. Friel (2007), Photoformation of hydroxyl radical on snow grains at Summit, Greenland, *Atmos. Environ.*, *41*(24), 5110–5121, doi:10.1016/j.atmosenv.2006.12.011.

Beine, H. J., I. Allegrini, R. Sparapani, A. Ianniello, and F. Valentini (2001), Three years of springtime trace gas and particle measurements at Ny-Alesund, Svalbard, *Atmos. Environ.*, *35*(21), 3645–3658, doi:10.1016/S1352-2310(00)00529-X.

Beine, H. J., R. E. Honrath, F. Domine, W. R. Simpson, and J. D. Fuentes (2002), NO_x during background and ozone depletion periods at Alert: Fluxes above the snow surface, *J. Geophys. Res.*, *107*(D21), 4584, doi:10.1029/2002JD002082.

Beine, H. J., F. Domine, A. Ianniello, M. Nardino, I. Allegrini, K. Teinila, and R. Hillamo (2003), Fluxes of nitrates between snow surfaces and the atmosphere in the European high Arctic, *Atmos. Chem. Phys.*, *3*, 335–346, doi:10.5194/acp-3-335-2003.

Beine, H. J., A. Amoroso, F. Domine, M. D. King, M. Nardino, A. Ianniello, and J. L. France (2006), Surprisingly small HONO emissions from snow surfaces at Browning Pass, Antarctica, *Atmos. Chem. Phys.*, *6*, 2569–2580, doi:10.5194/acp-6-2569-2006.

Beine, H., A. J. Colussi, A. Amoroso, G. Esposito, M. Montagnoli, and M. R. Hoffmann (2008), HONO emissions from snow surfaces, *Environ. Res. Lett.*, *3*(4), 045005, doi:10.1088/1748-9326/3/4/045005.

Beine, H. J., C. Anastasio, F. Domine, T. A. Douglas, M. Barret, J. L. France, M. D. King, S. R. Hall, and K. Ullmann (2012), Soluble chromophores in marine snow, seawater, sea-ice and frost flowers near Barrow, AK, *J. Geophys. Res.*, doi:10.1029/2011JD016650, in press.

Bloss, W. J., J. D. Lee, D. E. Heard, R. A. Salmon, S. J. B. Bauguitte, H. K. Roscoe, and A. E. Jones (2007), Observations of OH and HO_2 radicals in coastal Antarctica, *Atmos. Chem. Phys.*, *7*(16), 4171–4185, doi:10.5194/acp-7-4171-2007.

Bock, J., and H. W. Jacobi (2010), Development of a mechanism for nitrate photochemistry in snow, *J. Phys. Chem. A*, *114*(4), 1790–1796, doi:10.1021/jp909205e.

Bohren, C. F. (1986), Applicability of effective-medium theories to problems of scattering and absorption by nonhomogeneous atmospheric particles, *J. Atmos. Sci.*, *43*(5), 468–475, doi:10.1175/1520-0469(1986)043<0468:AOEMTT>2.0.CO;2.

Bond, T. C., and R. W. Bergstrom (2006), Light absorption by carbonaceous particles: An investigative review, *Aerosol Sci. Technol.*, *40*(1), 27–67, doi:10.1080/02786820500421521.

Boxe, C. S., and A. Saiz-Lopez (2008), Multiphase modeling of nitrate photochemistry in the quasi-liquid layer (QLL): Implications for NO_x release from the Arctic and coastal Antarctic snowpack, *Atmos. Chem. Phys.*, *8*(2), 6009–6034, doi:10.5194/acpd-8-6009-2008.

Boxe, C. S., A. J. Colussi, M. R. Hoffmann, I. M. Perez, J. G. Murphy, and R. C. Cohen (2006), Kinetics of NO and NO_2 evolution from illuminated frozen nitrate solutions, *J. Phys. Chem. A*, *110*(10), 3578–3583, doi:10.1021/jp055037q.

Chu, L., and C. Anastasio (2003), Quantum yields of hydroxyl radical and nitrogen dioxide from the photolysis of nitrate on ice, *J. Phys. Chem. A*, *107*(45), 9594–9602, doi:10.1021/jp0349132.

Chu, L., and C. Anastasio (2005), Formation of hydroxyl radical from the photolysis of frozen hydrogen peroxide, *J. Phys. Chem. A*, *109*(28), 6264–6271, doi:10.1021/jp051415f.

Chu, L., and C. Anastasio (2007), Temperature and wavelength dependence of nitrite photolysis in frozen and aqueous solutions, *Environ. Sci. Technol.*, *41*(10), 3626–3632, doi:10.1021/es062731q.

Cotter, E. S. N., A. E. Jones, E. W. Wolff, and S. J. B. Bauguitte (2003), What controls photochemical NO and NO_2 production from Antarctic snow? Laboratory investigation assessing the wavelength and temperature dependence, *J. Geophys. Res.*, *108*(D4), 4147, doi:10.1029/2002JD002602.

Couch, T. L., A. L. Sumner, T. M. Dassau, P. B. Shepson, and R. E. Honrath (2000), An investigation of the interaction of carbonyl compounds with the snowpack, *Geophys. Res. Lett.*, *27*(15), 2241–2244, doi:10.1029/1999GL011288.

Dassau, T. M., et al. (2002), Investigation of the role of the snowpack on atmospheric formaldehyde chemistry at Summit, Greenland, *J. Geophys. Res.*, *107*(D19), 4394, doi:10.1029/2002JD002182.

Dibb, J. E., L. G. Huey, D. L. Slusher, and D. J. Tanner (2004), Soluble reactive nitrogen oxides at South Pole during ISCAT 2000, *Atmos. Environ.*, *38*(32), 5399–5409, doi:10.1016/j.atmosenv.2003.01.001.

Doherty, S. J., S. G. Warren, T. C. Grenfell, A. D. Clarke, and R. E. Brandt (2010), Light-absorbing impurities in Arctic snow, *Atmos. Chem. Phys. Discuss.*, *10*(8), 18,807–18,878, doi:10.5194/acpd-10-18807-2010.

Domine, F., and P. B. Shepson (2002), Air-snow interactions and atmospheric chemistry, *Science*, *297*(5586), 1506–1510, doi:10.1126/science.1074610.

Domine, F., M. Albert, T. Huthwelker, H. W. Jacobi, A. A. Kokhanovsky, M. Lehning, G. Picard, and W. R. Simpson (2008), Snow physics as relevant to snow photochemistry, *Atmos. Chem. Phys.*, *8*(2), 171–208, doi:10.5194/acp-8-171-2008.

Domine, F., J.-C. Gallet, J. Bock, and S. Morin (2012), Structure, specific surface area and thermal conductivity of the snowpack around Barrow, Alaska, *J. Geophys. Res.*, doi:10.1029/2011JD016647, in press.

Dubowski, Y., A. J. Colussi, and M. R. Hoffmann (2001), Nitrogen dioxide release in the 302 nm band photolysis of spray-frozen aqueous

nitrate solutions. Atmospheric implications, *J. Phys. Chem. A*, *105*(20), 4928–4932, doi:10.1021/jp0042009.

Dubowski, Y., A. J. Colussi, C. Boxe, and M. R. Hoffmann (2002), Monotonic increase of nitrite yields in the photolysis of nitrate in ice and water between 238 and 294 K, *J. Phys. Chem. A*, *106*(30), 6967–6971, doi:10.1021/jp0142942.

Duggin, M. J., and W. R. Philipson (1982), Field measurement of reflectance: Some major considerations, *Appl. Opt.*, *21*(15), 2833–2840, doi:10.1364/AO.21.002833.

Fierz, C., R. L. Armstrong, Y. Durand, P. Etchevers, E. Greene, D. M. McClung, K. Nishimura, P. K. Satyawali, and S. A. Sokratov (2009), The International classification for seasonal snow on the ground, *IHP-VII Tech. Doc. Hydrol. 83*, UNESCO, Paris.

Fisher, F. N., M. D. King, and J. Lee-Taylor (2005), Extinction of UV-visible radiation in wet midlatitude (maritime) snow: Implications for increased NO_x emission, *J. Geophys. Res.*, *110*, D21301, doi:10.1029/2005JD005963.

France, J. L., M. D. King, and J. Lee-Taylor (2007), Hydroxyl (OH) radical production rates in snowpacks from photolysis of hydrogen peroxide (H_2O_2) and nitrate (NO_3^-), *Atmos. Environ.*, *41*(26), 5502–5509, doi:10.1016/j.atmosenv.2007.03.056.

France, J. L., M. D. King, and J. Lee-Taylor (2010), The importance of considering depth-resolved photochemistry in snow: A radiative-transfer study of NO_2 and OH production in Ny-Alesund snowpacks, *J. Glaciol.*, *56*(198), 655–663, doi:10.3189/002214310793146250.

France, J. L., M. D. King, J. Lee-Taylor, H. J. Beine, A. Ianniello, F. Domine, and A. MacArthur (2011a), Calculations of in-snow NO_2 and OH radical photochemical production and photolysis rates: A field and radiative-transfer study of the optical properties of Arctic (Ny-Ålesund, Svalbard) snow, *J. Geophys. Res.*, *116*, F04013, doi:10.1029/2011JF002019.

France, J. L., M. D. King, M. M. Frey, J. Erbland, G. Picard, S. Preunkert, A. MacArthur, and J. Savarino (2011b), Snow optical properties at Dome C (Concordia), Antarctica; implications for snow emissions and snow chemistry of reactive nitrogen, *Atmos. Chem. Phys.*, *11*(18), 9787–9801, doi:10.5194/acp-11-9787-2011.

Gallet, J. C., F. Domine, L. Arnaud, G. Picard, and J. Savarino (2010), Vertical profiles of the specific surface area of the snow at Dome C, Antarctica, *Cryosphere Discuss.*, *4*(3), 1647–1708, doi:10.5194/tcd-4-1647-2010.

George, I. J., and C. Anastasio (2007), Release of gaseous bromine from the photolysis of nitrate and hydrogen peroxide in simulated sea-salt solutions, *Atmos. Environ.*, *41*(3), 543–553, doi:10.1016/j.atmosenv.2006.08.022.

Gerland, S., J. G. Winther, J. B. Orbaek, G. E. Liston, N. A. Oritsland, A. Blanco, and B. Ivanov (1999), Physical and optical properties of snow covering Arctic tundra on Svalbard, *Hydrol. Processes*, *13*(14–15), 2331–2343, doi:10.1002/(SICI)1099-1085(199910)13:14/15<2331::AID-HYP855>3.0.CO;2-W.

Grannas, A. M., P. B. Shepson, and T. R. Filley (2004), Photochemistry and nature of organic matter in Arctic and Antarctic snow, *Global Biogeochem. Cycles*, *18*, GB1006, doi:10.1029/2003GB002133.

Grannas, A. M., et al. (2007), An overview of snow photochemistry: Evidence, mechanisms and impacts, *Atmos. Chem. Phys.*, *7*(16), 4329–4373, doi:10.5194/acp-7-4329-2007.

Grenfell, T. C., and G. A. Maykut (1977), The optical properties of ice and snow in the Arctic basin, *J. Glaciol.*, *10*, 445–463.

Grenfell, T. C., S. G. Warren, and P. C. Mullen (1994), Reflection of solar-radiation by the Antarctic snow surface at ultraviolet, visible, and near-infrared wavelengths, *J. Geophys. Res.*, *99*(D9), 18,669–18,684, doi:10.1029/94JD01484.

Grenfell, T. C., S. J. Doherty, A. D. Clarke, and S. G. Warren (2011), Light absorption from particulate impurities in snow and ice determined by spectrophotometric analysis of filters, *Appl. Opt.*, *50*, 2037–2048, doi:10.1364/AO.50.002037.

Hoffer, A., A. Gelencsér, P. Guyon, G. Kiss, O. Schmid, G. P. Frank, P. Artaxo, and M. O. Andreae (2006), Optical properties of humic-like substances (HULIS) in biomass-burning aerosols, *Atmos. Chem. Phys.*, *6*(11), 3563–3570, doi:10.5194/acp-6-3563-2006.

Honrath, R. E., M. C. Peterson, S. Guo, J. E. Dibb, P. B. Shepson, and B. Campbell (1999), Evidence of NO_x production within or upon ice particles in the Greenland snowpack, *Geophys. Res. Lett.*, *26*(6), 695–698, doi:10.1029/1999GL900077.

Honrath, R. E., M. C. Peterson, M. P. Dziobak, J. E. Dibb, M. A. Arsenault, and S. A. Green (2000a), Release of NO_x from sunlight-irradiated mid-latitude snow, *Geophys. Res. Lett.*, *27*(15), 2237–2240, doi:10.1029/1999GL011286.

Honrath, R. E., S. Guo, M. C. Peterson, M. P. Dziobak, J. E. Dibb, and M. A. Arsenault (2000b), Photochemical production of gas phase NOx from ice crystal NO_3^-, *J. Geophys. Res.*, *105*(D19), 24,183–24,190, doi:10.1029/2000JD900361.

Honrath, R. E., Y. Lu, M. C. Peterson, J. E. Dibb, M. A. Arsenault, N. J. Cullen, and K. Steffen (2002), Vertical fluxes of NO_x, HONO, and HNO_3 above the snowpack at Summit, Greenland, *Atmos. Environ.*, *36*(15–16), 2629–2640, doi:10.1016/S1352-2310(02)00132-2.

Hutterli, M. A., J. R. McConnell, R. C. Bales, and R. W. Stewart (2003), Sensitivity of hydrogen peroxide (H_2O_2) and formaldehyde (HCHO) preservation in snow to changing environmental conditions: Implications for ice core records, *J. Geophys. Res.*, *108*(D1), 4023, doi:10.1029/2002JD002528.

Hutterli, M. A., J. R. McConnell, G. Chen, R. C. Bales, D. D. Davis, and D. H. Lenschow (2004), Formaldehyde and hydrogen peroxide in air, snow and interstitial air at South Pole, *Atmos. Environ.*, *38*(32), 5439–5450, doi:10.1016/j.atmosenv.2004.06.003.

Jacobi, H. W., B. Kwakye-Awuah, and O. Schrems (2004), Photochemical decomposition of hydrogen peroxide (H_2O_2) and formaldehyde (HCHO) in artificial snow, *Ann. Glaciol.*, *39*, 29–33.

Jacobi, H.-W., D. Voisin, J.-L. Jaffrezo, Cozic, J., and T. A. Douglas (2012), Chemical composition of the snowpack during the OASIS spring campaign 2009 at Barrow, AK, *J. Geophys. Res.*, doi:10.1029/2011JD016654, in press.

Jones, A. E., R. Weller, E. W. Wolff, and H. W. Jacobi (2000), Speciation and rate of photochemical NO and NO_2 production in Antarctic snow, *Geophys. Res. Lett.*, *27*(3), 345–348, doi:10.1029/1999GL010885.

Jones, A. E., R. Weller, P. S. Anderson, H. W. Jacobi, E. W. Wolff, O. Schrems, and H. Miller (2001), Measurements of NO_x emissions from the Antarctic snowpack, *Geophys. Res. Lett.*, *28*(8), 1499–1502, doi:10.1029/2000GL011956.

King, M. D., and W. R. Simpson (2001), Extinction of UV radiation in Arctic snow at Alert, Canada (82°N), *J. Geophys. Res.*, *106*(D12), 12,499–12,507, doi:10.1029/2001JD900006.

Kokhanovsky, A. A., and E. P. Zege (2004), Scattering optics of snow, *Appl. Opt.*, *43*(7), 1589–1602, doi:10.1364/AO.43.001589.

Lee-Taylor, J., and S. Madronich (2002), Calculation of actinic fluxes with a coupled atmosphere-snow radiative transfer model, *J. Geophys. Res.*, *107*(D24), 4796, doi:10.1029/2002JD002084.

Long, C. N., and J. J. DeLuisi (1998), Development of an automated hemispheric sky imager for cloud fraction retrievals, paper presented at 10th Symposium on Meteorological Observations and Instrumentation, Am. Meteorol. Soc., Phoenix, Ariz.

Long, C. N., D. W. Slater, and T. Tooman (2001), Total Sky Imager model 880 status and testing results, *ARM TR-006*, 30 pp., U.S. Dep. of Energy, Washington, D. C.

Lyapustin, A., et al. (2010), Analysis of snow bidirectional reflectance from ARCTAS Spring-2008 Campaign, *Atmos. Chem. Phys.*, *10*(9), 4359–4375, doi:10.5194/acp-10-4359-2010.

McPeters, R. D., A. J. Krueger, P. K. Bhartia, and J. R. Herman (1998), Earth Probe Total Ozone Mapping Spectrometer (TOMS) data products user's guide, *NASA Tech. Publ.*, *1998–206895*, 70 pp.

Morin, S., J. Savarino, M. M. Frey, N. Yan, S. Bekki, J. W. Bottenheim, and J. M. F. Martins (2008), Tracing the origin and Fate of NO_x in the Arctic atmosphere using stable isotopes in nitrate, *Science*, *322*(5902), 730–732, doi:10.1126/science.1161910.

Oum, K. W., M. J. Lakin, and B. J. Finlayson-Pitts (1998), Bromine activation in the troposphere by the dark reaction of O_3 with seawater ice, *Geophys. Res. Lett.*, *25*(21), 3923–3926, doi:10.1029/1998GL900078.

Rowland, G. A., and A. M. Grannas (2011), A solid-phase chemical actinometer film for measurement of solar UV penetration into snowpack, *Cold Reg. Sci. Technol.*, *66*, 75–83, doi:10.1016/j.coldregions.2011.01.009

Shepson, P. B., A. P. Sirju, J. F. Hopper, L. A. Barrie, V. Young, H. Niki, and H. Dryfhout (1996), Sources and sinks of carbonyl compounds in the Arctic Ocean boundary layer: Polar Ice Floe Experiment, *J. Geophys. Res.*, *101*(D15), 21,081–21,089, doi:10.1029/96JD02032.

Simpson, W. R., M. D. King, H. J. Beine, R. E. Honrath, and X. L. Zhou (2002), Radiation-transfer modeling of snow-pack photochemical processes during ALERT 2000, *Atmos. Environ.*, *36*(15–16), 2663–2670, doi:10.1016/S1352-2310(02)00124-3.

Stamnes, K., S. C. Tsay, W. Wiscombe, and K. Jayaweera (1988), Numerically stable algorithm for discrete-ordinate-method radiative-transfer in multiple-scattering and emitting layered media, *Appl. Opt.*, *27*(12), 2502–2509, doi:10.1364/AO.27.002502.

Sturm, M., and G. E. Liston (2003), The snow cover on lakes of the Arctic coastal plain of Alaska, *J. Glaciol.*, *49*(166), 370–380, doi:10.3189/172756503781830539.

Sumner, A. L., et al. (2002), Atmospheric chemistry of formaldehyde in the Arctic troposphere at polar sunrise, and the influence of the snowpack, *Atmos. Environ.*, *36*(15–16), 2553–2562, doi:10.1016/S1352-2310(02)00105-X.

Thomas, J. L., J. Stutz, B. Lefer, L. G. Huey, K. Toyota, J. E. Dibb, and R. von Glasow (2011), Modeling chemistry in and above snow at Summit, Greenland - Part 1: Model description and results, *Atmos. Chem. Phys.*, *11*(10), 4899–4914, doi:10.5194/acp-11-4899-2011.

Villena, G., et al. (2011), Nitrous acid (HONO) during polar spring in Barrow, Alaska: A net source of OH radicals?, *J. Geophys. Res.*, *116*, D00R07, doi:10.1029/2011JD016643.

Wang, Y. H., Y. Choi, T. Zeng, D. Davis, M. Buhr, L. G. Huey, and W. Neff (2008), Assessing the photochemical impact of snow NO_x emissions over Antarctica during ANTCI 2003, *Atmos. Environ.*, *42*(12), 2849–2863, doi:10.1016/j.atmosenv.2007.07.062.

Warren, S. G. (1982), Optical properties of snow, *Rev. Geophys.*, *20*(1), 67–89, doi:10.1029/RG020i001p00067.

Warren, S. G. (1984), Impurities in snow—Effects on albedo and snowmelt review, *Ann. Glaciol.*, *5*, 177–179.

Warren, S. G., and R. E. Brandt (2008), Optical constants of ice from the ultraviolet to the microwave: A revised compilation, *J. Geophys. Res.*, *113*, D14220, doi:10.1029/2007JD009744.

Warren, S. G., and A. D. Clarke (1990), Soot in the atmosphere and snow surface of Antarctica, *J. Geophys. Res.*, *95*(D2), 1811–1816, doi:10.1029/JD095iD02p01811.

Warren, S. G., and W. J. Wiscombe (1980), A model for the spectral albedo of snow. 2. Snow containing atmospheric aerosols, *J. Atmos. Sci.*, *37*(12), 2734–2745, doi:10.1175/1520-0469(1980)037<2734:AMFTSA>2.0.CO;2.

Warren, S. G., and W. J. Wiscombe (1985), Dirty snow after nuclear war, *Nature*, *313*(6002), 467–470, doi:10.1038/313467a0.

Warren, S. G., R. E. Brandt, and T. C. Grenfell (2006), Visible and near-ultraviolet absorption spectrum of ice from transmission of solar radiation into snow, *Appl. Opt.*, *45*(21), 5320–5334, doi:10.1364/AO.45.005320.

Wiscombe, W. J., and S. G. Warren (1980), A model for the spectral albedo of snow. 1. Pure snow, *J. Atmos. Sci.*, *37*(12), 2712–2733, doi:10.1175/1520-0469(1980)037<2712:AMFTSA>2.0.CO;2.

Yang, J., R. E. Honrath, M. C. Peterson, J. E. Dibb, A. L. Sumner, P. B. Shepson, M. Frey, H. W. Jacobi, A. Swanson, and N. Blake (2002), Impacts of snowpack emissions on deduced levels of OH and peroxy radicals at Summit, Greenland, *Atmos. Environ.*, *36*(15–16), 2523–2534, doi:10.1016/S1352-2310(02)00128-0.

C. Anastasio and H. Beine, Department of Land, Air, and Water Resources, University of California, 1 Shields Ave., Davis, CA 95616-8627, USA.

F. Domine, H. W. Jacobi, and D. Voisin, Laboratoire de Glaciologie et Géophysique de l'Environnement, CNRS/Université Joseph Fourier – Grenoble 1, F-38402 St Martin d'Hères CEDEX, France.

J. L. France, M. D. King, and H. J. Reay, Department of Earth Sciences, Royal Holloway, University of London, Egham TW20 0EX, UK. (m.king@es.rhul.ac.uk)

J. Lee-Taylor, Atmospheric Chemistry Division, National Center for Atmospheric Research, Boulder, CO 80307, USA.

A. MacArthur, NERC Field Spectroscopy Facility, Grant Institute, School of GeoSciences, University of Edinburgh, Edinburgh EH9 3JW, UK.

Appendix 2

Snowpack in Barrow, Alaska: OASIS Spring Campaign 2009

A2.1 Introduction

A summary of the snowpacks investigated around the Barrow area for OASIS 09 are presented in chapters 2a and 2b, including basic stratigraphy, surface albedo, light attenuation within the snow, absorption spectra due to impurities and calculated in-snow photochemical reaction rates. The absorption profiles for the 7 snowpacks measured are presented here in Appendix 2.

A2.2 Absorption Cross-section

Figures A2.1-2.7 show the absorption cross-sections for the snowpack measurement during the Barrow OASIS 2009 campaign.

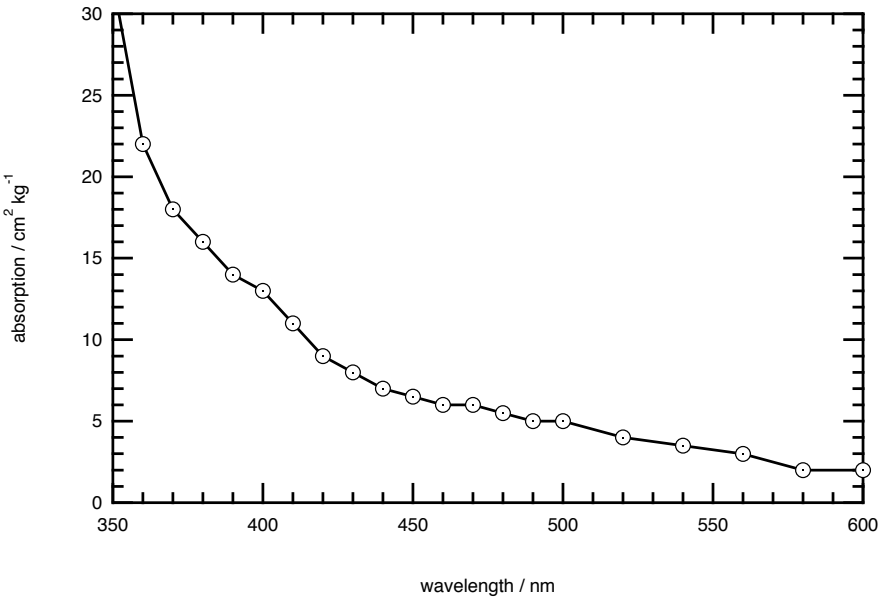

Figure A2.1. Absorption cross-section for the snowpack on Day 68. The *Upper Limit* for black carbon concentration in the snowpack, assuming all absorption at 600nm is due to black carbon, is 20 $ng_{(carbon)}g^{-1}_{(snow)}$.

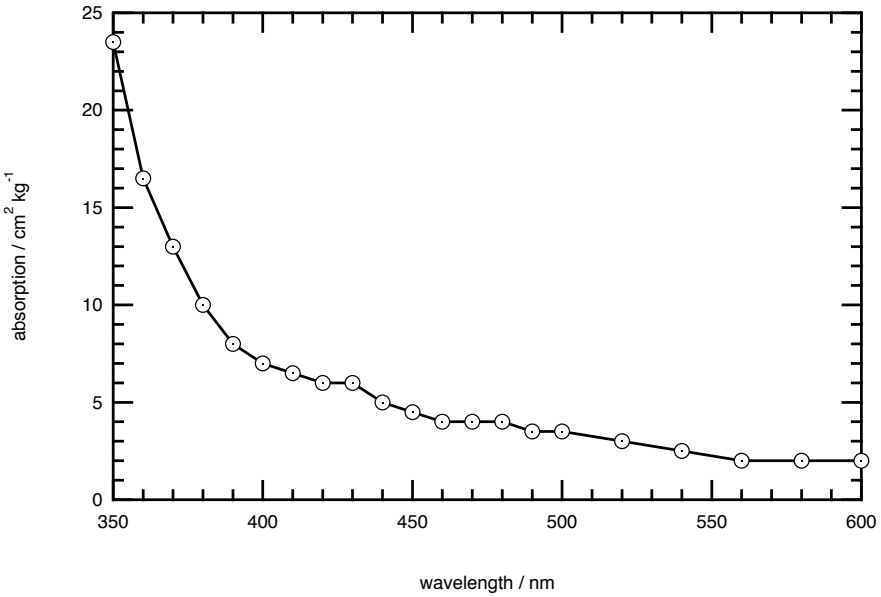

Figure A2.2. Absorption cross-section for the snowpack on Day 69. The *Upper Limit* for black carbon concentration in the snowpack, assuming all absorption at 600nm is due to black carbon, is 20 $ng_{(carbon)}g^{-1}_{(snow)}$.

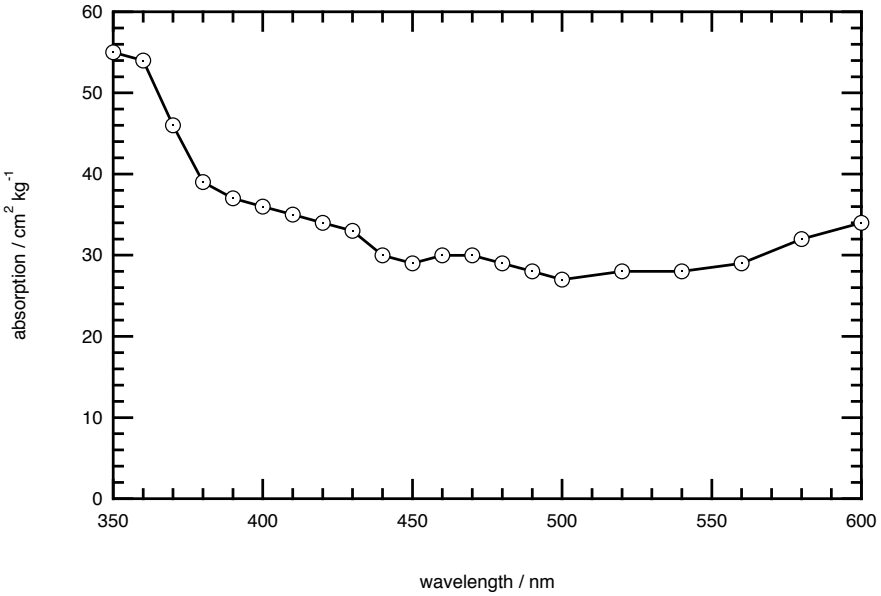

Figure A2.3. Absorption cross-section for the snowpack on Day 70. The *Upper Limit* for black carbon concentration in the snowpack, assuming all absorption at 600nm is due to black carbon, is 340 $ng_{(carbon)}g^{-1}_{(snow)}$.

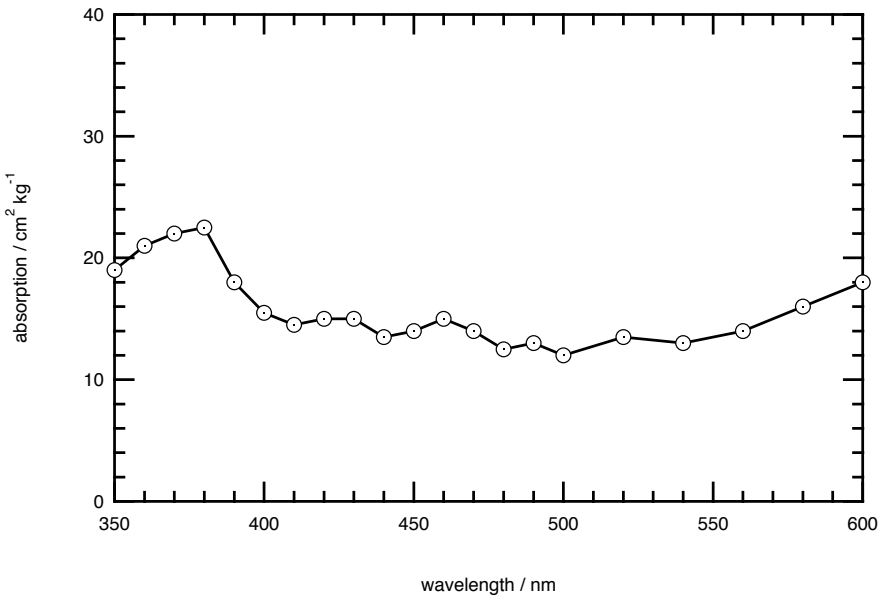

Figure A2.4. Absorption cross-section for the snowpack on Day 72. The *Upper Limit* for black carbon concentration in the snowpack, assuming all absorption at 600nm is due to black carbon, is 180 $ng_{(carbon)}g^{-1}_{(snow)}$.

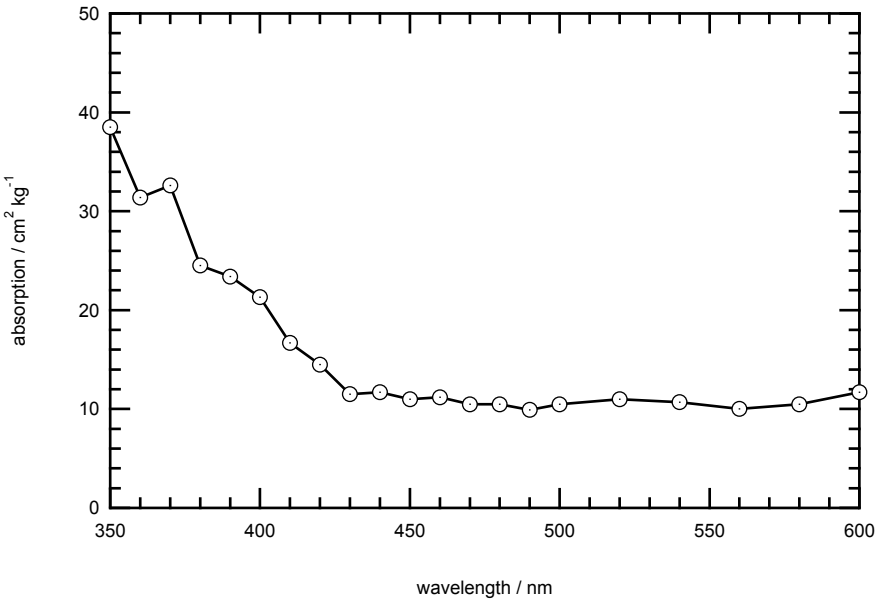

Figure A2.5. Absorption cross-section for the snowpack on Day 76. The *Upper Limit* for black carbon concentration in the snowpack, assuming all absorption at 600nm is due to black carbon, is 120 $ng_{(carbon)}g^{-1}_{(snow)}$.

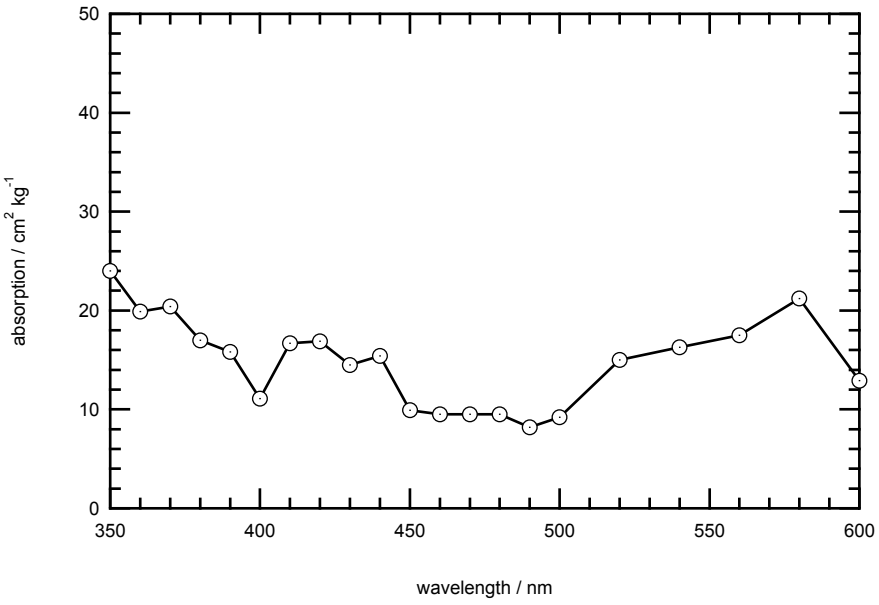

Figure A2.6. Absorption cross-section for the snowpack on Day 79. The *Upper Limit* for black carbon concentration in the snowpack, assuming all absorption at 600nm is due to black carbon, is 130 $ng_{(carbon)}g^{-1}_{(snow)}$.

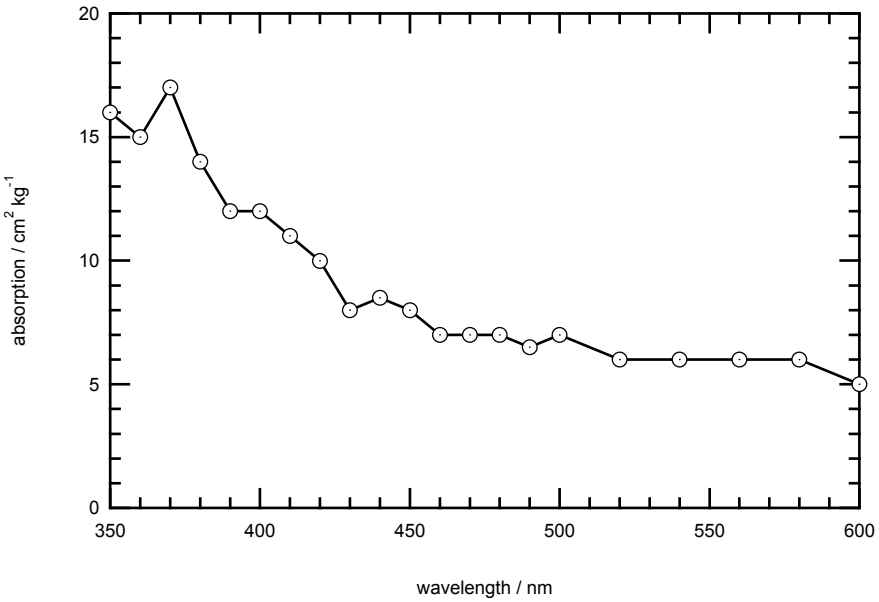

Figure A2.7. Absorption cross-section for the snowpack on Day 85. The *Upper Limit* for black carbon concentration in the snowpack, assuming all absorption at 600nm is due to black carbon, is 50 $ng_{(carbon)}g^{-1}_{(snow)}$.

A2.3 Scattering and absorption coefficients for the Barrow snowpack

The absorption and scattering coefficients, at 400 nm, for all snowpacks measured throughout the Barrow campaign can be found in Table A2.1.

Day Number	σ_{scatt} / **m^2 kg^{-1}**	σ^{+}_{abs} / **cm^2 kg^{-1}**
68	4	12
69	2.5	8
70	4	37
72	1.5	16
76	2	21
79	2	11
85	2	12

Table A2.1. Absorption and scattering coefficients derived to allow the calculation of in-snow photochemistry using TUV-snow.

Appendix 3

Decreased albedo, *e*-folding depth and photolytic OH radical and NO_2 production with increasing black carbon content in Arctic snow

Decreased albedo, *e*-folding depth and photolytic OH radical and NO_2 production with increasing black carbon content in Arctic snow

H. J. Reay,[1] J. L. France,[1] and M. D. King[1]

Received 28 July 2011; revised 17 April 2012; accepted 18 April 2012; published 12 June 2012.

[1] The contribution of snow photochemistry to snow and atmospheric oxidative capacity is controlled, in part, by snow albedo and *e*-folding depths in snow. Albedo and *e*-folding depths (and thus snow photochemistry) are a function of black carbon concentration in snow. The paper presented here demonstrates the complicated response of albedo, *e*-folding depth (wavelengths 300–600 nm) and depth-integrated production rates of NO_2 and OH radicals to increasing black carbon concentration in well-characterized snowpacks of the Barrow OASIS campaign, Alaska. All snowpacks were reworked layered windpacks and were found to have similar responses to changes in black carbon concentration. The radiative-transfer calculations demonstrate two light absorption regimes: ice-dominated and black carbon dominated. The ice-dominated and black carbon dominated behavior of albedo, *e*-folding depth and depth-integrated production rates with increasing black carbon concentrations are presented. For black carbon concentrations greater than 20 ng g^{-1} (wavelength range of 300–600 nm), *e*-folding depth and depth-integrated production rate have an inverse power law relationship with black carbon concentration. Doubling the black carbon concentration decreases the *e*-folding depth to ~70% of the initial value and for solar zenith angles greater than 60°, doubling the black carbon concentration decreases depth-integrated production rates of NO_2 and OH to ~70% and ~65% of their original values respectively.

Citation: Reay, H. J., J. L. France, and M. D. King (2012), Decreased albedo, *e*-folding depth and photolytic OH radical and NO_2 production with increasing black carbon content in Arctic snow, *J. Geophys. Res.*, *117*, D00R20, doi:10.1029/2011JD016630.

1. Introduction

[2] Recent climatic changes in the Arctic i.e., thinning sea-ice, early springs and glacier retreat is, in part, due to warming associated with increased black carbon content in Arctic snow [*Hansen and Nazarenko*, 2004]. Trace amounts of dust, HULIS (HUmic Like Substances) and black carbon deposited on or within a snowpack can reduce its albedo relative to pure snow [e.g., *Clarke and Noone*, 1985; *Warren*, 1982; *Warren and Wiscombe*, 1980b, 1985; *France et al.*, 2011b]. Changes in the extent of global snow and ice can account for up to fifty percent of interannual variability in planetary albedo [*Qu and Hall*, 2005]. Studies have shown that the albedo of snow can be reduced by ~1% with the addition of ~10 ng g^{-1} of black carbon in snow [*Clarke and Noone*, 1985; *Flanner et al.*, 2007; *Grenfell et al.*, 2002; *Hansen and Nazarenko*, 2004; *Jacobson*, 2004]. *Hansen and Nazarenko* [2004] suggest black carbon in snow is a factor of two more efficient than atmospheric carbon dioxide in altering global air temperatures and has a maximum global radiative forcing of +0.3 W m^{-2}. Typical concentrations of black carbon (found in snow throughout the world) are 0.2–60 ng g^{-1} with extreme values greater than 250 ng g^{-1} [e.g., *Clarke and Noone*, 1985; *Hansen and Nazarenko*, 2004, *Hegg et al.*, 2010]. Using the method developed by *Clarke and Noone* [1985], *Doherty et al.* [2010] reported equivalent black carbon, C^{BC}_{equiv}, (the mass of black carbon present in the snow to account for total light absorption in the snowpack) concentrations in the Canadian and Alaskan Arctic as 14 ± 7 ng g^{-1}. Increasing concentrations of black carbon in snow increases the amount of incident light absorbed by snow [*Warren*, 1984; *Warren et al.*, 2006] and decreases the *e*-folding depth of the snowpack. The *e*-folding depth is a useful metric in snow photochemistry and is the depth for irradiance to decrease to $\frac{1}{e}$ (or ~37%) of its initial value within a snowpack. The *e*-folding depth, ε, can be mathematically defined using equation (1)

$$\frac{I_d}{I_{d'}} = e^{-\frac{d-d'}{\varepsilon}} \quad (1)$$

[1]Department of Earth Sciences, Royal Holloway University of London, Egham, UK.

Corresponding author: M. D. King, Department of Earth Sciences, Royal Holloway University of London, Egham, TW20 0EX, UK. (m.king@es.rhul.ac.uk)

where I_d is the irradiance in snow at a depth d relative to a reference irradiance $I_{d'}$ at depth d'. Depth, d, is deeper than d'. Note d' is a few cm below the surface of the snowpack where all irradiance is isotropic [e.g., *King and Simpson*, 2001].

[3] Snowpack is an efficient medium for chemical photolysis [e.g., *Dominé and Shepson*, 2002; *Grannas et al.*, 2004, 2007] and reduction of the e-folding depth by increasing black carbon concentration in the snow will reduce the rate of photolysis of impurities and pollutants in the snowpack such as nitrate [e.g., *Fisher et al.*, 2005; *France et al.*, 2010; *King and Simpson*, 2001]. Photolysis of nitrate, NO_3^-, in the snowpack produces a molecular flux of NO_2 from the snowpack to the atmosphere (reaction (2)) [*Anastasio et al.*, 2007; *Beine et al.*, 2006, 2008; *Chu and Anastasio*, 2007; *Fisher et al.*, 2005; *France et al.*, 2007, 2010; *King and Simpson*, 2001; *Simpson et al.*, 2002] and a decrease in the molecular flux of NO_2 with increasing black carbon content is expected. Hydroxyl radicals, OH, are also produced in the snowpack by photolysis of the nitrate anion (2) and independently by the photolysis of hydrogen peroxide (4) (both naturally found in snowpacks).

$$NO_3^- + h\nu \rightarrow NO_2 + O^- \quad (2)$$

$$O^- + H_2O \rightarrow OH + OH^- \quad (3)$$

$$H_2O_2 + h\nu \rightarrow 2OH \quad (4)$$

Production of hydroxyl radicals may be responsible for halogen activation and fluxes of organic chemicals from the snow [e.g., *Abbatt*, 2003; *Chu and Anastasio*, 2005; *Dominé and Shepson*, 2002; *Peterson and Honrath*, 2001]. Larger molecular fluxes of NO_2 from the snowpack or larger yields of OH radicals in the snowpack are associated with a larger e-folding depth [e.g., *Fisher et al.*, 2005; *France et al.*, 2010] and less light absorption by snowpack or its impurities (i.e., less black carbon or other light-absorbing snow impurities such as dust or HULIS).

[4] Previous radiative-transfer calculations of light propagation in snowpack undertaken by the authors and others have always required the addition of black carbon to the snow to match the modeled snowpack reflectivity and e-folding depth with field measurements of e-folding depth and reflectivity of snowpacks [e.g., *Beine et al.*, 2006; *Fisher et al.*, 2005; *France et al.*, 2010; *King et al.*, 2005, *Lee-Taylor and Madronich*, 2002]. Increases in the concentration of black carbon may decrease the albedo, e-folding depth and flux of chemicals from the snowpack and vice versa. Previous studies have considered the effect of black carbon on snowpack albedo [e.g., *Aoki et al.*, 2000; *Chylek et al.*, 1983, 1987; *Flanner et al.*, 2007; *Warren and Wiscombe*, 1980b, 1985] but to the authors' knowledge the response of e-folding depth and depth-integrated production rate of chemicals from snowpack has not been quantified solely as a function of black carbon concentration in snowpack. The detailed field and modeling study of the Barrow snowpacks during the OASIS campaign [*France et al.*, 2012] provided enough data to allow e-folding depth, albedo and depth-integrated production rates to be calculated as a function of black carbon.

[5] The paper describes in detail one of these snowpacks and the results from all four snowpacks described in *France et al.* [2012] are in the auxiliary material.[1]

2. Modeling Procedure

[6] Albedo, e-folding depth and depth-integrated production rates of OH and NO_2 radicals for four Barrow snowpacks [*France et al.*, 2012] are calculated from irradiances within snowpack as a function of black carbon content, solar zenith angle and sky conditions (i.e., clear or completely cloudy skies). It is necessary to describe (a) the snowpits selected for this study (b) the radiative-transfer calculations of irradiance in the snow and (c) the calculations of albedo, e-folding depth and depth-integrated production rates from irradiances in the snow.

2.1. Snowpacks

[7] Generally the snowpack stratigraphy constituted a basal depth hoar with intermediate layers of faceted crystals and windpacked top layers frequently coated with a thin layer of diamond dust [*Domine et al.*, 2011]. The four snowpacks were 'soft', 'hard', 'snow on sea-ice' and 'inland' and the snowpack considered here is the hard snowpack. The hard snowpack (also considered in *France et al.* [2012]) was located at 71.31896°N, 156.6723°W and consisted of rounded grains with a density of 0.38 g cm^{-3} and a temperature of −15°C. Scattering values, σ_{scatt}, of 2.0, 2.0, 1.8, 1.8, 2.0, 2.2 and 3.0 were found at wavelengths of 300, 350, 400, 450, 500, 550 and 600 nm respectively. The snowpack is characteristic of the snowpack around the atmospheric chemistry experiments near the BARC building.

2.2. Radiative-Transfer Calculations

[8] Irradiances in the snowpack were calculated using the radiative-transfer code in the model TUV-snow [*Lee-Taylor and Madronich*, 2002]. TUV-snow is a coupled atmosphere-snow radiative-transfer model with an eight-stream discrete-ordinates scheme [*Stamnes et al.*, 1988]. Downwelling and spherical irradiances of short-wave radiation (λ = 280–700 nm, $\Delta\lambda$ = 1 nm) were calculated from the top of the atmosphere through sixty-five unequal layers, varying from 0.001, 0.01, 1 or 2 km, to 30 unequal snow layers varying from either 0.1, 0.5, 1, 5 or 10 cm (5 thinner layers (1 mm) are at the snow surface) all within a 1 m snowpack. The atmosphere was modeled with and without thick clouds to calculate irradiances (and thus photolysis rate coefficients) for photochemical reactions in snow for clear sky conditions and to calculate albedo and e-folding depths for diffuse sky conditions respectively. To obtain diffuse sky conditions a 100 m thick cloud layer is placed 1 km above the ground with an optical depth of 16, an asymmetry factor of 0.86 and single scattering albedo of 0.9999. For the work presented here the albedo of the snowpack was calculated as a ratio of upwelling and downwelling irradiance at the snow surface. The e-folding depth, ε, was calculated by fitting equation (1), to the downwelling irradiances, I_d, at depths, d, of 10, 20, 30 and 40 cm in the snowpack with a reference depth, d', of

[1] Auxiliary materials are available in the HTML. doi:10.1029/2011JD016630.

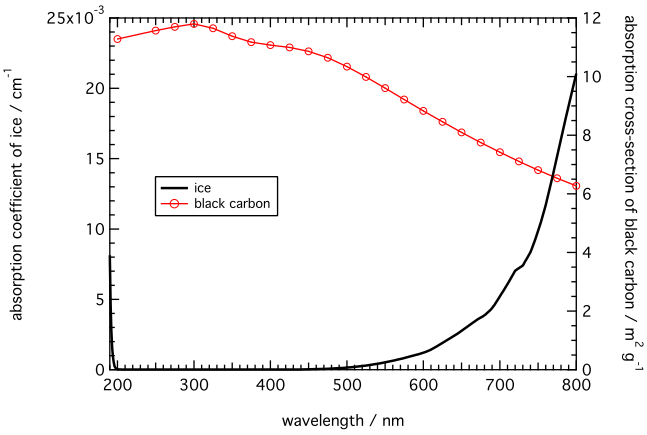

Figure 1. Absorption of ice and the absorption cross-section of a spherical black carbon particle calculated from Mie theory (density = 1 g cm^{-3}, complex index of refraction = 1.9–0.5i, media index of refraction = 1.0, particle size radius = 0.1 μm). See *Warren and Brandt* [2008, Figure 1], *Warren and Wiscombe* [1985, Figure 1], and *Warren and Wiscombe* [1980a, 1980b] for further details.

10 cm. The depths of 10, 20, 30 and 40 cm are within the asymptotic zone [*Simpson et al.*, 2002; *Warren*, 1982] where any direct radiation entering the snowpack is effectively diffused due to multiple scattering within the upper few cm of the snowpack.

[9] The albedo of a snowpack is a function of solar zenith angle [*Warren*, 1982, 1984; *Warren and Clarke*, 1986; *Warren and Wiscombe*, 1985]. The albedo measured under diffuse-only solar illumination (i.e., no direct radiation or solely isotropic radiation) is not dependent on solar zenith angle. The albedos are reported for diffuse solar radiation to demonstrate the effect of increasing black carbon on snowpack albedo and not the effect of solar zenith angle on snowpack albedo. The calculation of the *e*-folding depth is independent of the absolute values of irradiance incident on the snow surface and independent of the solar zenith angle as the *e*-folding depth is only measured in the asymptotic zone of the snowpack (i.e., below the top few cm) where all solar direct radiation has been converted to diffuse radiation by multiple scattering in the top few cm of snow [*France and King*, 2012; *King and Simpson*, 2001; *Lee-Taylor and Madronich*, 2002]. Depth-integrated production rates for the photolysis of H_2O_2 and NO_3^- (reactions (2) and (4)) were calculated for clear skies at four solar zenith angles: 60°, 69°, 75°, 86°. The Earth-Sun distance was based on the date of measurement of 11th March 2009, the ozone column was 428 Dobson units with no atmospheric aerosol (the presence or absence of atmospheric aerosol will not effect the calculation of *e*-folding depth or diffuse albedo). Exploratory calculations showed that the inclusion of an atmospheric aerosol profile described by *Elterman* [1968] reduces the photolysis coefficient for the photolysis of NO_2 by ~10% at 5 cm depth in the snowpack. Previous work by the authors [*Fisher et al.*, 2005; *France et al.*, 2007, 2010, 2011a, 2012; *King et al.*, 2005] have neglected atmospheric aerosol column and the work presented here is consistent with that work. The value of under-snow albedo is not important in the work described here as the snowpack thickness is large enough (typical >3–5 *e*-folding depths) to ensure it is optically semi-infinite as demonstrated in *France et al.* [2010] and previously by *Warren and Wiscombe* [1980a]. The asymmetry factor, g, used for snow was 0.89 [*Lee-Taylor and Madronich*, 2002]. *Aoki et al.* [2000] investigated the difference for single scattering parameters (asymmetry parameter, g) for snow grains between Mie theory and Henyey-Greenstein theory and note that for BRDF calculations at greater than 1.4 μm there is a difference in asymmetry parameters determined by the different methods. However, for albedo and at wavelengths less than 1.4 μm the Mie theory gives the same results as the Henyey-Greenstein theory.

[10] The optical properties of the snowpack may be characterized by wavelength dependent scattering and absorption cross-sections [*Lee-Taylor and Madronich*, 2002]. The absorption cross-section, σ_{abs}, is the sum of light absorption owing to water-ice, σ_{abs}^{ice}, and absorption owing to all light-absorbing species in the snowpack, σ_{abs}^{+}; for the study presented here, all absorption by light-absorbing species in the snowpack is due to black carbon. The absorption cross-section of ice was taken from *Warren and Brandt* [2008] and is plotted in Figure 1. The ice absorption cross-section is not well known in the wavelength region of 200–400 nm. *Warren and Brandt* [2008] noted the imaginary part of the refractive index of ice is effectively no different from zero (below 2×10^{-11}) in this wavelength region and therefore the value of the ice absorption cross-section used in this work is a linearly interpolated value between values for wavelengths of 200–400 nm.

[11] The absorption cross-section of black carbon particles was calculated after the work of *Warren and Wiscombe* [1985, 1980b] and using the Mie code of *Bohren and Huffman* [1983]. The absorption cross-section used for the black carbon particle is reproduced in Figure 1. Briefly the black carbon particles were assumed to be spheres of radius 0.1 μm, with a density of 1 g cm^{-3} and a complex refractive index of 1.8–0.5i. The uncertainty in these properties will be discussed later. The calculated absorption cross-section for black carbon agrees well with the measured black carbon absorption cross-section from *Bond and Bergstrom* [2006], as shown in *France et al.* [2012]. Albedo and *e*-folding depths were calculated at seven discrete wavelengths: 300, 350, 400, 450, 500, 550 and 600 nm while photolysis rate coefficients were calculated every nanometer over 290–600 nm. The albedo, *e*-folding depth and photolysis rate coefficients for reactions (2) and (4) were calculated with concentrations of black carbon in snow of 1, 2, 4, 8, 16, 32, 64, 128, 256, 512 and 1024 ng g^{-1}. The range encompasses the present-day black carbon concentrations of the Barrow snowpack but also with higher and lower concentrations to assess how increasing/decreasing black carbon concentration will affect the *e*-folding depth, albedo and photolysis rate coefficients. The concentrations of black carbon bracket the values found experimentally [*Doherty et al.*, 2010]. To demonstrate the accuracy of the radiative-transfer method described above, the albedo and *e*-folding depth were calculated for a Barrow snowpack described in *France et al.* [2012]. Figure 2 demonstrates a measured nadir reflectivity and *e*-folding depth, and a sample model fit to the

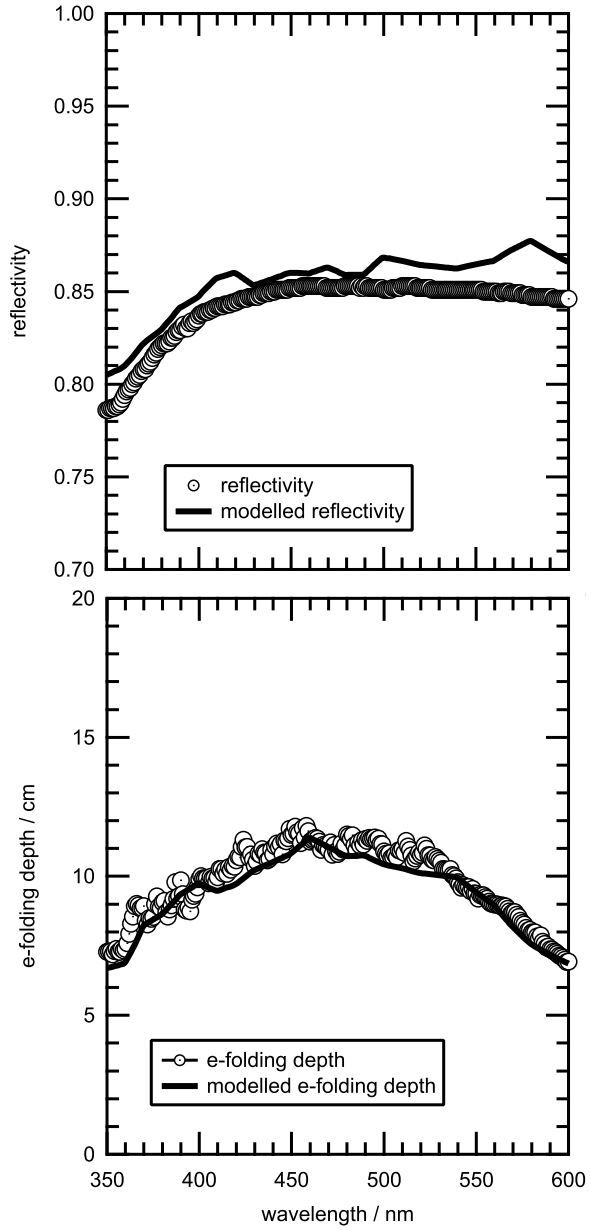

Figure 2. The *e*-folding depth and reflectance measured for the hard snowpack during the Barrow OASIS campaign [*France et al.*, 2012] compared to modeled *e*-folding depth and reflectance using TUV-snow [*Lee-Taylor and Madronich*, 2002], with wavelength variable snow optical properties (σ^{+}_{abs} and σ_{scatt}) and a snowpack density of 0.38 g cm^{-3}.

measurements using scattering cross-sections and absorption cross-sections in *France et al.* [2012]. Reproducing snow reflectivity and *e*-folding depth simultaneously is a rigorous test of the method as there are less parameters (more constrained) than fitting simply albedo [e.g., *Jacobson*, 2004].

2.3. Depth-Integrated Production Rate Calculations

[12] Detailed descriptions for the calculation of photolysis rate coefficients, *J*, and depth-integrated production rates are found in *France et al.* [2012]. Briefly, photolysis rate coefficients, *J*, for reactions (2) and (4) were calculated using,

$$J = \int_{\lambda=290\text{nm}}^{\lambda=600\text{nm}} \sigma(\lambda, \mathrm{T})\Phi(\lambda, \mathrm{T})\mathrm{I}(\theta, \lambda)\mathrm{d}\lambda, \quad (5)$$

where σ is the absorption cross-section for NO_3^- or H_2O_2 taken from *Chu and Anastasio* [2003, 2005] respectively, Φ is quantum yield (0.71 for H_2O_2 and 0.34 $\times$ 10^{-3} for NO_3^-) with values adjusted for temperature (T = -10°C) taken from *Chu and Anastasio* [2003, 2005] respectively; I is the spherical (or point) irradiance, sometimes termed 'actinic flux', calculated using TUV-snow [*Lee-Taylor and Madronich*, 2002] within the snowpack. *Warren and Wiscombe* [1980a] note that the diffuse albedo for snowpacks approximates the direct albedo at a solar zenith angle of ~60°. Thus, to a first approximation, the photolysis rate coefficient calculated at a solar zenith angle of 60° may be taken as representative of diffuse-only sky conditions. Depth-integrated production rates, F, of NO_2 and OH radicals were calculated using equation (6)

$$\mathrm{F} = [x] \int_{\mathrm{z}=0m}^{\mathrm{z}=1m} J\,\mathrm{dz} \quad (6)$$

where z is the depth into the snowpack and [*x*] is the concentration of NO_3^- or H_2O_2; 3.9 μmol L^{-1} [*Jacobi et al.*, 2012] and 0.4 μmol L^{-1} [*Beine et al.*, 2011] respectively. A depth-integrated production rate of NO_2 may be considered equal to a potential molecular flux of photolytically produced NO_2 from the snowpack to the atmosphere in the absence of secondary reactions, photolysis or any impediment by the crystal matrix. Hydroxyl radicals are very reactive and have a very short lifetime thus they are not considered to advect from the snowpack.

[13] Equation (6) assumes a depth-independent concentration of hydrogen peroxide or nitrate. *France et al.* [2007] demonstrated the concentration-depth dependence of a chromophore tends to decrease over an order of magnitude with depth compared to light irradiance which decreases over many orders of magnitude over the same snow depth. *France et al.* [2007] also demonstrated the depth-integrated production rate of hydroxyl radical from the South Polar snowpit varied by 3–5% when considering depth-dependent chromophore concentrations or constant depth chromophore concentrations.

3. Results

3.1. Effect of Black Carbon Concentration on *e*-folding Depth

[14] Figure 3 plots *e*-folding depth versus black carbon concentration. The variation of *e*-folding depth with black carbon has two regimes dependent on black carbon concentration: In the first regime, the concentration of black carbon is less than 20 ng g^{-1} and light absorption is dominated by ice. The wavelength dependence of *e*-folding depths (for wavelengths 450–600 nm) is due to the absorption cross-section of ice, σ_{ice}, increasing quickly with wavelength over the range 450–600 nm, as shown in

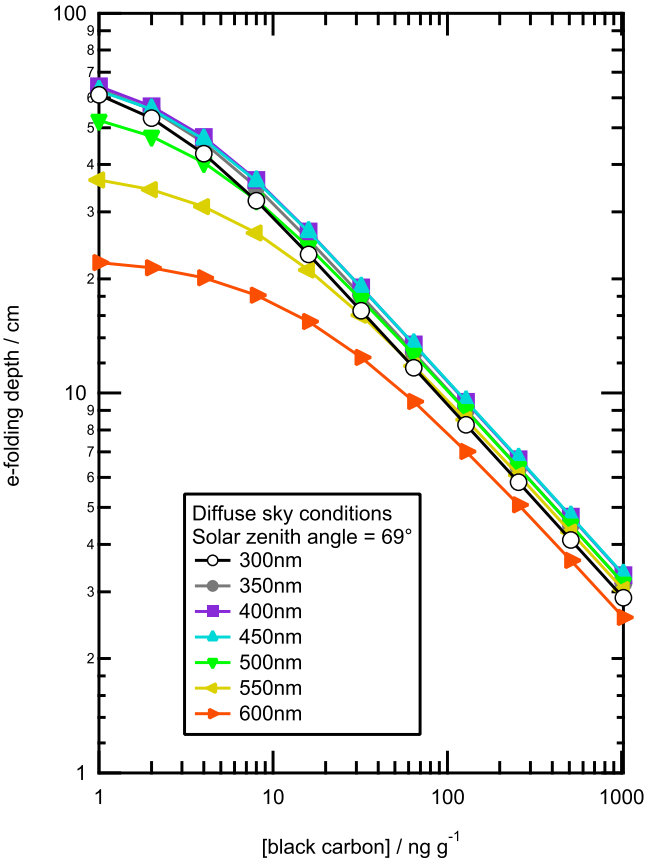

Figure 3. The *e*-folding depths plotted versus black carbon concentration for solar wavelengths of 300, 350, 400, 450, 500, 550 and 600 nm under diffuse sky conditions (nominal solar zenith angle of 69°).

Figure 1. In the second regime, black carbon concentration is greater than 20 ng g^{-1}, and the absorption of solar radiation in the snowpack is dominated by black carbon (Figure 3). The variation of the absorption cross-section of black carbon, σ^{+}_{abs}, with wavelength is small relative to ice and decreases from 300 nm to 1000 nm, i.e., opposite behavior to the absorption cross-section of ice with wavelength (Figure 1).

[15] For concentrations of black carbon greater than 10–20 ng g^{-1} (depending on wavelength), the variation of *e*-folding depth with respect to black carbon concentration obeys a simple power law (as shown in Figure 3).

$$e\text{-folding depth} = \alpha_E[\text{black carbon}]^{-\beta_E} \quad (7)$$

The curves in Figure 3 are fitted to equation (7) for each wavelength. The values of α_E and β_E are displayed in Table 1 along with the range of black carbon concentration over which the power law is valid. The exponent, β_E, in equation (7) is approximately −0.5 thus a doubling of the black carbon concentration (above 10–20 ng g^{-1}) will reduce the light penetration depth to ∼70% of its initial value. All values have an uncertainty of 1 standard deviation from fitting the power law.

3.2. Effect of Black Carbon Concentration on Albedo

[16] Figure 4 plots decreasing albedo with increasing black carbon concentration under diffuse sky conditions. Large decreases of the albedo for increasing black carbon are noted but the albedo response for each wavelength is different. As the black carbon concentration increases the wavelength dependence of the albedo reverses as the absorption of light within the snowpack is influenced more by black carbon and less by water-ice as described in section 3.1. The relationship in equation (7) is not valid for albedo. The decrease or increase in albedo for doubling or halving the concentration of black carbon around 32 ng g^{-1} is approximately 2–3%.

3.3. The Effect of Black Carbon Concentration on Snowpack Photochemistry

[17] Figures 5 and 6 plot the variation of $F(NO_2)$ and F(OH), respectively, as a function of black carbon concentration. The dependence of $F(NO_2)$ and F(OH) on the concentration of black carbon matches the behavior shown in Figure 3 for the *e*-folding depth, with ice dominated absorption below 20 ng g^{-1} and black carbon dominated absorption above 20 ng g^{-1}. The variation of $F(NO_2)$ and F(OH) with black carbon is fitted to the power law in equation (8) and the values of α_F and β_F are in Table 2.

$$F(NO_2 \text{ or } OH) = \alpha_F[\text{black carbon}]^{-\beta_F} \quad (8)$$

Note the value of β_F for all snowpack with black carbon concentrations greater than 16 ng g^{-1} and a solar zenith angle of greater than 60° is approximately −0.5 for $F(NO_2)$ and approximately −0.6 for F(OH). Thus, a doubling of snowpack black carbon concentration will reduce $F(NO_2)$ and F(OH) to ∼70% and ∼65% of initial values respectively.

[18] The decrease in depth-integrated production rates of OH radicals and NO_2 molecules with increasing black carbon concentrations were calculated at four different solar zenith angles and clear skies (Figures 5 and 6). The black carbon concentrations used in the calculations were between 1 and 1024 ng g^{-1}, a range that encompasses the present-day black carbon concentrations of the Barrow snowpack

Table 1. Power Law Coefficients For Relating *e*-Folding Depth, ε, to Black Carbon Concentration ($\varepsilon = \alpha_E[\text{black carbon}]^{-\beta_E}$) for Black Carbon Concentrations Greater Than 20 ng g^{-1}

Snow Type	Wavelength (nm)	α_E (cm ng^{β_E} $g^{-\beta_E}$)	$-\beta_E$	Range of [Black Carbon] Equation (7) is Valid Over (ng g^{-1})
Hard	300	89.1 ± 0.911	0.489 ± 0.00353	8–512
	350	96.2 ± 1.36	0.485 ± 0.00487	8–512
	400	100 ± 1.63	0.482 ± 0.00562	8–512
	450	98.8 ± 1.79	0.479 ± 0.00624	8–512
	500	92.3 ± 1.50	0.480 ± 0.0046	16–512
	550	81.2 ± 2.28	0.467 ± 0.00675	32–512
	600	55.8 ± 2.94	0.406 ± 0.0125	32–512

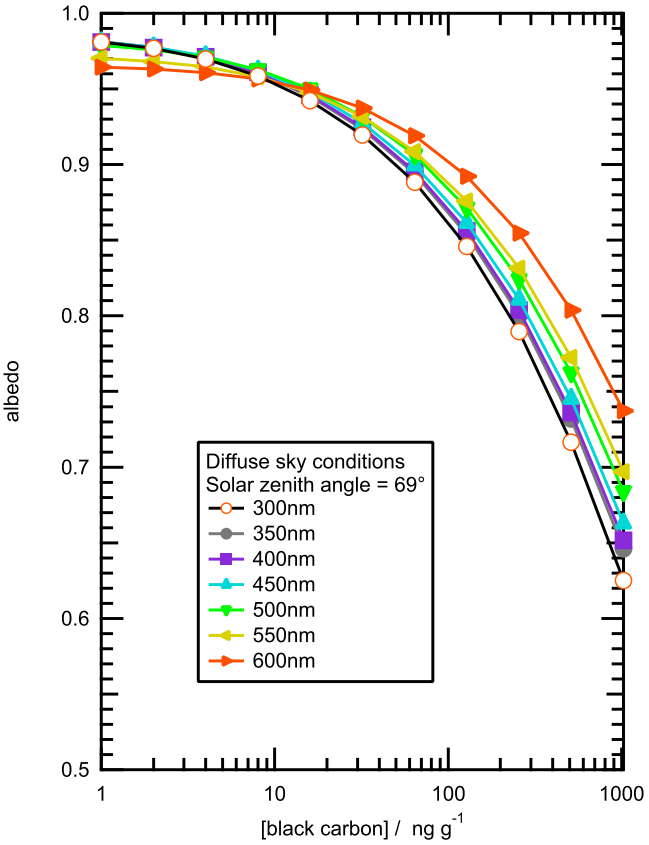

Figure 4. Albedos i.e., ratio of upwelling and downwelling irradiance plotted versus black carbon concentration for light wavelengths of 300, 350, 400, 450, 500, 550 and 600 nm under diffuse sky conditions (nominal solar zenith angle of 69°).

but also with higher and lower concentrations to assess how increasing/decreasing black carbon concentration will affect snowpack photochemistry. The large black carbon concentrations used in this study are probably unrealistically large. Depth-integrated photolytic production rates reported by *France et al.* [2012] are the actual values calculated for the OASIS 2009 campaign as absorption by both HULIS and black carbon is considered. Chemical measurements of black carbon and HULIS were made by *Voisin et al.* [2012]. The study presented here considers only black carbon absorption (the most efficient absorber per gram of carbon among aerosol carbonaceous constituents [*Hoffer et al.*, 2006]) to assess how varying black carbon concentrations will affect the photochemical production rates of snowpacks. Note the three other snowpacks studied by *France et al.* [2012] gave similar results as those shown in Figures 3–6 and are included for completeness in the auxiliary material.

4. Discussion

[19] The discussion will focus on five aspects of the work: the identity of the light-absorbing snowpack impurities, the absorption spectrum of black carbon and the effect of black carbon concentration on snowpack *e*-folding depth, albedo and snowpack photochemistry.

4.1. Identity of the Light-Absorbing Impurity

[20] The main sources of organic carbon to the atmosphere and to snowpack are anthropogenic activities and biomass burning [e.g., *Hegg et al.*, 2009; *Goldberg*, 1985; *McConnell et al.*, 2007], the optical parameters of organic carbon from biomass burning aerosols have been reported by *Kirchstetter et al.* [2004]. Brown carbon, which includes HULIS (Humic Like Substances), is highly abundant yet a weaker absorber of visible light than black carbon which has the highest absorption cross-section among carbonaceous constituents of aerosols and therefore contributes significantly to atmospheric absorption by aerosols [e.g., *Hoffer et al.*, 2006]. *France et al.* [2012] demonstrated that black carbon alone could not account for all the absorption seen in the Barrow snowpacks and an additional absorption by HULIS and other chromophores was necessary to explain variation of the cross-section of light-absorbing impurities in snowpack, σ^{+}_{abs}, with wavelength. It is important to note the effect of increased absorption due to impurities within the snowpack upon snowpack photochemistry, *e*-folding depth and albedo, especially black carbon as it is produced mainly by anthropogenic activity and therefore black carbon emissions are likely to be regulated or change in future. A reader of this work may adjust the results in Figures 3 and 4 for another light-absorbing impurity (or change the properties of the black carbon particle) without

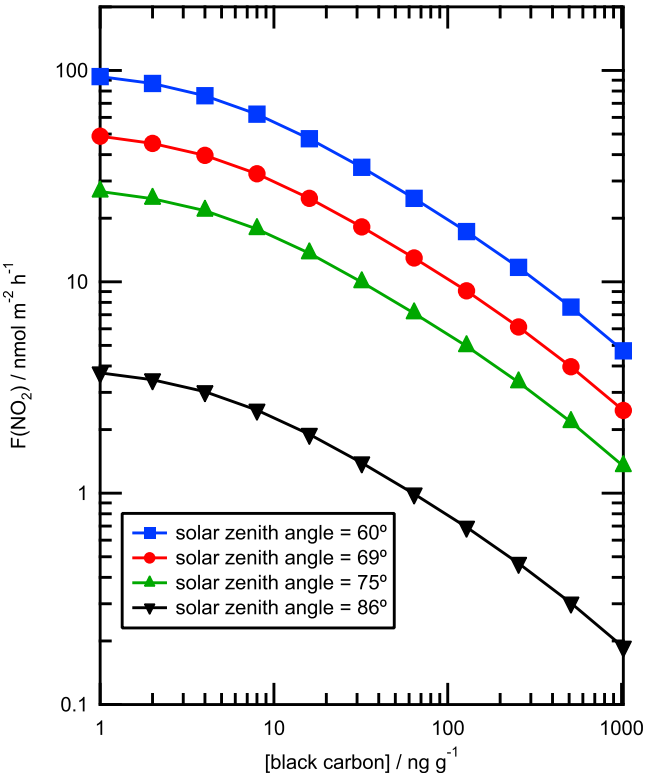

Figure 5. Depth-integrated production rates of NO_2, $F(NO_2)$, versus black carbon concentration from the Barrow OASIS campaign. The depth-integrated production rates are calculated with a NO_3^- concentration of 3.9 μmol L^{-1} [*Jacobi et al.*, 2012] and at solar zenith angles of 60°, 69°, 75° and 86° under clear sky conditions. Note that all axes are plotted on a logarithmic scale.

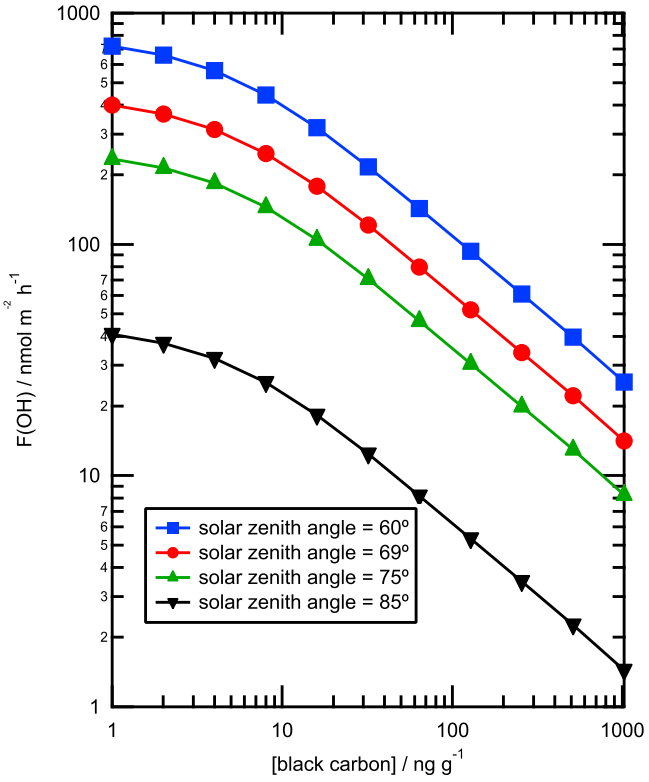

Figure 6. Depth-integrated production rates of OH radicals, F(OH), from the photolysis of hydrogen peroxide in the snowpack from the Barrow OASIS campaign. The depth-integrated production rates are calculated with an H_2O_2 concentration of 0.4 μmol L^{-1} [*Beine et al.*, 2011] and at solar zenith angles of 60°, 69°, 75° and 86° under clear sky conditions. Note that all axes are plotted on a logarithmic scale.

repeating the radiative-transfer calculations. The concentration of black carbon may be converted to a specific absorption by snowpack light absorbing impurities (i.e., σ^{+}_{abs} in *France et al.* [2012]) by multiplying values on the ordinate of Figures 3 and 4 with the absorption cross-section of black carbon (at the correct wavelength) in Figure 1. Dividing the specific absorption (σ^{+}_{abs}) by the cross-section of the new absorber at the correct wavelength will allow the albedo and *e*-folding depth in Figures 3 and 4 to be reported as a function of concentrations of the new absorber. An example (replacing black carbon with HULIS) is included in the auxiliary material as a useful example.

4.2. Black Carbon Absorption Spectrum

[21] A proxy for black carbon in snow was adopted from the literature [e.g., *Bohren*, 1986; *Roessler and Faxvog*, 1980; *Warren and Wiscombe*, 1980b, 1985]. The major sources of uncertainty of the black carbon absorption cross-section are the values of the index of refraction, size and location of the soot particle relative to the snow crystal/grain. A black carbon particle internal to the snow grain increases the absorption cross-section of the composite particle by a factor of 1.4 relative to the black carbon particle external to the snow grain [*Bohren*, 1986]. In this work the black carbon was deposited external to the snowpack i.e., the black carbon was rimed onto the snow during snowfall or collected on the snowpack by atmospheric deposition or wind pumping. *Chylek et al.* [1983] added black carbon throughout the snow grain and using a very similar radiative-transfer model to *Warren and Wiscombe* [1980a] calculated snow albedo. It is not clear if black carbon should be modeled internal or external to the snow grain and the study described here has taken the majority view. The imaginary index of refraction, and therefore the absorption spectrum, of black carbon span a factor of 5 [e.g., *Roessler and Faxvog*, 1980; *Bohren*, 1986]. *France et al.* [2012] demonstrate the black carbon absorption spectra in Figure 1 is consistent with experimental measurements [*Bond and Bergstrom*, 2006]. The third uncertainty is the shape of the black carbon, a spherical black carbon particle was used [e.g., *France et al.*, 2011a; *Warren and Wiscombe*, 1980b, 1985]. A needle or disk shape increases the absorption cross-section by a factor of 1.48 and 2.1 relative to the sphere [*Bohren*, 1986]. Comprehensive arguments by *Bohren* [1986] and *Warren and Wiscombe* [1980a, 1980b, 1985] justify the choice of black carbon properties used in this study. Fieldwork investigating black carbon in snow [i.e., *Hegg et al.*, 2009; *Clarke and Noone*, 1985; *Doherty et al.*, 2010; *Ming et al.*, 2009] show that the concentration values of black carbon chosen in this work are reasonable. *Jacobson* [2004], *Qian et al.* [2009], *Wang et al.* [2011], *Warren* [1984], and *Warren and Wiscombe* [1980a, 1980b, 1985, Figure 1] have all investigated the effect of black carbon on albedo. The study presented here is different because it takes into account real snowpacks characterized both by *e*-folding depth and albedo, and reports the effects of black carbon concentration on *e*-folding depth, albedo and photochemical fluxes. Atmospheric deposition of black carbon to

Table 2. Power Law Coefficients for Relating $F(NO_2)$ and F(OH) to Black Carbon Concentration ($\varepsilon = \alpha_F$[black carbon]$^{-\beta_F}$) for Black Carbon Concentrations Greater Than 20 ng g^{-1} and Solar Zenith Angles Greater Than 60°

		$F(NO_2)$			F(OH)		
Snow Type	Solar Zenith Angle (deg)	α_F (cm ng$^{\beta_F}$ g$^{-\beta_F}$)	$-\beta_F$	Range of [Black Carbon] Equation (7) is Valid Over (ng g^{-1})	α_F (cm ng$^{\beta_F}$ g$^{-\beta_F}$)	$-\beta_F$	Range of [Black Carbon] Equation (7) is Valid Over (ng g^{-1})
Hard	60	191 ± 9.39	0.497 ± 0.014	16–512	1650 ± 39.7	0.591 ± 0.00713	16–512
	69	100 ± 4.93	0.497 ± 0.0141	16–512	923 ± 22.6	0.591 ± 0.00727	16–512
	75	54.8 ± 2.71	0.497 ± 0.0141	16–512	541 ± 13.5	0.591 ± 0.00738	16–512
	86	7.64 ± 0.38	0.495 ± 0.0142	16–512	94.6 ± 2.4	0.591 ± 0.00753	16–512

Table 3. Comparison of Measured and Predicted *e*-Folding Depths in Snow With Optical Constants Obtained From Radiative-Transfer Calculations

Study	Snow Description	*e*-Folding Depth (cm (λ = 400 nm))		σ_{scatt} ($m^2\ kg^{-1}$)	σ^+_{abs} ($cm^2\ kg^{-1}$)
		Measured	Predicted		
Grenfell and Maykut [1977]	Arctic summer, dry snow	2.4	2.3	6.4	7.3
	Arctic summer, melting snow	5.3	5.4	1.1	7.8
King and Simpson [2001]	Arctic Spring, windblown	1.3	1.3	25–30	4–5
Beaglehole et al. [1998]	Coastal Antarctic snowdrift, summer	6.6[a]	6.2	7	~0.4
Beine et al. [2006]	Antarctic coastal hard windpack	17[b]	17.3	1.3	4.3
	Antarctic coastal soft windpack	3.3	3.5	6.3	24
	Antarctic coastal recent windblown	4.5	4.3	3.7	37
	Antarctic coastal precipitation	15	14.8	4.3	17
France et al. [2010]	Fresh Ny-Ålesund snowpack	6	5.7	16.7	2.7
	Melting Ny-Ålesund snowpack	9.9	9.7	0.8	19.8
Fisher et al. [2005]	Midlatitude maritime windslab, melting	13.9	-	1	1
	Midlatitude maritime windslab, dry	13.3	-	2–5	1–2
This Study	Hard snowpack	9.9	9.7	1.7	11
	Soft snowpack	9.4	9.5	2.0	11
	Inland snowpack	14.8	15.3	1.7	9
	Snow on sea-ice	9.4	8.8	1.8	15

[a]Values σ^+_{abs} and σ_{scatt} from *Lee-Taylor and Madronich* [2002] suggest that *Lee-Taylor and Madronich* [2002] interpreted the data in *Beaglehole et al.* [1998] as liquid equivalent *e*-folding depth in contrast to *King and Simpson* [2001] who interpret the *e*-folding data in *Beaglehole et al.* [1998] as not corrected for density.
[b]In the original paper *e*-folding depth was incorrectly reported. Details of this snowpack can be found in *France* [2008].

snowpack would (a) give a distribution of black carbon particle sizes from different sources and (b) give a distribution of different complex index of refractions from different sources. The work presented here has not considered such distributions and the reader could use the data plotted in Figures 3 and 4 to recalculate the effect on *e*-folding depth, albedo and depth-integrated production rates.

4.3. Effect of Black Carbon Concentration on Snowpack Penetration Depth

[22] To the authors' knowledge, there has been no systematic quantitative study on the effect of increasing black carbon concentrations on *e*-folding depths in snowpacks. Table 3 contains a survey of the previous *e*-folding depth measurements, their scattering and absorption cross-section as modeled by TUV-snow and the predicted *e*-folding depth using these cross-sections. Values of *e*-folding depth are reported for a wavelength of 400 nm. The values of the *e*-folding depth presented here are within the range of values previously reported for coastal Antarctica [*Beine et al.*, 2006]. The Barrow snowpacks were very similar to the coastal hard windpack, as reported by *Beine et al.* [2006]. Figure 2 shows the *e*-folding depth measured for the hard windpack in Barrow and the predicted *e*-folding depth using the model. The agreement between modeled and measured *e*-folding depths gives confidence to the method described in the work presented here. In the study presented here it was assumed the black carbon was uniformly mixed within the snowpack but the effect of layered snow containing different concentrations of black carbon in different layers is possible. Preliminary field and modeling work on layered windpacks does not demonstrate any need to consider different black carbon concentrations in different wind packed layers [*France et al.*, 2011a]. The snowpack studied had been re-worked by wind events and therefore the concentrations of particles are assumed to be well-mixed in the top layers of the snowpack, thus, a constant black carbon concentration with depth is assumed. Owing to the close proximity of our study sites to human activity in Barrow, Alaska the regional black carbon concentrations given by *Doherty et al.* [2010] may not be representative of the black carbon concentration in snow found around Barrow; ~70 ng g^{-1} of black carbon was found in the snowpack [*France et al.*, 2012]. It may be better to consider the black carbon concentrations in Barrow akin to that of Eastern Russia; mean C^{BC}_{equiv} values of (65 ± 44) ng g^{-1} [*Doherty et al.*, 2010].

4.4. Effect of Black Carbon Concentration on Albedo

[23] The amount of black carbon in snow controls the albedo and just a small concentration of black carbon, i.e., 5×10^{-8} g g^{-1}, increases the imaginary part of the refractive index by more than a factor of 10 [*Chylek et al.*, 1983]. There have been many modeling studies into the effect of black carbon concentration on albedo [e.g., *Jacobson*, 2004; *Qian et al.*, 2009; *Wang et al.*, 2011; *Warren*, 1984; *Warren and Wiscombe*, 1980a, 1980b, 1985] that have mainly dealt with hypothetical snowpacks and the study presented here, in contrast, uses measurements on a specific snowpack that were part of a wider field campaign and plots albedo versus black carbon concentration for a specific wavelength.

4.5. The Effect of Black Carbon Concentration on Snowpack Photochemistry and Future Outlook

[24] *Lee-Taylor and Madronich* [2002] produced a very useful plot to calculate $\int J(NO_3^-)dz/J(NO_2\downarrow)$, i.e., the depth-integrated photolysis rate constant of nitrate photolysis relative to surface downwelling photolysis coefficient for gaseous nitrogen dioxide (which is frequently measured for field campaigns) as a function of snow albedo, *e*-folding depth or σ^+_{abs}. It is not possible to use *Lee-Taylor and Madronich* [2002, Figure 5] to generate the figures (Figures 3 and 4) presented in this work as albedo and *e*-folding depth are also a

function of black carbon. The work of *Lee-Taylor and Madronich* [2002, Figure 5] is an excellent resource for field workers who may have measurements of albedo, *e*-folding depth and $J(NO_2 \downarrow)$ and want to estimate $\int J(NO_3^-)dz$ whereas the work presented here demonstrates how the albedo, *e*-folding depth and depth-integration photolysis coefficients of reactions (2) and (4) respond to increasing or decreasing black carbon concentrations for snowpacks characterized in Barrow, Alaska in Spring.

[25] Inspection of Table 2 demonstrates that for solar zenith angles greater than 60° and black carbon concentrations greater than 20 ng g^{-1}, the depth-integrated production rate of NO_2 production from snow approximately follows the inverse square-root of the concentration of black carbon (i.e., $F(NO_2) \propto \frac{1}{\sqrt{[\text{black carbon}]}}$). The depth-integrated production rate of OH radicals is similar but the power is closer to 0.6 (i.e., $F(OH) \propto \frac{1}{[\text{black carbon}]^{0.6}}$). Such a simple approximate relationship can be used to estimate depth-integrated production rate response to increasing or decreasing black carbon scenarios for black carbon concentrations greater than 20 ng g^{-1} i.e., doubling the black carbon in snow would reduce the depth-integrated production rates of NO_2 and OH radicals to ~70% and ~65% of their initial values.

[26] Future trends of black carbon concentrations within snow are difficult to predict as the main controls are anthropogenic processes. Black carbon concentrations in snow have varied significantly during the past 215 years, gradually rising toward the mid 1800s until industrialization caused a sharp increase in black carbon concentrations [*McConnell et al.*, 2007]. For around 50 years, after 1900, the seasonal variability of black carbon concentrations lessened as winter concentrations matched the normally higher summer concentrations but in the late 20th Century black carbon concentrations once again became seasonal [*McConnell et al.*, 2007]. Ice cores from Greenland show that by 2000, black carbon concentrations in snow/ice equaled the pre-industrial concentration of 1–2 ng g^{-1} in clean snowpack regions [*Doherty et al.*, 2010]. *Doherty et al.* [2010] reported no increase in the black carbon concentrations of Arctic snow since 1984. *Flanner et al.* [2009] suggest that black carbon in midlatitude snow may be contributing indirectly to melt Arctic sea-ice by enhancing warm-air advection into the Arctic. *Rosen et al.* [1981] show that aerosol at Barrow, Alaska has a large increase in black carbon during winter to spring, almost as large as found in urban areas. *Sharma et al.* [2006] and *Garrett et al.* [2011] indicate the large black carbon concentrations seen in Barrow in winter and spring are due to long-range transport of pollutants. Black carbon removal is most efficient at warmer temperatures and higher humidities, thus a future warmer and wetter Arctic could be cleaner [*Garrett et al.*, 2011].

[27] A decrease in black carbon concentrations in the snow will increase depth-integrated production rates of OH radicals and NO_2 molecules and increase the oxidative capacity of snowpack and the atmospheric boundary layer above [e.g., *Jones et al.*, 2001]. A "warmer" snowpack will tend to have a larger grain size and thus smaller values of σ_{scatt} leading to snowpacks with large *e*-folding depth, see Table 3 [*Fisher et al.*, 2005] and *Warren* [1982] for a detailed explanation. Thus "warmer" snowpacks may produce larger depth-integrated production rates of OH radicals and NO_2 [*Fisher et al.*, 2005] and as black carbon in snow causes warmer snowpacks, a future warmer climate could have two effects on snow photochemistry: First, snow photochemistry may become important (larger molecular fluxes from snowpack) in a warming world owing to more photochemistry occurring in the warm snowpack and second, a warming climate may cause a loss of snowpack thus snow photochemistry will become less important due to less snow cover. Thus a scenario may be envisaged where snow photochemistry may have a large effect on the oxidative potential of the overlying atmosphere but for a shorter duration.

5. Conclusions

[28] Increasing black carbon concentrations in snow reduces albedo, *e*-folding depths and depth-integrated production rates of photochemically derived species in a complicated way. For black carbon concentrations typically measured in the snow, *e*-folding depth, albedo and depth-integrated production rates of OH and NO_2 can switch from ice-dominated absorption to black carbon dominated absorption. The *e*-folding depths and depth-integrated production rates (of NO_2 and OH radicals) follow a power law relationship for black carbon concentrations greater than 20 ng g^{-1} and solar zenith angles greater than 60°.

[29] Black carbon amounts in snow are very closely linked to human activity and therefore the reduction or increase of depth-integrated production rates of OH and NO_2 are linked to the increase or reduction of black carbon in the snow.

[30] **Acknowledgments.** M.D.K. and J.L.F. thank NERC (NE/F010788/1 and NE/F004796/1) and NERC FSF (555.0608). H.J.R. thanks RHUL for a Thomas Holloway studentship. M.D.K. also gratefully acknowledges receipt of an RSF award from RHUL. We thank an anonymous reviewer for the suggested calculations involving HULIS in the auxiliary material.

References

Abbatt, J. P. D. (2003), Interactions of atmospheric trace gases with ice surfaces: Adsorption and reaction, *Chem. Rev.*, *103*, 4783–4800, doi:10.1021/cr0206418.

Anastasio, C., E. S. Galbavy, M. A. Hutterli, J. F. Burkhart, and D. K. Friel (2007), Photoformation of hydroxyl radical on snow grains at Summit, Greenland, *Atmos. Environ.*, *41*(24), 5110–5121, doi:10.1016/j.atmosenv.2006.12.011.

Aoki, T., T. Aoki, M. Fukabori, A. Hachikubo, Y. Tachibana, and F. Nishio (2000), Effects of snow physical parameters on spectral albedo and bidirectional reflectance of snow surface, *J. Geophys. Res.*, *105*(D8), 10,219–10,236, doi:10.1029/1999JD901122.

Beaglehole, D., B. Ramanathan, and J. Rumberg (1998), The UV to IR transmittance of Antarctic snow, *J. Geophys. Res.*, *103*(D8), 8849–8857, doi:10.1029/97JD03604.

Beine, H., A. Amoroso, F. Domine, M. King, M. Nardino, A. Ianniello, and J. France (2006), Surprisingly small HONO emissions from snow surfaces at browning pass, Antarctic, *Atmos. Chem. Phys.*, *6*, 2569–2580, doi:10/5194/acpd-6–615–2006.

Beine, H., A. J. Colussi, A. Amoroso, G. Esposito, M. Montagnoli, and M. R. Hoffman (2008), HONO emissions from snow surfaces, *Environ. Res. Lett.*, *3*, 045005, doi:10.1088/1748-9326/3/4/045005.

Beine, H., C. Anastasio, G. Esposito, K. Patten, E. Wilkening, F. Domine, D. Voisin, M. Barret, S. Houdier, and S. Hall (2011), Soluble, light-absorbing species in snow at Barrow, Alaska, *J. Geophys. Res.*, *116*, D00R05, doi:10.1029/2011JD016181.

Bohren, C. (1986), Applicability of effective-medium theories to problems of scattering and absorption by nonhomogeneous atmospheric particles, *J. Atmos. Sci.*, *43*(5), 468–475, doi:10.1175/1520-0469(1986)043<0468:AOEMTT>2.0.CO;2.

Bohren, C., and D. Huffman (1983), *Absorption and Scattering of Light by Small Particles*, Wiley-Interscience, New York.

Bond, T. C., and R. W. Bergstrom (2006), Light absorption by carbonaceous particles: An investigative review, *Aerosol Sci. Technol.*, *40*, 27–67, doi:10.1080/02786820500421521.

Chu, L., and C. Anastasio (2003), Quantum yield of hydroxyl radical and nitrogen dioxide from the photolysis of nitrate on ice, *J. Phys. Chem. A*, *107*(45), 9594–9602, doi:10.1021/jp0349132.

Chu, L., and C. Anastasio (2005), Formation of hydroxyl radical from the photolysis of frozen hydrogen peroxide, *J. Phys. Chem. A*, *109*(28), 6264–6271, doi:10.1021/jp051415f.

Chu, L., and C. Anastasio (2007), Temperature and wavelength dependence of nitrite photolysis in frozen and aqueous solutions, *Environ. Sci. Technol.*, *41*(10), 3626–3632, doi:10.1021/es062731q.

Chylek, P., V. Ramaswamy, and V. Srivastava (1983), Albedo of soot-contaminated snow, *J. Geophys. Res.*, *88*(C15), 10,837–10,843, doi:10.1029/JC088iC15p10837.

Chylek, P., V. Srivastava, L. Cahenzli, R. G. Pinnick, R. L. Dod, T. Novakov, T. L. Cook, and B. D. Hinds (1987), Aerosol and graphitic carbon content of snow, *J. Geophys. Res.*, *92*(D8), 9801–9809, doi:10.1029/JD092iD08p09801.

Clarke, A., and K. Noone (1985), Soot in the arctic snowpack–A cause for perturbations in radiative-transfer, *Atmos. Environ.*, *19*(12), 2045–2053, doi:10.1016/0004-6981(85)90113-1.

Doherty, S. J., S. G. Warren, T. C. Grenfell, A. D. Clarke, and R. E. Brandt (2010), Light-absorbing impurities in Arctic snow, *Atmos. Chem. Phys. Discuss.*, *10*, 18,807–18,878, doi:10.5194/acpd-10-18807-2010.

Dominé, F., and P. B. Shepson (2002), Air-snow interactions and atmospheric chemistry, *Science*, *297*(5586), 1506–1510, doi:10.1126/science.1074610.

Domine, F., J.-C. Gallet, M. Barret, S. Houdier, D. Voisin, T. A. Douglas, J. D. Blum, H. J. Beine, C. Anastasio, and F.-M. Bréon (2011), The specific surface area and chemical composition of diamond dust near Barrow, Alaska, *J. Geophys. Res.*, *116*, D00R06, doi:10.1029/2011JD016162.

Elterman, L. (1968), *UV, Visible and IR Attenuation for Altitudes up to 50 km*, *Environ. Res. Pap.*, vol. 285, U.S. Air Force, Off. of Aerosp. Res., Washington, D. C.

Fisher, F. N., M. D. King, and J. Lee-Taylor (2005), Extinction of UV-visible radiation in wet mid-latitude (maritime) snow: Implications for increase NO_x emission, *J. Geophys. Res.*, *110*, D21301, doi:10.1029/2005JD005963.

Flanner, M. G., C. S. Zender, J. T. Randerson, and P. J. Rasch (2007), Present-day climate forcing and response from black carbon in snow, *J. Geophys. Res.*, *112*, D11202, doi:10.1029/2006JD008003.

Flanner, M. G., C. S. Zender, P. G. Hess, N. M. Mahowald, T. H. Painter, V. Ramanathan, and P. J. Rasch (2009), Springtime warming and reduced snow cover from carbonaceous particles, *Atmos. Chem. Phys.*, *9*, 2481–2497, doi:10.5194/acp-9-2481-2009.

France, J. L. (2008), Chemical oxidation in snowpack, PhD thesis, Dep. Of Earth Science, Royal Holloway, Univ. of London, Egham, U. K.

France, J. L., and M. D. King (2012), The effect of measurement geometry on recording solar radiation attenuation in snowpack (*e*-folding depth) using fibre-optic probes, *J. Glaciol.*, *58*(208), doi:10.3189/2012JoG11J227.

France, J. L., M. D. King, and J. Lee-Taylor (2007), Hydroxyl (OH) radical production rates in snowpack from photolysis of hydrogen peroxide (H_2O_2) and nitrate (NO_3^-), *Atmos. Environ.*, *41*(26), 5502–5509, doi:10.1016/j.atmosenv.2007.03.056.

France, J. L., M. D. King, and J. Lee-Taylor (2010), The importance of considering depth-resolved photochemistry in snow: A radiative-transfer study of NO_2 and OH production in Ny-Alesund snowpacks, *J. Glaciol.*, *56*(198), 655–663, doi:10.3189/002214310793146250.

France, J. L., M. D. King, M. M. Frey, J. Erbland, G. Picard, S. Preunkert, A. MacArthur, and J. Savarino (2011a), Snow optical properties at Dome C (Concordia), Antarctica; implications for snow emissions and snow chemistry of reactive nitrogen, *Atmos. Chem. Phys.*, *11*(18), 9787–9801, doi:10.5194/acp-11-9787-2011.

France, J. L., M. D. King, J. Lee-Taylor, H. J. Beine, A. Ianniello, F. Domine, and A. MacArthur (2011b), Calculations of in-snow NO_2 and OH radical photochemical production and photolysis rates: A field and radiative-transfer study of the optical properties of Arctic (Ny-Ålesund, Svalbard) snow, *J. Geophys. Res.*, *116*, F04013, doi:10.1029/2011JF002019.

France, J. L., H. J. Reay, M. D. King, D. Voisin, H. W. Jacobi, F. Domine, H. Beine, C. Anastasio, A. MacArthur, and J. Lee-Taylor (2012), Hydroxyl radical and NO_x production rates, black carbon concentrations and light-absorbing impurities in snow from field measurements of light penetration and nadir reflectivity of onshore and offshore coastal Alaskan snow, *J. Geophys. Res.*, *117*, D00R12, doi:10.1029/2011JD016639.

Garrett, T. J., S. Brattström, S. Sharma, D. E. J. Worthy, and P. Novelli (2011), The role of scavenging in the seasonal transport of black carbon and sulfate to the Arctic, *Geophys. Res. Lett.*, *38*, L16805, doi:10.1029/2011GL048221.

Goldberg, E. D. (1985), *Black Carbon in the Environment: Properties and Distribution*, John Wiley, New York.

Grannas, A. M., P. B. Shepson, and T. R. Filley (2004), Photochemistry and nature of organic matter in Arctic and Antarctic snow, *Global Biogeochem. Cycles*, *18*, GB1006, doi:10.1029/2003GB002133.

Grannas, A. M., et al. (2007), An overview of snow photochemistry: Evidence, mechanisms and impacts, *Atmos. Chem. Phys.*, *7*, 4329–4373, doi:10.5194/acp-7-4329-2007.

Grenfell, T. C., and G. A. Maykut (1977), The optical properties of ice and snow in the Arctic basin, *J. Glaciol.*, *10*, 445–463.

Grenfell, T. C., B. Light, and M. Sturm (2002), Spatial distribution and radiative effects of soot in the snow and sea ice during the SHEBA experiment, *J. Geophys. Res.*, *107*(C10), 8032, doi:10.1029/2000JC000414.

Hansen, J., and L. Nazarenko (2004), Soot climate forcing via snow and ice albedos, *Proc. Natl. Acad. Sci. U. S. A.*, *101*(2), 423–428, doi:10.1073/pnas.2237157100.

Hegg, D. A., S. G. Warren, T. C. Grenfell, S. J. Doherty, T. V. Larson, and A. D. Clarke (2009), Source attribution of black carbon in arctic snow, *Environ. Sci. Technol.*, *43*(11), 4016–4021, doi:10.1021/es803623f.

Hegg, D. A., S. G. Warren, T. C. Grenfell, S. J. Doherty, and A. D. Clarke (2010), Sources of light-absorbing aerosol in arctic snow and their seasonal variation, *Atmos. Chem. Phys.*, *10*, 10,923–10,938, doi:10.5194/acp-10-10923-2010.

Hoffer, A., A. Gelencsér, P. Guyon, G. Kiss, G. P. Frank, P. Artaxo, and M. O. Andreae (2006), Optical properties of humic-like substances (HULIS) in biomass-burning aerosols, *Atmos. Chem. Phys.*, *6*(11), 3563–3570, doi:10.5194/acp-6-3563-2006.

Jacobi, H. W., D. Voisin, J. L. Jaffrezo, J. Cozic, and T. A. Douglas (2012), Chemical composition of the snowpack during the OASIS spring campaign 2009 at Barrow, Alaska, *J. Geophys. Res.*, *117*, D00R13, doi:10.1029/2011JD016654.

Jacobson, M. Z. (2004), Climate response of fossil fuel and biofuel soot, accounting for soot's feedback to snow and sea ice albedo and emissivity, *J. Geophys. Res.*, *109*, D21201, doi:10.1029/2004JD004945.

Jones, A. E., R. Weller, P. S. Anderson, W.-W. Jacobi, E. W. Wolff, O. Schrem, and H. Miller (2001), Measurements of NO_x emissions from the Antarctic snowpack, *J. Geophys. Res.*, *28*(8), 1499–1502, doi:10.1029/2000GL011956.

King, M., and W. Simpson (2001), Extinction of UV radiation in arctic snow at Alert, Canada (82 N), *J. Geophys. Res.*, *106*(D12), 12,499–12,507, doi:10.1029/2001JD900006.

King, M., J. France, F. Fisher, and H. Beine (2005), Measurement and modelling of UV radiation penetration and photolysis rates of nitrate and hydrogen peroxide in Antarctic sea-ice: An estimate of the production rate of hydroxyl radicals in first year sea-ice, *J. Photochem. Photobiol. Chem.*, *176*, 39–49, doi:10.1016/j.jphotochem.2005.08.032.

Kirchstetter, T. W., T. Novakov, and P. V. Hobbs (2004), Evidence that the spectral dependence of light absorption by aerosols is affected by organic carbon, *J. Geophys. Res.*, *109*, D21208, doi:10.1029/2004JD004999.

Lee-Taylor, J., and S. Madronich (2002), Calculation of actinic fluxes with a coupled atmosphere-snow radiative-transfer model, *J. Geophys. Res.*, *107*(D24), 4796, doi:10.1029/2002JD002084.

McConnell, J. R., R. Edwards, G. L. Kok, M. G. Flanner, C. S. Zender, E. S. Saltzman, J. R. Banta, D. R. Pasteris, M. M. Carter, and J. D. W. Kahl (2007), 20th-century industrial black carbon emissions altered arctic climate forcing, *Science*, *317*(5843), 1381–1384, doi:10.1126/science.1144856.

Ming, J., C. Xiao, H. Cachier, D. Qin, X. Qin, Z. Li, and J. Pu (2009), Black carbon (BC) in the snow of glaciers in west China and its potential effects on albedo, *Atmos. Res.*, *92*, 114–123, doi:10.1016/j.atmosres.2008.09.007.

Peterson, M. C., and R. E. Honrath (2001), Observations of rapid photochemical destruction of ozone in snowpack interstitial air, *Geophys. Res. Lett.*, *28*(3), 511–514, doi:10.1029/2000GL012129.

Qian, Y., W. I. Gustafson Jr., L. R. Leung, and S. J. Ghan (2009), Effects of soot-induced snow albedo change on snowpack and hydrological cycle in western United States based on Weather Research and Forecasting chemistry and regional climate simulations, *J. Geophys. Res.*, *114*, D03108, doi:10.1029/2008JD011039.

Qu, X., and A. Hall (2005), Surface contribution to planetary albedo variability in cryosphere regions, *J. Clim.*, *18*(24), 5239–5252, doi:10.1175/JCLI3555.1.

Roessler, D., and F. Faxvog (1980), Optical properties of agglomerated acetylene smoke particles at 0.5145-μ m and 10.6-μ m wavelengths, *J. Opt. Soc. Am.*, *70*(2), 230–235, doi:10.1364/JOSA.70.000230.

Rosen, H., T. Novakov, and B. A. Bodhaine (1981), Soot in the arctic, *Atmos. Environ.*, *15*(8), 1371–1374, doi:10.1016/0004-6981(81)90343-7.

Sharma, S., E. Andrews, L. A. Barrie, J. A. Ogren, and D. Lavoue (2006), Variations and sources of the equivalent black carbon in the high Arctic revealed by long-term observations at Alert and Barrow: 1989–2003, *J. Geophys. Res.*, *111*, D14208, doi:10.1029/2005JD006581.

Simpson, W., M. King, H. Beine, R. Honrath, and X. Zhou (2002), Radiation-transfer modelling of snow-pack photochemical processes during alert 2000, *Atmos. Environ.*, *36*, 2663–2670, doi:10.1016/S1352-2310(02)00124-3.

Stamnes, K., S.-C. Tsay, W. Wiscombe, and K. Jayaweera (1988), Numerically stable algorithm for discrete-ordinate-method radiative-transfer in multiple scattering and emitting layered media, *Appl. Opt.*, *27*(12), 2502–2509, doi:10.1364/AO.27.002502.

Voisin, D., et al. (2012), Carbonaceous species and HUmic LIke Substances (HULIS) in Arctic snowpack during OASIS field campaign in Barrow, *J. Geophys. Res.*, *117*, D00419, doi:10.1029/2011JD016612.

Wang, Q., et al. (2011), Sources of carbonaceous aerosols and deposited black carbon in the Arctic in winter-spring: Implications for radiative forcing, *Atmos. Chem. Phys. Discuss.*, *11*, 19,395–19,442, doi:10.5194/acpd-11-19395-2011.

Warren, S. (1982), Optical properties of snow, *Rev. Geophys.*, *20*(1), 67–89, doi:10.1029/RG020i001p00067.

Warren, S. (1984), Impurities in snow: Effects on albedo and snowmelt, *Ann. Glaciol.*, *5*, 177–179.

Warren, S. G., and R. E. Brandt (2008), Optical constants of ice from the ultraviolet to the microwave: A revised compilation, *J. Geophys. Res.*, *113*, D14220, doi:10.1029/2007JD009744.

Warren, S., and A. D. Clarke (1986), Soot from arctic haze: Radiative effect on the arctic snowpack, *Glaciol. Data Rep. GD-18*, World Data Cent. A for Glaciol., Boulder, Colo.

Warren, S. G., and W. J. Wiscombe (1980a), A model for the spectral albedo of snow I. Pure snow, *J. Atmos. Sci.*, *37*, 2712–2733.

Warren, S., and W. J. Wiscombe (1980b), A model for the spectral albedo of snow II. snow containing atmospheric aerosols, *J. Atmos. Sci.*, *37*(12), 2734–2745, doi:10.1175/1520-0469(1980)037<2734:AMFTSA>2.0.CO;2.

Warren, S., and W. Wiscombe (1985), Dirty snow after nuclear-war, *Nature*, *313*(6002), 467–470, doi:10.1038/313467a0.

Warren, S. G., R. E. Brandt, and T. C. Grenfell (2006), Visible and near-ultraviolet absorption spectrum of ice from the transmission of solar radiation into snow, *Appl. Opt.*, *45*(21), 5320–5334, doi:10.1364/AO.45.005320.

Appendix 4

Black carbon concentrations in Svalbard and Antarctic Snowpacks

A4.1 Introduction

The work presented in this appendix correlates with chapter 4 of the thesis. Each graph has been labelled with a subjective qualitative data quality score; A means the quality of data is good, B means the quality of data is subjective and C means the quality of data is poor. Examples of absorption spectra for individual transects and sampling sites can be seen in chapter 4, and the full set of absorption spectra have been included in this appendix.

A4.2 Absorption Spectra

A4.2.1 Svalbard

A4.2.1.1 Lappbreen Transect

Sampling site 2 (Figure A4.1) was situated in the central section of the glacier at 50 m along the Lappbreen transect.

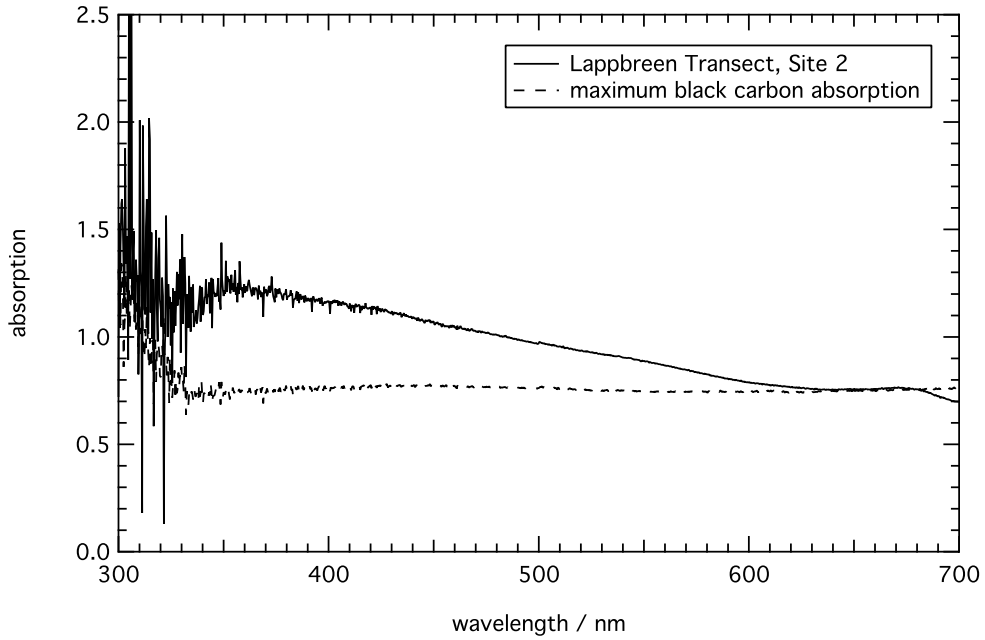

Figure A4.1. Absorption spectrum of site 2 of the Lappbreen transect. Data quality = A. Black carbon absorption factor = 1.7.

Sampling site 3 of the Lappbreen transect (Figure A4.2) was situated 100 m along the transect in the central section of the glacier.

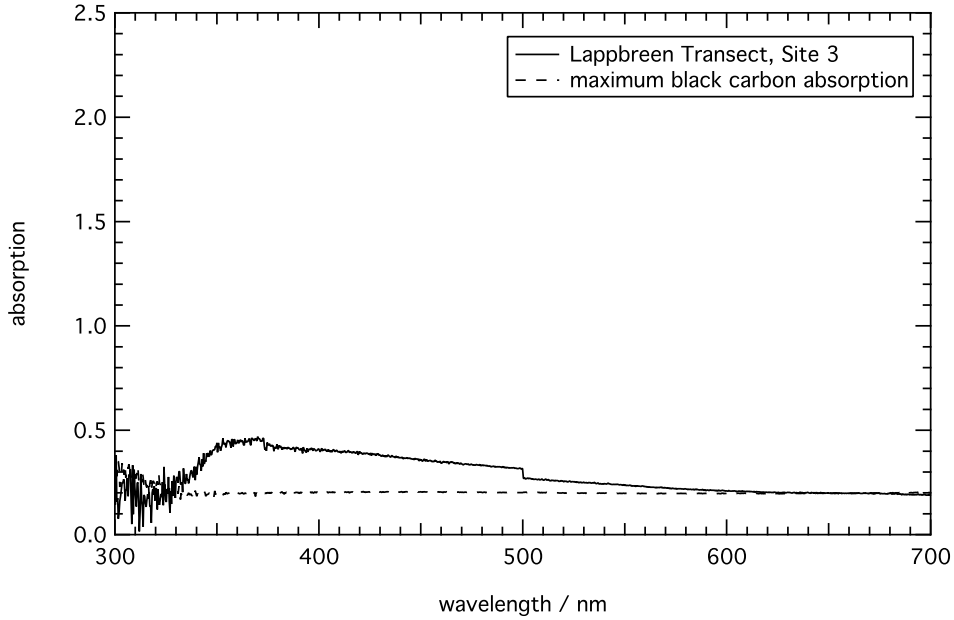

Figure A4.2. Absorption spectrum of site 3 of the Lappbreen transect. Data quality = A. Black carbon absorption factor = 0.45.

Sampling site 4 (Figure A4.3) was located 150 m along the transected in the central section of the glacier.

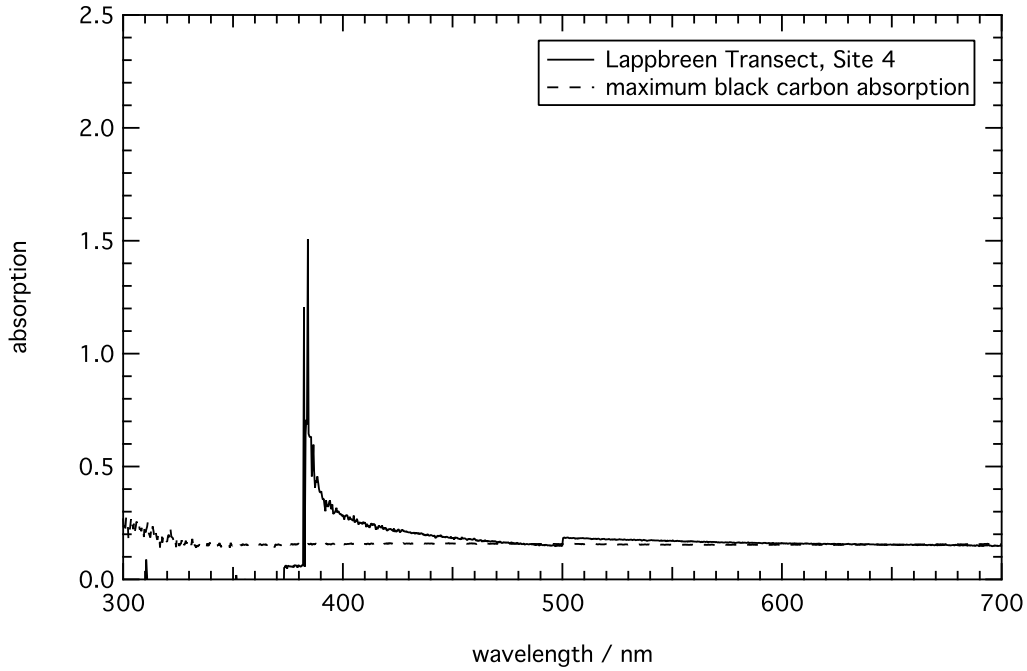

Figure A4.3. Absorption spectrum of site 4 of Lappbreen transect. Data quality = B. Major issues in data quality can be seen below 400 nm. Black carbon absorption factor = 0.35.

Sampling site 5 (Figure A4.4) was located on the slope of the glacier at 200 m along the transect. The snow sample was icy and some of the filters contained red algae.

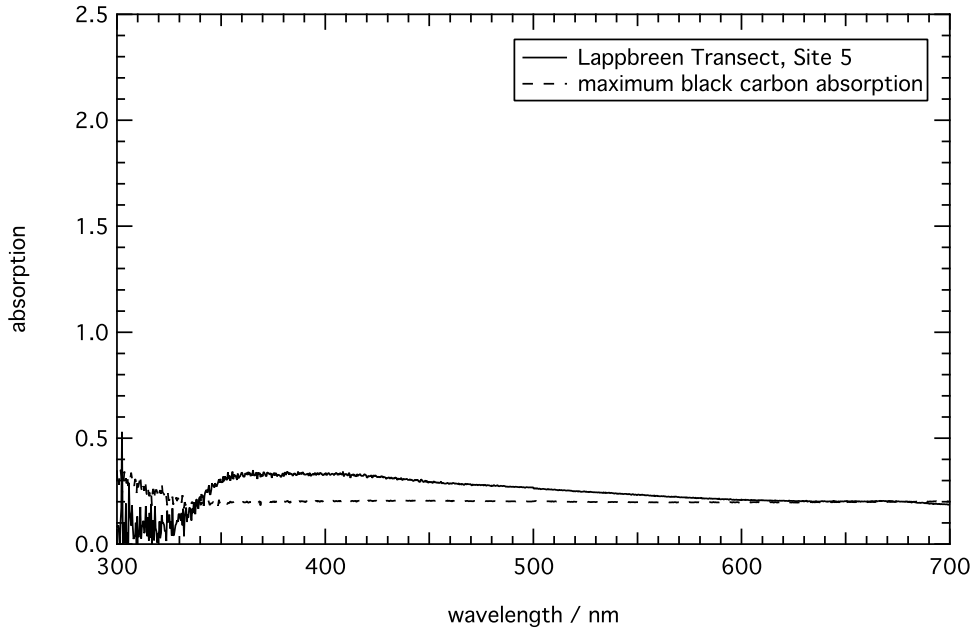

Figure A4.4. Absorption spectrum of site 5 of Lappbreen transect. Data quality = A. Black carbon absorption factor = 1.5.

Sampling site 6 (Figure A4.5) was situated on the edge of the glacier at 250 m along the transect and the snow sample was icy.

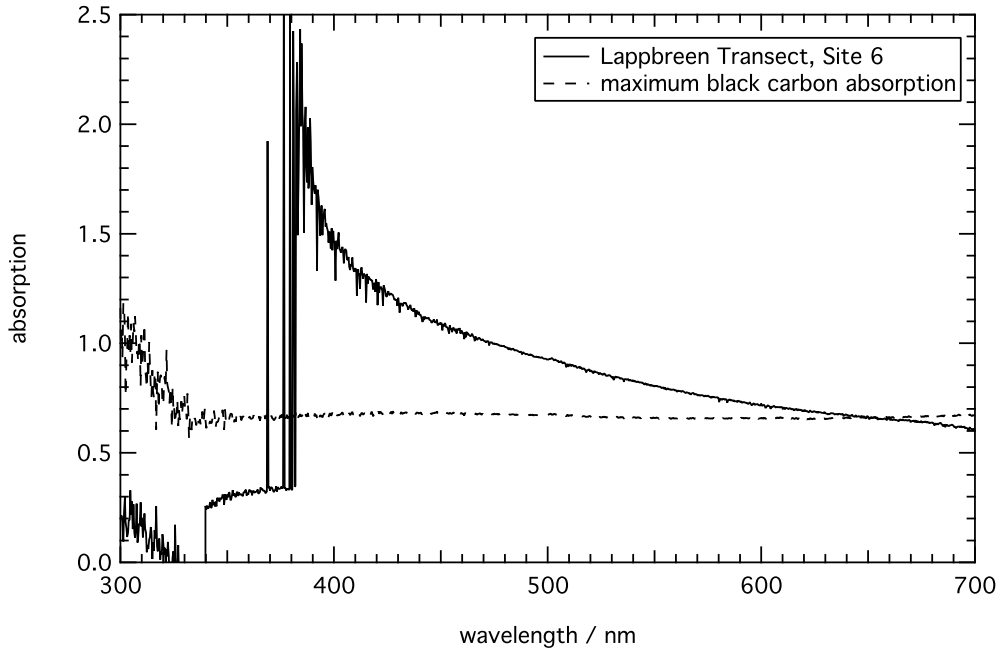

Figure A4.5. Absorption spectrum of site 6 of Lappbreen transect. Data quality = B. Black carbon absorption factor = 0.45. Major data quality issues below 400 nm.

A4.2.1.2 Lulefjellet Transect

Sampling site 2 (Figure A4.6) was located 50 m along the transect.

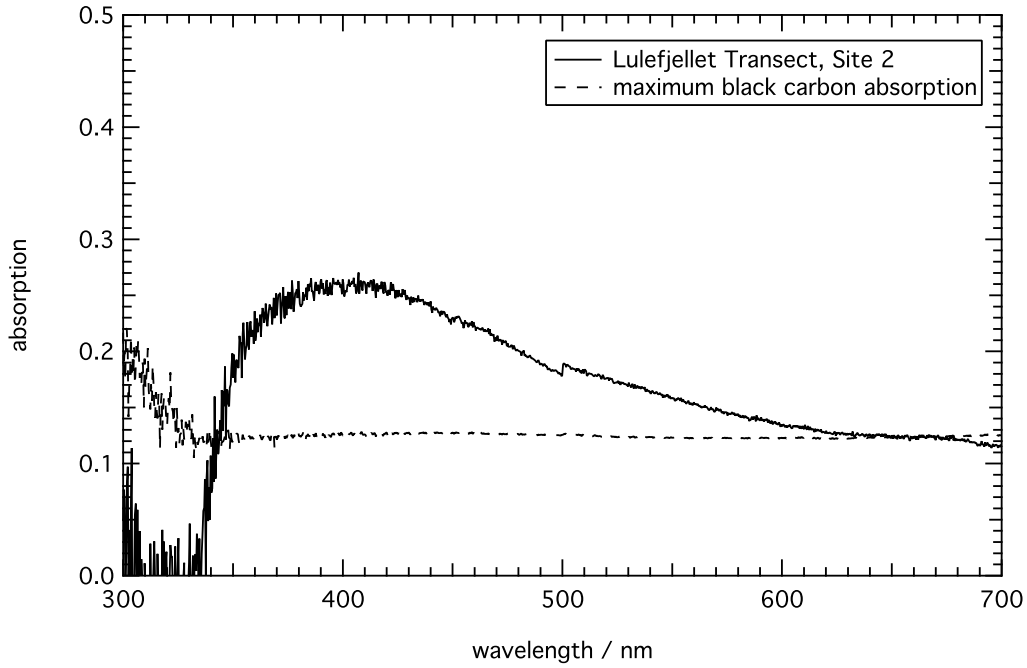

Figure A4.6. Absorption spectrum of site 2 of Lulefjellet transect. Data quality = A. Black carbon absorption factor = 0.23.

Sampling site 3 (Figure A4.7) was situated 100 m along the transect.

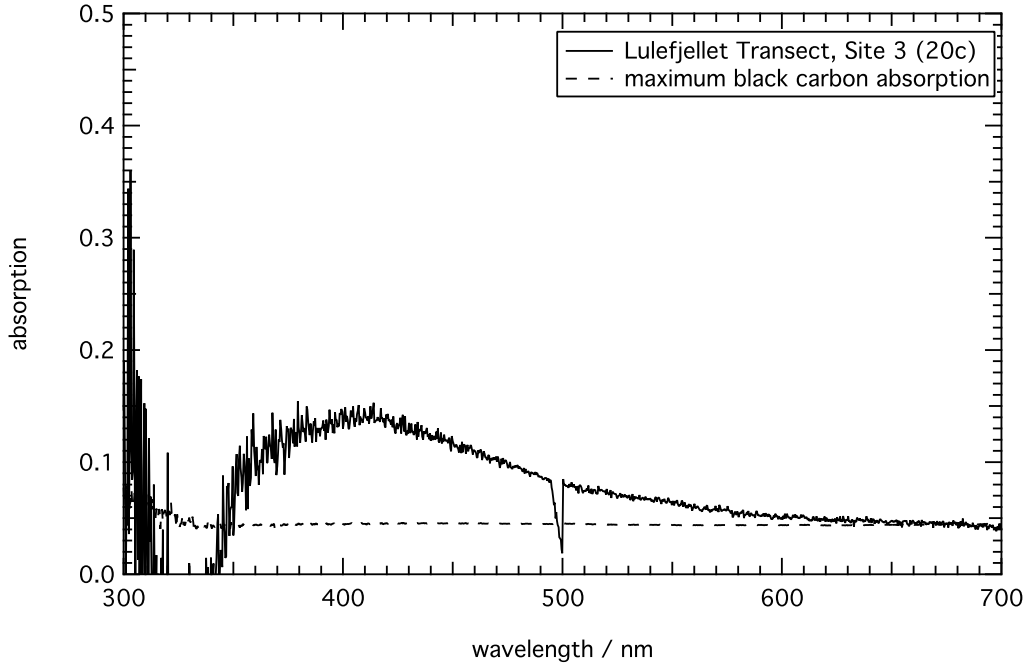

Figure A4.7. Absorption spectrum of site 3 of Lulefjellet transect. Data quality = C. Black carbon absorption factor = 0.1.

Sampling site 4 (Figure A4.8) was situated 150 m along the transect.

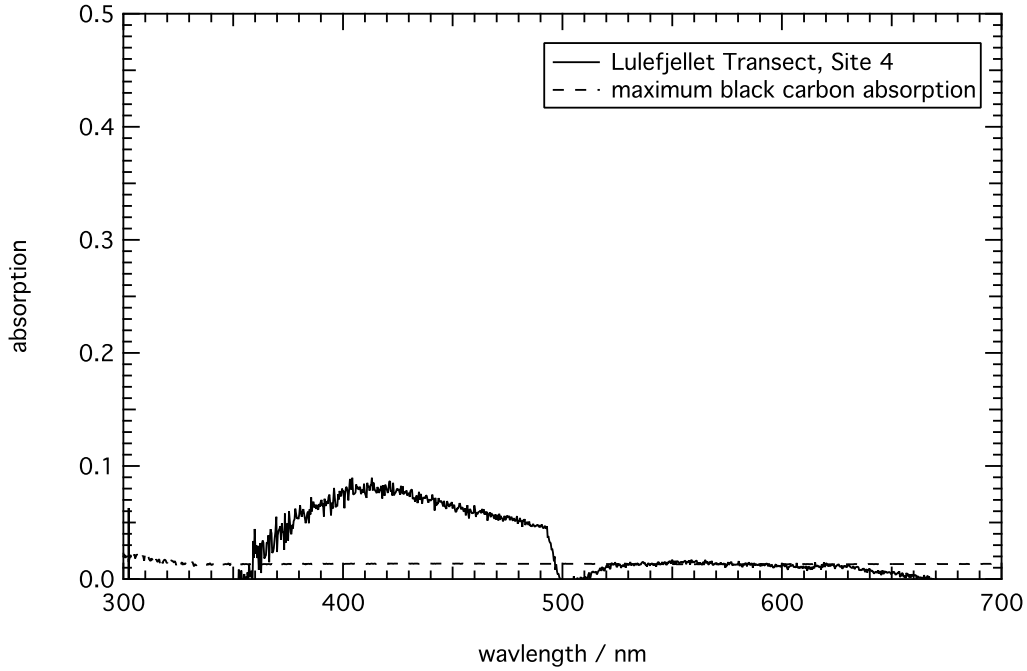

Figure A4.8. Absorption spectrum of site 4 of Lulefjellet transect. Data quality = B/C. Black carbon absorption factor = 0.03. Transition between saturated and unsaturated spectra is poor.

Sampling site 5 (Figure A4.9) was situated 200 m along the transect.

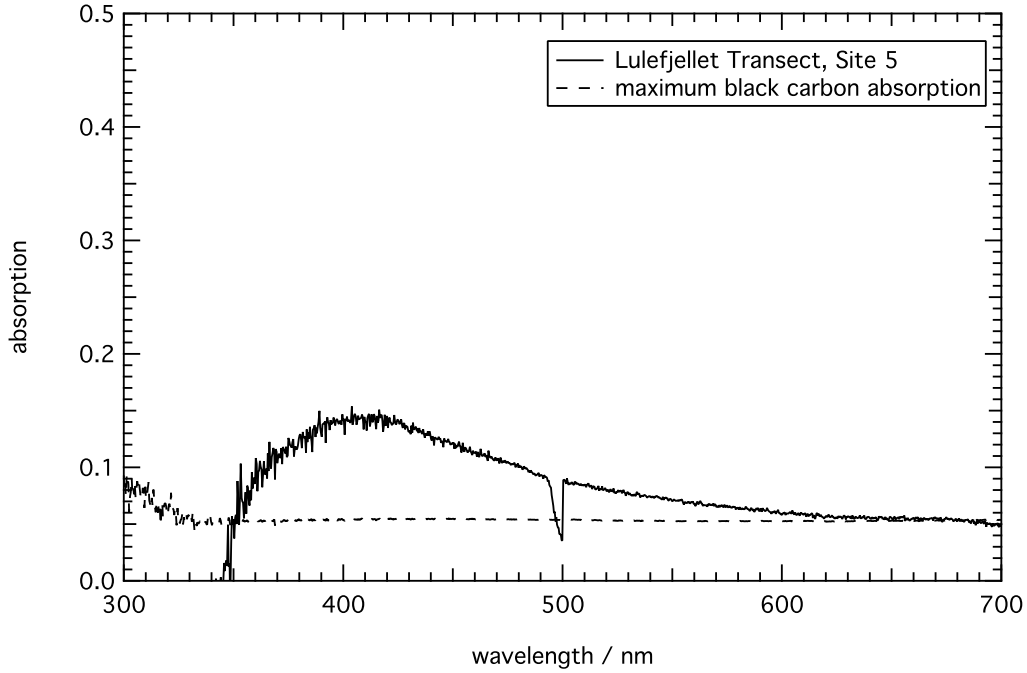

Figure 4.9. Absorption spectrum of site 5 of Lulefjellet transect. Data quality = A. Black carbon absorption factor = 0.28.

Sampling site 6 (Figure A4.10) was situated 250 m along the transect.

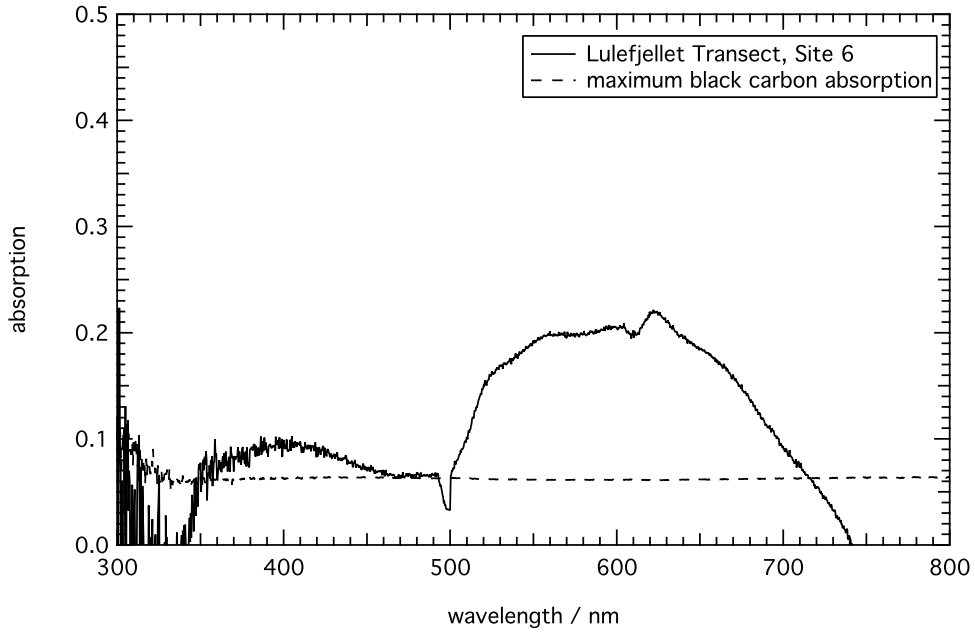

Figure A4.10. Absorption spectrum of site 6 of Lulefjellet transect. Data quality = C. Black carbon absorption factor = 0.14. Poor quality due to discrepancies between dark spectra.

A4.2.1.3 Lappbreen Slope Transect

Sampling site 2 (Figure A4.11) was collected 50 m along the transect.

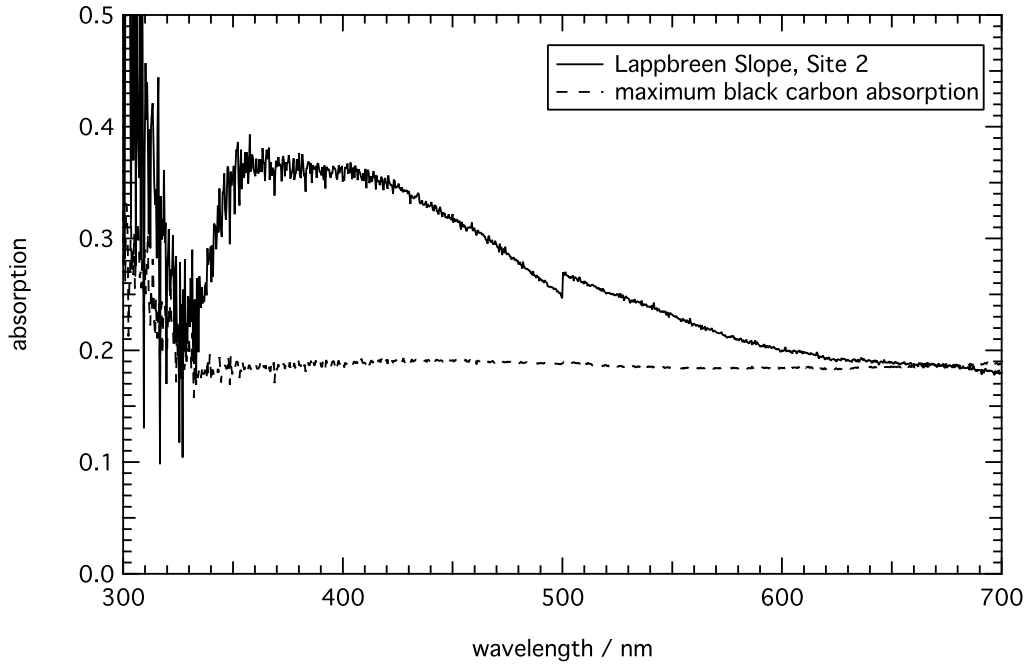

Figure A4.11. Absorption spectrum for site 2 of the Lappbreen slope transect. Data quality = A. Black carbon absorption factor = 0.42.

Sampling site 3 (Figure A4.12) was located 100 m along the transect. The snow sampled took a long time to melt.

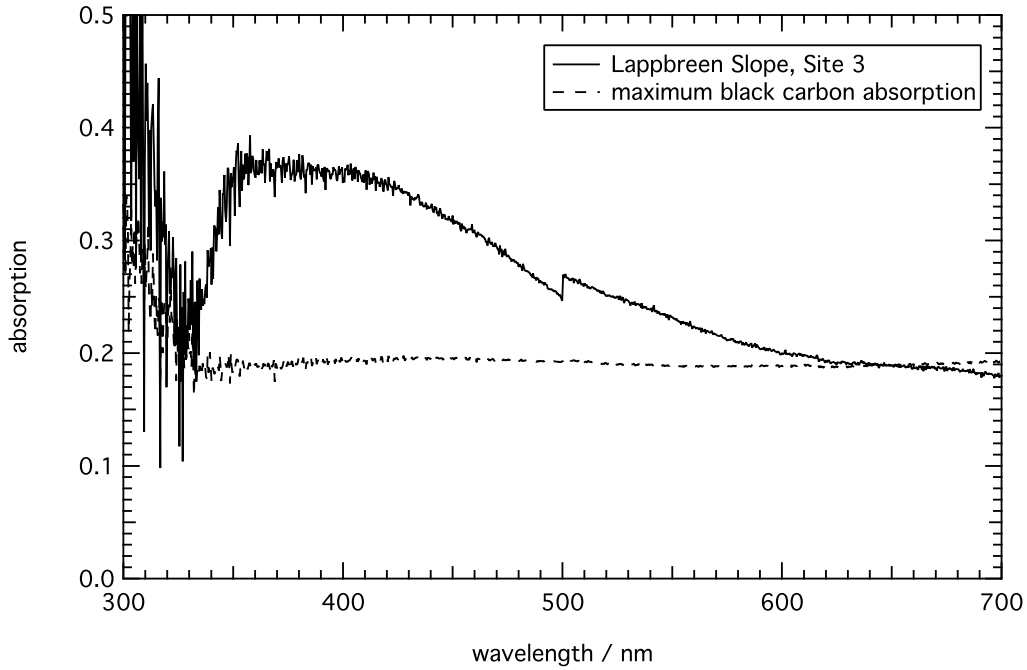

Figure A4.12. Absorption spectrum for site 3 of Lappbreen slope. Data quality = A. Black carbon absorption factor = 0.43.

Sampling site 4 (Figure A4.13) was located 150 m along the transect and the snow sampled took a long time to melt.

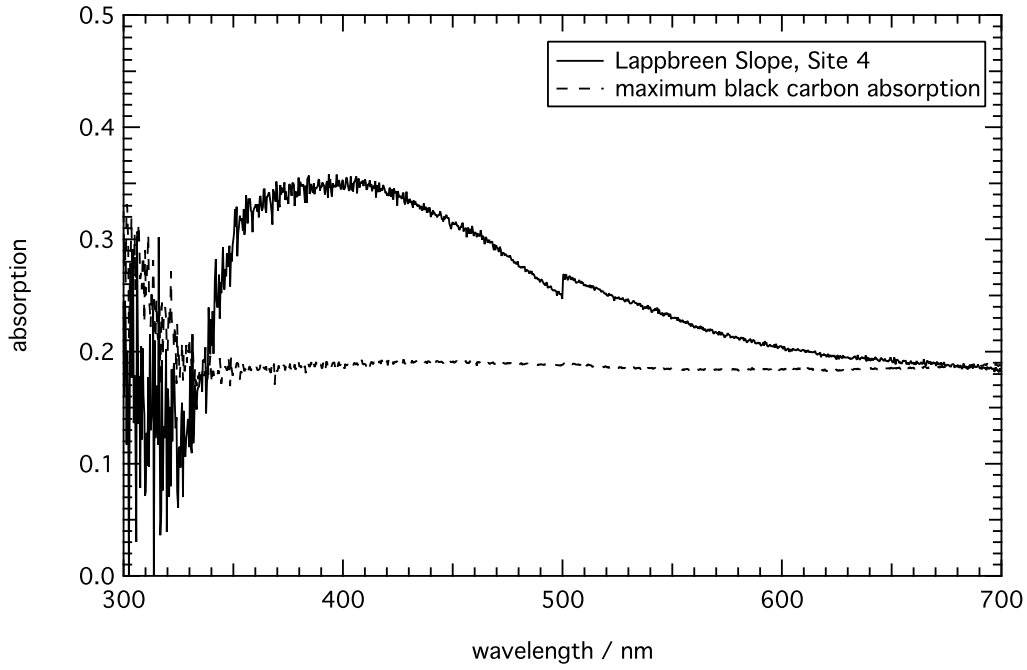

Figure A4.13. Absorption spectrum for site 4 of the Lappbreen slope transect. Data quality = A. Black carbon absorption factor = 0.42.

Sampling site 5 (Figure A4.14) was located 200 m along the transect.

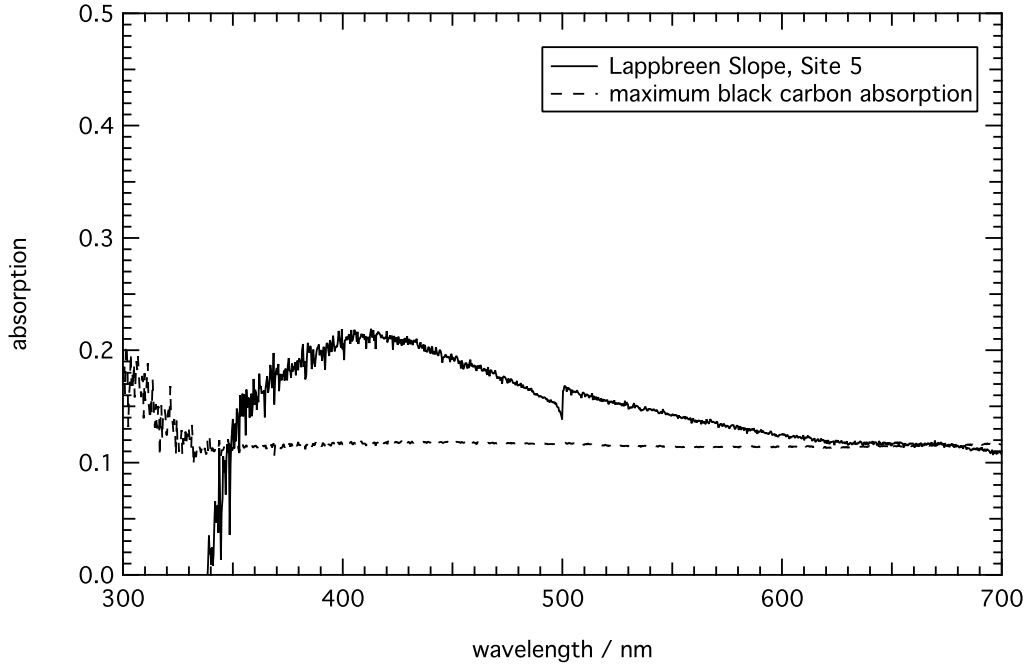

Figure A4.14. Absorption spectrum for site 5 of the Lappbreen slope transect. Data quality = A. Black carbon absorption factor = 0.26.

Sampling site 6 (Figure A4.15) was located at the top of the slope, 250 m along the transect.

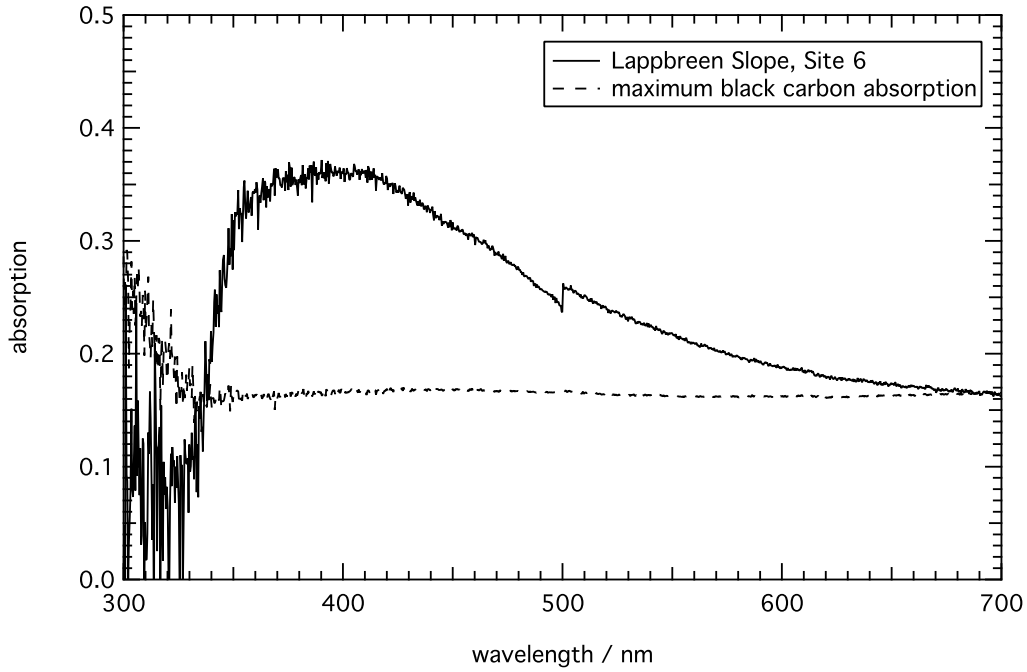

Figure A4.15. Absorption spectrum for site 6 of the Lappbreen slope transect. Data quality = A. Black carbon absorption factor = 0.37.

A4.2.1.4 Snowpits

Figures A4.16 – A4.18 show the individual snow layers for snowpit 2 and Figure A4.19 shows all 3 layers of the snowpit together.

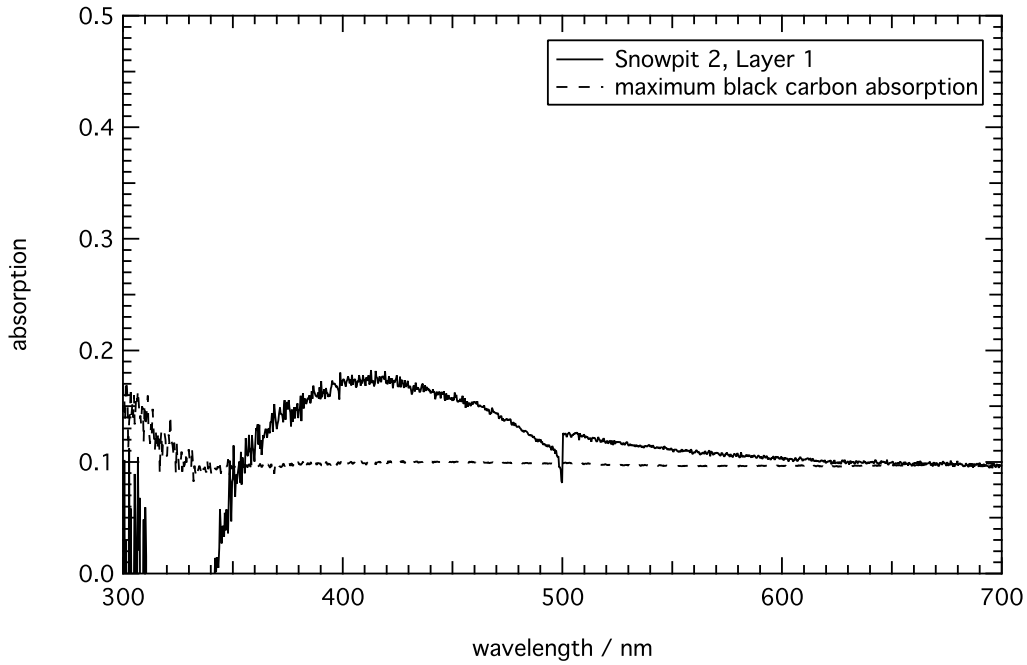

Figure A4.16. Absorption spectrum for layer 1 of snowpit 2. Data quality = A. Black carbon absorption factor = 0.22.

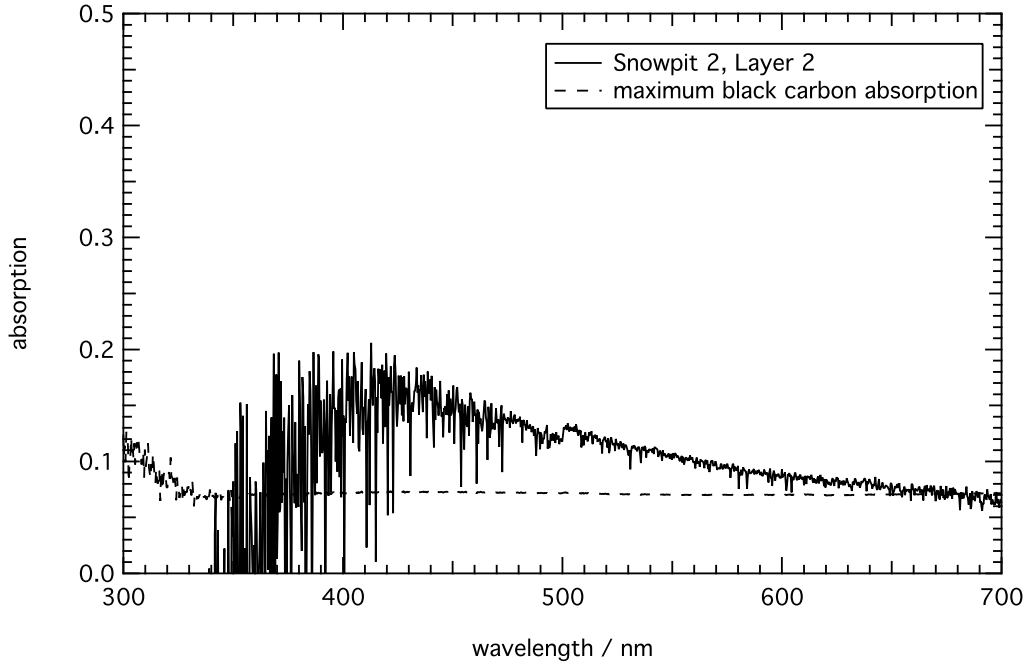

Figure A4.17. Absorption spectrum for layer 2 of snowpit 2. Data quality = B. Black carbon absorption factor = 0.16.

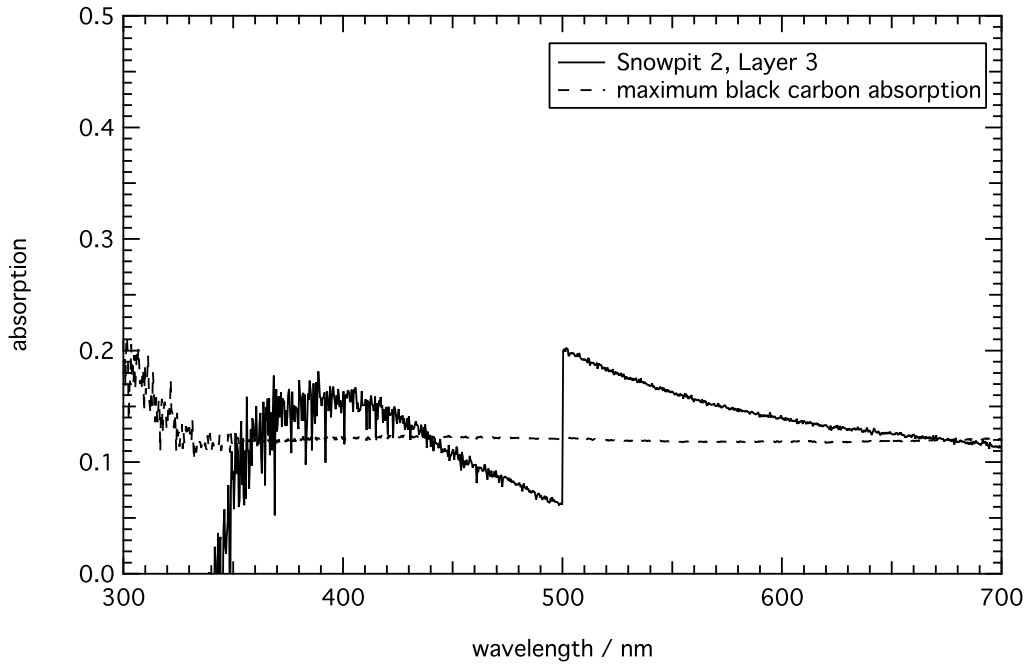

Figure A4.18. Absorption spectrum for layer 3 of snowpit 2. Data quality = C. Black carbon absorption factor = 0.27.

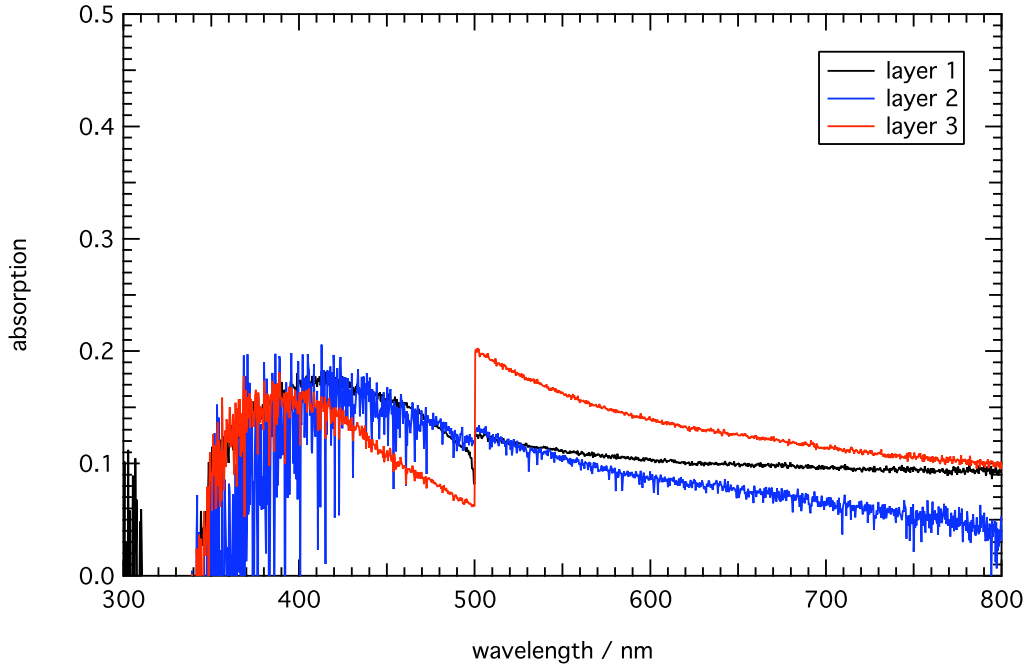

Figure A4.19. Absorption spectrum for layers 1, 2 and 3 of snowpit 2.

Appendix 5

Assessment of Bi-Directional Reflectivity Distribution Function Measurements in Cold Climates

A5.1 Introduction

Contour plots at 500 nm and 1100 nm are presented for each day in Chapter 5. The contour plots included in this appendix show the reflectivity of the snow surface between 400-1500 nm in 100 m intervals.

A5.2 Contour Plots

A5.2.2 Day 1

The first day of measurements taken at Tethys Bay using GRASS occurred on the 11th December 2010. The location for the measurements was 74° 41.3306 S, 164° 03.1543 E, the temperatures was -2.4 °C and sky conditions consisted of no cloud but high wind. The sea-ice was > 1 m thick and the measurements surface was bare sea-ice with a melting surface.

A5.2.2.1 Day 1, Site 2

Figure A5.1 shows the complete set of reflected contour plots measured at site 2 on day 1, over the wavelength range of 400–1500 nm.

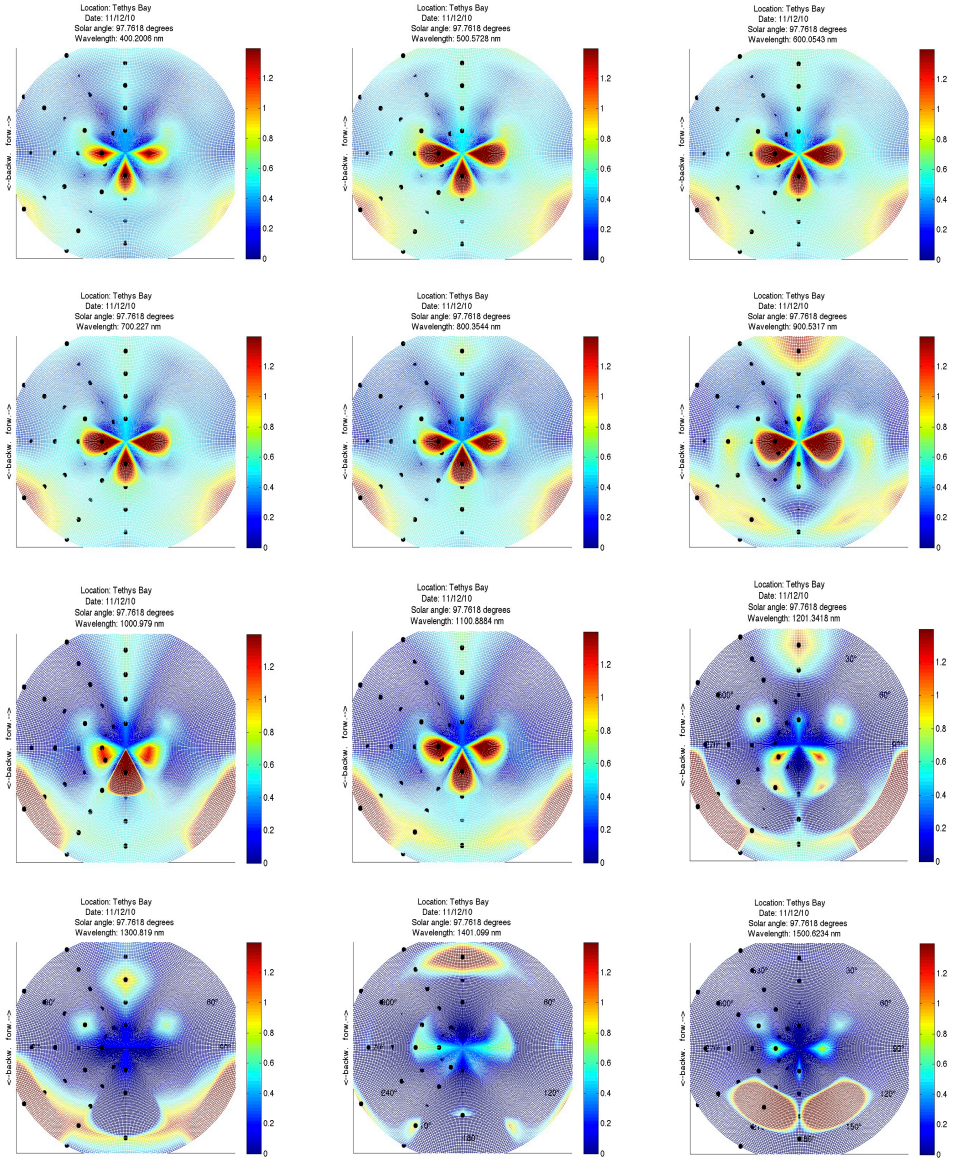

Figure A5.1. Reflected contour plots presenting the intensity of reflectivity between 400–1500 nm, at 100 nm intervals. Reflectivity measurements taken on 11th December 2010 at Tethys Bay. The HCRF value is the intensity (indicated by the colour scale). The solar zenith angle at which the measurements were taken was 52°.

A5.2.3 Day 2

The second day of measurements taken at Tethys Bay using GRASS occurred on the 20th December 2010. The location for the measurements was 74° 41.3306 S, 164° 03.1543 E, the temperatures was -2.46 °C and sky conditions consisted of no

cloud and no wind. The sea-ice was > 1 m think and the measurement surface was sea-ice covered in a faceted snow crystal layer 1-2 cm thick.

A5.2.3.1 Day 2, Site 1

Figure A5.2 shows the complete set of rotated contour plots measured at site 1 on day 2, over the wavelength range of 400–1500 nm.

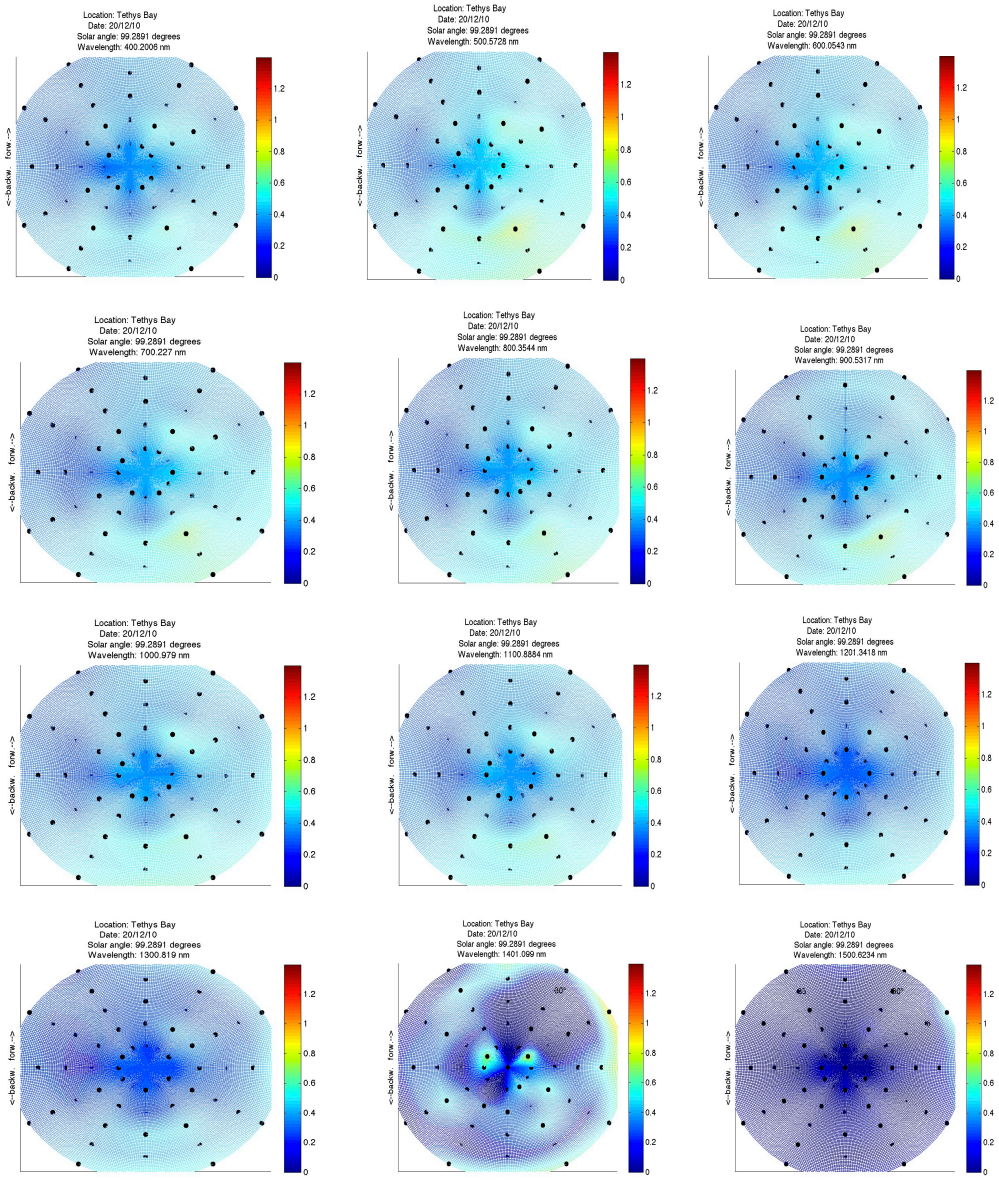

Figure A5.2. Rotated contour plots presenting the intensity of reflectivity between 400–1500 nm, at 100 nm intervals. Reflectivity measurements taken on 20th December 2010 at Tethys Bay. The HCRF value is the intensity (indicated by the colour scale). The solar zenith angle at which the measurements were taken was 53°.

A5.2.3.2 Day 2, Site 2

Figure A5.3 shows the complete set of reflected contour plots measured at site 2 on day 2, over the wavelength range of 400–1500 nm.

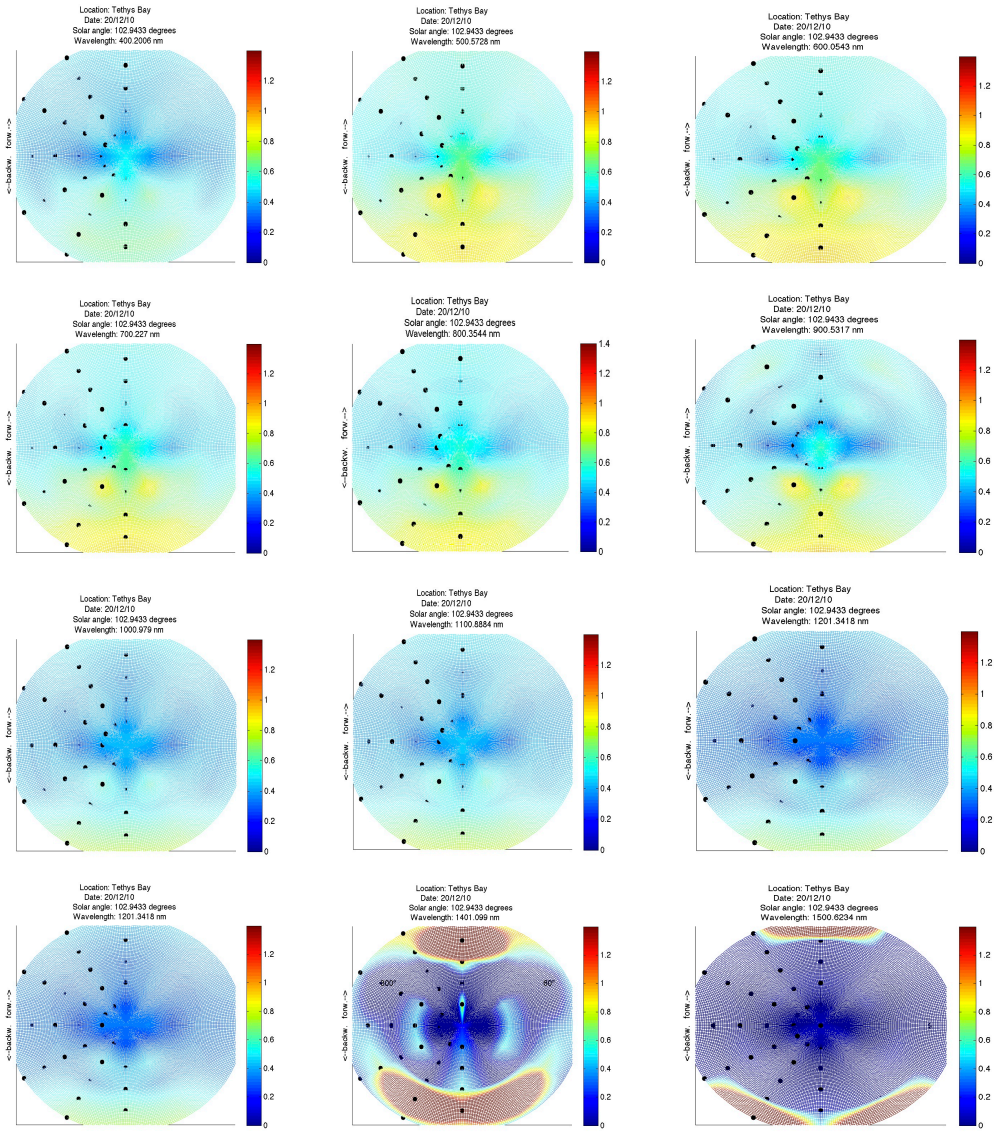

Figure A5.3. Reflected contour plots presenting the intensity of reflectivity between 400–1500 nm, at 100 nm intervals. Reflectivity measurements taken on 20th December 2010 at Tethys Bay. The HCRF value is the intensity (indicated by the colour scale). The solar zenith angle at which the measurements were taken was 57°.

Figure A5.4 shows the complete set of rotated contour plots measured at site 2 on day 2, over the wavelength range of 400–1500 nm.

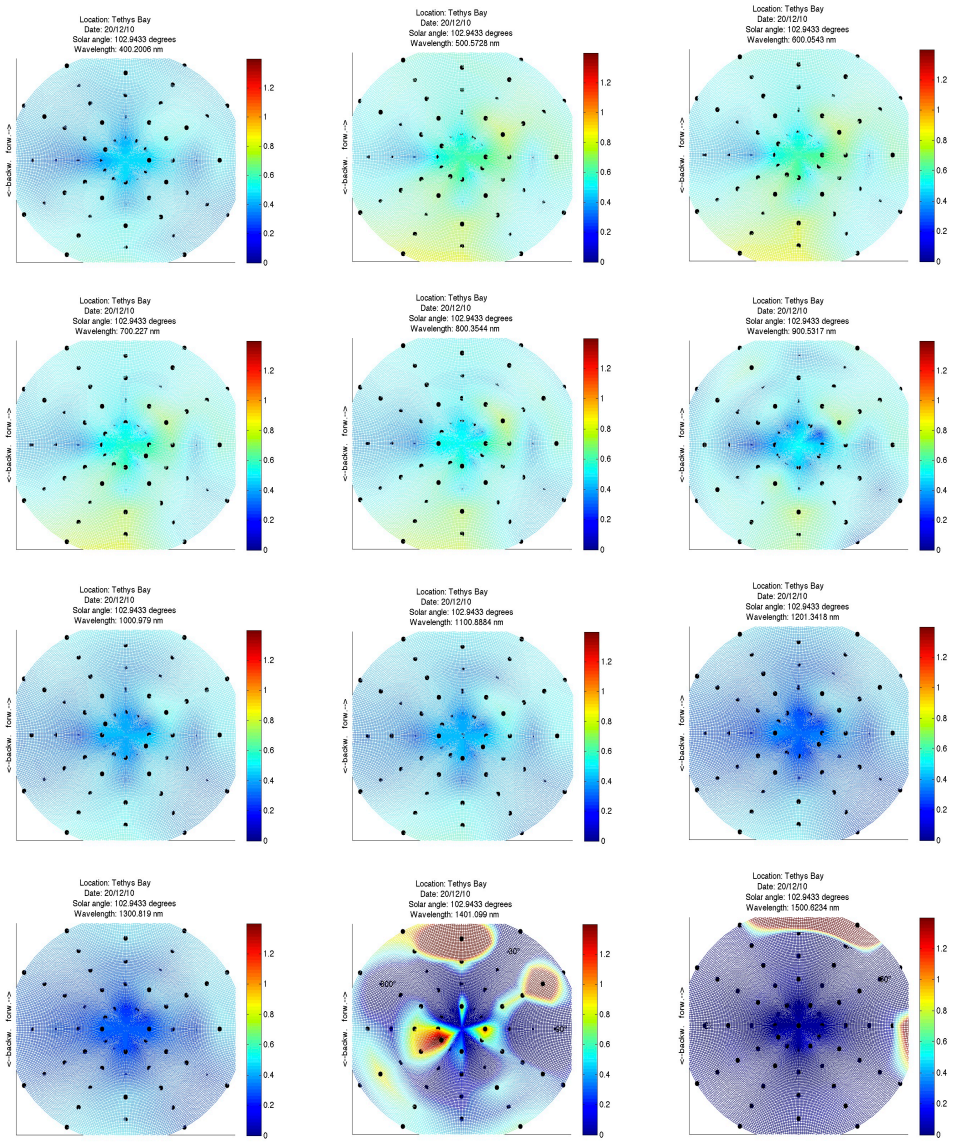

Figure A5.4. Rotated contour plots presenting the intensity of reflectivity between 400–1500 nm, at 100 nm intervals. Reflectivity measurements taken on 20th December 2010 at Tethys Bay. The HCRF value is the intensity (indicated by the colour scale). The solar zenith angle at which the measurements were taken was 57°.